

Compound Semiconductors Materials Science

MSE 5460 / ECE 5570

Spring, 2016

Debdeep Jena (djena@cornell.edu)

ECE & MSE, Cornell University

About the course



[← Back](#)

MSE 5460 Compound Semiconductors Materials Science

Course information provided by the [Courses of Study 2015-2016](#).

Course provides comprehensive understanding of compound semiconductors, stressing how differences with Si enable unique applications in electronics, photonics, and thermoelectrics. Materials include group IV (SiGe, SiC), III-V (GaAs, InP, GaN), II-VI (ZnO, CdTe), and layered semiconductors (Bi₂Se₃, BN, MoS₂), and will touch on organic and dilute magnetic semiconductors. Methods of crystal growth, doping, strain control, and fabrication will be discussed. Electronic bandstructure will be used to develop band diagrams of complex heterostructures and nanostructures including quantum wells, wires, and dots. Examples of these materials in electronic, photonic, thermoelectric, and solar cell applications will be used to motivate the materials science.

When Offered: Fall or spring.

Prerequisites/Corequisites: Prerequisite: MSE 2620 or equivalent.

[▼ Collapse Enrollment Information](#)

Enrollment Information

Combined with: [ECE 5570](#)

17969



LEC 001

TR

9:55am

8:40am -

[Jena, D](#)

3 Credits
Graded

[Bard Hall 140](#)

Spring 2016 ▼

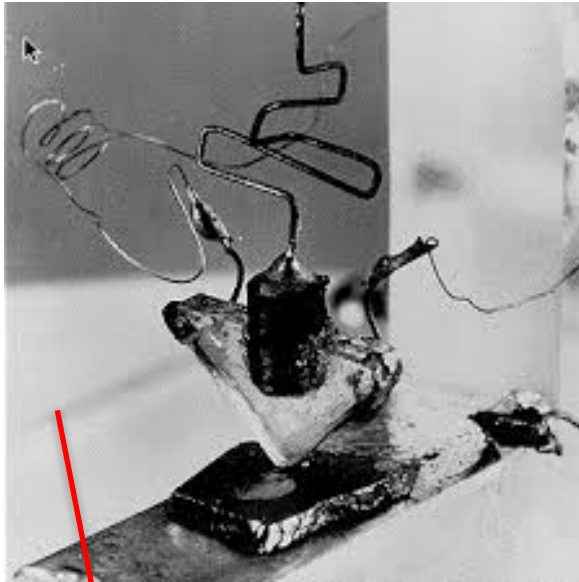
Share



Or send this URL:

<https://classes.cornell.edu/>

The first transistor



	5 B	6 C	7 N	8 O	9 F
	13 Al	14 Si	15 P	16 S	17 Cl
30 Zn	31 Ga	32 Ge	33 As	34 Se	35 Br
48 Cd	49 In	50 Sn	51 Sb	52 Te	53 I
80 Hg	81 Tl	82 Pb	83 Bi	84 Po	85 At



The Nobel Prize in Physics 1956

William B. Shockley, John Bardeen, Walter H. Brattain

Share this: [f](#) [G+](#) [T](#) [+](#) 36 [E](#)

The Nobel Prize in Physics 1956



William Bradford Shockley

Prize share: 1/3



John Bardeen

Prize share: 1/3



Walter Houser Brattain

Prize share: 1/3

The Nobel Prize in Physics 1956 was awarded jointly to William Bradford Shockley, John Bardeen and Walter Houser Brattain *"for their researches on semiconductors and their discovery of the transistor effect"*.

Photos: Copyright © The Nobel Foundation

First Demonstration of Amplification at 1 THz Using 25-nm InP High Electron Mobility Transistor Process

Xiaobing Mei, Wayne Yoshida, Mike Lange, Jane Lee, Joe Zhou, Po-Hsin Liu, Kevin Leong, *Member, IEEE*, Alex Zamora, Jose Padilla, Stephen Sarkozy, Richard Lai, *Fellow, IEEE*, and William R. Deal, *Senior Member, IEEE*

Abstract—We report the first ever terahertz monolithic integrated circuit amplifier based on 25-nm InP high electron mobility transistor (HEMT) process demonstrating amplification at 1 THz (1000 GHz) with 9-dB measured gain at 1 THz. This milestone was achieved with a 25-nm InP HEMT transistor, which exhibits 3.5-dB maximum available gain at 1 and 1.5 THz projected f_{MAX} .

Index Terms—High electron mobility transistor (HEMT), high frequency, terahertz monolithic integrated circuit (TMIC), 25 nm gate, indium phosphide (InP).

I. INTRODUCTION

THE last decade has shown marked improvement in transistor speed capabilities. A variety of MMIC compatible processes, including HEMT and HBT, with a cut off frequency f_T in excess of 600 GHz and a maximum frequency of oscillation f_{MAX} approaching or exceeding 1.0 THz have been reported [1]–[5]. This improvement in capabilities has led to a rapid increase in integrated circuit capabilities, with amplifiers being demonstrated at frequencies in excess of 600 GHz [6]–[10].

Looks legit!

TABLE I
SUMMARY OF InP HEMT PROCESSES DEVELOPED AT NGAS

Gate length	100nm	70 nm	35 nm	30 nm	25 nm (this work)
Year Introduced	1998	2003	2007	2010	2013
In(n)Ga(1-x)As channel					
Indium composition	60%	75%	100%	100%	100%
Source-Drain Spacing (μm)	2	2	1.5	1.0	0.5
Rc (m Ω .mm)	0.12	0.1	0.04	0.04	0.04
Gmp @ 1V (mS/mm)	1000	1400	2000	2500	3000
f_{max} (THz)	0.4	0.6	1.1	1.3	1.5
Associated f_T (THz)	0.2	0.25	0.4	0.5	0.61
Highest frequency amplifier demonstrated (THz)	0.19	0.24	0.48	0.85	1.0
Associated amplifier device width (μm)	30	30	20	14	8

of the model extraction. Further milestone achievements in amplification at higher frequencies with subsequent generation of transistors and designs at 480 GHz [11], 670 GHz [8] and 850 GHz [9] have improved the validity and accuracy

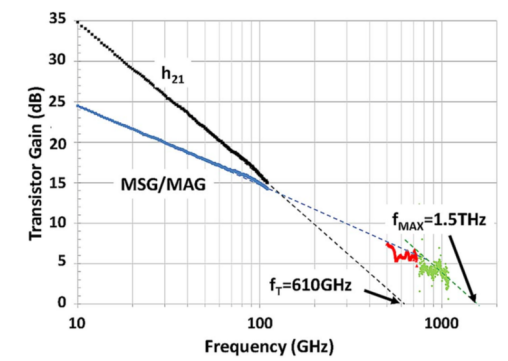
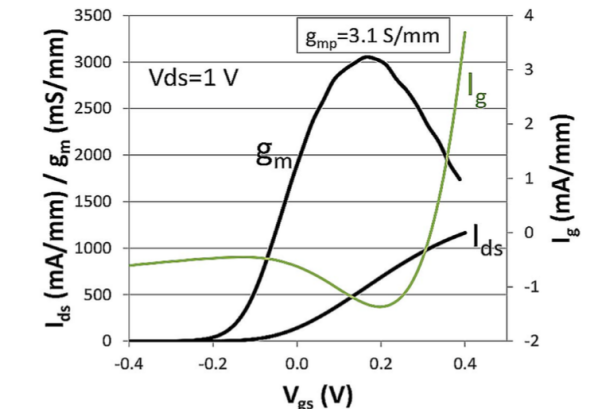
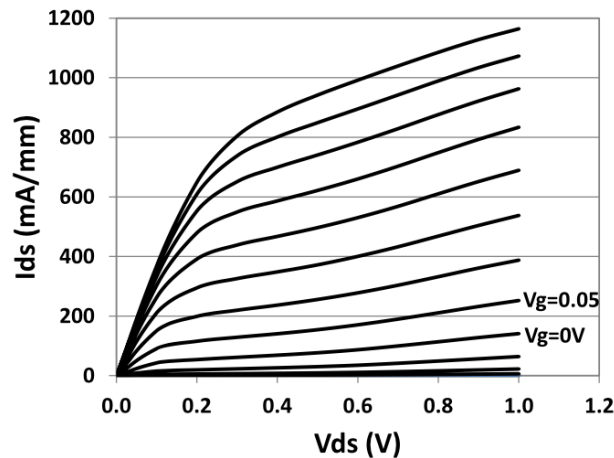


Fig. 4. Measured MAG/MSG and the associated h_{21} of a 2-finger 10 μm device biased at $V_d = 1.2$ V and $I_d = 450$ mA/mm. The dashed lines represent data extrapolations with -20 dB/decade and -10 dB/decade slopes for the estimation of f_T and f_{MAX} .

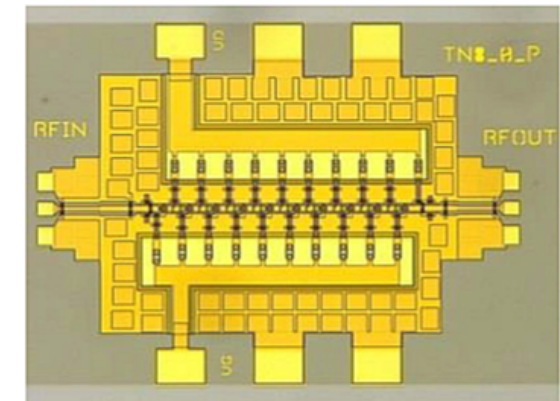


Fig. 5. Microphotograph of 1.0 THz TMIC amplifier.

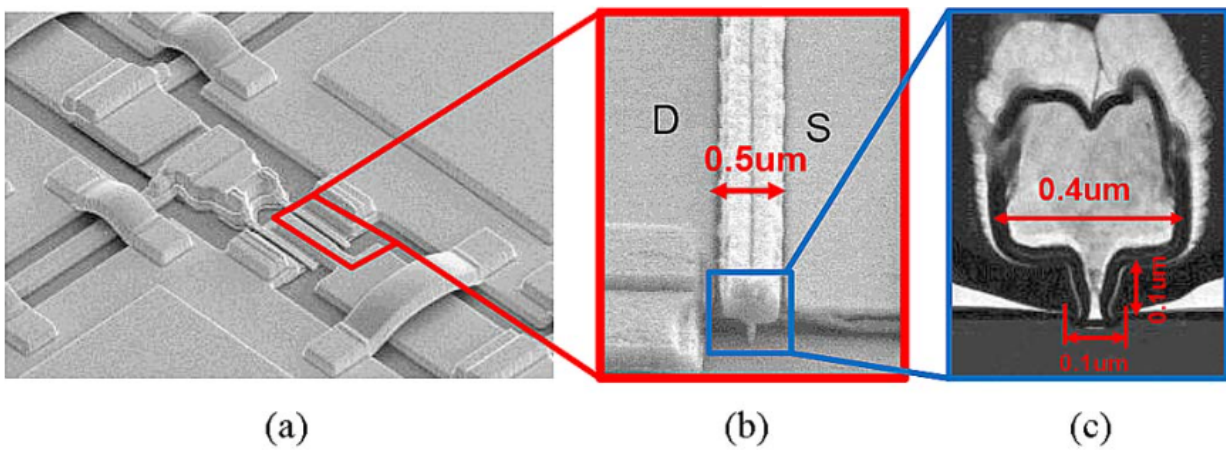


Fig. 1. 1a. SEM image of TMIC; 1b. End view SEM of the transistor with $0.5 \mu\text{m}$ source-drain distance; 1c. STEM image of the device cross-section.

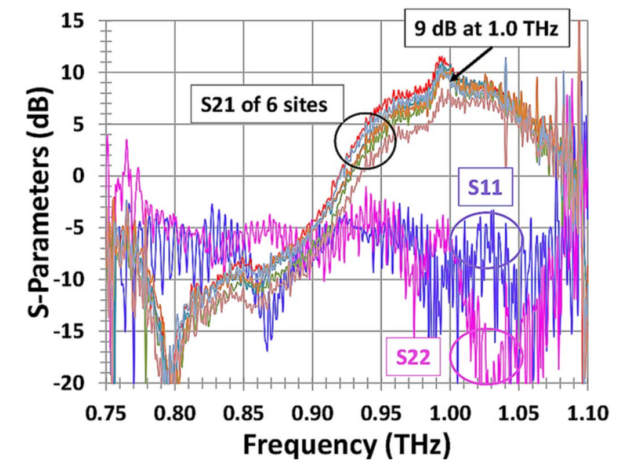
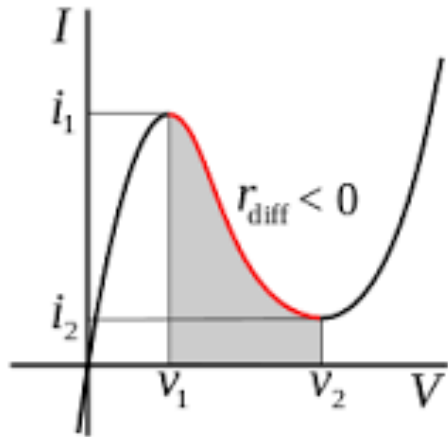


Fig. 6. On wafer measurement results showing 9 dB on-wafer gain at 1.0 THz.

New science discovered in Transistors



The Nobel Prize in Physics 1973

Leo Esaki, Ivar Giaever, Brian D. Josephson

Share this: [f](#) [G+](#) [t](#) [+](#) [3](#) [e](#)

Leo Esaki - Facts



Leo Esaki

Born: 12 March 1925, Osaka, Japan

Affiliation at the time of the award: IBM Thomas J. Watson Research Center, Yorktown Heights, NY, USA

Prize motivation: "for their experimental discoveries regarding tunneling phenomena in semiconductors and superconductors, respectively"

Field: condensed matter physics, semiconductors

Prize share: 1/4

- Science of electrons

New science discovered in Transistors

VOLUME 45, NUMBER 6

PHYSICAL REVIEW LETTERS

11 AUGUST 1980

New Method for High-Accuracy Determination of the Fine-Structure Constant Based on Quantized Hall Resistance

K. v. Klitzing

Physikalisches Institut der Universität Würzburg, D-8700 Würzburg, Federal Republic of Germany, and Hochfeld-Magnetlabor des Max-Planck-Instituts für Festkörperforschung, F-38042 Grenoble, France

and

G. Dorda

Forschungslaboratorien der Siemens AG, D-8000 München, Federal Republic of Germany

and

M. Pepper

Cavendish Laboratory, Cambridge CB3 0HE, United Kingdom

(Received 30 May 1980)

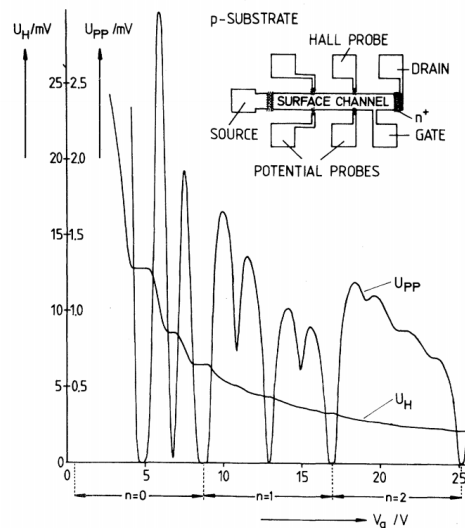
Measurements of the Hall voltage of a two-dimensional electron gas, realized with a silicon metal-oxide-semiconductor field-effect transistor, show that the Hall resistance at particular, experimentally well-defined surface carrier concentrations has fixed values which depend only on the fine-structure constant and speed of light, and is insensitive to the geometry of the device. Preliminary data are reported.

PACS numbers: 73.25.+i, 06.20.Jr, 72.20.My, 73.40.Qv

In this paper we report a new, potentially high-accuracy method for determining the fine-structure constant, α . The new approach is based on the fact that the degenerate electron gas in the inversion layer of a MOSFET (metal-oxide-semiconductor field-effect transistor) is fully quantized when the transistor is operated at helium temperatures and in a strong magnetic field of order 15 T.¹ The inset in Fig. 1 shows a schematic diagram of a typical MOSFET device used in this work. The electric field perpendicular to the surface (gate field) produces subbands for the motion normal to the semiconductor-oxide interface, and the magnetic field produces Landau quantization of motion parallel to the interface. The density of states $D(E)$ consists of broadened δ functions²; minimal overlap is achieved if the magnetic field is sufficiently high. The number of states, N_L , within each Landau level is given by

$$N_L = eB/h, \quad (1)$$

where we exclude the spin and valley degeneracies. If the density of states at the Fermi energy, $N(E_F)$, is zero, an inversion layer carrier cannot be scattered, and the center of the cyclo-



The Nobel Prize in Physics 1985

Klaus von Klitzing

Share this:

The Nobel Prize in Physics 1985



Klaus von Klitzing

Prize share: 1/1

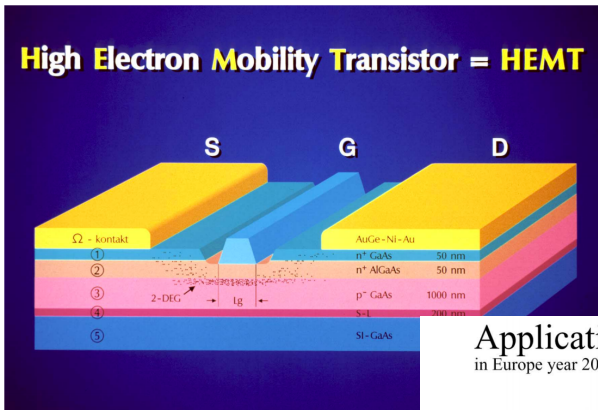
The Nobel Prize in Physics 1985 was awarded to Klaus von Klitzing "for the discovery of the quantized Hall effect".

Photos: Copyright © The Nobel Foundation

• Science of electrons

New science discovered in Transistors

High Electron Mobility Transistor = HEMT



Applications >20 GHz
in Europe year 2008

Figure 7: The different semiconducting layers comprising a High Elect high mobility of the two-dimensional electron gas (2DEG) just below the short length of the gate have enabled very high frequency use of these

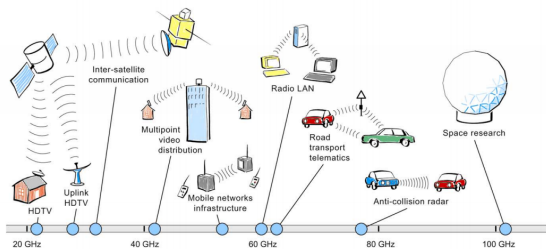
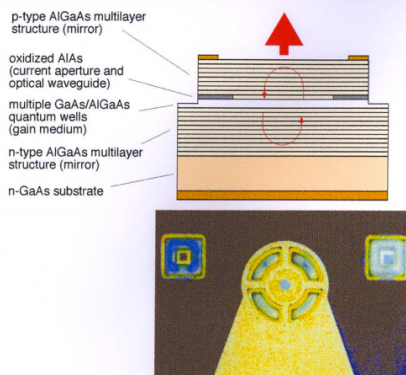


Figure 9: The figure shows several types of heterojunction transistor applications within the microwave to millimeter wave spectrum. It was drawn in 1994 and illustrates that within the field of microelectronics, new devices often reach the market at half the time projected instead of the customary twice the time. Several of the applications are already on the market today, or will soon be. The largest (commercial) breakthrough has occurred in the mobile phone frequency range, which is of the order of 1 GHz.



Properties:

- Surface emitting
- Array integration (1D and 2D)
- On wafer testing (low cost)
- Device size = $10 \times 10 \mu\text{m}$
- Threshold current $\approx 1 \text{ mA}$
- Output power \approx few mW's
- Power efficiency $\approx 50\%$
- Modulation bandwidth $\approx 20 \text{ GHz}$
- Low divergence circular beam (simplifies coupling to optical fibers)

"High performance laser to the cost of an LED"

- Heterostructure containing about 200 epitaxial layers of different composition, thickness, and doping
- Layer thicknesses in the range 60-900 Å
- Requirements in layer thickness precision $\approx \pm 0.5 \%$



The Nobel Prize in Physics 2000

Zhores I. Alferov, Herbert Kroemer, Jack S. Kilby

Share this: [f](#) [G+](#) [Twitter](#) [+](#) [Email](#) 15

The Nobel Prize in Physics 2000



Zhores I. Alferov
Prize share: 1/4



Herbert Kroemer
Prize share: 1/4



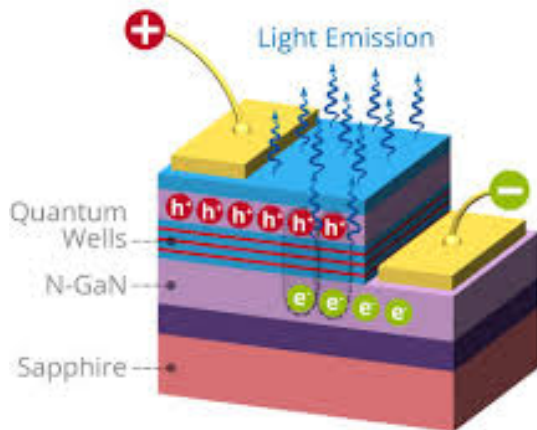
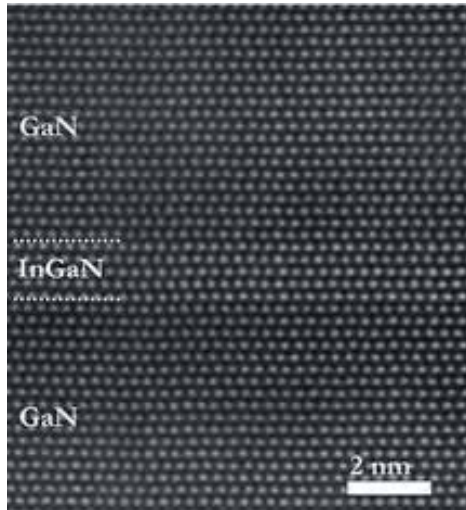
Jack S. Kilby
Prize share: 1/2

The Nobel Prize in Physics 2000 was awarded "for basic work on information and communication technology" with one half jointly to Zhores I. Alferov and Herbert Kroemer "for developing semiconductor heterostructures used in high-speed- and optoelectronics" and the other half to Jack S. Kilby "for his part in the invention of the integrated circuit".

Photos: Copyright © The Nobel Foundation

• Science of electrons

New science discovered in Transistors



The Nobel Prize in Physics 2014

Isamu Akasaki, Hiroshi Amano, Shuji Nakamura

Share this: [f](#) [G+](#) [Twitter](#) [+](#) 2.5K [Email](#)

The Nobel Prize in Physics 2014



Photo: A. Mahmoud

Isamu Akasaki

Prize share: 1/3



Photo: A. Mahmoud

Hiroshi Amano

Prize share: 1/3



Photo: A. Mahmoud

Shuji Nakamura

Prize share: 1/3

The Nobel Prize in Physics 2014 was awarded jointly to Isamu Akasaki, Hiroshi Amano and Shuji Nakamura *"for the invention of efficient blue light-emitting diodes which has enabled bright and energy-saving white light sources"*.

- Science of light

Kroemer's 'theorem' on New Technologies



• One shouldn't work on semiconductors, that is a filthy mess; who knows whether any semiconductors exist.

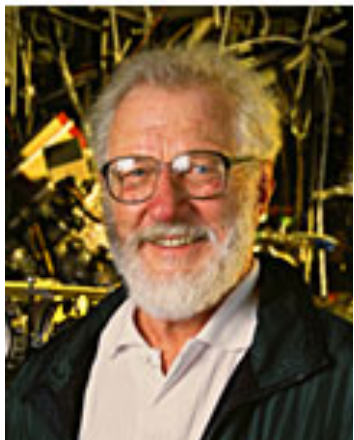
- *Über Halbleiter soll man nicht arbeiten, das ist eine Schweinerei; wer weiss, ob es überhaupt Halbleiter gibt.*
- Letter to Peierls, 29 September 1931, *Wolfgang Pauli – Wissenschaftlicher Briefwechsel mit Bohr, Einstein, Heisenberg u.a. Band II: 1930–1939*, Springer, 1985, p. 94.

1931

Wolfgang Pauli



Verdict: *Physics curiosity!*



2000

Herbert Kroemer

ON HOW NOT TO JUDGE NEW TECHNOLOGY

The principal applications of any sufficiently new and innovative technology always have been—and will continue to be—applications *created* by that technology.

Verdict: *Real! But... for what? Keep looking...*

Compounds semiconductors: Science

TABLE OF CONTENTS

PREFACE	<i>Rockett: MSS</i>	VII
Objectives	vii	
Topics and use of the book	viii	
Acknowledgements.....	ix	
1. AN ENVIRONMENT OF CHALLENGES		1
1.1 Overview	1	
1.2 A history of modern electronic devices.....	2	
1.3 An issue of scale	7	
1.4 Defining electronic materials	11	
1.5 Purity.....	13	
1.6 Performance.....	14	
1.7 Summary points.....	17	
1.8 Homework problems	18	
1.9 Suggested readings & references.....	19	
2. THE PHYSICS OF SOLIDS		21
2.1 Electronic band structures of solids.....	21	
2.1.1 Free electrons in solids.....	23	
2.1.2 Free electrons in a periodic potential	24	
2.1.3 Nearly free electrons	25	
2.1.4 Energy vs. momentum in 3d	28	
2.1.5 Electrons and holes	32	
2.1.6 Direct and indirect semiconductors.....	35	
2.1.7 Effective mass	37	
2.1.8 Density of states	38	
2.2 Intrinsic and extrinsic semiconductors	40	
2.2.1 Intrinsic semiconductors	40	
2.2.2 Extrinsic semiconductors	42	
2.3 Properties and the band structure	44	
2.3.1 Resistance, capacitance, and inductance.....	44	
2.3.2 Optical properties	53	
2.3.3 Thermal properties	54	
2.4 Quantum wells and confined carriers.....	59	

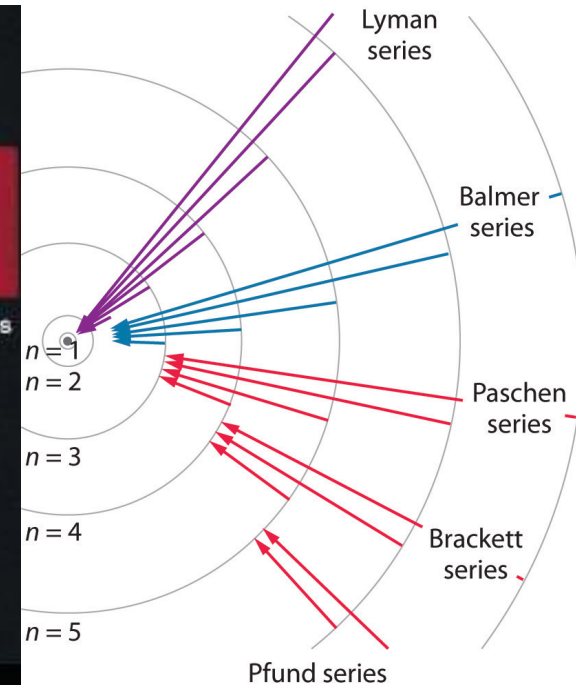
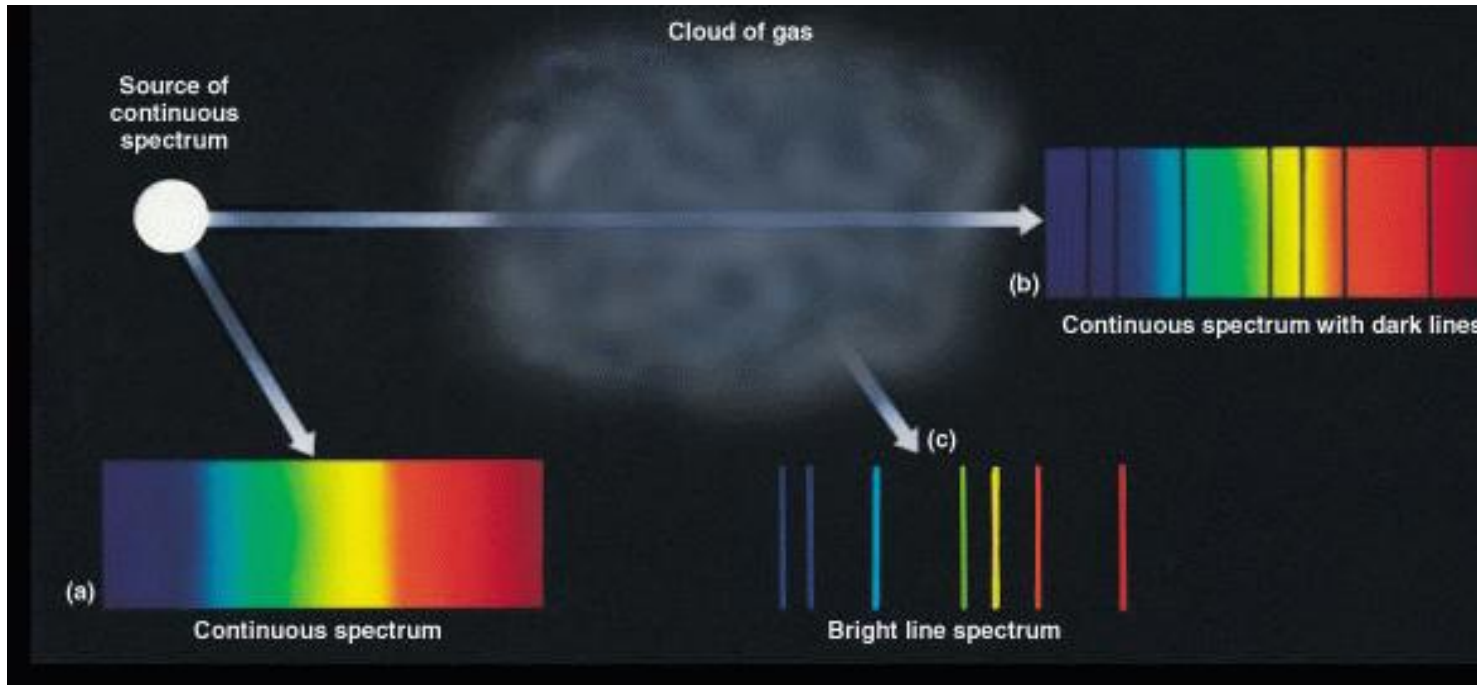
Contents

	<i>Weisbuch & Vinter: QSS</i>	
FOREWORD		ix
PREFACE		xi
I. Introduction		1
1. The Advent of Ultrathin, Well-Controlled Semiconductor Heterostructures		1
2. A Prerequisite: The Mastering of Semiconductor Purity and Interfaces		5
II. The Electronic Properties of Thin Semiconductor Heterostructures		11
3. Quantum Well Energy Levels		11
a. Conduction Electron Energy Levels		11
b. Hole Energy Levels		15
4. Triangular Quantum Well Energy Levels		19
5. Two-Dimensional Density of States		20
6. Excitons and Shallow Impurities in Quantum Wells		22
7. Tunneling Structures, Coupled Quantum Wells, and Superlattices		27
a. The Double-Well Structure		28
b. The Communicating Multiple-Quantum-Well Structure or Superlattice— Tight-Binding Calculations		28
c. Tunneling		33
d. Continuum States		37
8. Modulation Doping of Heterostructures		38
a. Charge Transfer in Modulation-Doped Heterojunctions		39
b. Electrostatic Potential		42
c. Energy-Level Calculation		43
d. Thermodynamic Equilibrium		44
9. $n-i-p-i$ Structures		51
III. Optical Properties of Thin Heterostructures		57
10. Optical Matrix Element		57
a. Interband Transitions		57
b. Oscillator Strength of Interband Transitions		60

v

Science and Future

Optical absorption and emission by atoms



- Absorption and emission spectra of atoms was the first hint that electron energies are **quantized**.
- Lead to the development of quantum mechanics, and finds a wide range of applications today.

Optical absorption in Compound Semiconductors

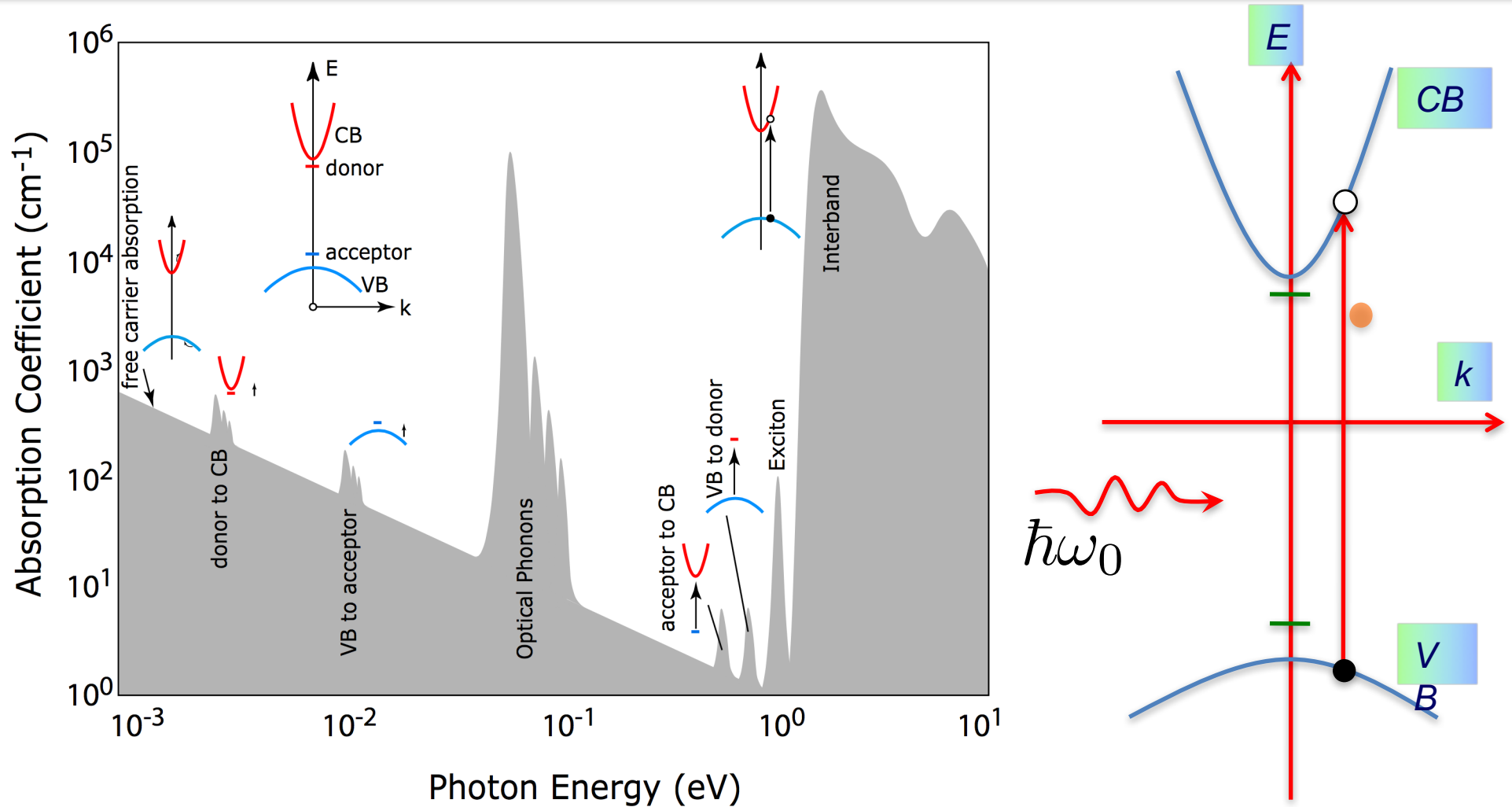


FIGURE 26.1: Schematic absorption spectrum $\alpha(\hbar\omega)$ of bulk semiconductors. The insets depict various state transitions upon absorption of photons.

- Absorption spectrum of typical compound semiconductors
- Can be completely explained using bandstructure+time-dep. Perturbation theory.

Optical absorption in Compound Semiconductors

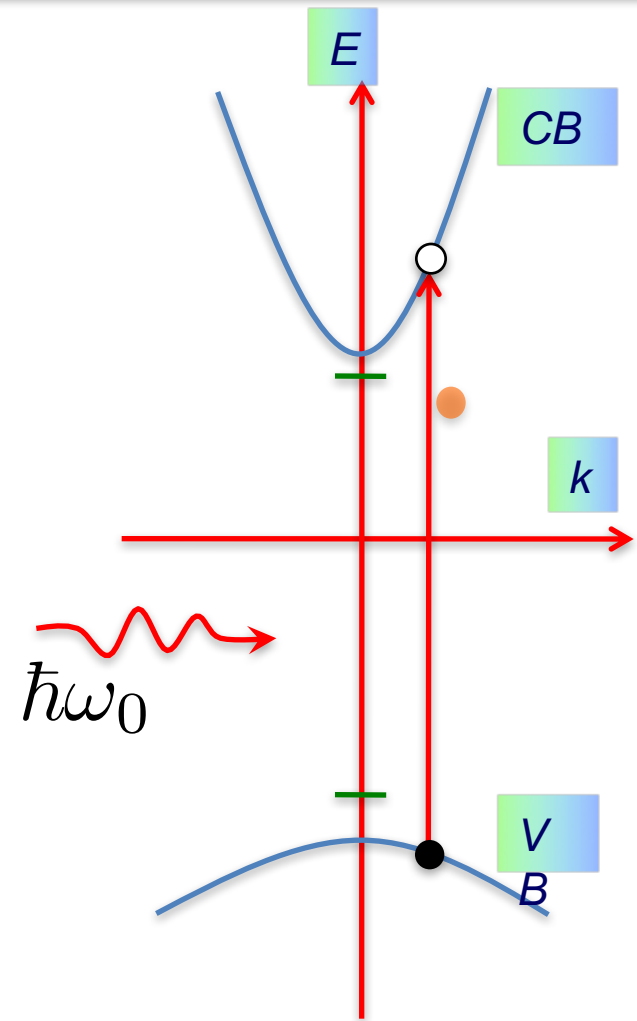
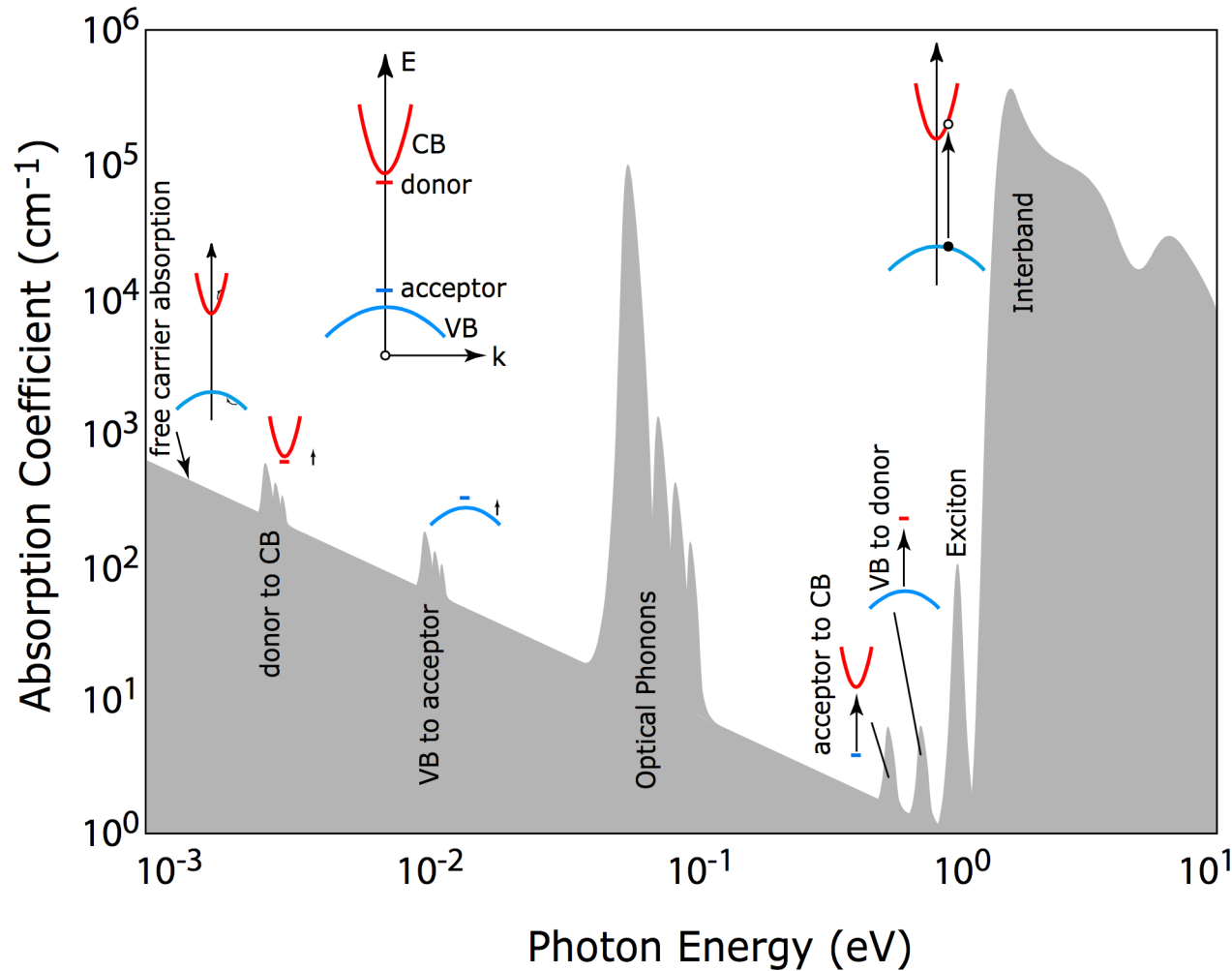


FIGURE 26.1: Schematic absorption spectrum $\alpha(\hbar\omega)$ of bulk semiconductors. The insets depict various state transitions upon absorption of photons.

- Absorption power is Quantified by “Absorption Coefficient”
- A negative absorption coefficient is equivalent to optical gain!

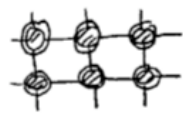
• Adapted from: Wolfe/Holonyak/Stillman
Physical Properties of Semiconductors

Atoms to Crystals

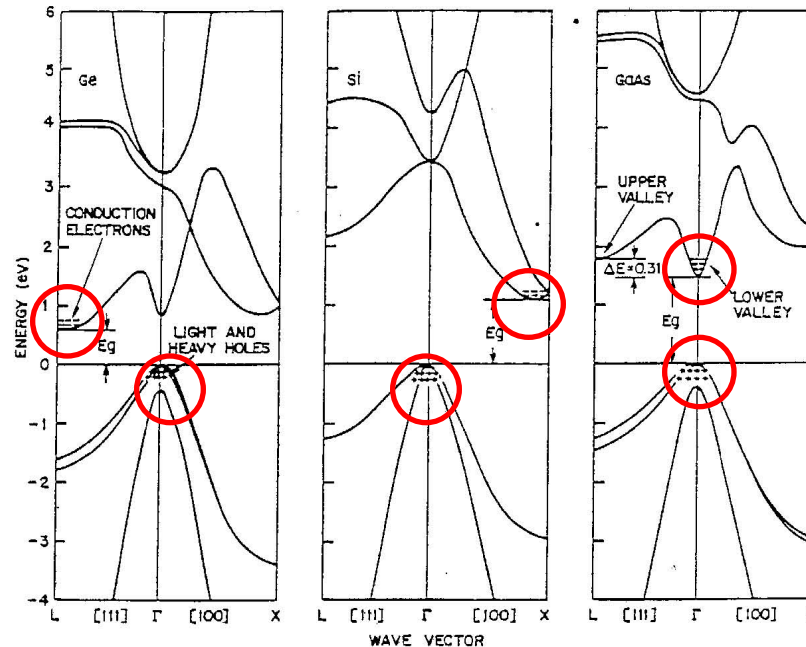
Quantum Mechanics



ϵ_3
 ϵ_2
 ϵ_1
 Discrete Energy levels

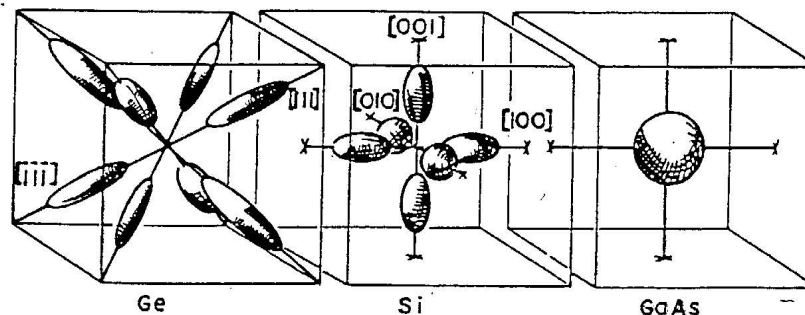
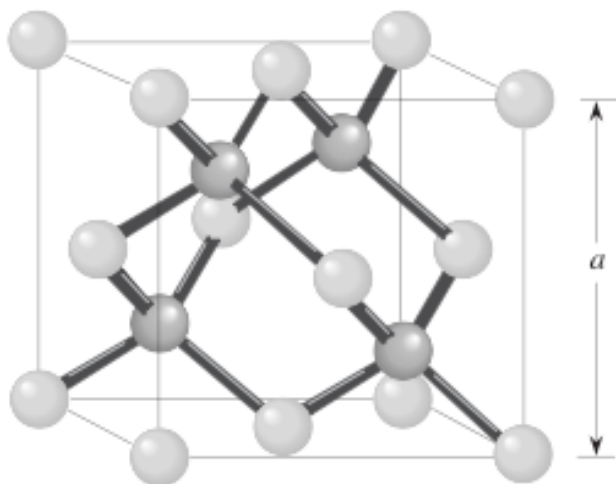


GAP (FORBIDDEN)
 ENERGY BAND
 'BANDS'



Indirect

Direct



Crystal \longrightarrow Bandstructure

The elements

Periodic Table of Elements

1	2	3	4	5	6	7	8	9	10	11	12	13	14	15	16	17	18																																																																				
1 H Hydrogen 1.00794	<table border="1"> <tr> <td>C Solid</td> <td colspan="10">Metals</td> <td colspan="6">Nonmetals</td> </tr> <tr> <td>Hg Liquid</td> <td>Alkali metals</td> <td>Alkaline earth metals</td> <td>Lanthanoids</td> <td>Actinoids</td> <td>Transition metals</td> <td>Poor metals</td> <td>Other nonmetals</td> <td>Noble gases</td> <td colspan="8"></td> </tr> <tr> <td>H Gas</td> <td colspan="16"></td> </tr> <tr> <td>Rf Unknown</td> <td colspan="16"></td> </tr> </table>																C Solid	Metals										Nonmetals						Hg Liquid	Alkali metals	Alkaline earth metals	Lanthanoids	Actinoids	Transition metals	Poor metals	Other nonmetals	Noble gases									H Gas																	Rf Unknown																	2 He Helium 4.002602
C Solid	Metals										Nonmetals																																																																										
Hg Liquid	Alkali metals	Alkaline earth metals	Lanthanoids	Actinoids	Transition metals	Poor metals	Other nonmetals	Noble gases																																																																													
H Gas																																																																																					
Rf Unknown																																																																																					
3 Li Lithium 6.941	4 Be Beryllium 9.012182											5 B Boron 10.811	6 C Carbon 12.0107	7 N Nitrogen 14.0057	8 O Oxygen 15.9994	9 F Fluorine 18.9984032	10 Ne Neon 20.1797																																																																				
11 Na Sodium 22.98976928	12 Mg Magnesium 24.3050											13 Al Aluminium 26.9815386	14 Si Silicon 28.0855	15 P Phosphorus 30.973762	16 S Sulfur 32.065	17 Cl Chlorine 35.453	18 Ar Argon 39.948																																																																				
19 K Potassium 39.0983	20 Ca Calcium 40.078	21 Sc Scandium 44.955912	22 Ti Titanium 47.867	23 V Vanadium 50.9415	24 Cr Chromium 51.9961	25 Mn Manganese 54.938045	26 Fe Iron 55.845	27 Co Cobalt 58.933195	28 Ni Nickel 58.6934	29 Cu Copper 63.546	30 Zn Zinc 65.38	31 Ga Gallium 69.723	32 Ge Germanium 72.64	33 As Arsenic 74.92160	34 Se Selenium 78.96	35 Br Bromine 79.904	36 Kr Krypton 83.798																																																																				
37 Rb Rubidium 85.4678	38 Sr Strontium 87.62	39 Y Yttrium 88.90585	40 Zr Zirconium 91.224	41 Nb Niobium 92.90638	42 Mo Molybdenum 95.96	43 Tc Technetium (97.9072)	44 Ru Ruthenium 101.07	45 Rh Rhodium 102.90550	46 Pd Palladium 106.42	47 Ag Silver 107.8682	48 Cd Cadmium 112.411	49 In Indium 114.818	50 Sn Tin 118.710	51 Sb Antimony 121.760	52 Te Tellurium 127.60	53 I Iodine 126.90447	54 Xe Xenon 131.293																																																																				
55 Cs Caesium 132.9054519	56 Ba Barium 137.327	57-71	72 Hf Hafnium 178.49	73 Ta Tantalum 180.94788	74 W Tungsten 183.84	75 Re Rhenium 186.207	76 Os Osmium 190.23	77 Ir Iridium 192.217	78 Pt Platinum 195.084	79 Au Gold 196.966569	80 Hg Mercury 200.59	81 Tl Thallium 204.3833	82 Pb Lead 207.2	83 Bi Bismuth 208.98040	84 Po Polonium (208.9824)	85 At Astatine (208.9871)	86 Rn Radon (222.0176)																																																																				
87 Fr Francium (223)	88 Ra Radium (226)	89-103	104 Rf Rutherfordium (261)	105 Db Dubnium (262)	106 Sg Seaborgium (266)	107 Bh Bohrium (264)	108 Hs Hassium (277)	109 Mt Meitnerium (268)	110 Ds Darmstadtium (271)	111 Rg Roentgenium (272)	112 Uub Ununbium (285)	113 Uut Ununtrium (284)	114 Uuq Ununquadium (289)	115 Uup Ununpentium (288)	116 Uuh Ununhexium (292)	117 Uus Ununseptium	118 Uuo Ununoctium (294)																																																																				

For elements with no stable isotopes, the mass number of the isotope with the longest half-life is in parentheses.

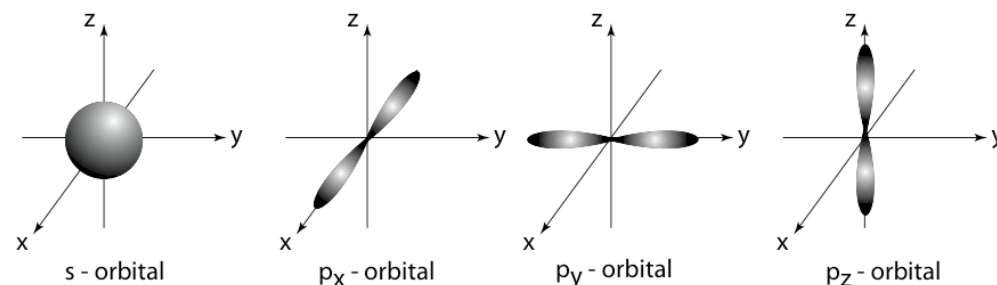
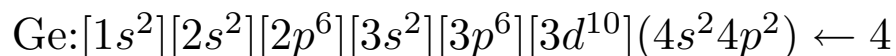
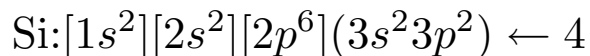
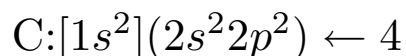
Design and Interface Copyright © 1997 Michael Dayah (michael@dayah.com). <http://www.ptable.com/>



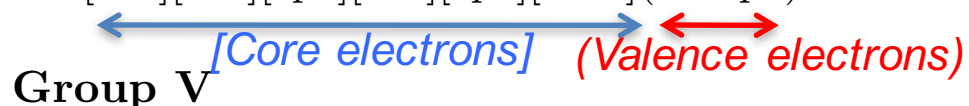
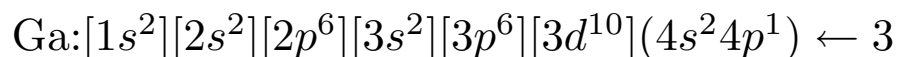
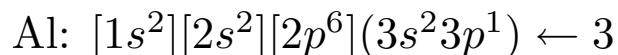
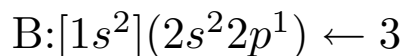
57 La Lanthanum 138.90547	58 Ce Cerium 140.116	59 Pr Praseodymium 140.90765	60 Nd Neodymium 144.242	61 Pm Promethium (145)	62 Sm Samarium 150.36	63 Eu Europium 151.964	64 Gd Gadolinium 157.25	65 Tb Terbium 158.92535	66 Dy Dysprosium 162.500	67 Ho Holmium 164.93032	68 Er Erbium 167.259	69 Tm Thulium 168.93421	70 Yb Ytterbium 173.054	71 Lu Lutetium 174.9688
89 Ac Actinium (227)	90 Th Thorium 232.03806	91 Pa Protactinium 231.03688	92 U Uranium 238.02891	93 Np Neptunium (237)	94 Pu Plutonium (244)	95 Am Americium (243)	96 Cm Curium (247)	97 Bk Berkelium (247)	98 Cf Californium (251)	99 Es Einsteinium (252)	100 Fm Fermium (257)	101 Md Mendelevium (258)	102 No Nobelium (259)	103 Lr Lawrencium (262)

Semiconductor Orbital Structures

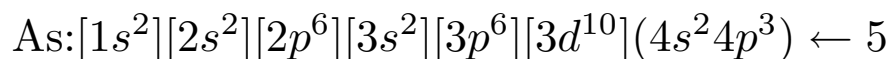
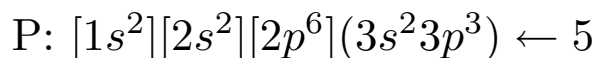
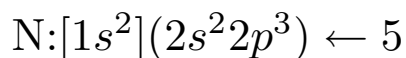
Group IV



Group III

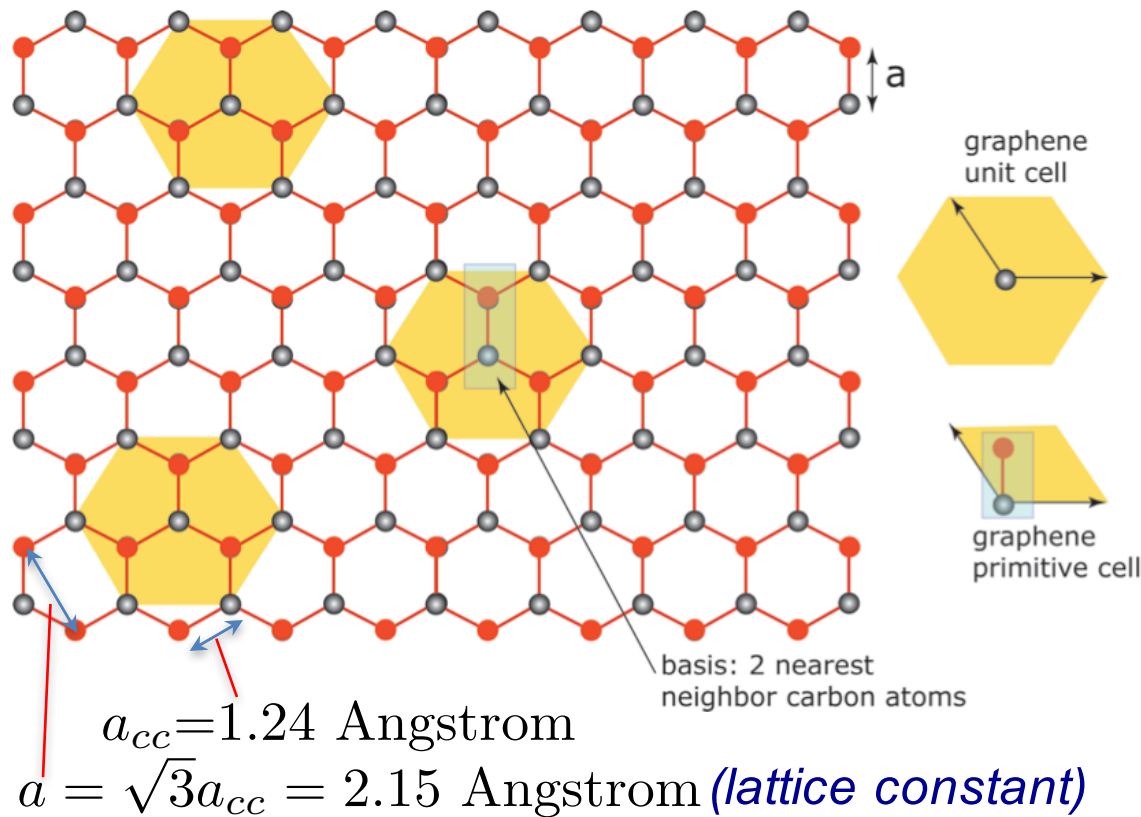


Group V

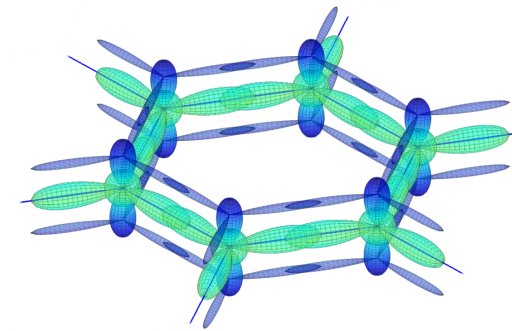
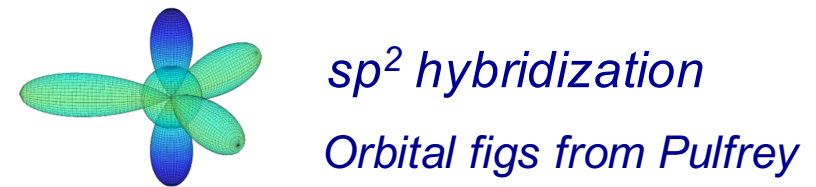


5 B Boron 10.811	6 C Carbon 12.0107	7 N Nitrogen 14.0067	8 O Oxygen 15.9994
13 Al Aluminium 26.9815386	14 Si Silicon 28.0855	15 P Phosphorus 30.973762	16 S Sulfur 32.065
30 Zn Zinc 65.38	31 Ga Gallium 69.723	32 Ge Germanium 72.64	33 As Arsenic 74.92160
48 Cd Cadmium 112.411	49 In Indium 114.818	50 Sn Tin 118.710	51 Sb Antimony 121.760
80 Hg Mercury 200.59	81 Tl Thallium 204.3833	82 Pb Lead 207.2	83 Bi Bismuth 208.98040
			84 Po Polonium (208.9824)

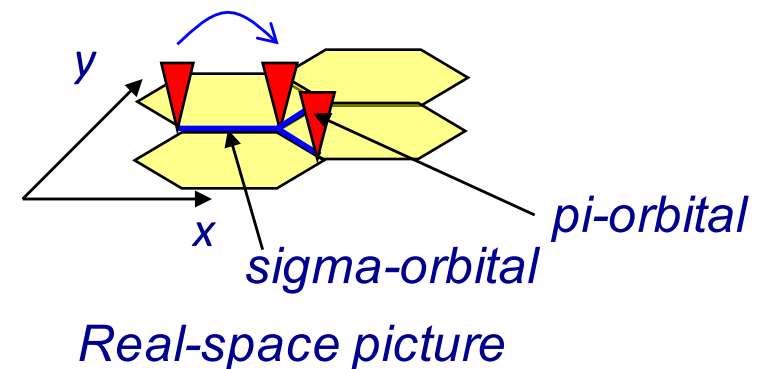
A Simple Example: 2D Graphene and Boron Nitride



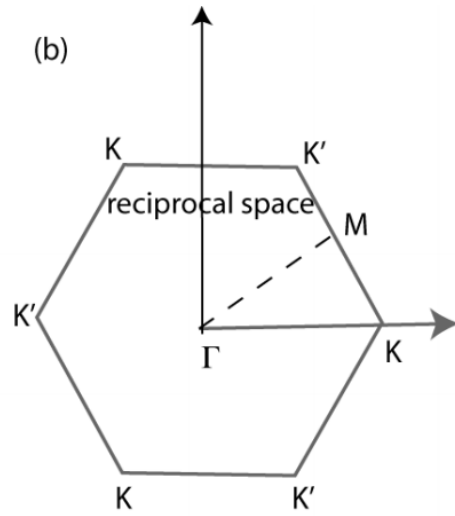
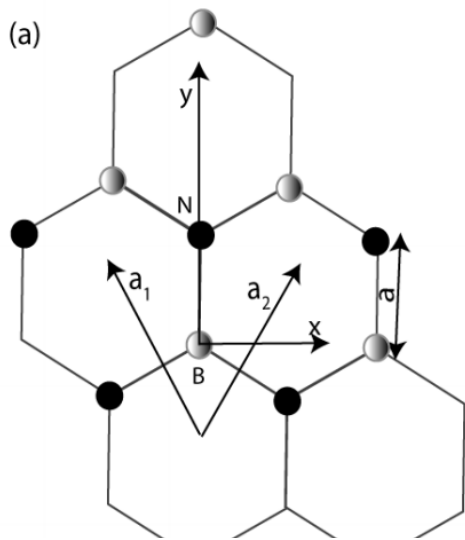
- *Sigma-orbitals hold the atoms together.*
(3 electrons/carbon atom, one left over)
- *Pi-orbitals are responsible for conduction.*
(1 electron/carbon atom)



Hopping energy: $\gamma_0 \approx 3$ eV



A Simple Example: 2D Graphene and Boron Nitride



Find the real space lattice vectors

$$\mathbf{a}_1 = \left(\frac{\sqrt{3}}{2}, \frac{3}{2} \right) \quad \mathbf{a}_2 = \left(-\frac{\sqrt{3}}{2}, \frac{3}{2} \right)$$

Write down the tight-binding Hamiltonian Matrix

$$\mathcal{H} = \begin{pmatrix} \epsilon_B & h(k) \\ h(k)^* & \epsilon_N \end{pmatrix}$$

hopping energy to each neighbor with phase factor

on-site energies of each atom in basis

$$h(k) = -t \left[1 + e^{i\mathbf{k} \cdot \mathbf{a}_1} + e^{i\mathbf{k} \cdot \mathbf{a}_2} \right]$$

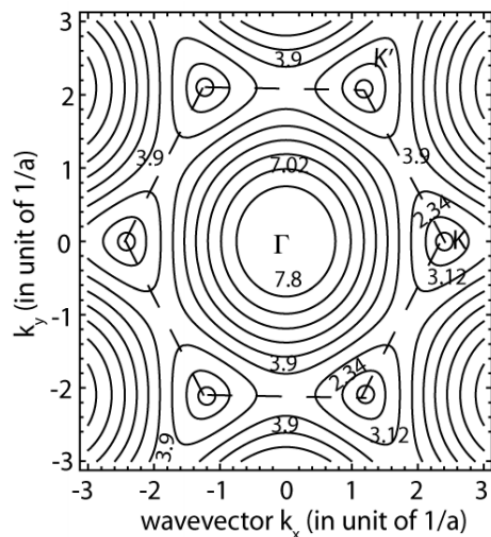
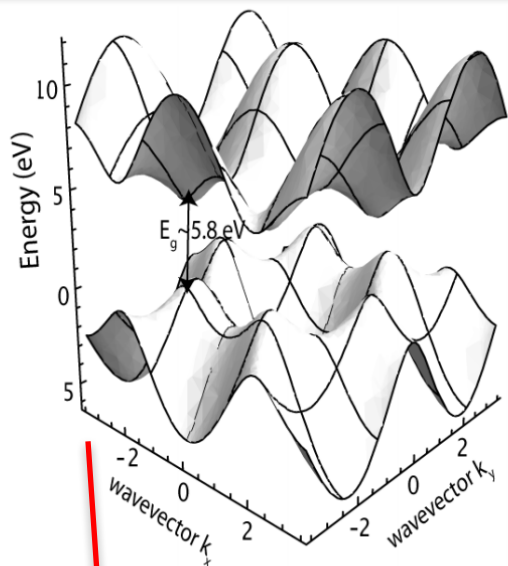
Find the eigenvalues of the Hamiltonian to get the bandstructure

$$\mathcal{E}_{\pm}(k_x, k_y) = A \pm \sqrt{B^2 + t^2 \left[1 + 4 \cos(3k_x a/2) \cos(\sqrt{3}k_y a/2) + 4 \cos^2(\sqrt{3}k_y a/2) \right]}$$

$$A = (\epsilon_B + \epsilon_N)/2$$

$$B = (\epsilon_B - \epsilon_N)/2$$

A Simple Example: 2D Graphene and Boron Nitride



Find the real space lattice vectors

$$\mathbf{a}_1 = \left(\frac{\sqrt{3}}{2}, \frac{3}{2} \right) \quad \mathbf{a}_2 = \left(-\frac{\sqrt{3}}{2}, \frac{3}{2} \right)$$

Write down the tight-binding Hamiltonian Matrix

$$\mathcal{H} = \begin{pmatrix} \epsilon_B & h(k) \\ h(k)^* & \epsilon_N \end{pmatrix}$$

hopping energy to each neighbor with phase factor

on-site energies of each atom in basis

$$h(k) = -t \left[1 + e^{i\mathbf{k} \cdot \mathbf{a}_1} + e^{i\mathbf{k} \cdot \mathbf{a}_2} \right]$$

Find the eigenvalues of the Hamiltonian to get the bandstructure

$$\mathcal{E}_{\pm}(k_x, k_y) = A \pm \sqrt{B^2 + t^2 \left[1 + 4 \cos(3k_x a/2) \cos(\sqrt{3}k_y a/2) + 4 \cos^2(\sqrt{3}k_y a/2) \right]}$$

$$A = (\epsilon_B + \epsilon_N)/2$$

$$B = (\epsilon_B - \epsilon_N)/2$$

A Simple Example: 2D Graphene and Boron Nitride

Find the eigenvalues of the Hamiltonian to get the bandstructure

$$\mathcal{E}_{\pm}(k_x, k_y) = A \pm \sqrt{B^2 + t^2 \left[1 + 4 \cos(3k_x a/2) \cos(\sqrt{3}k_y a/2) + 4 \cos^2(\sqrt{3}k_y a/2) \right]}$$

$$A = (\epsilon_B + \epsilon_N)/2$$

$$B = (\epsilon_B - \epsilon_N)/2$$

$$E_g = \mathcal{E}_+ - \mathcal{E}_- = 2B = 5.8 \text{ eV}$$

$$\epsilon_B \sim +2.9 \text{ eV}, \epsilon_N \sim -2.9 \text{ eV}$$

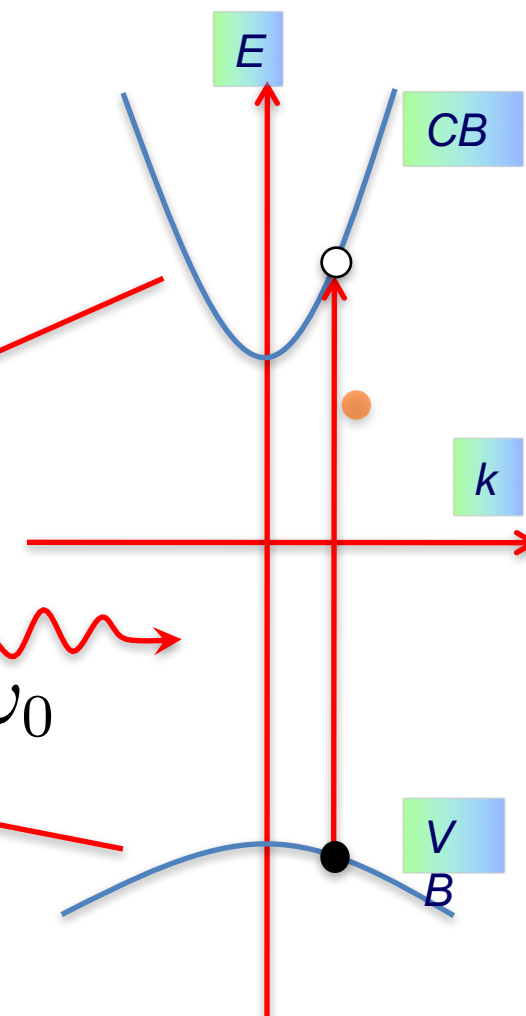
$$E_g = 5.8 \text{ eV}, t = 2.92 \text{ eV}, a \sim 0.15 \text{ nm}$$

Find the conduction and valence band structures and effective masses

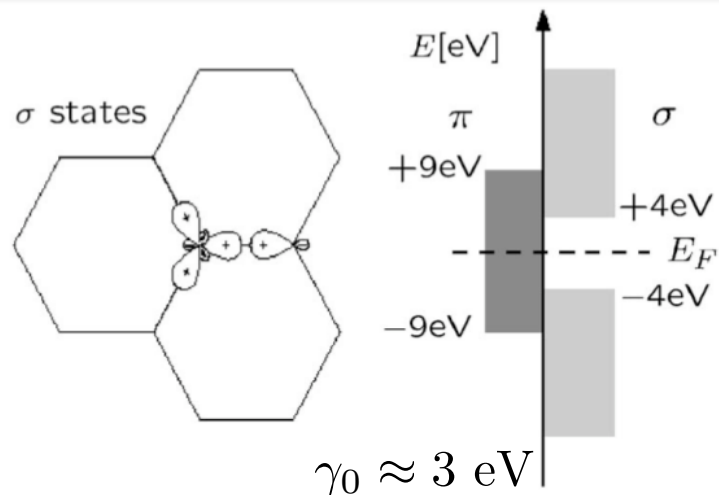
$$\mathcal{E}_c(k) = E_g + \frac{\hbar^2 k^2}{2m^*}, \quad (\text{conduction band})$$

$$\mathcal{E}_v(k) = -\frac{\hbar^2 k^2}{2m^*}, \quad (\text{valence band})$$

$$m^* = \frac{2\hbar^2 E_g}{9a^2 t^2} \sim 0.6m_0$$

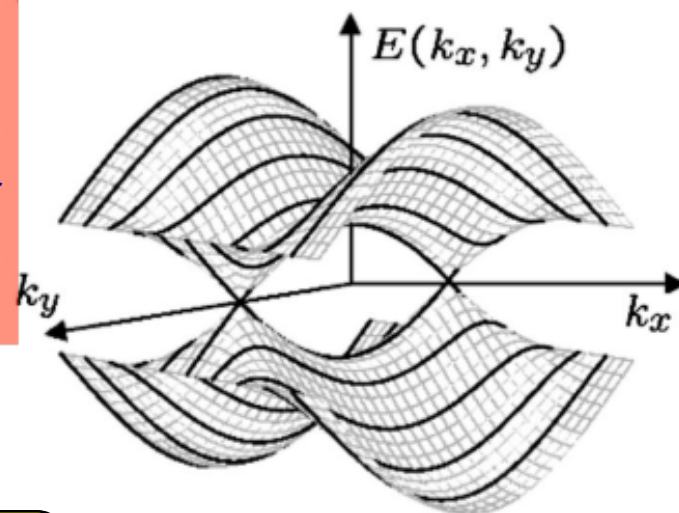


A Simple Example: 2D Graphene Bonds and Bands



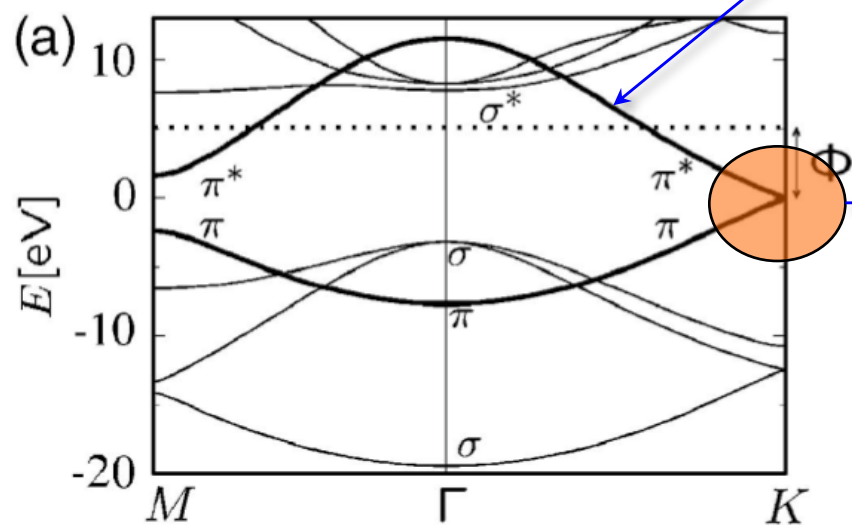
For 2D Graphene, because the on-site energies are the SAME, the gap is ZERO!

BN is the compound semiconductor counterpart of Graphene; the broken symmetry opens a very large bandgap.



$$\mathcal{E}(k_x, k_y) = \mathcal{E}_F \pm \gamma_0 \sqrt{1 + 4 \cos\left(\frac{\sqrt{3}k_x a}{2}\right) \cos\left(\frac{k_y a}{2}\right) + 4 \cos^2\left(\frac{k_y a}{2}\right)}$$

• Expand around the Dirac point



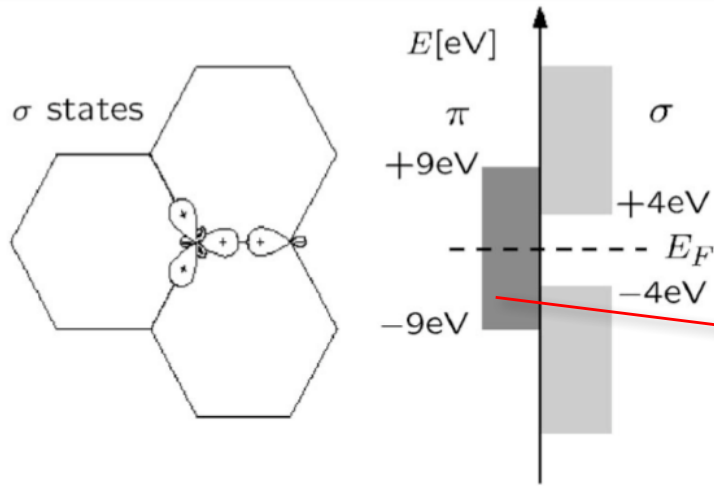
$$\mathcal{E}(k_x, k_y) \approx \hbar v_F \sqrt{k_x^2 + k_y^2}$$

$$v_F \sim 10^8 \text{ cm/s}$$

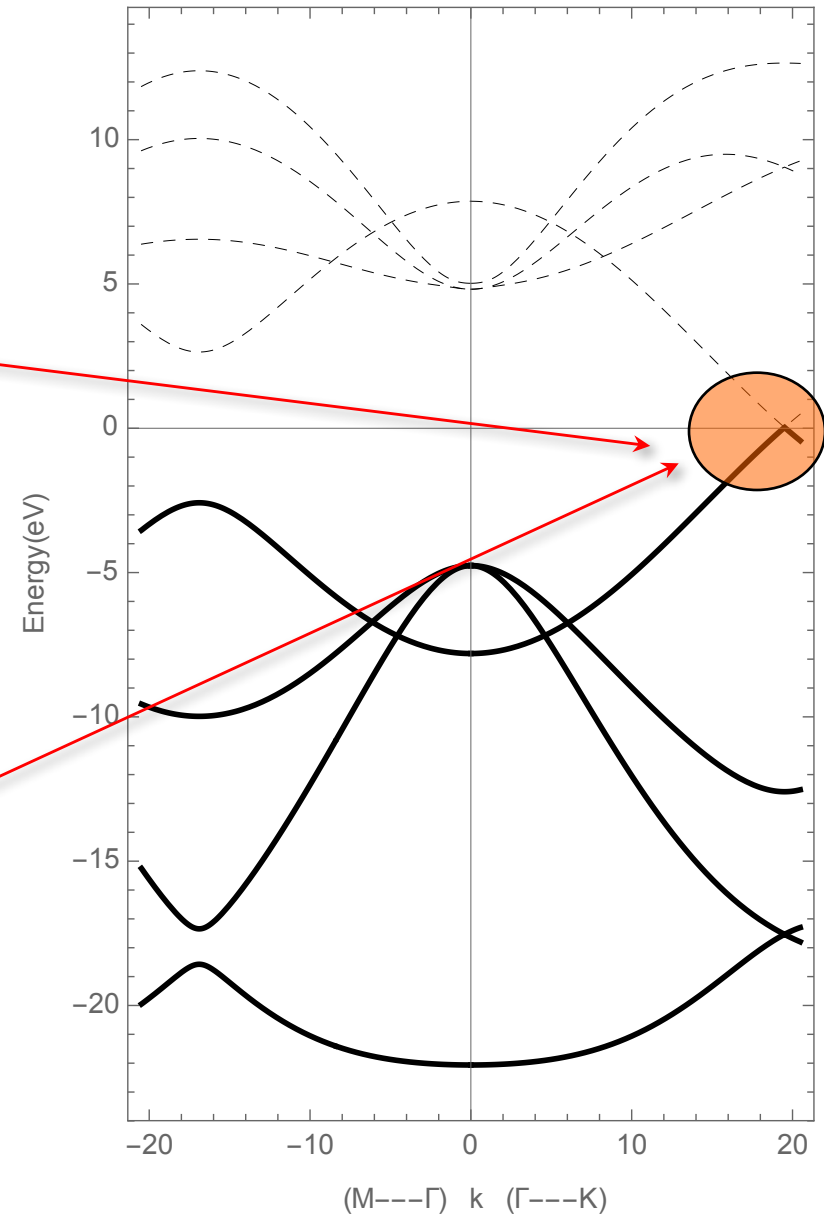
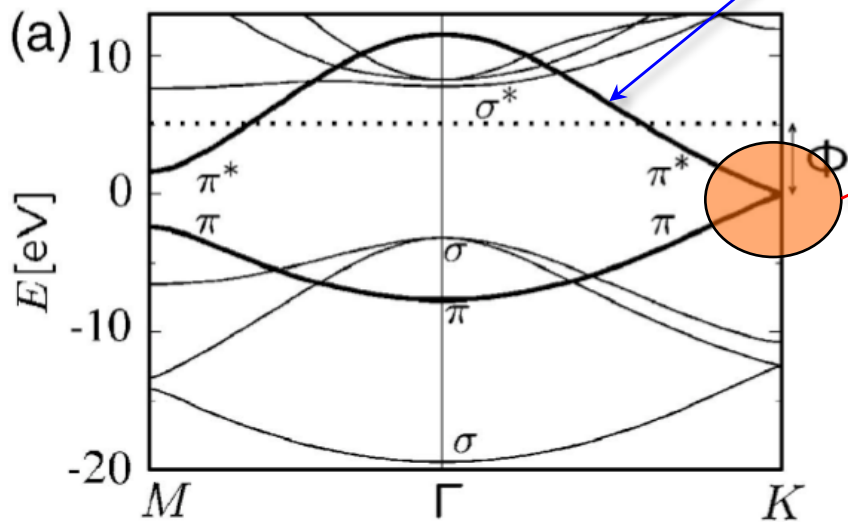
Conical! $g_{spin} = 2$
 Linear dispersion $g_{valley} = 2$

• Reviews of Modern Physics, 79 677 (2007).

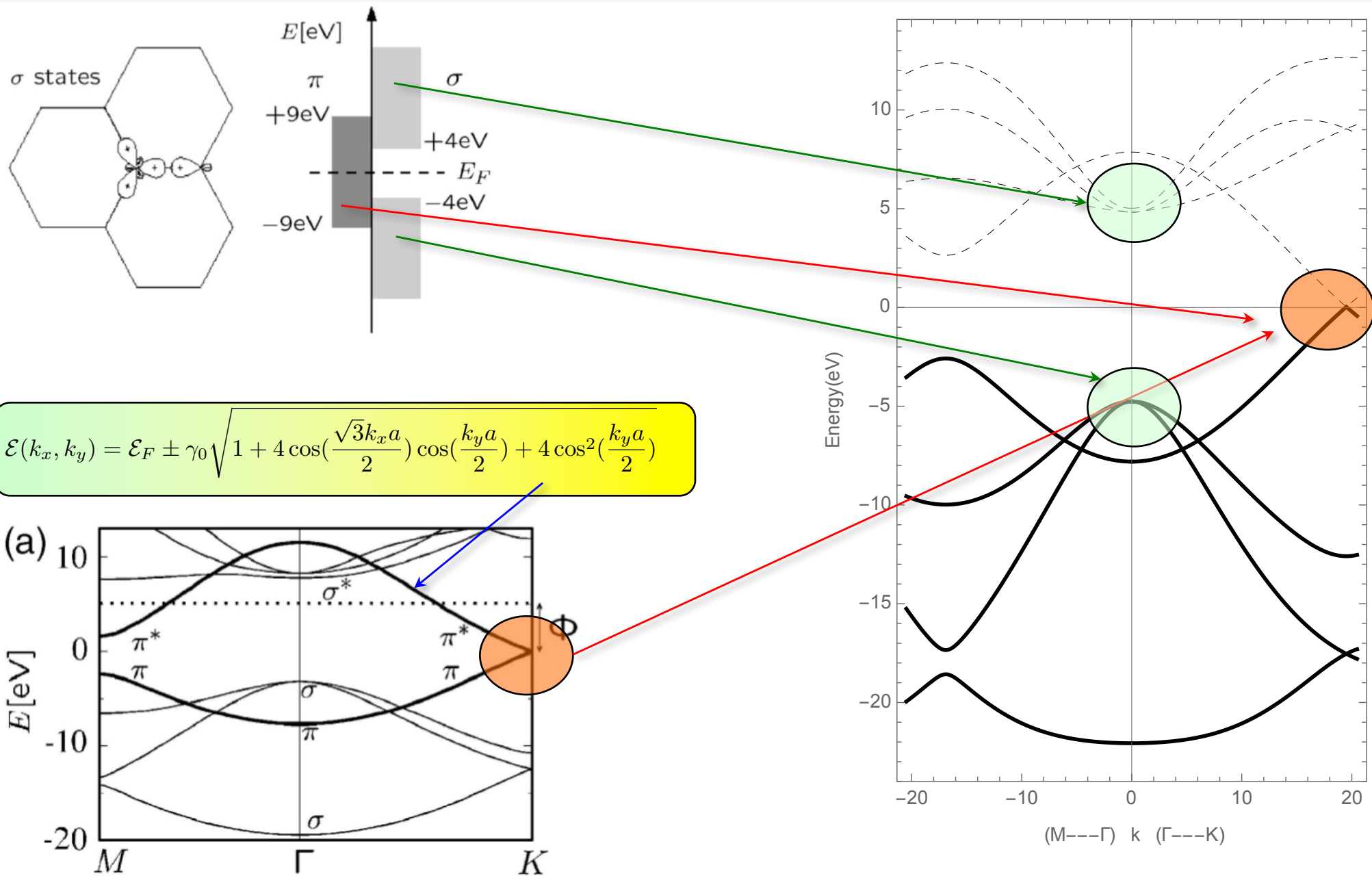
A Simple Example: 2D Graphene Bonds and Bands



$$\mathcal{E}(k_x, k_y) = \mathcal{E}_F \pm \gamma_0 \sqrt{1 + 4 \cos\left(\frac{\sqrt{3}k_x a}{2}\right) \cos\left(\frac{k_y a}{2}\right) + 4 \cos^2\left(\frac{k_y a}{2}\right)}$$



A Simple Example: 2D Graphene Bonds and Bands



Typical 3D semiconductor crystal structures

Due to the covalent bond structure (the bonding orbitals are s-p hybrids), most common semiconductors are found in three distinct structures:

- i) The diamond lattice type: e.g. Si, Ge
- ii) The zinkblende type: e.g. GaAs, InP
- iii) The wurtzite type (hexagonal): e.g. GaN, ZnO

	5 B Boron 10.811	6 C Carbon 12.0107	7 N Nitrogen 14.0067	8 O Oxygen 15.9994
	13 Al Aluminum 26.9815386	14 Si Silicon 28.0855	15 P Phosphorus 30.973762	16 S Sulfur 32.065
30 Zn Zinc 65.38	31 Ga Gallium 69.723	32 Ge Germanium 72.64	33 As Arsenic 74.92160	34 Se Selenium 78.96
48 Cd Cadmium 112.411	49 In Indium 114.818	50 Sn Tin 118.710	51 Sb Antimony 121.760	52 Te Tellurium 127.60
80 Hg Mercury 200.59	81 Tl Thallium 204.3833	82 Pb Lead 207.2	83 Bi Bismuth 208.98040	84 Po Polonium (208.9824)

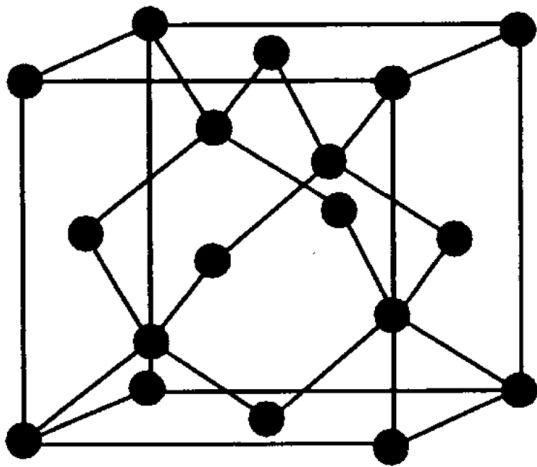
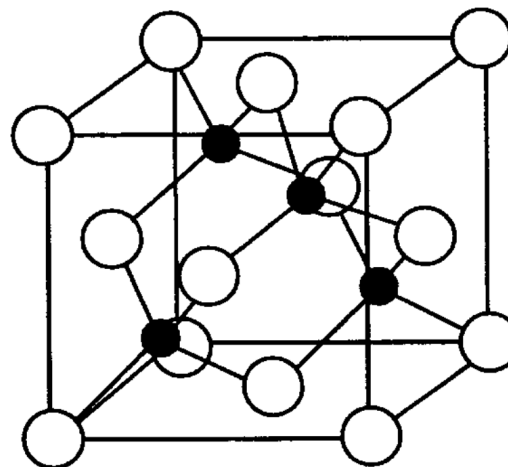
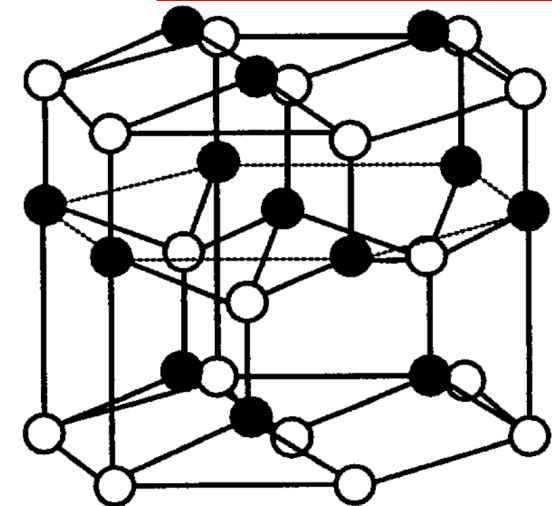


Fig. 1.2 Diamond lattice structure.



(a)



(b)

Fig. 1.3 (a) Zincblende lattice structure and (b) Wurtzite lattice structure. (○) A atom, (●) B atom.

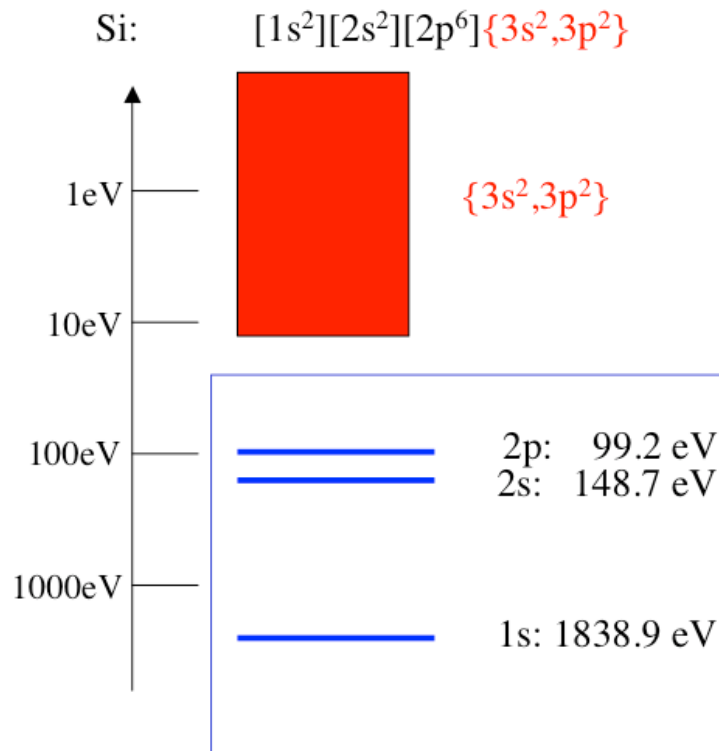
(Denninger, Oda)

Semiconductor Crystal Structures

Which electrons have to be included in band structure calculations?

In principle all, but the inner core electrons are strongly bound and their spatial extension is so small, that no significant overlap of the wavefunctions occur.

In silicon (Si), the 1s, 2s and 2p electrons are inner core electrons.



Most bandstructure calculations only take into account the $\{3s^2,3p^2\}$ valence electrons.

These are **4 electrons per atom**, which essentially form the chemical bonds in tetrahedral coordination.

The binding energies for the inner core electrons are taken from X-ray photoemission experiments.

The source is:

Handbook of Chemistry and Physics, E-184

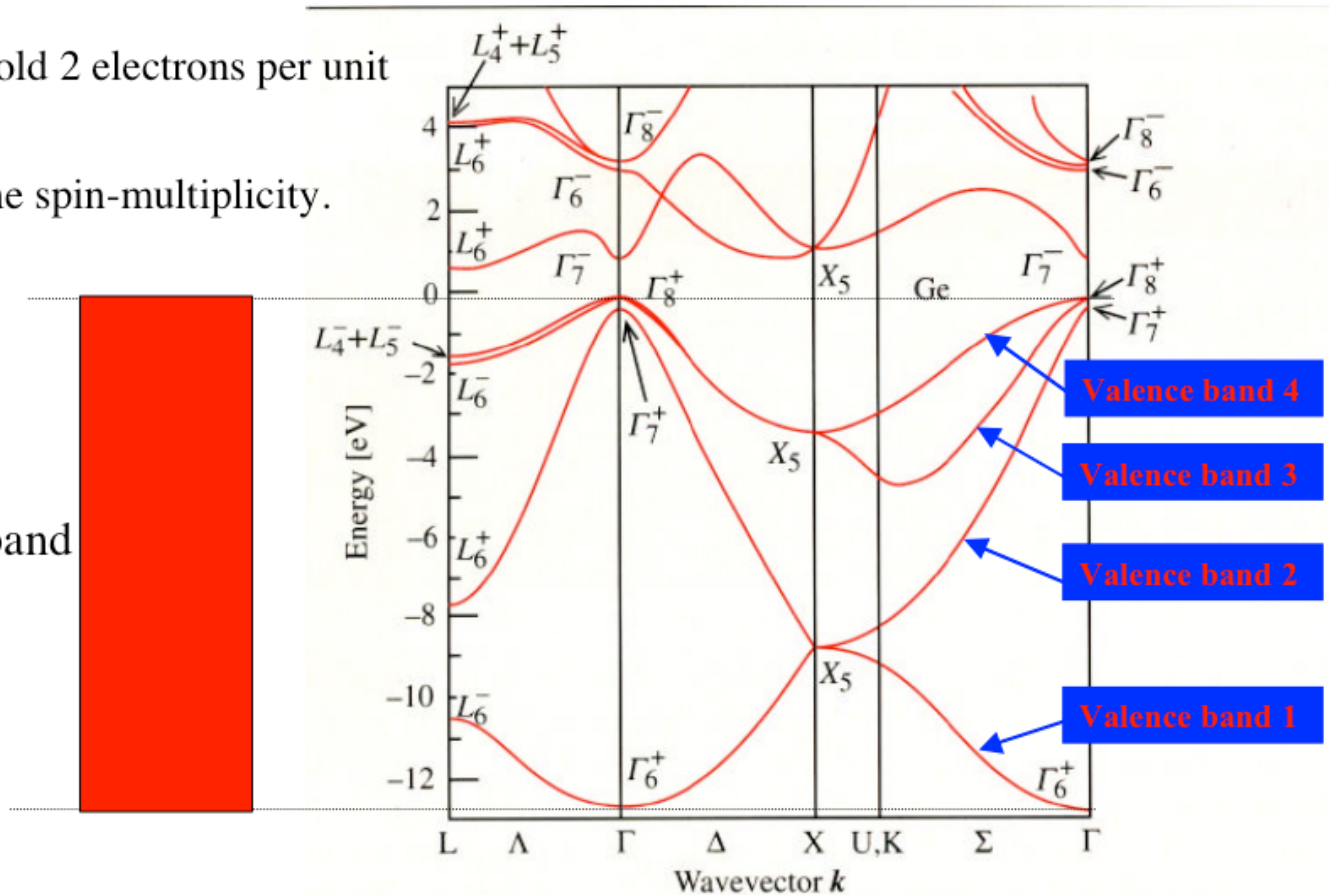
(Denninger)

Semiconductor Crystal Structures

Each band can hold 2 electrons per unit cell.

The factor 2 is the spin-multiplicity.

Valence band area



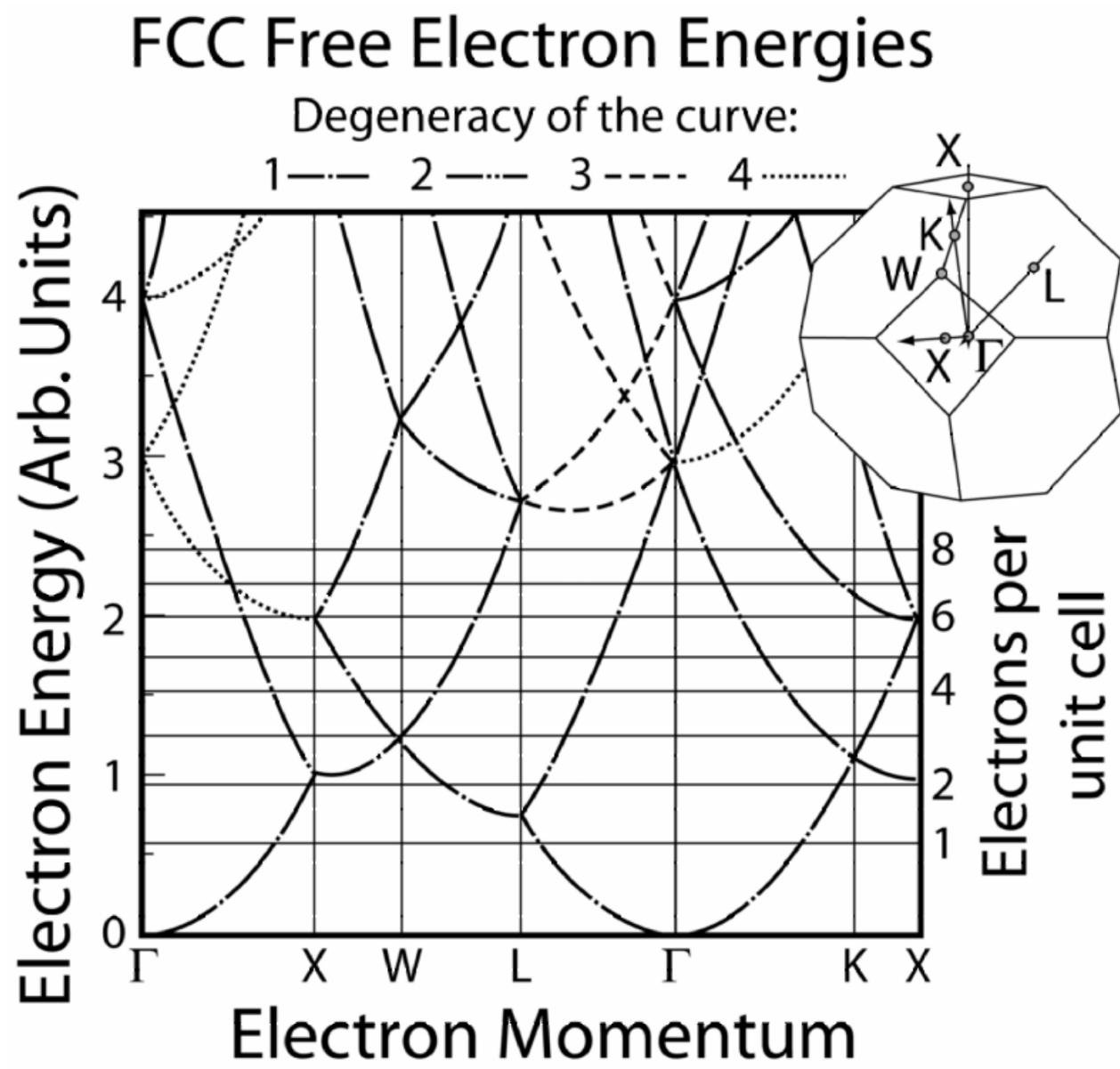
Valence bands: 4 bands

2 atoms per unit cell 4 electrons per atom

8 electrons in 4 bands

(Denninger)

Nearly free electron bandstructure, k-space points



(Rockett)

Orbital overlaps and bonds in semiconductors

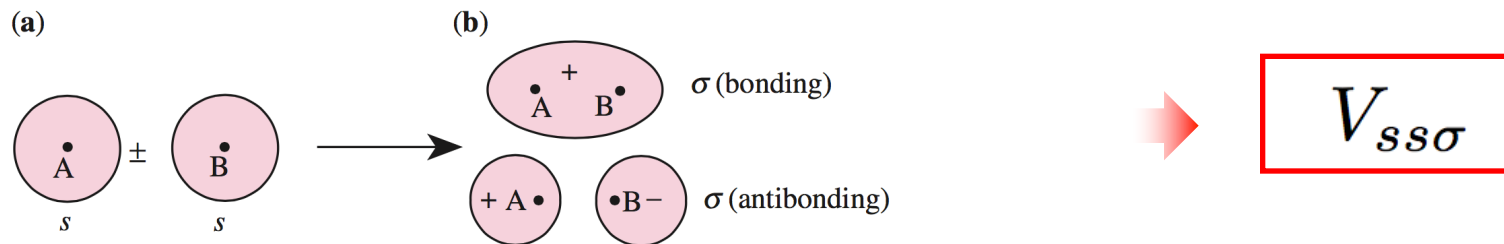


Fig. 2.17a,b. Overlap of two s orbitals to form bonding and antibonding σ orbitals

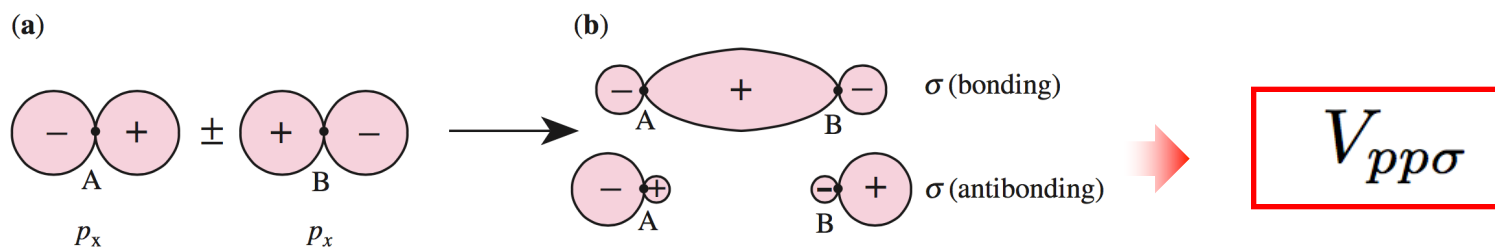


Fig. 2.18a,b. Overlap of two p_x orbitals along the x axis to form bonding and antibonding σ orbitals

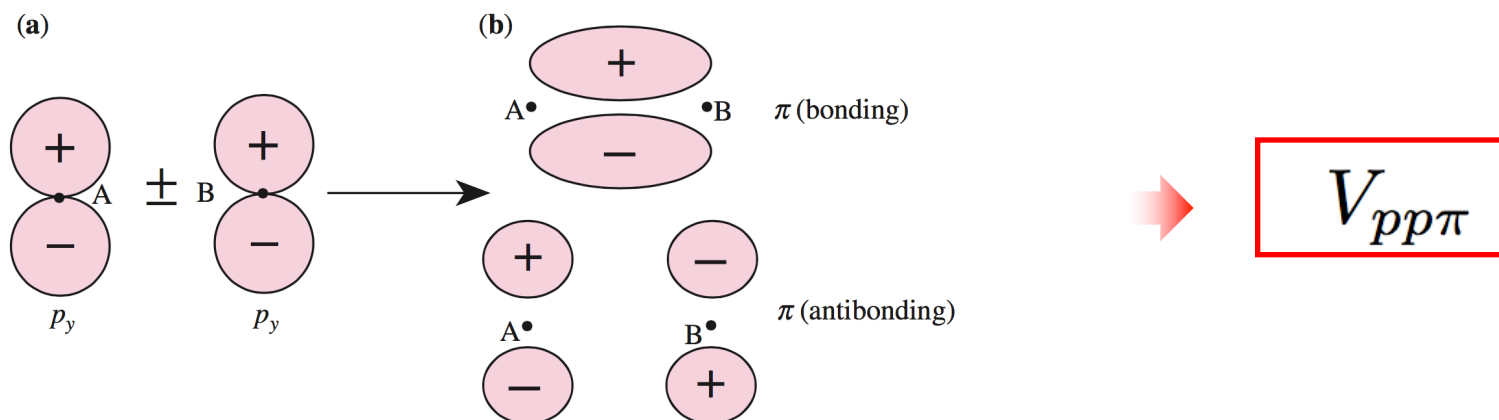
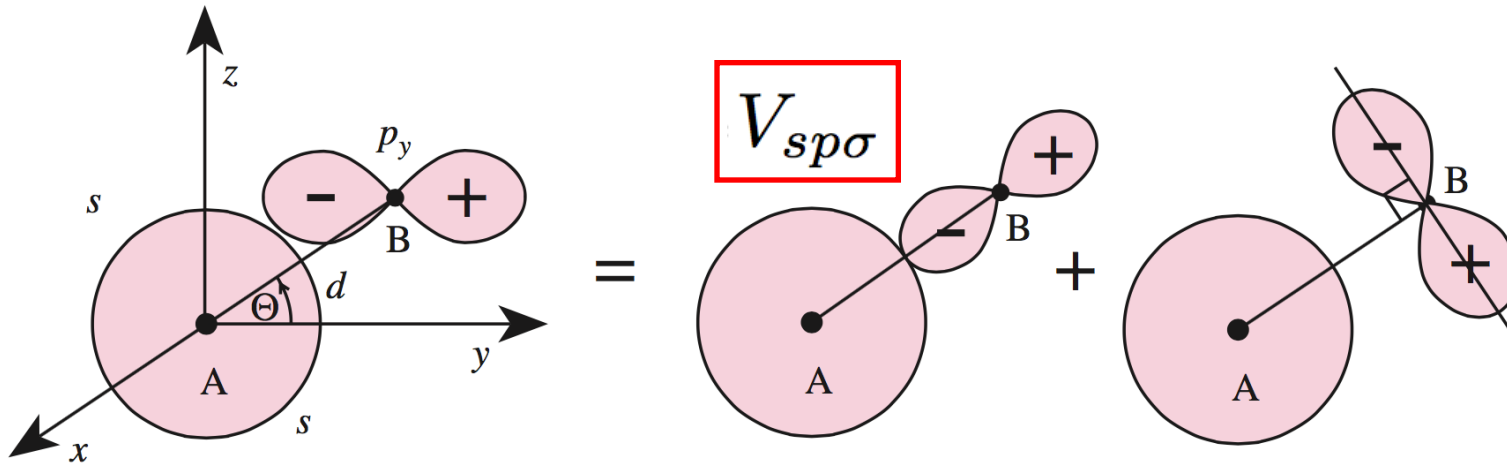


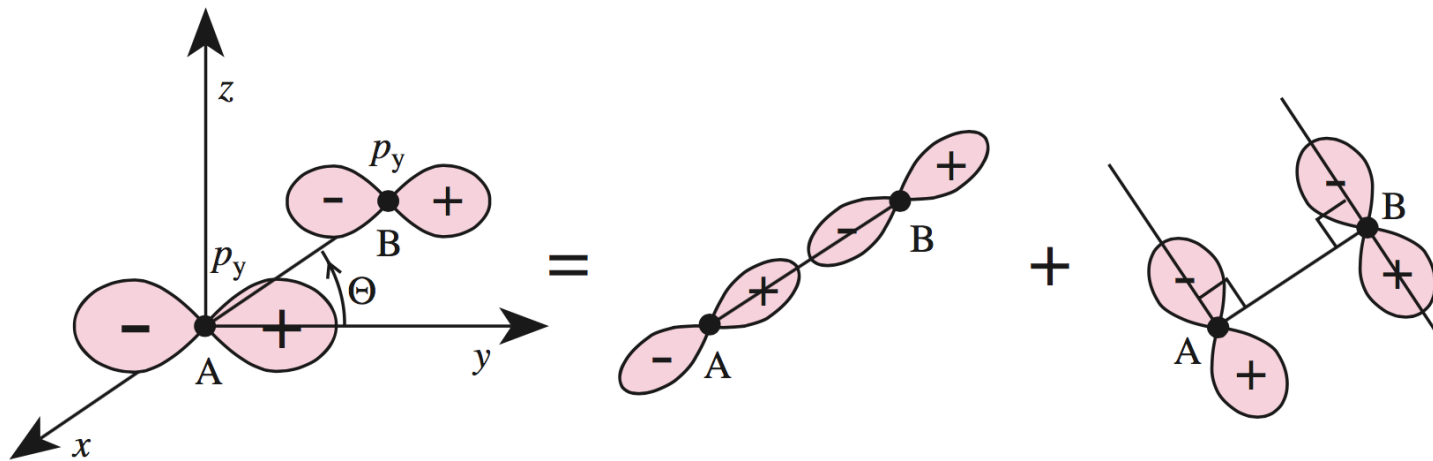
Fig. 2.19a,b. Overlap of two p_y orbitals to form bonding and antibonding π orbitals

(Cardona/Yu)

Orbital overlaps and bonds in semiconductors



$$\langle s | H | p_y \rangle = V_{sp\sigma} \cos\theta + 0 \sin\theta$$

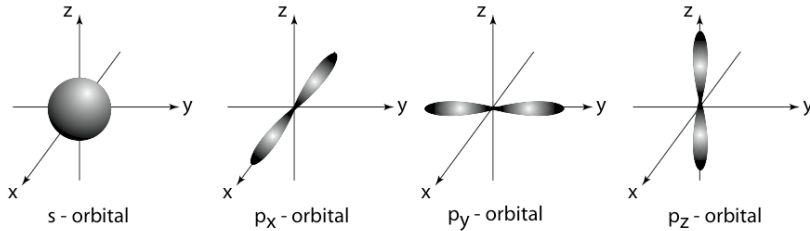


$$\langle p_y | H | p_y \rangle = V_{pp\sigma} \cos^2\theta + V_{pp\pi} \sin^2\theta$$

(Cardona/Yu)

Tight-Binding Bandstructure Matrix

$$\mathbf{a}_1 = \frac{a}{4}(1, 1, 1), \quad \mathbf{a}_2 = \frac{a}{4}(-1, -1, 1), \quad \mathbf{a}_3 = \frac{a}{4}(-1, 1, -1), \quad \mathbf{a}_4 = \frac{a}{4}(1, -1, -1)$$



$$V_0 = V_{ss\sigma},$$

$$V_1 = \frac{1}{\sqrt{3}} V_{sp\sigma},$$

$$V_2 = \frac{1}{3} V_{pp\sigma} - \frac{2}{3} V_{pp\pi}$$

$$V_3 = \frac{1}{3} V_{pp\sigma} + \frac{1}{3} V_{pp\pi}$$

$$g_0(\mathbf{k}) = e^{i\mathbf{k}\cdot\mathbf{a}_1} + e^{i\mathbf{k}\cdot\mathbf{a}_2} + e^{i\mathbf{k}\cdot\mathbf{a}_3} + e^{i\mathbf{k}\cdot\mathbf{a}_4},$$

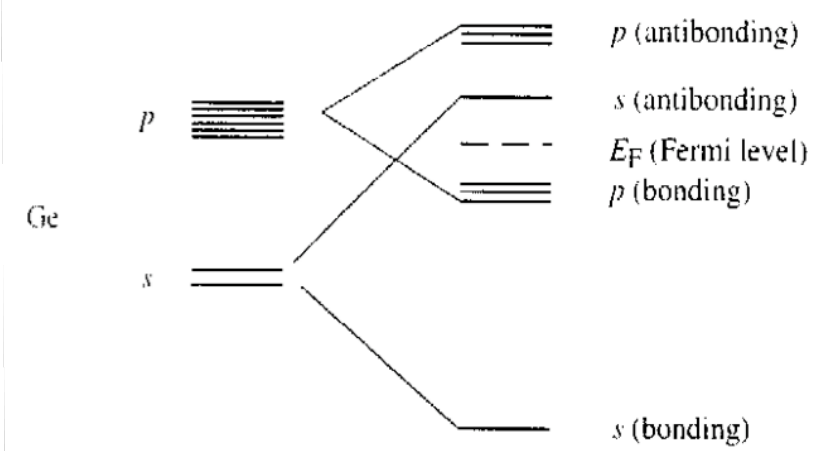
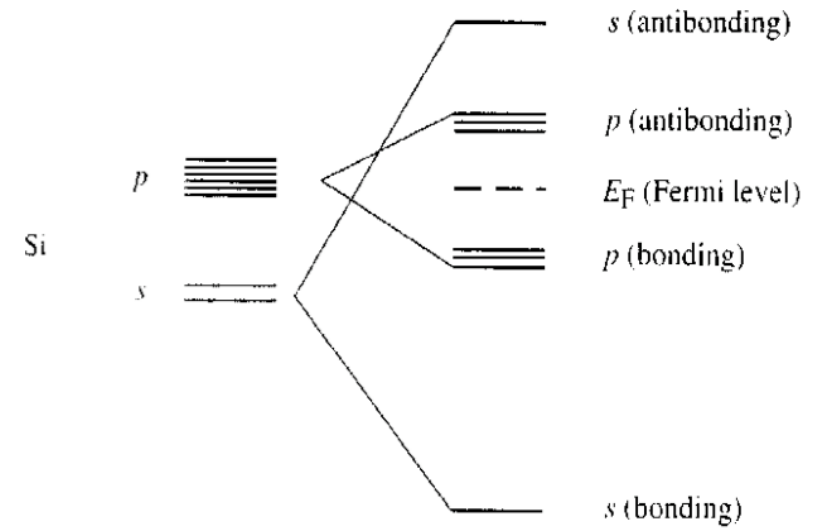
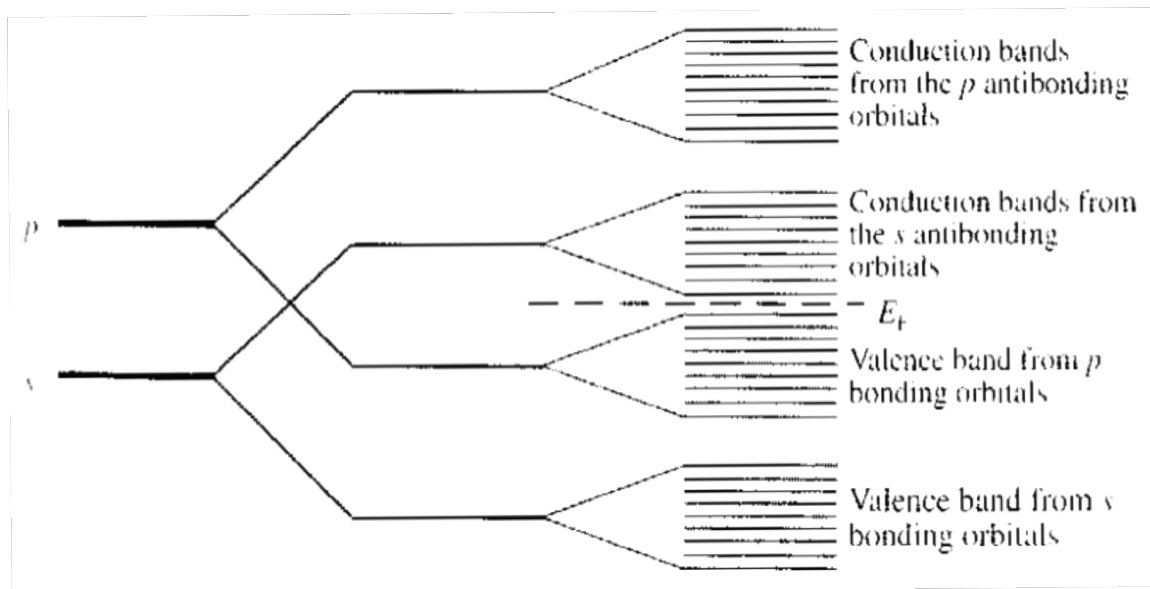
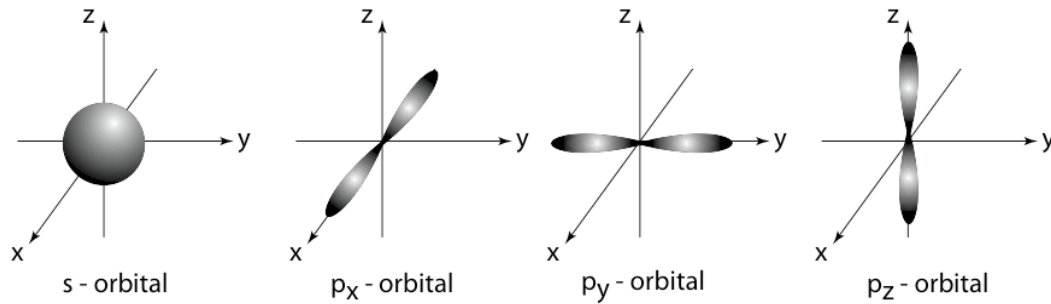
$$g_1(\mathbf{k}) = e^{i\mathbf{k}\cdot\mathbf{a}_1} - e^{i\mathbf{k}\cdot\mathbf{a}_2} - e^{i\mathbf{k}\cdot\mathbf{a}_3} + e^{i\mathbf{k}\cdot\mathbf{a}_4},$$

$$g_2(\mathbf{k}) = e^{i\mathbf{k}\cdot\mathbf{a}_1} - e^{i\mathbf{k}\cdot\mathbf{a}_2} + e^{i\mathbf{k}\cdot\mathbf{a}_3} - e^{i\mathbf{k}\cdot\mathbf{a}_4},$$

$$g_3(\mathbf{k}) = e^{i\mathbf{k}\cdot\mathbf{a}_1} + e^{i\mathbf{k}\cdot\mathbf{a}_2} - e^{i\mathbf{k}\cdot\mathbf{a}_3} - e^{i\mathbf{k}\cdot\mathbf{a}_4}$$

$$\begin{array}{c} \langle s^A | \\ \langle p_x^A | \\ \langle p_y^A | \\ \langle p_z^A | \\ \langle s^B | \\ \langle p_x^B | \\ \langle p_y^B | \\ \langle p_z^B | \end{array} \begin{pmatrix} |s^A\rangle & |p_x^A\rangle & |p_y^A\rangle & |p_z^A\rangle & |s^B\rangle & |p_x^B\rangle & |p_y^B\rangle & |p_z^B\rangle \\ E_s^A & 0 & 0 & 0 & -V_0 g_0(\mathbf{k}) & V_1 g_1(\mathbf{k}) & V_1 g_2(\mathbf{k}) & V_1 g_3(\mathbf{k}) \\ 0 & E_p^A & 0 & 0 & -V_1 g_1(\mathbf{k}) & V_2 g_0(\mathbf{k}) & V_3 g_3(\mathbf{k}) & V_3 g_2(\mathbf{k}) \\ 0 & 0 & E_p^A & 0 & -V_1 g_2(\mathbf{k}) & V_3 g_3(\mathbf{k}) & V_2 g_0(\mathbf{k}) & V_3 g_1(\mathbf{k}) \\ 0 & 0 & 0 & E_p^A & -V_1 g_3(\mathbf{k}) & V_3 g_2(\mathbf{k}) & V_3 g_1(\mathbf{k}) & V_2 g_0(\mathbf{k}) \\ \text{c.c.} & \text{c.c.} & \text{c.c.} & \text{c.c.} & E_s^B & 0 & 0 & 0 \\ \text{c.c.} & \text{c.c.} & \text{c.c.} & \text{c.c.} & 0 & E_p^B & 0 & 0 \\ \text{c.c.} & \text{c.c.} & \text{c.c.} & \text{c.c.} & 0 & 0 & E_p^B & 0 \\ \text{c.c.} & \text{c.c.} & \text{c.c.} & \text{c.c.} & 0 & 0 & 0 & E_p^B \end{pmatrix}$$

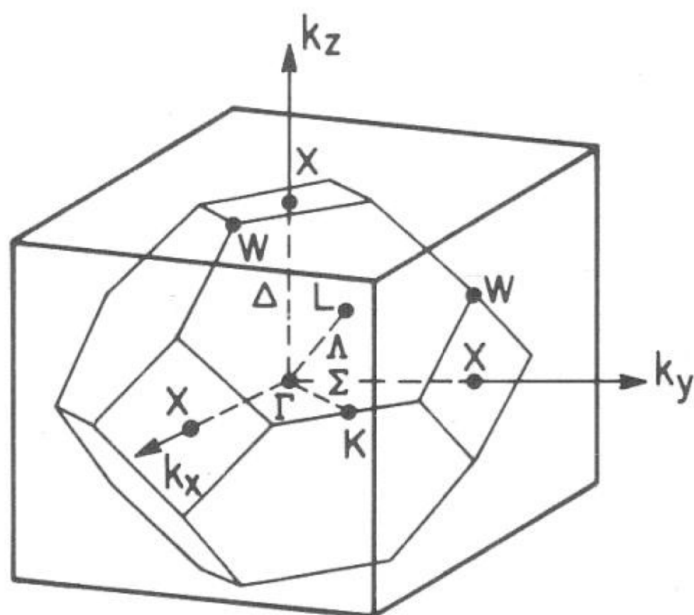
Semiconductor Bandstructures



Origin of s and p 'contents' in semiconductor bandstructure

Semiconductor Bandstructures

Tight Binding Solution for GaAs



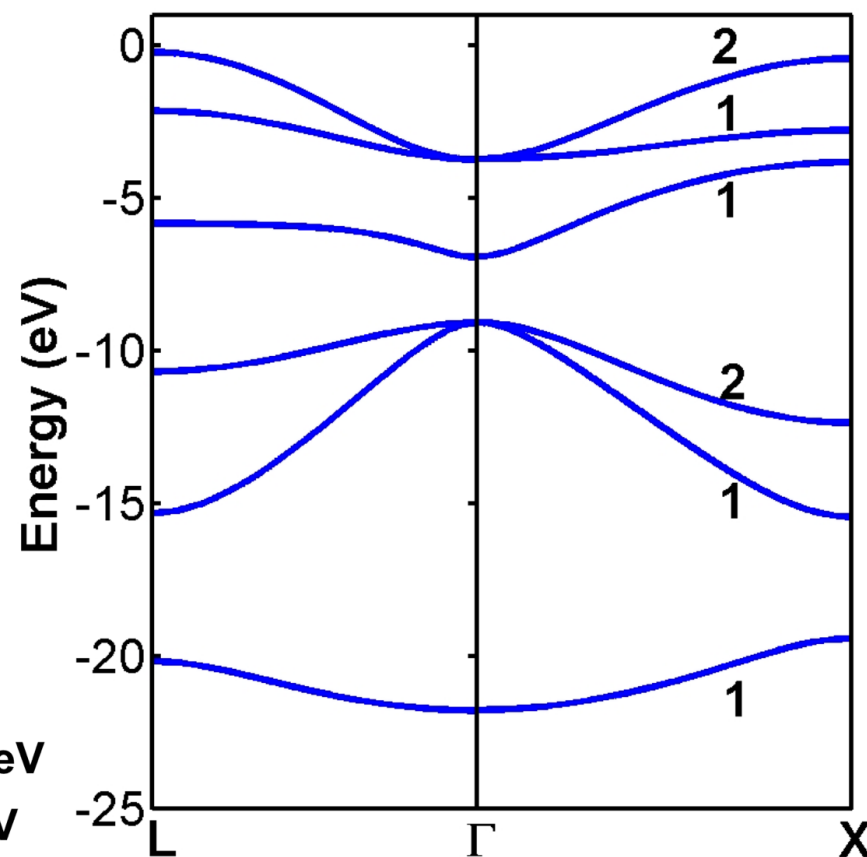
Parameter values for GaAs:

$$E_{SG} = -11.37 \text{ eV} \quad E_{SA} = -17.33 \text{ eV}$$

$$E_{PG} = -4.90 \text{ eV} \quad E_{PA} = -7.91 \text{ eV}$$

$$V_{ss\sigma} = 1.70 \text{ eV} \quad V_{pp\sigma} = 3.44 \text{ eV}$$

$$V_{sp\sigma} = 2.15 \text{ eV} \quad V_{pp\pi} = 0.89 \text{ eV}$$



Tight Binding Solution

Semiconductor Bandstructures

Tight Binding Solution for GaAs: States at the Γ -Point

At the Γ -point:

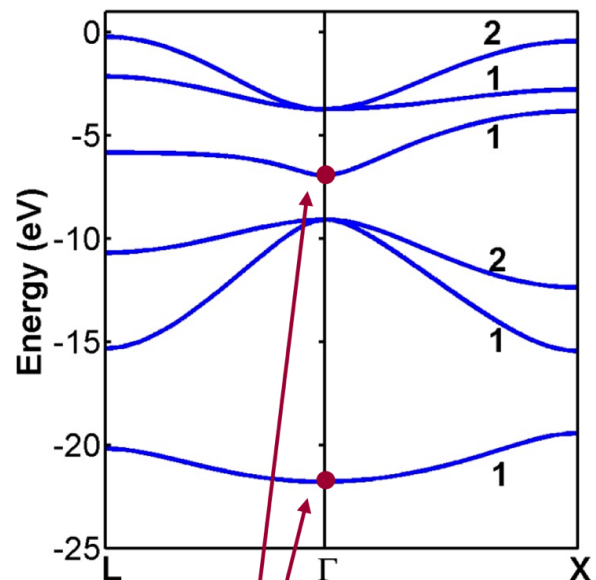
$$g_0(\vec{k} = 0) = 4$$

$$g_1(\vec{k}) = g_2(\vec{k}) = g_3(\vec{k}) = 0$$

⇒ Energy eigenvalues can be found analytically

Two of the eigenvalues at the Γ -point are:

$$E_{\pm 1}(\vec{k} = 0) = \left(\frac{E_{SG} + E_{SA}}{2} \right) \pm \sqrt{\left(\frac{E_{SG} - E_{SGA}}{2} \right)^2 + (4V_{ss\sigma})^2}$$



The Bloch function of the lowest energy band and of the conduction band at Γ -point are made up of ONLY s-orbitals from the Ga and As atoms

$$\psi_{c,\vec{k}=0}(\vec{r}) = \sum_m \frac{1}{\sqrt{N}} \left[c_1 |\phi_1(\vec{r} - \vec{R}_m)\rangle + c_5 |\phi_5(\vec{r} - \vec{R}_m - \vec{d}_2)\rangle \right]$$

Semiconductor Bandstructures

Tight Binding Solution for GaAs: States at the Γ -Point

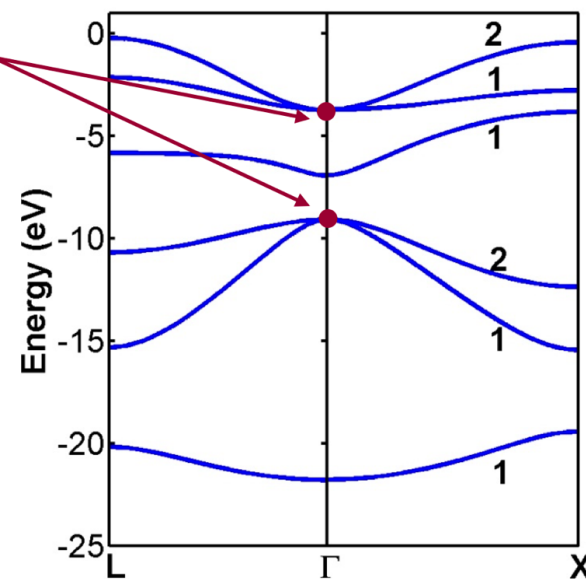
Six remaining eigenvalues at the Γ -point are:

$$E_{\substack{678 \\ 234}}(\vec{k} = 0) = \left(\frac{E_{PG} + E_{PA}}{2} \right) \pm \sqrt{\left(\frac{E_{PG} - E_{PA}}{2} \right)^2 + (4V_1)^2}$$

Each eigenvalue above is triply degenerate

The Bloch function of the highest three energy bands and of the three valence bands at Γ -point are made up of ONLY p-orbitals from the Ga and As atoms

$$\psi_{v, \vec{k}=0}(\vec{r}) = \sum_m \frac{1}{\sqrt{N}} \left[\begin{array}{l} \sum_{j=2}^4 c_j |\phi_j(\vec{r} - \vec{R}_m)\rangle \\ + \sum_{j=6}^8 c_j |\phi_j(\vec{r} - \vec{R}_m - \vec{d}_2)\rangle \end{array} \right]$$

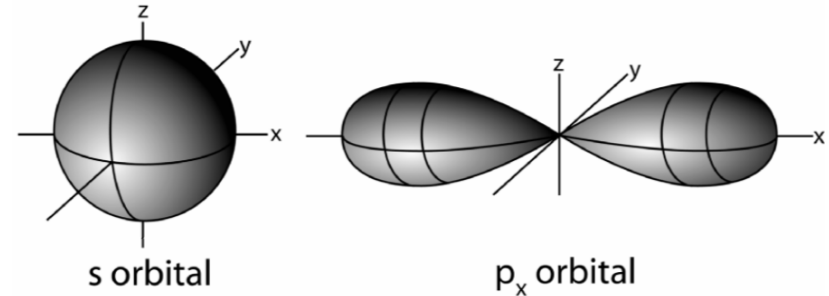


Semiconductor Bandstructures

5. ENGINEERING ELECTRONIC STRUCTURE 195

5.1 Linking atomic orbitals to bands	196
5.1.1 Homopolar semiconductors	197
5.1.2 Heteropolar compounds	201
5.2 LCAO: from atomic orbitals to bands	206
5.3 Common semiconductor energy bands	215
5.4 Pressure and temperature dependence	223
5.5 Applications	226
5.5.1 Experimental band structures	226
5.5.2 Gunn diodes	228
5.6 Summary points	232
5.7 Homework	233
5.8 Suggested readings & references	235

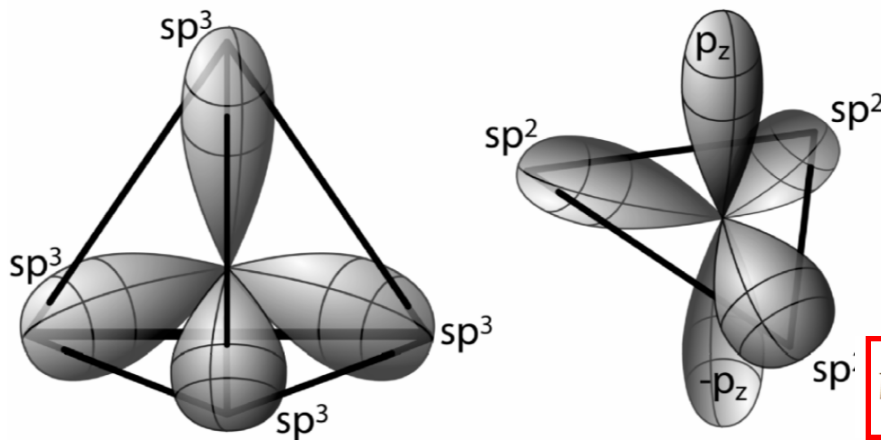
Rockett: MSS



$$\psi_s = \frac{2a_0^{-3/2}}{\sqrt{\pi}} \left(1 - \frac{r}{2a_0}\right) e^{-r/2a_0}$$

$$\psi_{p_x} = \frac{2a_0^{-3/2}}{\sqrt{\pi/3}} \left(1 - \frac{r}{2a_0}\right) e^{-r/2a_0} \cos\theta$$

Figure 5.1: Shows the shape of the s and p_x orbitals and the equations that describe them. a_0 is the atomic orbital size, r is the radius from the nucleus, and θ is the angle in the x,y plane.



$$V_2 \approx 4.4 \frac{\hbar^2}{md^2} \text{ eV}$$

Figure 5.2: Shows the symmetry of the hybridized sp^3 and sp^2 molecular orbitals. The sp^2 orbitals lie in a plane perpendicular to the p_z orbitals and are equal lengths. The sp^3 orbitals are all equivalent to each other and stretch to corners of a tetrahedron.

Wave function amplitudes (probability of finding an electron)

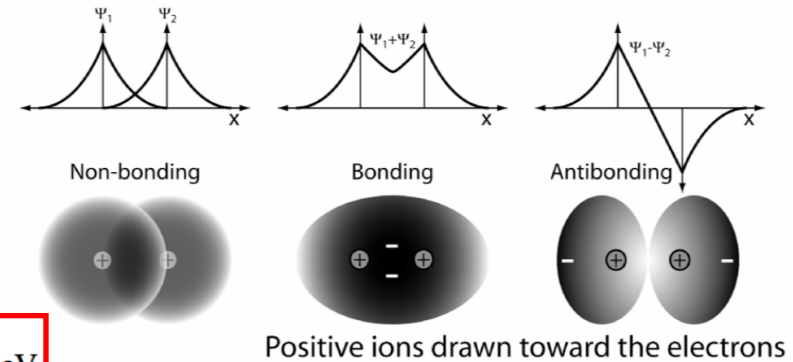


Figure 5.3: A schematic diagram illustrating the basis of cohesion in solids resulting from symmetric and antisymmetric combinations of atomic orbitals. The center of electron charge lies between the positive ions for a symmetric bonding orbital and outside of the positive ions for an antisymmetric orbital combination.

Origin of s and p 'contents' in semiconductor bandstructure

(Rockett)

Semiconductor Bandstructures

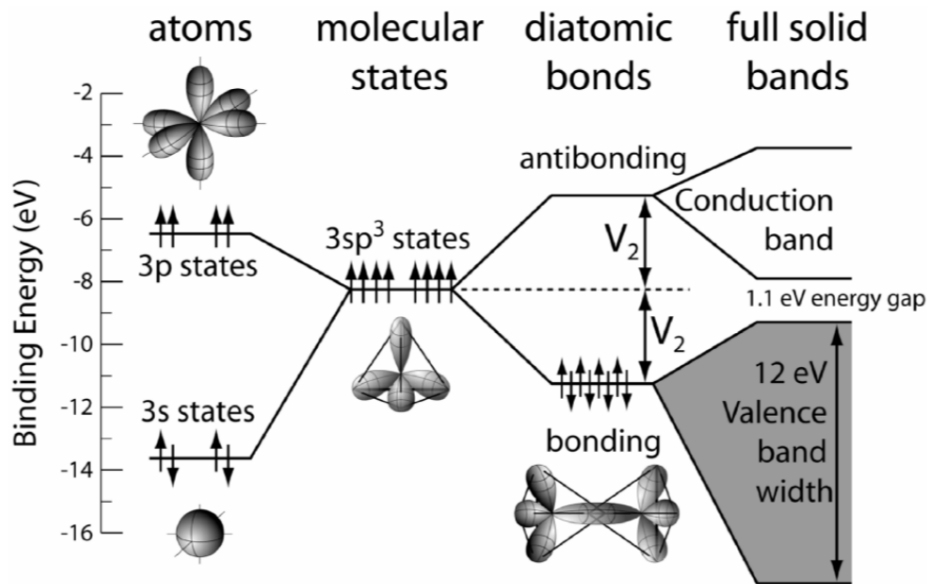


Figure 5.4: A schematic diagram of the evolution of bonding of Si atoms. The filled 3s and partially filled 3p atomic orbitals of two atoms combine to form half-filled sp³ hybrid molecular orbitals. These combine to form bonding and antibonding orbitals. As more atoms collect atoms collect to create a bulk solid, bands form.

Silicon

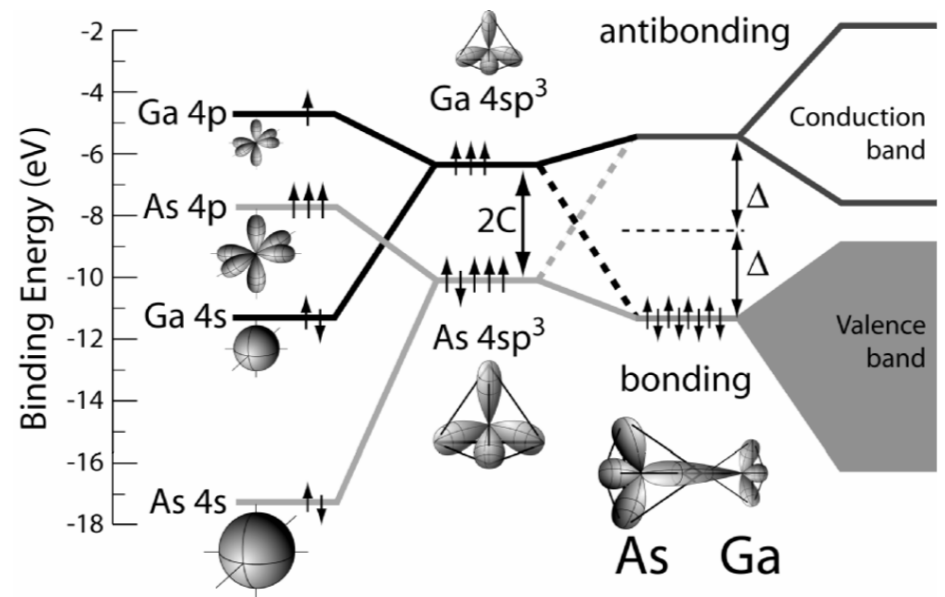


Figure 5.5: Shows the evolution of atomic orbital energies to form bonds and ultimately bands. The geometries of the atomic and hybrid orbitals are shown schematically as insets.

GaAs

(Rockett)

Semiconductor Bandstructures

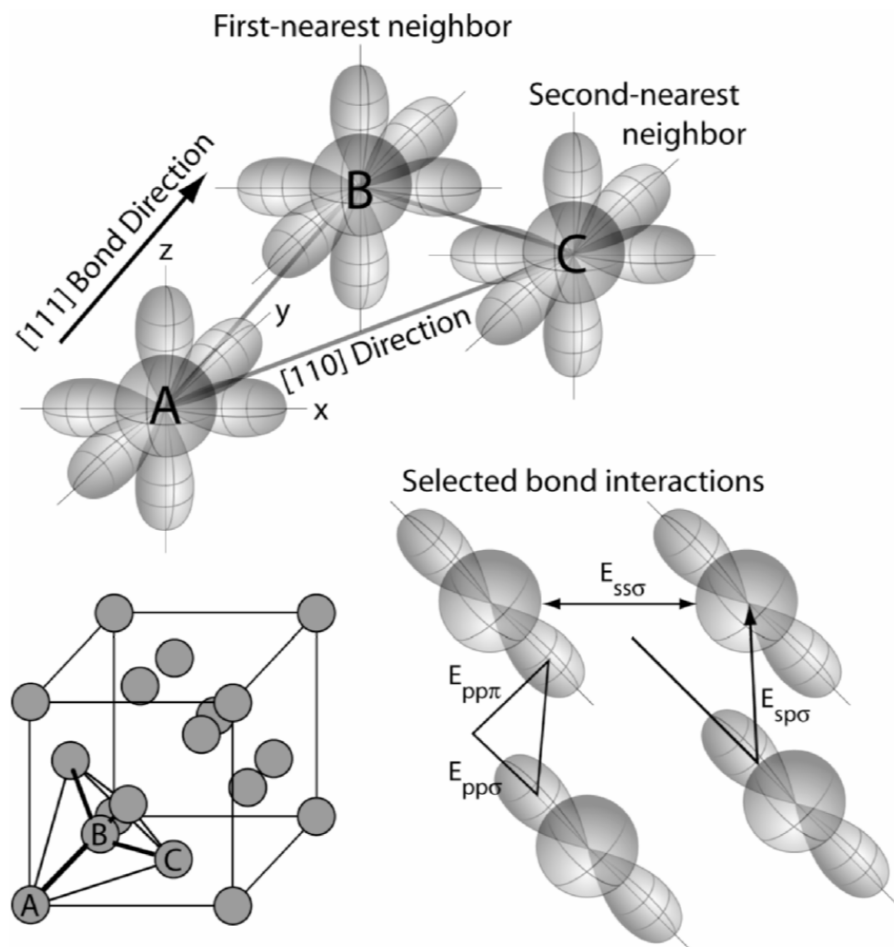


Figure 5.6: A schematic diagram showing the interactions of selected atomic orbitals and the geometry of these orbitals with respect to the crystal lattice in a zincblende or diamond structure material.

Table 5.3: Energy Gaps and Lattice Parameters

Semiconductor Class	Semiconductor	Lattice Parameter	Energy Gap, eV (at 20°C)	E_c (eV)	E_v (eV)
Cubic		nm			
IV	C (diamond)	0.35597	5.5		
IV	Si	0.54307	1.12 (indirect)	4.05	5.17
IV	Ge	0.56754	0.67 (indirect)	4.0	4.67
IV	a-Sn	0.64912	0.08		
III-V	GaP	0.54505	2.26 (indirect)	3.8	6.1
III-V	GaAs	0.56532	1.42	4.07	5.49
III-V	GaSb	0.609593	0.726	4.06	4.79
III-V	InP	0.58687	1.344	4.38	5.72
III-V	InAs	0.60583	0.354	4.9	5.25
III-V	InSb	0.6479	0.17	4.59	4.76
II-VI	ZnSe (cubic)	0.567	2.58	4.1	6.7
I-VII	CuBr	5.69	2.94	4.35	7.29
I-III-VI ₂	CuInSe ₂	0.578	0.98	4.0	5.0
II-IV-V ₂	ZnGeAs ₂	0.567	0.85		
Hexagonal					
III-V	AlN	0.3111 (a) 0.4978 (c)	5.9	0.6	6.5
III-V	GaN	0.3190 (a) 0.5189 (c)	3.45	4.0	7.4
III-V	InN	0.3533 (a) 0.5693 (c)	0.7 (note values vary greatly)		
II-VI	ZnS	0.3814 (a) 0.6258 (c)	3.911		
II-VI	CdSe	0.4299 (a) 0.7010 (c)	1.751 eV		

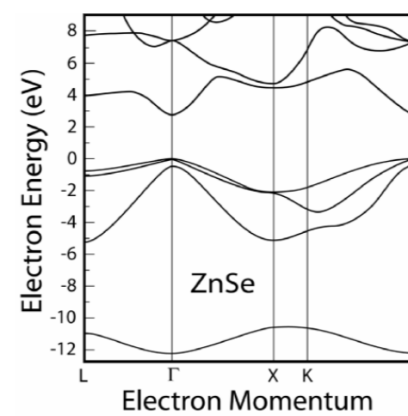
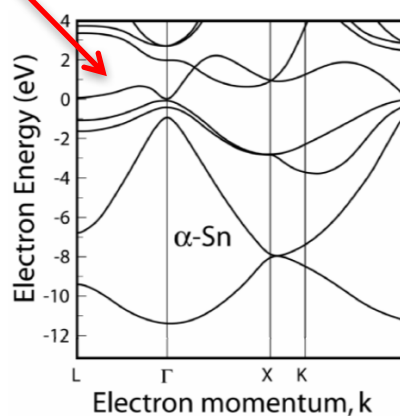
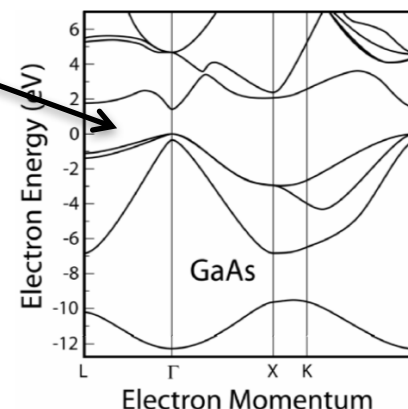
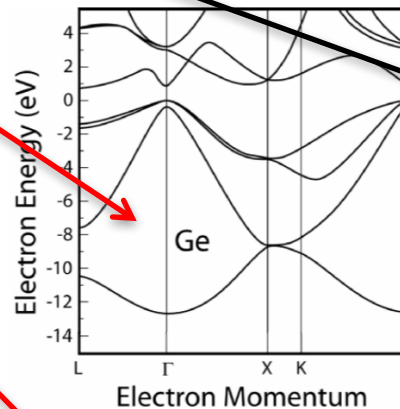
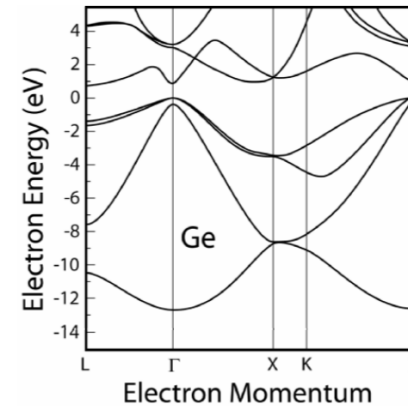
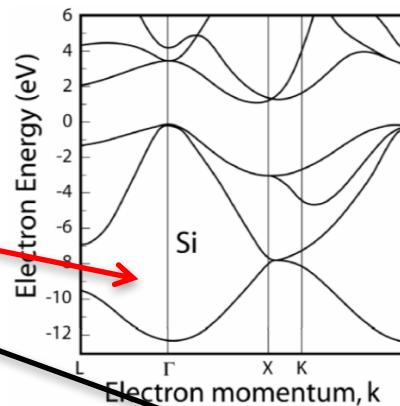
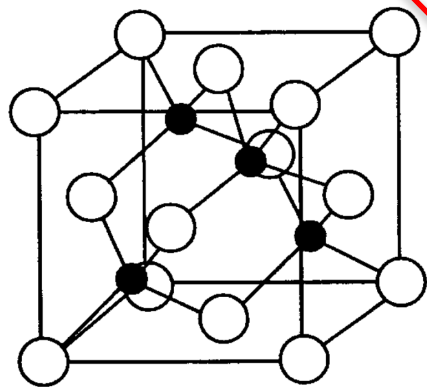
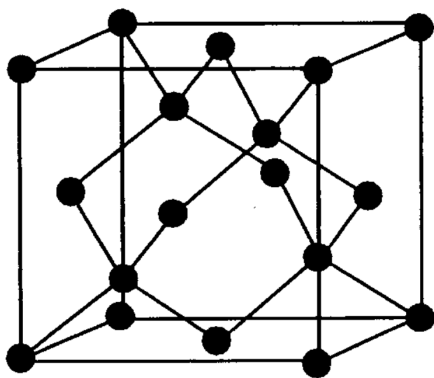
E_c (the electron affinity) and E_v (electron affinity + energy gap) measured with respect to the vacuum level. Lattice parameters in nm.

Chemical bonding, Lattice Constants, Band edges, and Band Gaps for various Semiconductors

(Rockett)

Semiconductor Bandstructures

Noble gases	5 B Boron 10.811	6 C Carbon 12.0107	7 N Nitrogen 14.0067	8 O Oxygen 15.9994
	13 Al Aluminium 26.9815386	14 Si Silicon 28.0855	15 P Phosphorus 30.973762	16 S Sulfur 32.065
	30 Zn Zinc 65.38	31 Ga Gallium 69.723	32 Ge Germanium 72.64	33 As Arsenic 74.92160
	48 Cd Cadmium 112.411	49 In Indium 114.818	50 Sn Tin 118.710	51 Sb Antimony 121.750
80 Hg Mercury 200.59	81 Tl Thallium 204.3833	82 Pb Lead 207.2	83 Bi Bismuth 208.98040	84 Po Polonium (208.9824)



Bandstructures of Elemental and Compound Semiconductors

Semiconductor Bandstructures

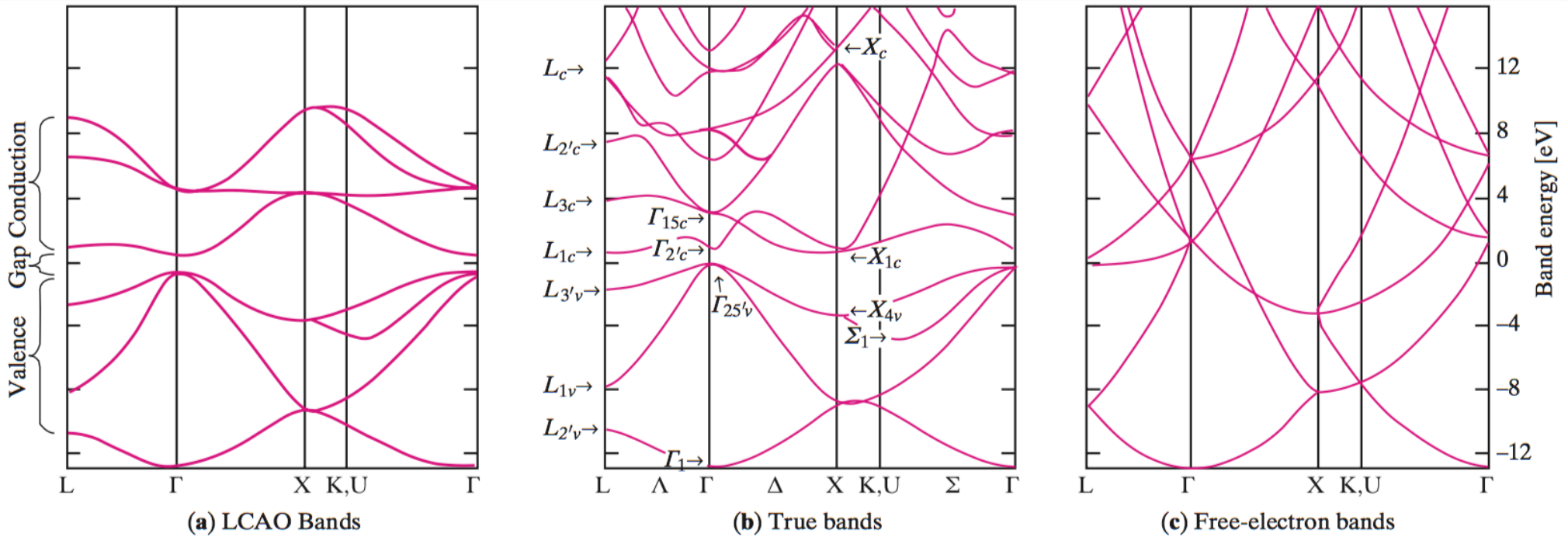


Fig. 2.25. A comparison between the band structure of Ge calculated by (a) the tight-binding method, (b) the empirical pseudopotential method, and (c) the nearly free electron model [Ref. 2.24, p. 79]

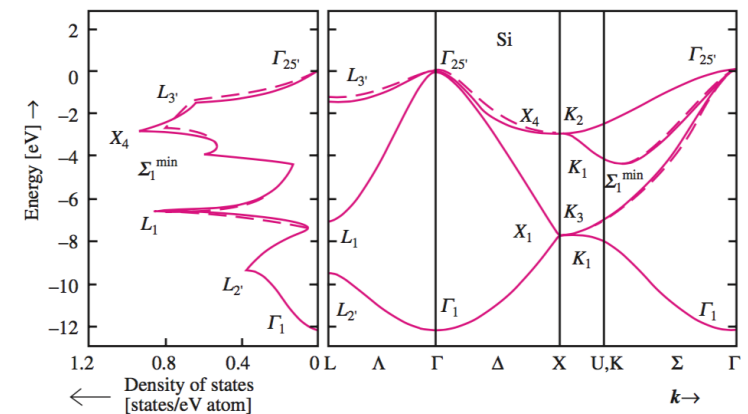
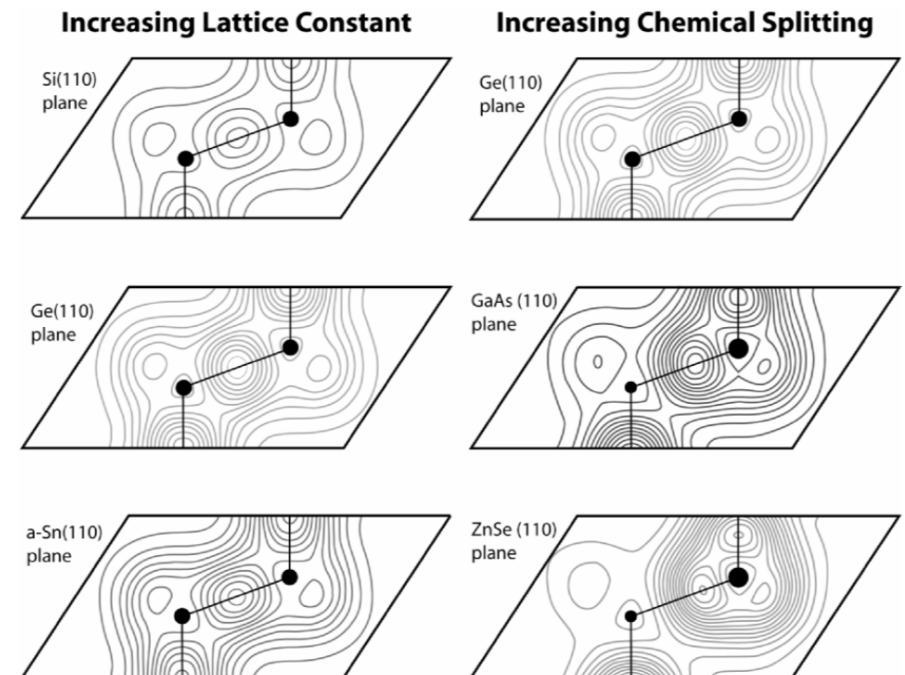
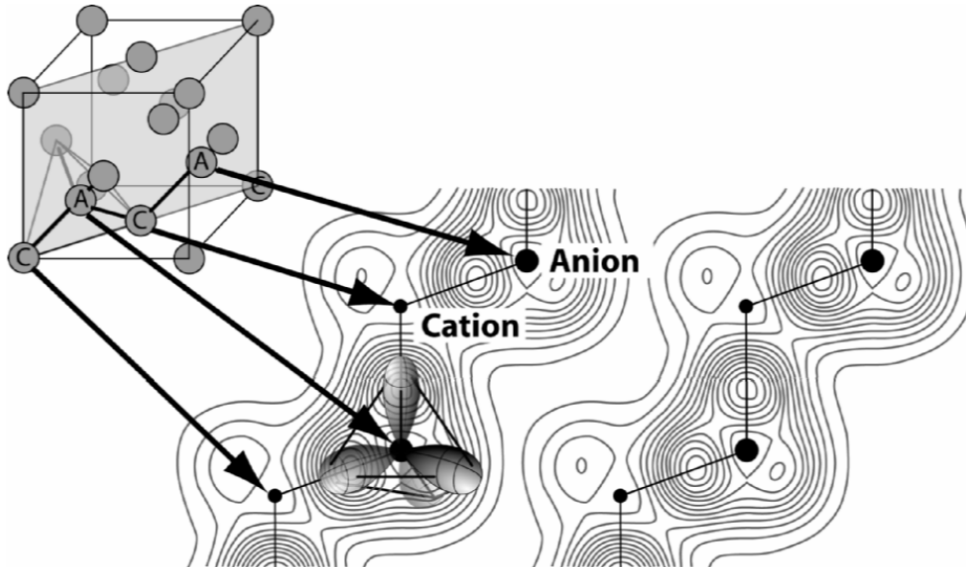


Fig. 2.24. The valence band structure and density of states (see Sect. 4.3.1 for definition) of Si calculated by the tight-binding method (broken curves) and by the empirical pseudopotential method (solid lines) [2.25]

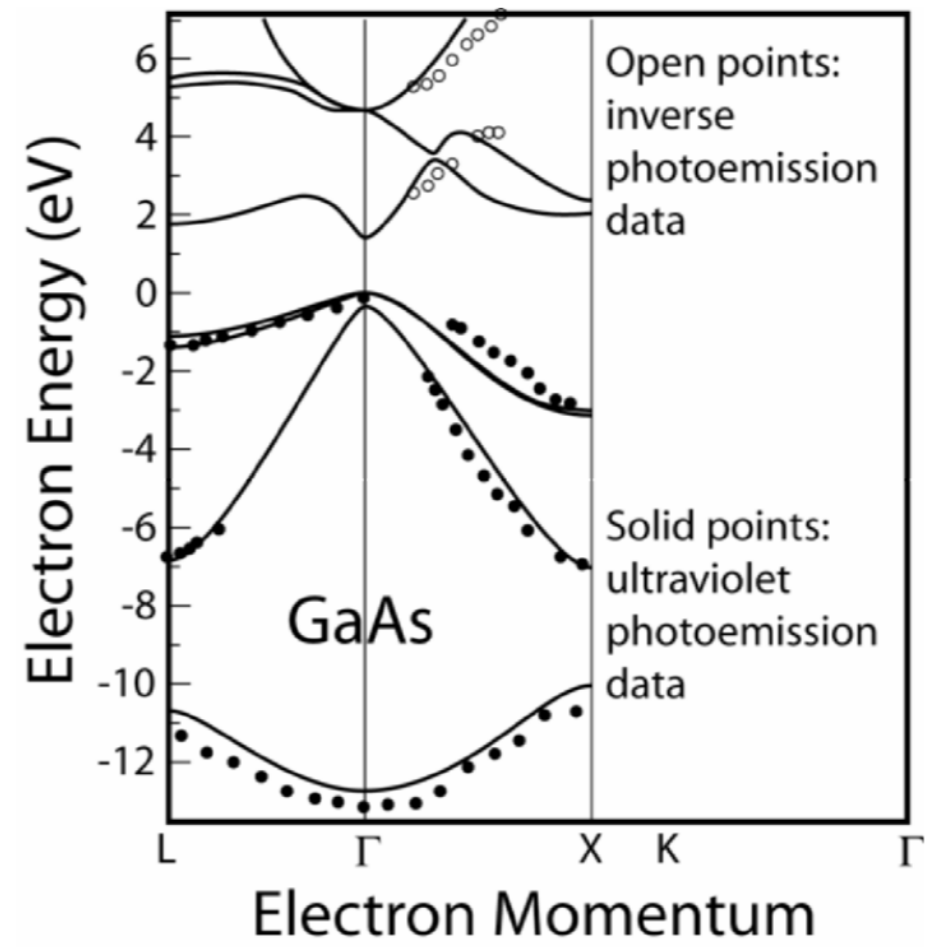
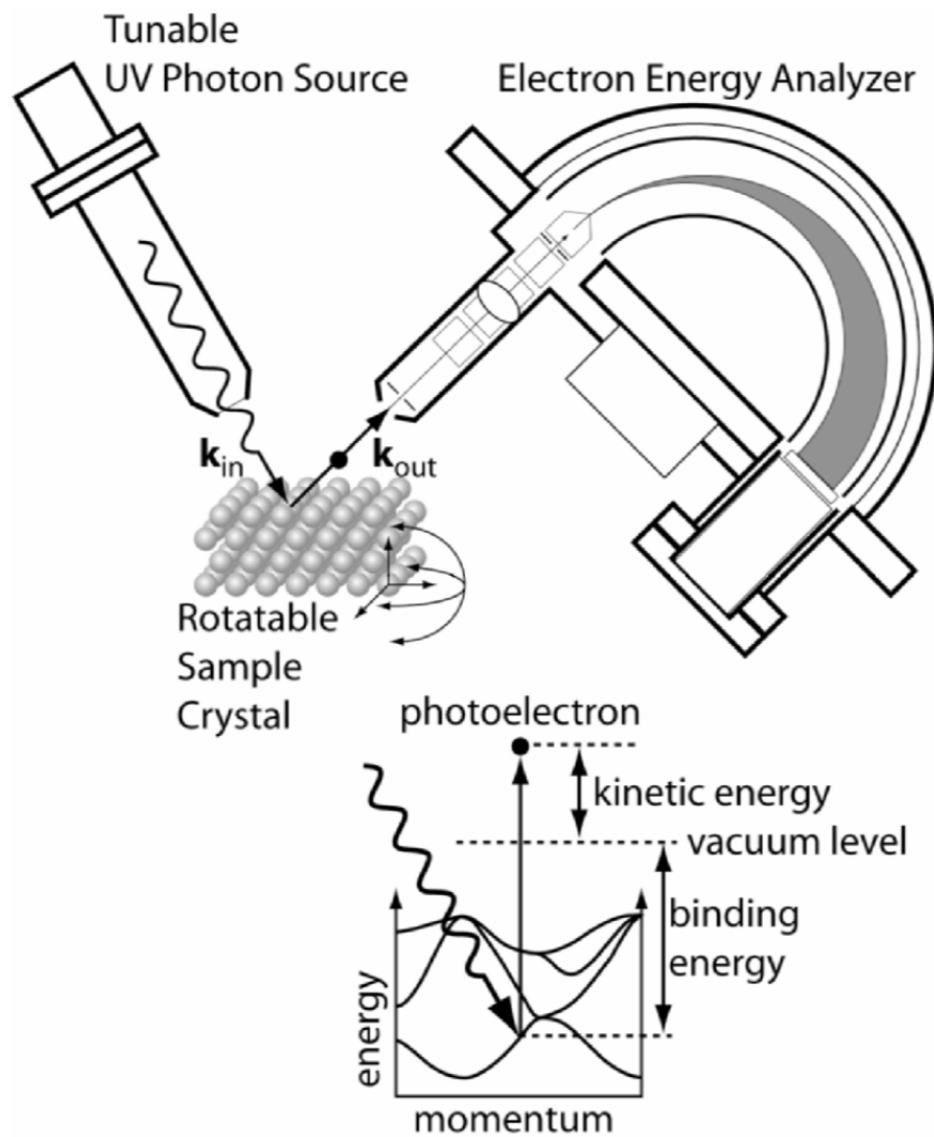
Electron clouds in semiconductors



Electron wavefunction squared = probability density of finding electrons

(Rockett)

Measurement of Semiconductor Bandstructures



Angle-Resolved Photo-Emission Spectroscopy (ARPES)

(Rockett)

Semiconductor Bandstructures

Free electron vs. real bandstructure

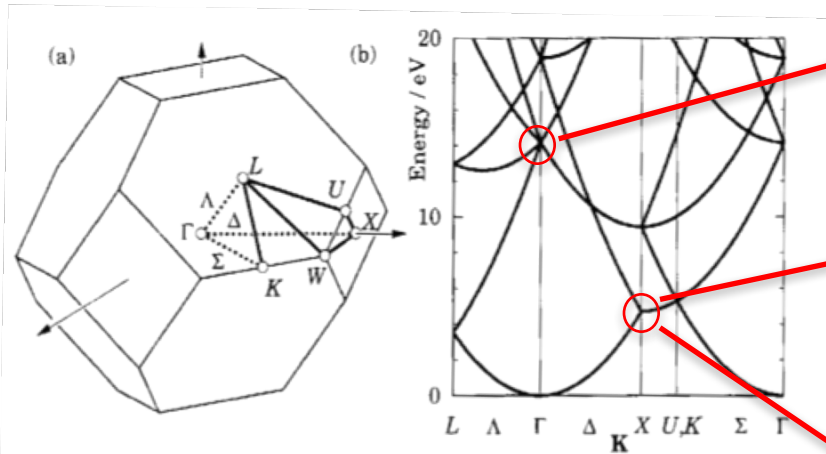


FIGURE 2.15. (a) Brillouin zone for a face-centered cubic crystal, showing the notation for special points and directions. Solid lines are on the surface with broken lines inside the zone. (b) Band structure in the free-electron model, showing the effect of folding back the parabola into the reduced zone.

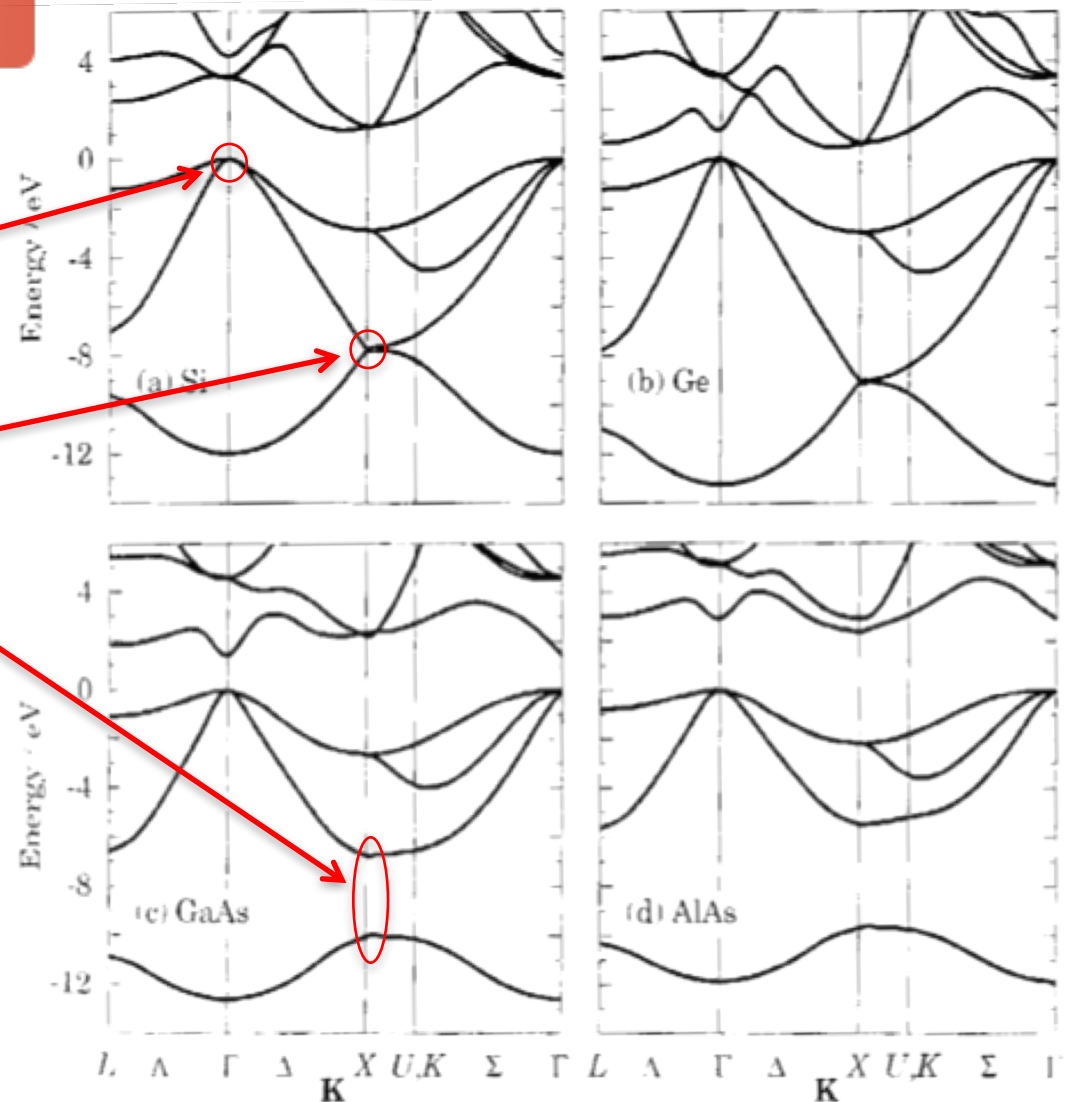
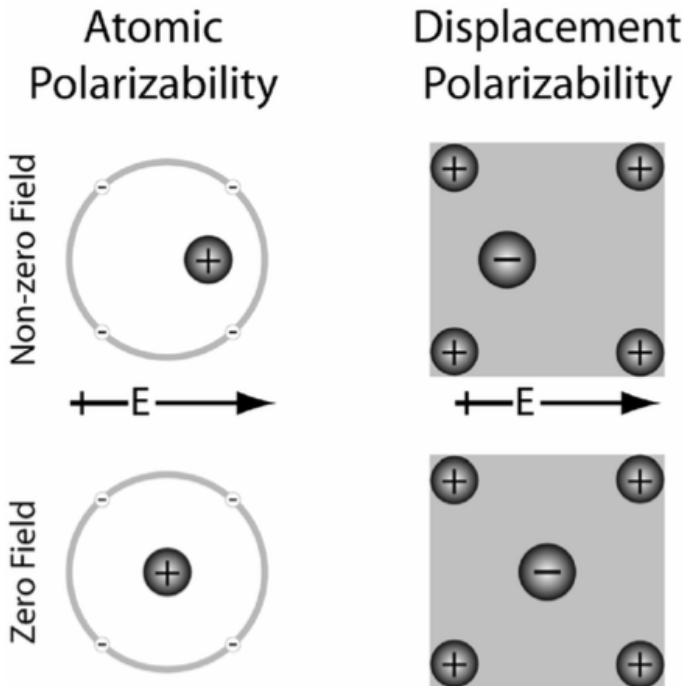
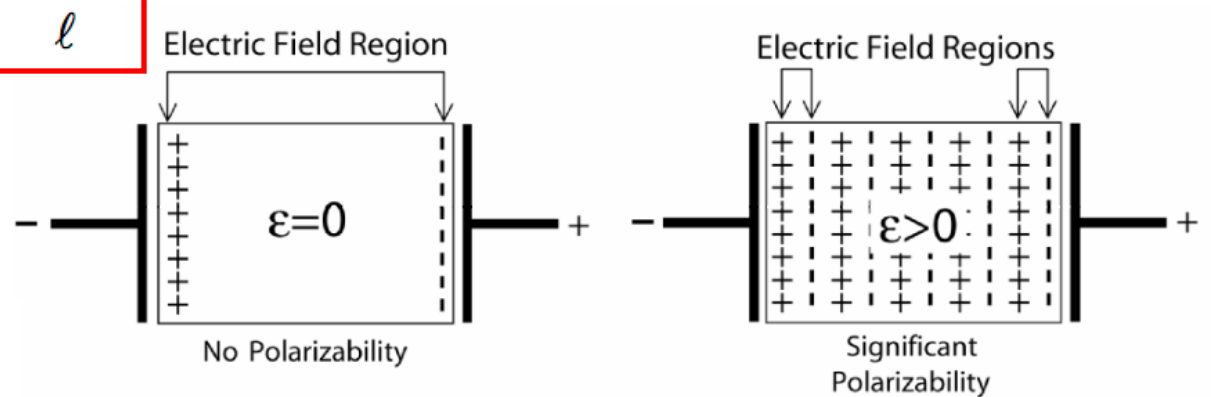


FIGURE 2.16. Band structure of four common semiconductors: silicon, germanium, gallium arsenide, and aluminium arsenide. The calculations do not include the spin-orbit coupling. [Results kindly supplied by Prof. G. P. Srivastava, University of Exeter.]

Semiconductor dielectric constants & polarization

$$C = \frac{\epsilon A}{d} \quad R = \frac{\rho l}{A} \quad L = \mu_B \frac{N^2 A}{l}$$



$$\alpha_{\text{displacement}} = \frac{Z^2 q^2}{(\bar{\omega}^2 - \omega^2)} \left(\frac{1}{M^+} + \frac{1}{M^-} \right)$$

$$\begin{aligned} \epsilon(\mathbf{q}, 0) &\approx 1 + \frac{4\pi e^2}{q^2} \frac{n}{\mathcal{E}_{\text{gap}}} \frac{\hbar^2 q^2}{2m} \frac{2}{\mathcal{E}_{\text{gap}}} \\ &= 1 + \frac{4\pi n e^2 \hbar^2}{m (\mathcal{E}_{\text{gap}})^2} \\ &= 1 + \left(\frac{\hbar \omega_p}{\mathcal{E}_{\text{gap}}} \right)^2, \end{aligned}$$

The "Moss" relation of dielectric constants of semiconductors

$$\omega_p = \left(\frac{4\pi n e^2}{m} \right)^{\frac{1}{2}}$$

Plasma frequency

(Rockett)

Semiconductor density of states

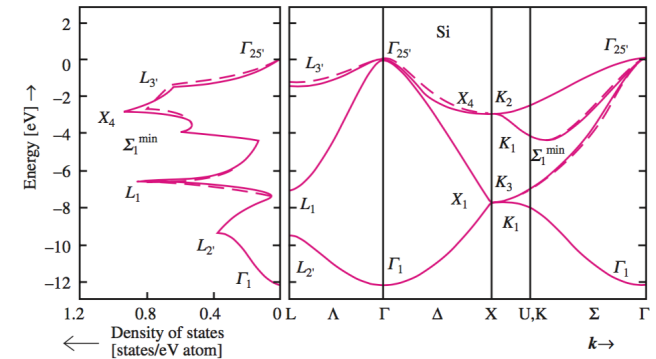
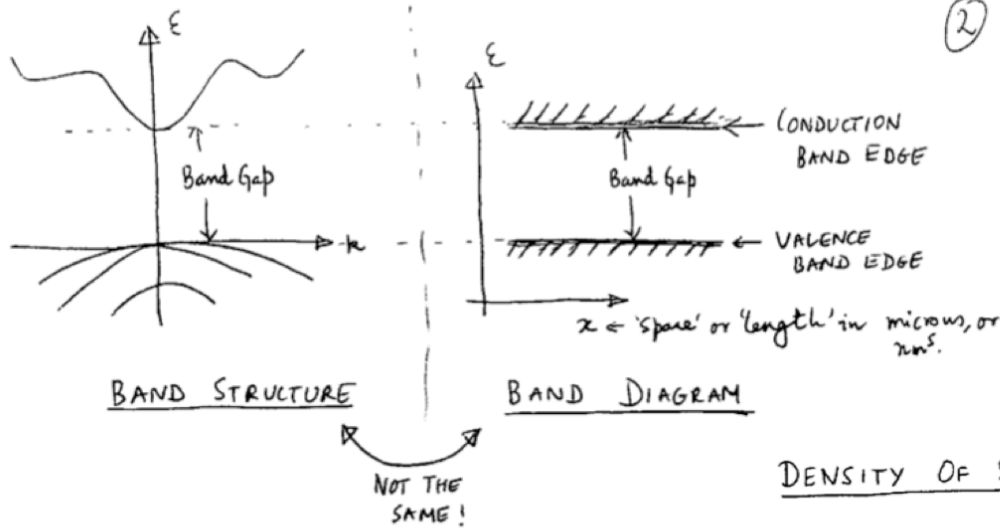


Fig. 2.24. The valence band structure and density of states (see Sect. 4.3.1 for definition) of Si calculated by the tight-binding method (broken curves) and by the empirical pseudopotential method (solid lines) [2.25]

DENSITY OF STATES (DOS)

General results

3D: $g_{3D}(E) = \frac{1}{2\pi^2} \left(\frac{2m^*}{\hbar^2}\right)^{3/2} \sqrt{E}$

$\sim \sqrt{E}$

Similarly, $g_{2D}(E) \sim E^0 \left(\text{const}\right)$

$g_{1D}(E) \sim 1/\sqrt{E}$

For a semiconductor (bulk, 3D),

Valence band DOS

Conduction band DOS

Available energy states

DOS effective mass

$$g_c(E) = g_{cv} \frac{1}{2\pi^2} \left(\frac{2m_c^*}{\hbar^2}\right)^{3/2} \sqrt{E - E_c}$$

Conduction band valley degeneracy

Conduction band edge

\therefore valid for $E > E_c$

$\left\{ \begin{array}{l} 1 \text{ for GaAs} \\ 6 \text{ for Si} \\ 4 \text{ for Ge} \end{array} \right.$

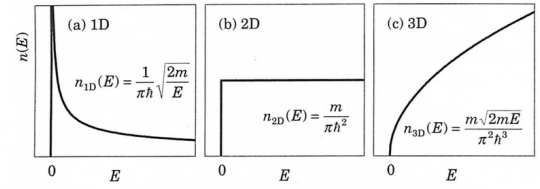
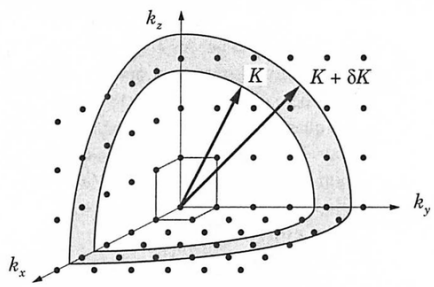
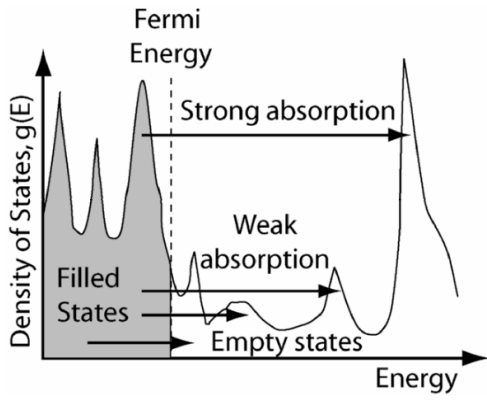


FIGURE 1.9. Densities of states for free electrons in one, two, and three dimensions.

Semiconductor carrier statistics

ENERGY distribution of electrons :

(3)

Carrier Statistics (Electrons/Holes)

Determined by the FERMI-DIRAC DISTRIBUTION FN.

$$f(\epsilon) = \frac{1}{1 + \exp\left(\frac{\epsilon - \epsilon_F}{kT}\right)}$$

ϵ_F : FERMI ENERGY

ELECTRON density in the conduction band:

$$n = \int_{E_c}^{\infty} dE g_c(E) f(E)$$

$$n = N_c F_{1/2}(\eta)$$

EFFECTIVE DOS

$$N_c = 2 \left(\frac{m^* kT}{2\pi \hbar^2} \right)^{3/2}$$

FERMI-DIRAC INTEGRAL

$$F_j(\eta) = \frac{1}{\Gamma(j+1)} \int_0^{\infty} dx \frac{x^j}{1 + e^{x-\eta}} \quad \text{order 'j'}$$

$$F_{1/2}(\eta) = \frac{2}{\sqrt{\pi}} \int_0^{\infty} dx \frac{x^{1/2}}{1 + e^{x-\eta}}$$

$$\eta = \frac{E_F - E_c}{kT}$$

For Non-Degenerate semiconductors, $\eta \ll -1 \Rightarrow$ BOLZMANN APPROX.

$$\Rightarrow F_{1/2}(\eta) \approx e^{\eta} \Rightarrow$$

$$n \approx N_c \exp\left(\frac{E_F - E_c}{kT}\right)$$

(* True for any order)
 $F_{j+1} \approx e^{\eta}$

USED VERY OFTEN!

Semiconductor carrier statistics

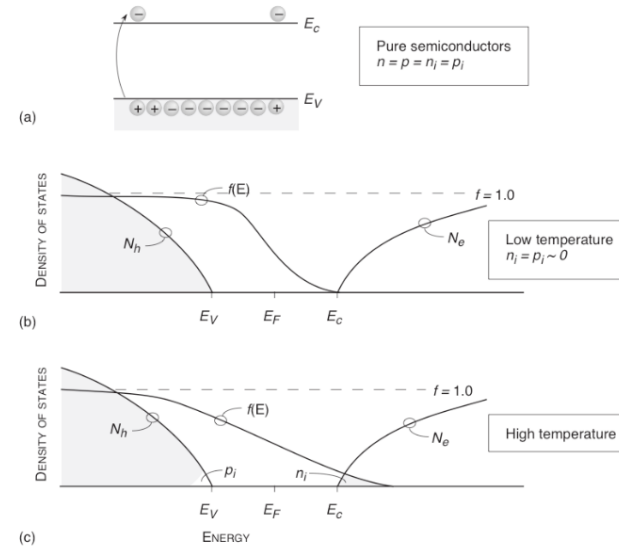
Carrier Statistics (Electrons/Holes)

$$p \approx N_v \exp\left(\frac{E_v - E_F}{kT}\right)$$

$$\Rightarrow np = n_i^2 = \left(\underbrace{\sqrt{N_c N_v} \exp\left(-\frac{E_g}{2kT}\right)}_{n_i} \right)^2$$

SEMICONDUCTOR

Intrinsic Carrier Concentration.

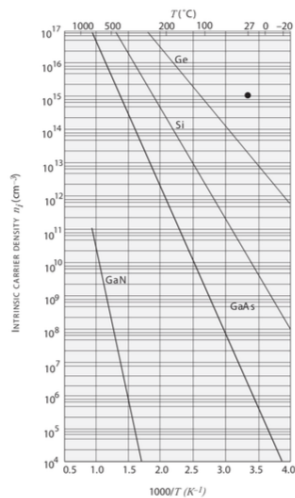


Where is the Fermi Level E_F ?

BASIC UNDERLYING PRINCIPLE:

CHARGE NEUTRALITY

WILL DETERMINE THE FERMIL LEVEL E_F ! - MORE LATER.



Intrinsic Semiconductor:

$$n = p = n_i = \sqrt{N_c N_v} \exp\left(-\frac{E_g}{2kT}\right)$$

$$E_F = E_i = \frac{E_c + E_v}{2} + \frac{kT}{2} \ln\left(\frac{N_v}{N_c}\right)$$

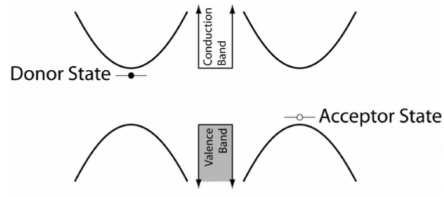
'Intrinsic' Fermi-Level.

Semiconductor doping

SEMICONDUCTOR
↓
INTRINSIC - PURE

↓
EXTRINSIC - DOPED - p-type
n-type

↓
COMPENSATED - DOPED - p + n type.



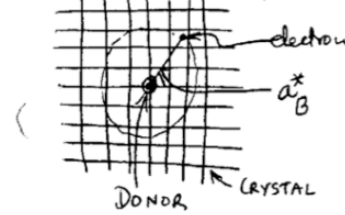
DOPANT: ATOM that replaces an atom of the intrinsic semiconductor

DONOR: ATOM with an EXTRA electron than the atom it replaces; the extra electron can be 'DONATED' to the cond. band.

ACCEPTOR: ATOM with one less electron than the atom it replaces; it can accept one electron from the valence band (same as forming a hole in VB).

$$N_D^+ = N_D \left[1 - \frac{1}{1 + \frac{1}{g_D} \exp\left(\frac{E_D - E_F}{kT}\right)} \right]$$

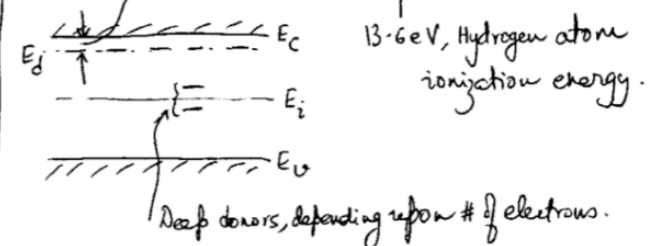
$$N_A^- = N_A \frac{1}{1 + g_A \exp\left(\frac{E_A - E_F}{kT}\right)}$$



'Shallow' donor ~~ionization~~ ionization energy

$$E_C - E_D \approx \frac{m_c^*}{E_r^2} R_{\infty} < kT$$

↑ to be shallow



'Effective Bohr radius'

$$a_B^* \approx \frac{\epsilon_r}{m_c^*} a_0$$

0.53 Å, H-atom Bohr radius.

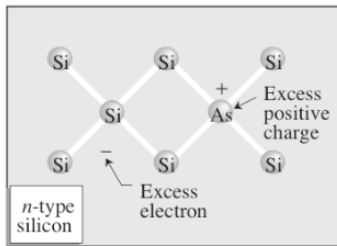
Typically: $a_B^* \gg a_0$.

EXAMPLE: n-doped semiconductor:

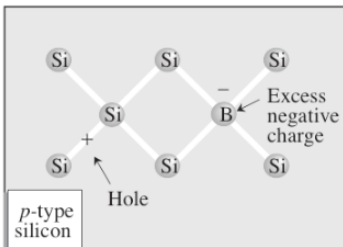
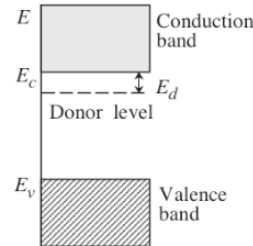
$$n = p + N_D^+, \quad np = n_i^2$$

Shallow donor $\Rightarrow N_D^+ \approx N_D \Rightarrow n \approx \frac{\sqrt{(N_D)^2 + 4n_i^2} + N_D}{2}$

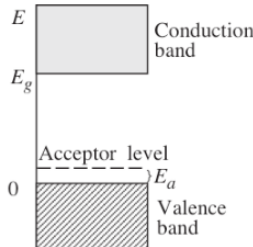
if $N_D \gg n_i$, $n \approx N_D \Rightarrow$ As many electrons in CB as # of donors!



Arsenic (As) atom donates one electron to the conduction band to produce an n-type silicon



One electron taken from the valence band to complete the bonding of the boron atom \rightarrow hole

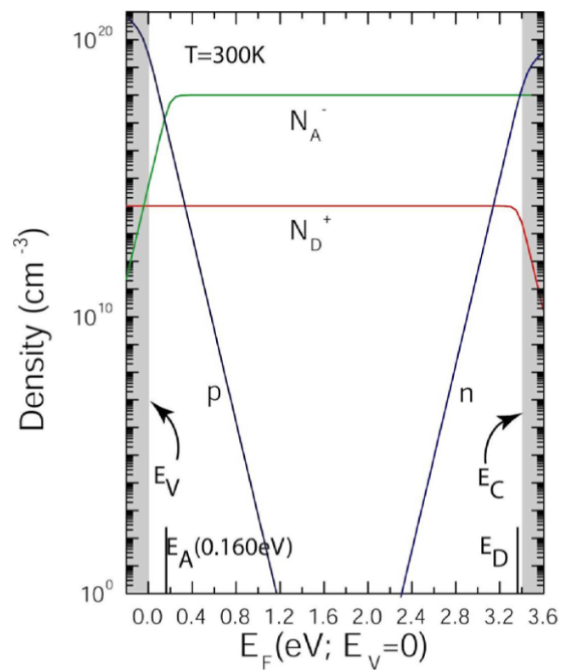


Semiconductor doping

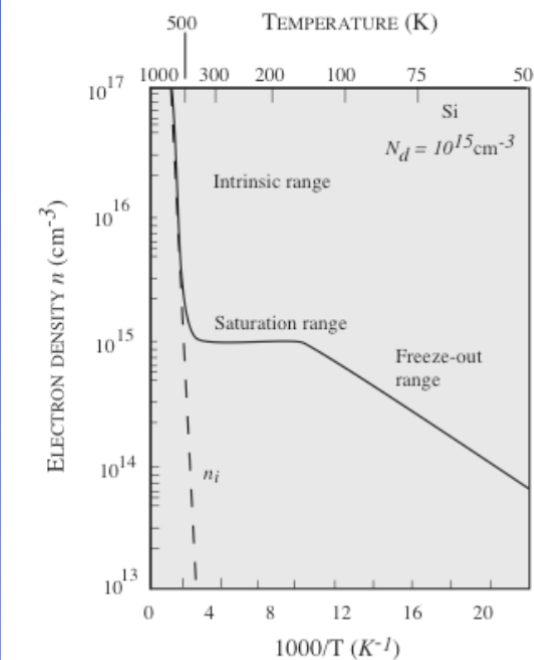
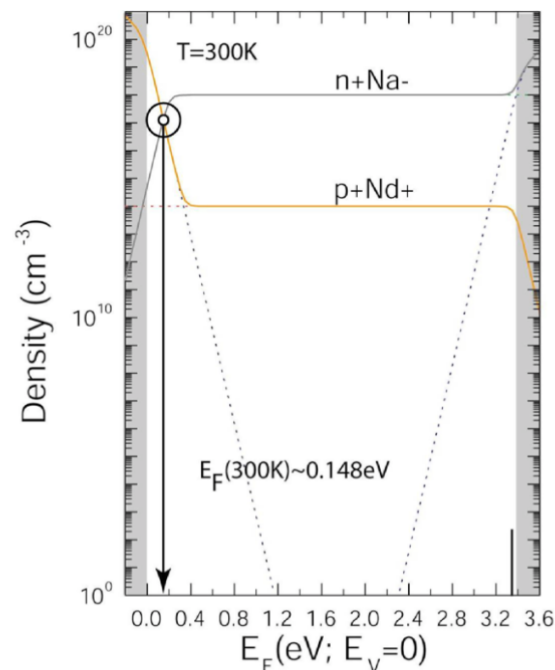
Graphical Solution for Locating the Fermi Level

Charge Neutrality: $n + N_A^- = p + N_D^+$

Solve to find the Fermi Level



Example for GaN ($N_A=10^{18}/\text{cm}^3$, $N_D=10^{14}/\text{cm}^3$)



Temperature dependence of mobile carrier density in doped Silicon

Semiconductor doping

Controlling resistivity of semiconductors by doping

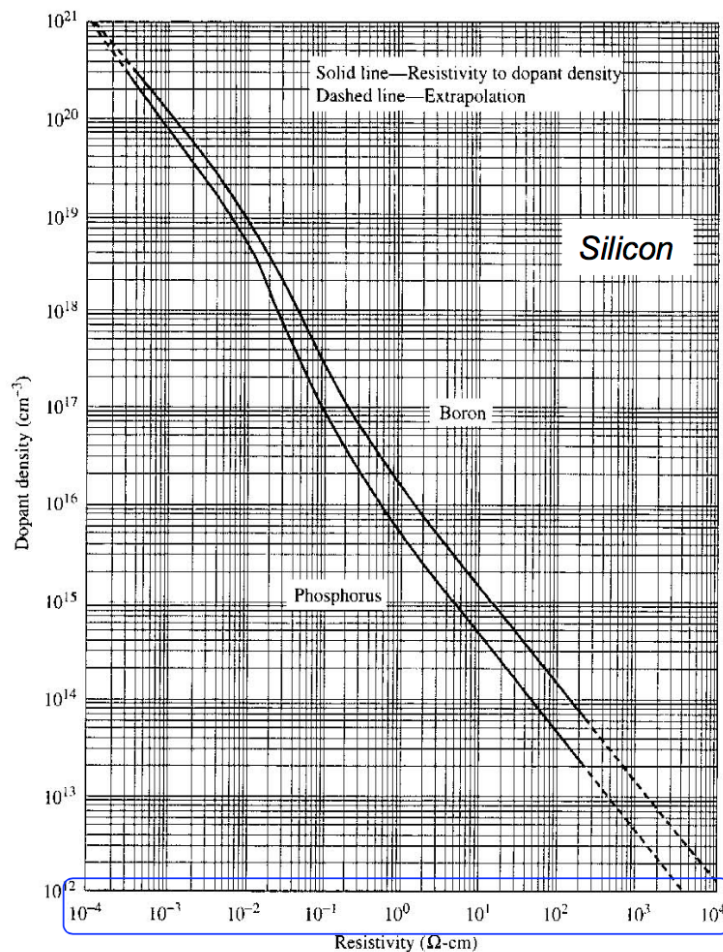


FIGURE 1.15 Dopant density versus resistivity at 23°C (296 K) for silicon

Resistivity of

- Metals $\sim 10^{-6}$ Ohm-cm
- SiO₂ (insulator) $\sim 10^{14}$ Ohm-cm

Various methods of “Doping”

Traditional Bulk Semiconductors -

- Impurity doping (bulk, uniform)
- Impurity doping (graded, delta-doping) (Since '50s)

Impurity + Heterostructures -

- Modulation Doping (Since '80s)

Polar Semiconductor Heterostructures –

- Polarization-induced doping (Since late '90s)

Other “Dynamic” methods –

- Electrostatic gating
- Optical excitation
- Thermal excitation

These are the various methods for Creating mobile carriers in the conduction & valence bands

Mobility and Transport

Charge Transport: Drift

CHARGE TRANSPORT - DRIFT + DIFFUSION

(6)

Drift:

$v_d = \mu F$ ← Electric field.
 ↑
 Drift velocity Mobility = $\frac{e\tau}{m^*}$ ← scattering time, order $\sim 10^{-12}$ s = ps.

$$J_{\text{drift}} = \underbrace{en}_{\text{flux}} v_d = en\mu F$$

v_d -F not always linear; v_d -F plots saturate.

$\mu \rightarrow$ depends on

- Temperature (Phonons)
- Doping densities
- Impurities

$$l = v_d \tau = \text{"mean free path"}$$

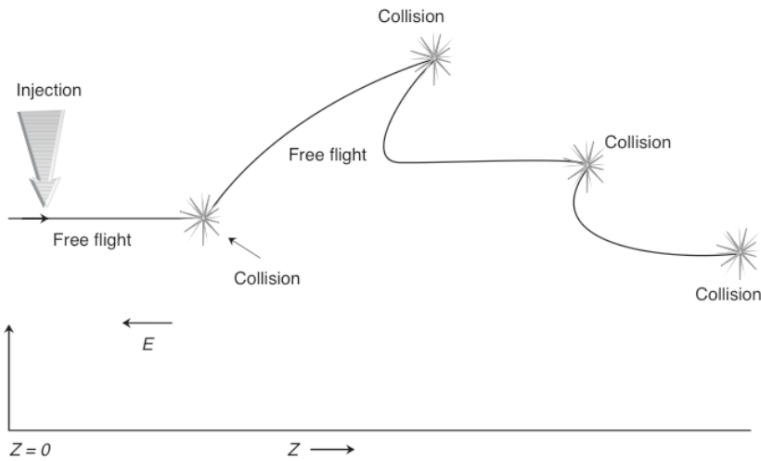
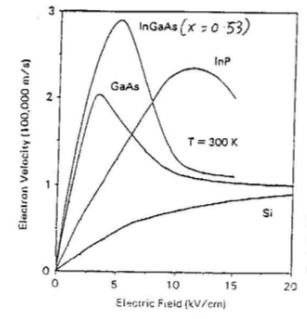
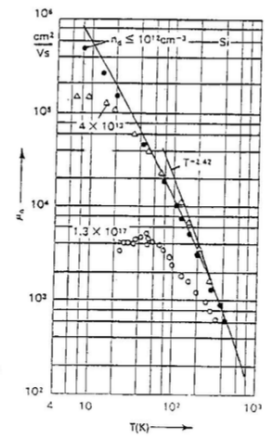
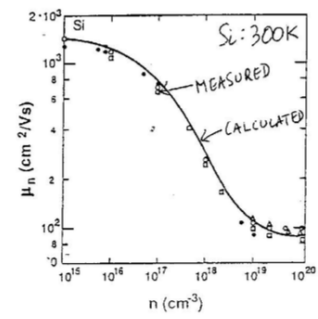
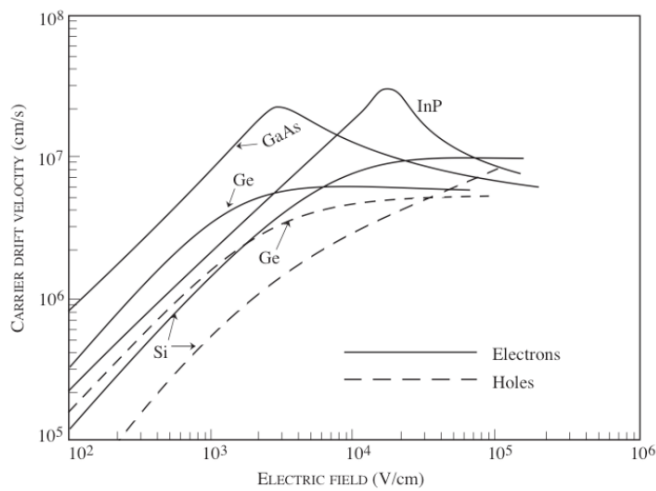


Table 1.6 Effective Mass and Mobility for Various Semiconductors

Material	Effective Mass			Mobility		
	m_e^*	m_p^*	m_{p1}^*	μ_e	μ_h	
IV	Si	0.26	0.55	0.24	1350	475
	Ge	0.56	0.37	-	3800	1900
III-V	GaP	0.12	0.86	0.14	200	120
	GaAs	0.065	0.45	0.082	8500	420
	GaSb	0.049	0.33	0.056	7700	1400
II-VI	InP	0.077	0.56	0.12	6060	150
	InAs	0.027	0.41	0.024	33000	460
	InSb	0.0135	0.438	0.016	78000	1700
II-VI	ZnS	0.28	1.4	-	140	5
	ZnSe	0.17	-0.7	-	530	28
	ZnTe	0.122	0.42	0.17	340	110
	CdS	0.171	-5	-	350	15
	CdTe	0.112	>1.0	-	650	80



Compound Semiconductor Families

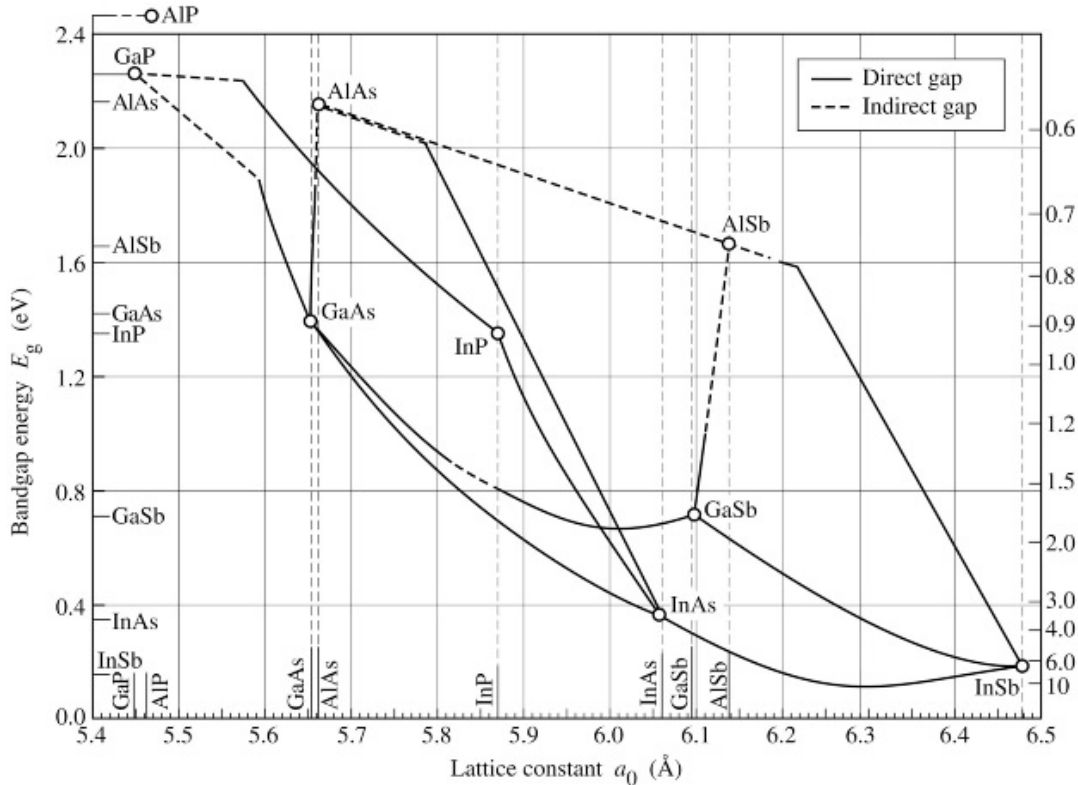
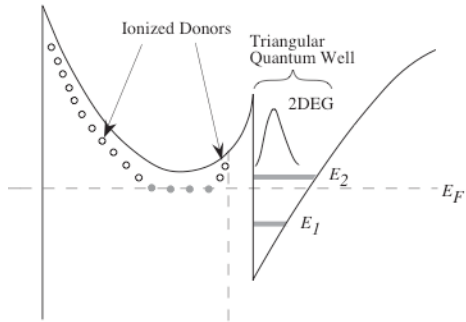


Fig. 7.6. Bandgap energy and lattice constant of various III-V semiconductors at room temperature (adopted from Tien, 1988).

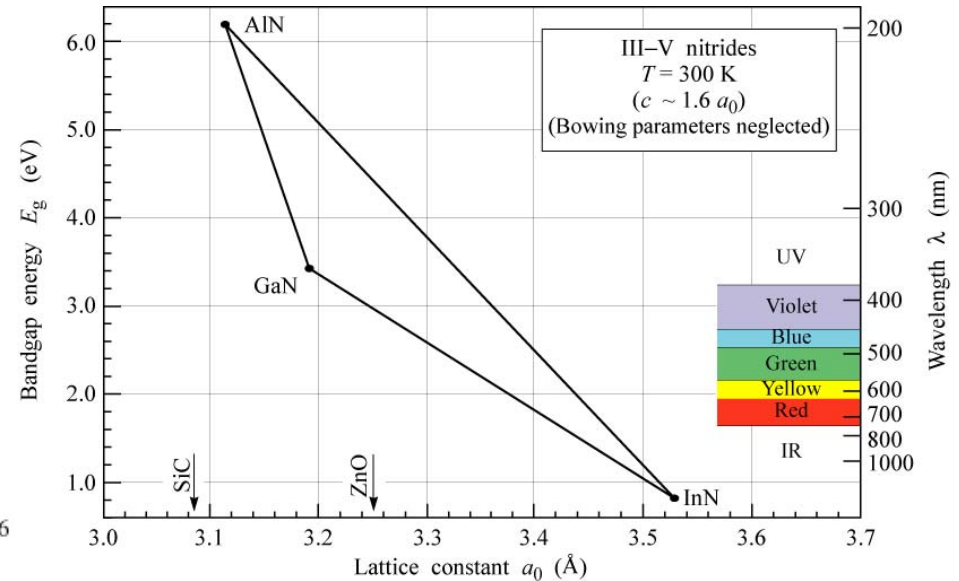


Fig. 12.12. Bandgap energy versus lattice constant of III-V nitride semiconductors at room temperature.

E. F. Schubert

Major HFET families:

- GaAs-based (AlGaAs/GaAs) (strain-free, or pseudomorphic)
- InP based (InGaAs channels)
- 6.1 Angstrom/narrow gap channels (generally grown metamorphically on GaAs)
- GaN-based (AlGaN/GaN and AlN/GaN) (typically pseudomorphic)

Compound Semiconductor Families

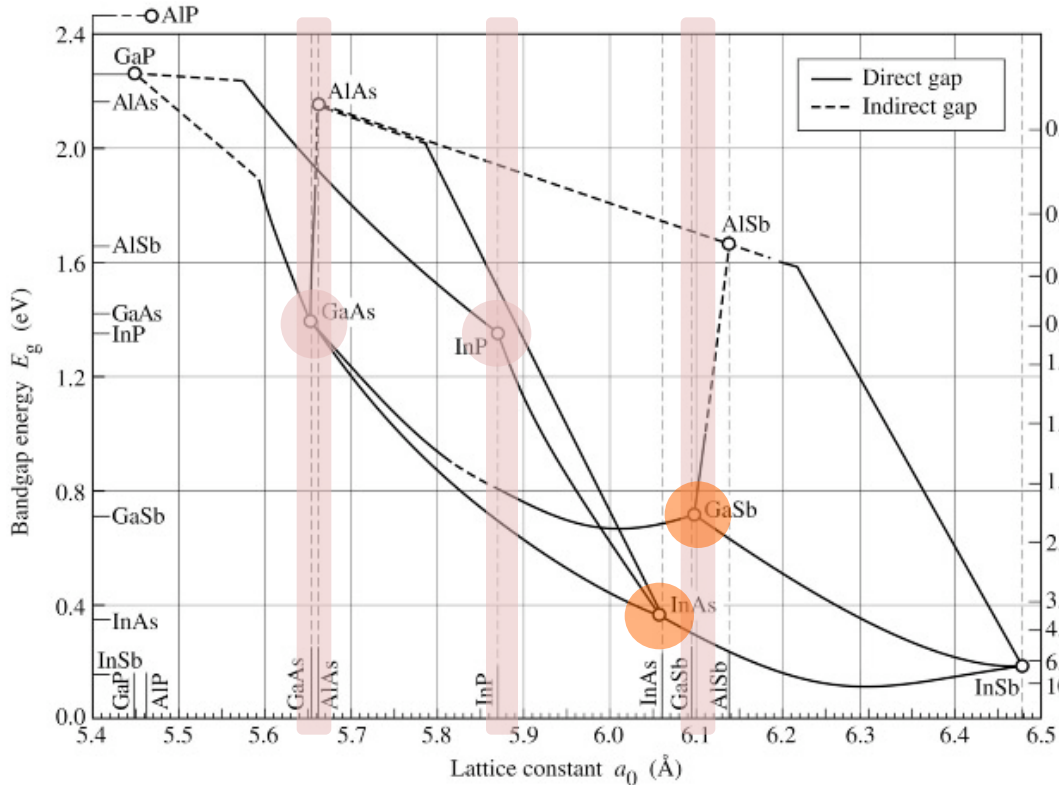
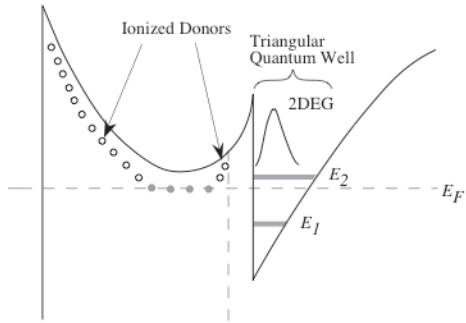


Fig. 7.6. Bandgap energy and lattice constant of various III-V semiconductors at room temperature (adopted from Tien, 1988).

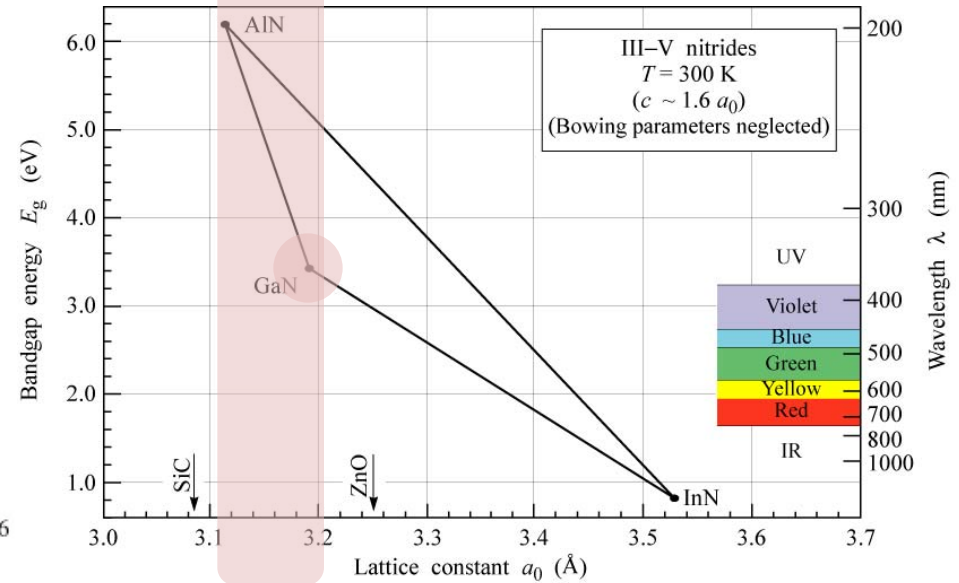


Fig. 12.12. Bandgap energy versus lattice constant of III-V nitride semiconductors at room temperature.

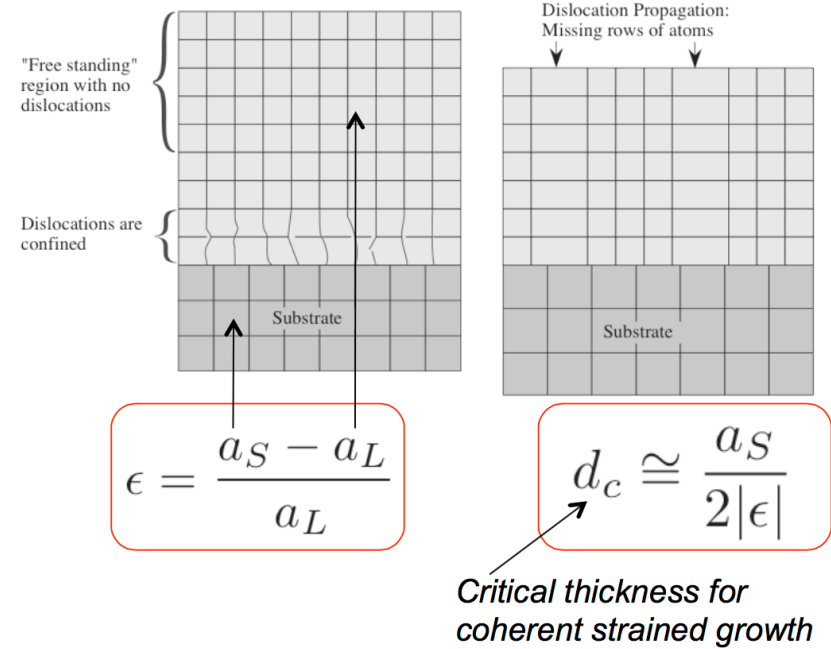
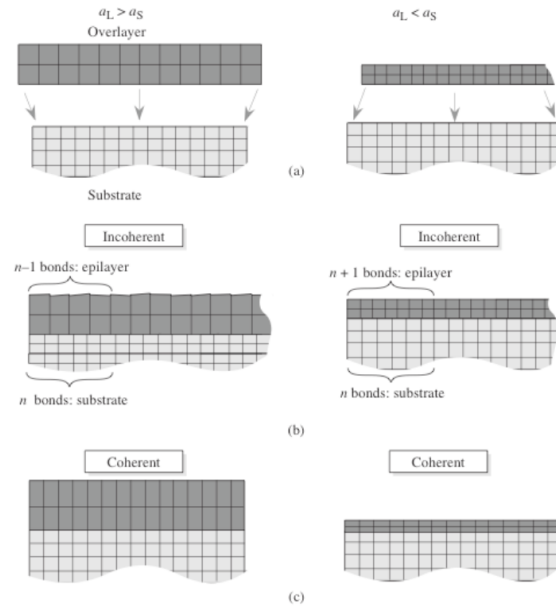
E. F. Schubert

Major HFET families:

- GaAs-based (AlGaAs/GaAs) (strain-free, or pseudomorphic)
- InP based (InGaAs channels)
- 6.1 Angstrom/narrow gap channels (generally grown metamorphically on GaAs)
- GaN-based (AlGaN/GaN and AlN/GaN) (typically pseudomorphic)

Compound Semiconductor Heterostructures: Strain

Lattice-Matching, Strain



Example: AlN on GaN, $d_c \sim 7$ nm

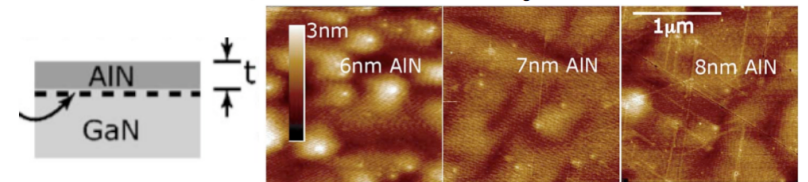


FIG. 1. (Color online) AFM images showing $2 \times 2 \mu\text{m}^2$ scans of the AlN surfaces after growth.

APPLIED PHYSICS LETTERS 90, 182112 (2007)

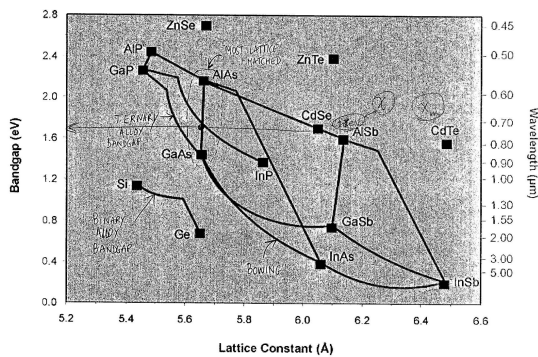
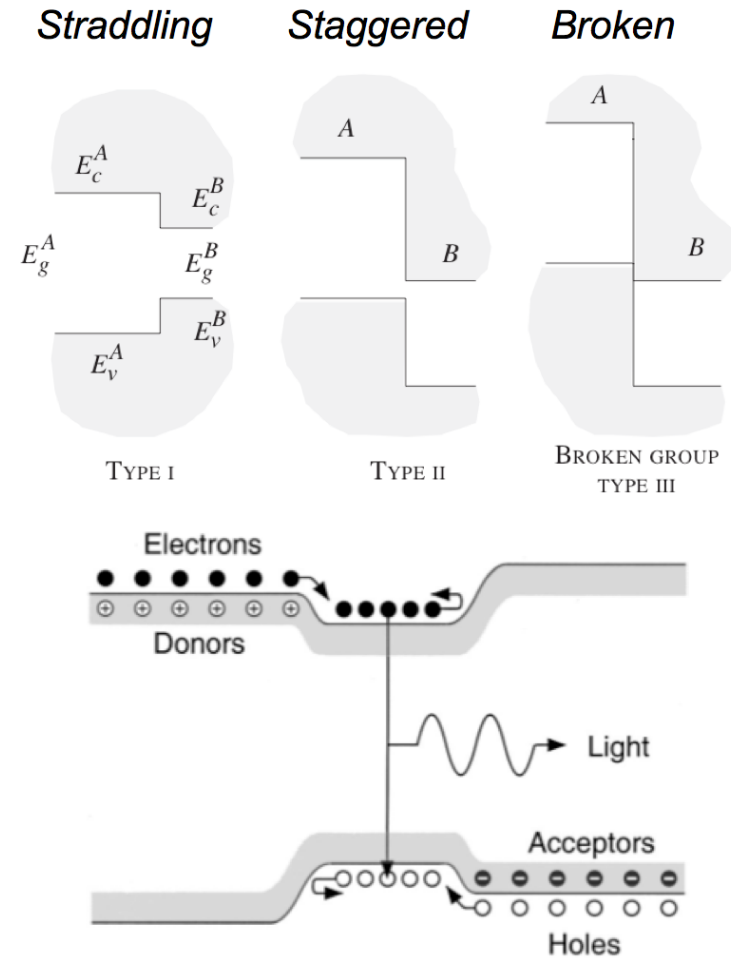
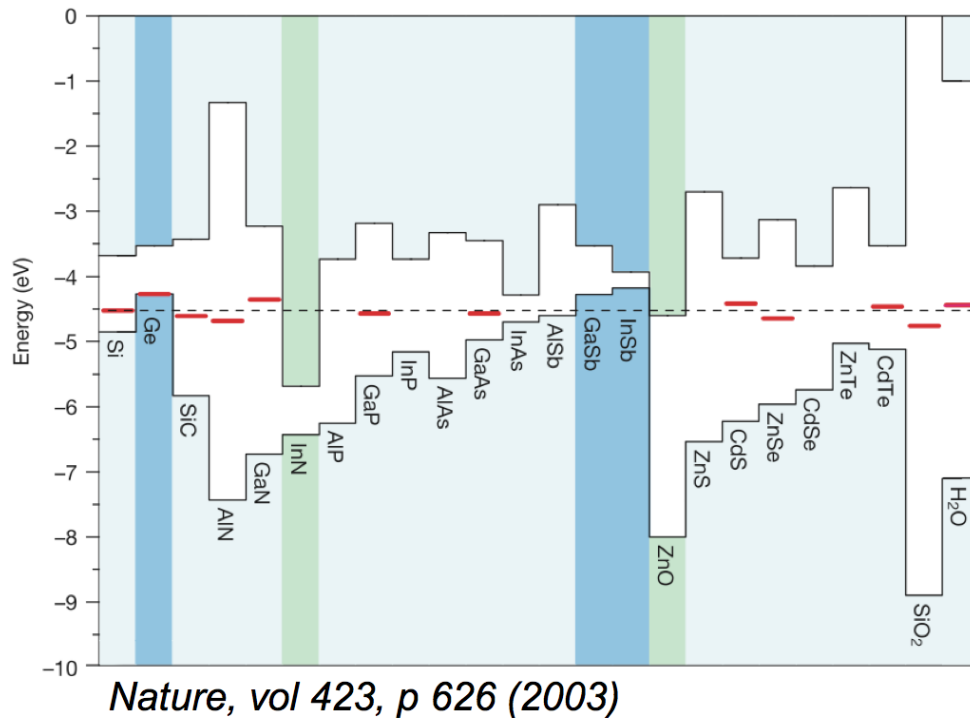


Figure 1.16: (a) The conceptual exercise in which an overlayer with one lattice constant is placed without distortion on a substrate with a different lattice constant. (b) Dislocations are generated at positions where the interface bonding is lost. (c) The case is shown where the overlayer is distorted so that no dislocation is generated.

Compound semiconductors: Heterostructures

Semiconductor Heterostructures



Semiconductor bands line up with each other in 3 ways.

Based on the lineups, one can create

- Barriers
- Wells
- Quasi-Electric fields

For both electrons and holes independently with suitable material choices.

Example –
Double Heterostructure LED/Laser

Being the Quantum Mechanic

$$\left[-\frac{\hbar^2}{2m^*} \frac{d^2}{dx^2} + V(x)\right]\psi(x) = E\psi(x)$$

$$V(x) = 0 \text{ for } -L \leq x \leq +L$$

$$V(x) = \infty \text{ for } |x| \geq L$$

$$\psi(x) = Ae^{ikx} + Be^{-ikx}$$

$$k = \frac{2\pi}{\lambda} = \sqrt{\frac{2m^*(E - V)}{\hbar^2}}$$

$$\psi(+L) = \psi(-L) = 0 \rightarrow k_n = \frac{n\pi}{2L}$$

$$\psi_{\text{even}}(x) = A_n \cos\left(\frac{n\pi}{2L}x\right) \text{ for } n = \pm 1, \pm 2, \dots$$

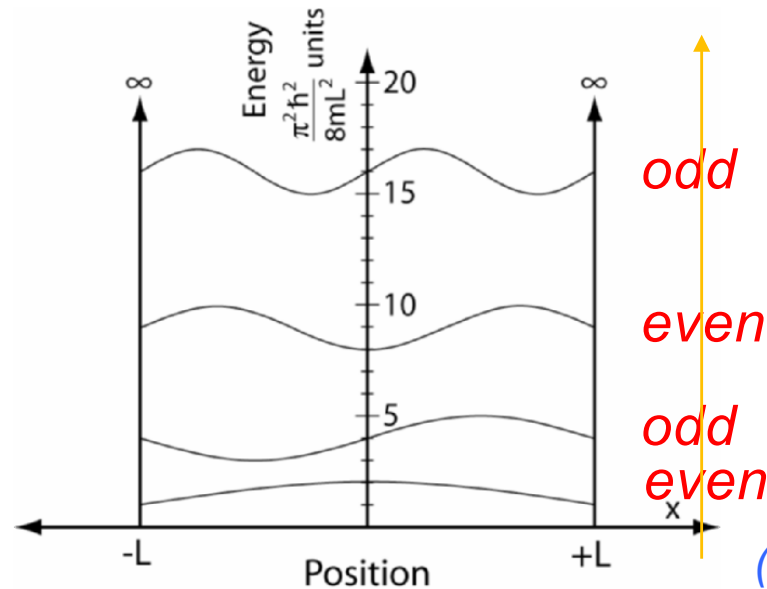
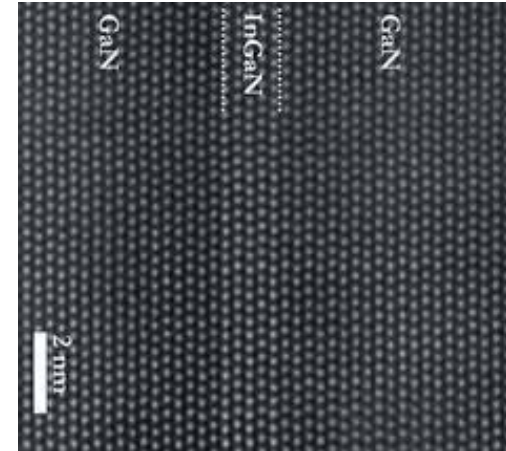
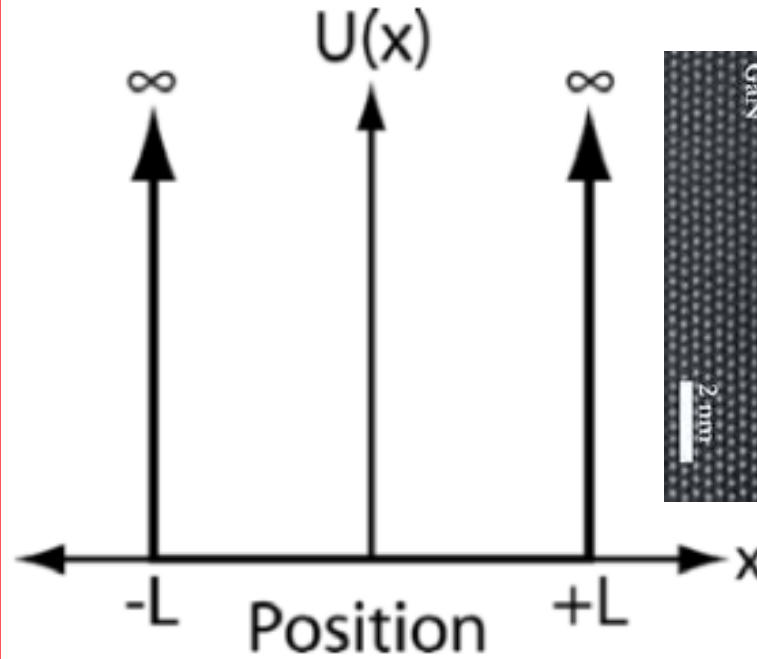
$$\psi_{\text{odd}}(x) = A_n \sin\left(\frac{n\pi}{2L}x\right) \text{ for } n = \pm 2, \pm 4, \dots$$

$$E_1^\infty = \frac{\pi^2 \hbar^2}{8m^* L^2} = \frac{\pi^2 \hbar^2}{2m^* L_w^2}$$

$$E_1^\infty = \frac{3.76}{\left(\frac{m^*}{m_0}\right) \left(\frac{L_w}{10 \text{ nm}}\right)^2} \text{ meV}$$

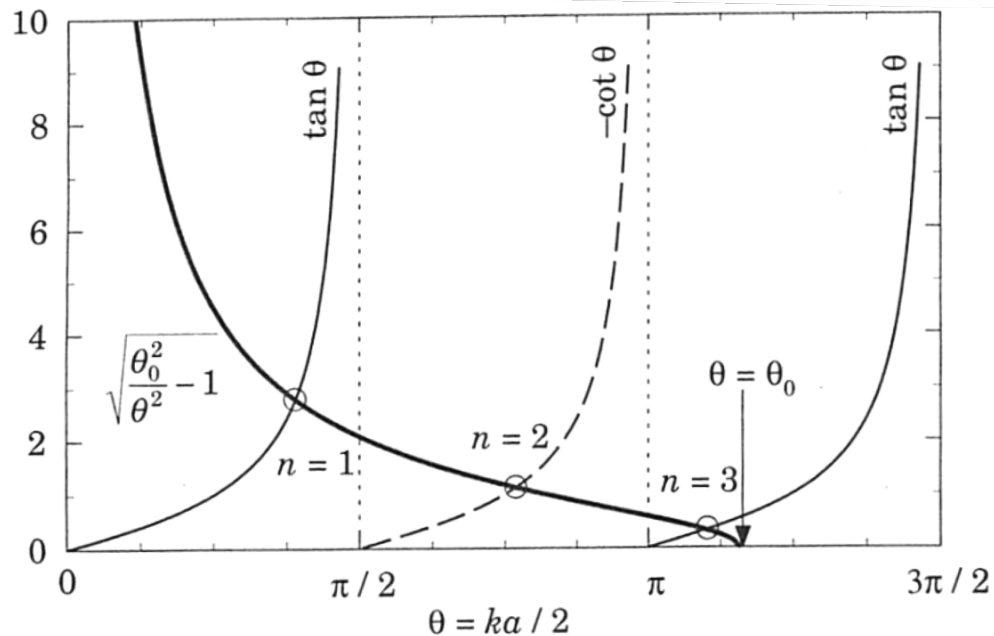
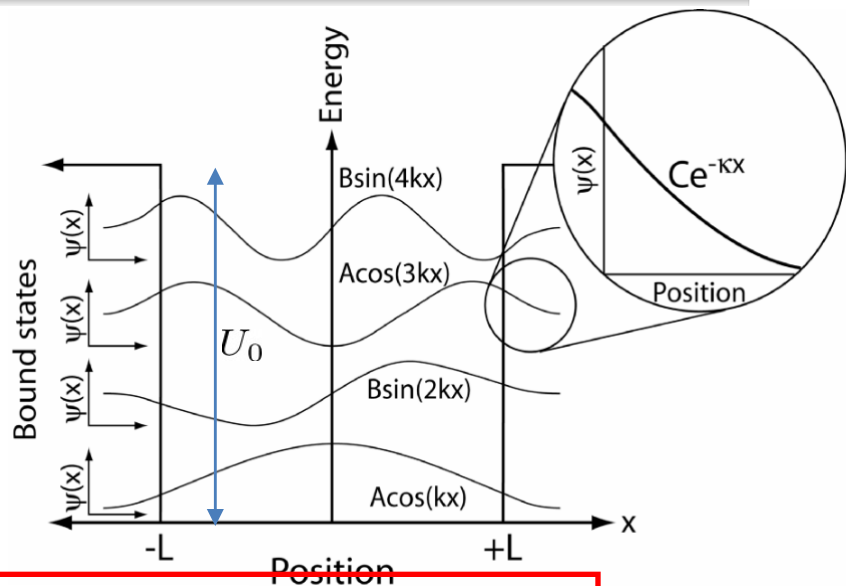
$$E_n = n^2 E_1^\infty$$

The particle in a box problem



(Rockett)

Being the Quantum Mechanic



$$\frac{d^2 \psi}{dx^2} + \kappa^2 \psi = 0$$

$$\kappa^2 = \frac{2mE}{\hbar^2}$$

$$\begin{aligned} \psi(x) &= Ce^{\kappa x} & x < -L \\ \psi(x) &= A \cos(kx) + B \sin(kx) & -L < x < +L \\ \psi(x) &= De^{-\kappa x} & x > +L \end{aligned}$$

$$k^2 = -\frac{2m}{\hbar^2}(U_0 + |E|) > 0$$

$$\sqrt{\frac{2mU_0}{\hbar^2 k^2} - 1} = \begin{cases} \tan(kL) & \text{Even solutions} \\ -\cot(kL) & \text{Odd solutions} \end{cases}$$

The particle in a box problem

FIGURE 4.2. Graphical solution of equation (4.12) for a square well in GaAs with depth $V_0 = 0.3$ eV and width $a = 10$ nm, giving $\theta_0^2 = 13.2$. There are three bound states.

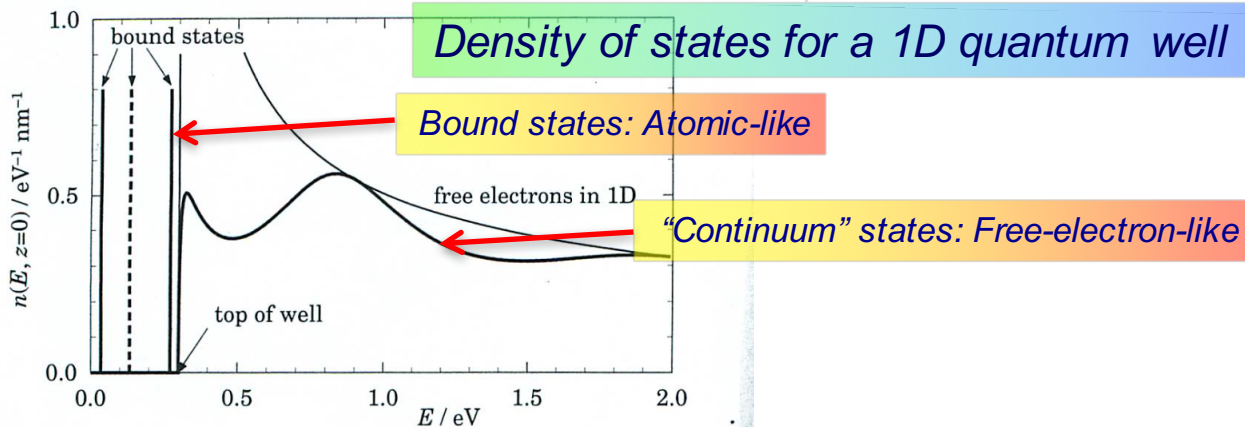


FIGURE 4.3. Local density of states $n(E, z = 0)$ in the middle of a square well in GaAs of width 10 nm and depth 0.3 eV. The result for free electrons, proportional to $E^{-1/2}$, is shown for comparison.

(Rockett/Davies)

Being the Quantum Mechanic: Quantum well states

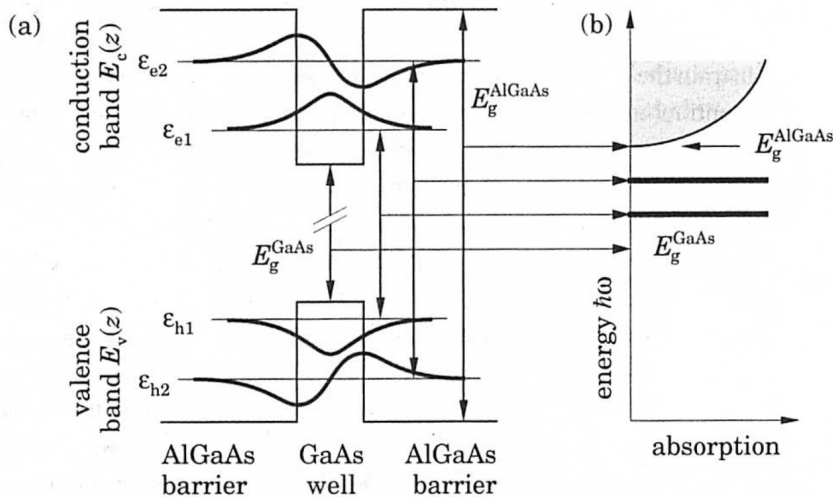


FIGURE 1.3. Optical absorption in a quantum well formed by a layer of GaAs surrounded by AlGaAs. (a) Potential well in conduction and valence band, showing two bound states in each; the energy gap of GaAs is really much larger than this diagram implies. (b) Transitions between states in the quantum well produce absorption lines between the band gaps of the GaAs well and AlGaAs barrier.

Quasi-2D systems: Quantum Wells

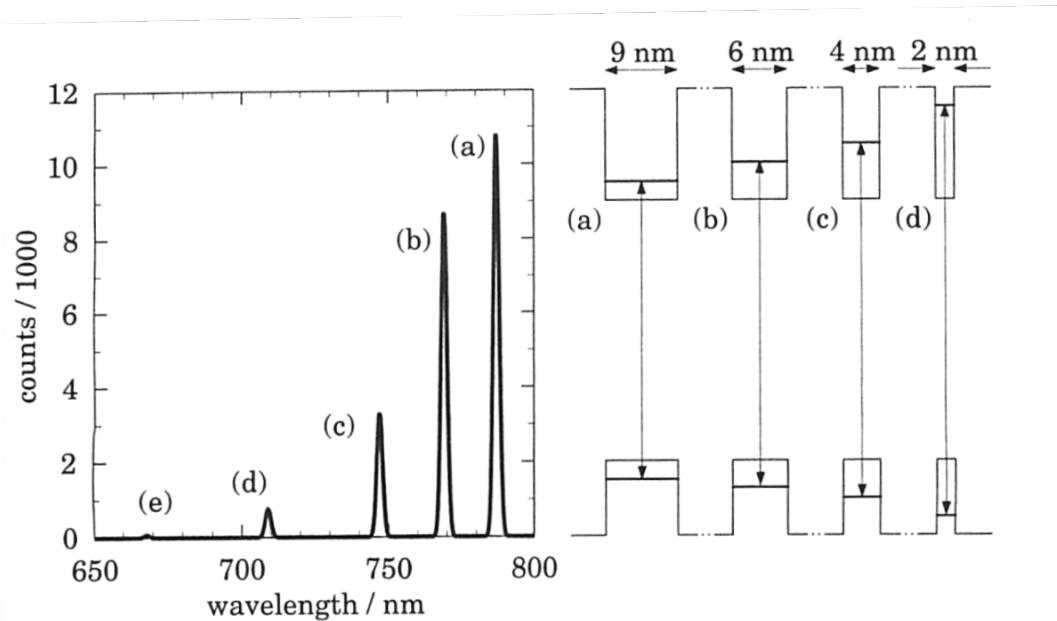


FIGURE 1.4. Photoluminescence as a function of wavelength for a sample with four quantum wells of different widths, whose conduction and valence bands are shown on the right. The barriers between the wells are much thicker than drawn. [Data kindly supplied by Prof. E. L. Hu, University of California at Santa Barbara.]

Photoluminescence spectra of quantum wells

(Davies)

Being the Quantum Mechanic: Designer Quantum wells

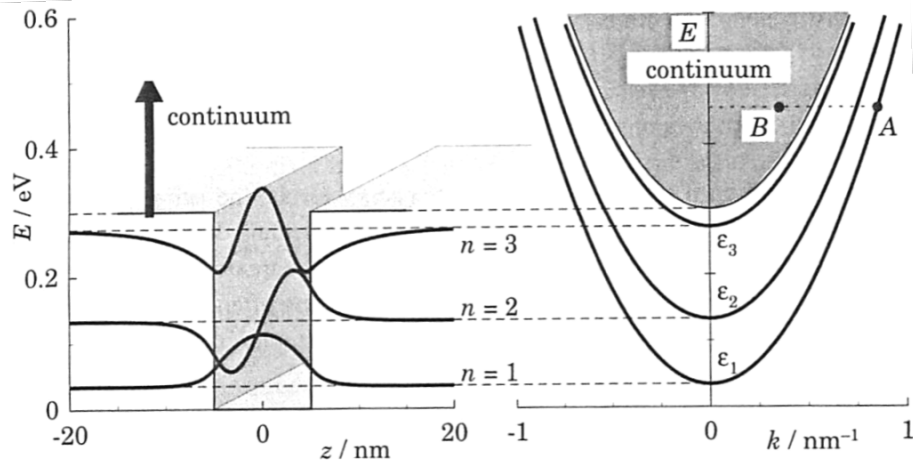


FIGURE 4.9. Quasi-two-dimensional system in a potential well of finite depth. Electrons with the same total energy can be bound in the well (A) or free (B).

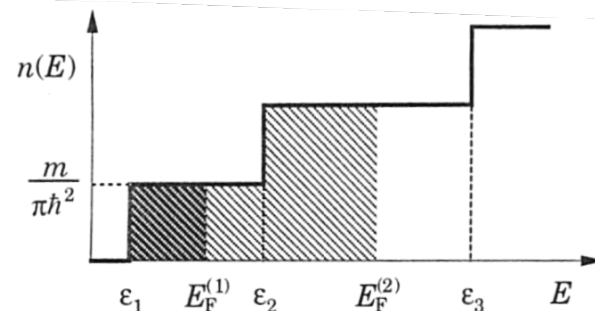


FIGURE 4.8. Occupation of steplike density of states for a quasi-two-dimensional system. Only one subband is occupied if the Fermi energy takes the lower value $E_F^{(1)}$, but two are occupied at the higher value $E_F^{(2)}$.

Rectangular quantum wells

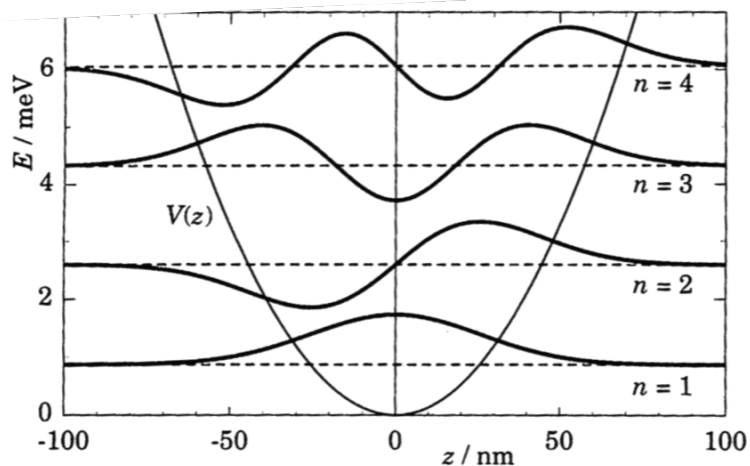


FIGURE 4.4. Potential well $V(z)$, energy levels, and wave functions of a harmonic oscillator. The potential is generated by a magnetic field of 1 T acting on electrons in GaAs.

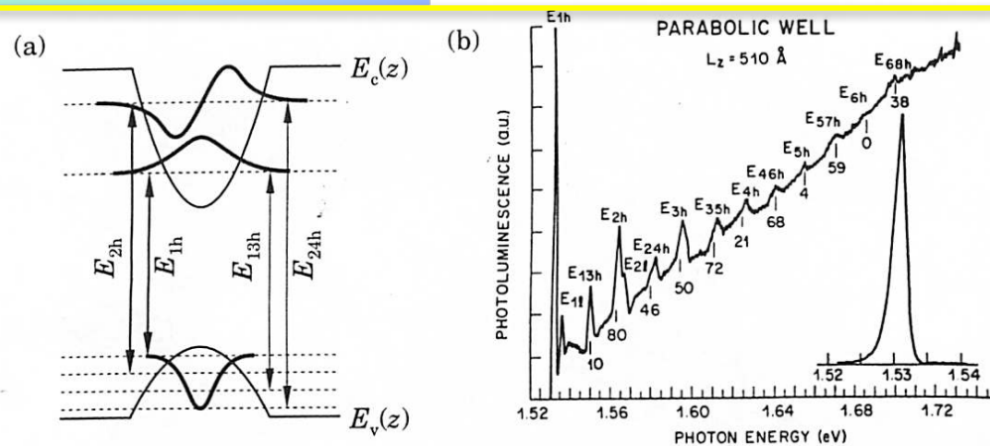
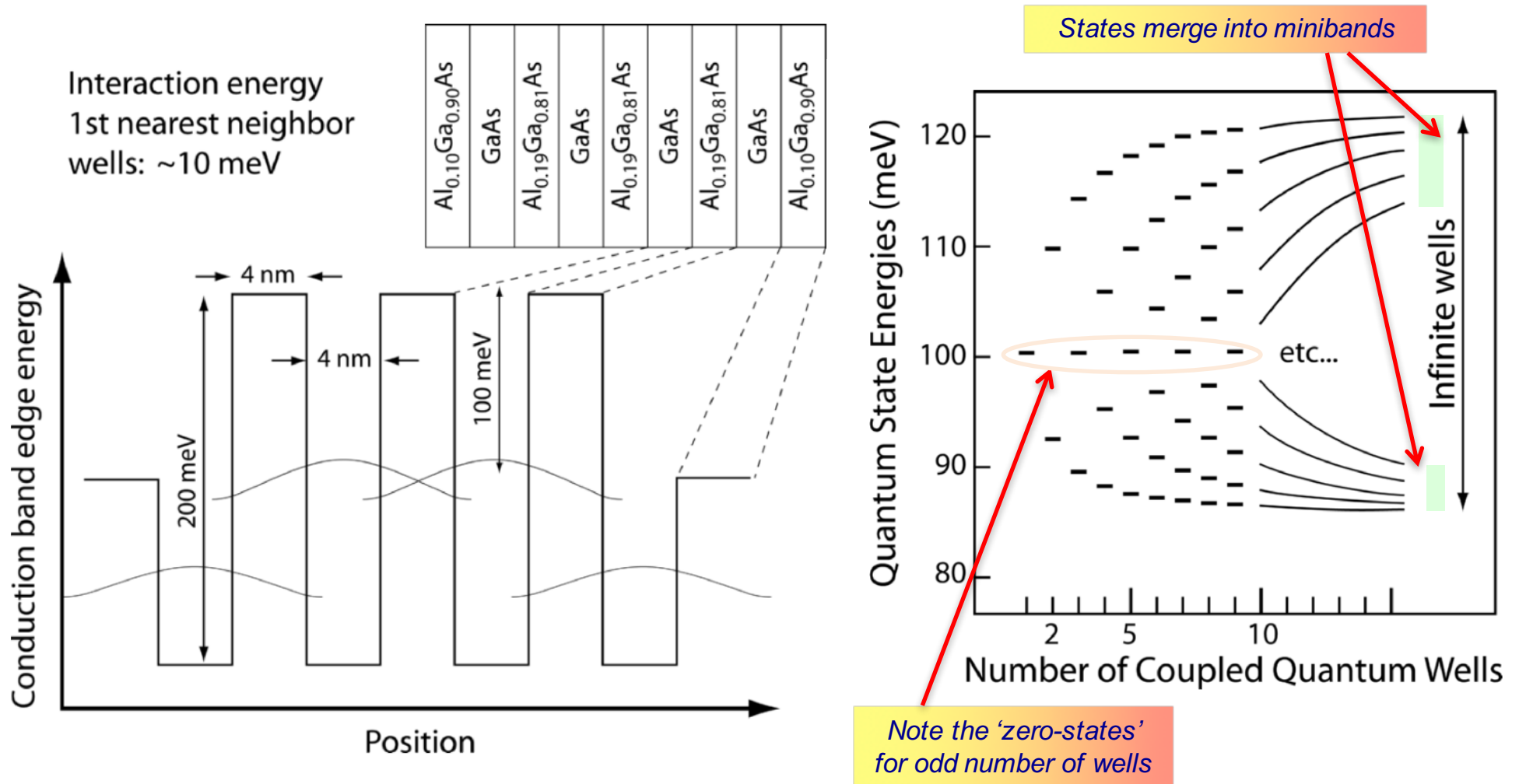


FIGURE 4.5. (a) Parabolic potential in both conduction and valence bands grown into GaAs by a graded composition of $\text{Al}_x\text{Ga}_{1-x}\text{As}$. The band gap has been reduced in this sketch, and only heavy holes are shown. (b) Photoluminescence in parabolic wells. [From Miller et al. (1984).]

Parabolic quantum wells: Harmonic Oscillator States!

(Davies)

Being the Quantum Mechanic: Multiple Quantum Wells



(Rockett)

The Quantum Mechanic: Designer Quantum States

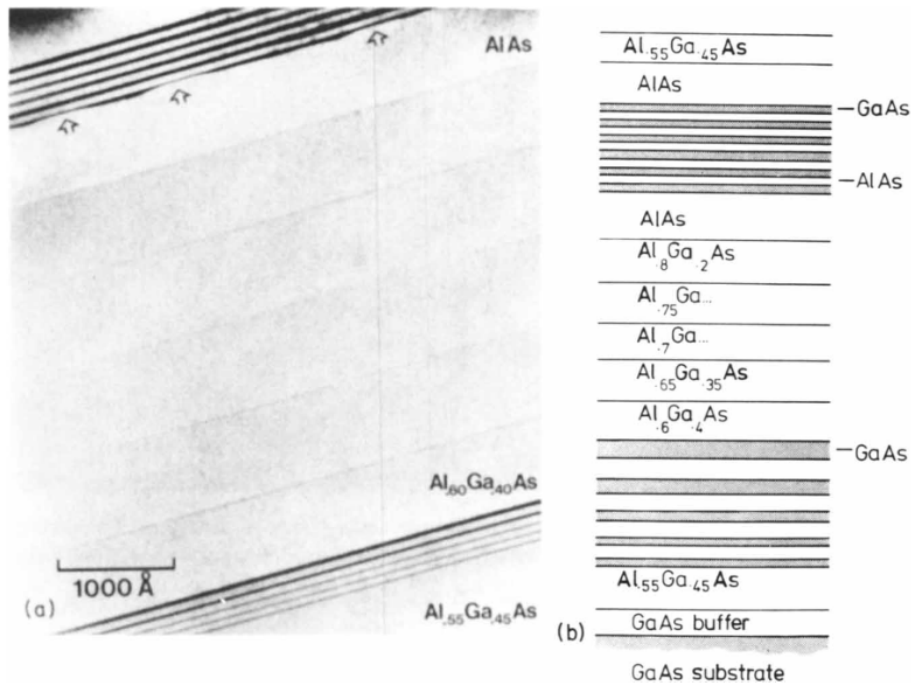
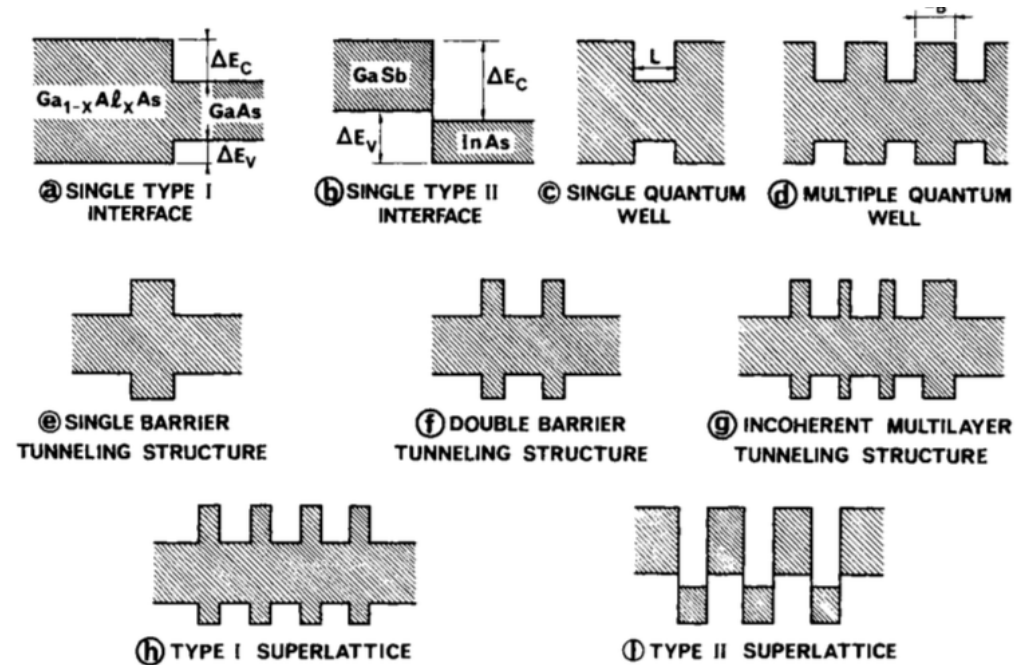


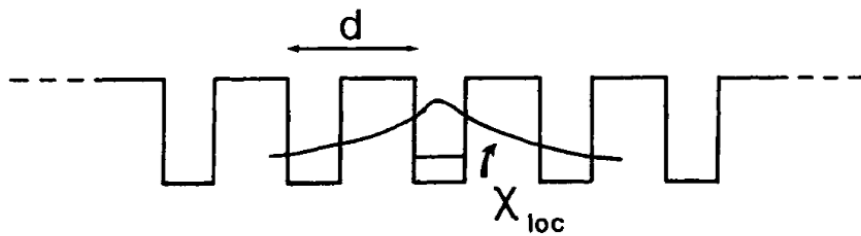
FIG. 3. (a) TEM characterization of a test sample grown by MOCVD. The growth sequence and the structure are shown in (b). The remarkable features are the sharpness of the very narrow GaAs layers (minimum $\approx 25 \text{ \AA}$) appearing at the lower right-hand side corner, the interface roughness showing up at the uppermost interface of the AlAs layer, and the subsequent smoothing of this roughness by the multilayer growth (upper left-hand side corner) (after Leys *et al.*⁶¹).



(Weisbuch/Vinter)

Heterostructure superlattices

SUPERLATTICES



N WELLS

N-DEGENERATE GROUND STATE

TIGHT-BINDING APPROXIMATION

$$\Psi_q(z) = \frac{1}{N^{1/2}} \sum e^{iqnd} \chi_{loc}(z-nd)$$

$$E = E_1 + S + 2T \cos qd$$

$$S = \int \chi_{loc}(z-d) V(z) \chi_{loc}(z-d) dz$$

$$T = \int \chi_{loc}(z-d) V(z) \chi_{loc}(z) dz$$

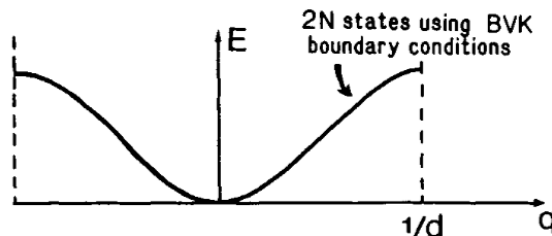


FIG. 15. Tight-binding model of superlattices.

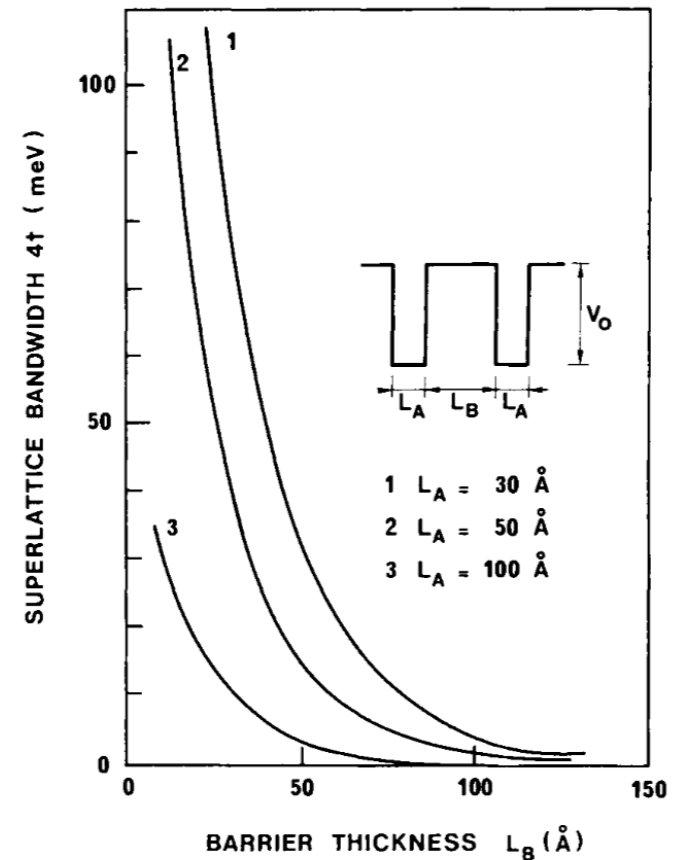


FIG. 16. Tight-binding model of GaAs/GaAlAs superlattices: Variation of the fundamental state bandwidth $[4t]$, of Eq. (30) in the tight-binding model as a function of barrier thickness for three different well thicknesses. $X = 0.2$; $V_0 = 212$ meV (after Bastard¹²⁵).

(Weisbuch/Vinter)

Heterostructure superlattices

SUPERLATTICES

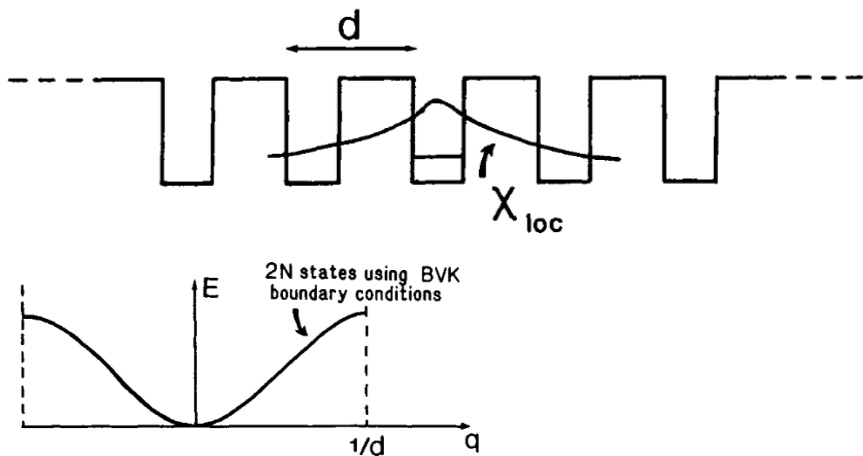


FIG. 15. Tight-binding model of superlattices.

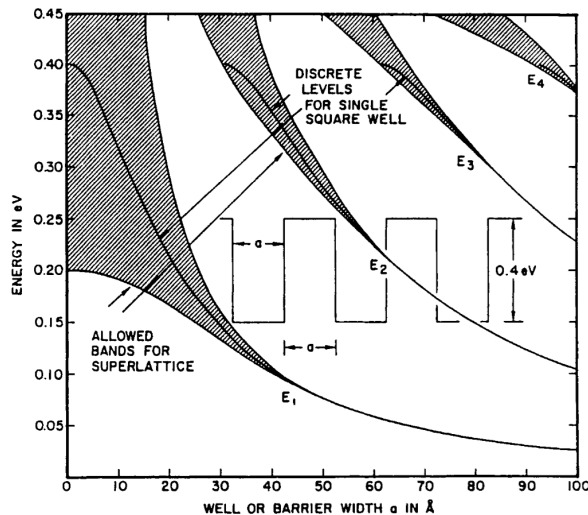


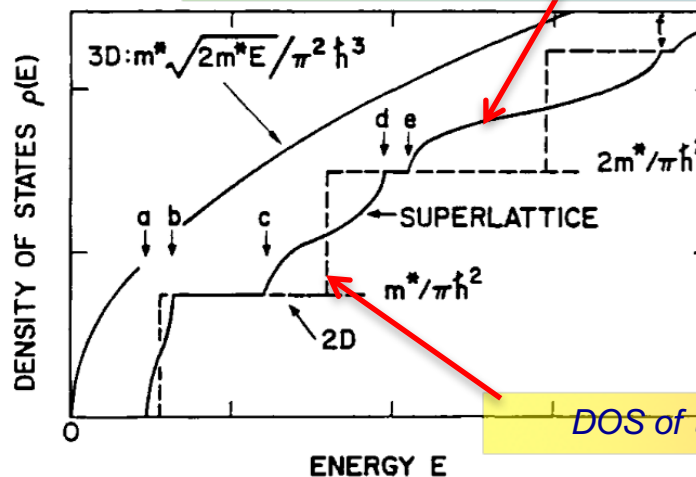
FIG. 18c. Allowed energy bands E_1 , E_2 , E_3 , and E_4 (hatched) calculated as a function of well or barrier width ($L_z = L_B = a$) in a superlattice with a barrier potential $V = 0.4$ V. Note the existence of forbidden gaps even above the barrier potential (Reprinted with permission from World Scientific Pub. Co., L. Esaki, "Recent Topics in Semiconductor Physics" (H. Kamimura and Y. Toyozawa, eds.), 1983.)

$$E = E_1 + S + 2T \cos qd$$

$$\varepsilon_{n^*}(q, k_{\perp}) = \hbar^2 k_{\perp}^2 / 2m + \varepsilon_n(q)$$

$$\rho_n(\varepsilon) = N \frac{m^*}{\pi \hbar^2} \arccos \left(\frac{\varepsilon_i - E_i - S_i}{2t_i} \right)$$

Density of states of a superlattice

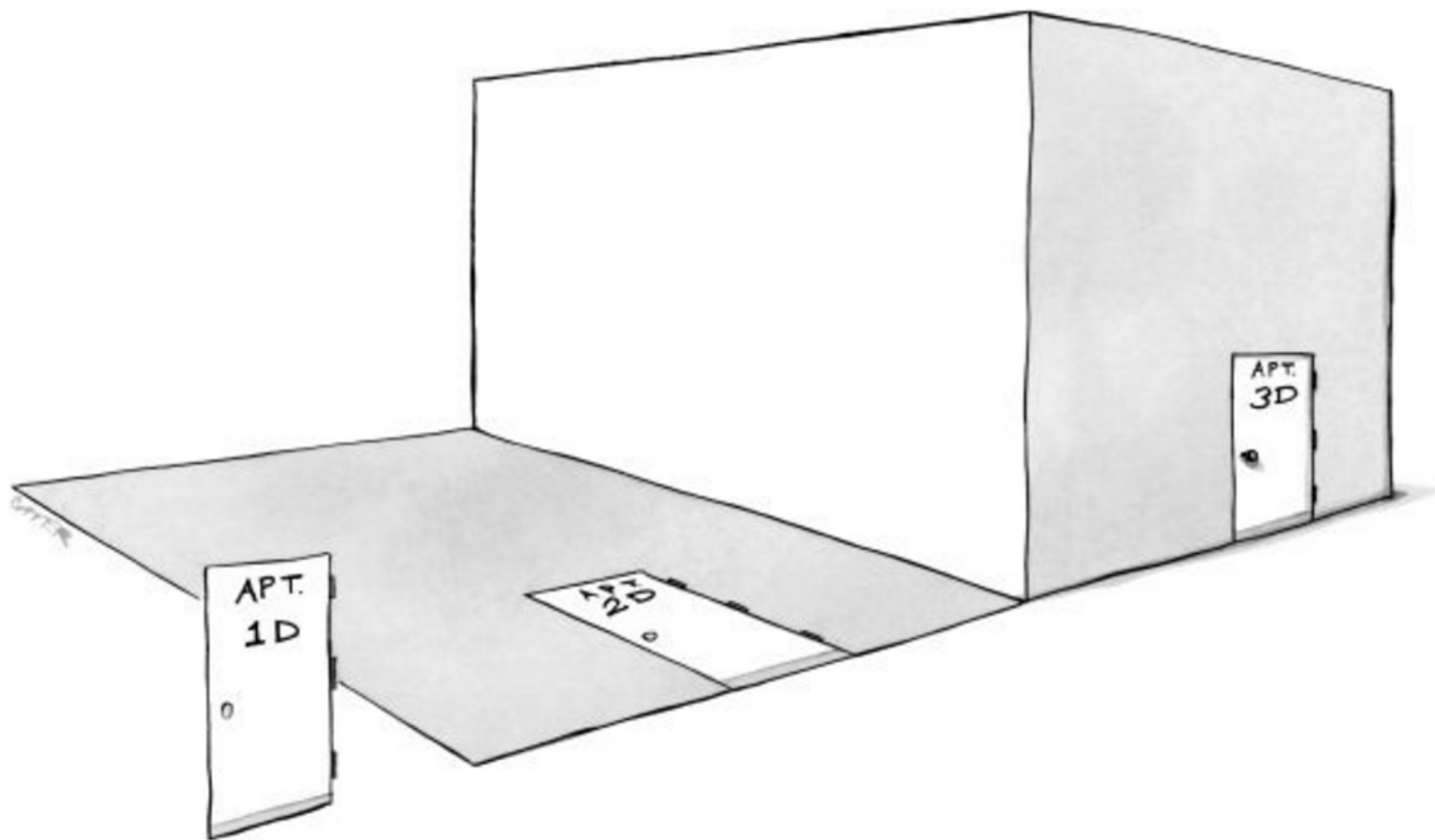


DOS of uncoupled 2D wells

FIG. 17. Comparison of the DOS of a superlattice with that of a 2D system (—) and a 3D isotropic system. Note the broadening of the superlattice band with band index as the overlap of wave functions increases with energy E in the tight-binding description, increasing the transfer matrix element t_i (Reprinted with permission from World Scientific Pub. Co., L. Esaki, "Recent Topics in Semiconductor Physics" (H. Kamimura and Y. Toyozawa, eds.), 1983.)

(Weisbuch/Vinter)

Lower dimensions have lower DOS!



Overview of Semiconductor Devices

3. OVERVIEW OF ELECTRONIC DEVICES 73

3.1 Diffusion and drift of carriers.....	74
3.1.1 Chemical potential	74
3.1.2 Carrier motion in a chemical potential gradient.....	74
3.2 Simple diodes	75
3.2.1 The junction contact potential.....	77
3.2.2 Biased junctions	81
3.2.3 Non-ideal diode behaviors	88
3.3 Schottky barriers and ohmic contacts.....	96
3.3.1 Ideal metal/semiconductor junctions	96
3.3.2 Real schottky diodes	101
3.4 Semiconductor heterojunctions	102
3.4.1 Heterojunctions at equilibrium.....	103
3.4.2 Heterojunctions as diodes	109
3.5 Transistors	111
3.5.1 Bipolar junction transistors	111
3.5.2 Field-effect transistors.....	114
3.6 Light-emitting devices.....	119
3.6.1 Light-emitting diodes.....	120
3.6.2 Laser diodes.....	124
3.7 Summary.....	134
3.8 Homework problems	136
3.9 Suggested readings & references.....	139

Rockett: MSS

$$F = -C \frac{d\mu}{dx}$$

$$J = q\mu_n n \frac{d\mu}{dx}$$

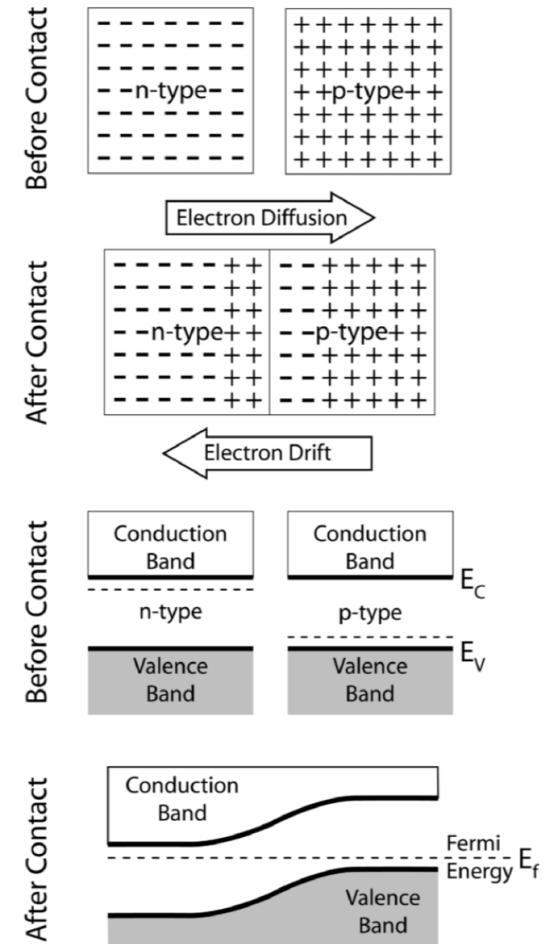
$$E = -\frac{dV}{dx} = \frac{d\mu}{dx}$$

$$\frac{d\mu}{dx} = \frac{k_B T}{qn} \frac{dn}{dx}$$

$$\frac{d\mu}{dx} = \frac{k_B T}{qn} \frac{dn}{dx} - \frac{dV}{dx}$$

Constitutive relations for charge transport in any semiconductor

(Rockett)

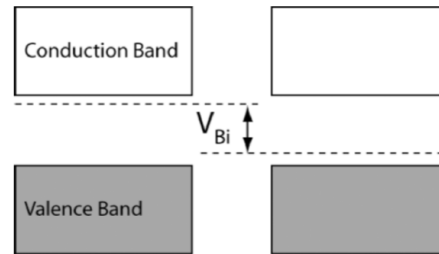


P-n diode electrostatics

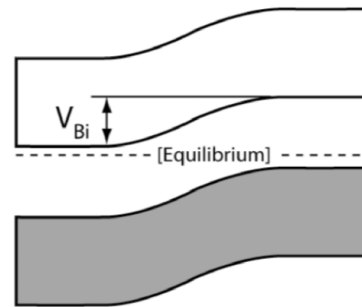
$$J = q\mu_n n \left[\frac{k_B T}{qn} \frac{dn}{dx} + E \right] = \left[\mu_n k_B T \frac{dn}{dx} + q\mu_n n E \right]$$

$$D = \mu_n k_B T / q$$

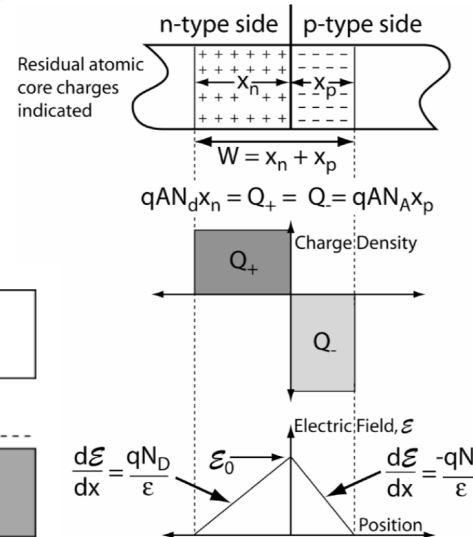
$$J = qD \frac{dn}{dx} + q\mu_n n E$$



Before Contact



After Contact



$$V_{bi} = \frac{qN_A x_p W}{2\epsilon}$$

$$x_p N_A = x_n N_D$$

Charge neutrality

$$W = x_p (1 + N_A/N_D)$$

$$x_p = W \frac{N_D}{N_A + N_D}$$

$$V_{bi} = \frac{qW^2}{2\epsilon} \frac{N_A N_D}{N_A + N_D}$$

$$V_{bi} = \frac{k_B T}{q} \ln \left[\frac{n_n}{n_p} \right]$$

$$qV_{bi} = E_{gap} + k_B T \ln \left[\frac{N_A N_D}{N_C N_V} \right]$$

$$V_{bi} = \frac{k_B T}{q} \ln \frac{N_A N_D}{n_i^2}$$

Built-in voltage of a p-n diode

$$W = \left[\frac{2\epsilon k_B T}{q^2} \left(\ln \frac{N_A N_D}{n_i^2} \right) \left(\frac{1}{N_A} + \frac{1}{N_D} \right) \right]^{1/2}$$

Depletion width of a p-n diode

(Rockett)

Breakdown voltage of pn diodes

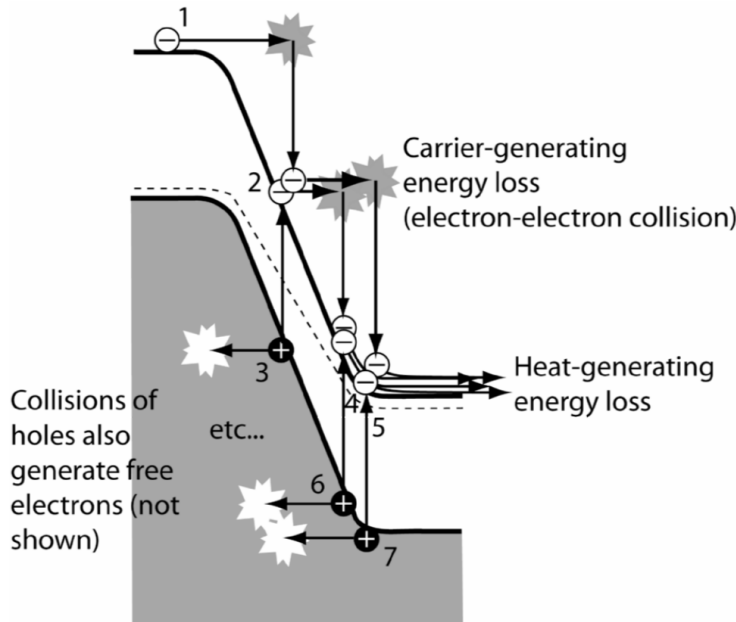


Figure 3.12: A schematic of the avalanche breakdown process.

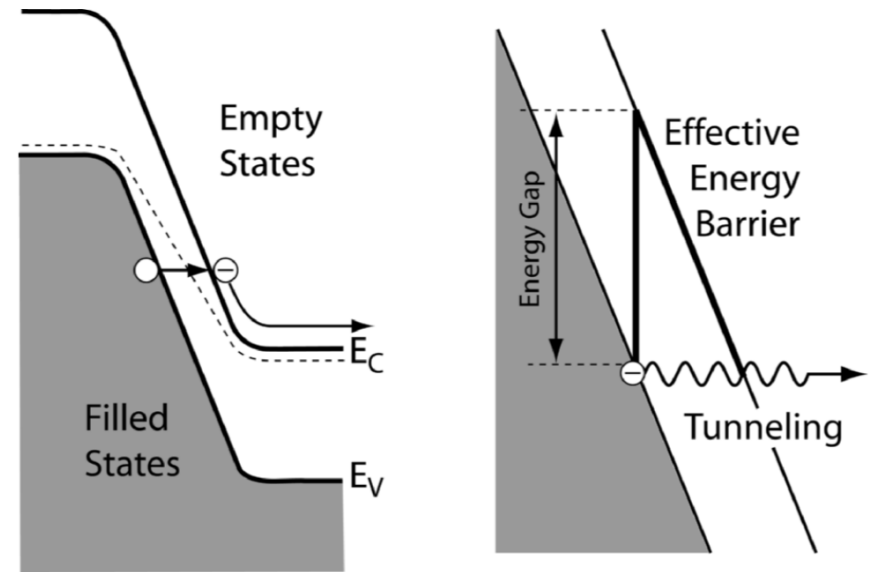
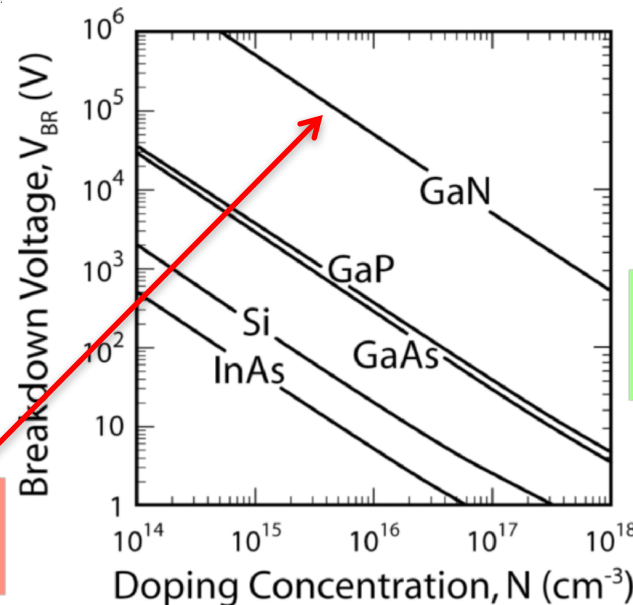


Figure 3.14: A schematic of the tunneling breakdown process.



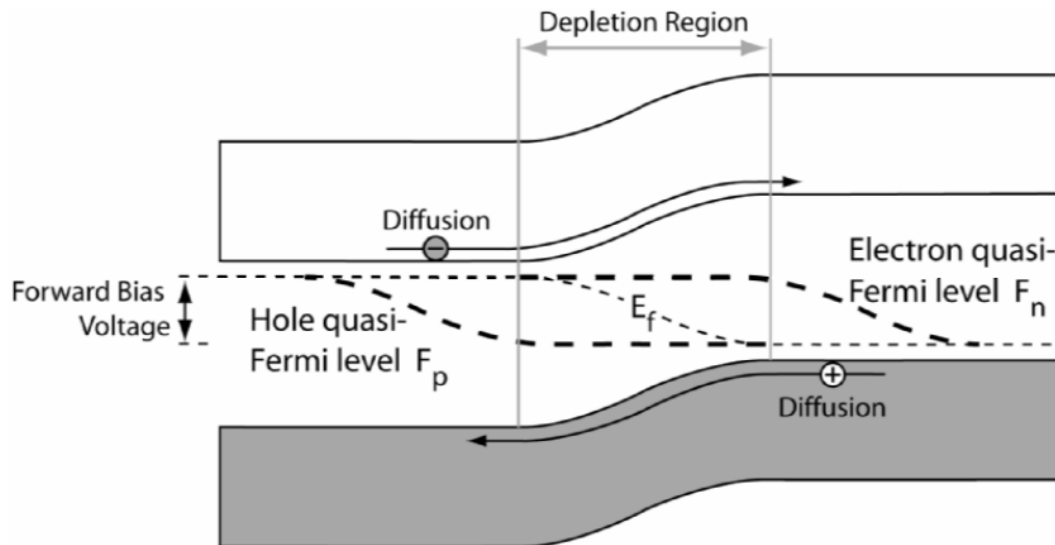
Wider bandgap semiconductors allow higher breakdown voltages

$$-V_{BR} = \frac{2\epsilon}{q} \left(\frac{E_{gap}}{m^* v \mu_e} \right)^2 \frac{N_A + N_D}{N_A N_D}$$

Avalanche breakdown voltage of a p-n diode

(Rockett)

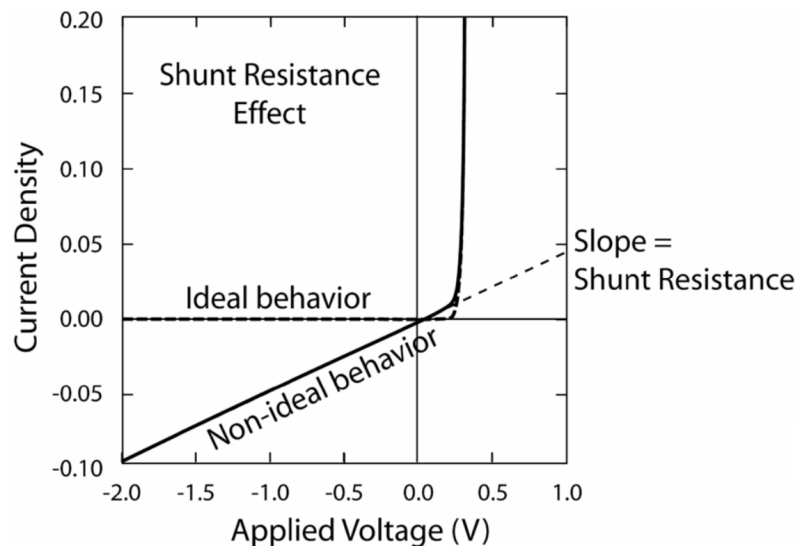
Electrostatics and current flow in a p-n diode



$$W = \left[\frac{2\epsilon(V_{bi} - V_{applied})}{q} \left(\frac{N_A + N_D}{N_A N_D} \right) \right]^{1/2}$$

Depletion width at an applied bias

$$\frac{1}{N_{net}(V_R)} = \frac{q\epsilon}{2} \frac{\partial C_{junction}^{-2}}{\partial V_R}$$



Non-ideal p-n diode: parallel leakage

$$J_{forward} = q \left(\frac{D_p}{L_p} p_n + \frac{D_n}{L_n} n_p \right) e^{qV_{applied}/k_B T} = J_0 e^{qV_{applied}/k_B T}$$

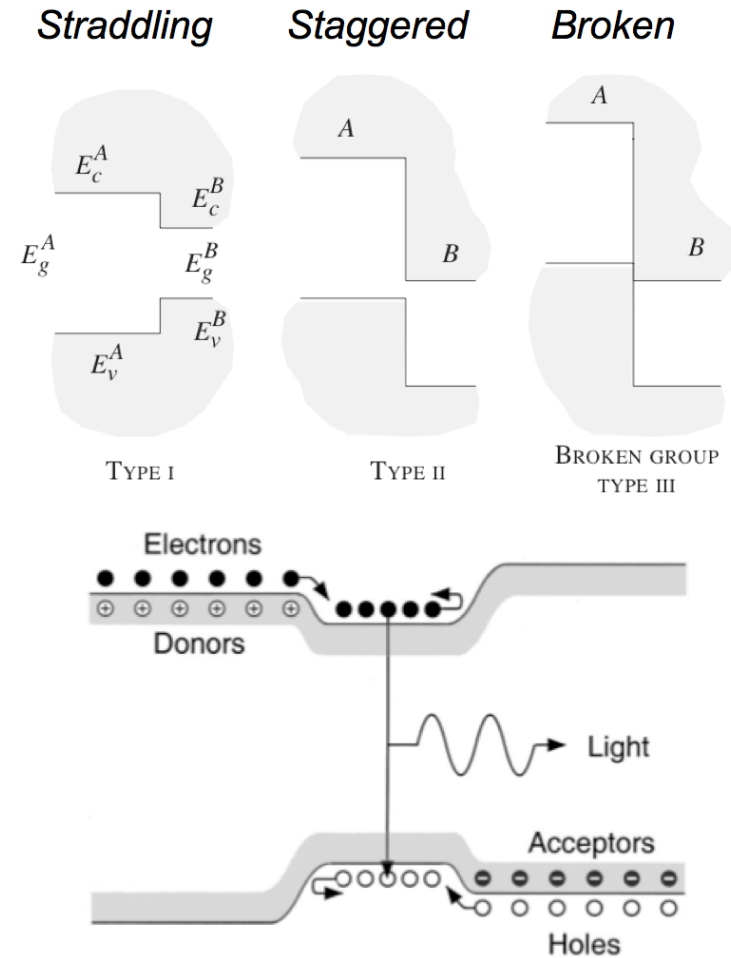
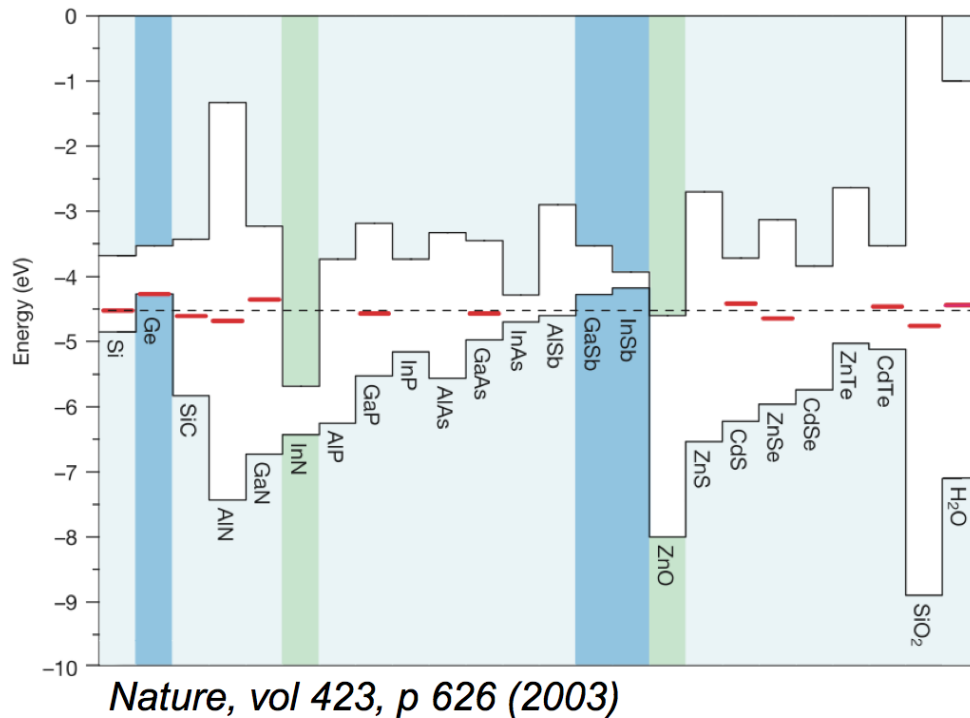
Current-voltage characteristics of a p-n diode

If one assumes a p⁺-n diode → $J_0 \approx -\frac{qD_p N_C N_V}{L_p N_D} e^{-E_{gap}/k_B T}$

(Rockett)

Compound semiconductors: Heterostructures

Semiconductor Heterostructures



Semiconductor bands line up with each other in 3 ways.

Based on the lineups, one can create

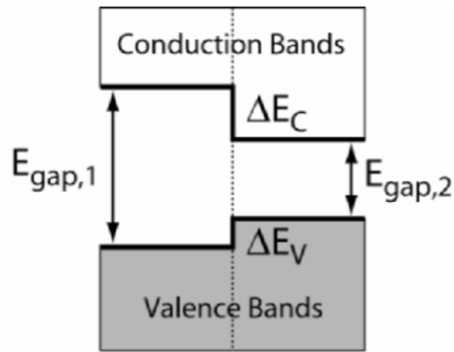
- Barriers
- Wells
- Quasi-Electric fields

For both electrons and holes independently with suitable material choices.

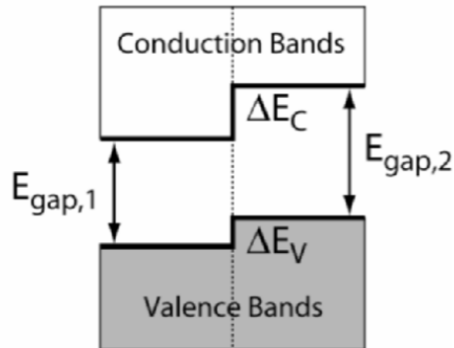
Example –
Double Heterostructure LED/Laser

Compound semiconductor heterostructure band offsets

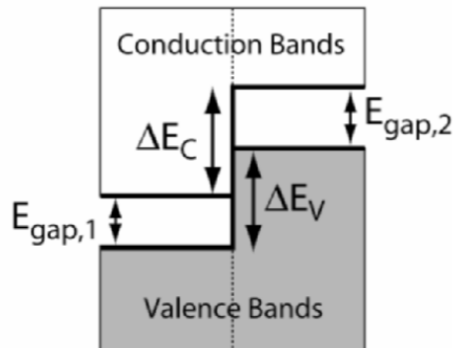
Straddling Gap



Offset Gap



Broken Gap

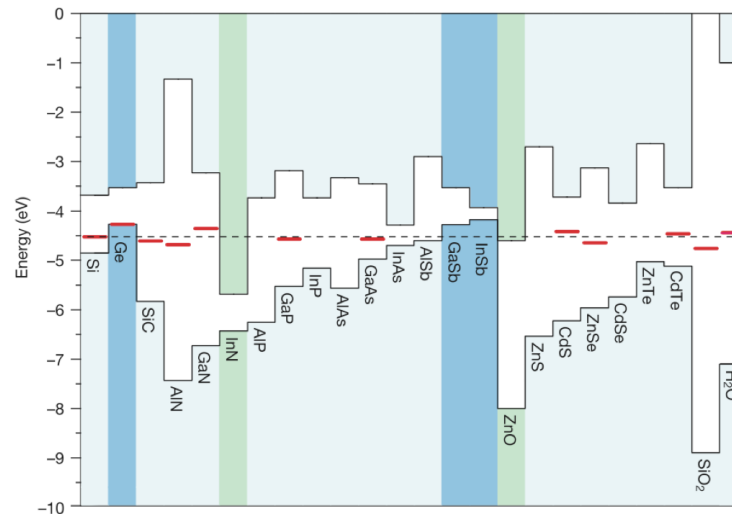


$$\Delta E_V(A : B) + \Delta E_V(B : C) + \Delta E_V(C : A) = 0.$$

Transitivity of band offsets

The Common Anion Rule: When the anion (the electron accepting atom such as As in GaAs and InAs) is in common across a semiconductor heterojunction, the change in the conduction band edge is greater than the change in the valence band edge across the semiconductor heterojunction. Mathematically, $\Delta E_V < \Delta E_C$.

The Common Cation Rule: When the cation (e.g. Ga in GaAs or GaSb) is in common across the junction, the valence band edge energies scale with the anion electronegativities. For example, the valence band edge of phosphide semiconductors will lie below those for arsenides which will lie below those of antimonides. Mathematically, $E_V(CA_1) < E_V(CA_2) < E_V(CA_3)$, where C designates a cation, and $A_1, A_2,$ and A_3 designate three anions with decreasing electronegativities.



5 B Boron 10.811	6 C Carbon 12.0107	7 N Nitrogen 14.0067	8 O Oxygen 15.9994
13 Al Aluminum 26.9815386	14 Si Silicon 28.0855	15 P Phosphorus 30.973762	16 S Sulfur 32.065
30 Zn Zinc 65.38	31 Ga Gallium 69.723	32 Ge Germanium 72.64	33 As Arsenic 74.92160
48 Cd Cadmium 112.411	49 In Indium 114.818	50 Sn Tin 118.710	51 Sb Antimony 121.760
80 Hg Mercury 200.59	81 Tl Thallium 204.3833	82 Pb Lead 207.2	83 Bi Bismuth 208.98040
			84 Po Polonium (209 8824)

(Rockett)

Quasi electric fields in semiconductor heterostructures

Semiconductor Heterostructures & Quasi-Electric Fields



The Nobel Prize in Physics 2000

"for basic work on information and communication technology"

"for developing semiconductor heterostructures used in high-speed- and opto-electronics"

"for his part in the invention of the integrated circuit"



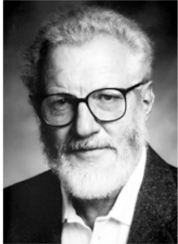
Zhores I. Alferov

1/4 of the prize

Russia

A.F. Ioffe Physico-Technical Institute
St. Petersburg, Russia

b. 1930



Herbert Kroemer

1/4 of the prize

Federal Republic of Germany

University of California
Santa Barbara, CA, USA

b. 1928



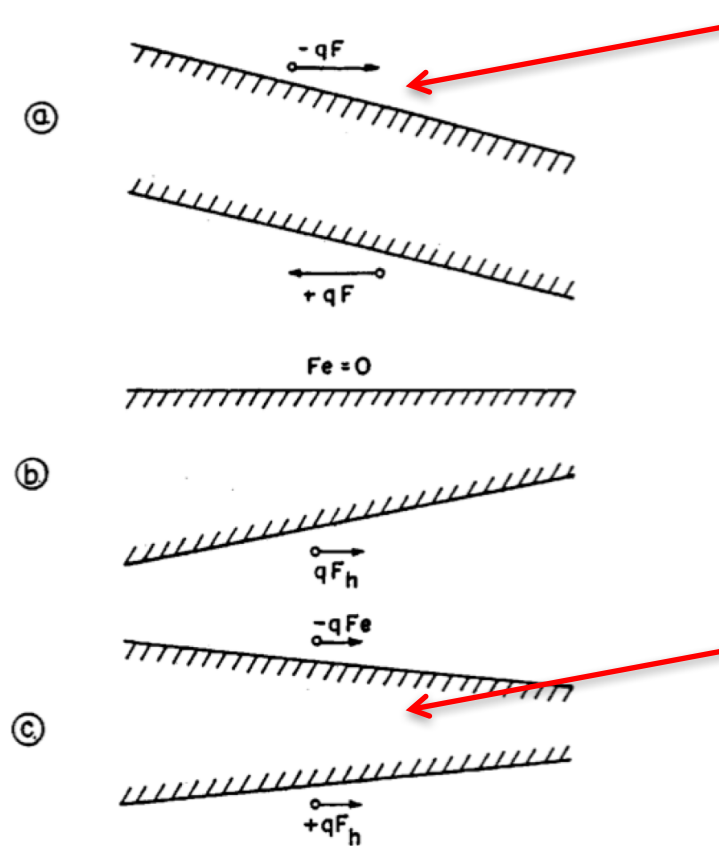
Jack S. Kilby

1/2 of the prize

USA

Texas Instruments
Dallas, TX, USA

b. 1923
d. 2005



Equal force on electrons and holes

...a drift field may also be generated through a variation of the energy gap itself, by making the base region from a nonstoichiometric mixed crystal of different semiconductors with different energy gaps (for example, Ge-Si), with a composition that varies continuously through the base. (Translated from Krömer, 1954)

Forces different for electrons and holes

Rev. Mod. Phys., vol 73, p 783 (2001)

FIG. 1. Quasielectric fields: (a) A true electric field simply tilts the bands; (b) quasielectric fields, with no force on electrons, but a force on holes; (c) quasielectric fields forcing electrons and holes in the same direction. From Kroemer, 1957a.

Compound semiconductors: Heterostructures

Nobel Lecture: Quasielectric fields and band offsets: teaching electrons new tricks*

Herbert Kroemer

*Electrical and Computer Engineering Department, University of California, Santa Barbara,
California 93106-9560*

(Published 22 October 2001)

I. INTRODUCTION

Heterostructures, as I use the word here, may be defined as heterogeneous semiconductor structures built from two or more different semiconductors, in such a way that the transition region or interface between the different materials plays an essential role in any device action. Often, it may be said that the interface is the device.

The participating semiconductors all involve elements from the central portion of the periodic table of the elements (Table I). In the center is silicon, the backbone of modern electronics. Below Si is germanium. Although Ge is rarely used by itself, Ge-Si alloys with a composition-dependent position play an increasingly important role in today's heterostructure technology. In fact, historically this was the first heterostructure device system proposed, although it was also the system that took longest to bring to practical maturity, largely because of the 4% mismatch between the lattice constants of Si and Ge.

Silicon plays the same central role in electronic metallurgy that steel plays in structural metallurgy. But just

Similar to the III-V compounds, every element shown in column II may be used together with every element in column VI to create II-VI compounds, and again alloying is possible to create a continuous range of the latter.

II. BAND DIAGRAMS AND QUASIELECTRIC FORCES

Whenever I teach my semiconductor device physics course, one of the central messages I try to get across early is the importance of energy-band diagrams. I often put this in the form of "Kroemer's Lemma of Proven Ignorance":

If, in discussing a semiconductor problem, you cannot draw an *Energy-Band-Diagram*, this shows that you don't know what you are talking about,

with the corollary

If you can draw one, but don't, then your audience won't know what you are talking about.

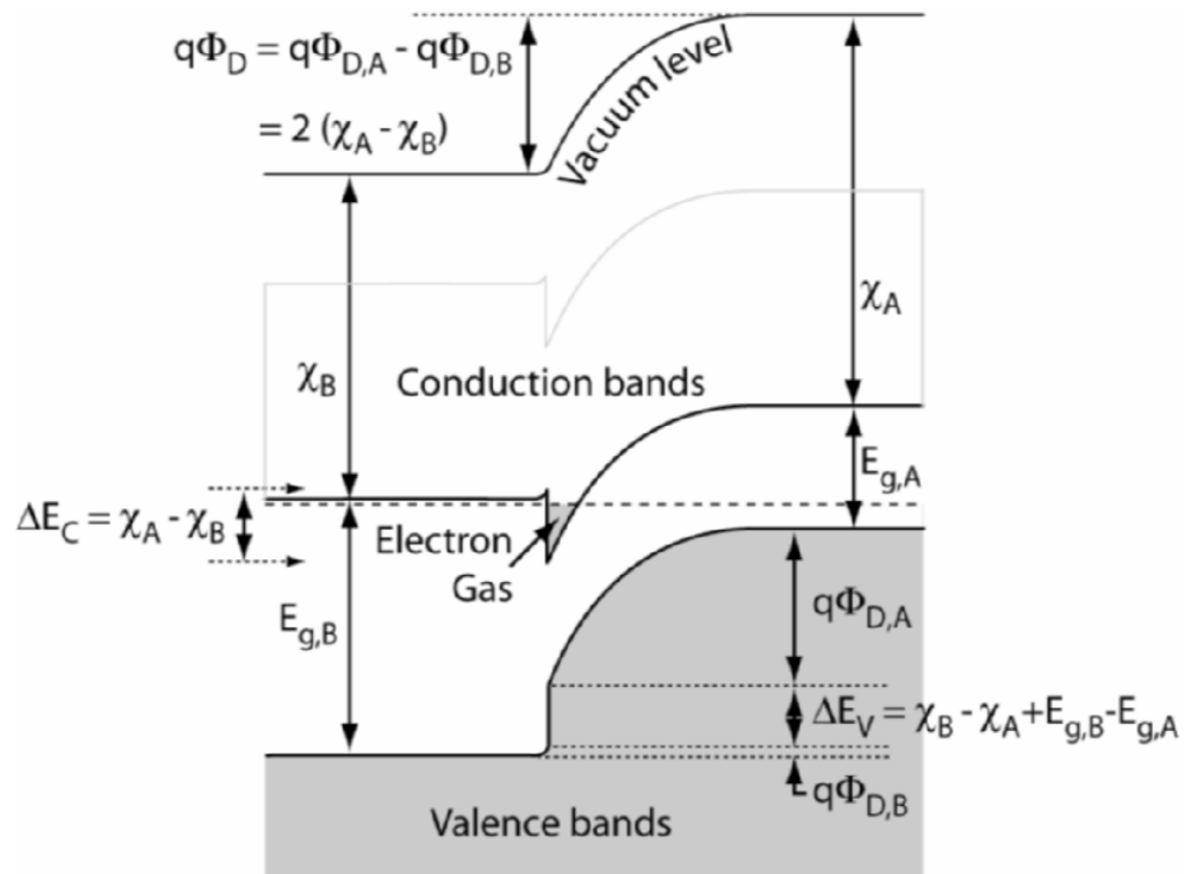
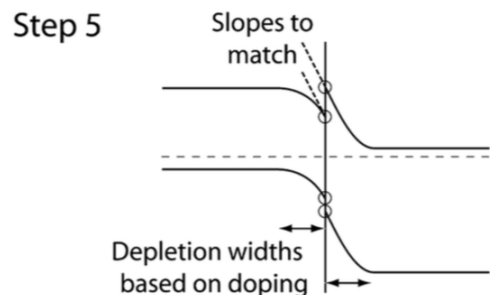
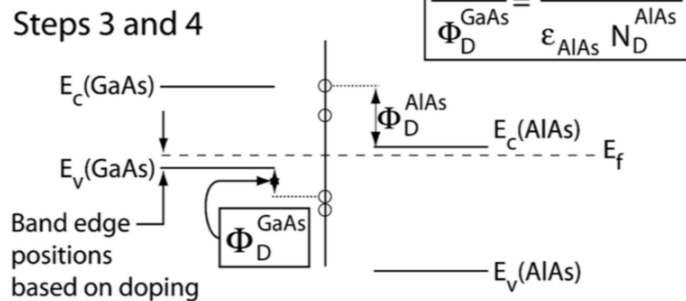
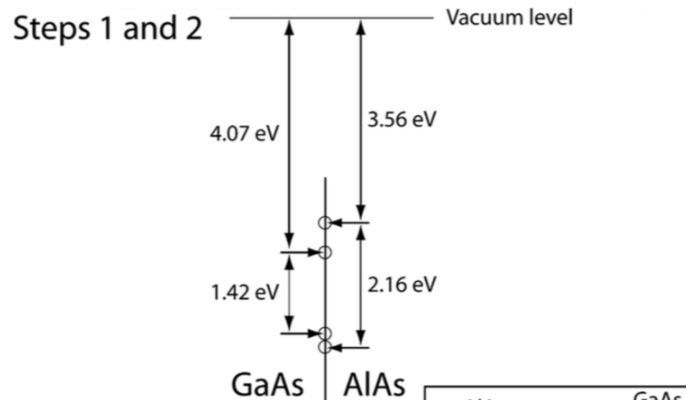
Nowhere is this more true than in the discussion of heterostructures, and much of the understanding of the latter is based on one's ability to draw their band diagrams—and knowing what they mean.

- Rev. Mod. Phys., vol 73, pg. 783 (2001)

Heterojunction Energy-Band Diagrams

Data used in drawing this figure:

Compound	Electron Affinity	Energy Gap
n-AlAs	3.56 eV	2.16 eV
p-GaAs	4.07 eV	1.42 eV
$N_A(\text{GaAs}) \sim N_D(\text{AlAs})$		



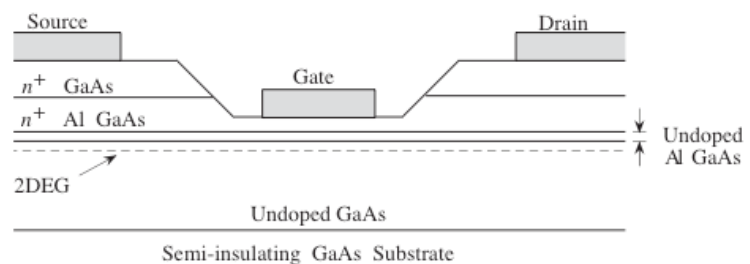
How to draw the energy band diagram for a heterostructure

$$\frac{\Phi_D^B}{\Phi_D^A} \approx \frac{\epsilon_A N_{dopant}^A}{\epsilon_B N_{dopant}^B}$$

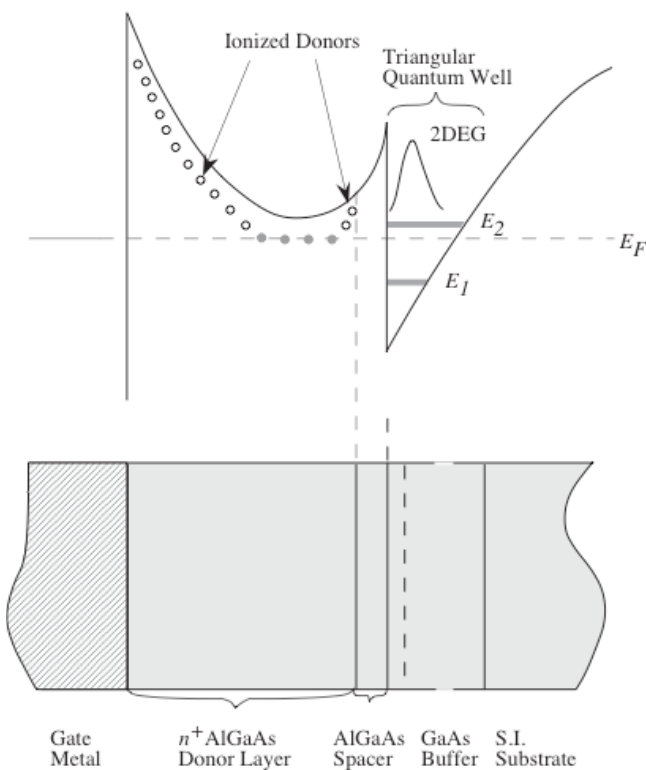
(Rockett)

High Electron Mobility Transistors (HEMTs, or HFETs)

Conductive channel is a 2DEG in a heterostructure quantum well



(a)



(b)

Key Advantages of HFETs:

- High mobility (suppressed ionized impurity scattering)
- Superior low-temperature performance (no freezeout)
- Choices: superior channel materials, heterostructures
- High sheet charge densities & channel conductance

Key material Requirements for HFETs:

- Semi-insulating substrates
- Large band offsets for carrier quantum confinement
- High mobility in conductive channel
- Low resistance Ohmic contacts
- Low-leakage Gate (Schottky, MOS structure, or variants)

HEMTs / HFETs

Semiconductor combinations for HFETs

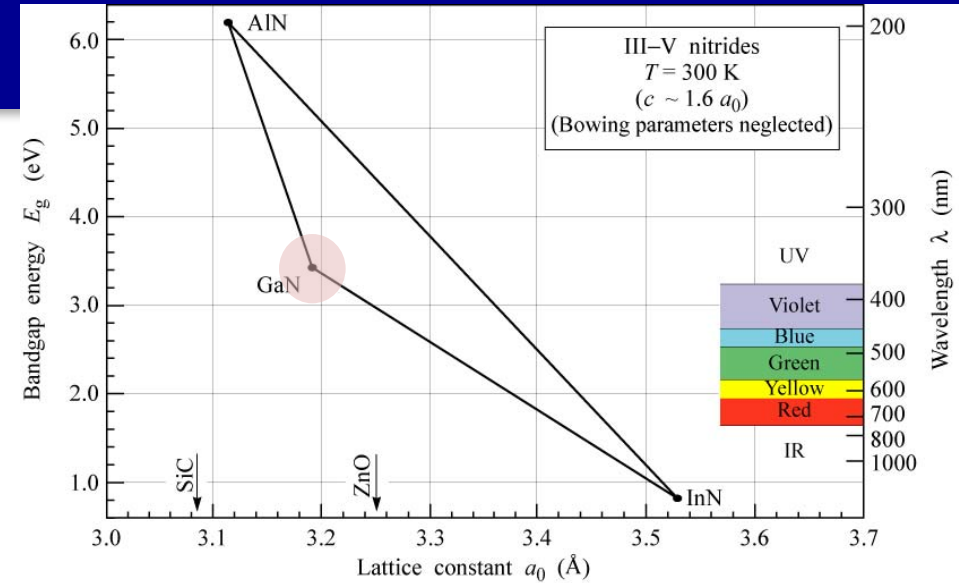
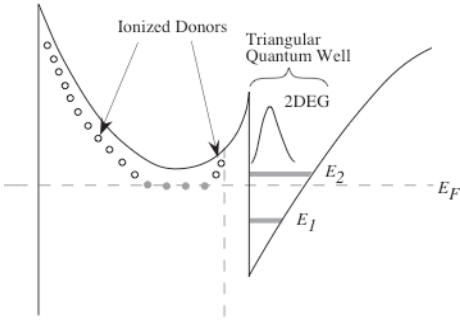


Fig. 12.12. Bandgap energy versus lattice constant of III-V nitride semiconductors at room temperature.

E. F. Schubert

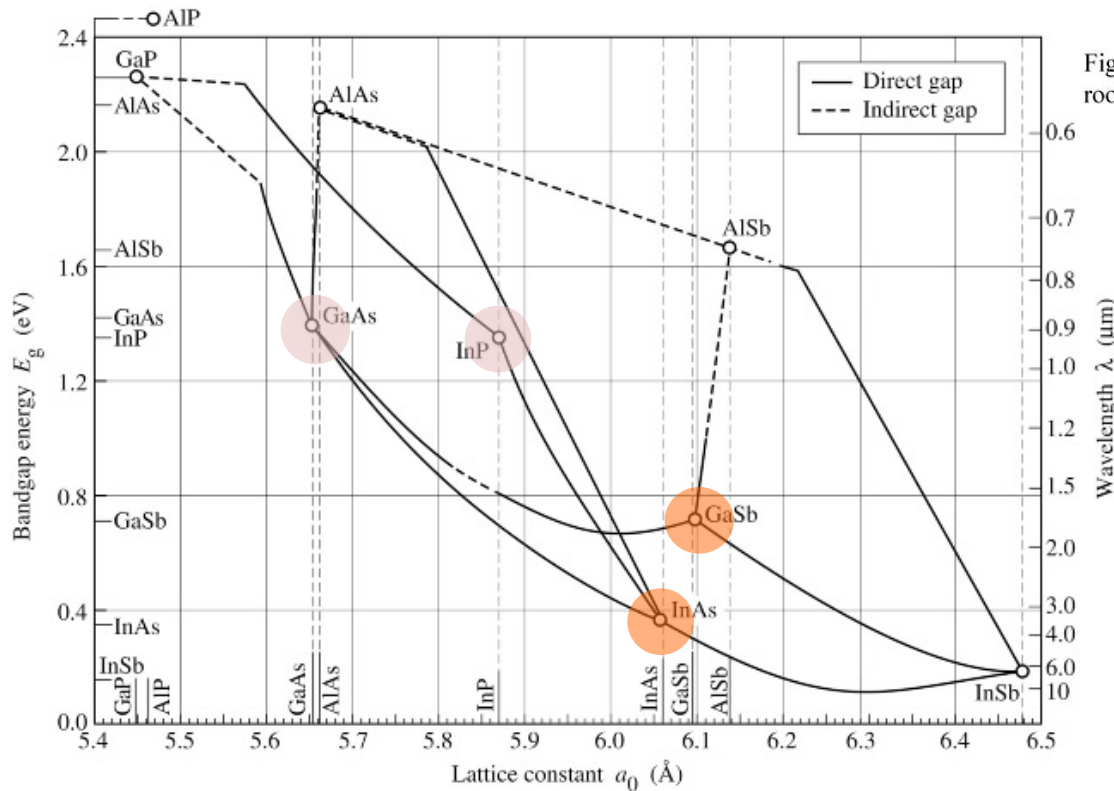


Fig. 7.6. Bandgap energy and lattice constant of various III-V semiconductors at room temperature (adopted from Tien, 1988).

HEMTs / HFETs

Semiconductor combinations for HFETs

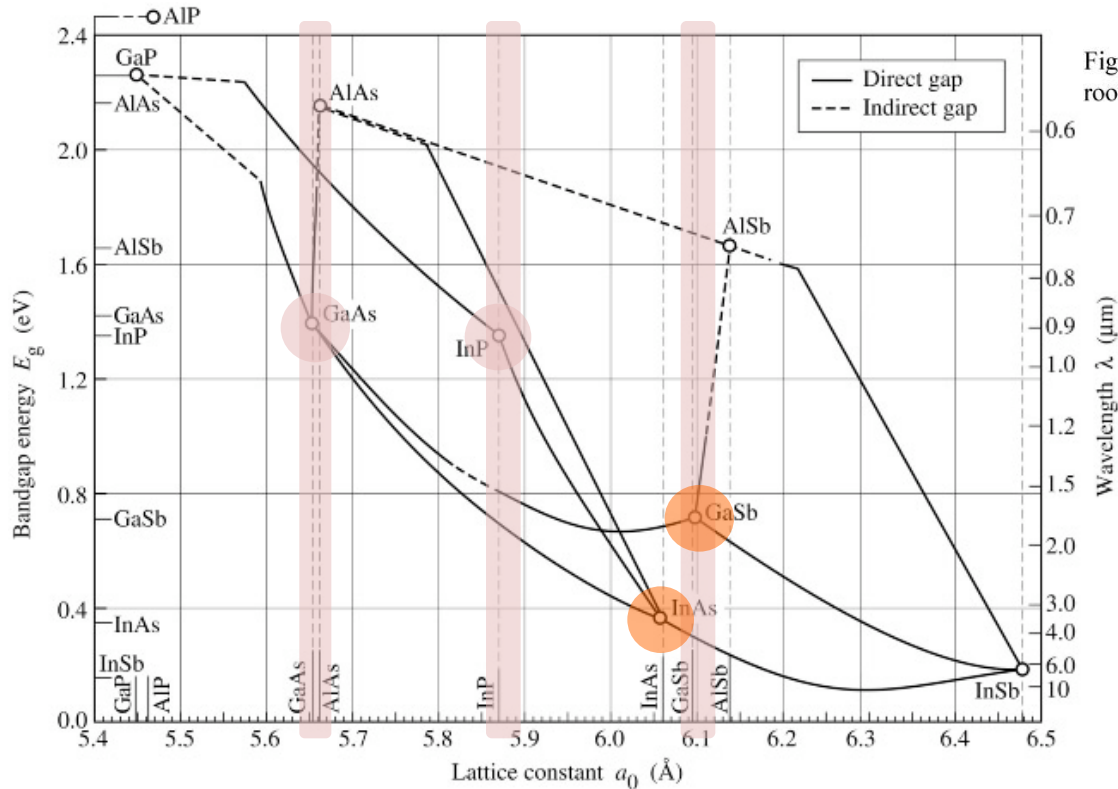
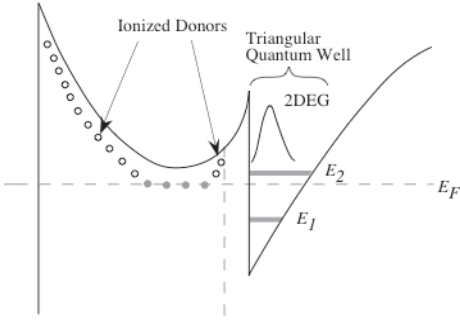


Fig. 7.6. Bandgap energy and lattice constant of various III-V semiconductors at room temperature (adopted from Tien, 1988).

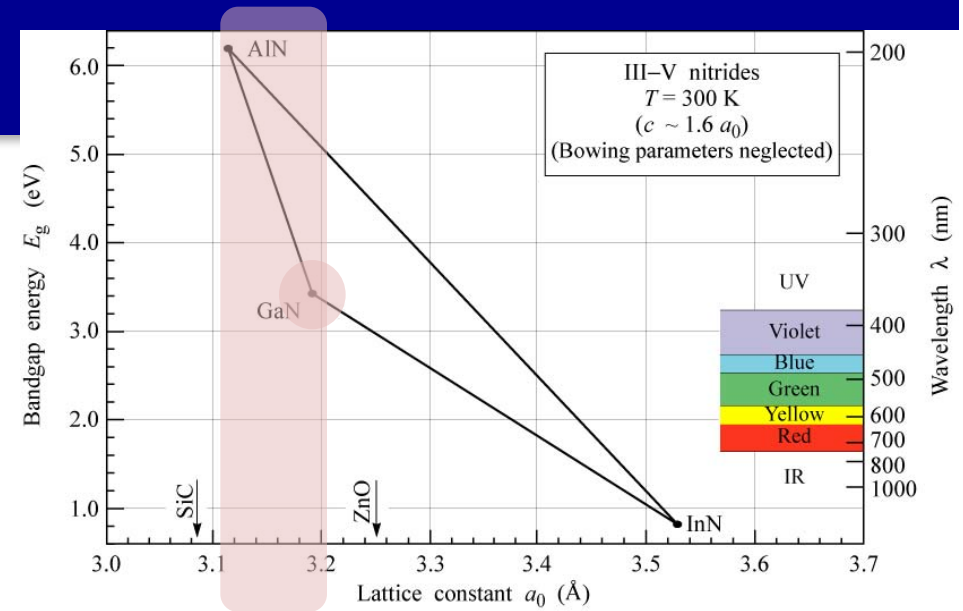


Fig. 12.12. Bandgap energy versus lattice constant of III-V nitride semiconductors at room temperature.

E. F. Schubert

Major HFET families:

- GaAs-based (AlGaAs/GaAs) (strain-free, or pseudomorphic)
- InP based (InGaAs channels)
- 6.1 Angstrom/narrow gap channels (generally grown metamorphically on GaAs)
- GaN-based (AlGaN/GaN and AlN/GaN) (typically pseudomorphic)

HEMTs / HFETs

Semiconductor combinations for HFETs

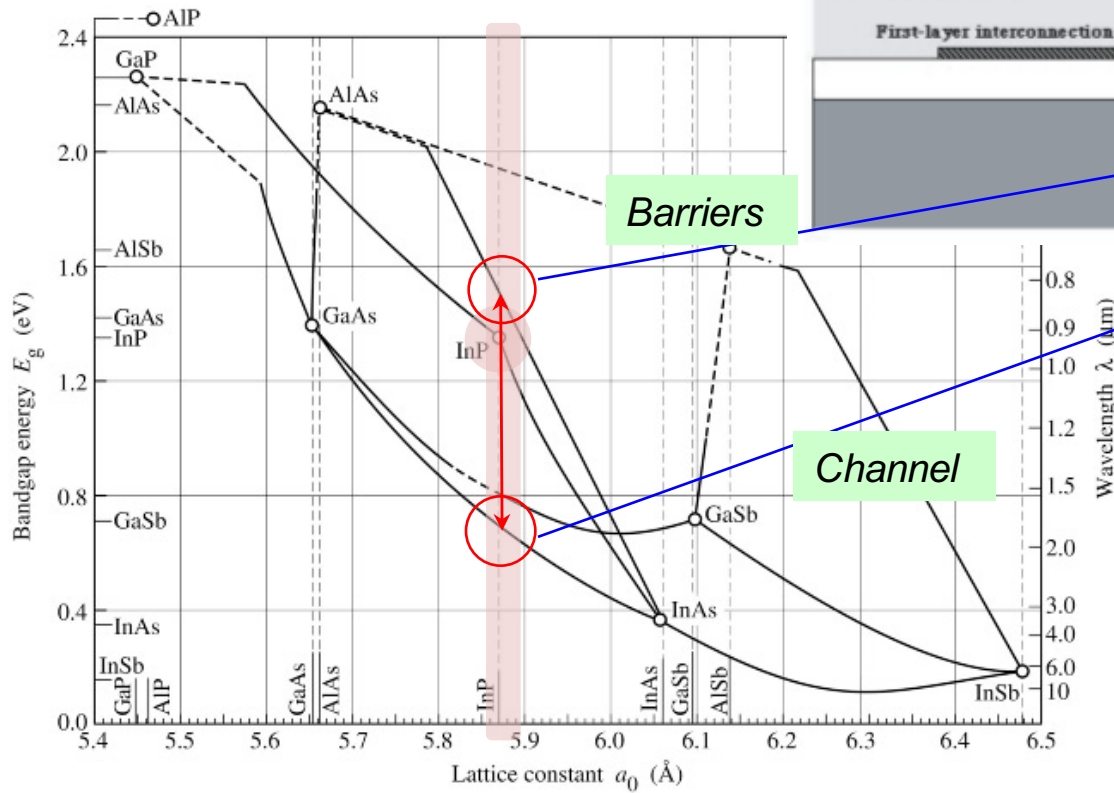
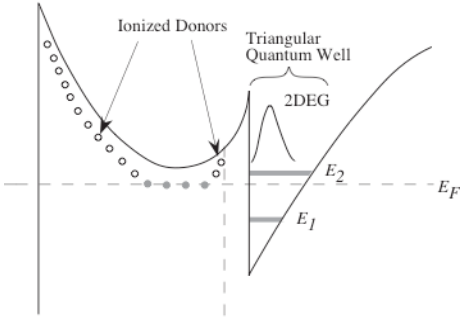
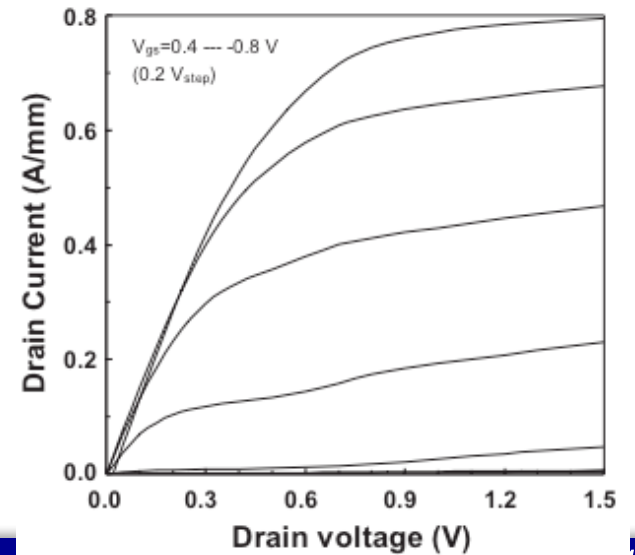
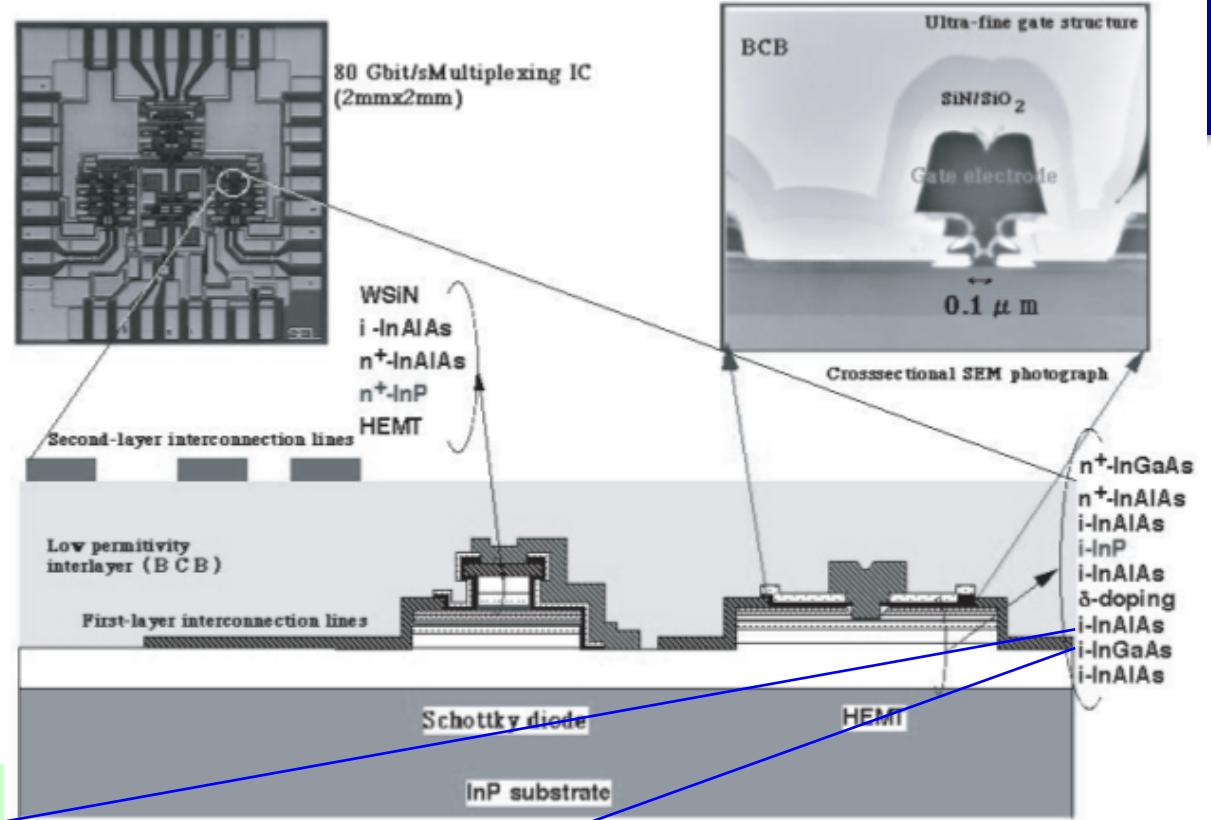


Fig. 7.6. Bandgap energy and lattice constant of various III-V semiconductors at room temperature (adopted from Tien, 1988).



HEMTs / HFETs: 2D Electron Gases

Charge Control Model

Charge Neutrality: $N_d^+ = n_m + n_{par} + n_s$

Gate Capacitance: $C_G = \frac{\epsilon}{d + \Delta d} \leftrightarrow V_{GS,int} = V_{GS} - (E_{F,ch} - E_{F,s})$

'Quantum' Capacitance: $C_Q = \epsilon / \Delta d \approx q^2 \times DOS$

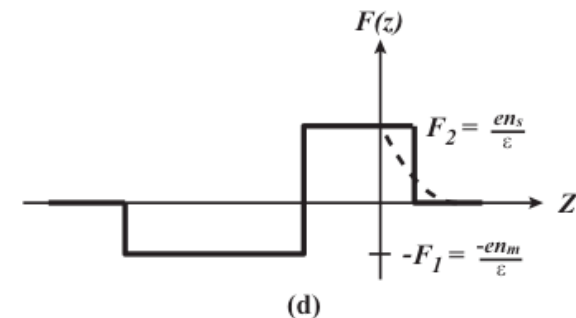
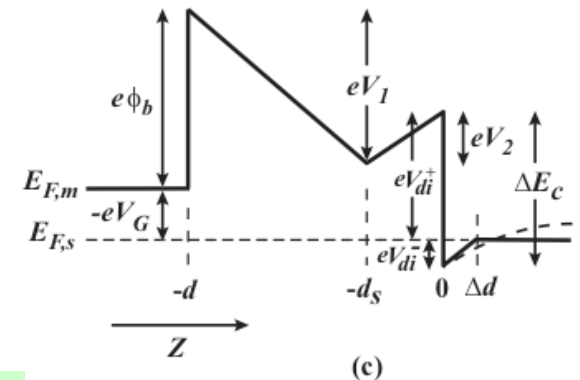
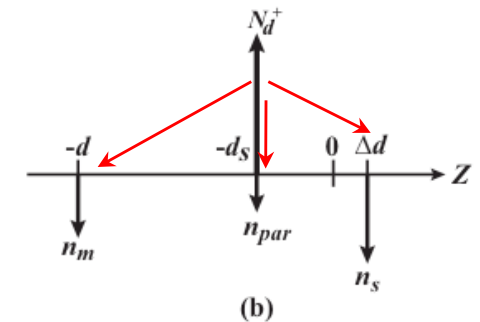
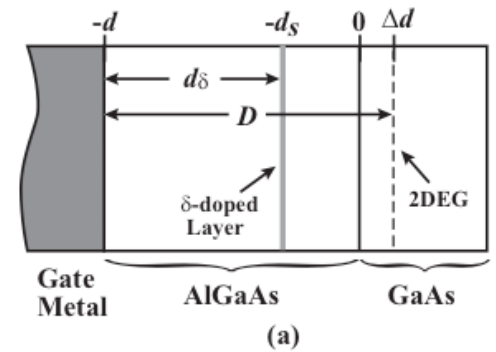
$$C_G = \frac{C_{G0} C_Q}{C_{G0} + C_Q}$$

$$C_Q = \epsilon / \Delta d \approx q^2 \times DOS$$

$$\rightarrow \Delta d \approx \frac{\epsilon \pi \hbar^2}{q^2 m^*} \quad \begin{array}{l} \sim 8 \text{ nm (GaAs)} \\ \sim 2 \text{ nm (GaN, Si MOSFETs)} \end{array}$$

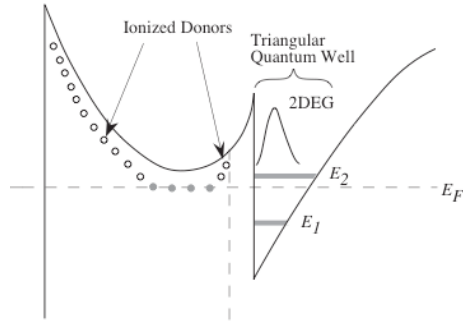
Effect of low Quantum Capacitance (low effective mass):

- More gate voltage needed for same carrier concentration
- Bad for gate modulation & transconductance
- This is a feature of 2DEGs (1D nanostructures can eliminate QC!)



HEMTs / HFETs: Threshold Voltage

Charge Control Model



QW energy eigenvalues (Airy functions):

$$E_i \approx \left(\frac{\hbar^2}{2m^*} \right)^{1/3} \left[\frac{3}{2} eF_2 \pi \left(i + \frac{3}{4} \right) \right]^{2/3}$$

Voltage drop in QW due to quantum capacitance:

$$qV_{di}^- \approx E_F - E_0 = \frac{\pi \hbar^2}{m^*} n_s$$

Energy Conservation:

$$-V_G + \phi_b - V_1 + V_2 - \frac{\Delta E_c}{e} + V_{di}^- = 0$$

Gauss' Law:

$$V_1 = \frac{en_m (d - d_s)}{\epsilon}$$

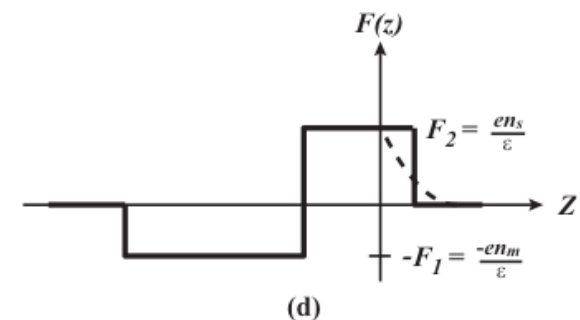
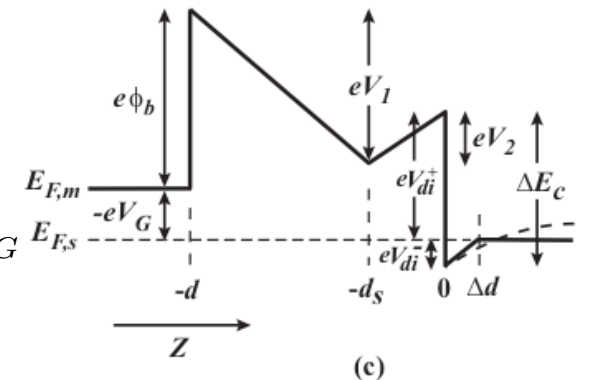
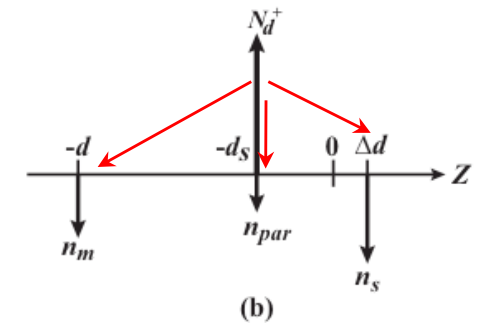
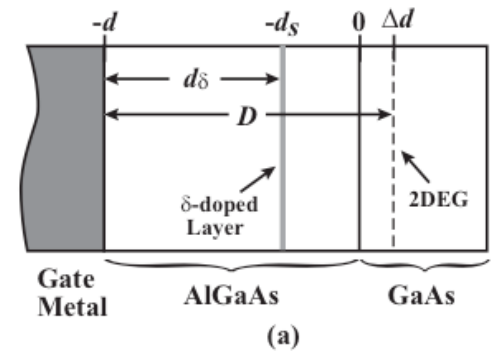
$$V_2 = \frac{en_s d_s}{\epsilon}$$

$$q\Delta n_s = \left(\frac{\epsilon}{d + \Delta d} \right) \Delta V_G = C_G \Delta V_G$$

Charge control Law:

$$n_s(V_G) = \frac{eN_d^+ d_\delta + \epsilon [V_G - (\phi_b - \Delta E_c/e)]}{eD}$$

Threshold Voltage ($n_s=0$) \rightarrow $V_p = -\frac{eN_d^+ d_\delta}{\epsilon} + (\phi_b - \Delta E_c/e)$



Overview of Semiconductor Devices

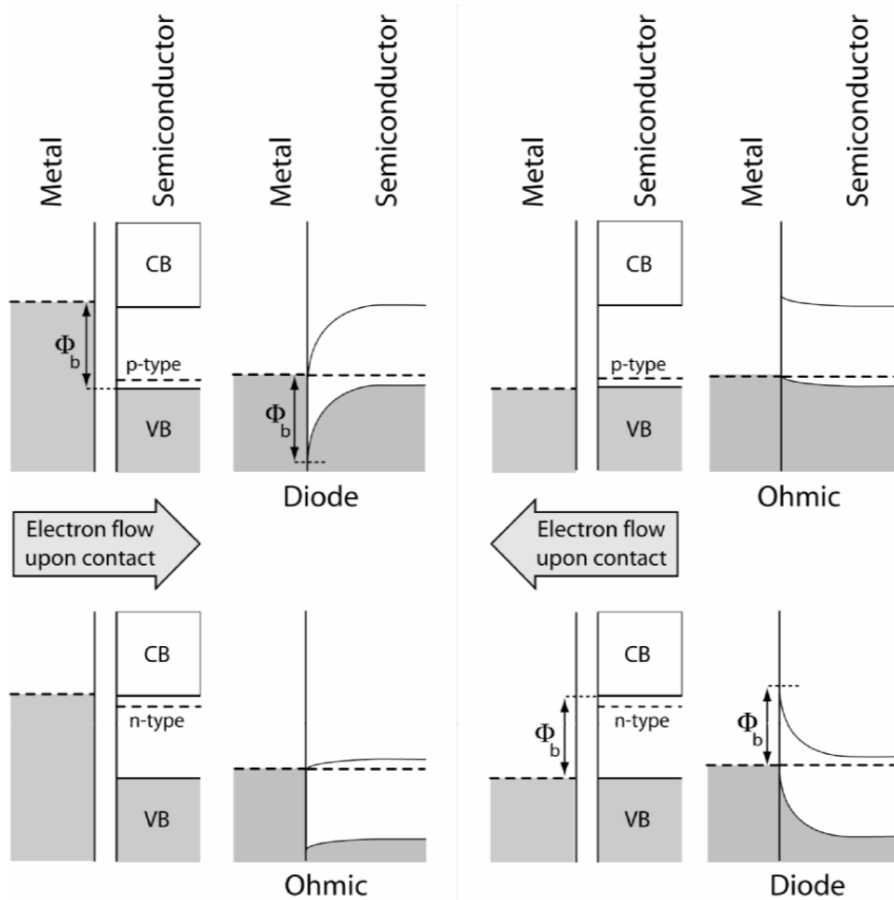
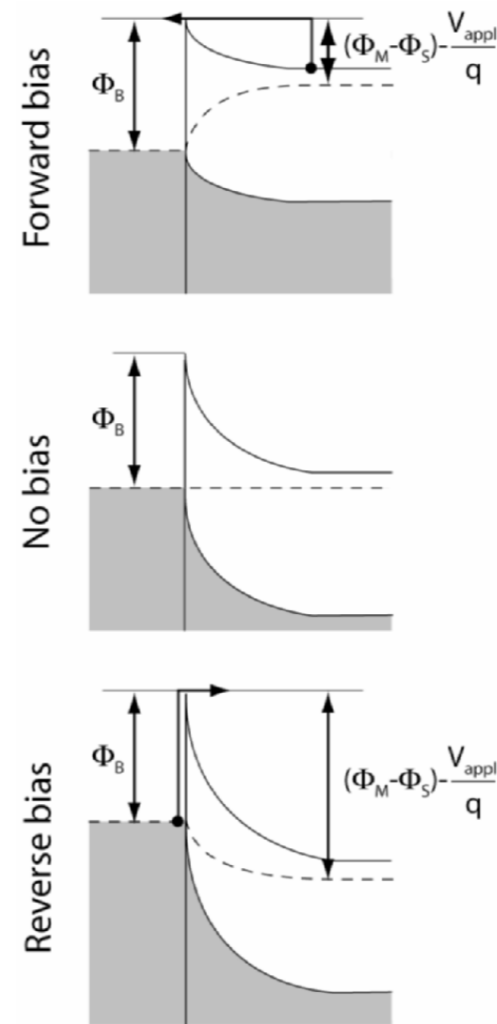
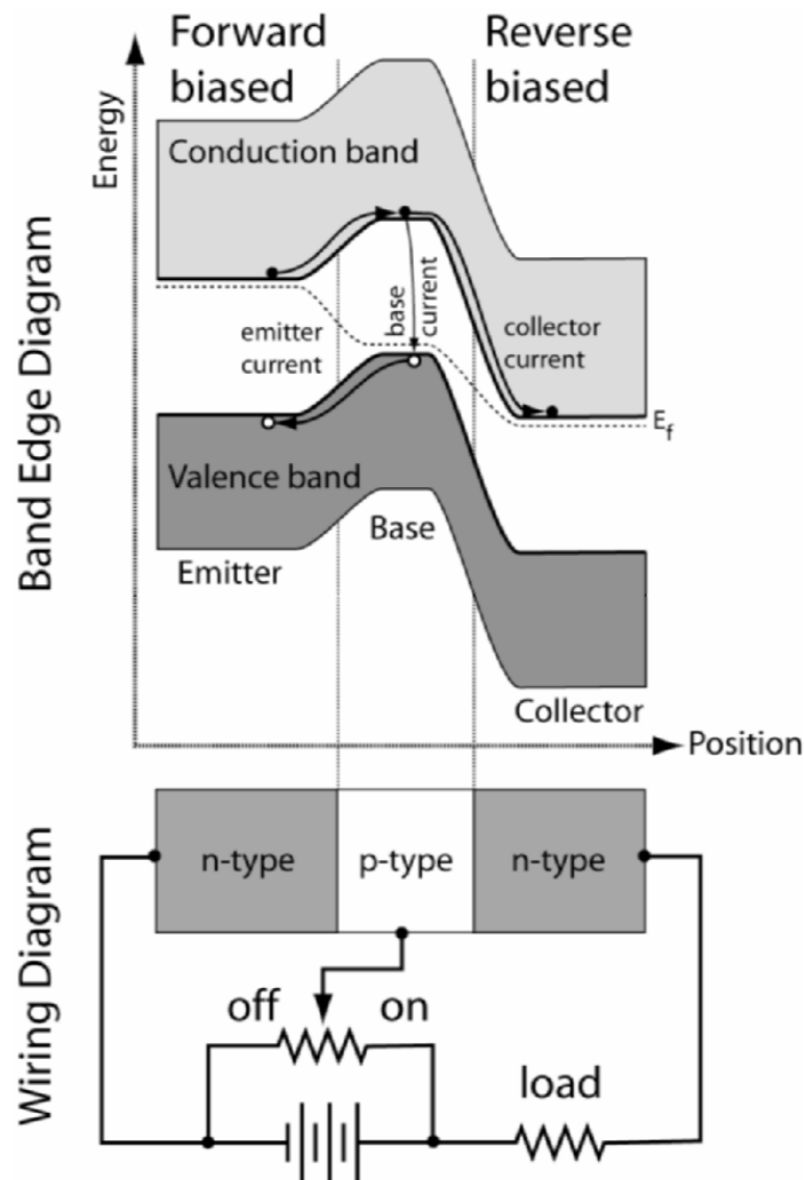
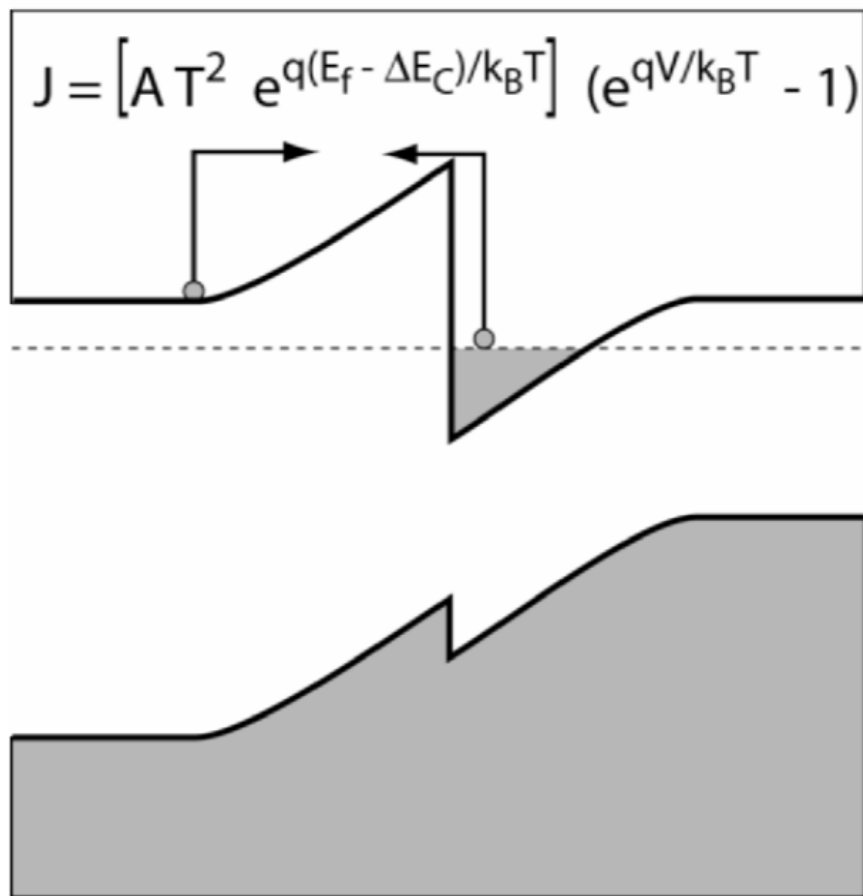


Figure 3.17: The four possible metal-semiconductor cases before and after contact. Two of the four produce ohmic contacts (resistors) while the others produce Schottky diodes.



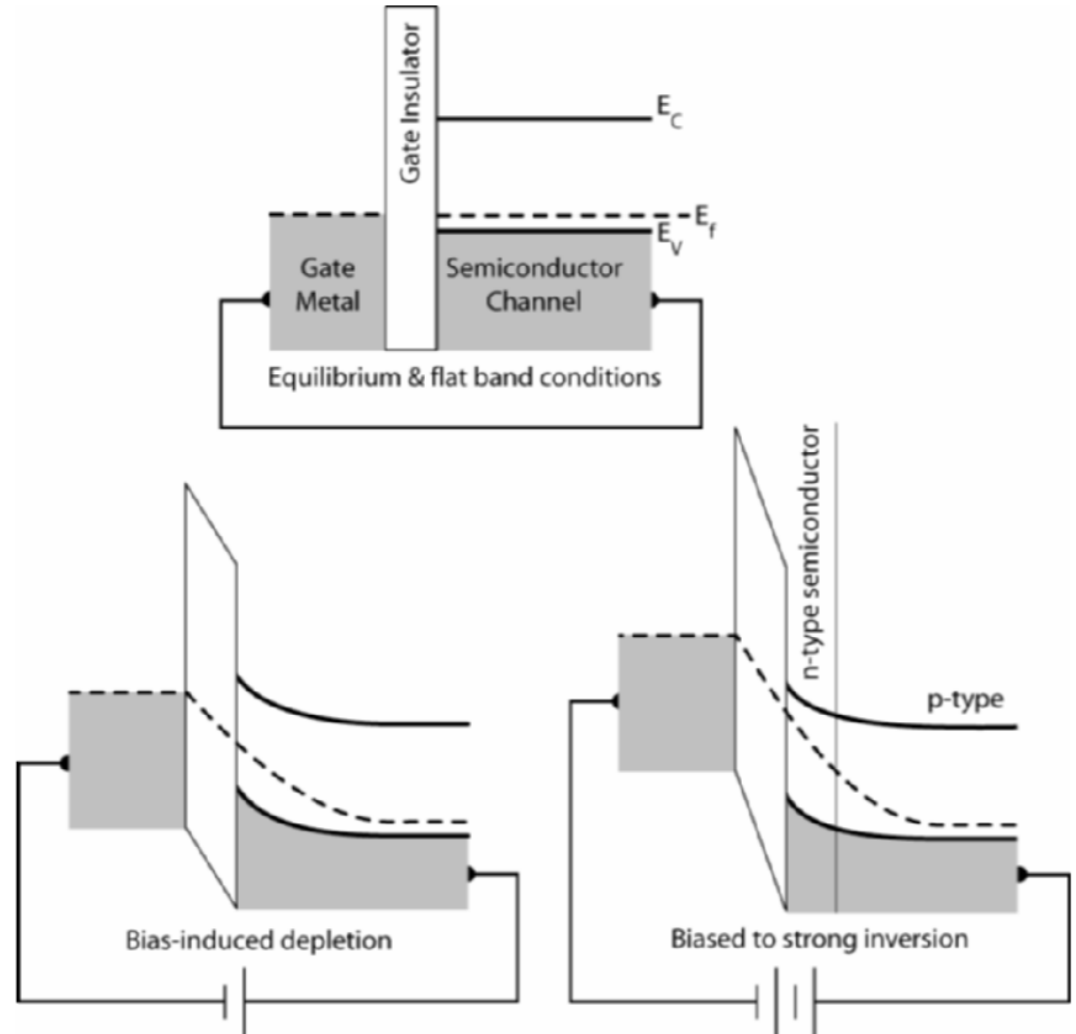
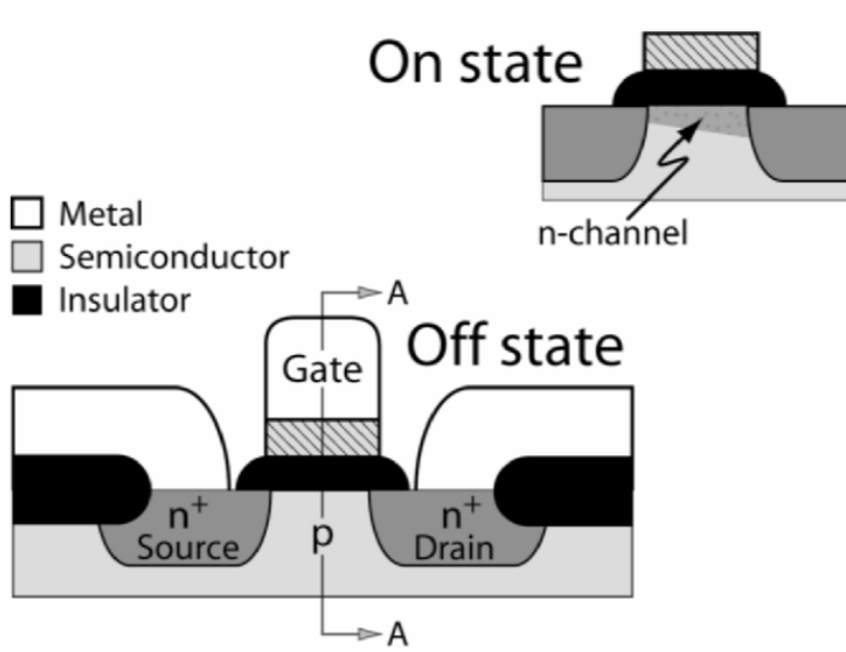
(Rockett)

Compound Semiconductor Heterojunction Devices



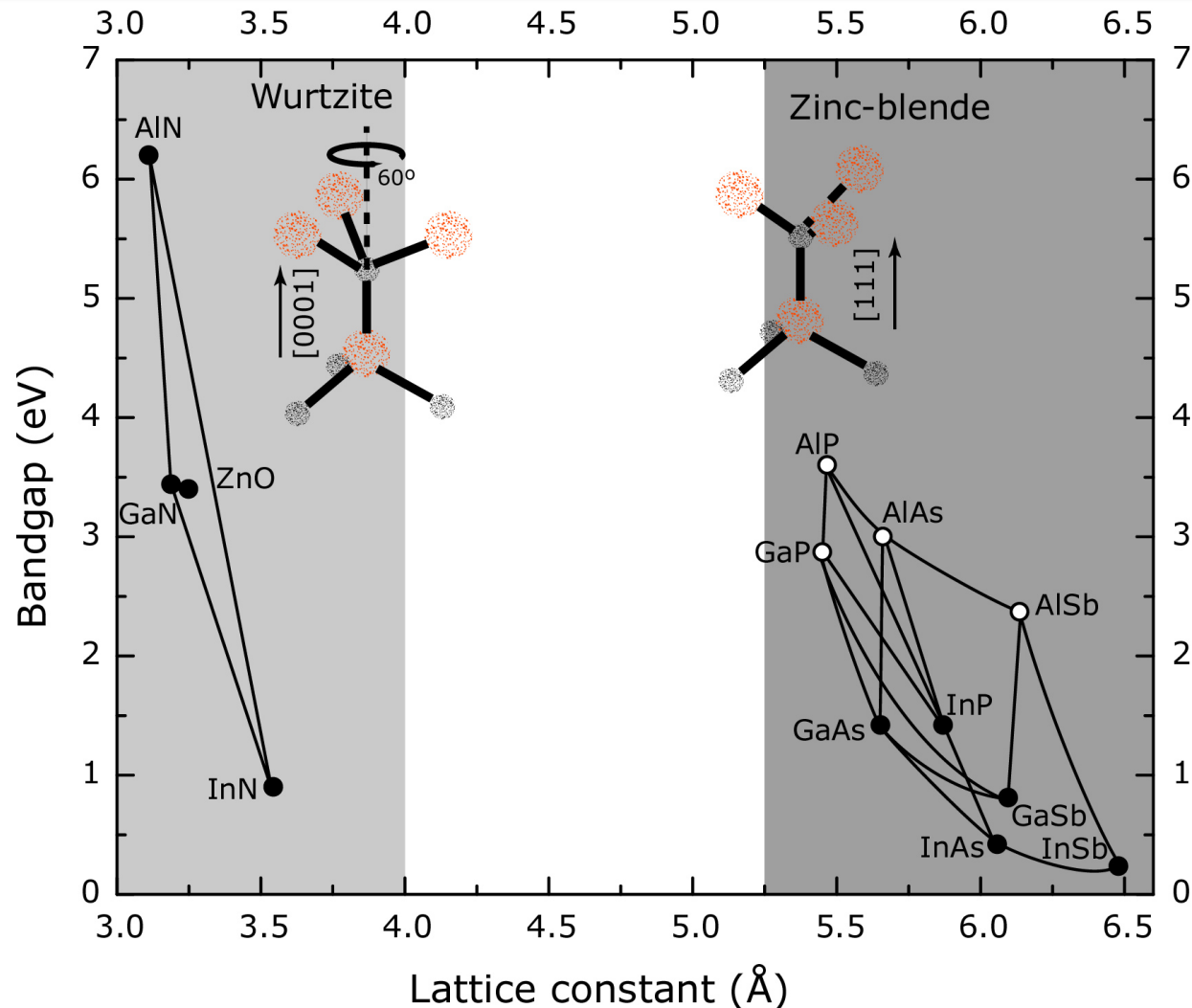
(Rockett)

Compound Semiconductor Heterojunction Devices



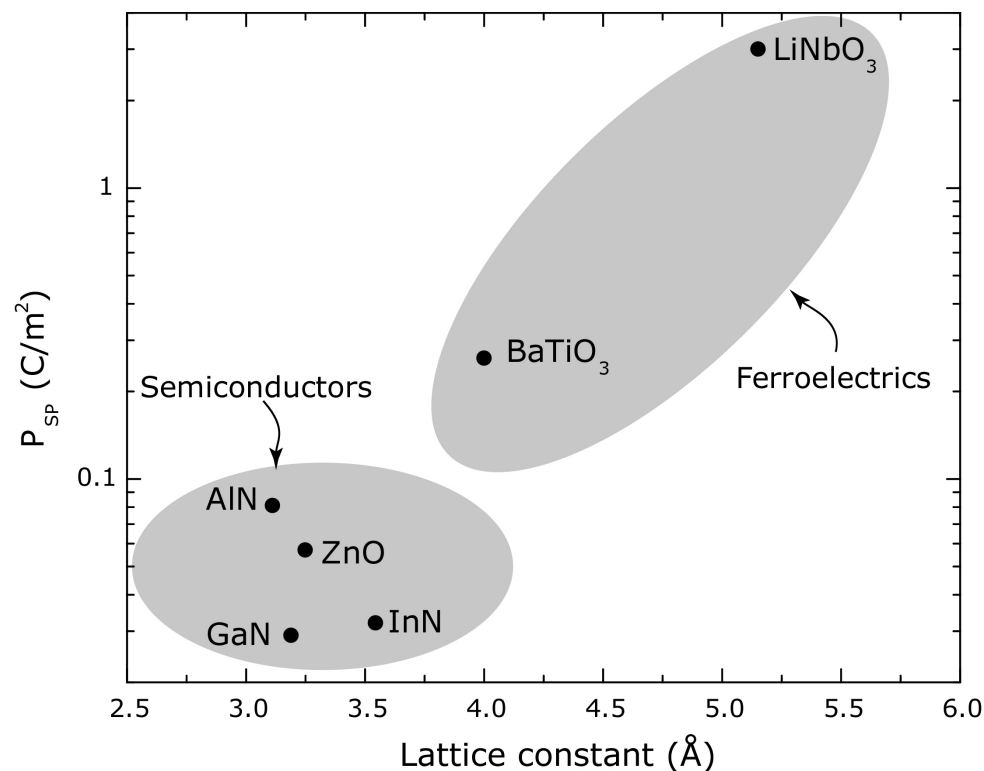
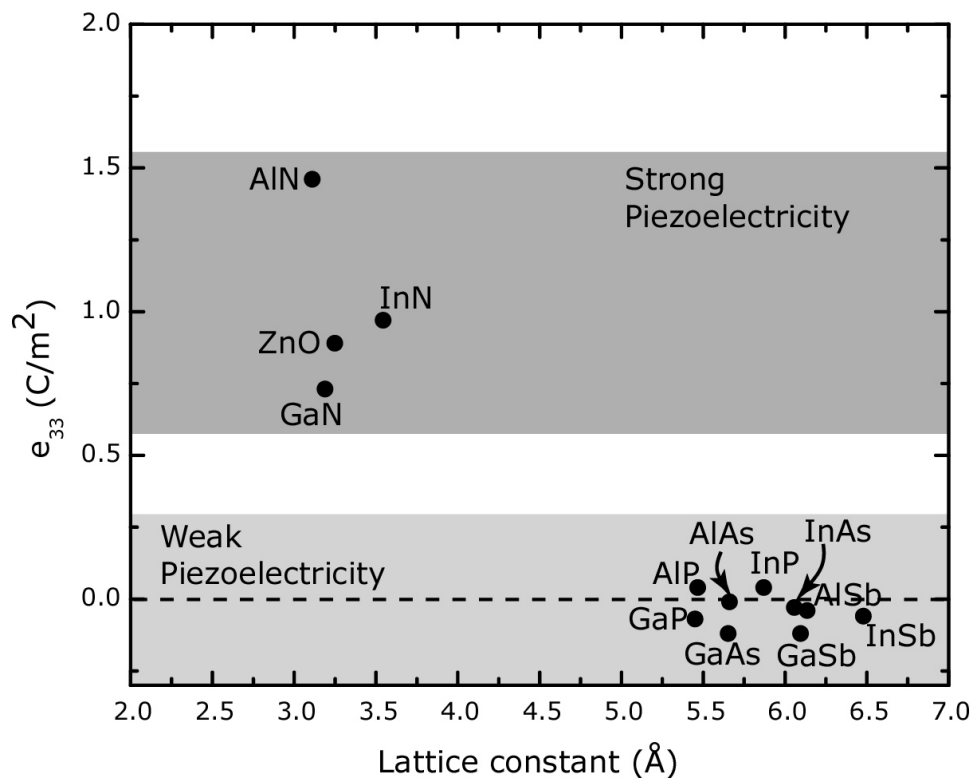
(Rockett)

GaN family (Wurtzite III-Vs)



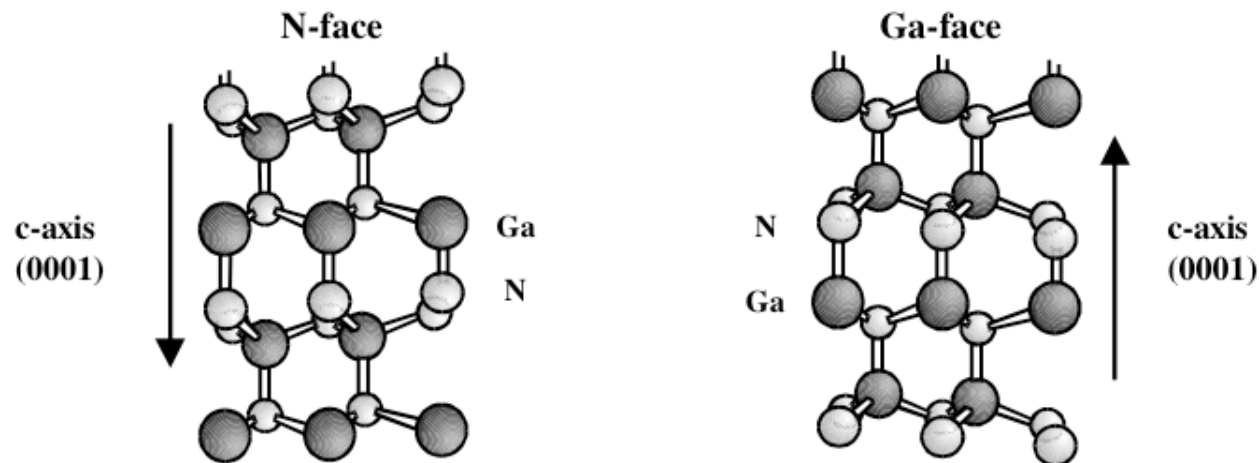
- III-V nitride semiconductors crystallize in the wurtzite structure
- All three semiconductors (InN, GaN, and AlN) are direct gap
- Bandgaps range from the IR thru visible to deep UV

Spontaneous & Piezoelectric polarization in the Nitrides

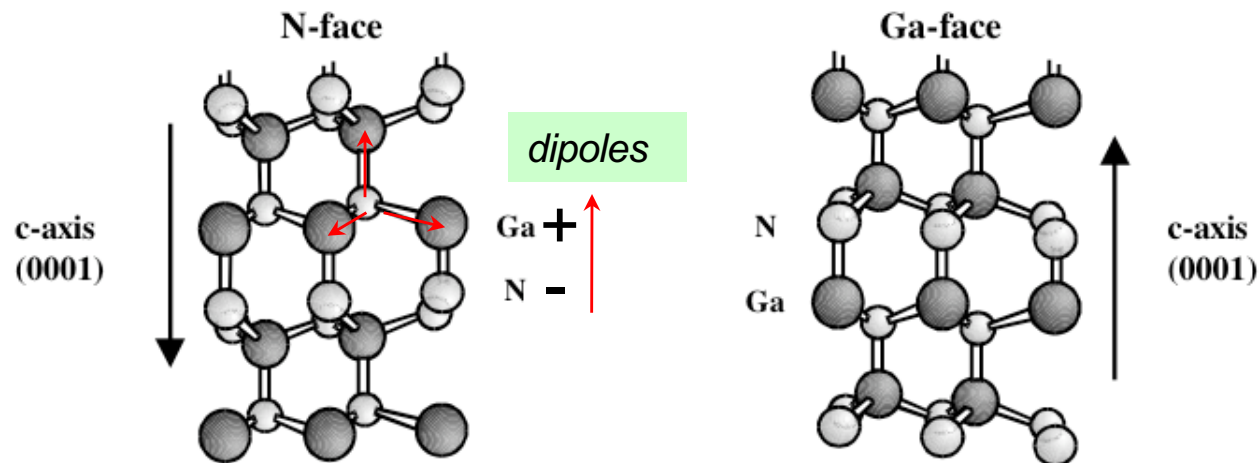


- *III-V Nitrides have an order of magnitude higher piezo-polarization than ZB III-Vs*
- *Piezoelectric polarization of Al(Ga)N is higher than GaN*
- *Alloys scale roughly linearly with composition (Vegard's law)*

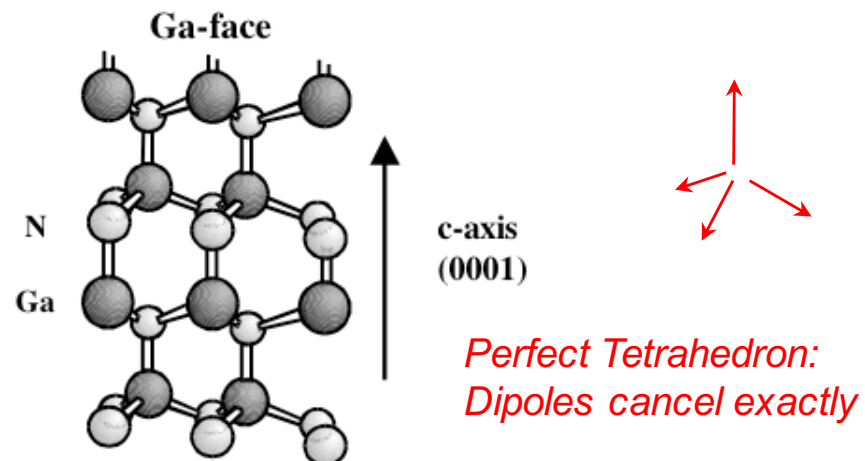
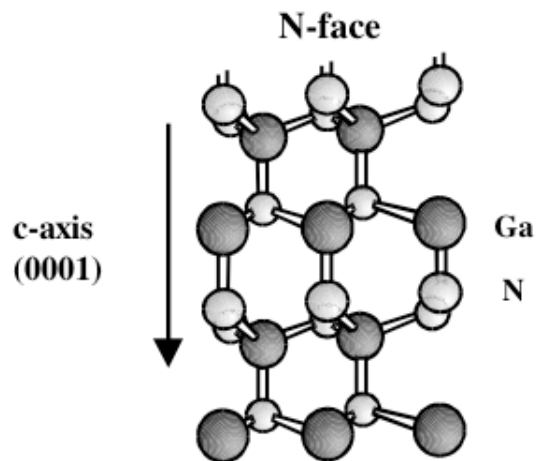
GaN HEMTs: Origin of Polarization



GaN HEMTs: Origin of Polarization

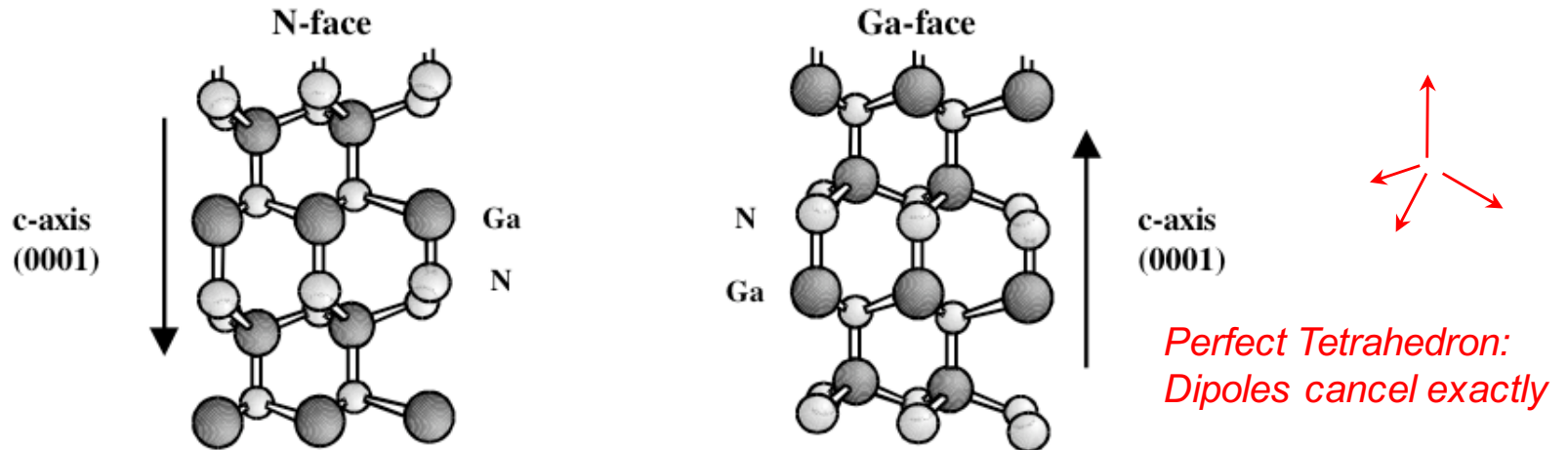


GaN HEMTs: Origin of Polarization



If $\frac{c}{a} = \sqrt{\frac{8}{3}}$, $\sum \mathbf{p}_i = 0!$

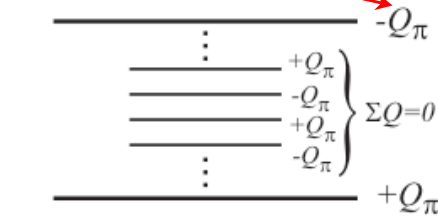
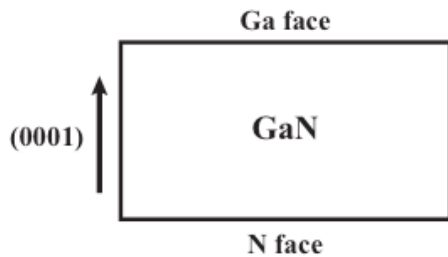
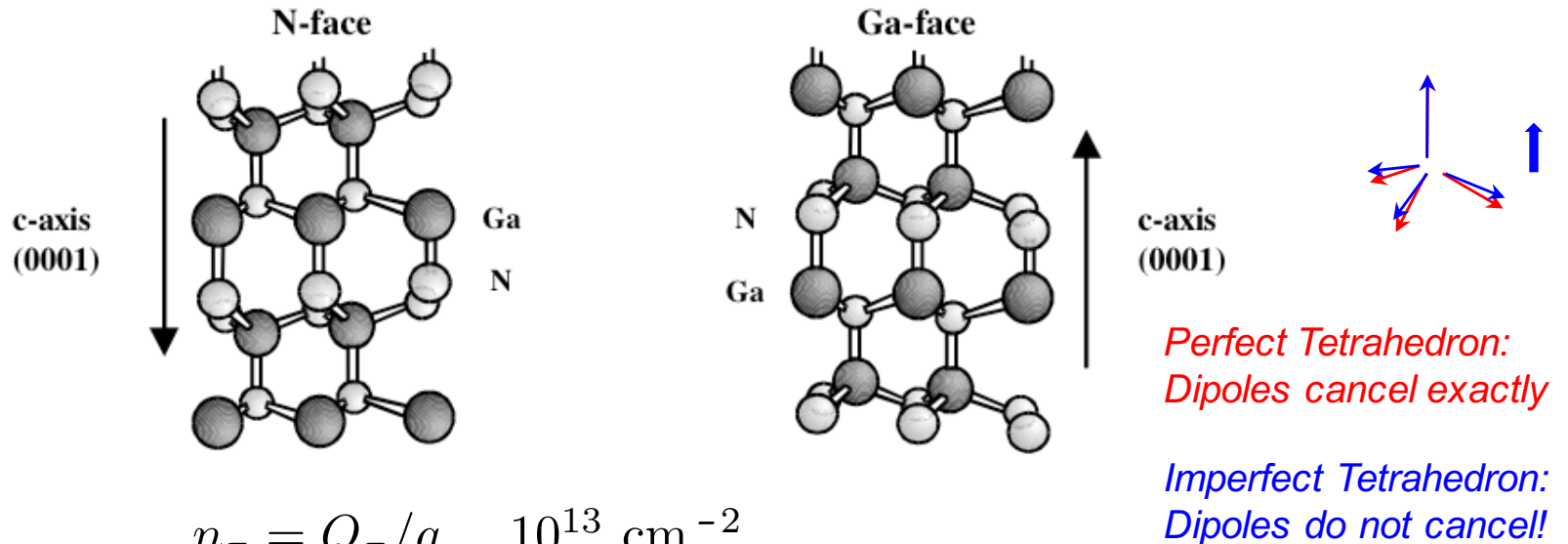
GaN HEMTs: Origin of Polarization



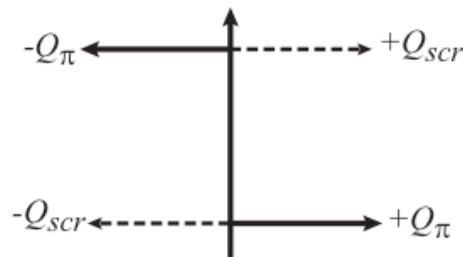
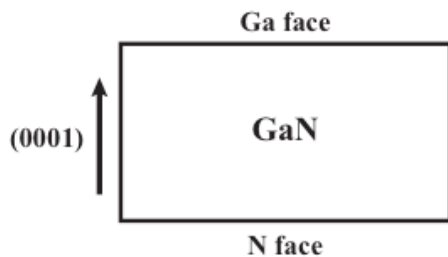
$$\text{If } \frac{c}{a} = \sqrt{\frac{8}{3}}, \quad \sum \mathbf{p}_i = 0!$$

In Nitrides, $\frac{c}{a} < \sqrt{\frac{8}{3}}$, $\rightarrow \sum \mathbf{p}_i \neq 0 \rightarrow$ Spontaneous Polarization

GaN HEMTs: Origin of Polarization



(a)



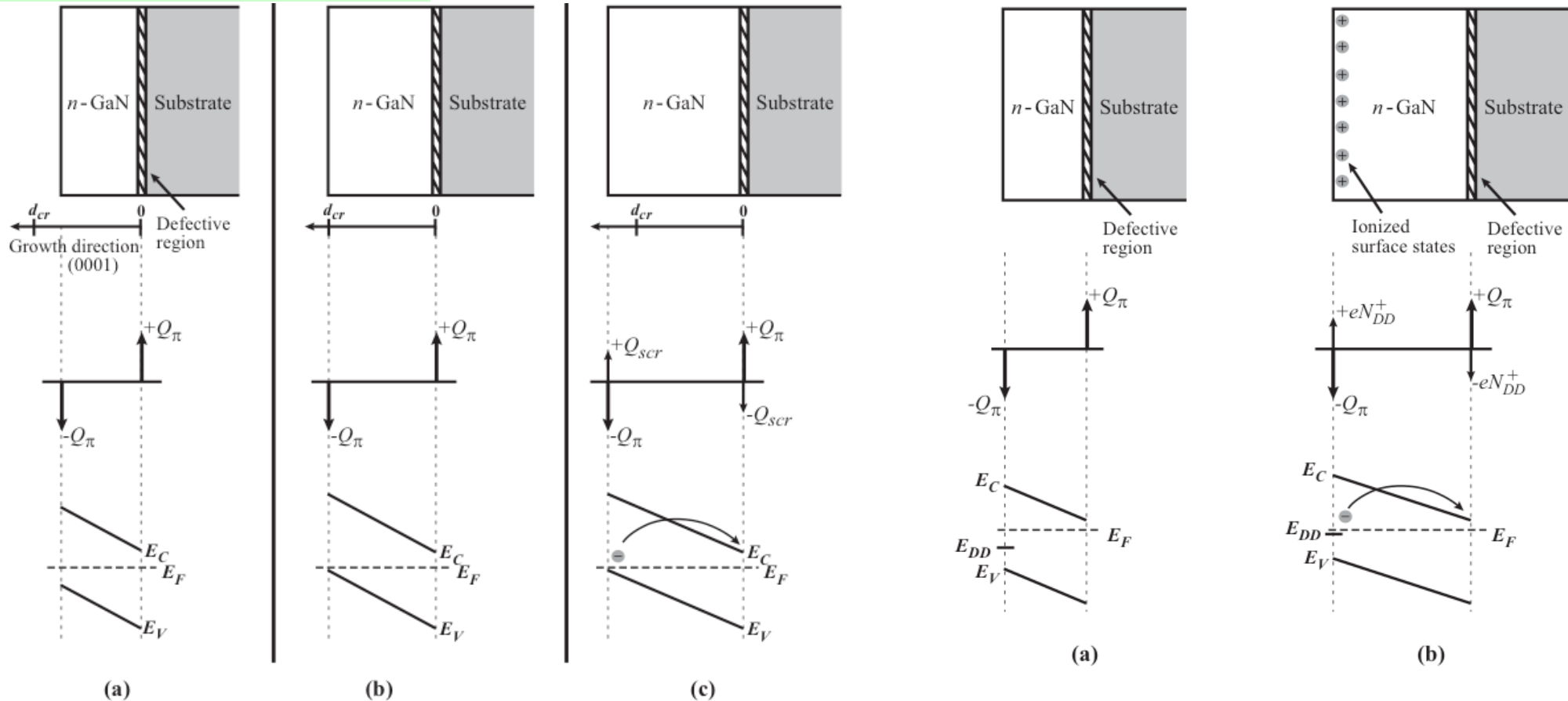
(b)

Polarization in III-V Nitride Semiconductors:

- Due to highly polar bonds & non-ideal crystal structure
- Magnitude of sheet charges \sim several $10^{13}/\text{cm}^2$
- Polarization charges are BOUND, but induce mobile carriers
- Two components: Spontaneous + Piezoelectric

GaN HEMTs: Consequence of Polarization Fields

Consequences of Polarization



Fixed sheet charges at the surfaces: Electric Field, Band Bending

$$F_\pi = qn_\pi/\epsilon \approx 1.6 \text{ MV/cm}$$

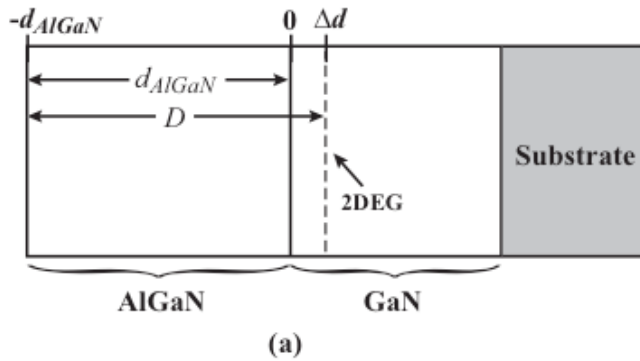
Band bending: $q \times F_\pi \times d = 160 \text{ eV}$ for $d = 1 \mu\text{m}$!

Maximum Band bending at equilibrium = Bandgap

$d_{cr} \sim \mathcal{E}_g/qF_\pi$, and for $d > d_{cr}$, a screening dipole is formed.

Polar Heterostructures

Charge Control Model



Polarization sheet charge: $Q_{\pi}(\text{net}) = Q_{\pi}(\text{AlGaN}) - Q_{\pi}(\text{GaN})$

Energy conservation (ungated): $\phi_s - V_1 - \frac{\Delta E_c}{e} + V_{di}^- = 0$

Gauss' s Law:

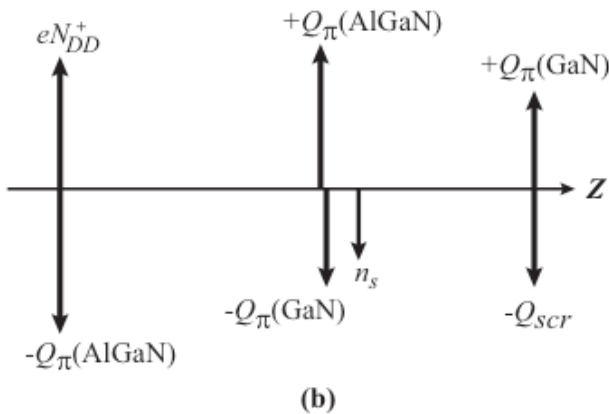
$$V_1 = \frac{[Q_{\pi}(\text{net}) - en_s] d_{\text{AlGaN}}}{\epsilon}$$

Charge density (ungated):

$$n_s = \frac{Q_{\pi}(\text{net}) \cdot d_{\text{AlGaN}} - \epsilon (\phi_s - \Delta E_c/e)}{eD}$$

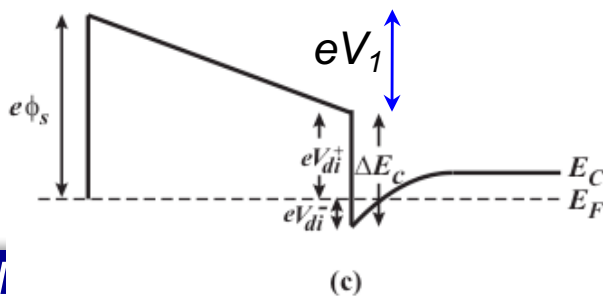
Charge density (gated):

$$n_s(V_G) = \frac{Q_{\pi}(\text{net}) \cdot d_{\text{AlGaN}} + \epsilon [V_G - (\phi_b - \Delta E_c/e)]}{eD}$$

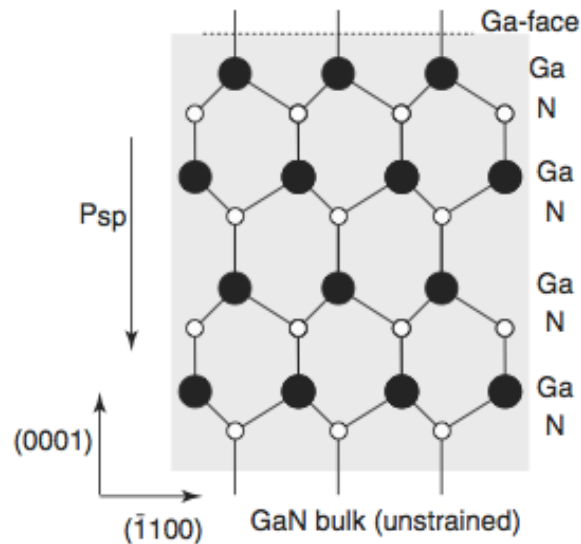


GaN-based polar HFETs:

- Wide bandgap >> High breakdown voltages
- Wide bandgap >> Thermal stability
- 2DEG channel due to polarization (very high densities possible)

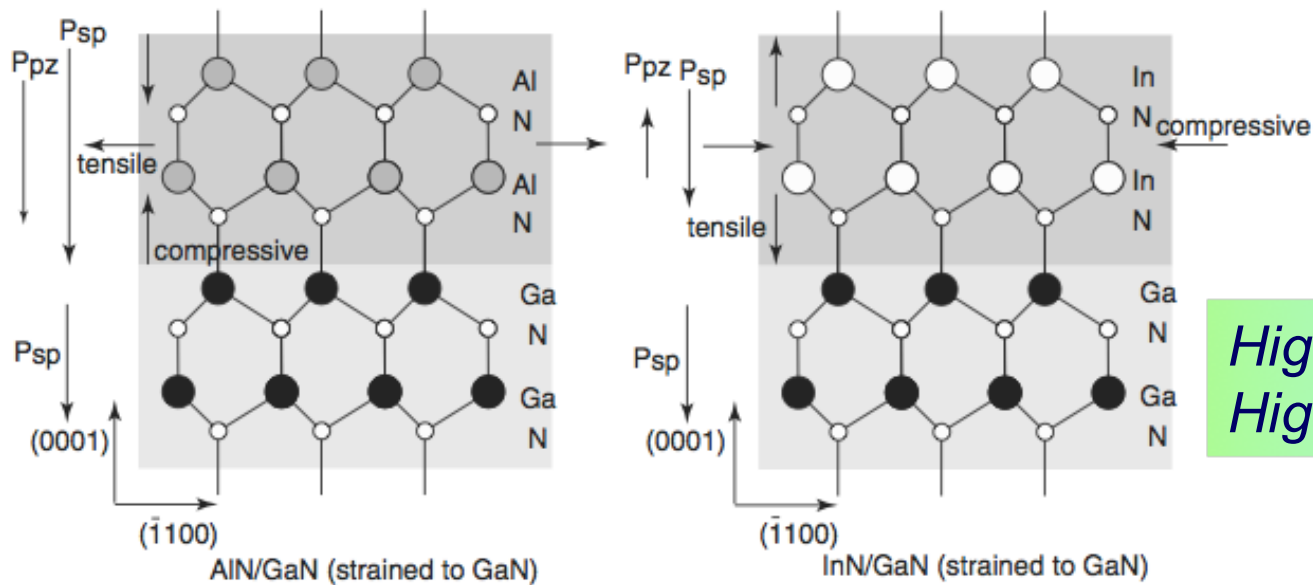


Polarization charges at Heterojunctions



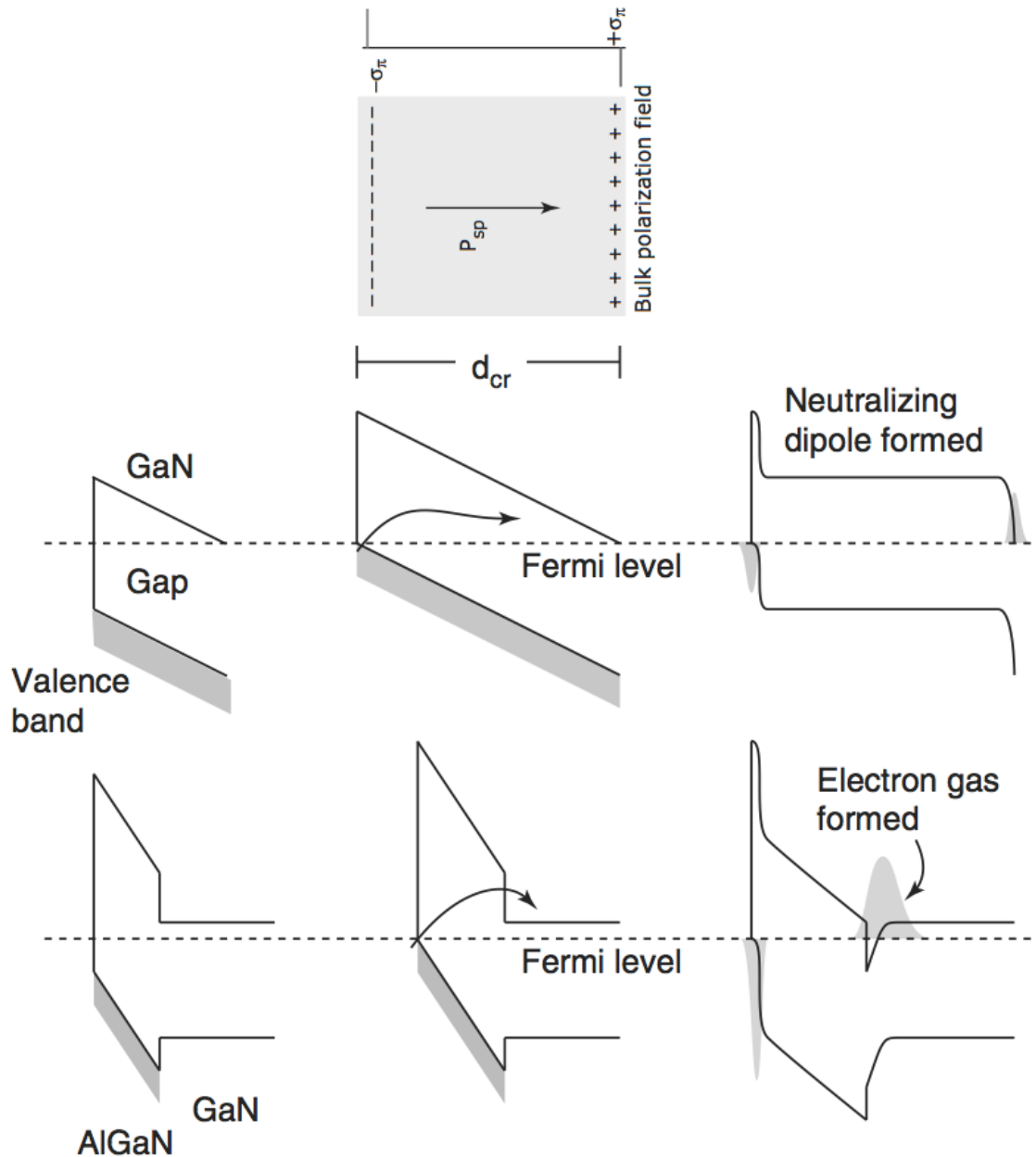
$$\frac{\sigma_{\pi}}{e} = \frac{1}{e} (\mathbf{P}_{AlN} - \mathbf{P}_{GaN}) \cdot \mathbf{n} = 6.4 \times 10^{13} / \text{cm}^2.$$

$$F_{\pi} \approx 1 - 10 \text{ MV/cm}$$



High polarization charges:
High electric fields

Polarization charges @ heterojunctions: Consequences



High polarization charges:
High electric fields



High electric fields:
Energy band bending



Semiconductors: Bands
cannot bend forever!

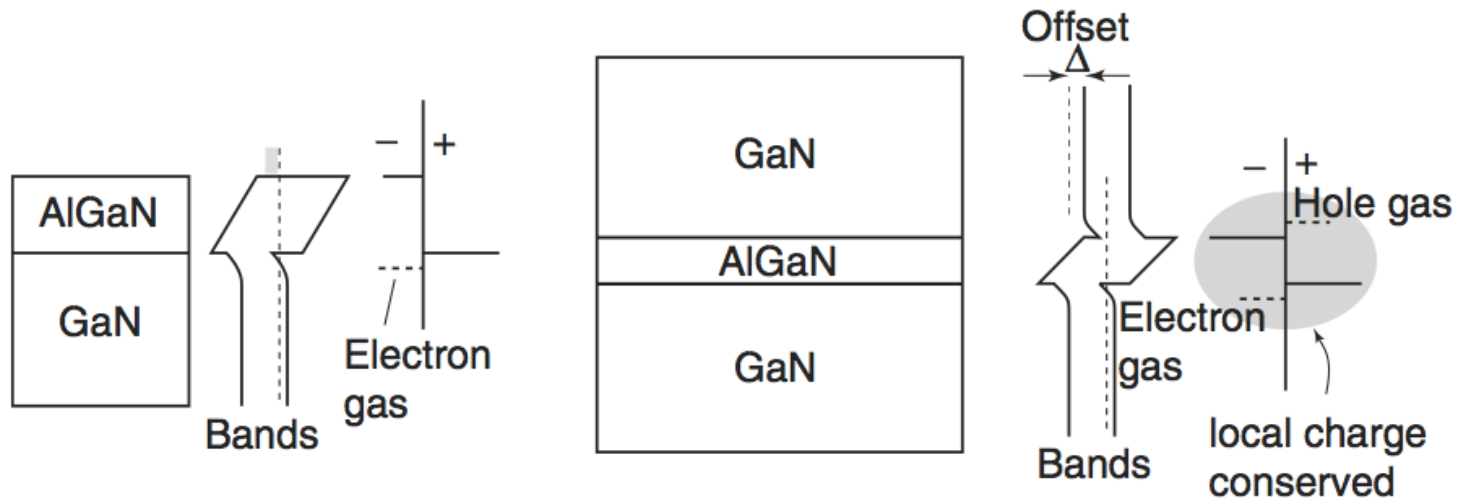


$$d_{cr} = E_g / F_{\pi}$$

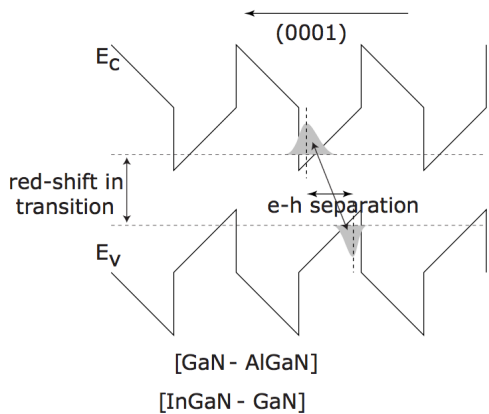


Creation of
"Neutralizing Dipole" ->
Mobile carriers!

Polarization Engineering in III-Nitride Heterostructures



Polarization creates mobile electron and hole gases: WITHOUT DOPING!



“Dipole Engineering”-
Polarization dipoles can create artificial
band-offsets in GaN heterostructures

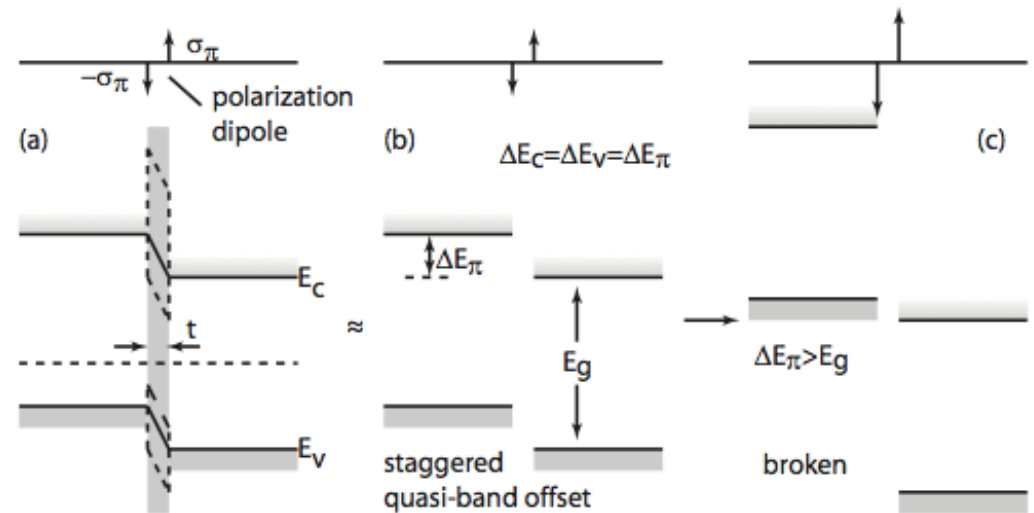


Figure 2 An ultrathin polarization dipole layer results in a quasi band-offset leading to staggered or broken gap alignments.

Polarization and Band Parameters for III-Nitrides

Parameters for InN, GaN, AlN, and Their Ternary Compounds

Table D.1 Recommended Band Structure Parameters for Wurtzite Nitride Binaries^a

Parameters	GaN	AlN	InN
a (Å) at $T = 300\text{K}$	3.189	3.112	3.545
c (Å) at $T = 300\text{K}$	5.185	4.982	5.703
E_g (eV) at $T = 0\text{K}$	3.510	6.25	0.69 ^b
at $T = 300\text{K}$	3.44	6.16	0.64
α (meV/K)	0.909	1.799	0.41 ^b
β (K)	830	1462	454 ^b
Δ_{cr} (eV)	0.010	-0.169	0.040
Δ_{so} (eV)	0.017	0.019	0.005
m_e^{\parallel}/m_0	0.20	0.32	0.07
m_e^{\perp}/m_0	0.20	0.30	0.07
A_1	-7.21	-3.86	-8.21
A_2	-0.44	-0.25	-0.68
A_3	6.68	3.58	7.57
A_4	-3.46	-1.32	-5.23
A_5	-3.40	-1.47	-5.11
A_6	-4.90	-1.64	-5.96
A_7 (eV Å)	0.0937	0	0
a_1 (eV)	-4.9	-3.4	-3.5
a_2 (eV)	-11.3	-11.8	-3.5
D_1 (eV)	-3.7	-17.1	-3.7
D_2 (eV)	4.5	7.9	4.5
D_3 (eV)	8.2	8.8	8.2
D_4 (eV)	-4.1	-3.9	-4.1
D_5 (eV)	-4.0	-3.4	-4.0
D_6 (eV)	-5.5	-3.4	-5.5
C_{11} (GPa)	390	396	223
C_{12} (GPa)	145	137	115
C_{13} (GPa)	106	108	92

(Continued)

Table D.2 Band Gap of In_xGa_{1-x}N, Al_xGa_{1-x}N, and Al_xIn_{1-x}N

General Interpolation Formula for Ternary Compound Parameters P:

$$P(A_xB_{1-x}C) = xP(AC) + (1-x)P(BC)$$

Except Band-Gap Energy:

$$P(A_xB_{1-x}C) = xP(AC) + (1-x)P(BC) - bx(1-x)$$

In_xGa_{1-x}N

$$E_g(x) = xE_g(\text{InN}) + (1-x)E_g(\text{GaN}) - 1.4x(1-x) \text{ (eV)}$$

$$P^{SP}(x) = [-0.042x - 0.034(1-x) + 0.037x(1-x)] \text{ C/m}^2$$

$$P_{\text{In,Ga}_{1-x}\text{N}/\text{InN}}^{Pz}(x) = [-0.113(1-x) - 0.0276x(1-x)] \text{ C/m}^2$$

$$P_{\text{In,Ga}_{1-x}\text{N}/\text{GaN}}^{Pz}(x) = [0.148x - 0.0424x(1-x)] \text{ C/m}^2$$

$$P_{\text{In,Ga}_{1-x}\text{N}/\text{AlN}}^{Pz}(x) = [0.182x - 0.026(1-x) - 0.0456x(1-x)] \text{ C/m}^2$$

Al_xGa_{1-x}N

$$E_g(x) = xE_g(\text{AlN}) + (1-x)E_g(\text{GaN}) - 0.7x(1-x) \text{ (eV)}$$

$$P^{SP}(x) = [-0.090x - 0.034(1-x) + 0.021x(1-x)] \text{ C/m}^2$$

$$P_{\text{Al,Ga}_{1-x}\text{N}/\text{InN}}^{Pz} = [-0.28x - 0.113(1-x) + 0.42x(1-x)] \text{ C/m}^2$$

$$P_{\text{Al,Ga}_{1-x}\text{N}/\text{GaN}}^{Pz} = [-0.0525x + 0.0282x(1-x)] \text{ C/m}^2$$

$$P_{\text{Al,Ga}_{1-x}\text{N}/\text{AlN}}^{Pz} = [0.026(1-x) - 0.0248x(1-x)] \text{ C/m}^2$$

Al_xIn_{1-x}N

$$E_g(x) = xE_g(\text{AlN}) + (1-x)E_g(\text{InN}) - 2.5x(1-x) \text{ (eV)}$$

$$P^{SP}(x) = [-0.090x - 0.042(1-x) + 0.070x(1-x)] \text{ C/m}^2$$

$$P_{\text{Al}_x\text{In}_{1-x}\text{N}/\text{InN}}^{Pz}(x) = [-0.28x + 0.104x(1-x)] \text{ C/m}^2$$

$$P_{\text{Al}_x\text{In}_{1-x}\text{N}/\text{GaN}}^{Pz}(x) = [-0.0525x + 0.148(1-x) + 0.0938x(1-x)] \text{ C/m}^2$$

$$P_{\text{Al}_x\text{In}_{1-x}\text{N}/\text{AlN}}^{Pz} = [0.182(1-x) + 0.092x(1-x)] \text{ C/m}^2$$

Parameters	GaN	AlN	InN
C_{33} (GPa)	398	373	224
C_{44} (GPa)	105	116	48
d_{13} (pm/V)	-1.6	-2.1	-3.5
d_{33} (pm/V)	3.1	5.4	7.6
d_{15} (pm/V)	3.1	3.6	5.5
P_{sp} (C/m ²)	-0.034	-0.090	-0.042

Note: $E_g(T) = E_g(0) - \frac{\alpha T^2}{T + \beta}$

Piezoelectric Polarization in III-Nitrides

$$P_{pz,i} = e_{ijk}\epsilon_{jk} = d_{ijk}\sigma_{jk}$$

Piezoelectric Polarization Field

$$e = \begin{pmatrix} 0 & 0 & 0 & 0 & e_{14} & 0 \\ 0 & 0 & 0 & e_{15} & 0 & 0 \\ e_{31} & e_{31} & e_{33} & 0 & 0 & 0 \end{pmatrix} \quad e_{jk} = c_{ij}d_{ik}$$

$$c = \begin{pmatrix} c_{11} & c_{12} & c_{13} & 0 & 0 & 0 \\ c_{12} & c_{11} & c_{13} & 0 & 0 & 0 \\ c_{13} & c_{13} & c_{11} & 0 & 0 & 0 \\ 0 & 0 & 0 & c_{44} & 0 & 0 \\ 0 & 0 & 0 & 0 & c_{44} & 0 \\ 0 & 0 & 0 & 0 & 0 & \frac{1}{2}(c_{11} - c_{12}) \end{pmatrix}$$

$$P_3 = e_{33}\epsilon_3 + e_{31}(\epsilon_1 + \epsilon_2)$$

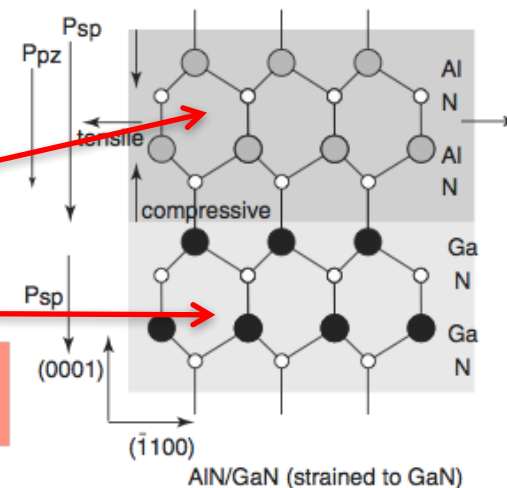
$$\epsilon_3 = -2\epsilon_1(c_{13}/c_{33})$$

$$P_{pz,[0001]} = 2(e_{31} - e_{33}\frac{c_{13}}{c_{33}})\epsilon_1$$

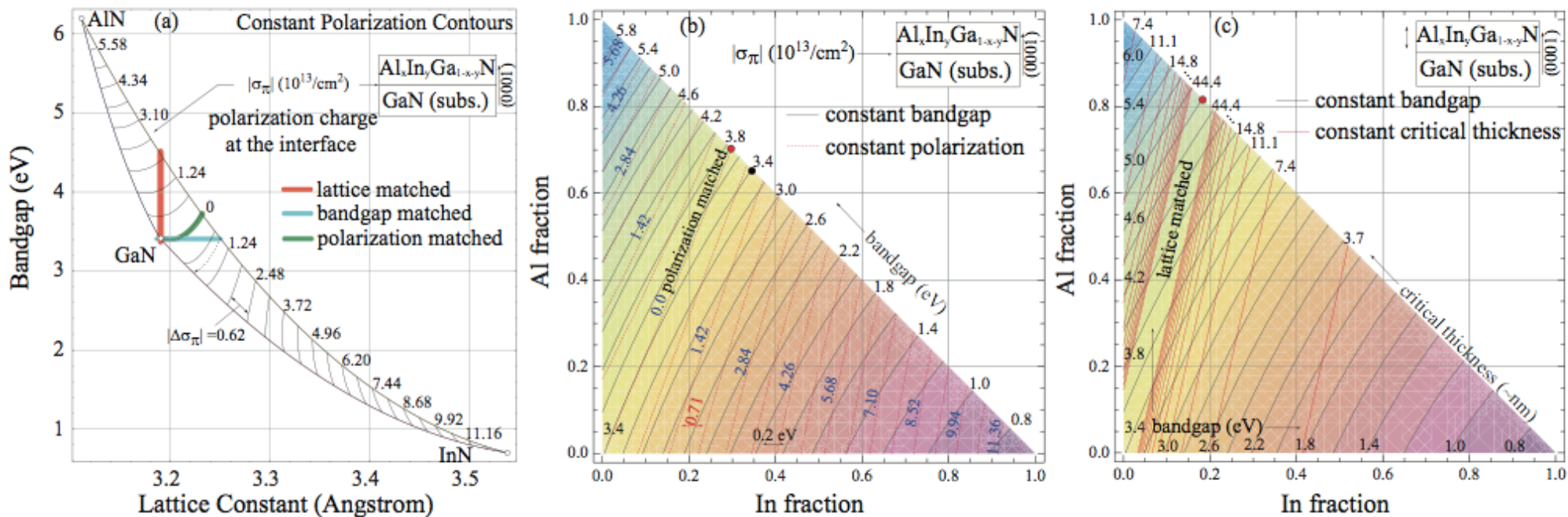
Piezoelectric Polarization Field in Wurtzite GaN Heterostructures

$$\epsilon_1 = (a - a_{GaN})/a_{GaN}$$

Lattice constant of the substrate



Polarization Engineering in III-Nitride Heterostructures



- Lattice matched heterostructures – same lattice constants
- Polarization-matched heterostructures – same polarization

Semiconductors for Photonics

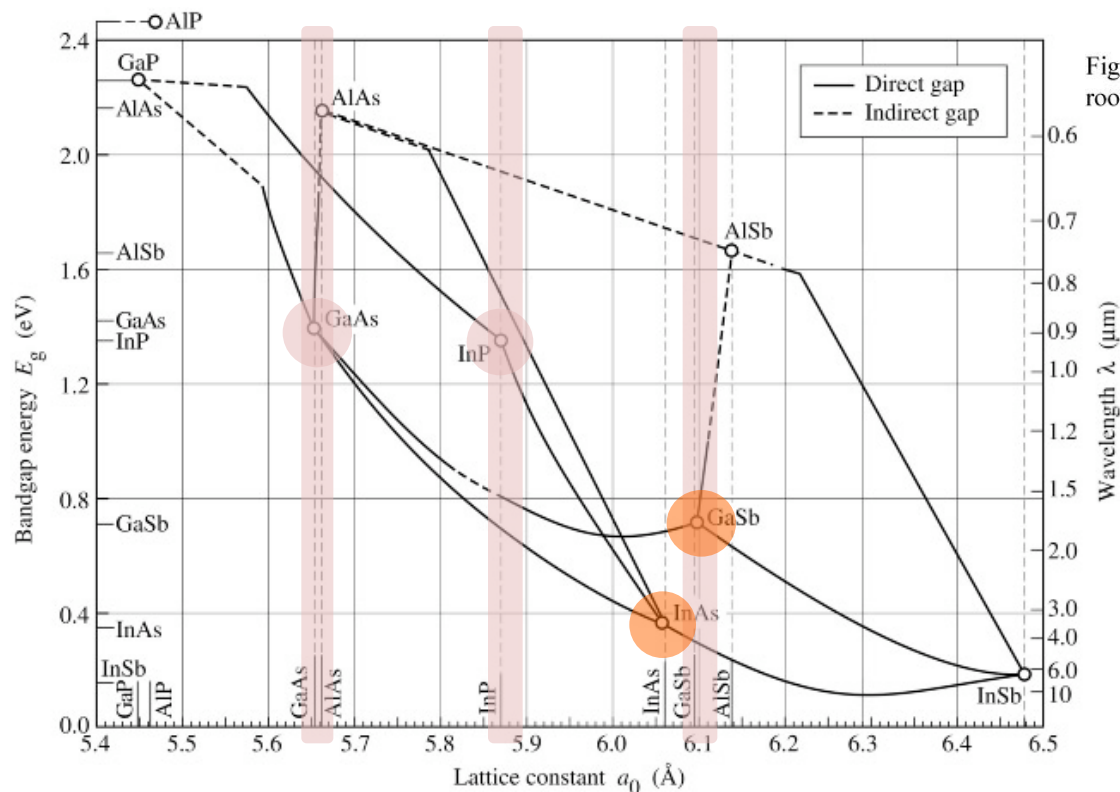


Fig. 7.6. Bandgap energy and lattice constant of various III-V semiconductors at room temperature (adopted from Tien, 1988).

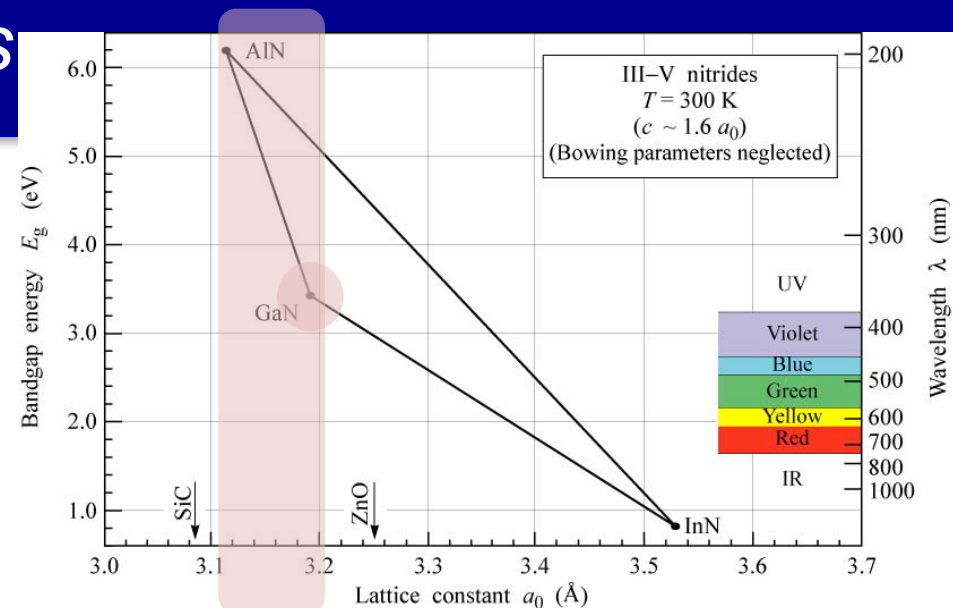


Fig. 12.12. Bandgap energy versus lattice constant of III-V nitride semiconductors at room temperature.

E. F. Schubert

Major III-V Semiconductor families:

- GaAs-based (AlGaAs/GaAs) (strain-free, or pseudomorphic)
- InP based (InGaAs channels)
- 6.1 Angstrom/narrow gap channels (generally grown metamorphically on GaAs)
- GaN-based (InGaN/GaN and AlGaN/GaN) (typically pseudomorphic)

Optical absorption in Compound Semiconductors

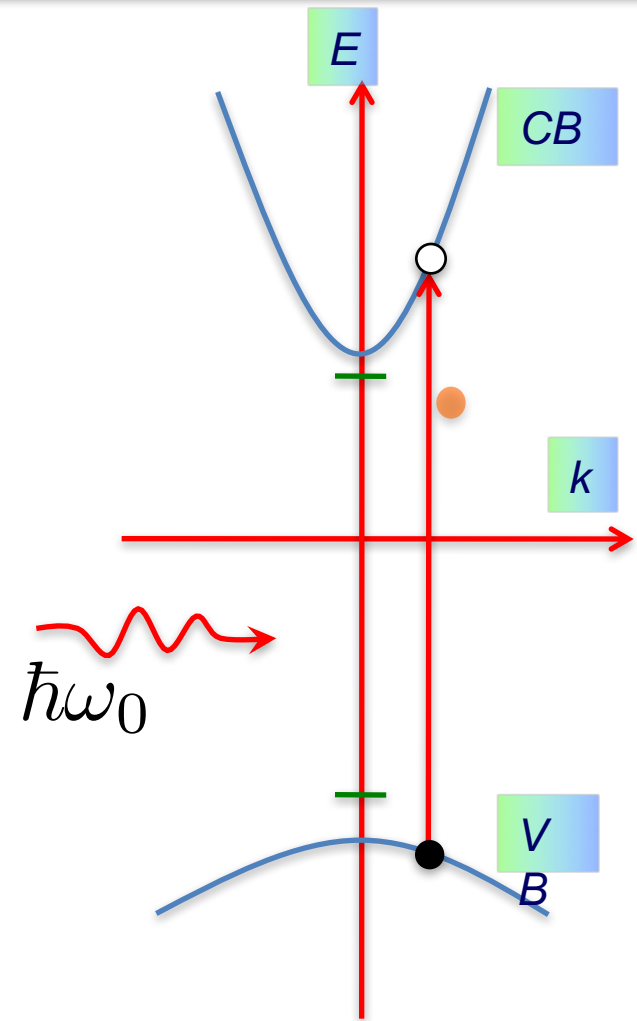
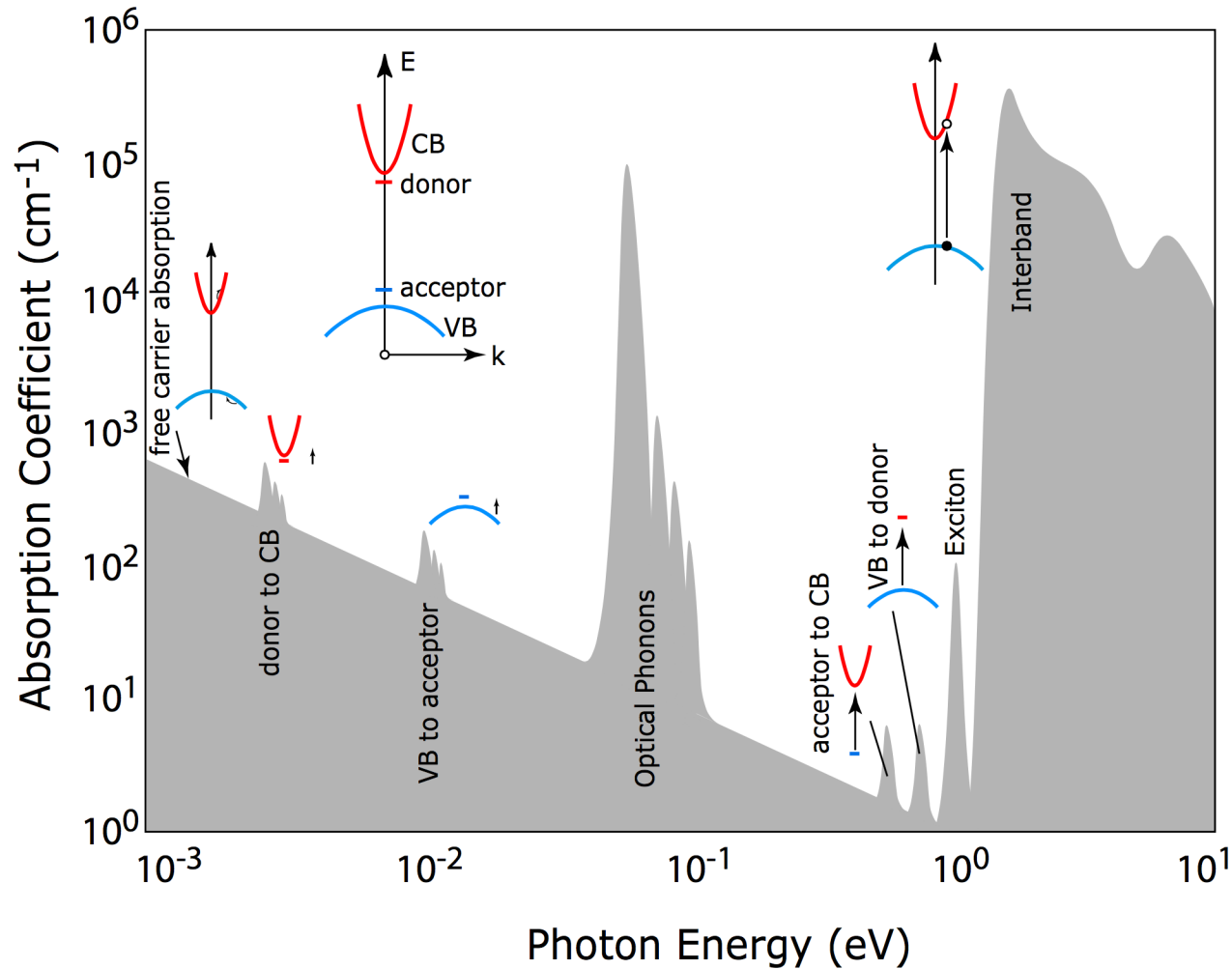
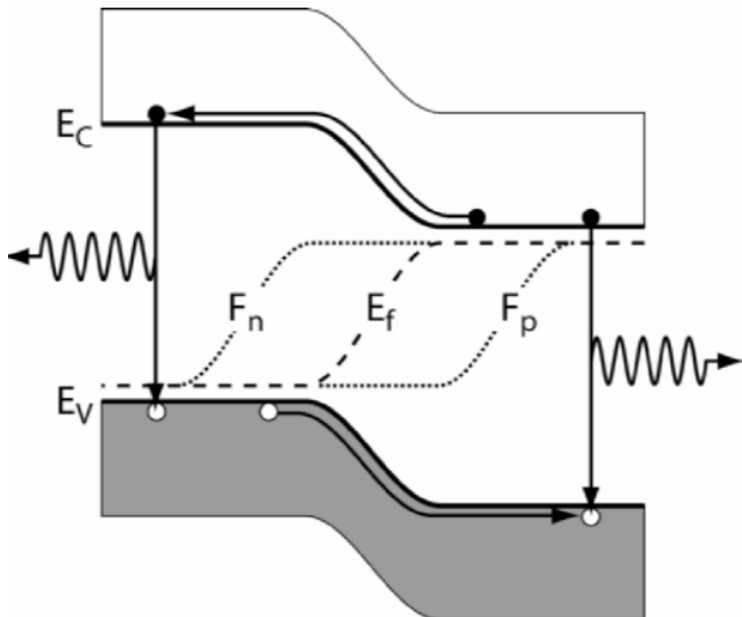


FIGURE 26.1: Schematic absorption spectrum $\alpha(\hbar\omega)$ of bulk semiconductors. The insets depict various state transitions upon absorption of photons.

- Absorption power is Quantified by “Absorption Coefficient”
- A negative absorption coefficient is equivalent to optical gain!

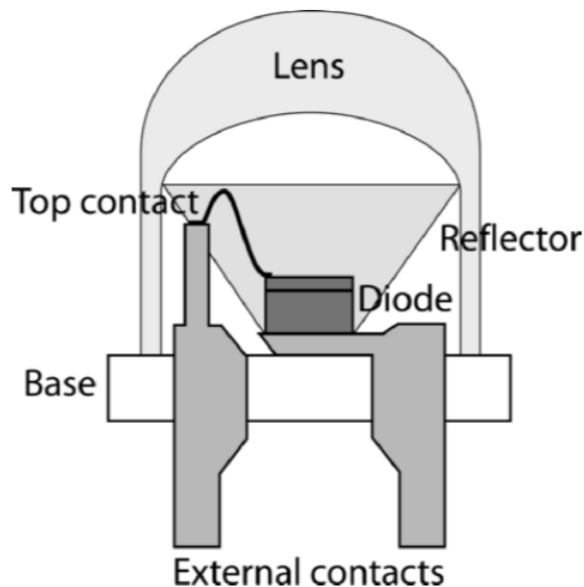
• Adapted from: Wolfe/Holonyak/Stillman
Physical Properties of Semiconductors

Compound Semiconductor Heterojunction LEDs



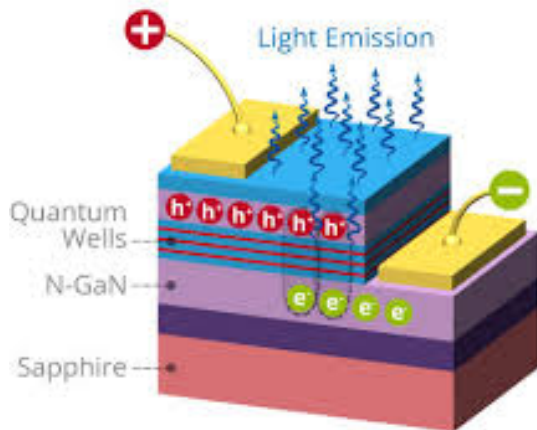
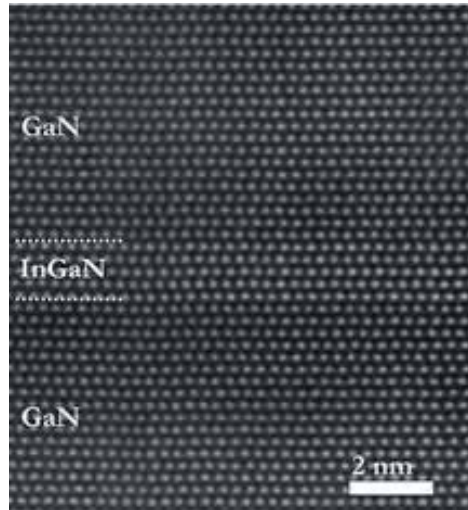
$$R_{\text{radiative}} = npv_{\text{th}}S_{\text{R}}/2\eta^2$$

$$S_{\text{R}} \approx 5 \times 10^{-25} \eta^2 E_{\text{gap}}^2 \alpha (m_e^* m_h^*)^{-3/2} (300/T)^{5/2} \text{ cm}^2$$



(Rockett)

GaN based Visible LEDs and Lasers



The Nobel Prize in Physics 2014

Isamu Akasaki, Hiroshi Amano, Shuji Nakamura

Share this: [f](#) [G+](#) [t](#) [+](#) 2.5K [✉](#)

The Nobel Prize in Physics 2014



Photo: A. Mahmoud

Isamu Akasaki

Prize share: 1/3



Photo: A. Mahmoud

Hiroshi Amano

Prize share: 1/3



Photo: A. Mahmoud

Shuji Nakamura

Prize share: 1/3

The Nobel Prize in Physics 2014 was awarded jointly to Isamu Akasaki, Hiroshi Amano and Shuji Nakamura *"for the invention of efficient blue light-emitting diodes which has enabled bright and energy-saving white light sources"*.

- Science of light

How to make a Semiconductor Light Emitter

REVIEWS OF MODERN PHYSICS, VOLUME 87, OCTOBER–DECEMBER 2015

Nobel Lecture: Background story of the invention of efficient blue InGaN light emitting diodes*

Shuji Nakamura

University of California, Santa Barbara, California, USA

(published 5 October 2015)

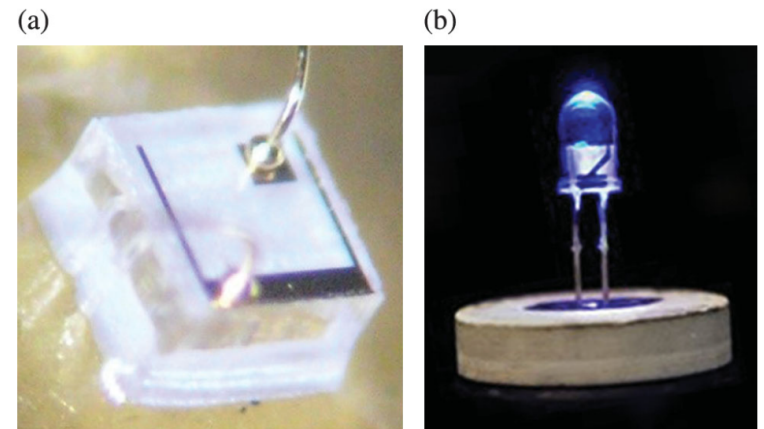
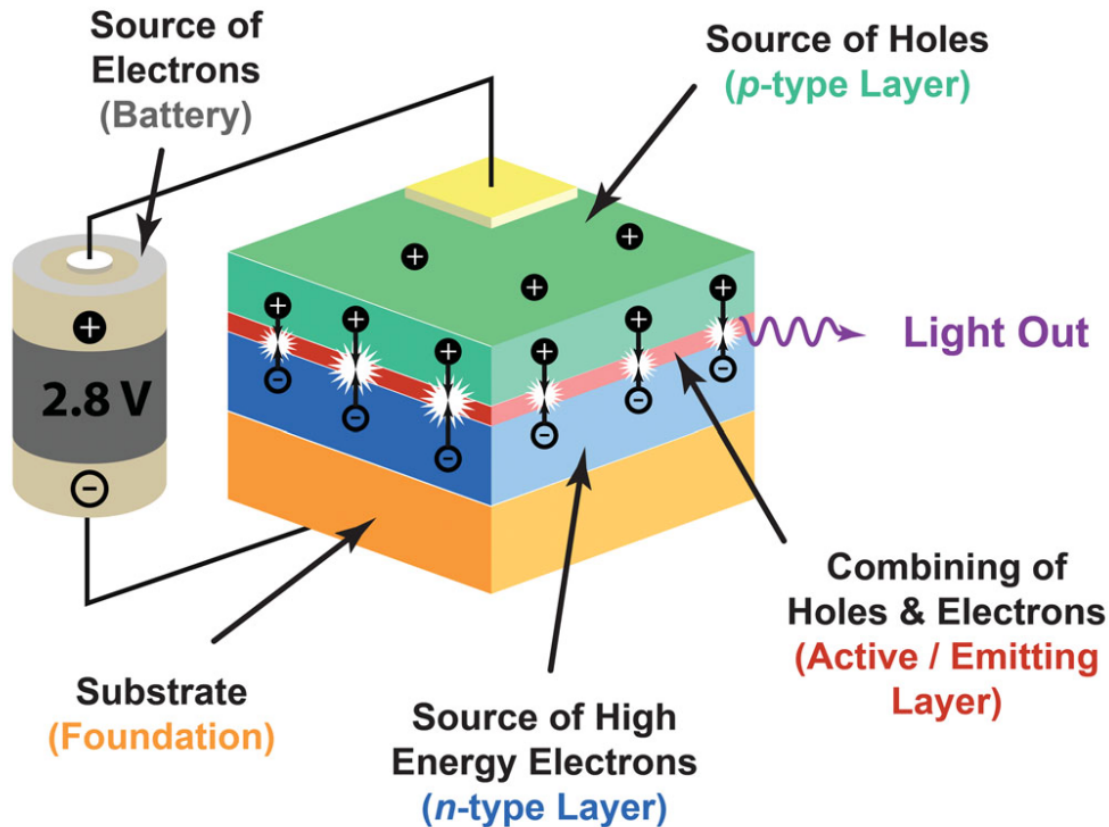
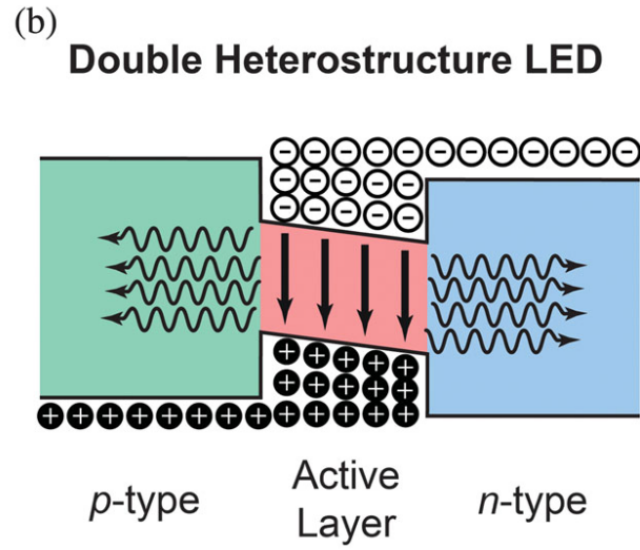
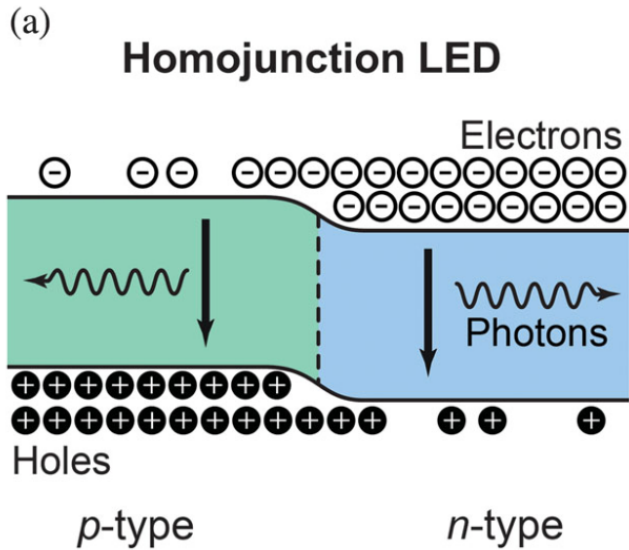
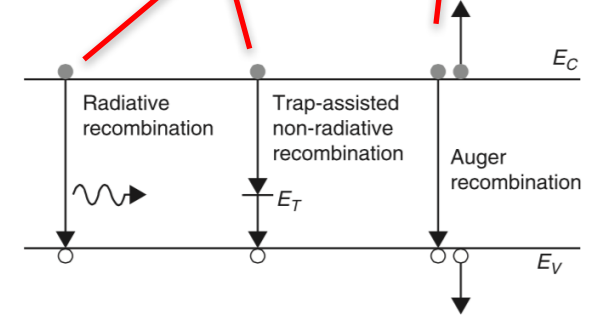
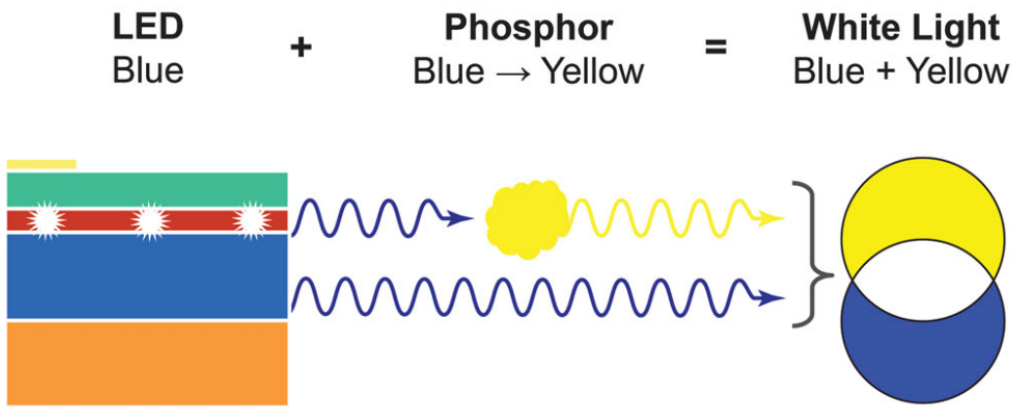


FIG. 2 (color). (a) Image of a blue GaN LED with attached gold wire contacts (size of diode $0.4 \times 0.4 \text{ mm}^2$) and (b) the same LED packaged as a commercial product. From Nakamura, Mukai, and Senoh, 1994.

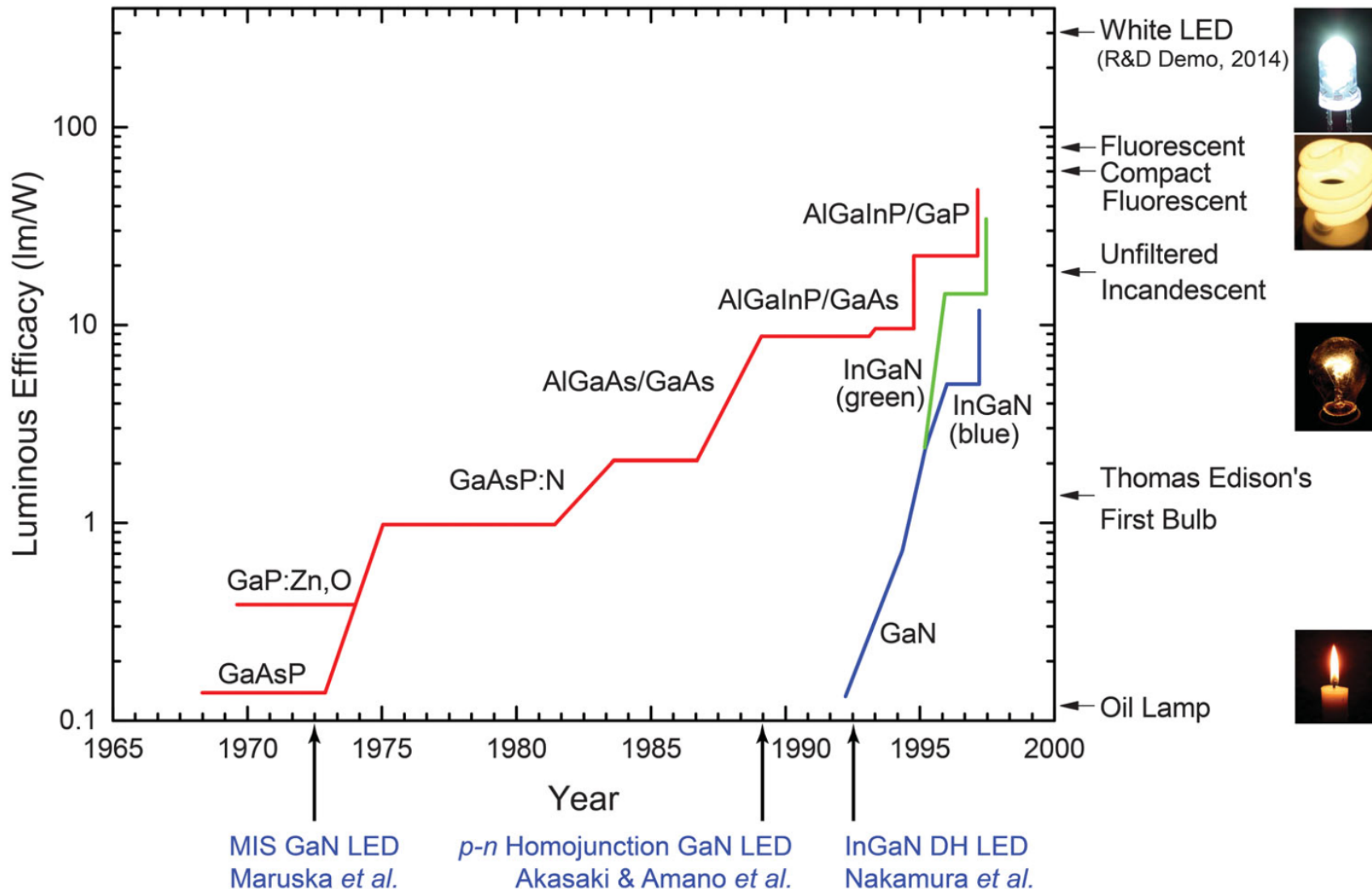
How to make white light with semiconductors



$$\begin{aligned}
 \text{IQE} &= \frac{\text{Light generated}}{\text{Electrons injected}} \\
 &= \frac{R_{\text{radiative}}}{R_{\text{radiative}} + R_{\text{nonradiative}}} \\
 &= \frac{Bn^2}{An + Bn^2 + Cn^3}
 \end{aligned}$$



Solid state lighting: The lighting of the future



Effect of Defects and Quantum Wells on Efficiency

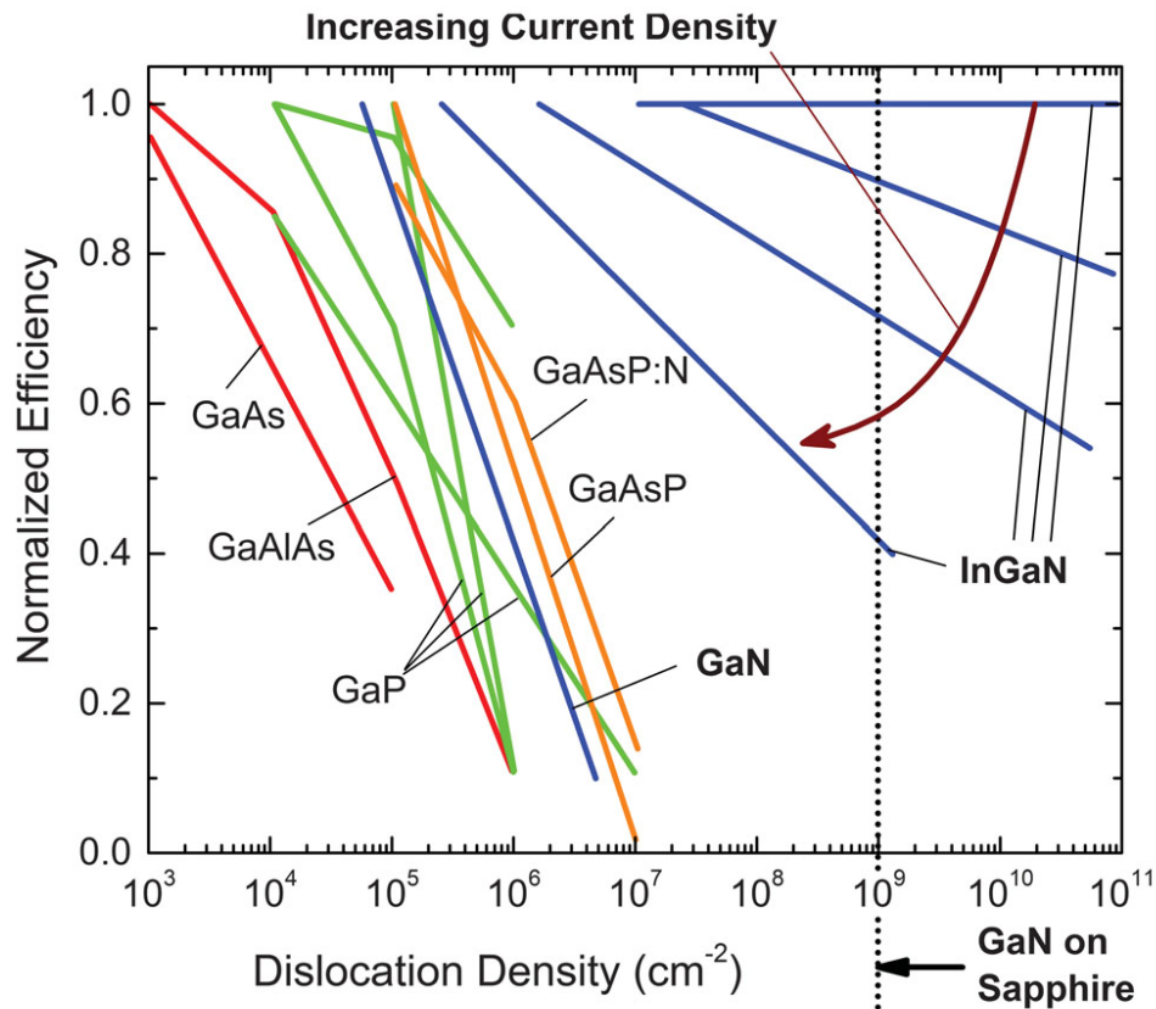


FIG. 13 (color). Dependence of LED efficiency on dislocation density for various semiconductor materials. From Lester *et al.*, 1995, Chichibu *et al.*, 1996, and Nakamura, 1998.

Absorption Coefficient of Compound Semiconductors

$$\alpha(\hbar\omega) = \frac{\text{Number of photons absorbed per unit volume per second}}{\text{Number of photons incident per unit area per second}}$$

$$\alpha(\hbar\omega) = \frac{R}{S/\hbar\omega}$$

Number of photons incident per unit area per second:

Vector potential:

$$\mathbf{A}(\mathbf{r}, t) = \hat{e}A_0 \cos(\mathbf{k}_{op} \cdot \mathbf{r} - \omega t)$$



Electric Field:

$$\begin{aligned} \mathbf{E}(\mathbf{r}, t) &= -\frac{\partial}{\partial t} \mathbf{A}(\mathbf{r}, t) \\ &= -\hat{e}\omega A_0 \sin(\mathbf{k}_{op} \cdot \mathbf{r} - \omega t) \end{aligned}$$



Magnetic Field:

$$\begin{aligned} \mathbf{H}(\mathbf{r}, t) &= \frac{1}{\mu} \nabla \times \mathbf{A}(\mathbf{r}, t) \\ &= -\frac{1}{\mu} \mathbf{k}_{op} \times \hat{e}A_0 \sin(\mathbf{k}_{op} \cdot \mathbf{r} - \omega t) \end{aligned}$$

Poynting Vector:

$$\begin{aligned} \mathbf{S}(\mathbf{r}, t) &= \mathbf{E}(\mathbf{r}, t) \times \mathbf{H}(\mathbf{r}, t) \\ &= \mathbf{k}_{op} \frac{\omega A_0^2}{\mu} \sin^2(\mathbf{k}_{op} \cdot \mathbf{r} - \omega t) \end{aligned}$$

$$\langle \mathbf{S}(\mathbf{r}, t) \rangle = \frac{\omega A_0^2}{2\mu} \mathbf{k}_{op}$$

Incident energy per unit area per second:

$$S = |\langle \mathbf{S}(\mathbf{r}, t) \rangle| = \frac{\omega A_0^2}{2\mu} k_{op} = \frac{n_r c \epsilon_0 \omega^2 A_0^2}{2}$$

- Incident photon number per unit area per second: $|\text{Poynting vector}| / \text{photon energy}$
- Goes as square of the amplitude of vector potential (or electric field, or magnetic field)

Absorption Spectra of Compound Semiconductors

$$E_c(\mathbf{k}) = E_g + \frac{\hbar^2 k^2}{2m_e^*}$$

$$E_v(\mathbf{k}) = -\frac{\hbar^2 k^2}{2m_h^*}$$

$$E_c(\mathbf{k}) - E_v(\mathbf{k}) = E_g + \frac{\hbar^2 k^2}{2m_r^*}$$

$$\frac{1}{m_r^*} = \frac{1}{m_e^*} + \frac{1}{m_h^*}$$

first assume
 $f_v(k)=1, f_c(k)=0$

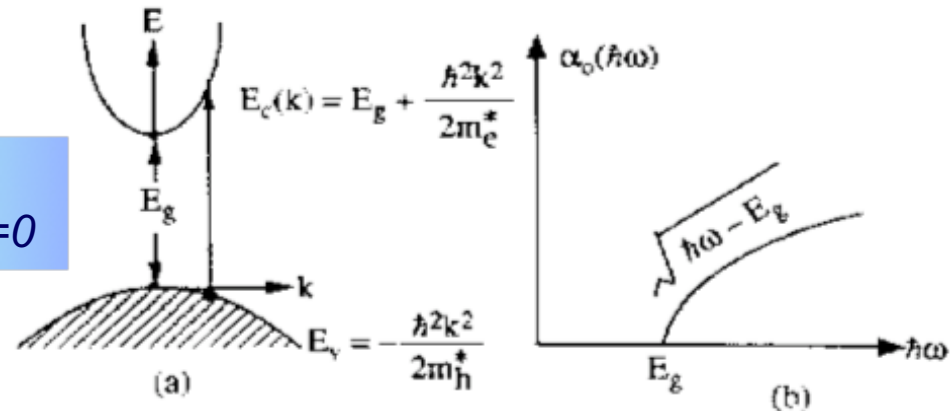


Figure 9.5 (a) Optical absorption in a direct-band-gap semiconductor (b) The absorption spectrum due to the interband transitions

$$\alpha_0(\hbar\omega) = C_0 |\hat{e} \cdot \mathbf{p}_{cv}|^2 \times (g_s g_v) \times \int_{\mathbf{k}} \frac{d^3 \mathbf{k}}{(2\pi)^3} \delta[E_c(\mathbf{k}) - (E_v(\mathbf{k}) + \hbar\omega)]$$

$$\gamma_{abs} = \frac{2\pi}{\hbar} |\langle b|W(\mathbf{r})|a \rangle|^2 \delta[E_b - (E_a + \hbar\omega)]$$

Fermi's Golden Rule

$$\gamma_{em} = \frac{2\pi}{\hbar} |\langle a|W(\mathbf{r})|b \rangle|^2 \delta[E_a - (E_b - \hbar\omega)]$$

$$\alpha_0(\hbar\omega) = C_0 |\hat{e} \cdot \mathbf{p}_{cv}|^2 \cdot \rho_r(\hbar\omega - E_g)$$

Optical absorption coeff. of bulk semiconductor
(general form applicable to quantum wells, etc...)

$$\rho_r(u) = g_s g_v \cdot \frac{1}{(2\pi)^2} \cdot \left(\frac{2m_r^*}{\hbar^2}\right)^{\frac{3}{2}} \cdot \sqrt{u}$$

"Joint" density of states of (VB, CB)

$$C_0 = \frac{\pi e^2}{n_r c \epsilon_0 m_0^2 \omega}$$

This and next few slides:

From: S. L. Chuang (Photonic Devices)

Optical Matrix Elements for Transitions

$$\alpha_0(\hbar\omega) = \frac{2.64 \times 10^5}{\eta_r} \cdot \underbrace{\frac{2|\hat{e} \cdot \mathbf{p}_{cv}|^2/m_0}{\hbar\omega}}_{\text{'oscillator strength'}} \cdot \underbrace{\left(\frac{2m_r^*}{m_0}\right)^{\frac{3}{2}} \cdot \sqrt{\hbar\omega - E_g}}_{\propto \text{reduced DOS}} \text{ cm}^{-1}$$

Absorption spectrum of a general III-V semiconductor at equilibrium

Momentum matrix elements for bulk & quantum well structures

$$M_b^2 = \frac{1}{3} P_x^2 = \frac{m_0^2}{3\hbar^2} P^2$$

$$= \left(\frac{m_0}{m_c^*} - 1 \right) \frac{m_0 E_g (E_g + \Delta)}{6(E_g + \frac{2}{3}\Delta)}$$

Table 9.1 Summary of the Momentum Matrix Elements in Parabolic Band Model ($|\hat{e} \cdot \mathbf{p}_{cv}|^2 = |\hat{e} \cdot \mathbf{M}|^2$)

Bulk $|\hat{x} \cdot \mathbf{p}_{cv}|^2 = |\hat{y} \cdot \mathbf{p}_{cv}|^2 = |\hat{z} \cdot \mathbf{p}_{cv}|^2 = M_b^2 = \frac{m_0}{6} E_p$

Quantum Well

TE Polarization ($\hat{e} = \hat{x}$ or \hat{y})

$$\langle |\hat{e} \cdot \mathbf{M}_{c-hh}|^2 \rangle = \frac{3}{4}(1 + \cos^2 \theta) M_b^2$$

$$\langle |\hat{e} \cdot \mathbf{M}_{c-lh}|^2 \rangle = \left(\frac{5}{4} - \frac{3}{4}\cos^2 \theta\right) M_b^2$$

TM Polarization ($\hat{e} = \hat{z}$)

$$\langle |\hat{e} \cdot \mathbf{M}_{c-hh}|^2 \rangle = \frac{3}{2}\sin^2 \theta M_b^2$$

$$\langle |\hat{e} \cdot \mathbf{M}_{c-lh}|^2 \rangle = \frac{1}{2}(1 + 3\cos^2 \theta) M_b^2$$

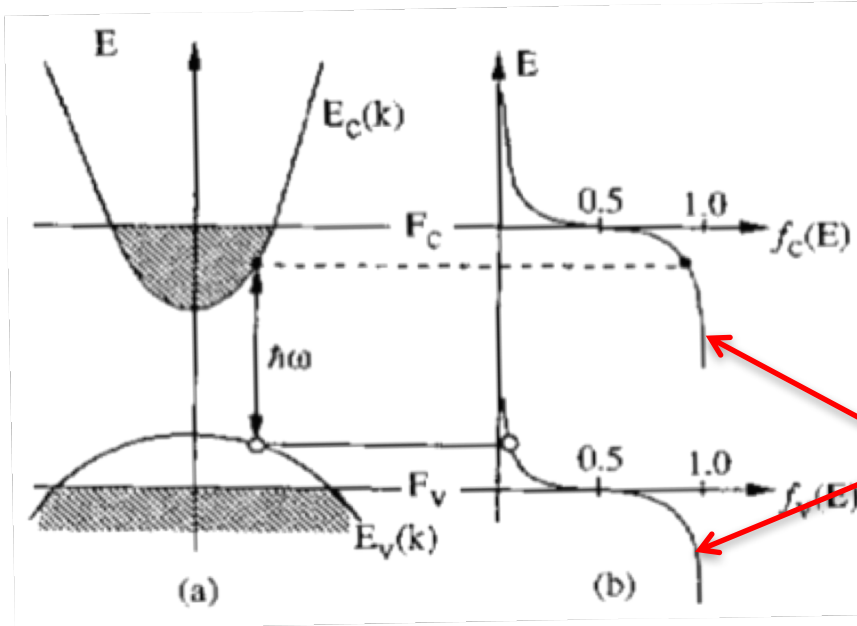
Conservation Rule

$$\langle |\hat{x} \cdot \mathbf{M}_{c-h}|^2 \rangle + \langle |\hat{y} \cdot \mathbf{M}_{c-h}|^2 \rangle + \langle |\hat{z} \cdot \mathbf{M}_{c-h}|^2 \rangle = 3M_b^2, (h = hh \text{ or } lh)$$

$$\langle |\hat{e} \cdot \mathbf{M}_{c-hh}|^2 \rangle + \langle |\hat{e} \cdot \mathbf{M}_{c-lh}|^2 \rangle = 2M_b^2$$

Optical Gain in Semiconductors

- We have looked at light absorption by a semiconductor (useful for photodetectors & solar cells)
- But LEDs and LASERs are electrically injected light emitters
- The same theory that explains absorption explains emission under electrical injection as well



Non-equilibrium Fermi-Dirac functions with electron quasi-Fermi levels (note: not necessary to talk about holes here)
 F_c : Conduction Band quasi-Fermi level
 F_v : Valence Band quasi-Fermi level

$$f_v(\mathbf{k}) = \frac{1}{1 + e^{(E_v(\mathbf{k}) - F_v)/k_B T}}$$

$$f_c(\mathbf{k}) = \frac{1}{1 + e^{(E_c(\mathbf{k}) - F_c)/k_B T}}$$

$$\alpha(\hbar\omega) = C_0 |\hat{e} \cdot \mathbf{p}_{cv}|^2 \times (g_s g_v) \times \int_{\mathbf{k}} \frac{d^3 \mathbf{k}}{(2\pi)^3} \delta[E_g + \frac{\hbar^2 k^2}{2m_r^*} - \hbar\omega] \times [f_v(\mathbf{k}) - f_c(\mathbf{k})]$$

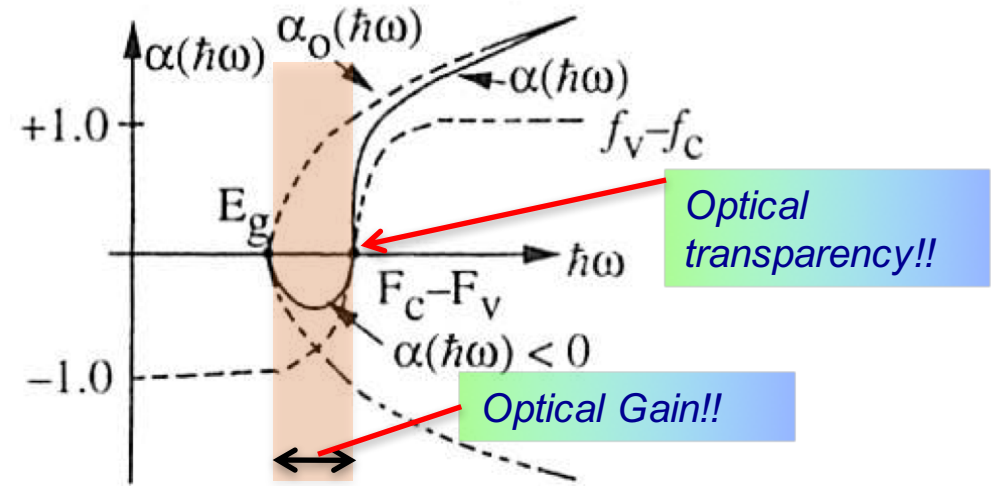
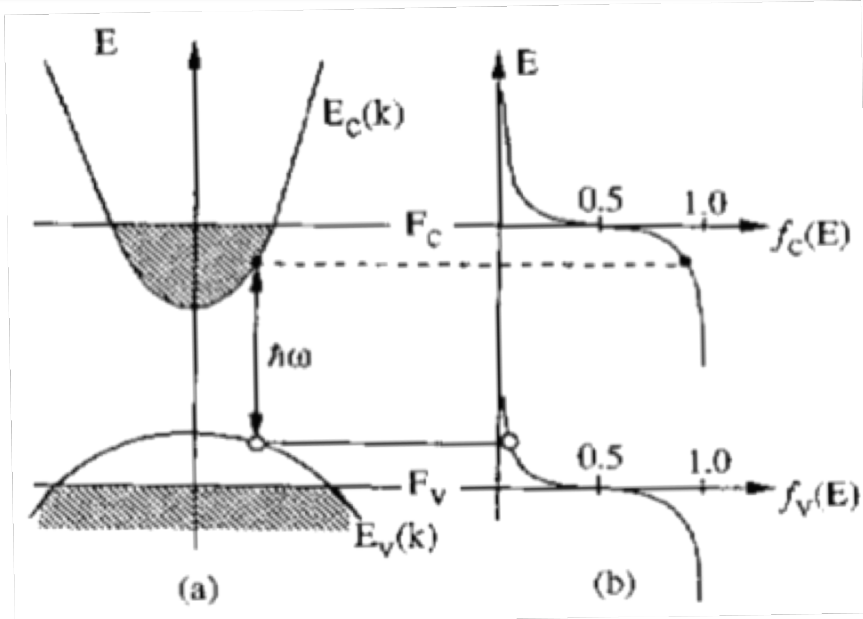
Non-equilibrium absorption coefficient

$$\alpha(\hbar\omega) = \alpha_0(\hbar\omega) \times [f_v(k_0) - f_c(k_0)]$$

$$k_0 = \sqrt{\frac{2m_r^*}{\hbar^2} (\hbar\omega - E_g)}$$

Fundamental result for understanding LEDs and LASERs

Optical Gain in Non-Equilibrium Conditions



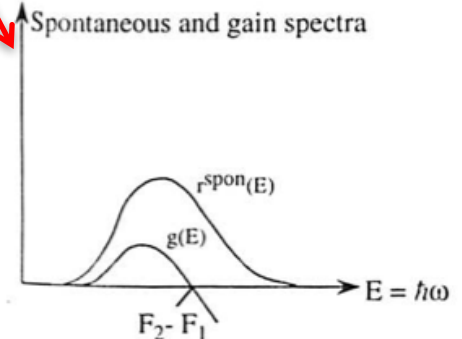
$$\alpha(\hbar\omega) = \alpha_0(\hbar\omega) \times [f_v(k_0) - f_c(k_0)] \quad k_0 = \sqrt{\frac{2m_r^*}{\hbar^2}(\hbar\omega - E_g)}$$

$$f_v(k_0) - f_c(k_0) = \frac{\exp\left(\frac{E_c - F_c}{kT}\right) - \exp\left(\frac{E_v - F_v}{kT}\right)}{\left[1 + \exp\left(\frac{E_v - F_v}{kT}\right)\right]\left[1 + \exp\left(\frac{E_c - F_c}{kT}\right)\right]} < 0 \rightarrow$$

$$\exp\left(\frac{E_c - F_c}{kT}\right) < \exp\left(\frac{E_v - F_v}{kT}\right)$$

$$F_c - F_v > E_c - E_v = \hbar\omega$$

Bernard-Duraffourg inversion condition



The inversion conditions can be achieved by

- Optical pumping (gas lasers), or
- Electrical pumping (semiconductor LEDs & Lasers)

A laser requires a light emitter to be placed in a high-finesse (hi-Q) optical cavity to amplify a specific mode.

Absorption Coefficient/Optical Gain in Quantum Wells

$$\psi_v(r) = u_v(\mathbf{r}) \times \left[\frac{1}{\sqrt{A}} e^{i\mathbf{k}_t \cdot \rho} \right] \times V(n_v, z)$$

$$\psi_c(r) = u_c(\mathbf{r}) \times \left[\frac{1}{\sqrt{A}} e^{i\mathbf{k}'_t \cdot \rho} \right] \times C(n_c, z)$$

$$\mathbf{p}_{ba} = \langle \psi_c | \mathbf{p} | \psi_v \rangle \approx \langle u_c | \mathbf{p} | u_v \rangle \times \delta_{\mathbf{k}_t, \mathbf{k}'_t} \times I_{v, n_v}^{c, n_c}$$

$$I_{hm}^{en} = \int_{-\infty}^{+\infty} dz C^*(n_c, z) V(n_v, z)$$

Effective-mass functions!!

Determines selection rules

General form of absorption coefficient:

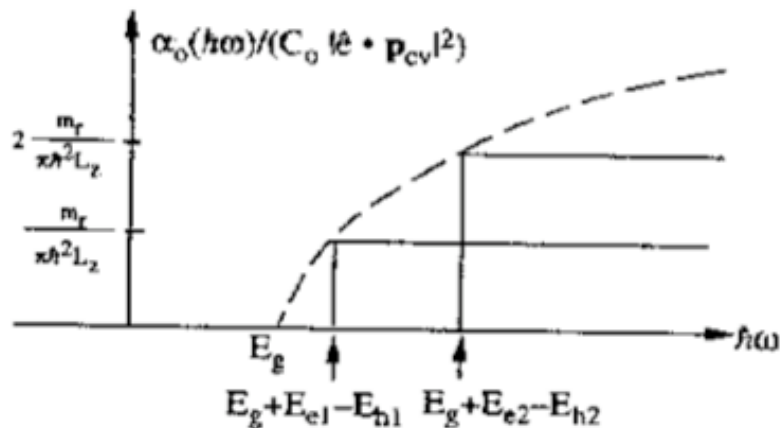
$$\alpha_0(\hbar\omega) = C_0 |\hat{e} \cdot \mathbf{p}_{cv}|^2 \cdot \rho_r(\hbar\omega - E_g)$$

$$C_0 = \frac{\pi e^2}{n_r c \epsilon_0 m_0^2 \omega}$$

$$\rho_r^{2D} = \frac{m_r}{\pi \hbar^2 L_z}$$

$$\frac{\alpha_0(\hbar\omega)}{C_0 |\hat{e} \cdot \mathbf{p}_{c,v}|^2} = \begin{cases} \frac{m_r}{\pi \hbar^2 L_z} & \text{for } E_{h1}^{e1} < \hbar\omega < E_{h2}^{e2} \\ 2 \frac{m_r}{\pi \hbar^2 L_z} & \text{for } E_{h2}^{e2} < \hbar\omega < E_{h3}^{e3} \\ 3 \frac{m_r}{\pi \hbar^2 L_z} & \text{for } E_{h3}^{e3} < \hbar\omega < E_{h4}^{e4} \\ \text{etc.} \end{cases}$$

Optical Gain in Quantum Wells



$$\frac{\alpha_0(\hbar\omega)}{C_0|\hat{e} \cdot \mathbf{p}_{cv}|^2} = \begin{cases} \frac{m_r}{\pi\hbar^2L_z} & \text{for } E_{h1}^{e1} < \hbar\omega < E_{h2}^{e2} \\ 2\frac{m_r}{\pi\hbar^2L_z} & \text{for } E_{h2}^{e2} < \hbar\omega < E_{h3}^{e3} \\ 3\frac{m_r}{\pi\hbar^2L_z} & \text{for } E_{h3}^{e3} < \hbar\omega < E_{h4}^{e4} \\ \text{etc.} \end{cases}$$

Figure 9.7. The stepwise absorption spectrum for a quantum-well structure.

Equilibrium absorption coefficient in QW is proportional to the joint DOS and has 2D subband features

$$\alpha(\hbar\omega) = \alpha_0(\hbar\omega) [f_c^m(E_t = \hbar\omega - E_{hm}^{en}) - f_c^n(E_t = \hbar\omega - E_{hm}^{en})]$$

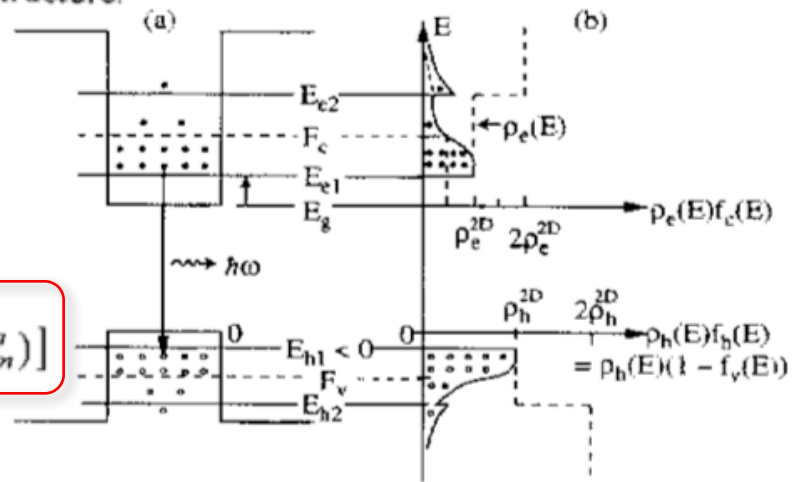
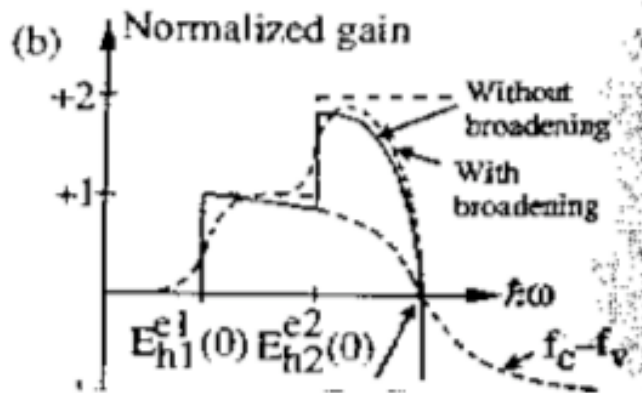
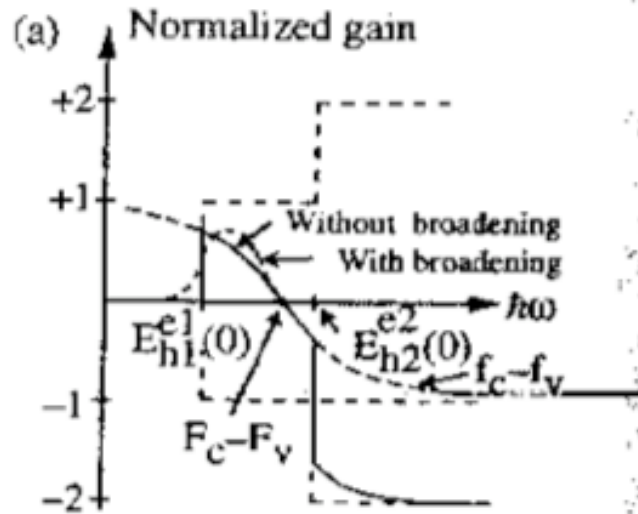
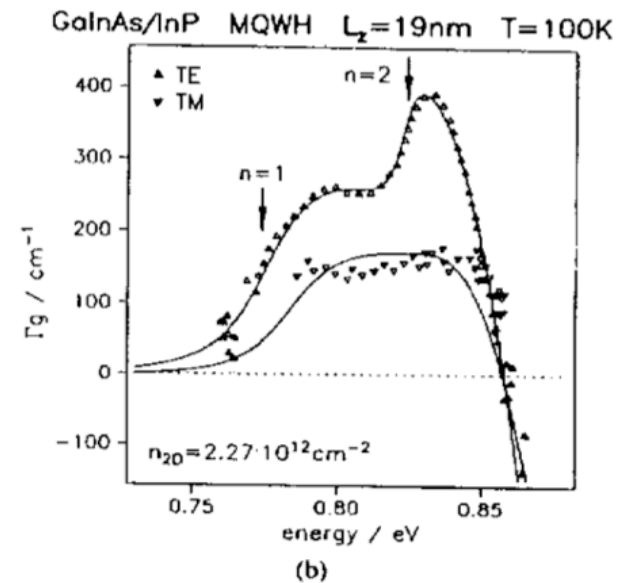
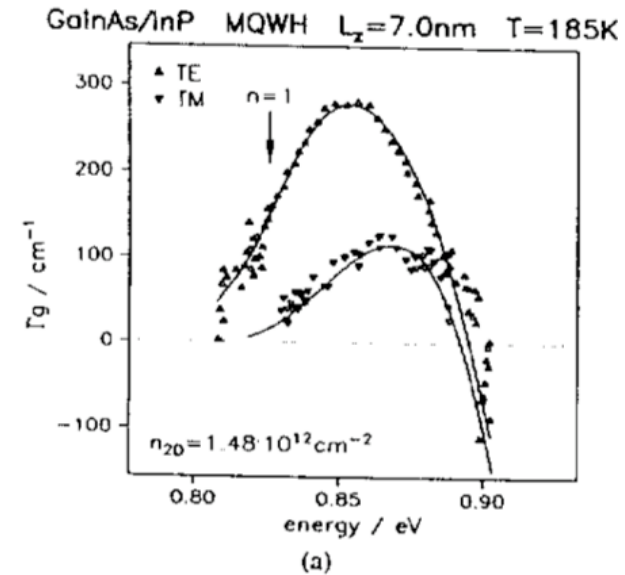


Figure 9.8. (a) Population inversion in a quantum well such that $F_c - F_v > \hbar\omega > E_{e1} + E_{h1} - E_{hm}$. Here F_c is measured from the valence band edge where the energy level is chosen to be zero. (b) The products of the density of states and the occupation probability for electrons in the conduction band $\rho_e^{2D} f_c(E)$ and holes in the valence band $\rho_h^{2D} f_h(E) = \rho_h^{2D} [1 - f_v(E)]$ are plotted vs the energy E in the vertical scale.

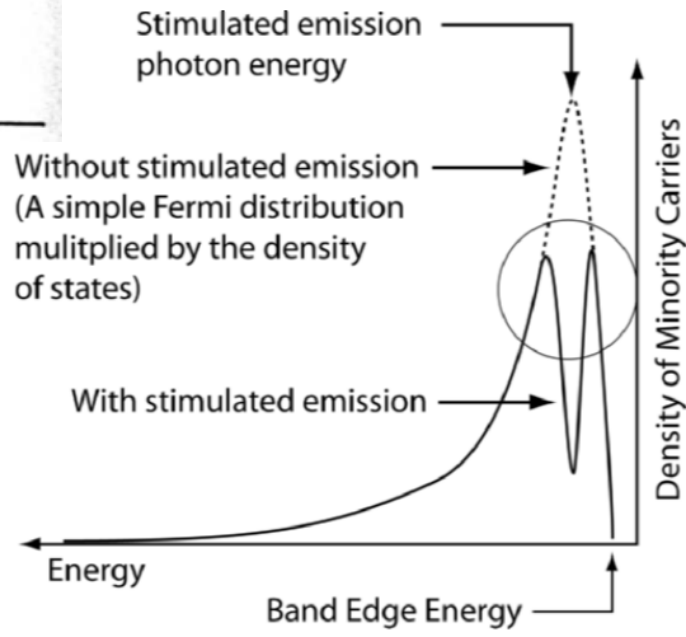
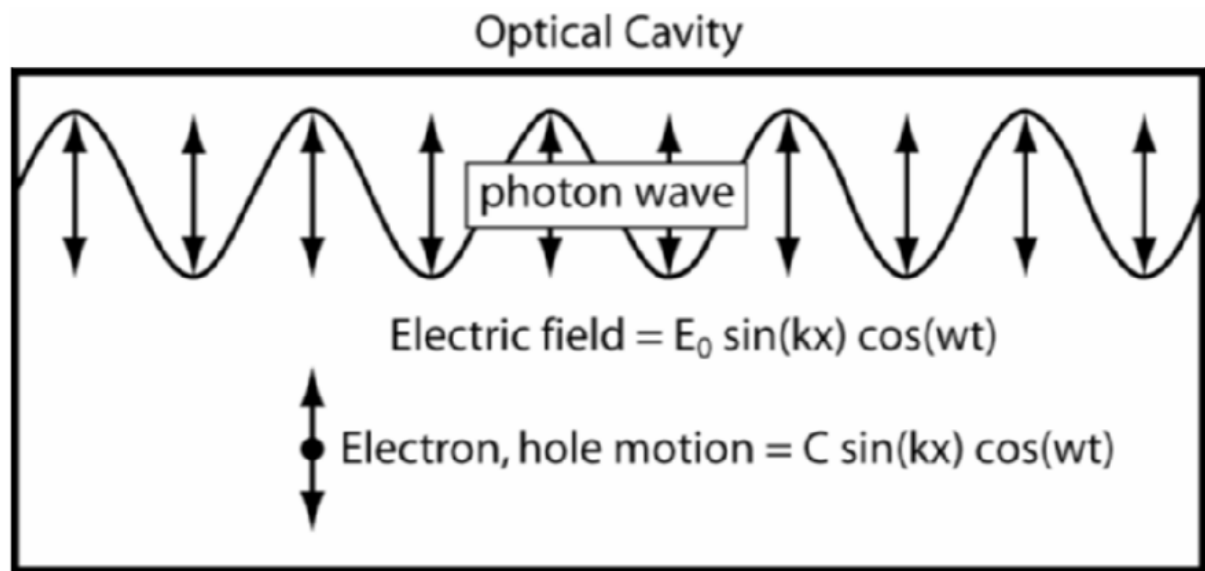
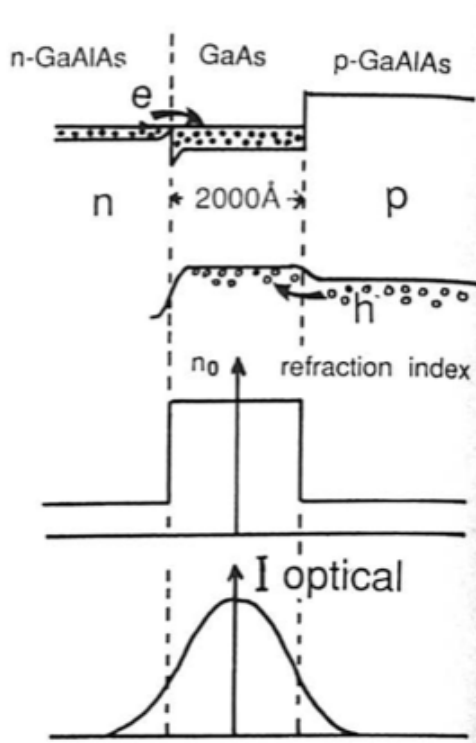
Measured Gain Spectra in III-V Quantum Wells



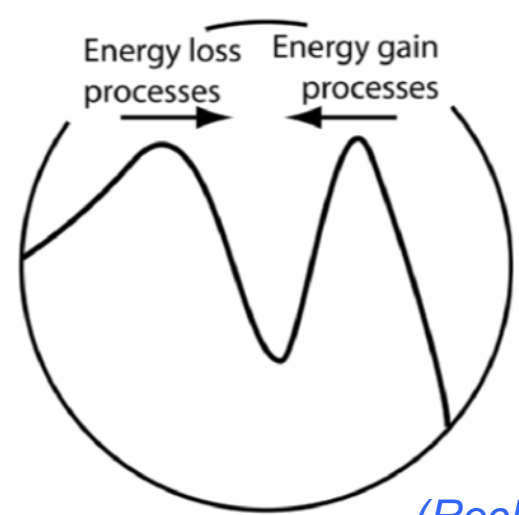
Gain spectrum in QWs follows the equilibrium JDOS modulated by the Fermi Dirac functions in accordance with the Bernard-Duraffourg condition.



Compound Semiconductor Laser Diodes



Refilling of occupied states



(Rockett)

Interband and Intersubband Optical Transitions in QWs

Using effective-mass theory, optical matrix elements in quantum wells:

$$M \propto \langle f | \mathbf{r} \cdot \boldsymbol{\eta} | i \rangle = \int \chi_e(z) e^{i\mathbf{k}_{e\perp} \cdot \mathbf{r}_{\perp}} u_{c\mathbf{k}_e}(\mathbf{r}) \boldsymbol{\eta} \cdot \mathbf{r} \chi_h(z) e^{i\mathbf{k}_{h\perp} \cdot \mathbf{r}_{\perp}} u_{v\mathbf{k}_h}(\mathbf{r}) d\mathbf{r}$$

For **INTERBAND** transitions:

$$M \approx \sum_{\mathbf{R}_i} \chi_e(\mathbf{R}_i) \chi_h(\mathbf{R}_i) e^{i(\mathbf{k}_{h\perp} - \mathbf{k}_{e\perp}) \cdot \mathbf{R}_i} \int_{\text{cell}} u_{c\mathbf{k}_e}(\mathbf{r}) \boldsymbol{\eta} \cdot \mathbf{r} u_{v\mathbf{k}_h}(\mathbf{r}) d\mathbf{r}$$

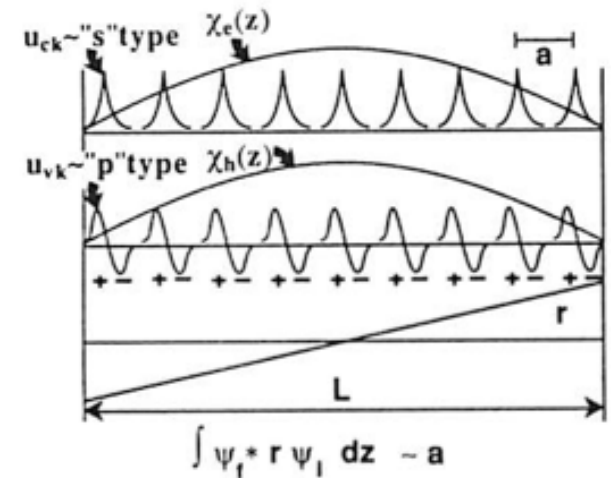
$$M_{\text{interband}} \sim a_0, \text{ dipole length} \sim \text{lattice constant}$$

For **INTERSUBBAND** (intra-band) transitions:

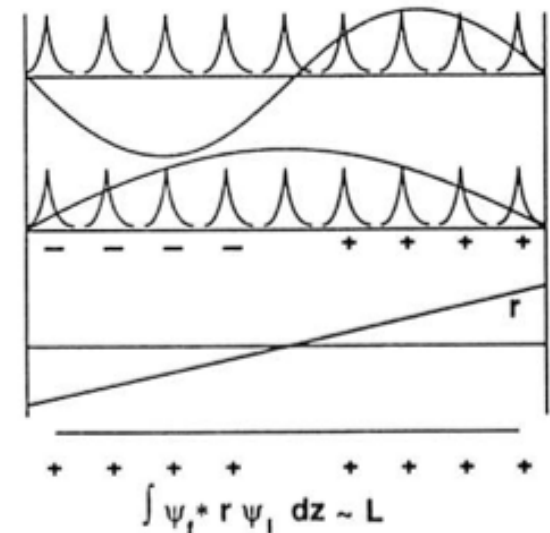
$$M \sim \int_{\text{crystal}} \chi_e(z) \boldsymbol{\eta} \cdot \mathbf{r} \chi_e'(z) dz \int_{\text{cell}} u_{c\mathbf{k}_e}(\mathbf{r}) u_{c\mathbf{k}_e}^*(\mathbf{r}) d^3r$$

$$M_{\text{intersubband}} \sim L_{\text{well}}, \text{ dipole length} \sim \text{Quantum Well Width (giant dipole effect!!)}$$

(b) **INTERBAND TRANSITION**
1h → 1e



(c) **INTRABAND TRANSITION**
1e → 2e



Intersubband Optical Transitions

Optical transitions for intersubband processes

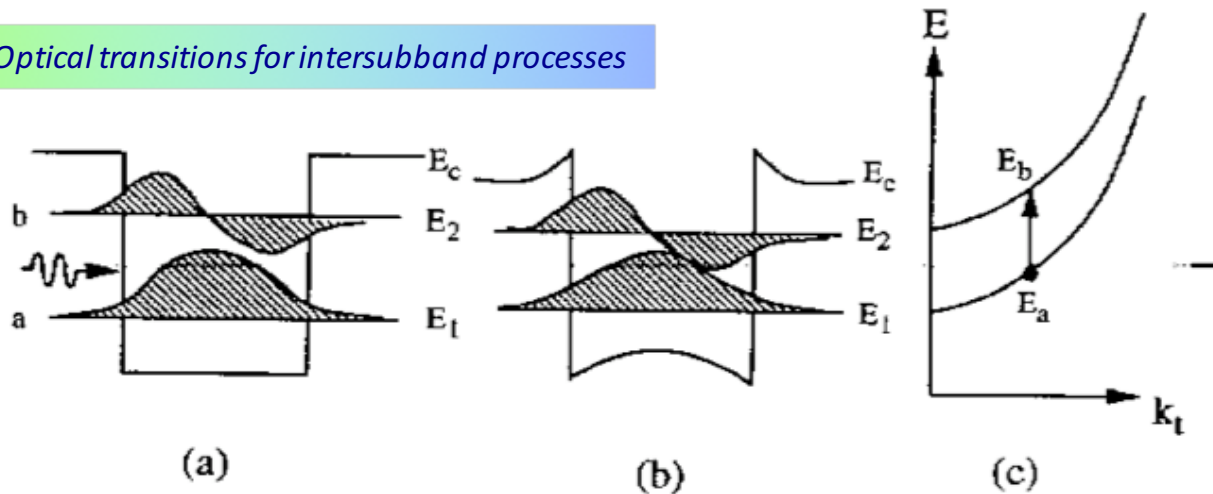


Figure 9.11. (a) A simple quantum well with a small doping concentration. (b) A modulation-doped quantum well with a significant amount of screening due to a large doping concentration. (c) The subband energy diagram in the k_t space. A direct vertical transition occurs because of the k -selection rule in the plane of quantum wells.

For **INTERSUBBAND** (intra-band) transitions:

$$M \sim \int_{\text{crystal}} \chi_c(z) \boldsymbol{\eta} \cdot \mathbf{r} \chi_c'(z) dr \int_{\text{cell}} u_{cke}(\mathbf{r}) u_{cke}^*(\mathbf{r}) d^3r$$

$M_{\text{intersubband}} \sim L_{\text{well}}$, dipole length \sim Quantum Well Width
(giant dipole effect!!)

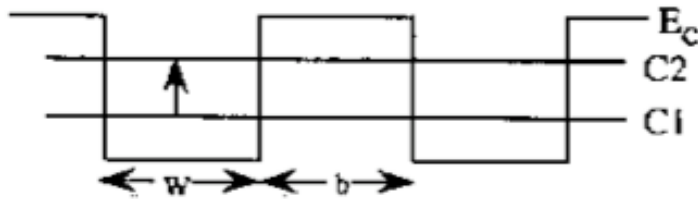
$$\psi_a(\mathbf{r}) = u_c(\mathbf{r}) \times \left[\frac{1}{\sqrt{A}} e^{i\mathbf{k}_t \cdot \boldsymbol{\rho}} \right] \times \phi_1(z)$$

$$\psi_b(\mathbf{r}) = u_c(\mathbf{r}) \times \left[\frac{1}{\sqrt{A}} e^{i\mathbf{k}'_t \cdot \boldsymbol{\rho}} \right] \times \phi_2(z)$$

$$\begin{aligned} \mu_{ba} &= \langle \psi_b | e\mathbf{e} | \psi_a \rangle \approx \langle u_c | u_c \rangle \times \left\langle \frac{1}{\sqrt{A}} e^{i\mathbf{k}_t \cdot \boldsymbol{\rho}} \left| e\mathbf{r} \right| \frac{1}{\sqrt{A}} e^{i\mathbf{k}'_t \cdot \boldsymbol{\rho}} \right\rangle \\ &\approx \delta_{\mathbf{k}_t, \mathbf{k}'_t} \langle \phi_2 | e z | \phi_1 \rangle \hat{z} \approx \delta_{\mathbf{k}_t, \mathbf{k}'_t} \times e z_{12} \end{aligned}$$

Intersubband Optical Transitions

(a) Bound-to-bound transition



$$\alpha(\hbar\omega) = \left(\frac{\omega}{n_r c \epsilon_0} \right) \frac{|\mu_{21}|^2 (\Gamma/2)}{(E_2 - E_1 - \hbar\omega)^2 + (\Gamma/2)^2} \left(\frac{m_e^* k_B T}{\pi \hbar^2 L} \right) \ln \left(\frac{1 + e^{(E_F - E_1)/k_B T}}{1 + e^{(E_F - E_2)/k_B T}} \right)$$

(b) Bound-to-continuum miniband transitions

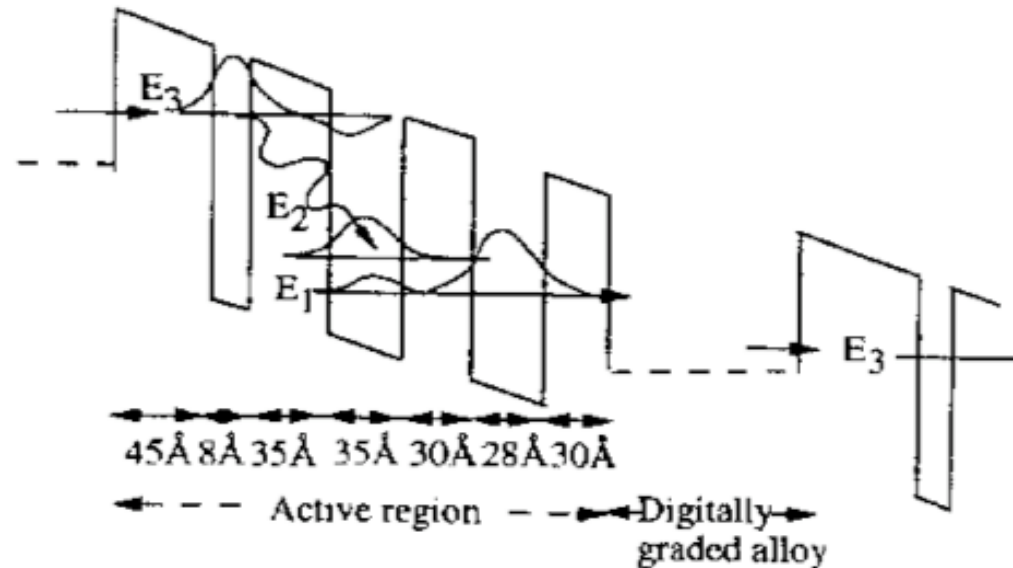
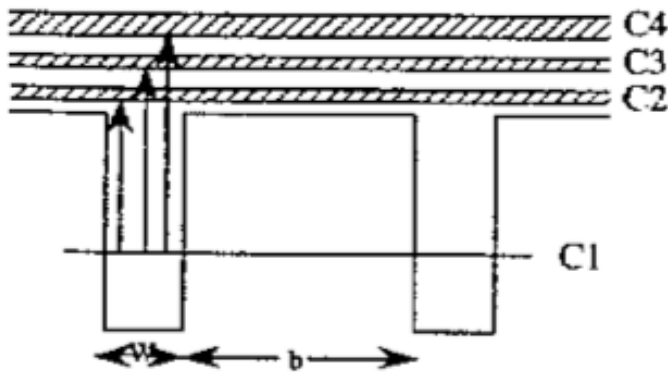
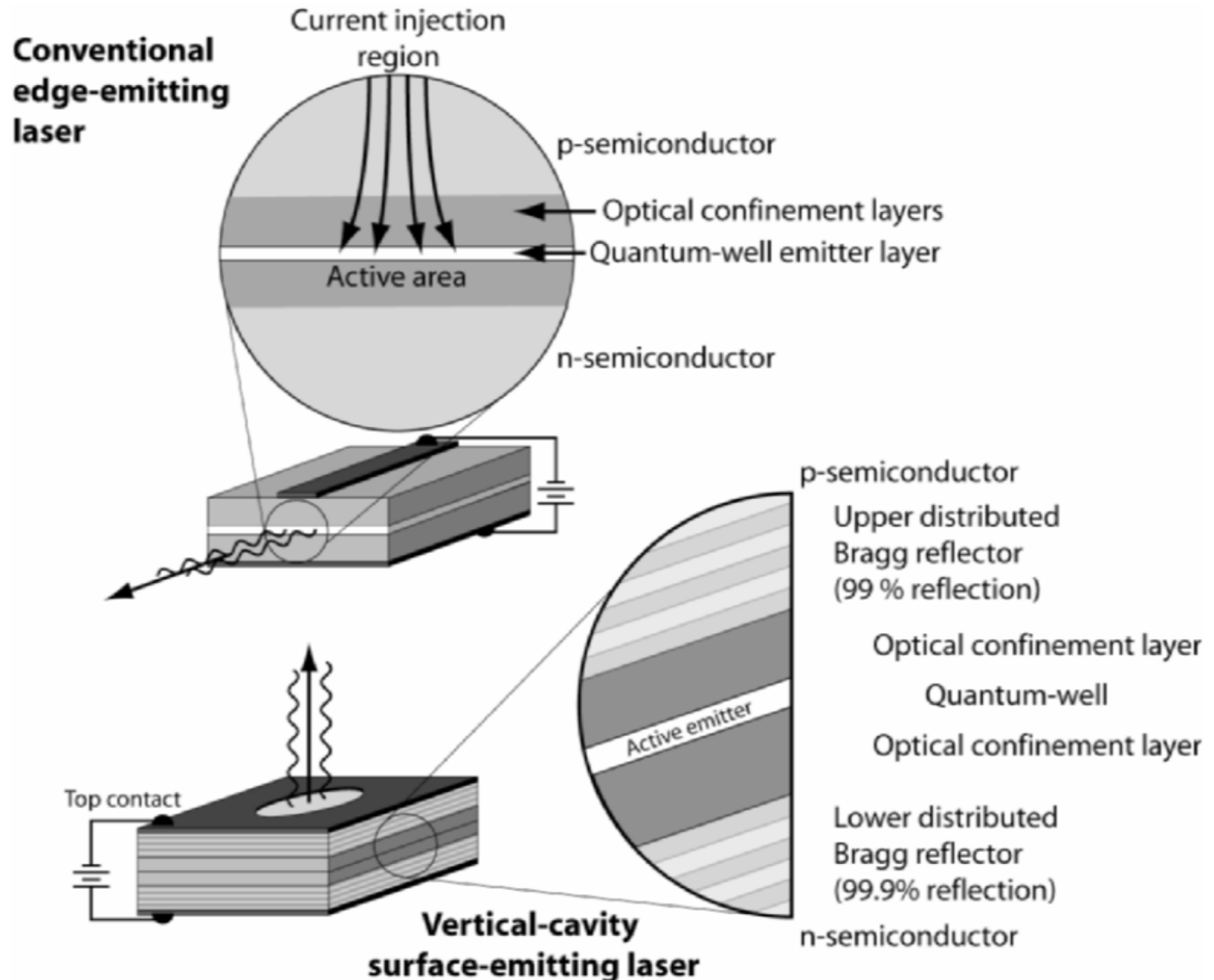
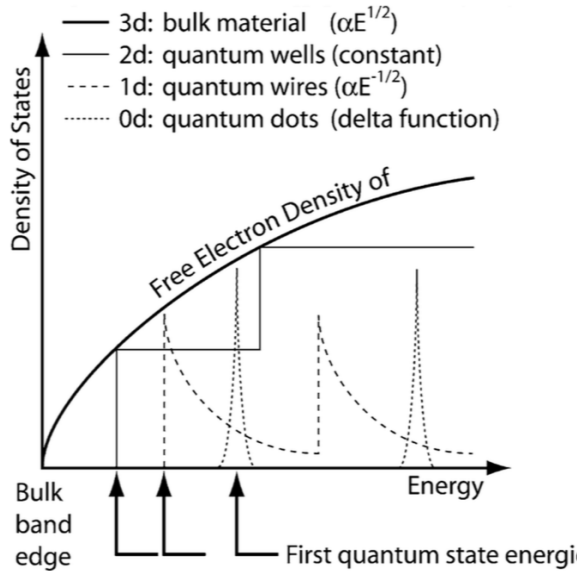


Figure 9.15. A period of a quantum cascade laser [27] using intersubband transition between E_3 and E_2 . The barriers are $\text{Al}_{0.48}\text{In}_{0.52}\text{As}$ and the wells are $\text{In}_{0.47}\text{Ga}_{0.53}\text{As}$ materials. The calculated values are $E_3 - E_2 = 295 \text{ meV}$ and $E_2 - E_1 = 30 \text{ meV}$.

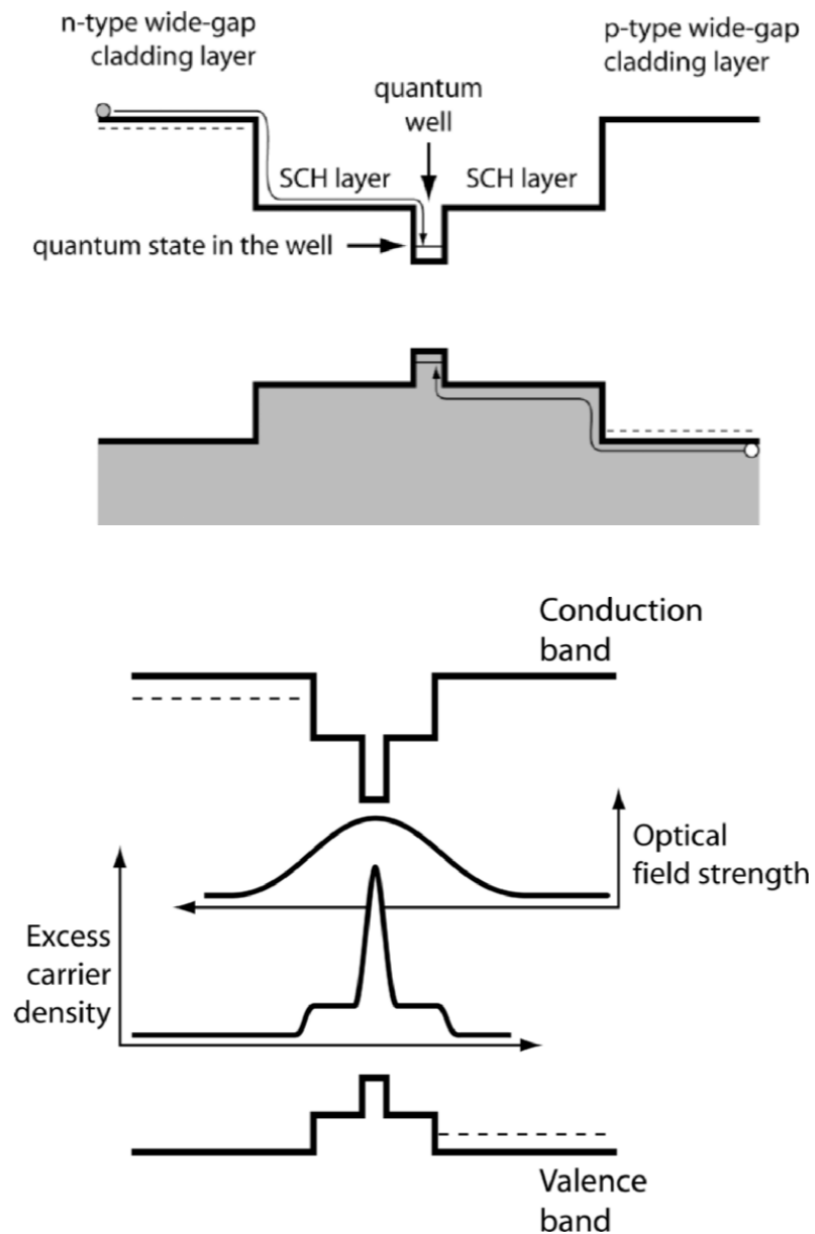
Applications of ISB transitions: In Quantum Cascade Lasers

Compound Semiconductor Heterojunction Devices



(Rockett)

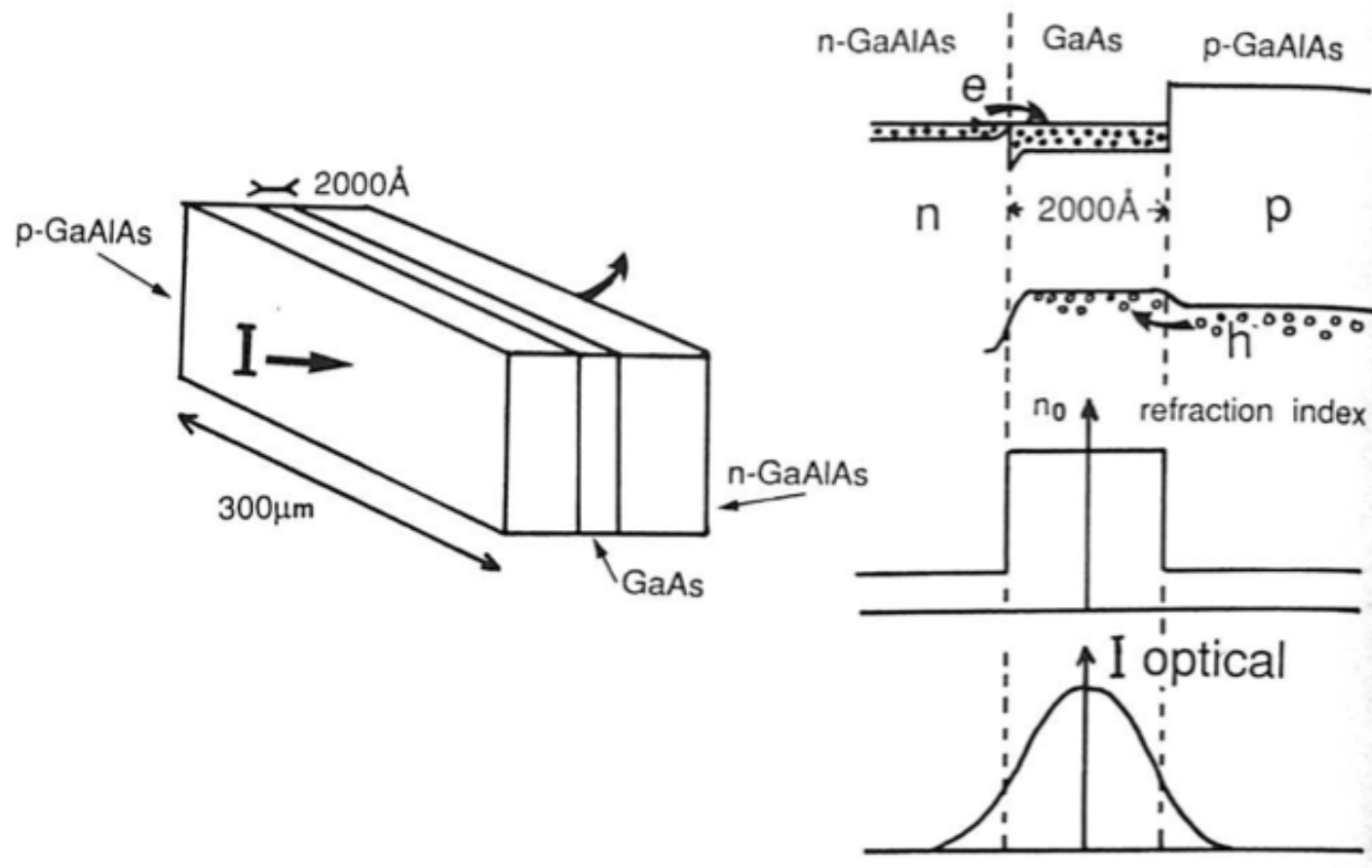
Compound Semiconductor Heterojunction Devices



(Rockett)

Applications: The Double-Heterostructure Laser

DOUBLE-HETEROSTRUCTURE LASER



Compound Semiconductor Laser Designs

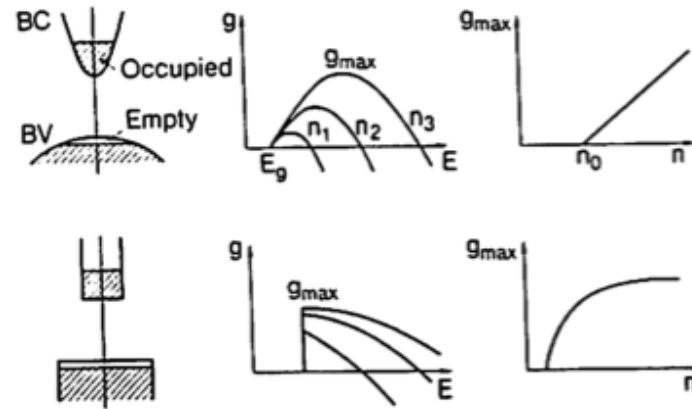


FIG. 91. Schematics of the gain formation in DH lasers (top) and QW lasers (bottom).

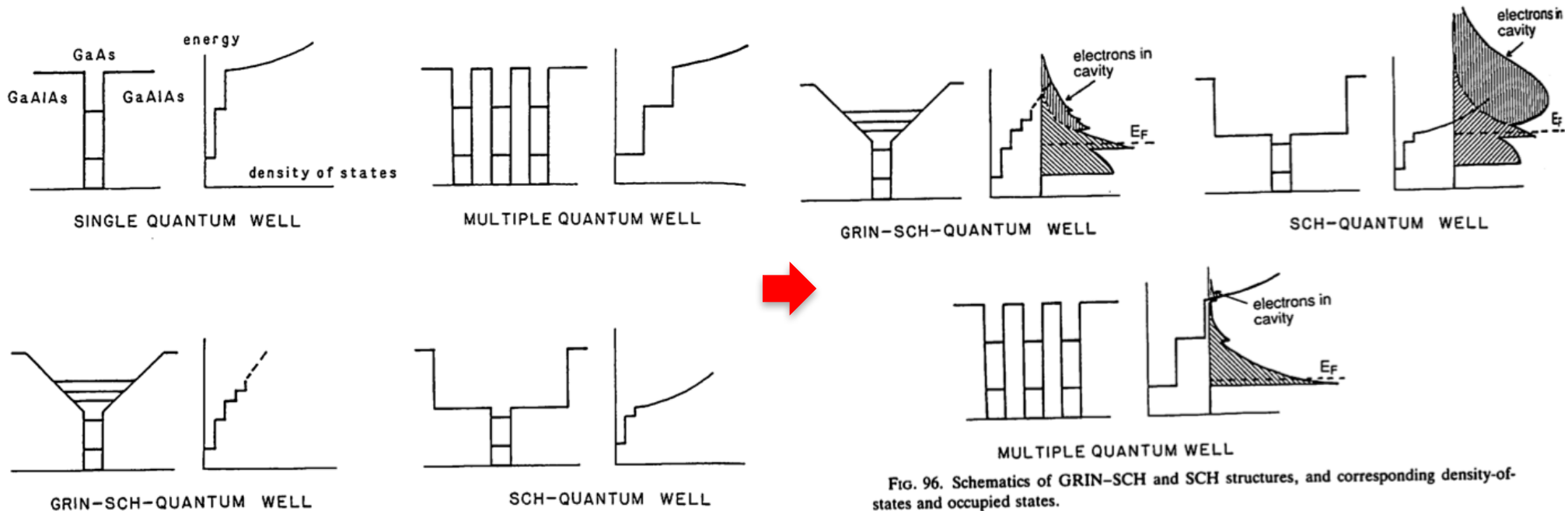


FIG. 96. Schematics of GRIN-SCH and SCH structures, and corresponding density-of-states and occupied states.

FIG. 93. The various QW structures used as active layers in lasers and the associated density of states.

(Weisbuch/Vinter)

Compound Semiconductor Laser Designs

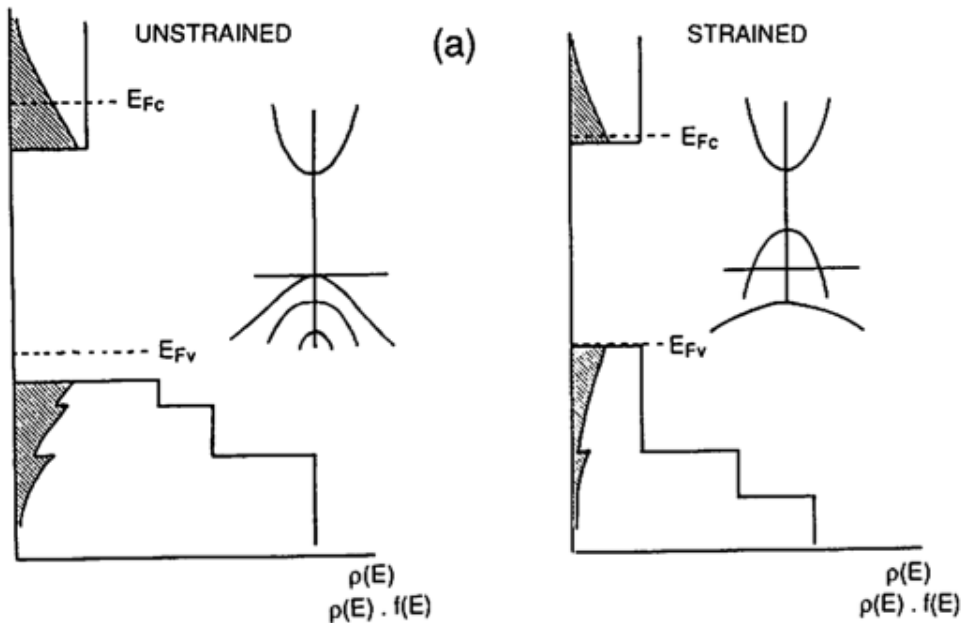


FIG. 100a. Schematics of band-filling for conduction and valence band states for equal numbers of injected electrons and holes in unstrained (left) and strained (right) QW active layers.

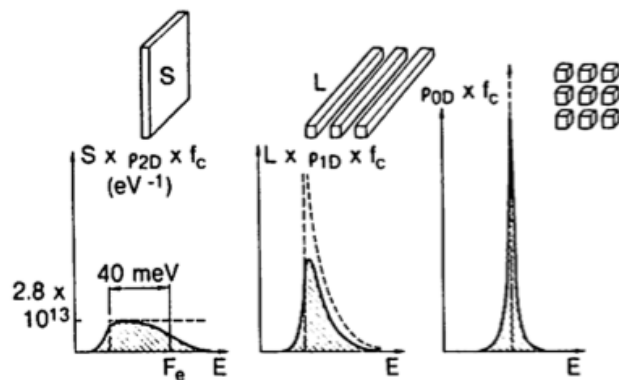


FIG. 113. Schematics of gain curves in 2D, 1D, and 0D structures. Similar numbers of electrons and holes are being injected above transparency, yielding equal integrated gain. (From Nagle and Weisbuch.⁴⁶⁵)

When $L \gg \bar{a}_B$, (but still well-separated, confined energy levels), a “giant” oscillator strength situation develops, which yields a transition matrix element⁵⁷⁵⁻⁷

$$f \approx f_{at} \cdot (V_{box}/V_{exc}) \quad (112)$$

where V_{box} and V_{exc} are the QB and exciton volume, respectively. The enhancement of the oscillator strength originates in the coherent excitation of the QB volume (somewhat analogous to the intersubband giant dipole moment of Eq. (54e)), which yields an increased dipole moment.

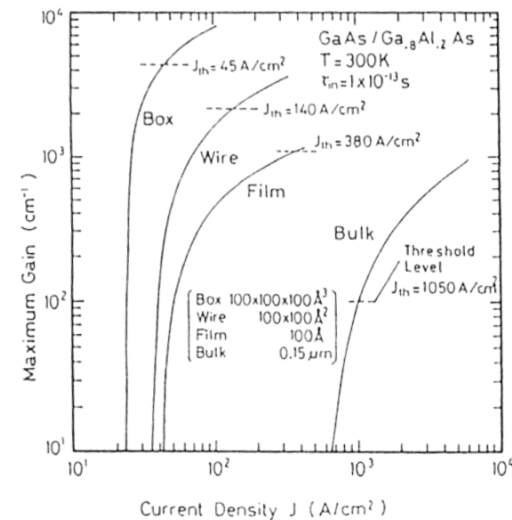
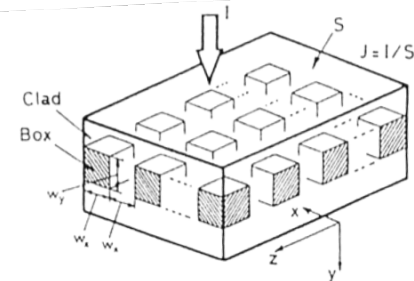
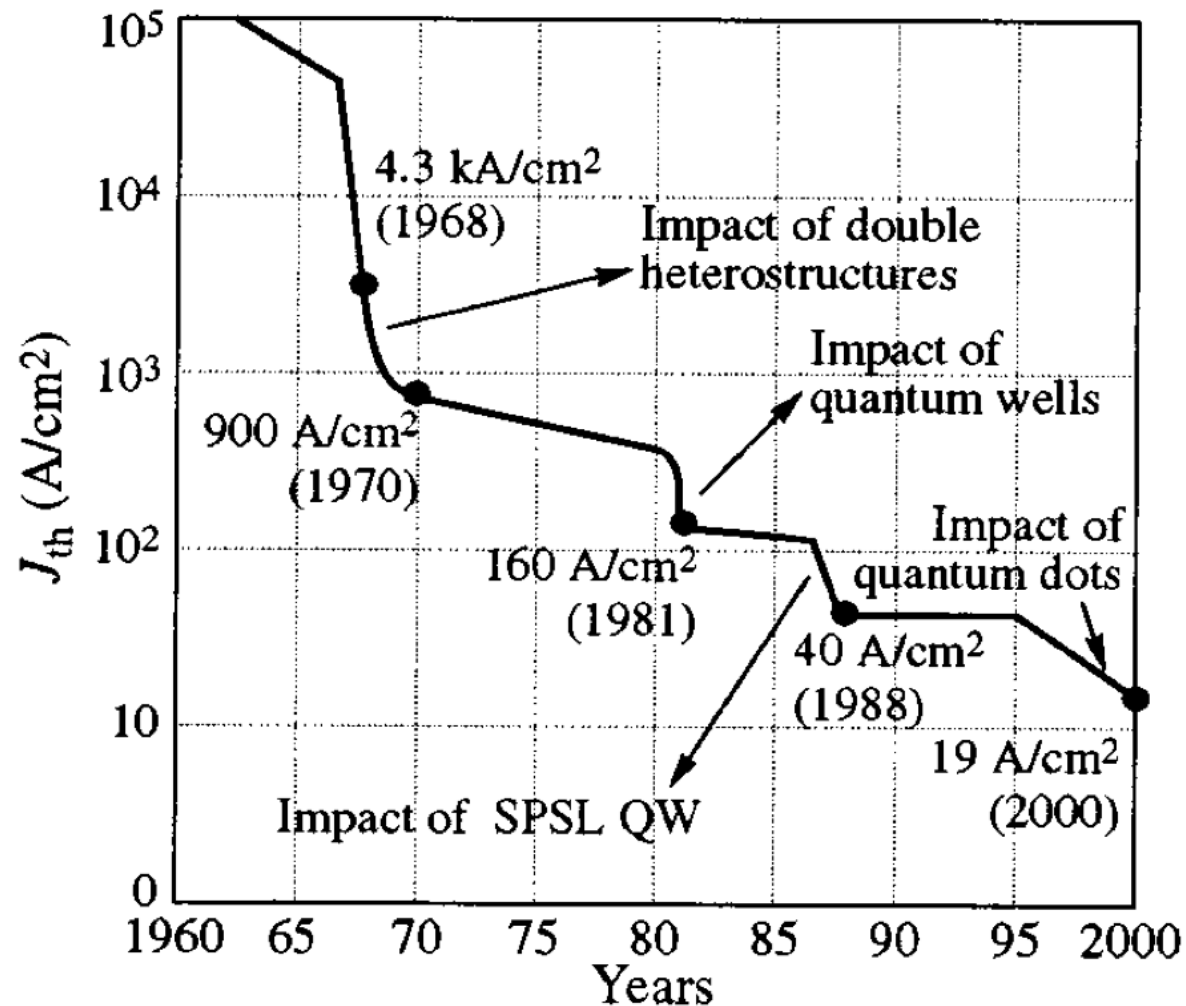


FIG. 114. Schematics of quantum box structure and gain curves 3D, 2D, 1D, 0D lasers, with optimized optical confinement in each case. (Adapted from M. Asada, Y. Miyamoto, and Y. Suematsu, IEEE J. Quantum Electron. QE-22, 1915, © 1986 IEEE.)

(Weisbuch/Vinter)

Reduction of lasing threshold current density



Alferov Nobel Lecture 2000

Lasers outperform LEDs in efficiency!

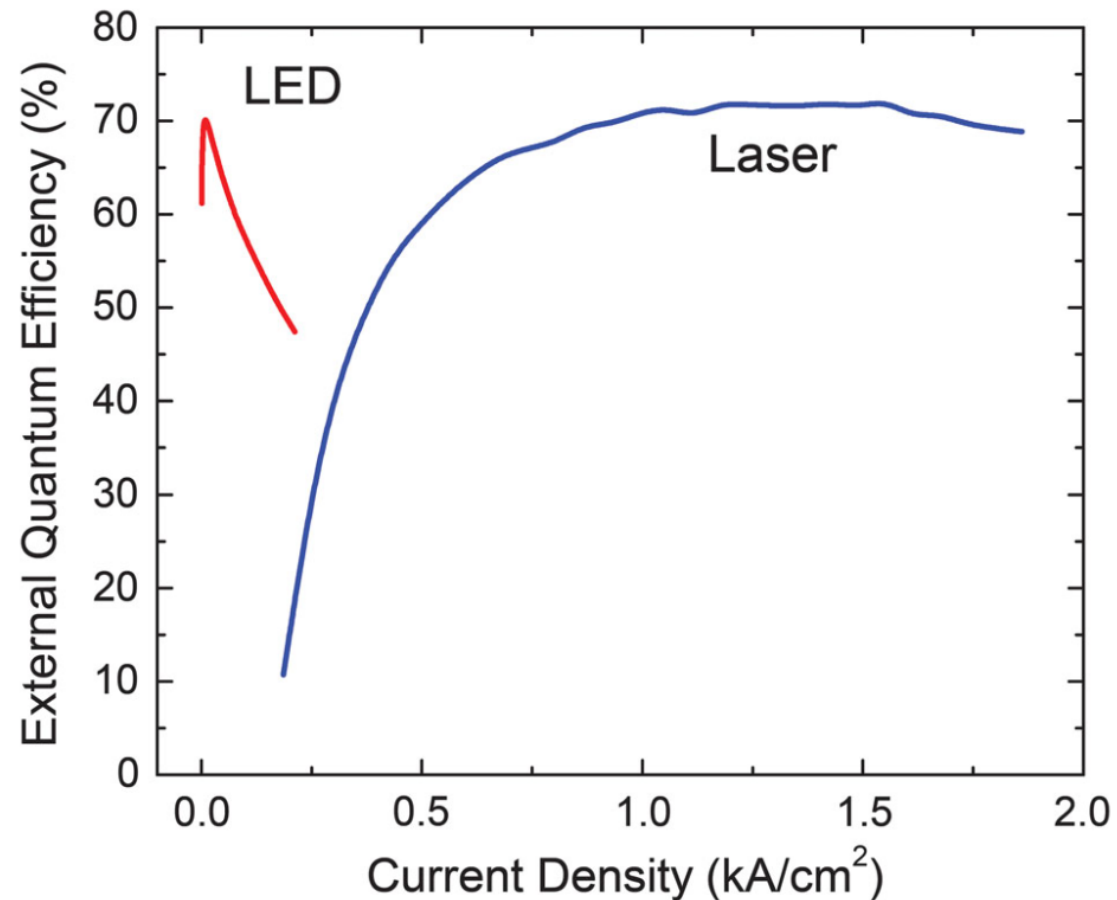


FIG. 17 (color). Comparison of external quantum efficiency (EQE) of a commercial LED and laser with increasing current density. From Pourhashemi *et al.*, 2013.

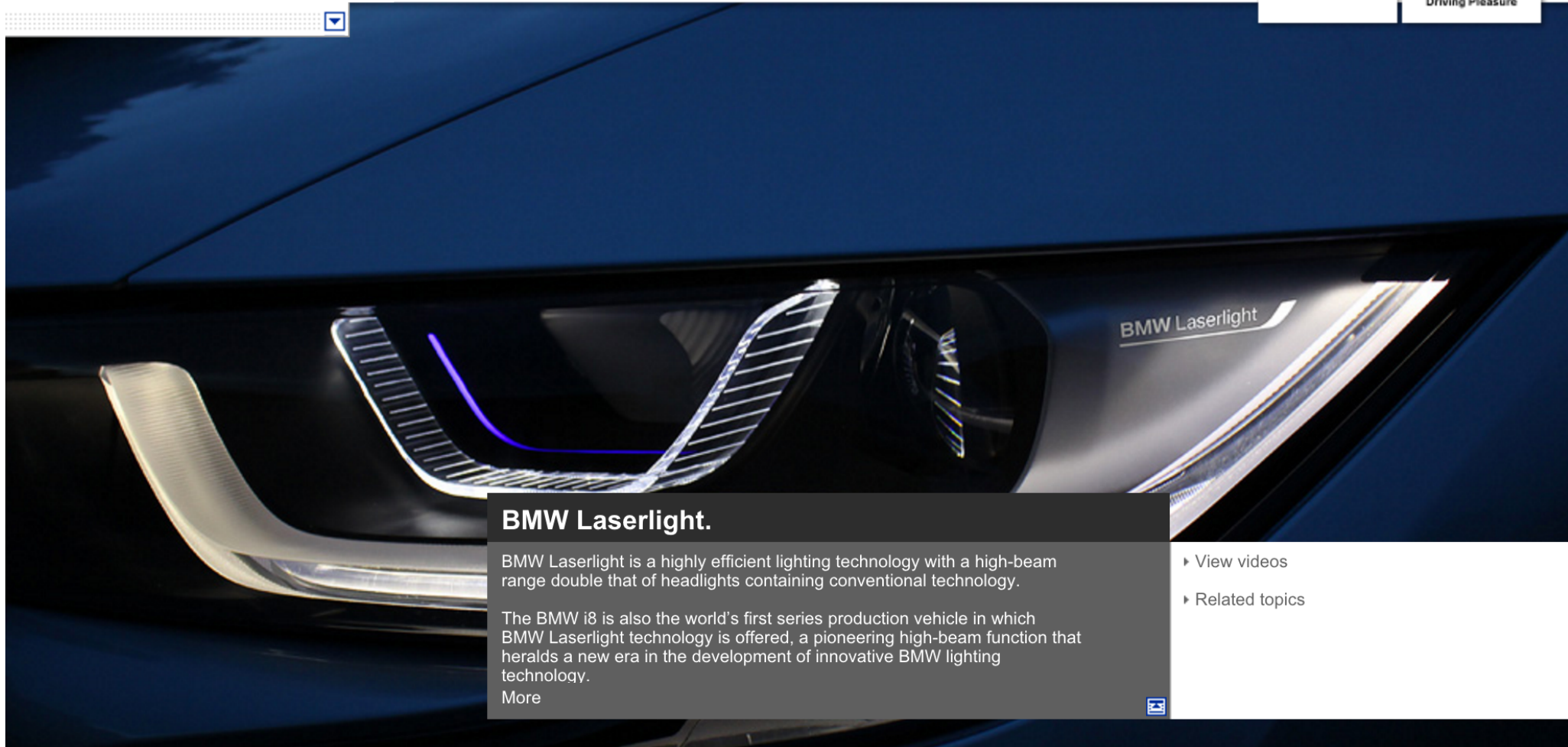
Lasers outperform LEDs in efficiency!

[BMW dealer](#) [Brochures](#) [Corporate/Direct Sales](#) [Shop](#) [BMW Financial Services](#) [Used Automobiles](#)

[Home](#) [1](#) [2](#) [3](#) [4](#) [5](#) [6](#) [7](#) [X](#) [Z4](#) [BMW M](#) [BMW i](#) [BMW Owners](#) [BMW Insights](#)

[BMW Technology Guide](#)

The international
BMW website



BMW Laserlight.

BMW Laserlight is a highly efficient lighting technology with a high-beam range double that of headlights containing conventional technology.

The BMW i8 is also the world's first series production vehicle in which BMW Laserlight technology is offered, a pioneering high-beam function that heralds a new era in the development of innovative BMW lighting technology.

[More](#)

[View videos](#)

[Related topics](#)

Please read...

Rockett: MSS

3. OVERVIEW OF ELECTRONIC DEVICES 73

3.1 Diffusion and drift of carriers.....	74
3.1.1 Chemical potential	74
3.1.2 Carrier motion in a chemical potential gradient.....	74
3.2 Simple diodes	75
3.2.1 The junction contact potential.....	77
3.2.2 Biased junctions	81
3.2.3 Non-ideal diode behaviors	88
3.3 Schottky barriers and ohmic contacts.....	96
3.3.1 Ideal metal/semiconductor junctions	96
3.3.2 Real schottky diodes	101
3.4 Semiconductor heterojunctions	102
3.4.1 Heterojunctions at equilibrium.....	103
3.4.2 Heterojunctions as diodes	109
3.5 Transistors	111
3.5.1 Bipolar junction transistors.....	111
3.5.2 Field-effect transistors.....	114
3.6 Light-emitting devices.....	119
3.6.1 Light-emitting diodes.....	120
3.6.2 Laser diodes.....	124
3.7 Summary.....	134
3.8 Homework problems	136
3.9 Suggested readings & references.....	139

Weisbuch & Vinter: QSS

III. Optical Properties of Thin Heterostructures	57
10. Optical Matrix Element.....	57
a. Interband Transitions.....	57
b. Oscillator Strength of Interband Transitions.....	60
c. Intraband (Intersubband) Transitions.....	61
d. Excitonic Effects.....	62
11. Selection Rules.....	65
a. Interband Transitions.....	65
b. Exciton Effects.....	69
c. Intraband Transitions.....	69
12. Energy Levels, Band Discontinuities, and Layer Fluctuations.....	69
13. Low-Temperature Luminescence.....	79
14. Carrier and Exciton Dynamics.....	83
15. Inelastic Light Scattering.....	85
16. Nonlinear and Electro-Optic Effects.....	87
a. Quantum-Confined Wavefunctions and Electro-optic Effects.....	88
b. Nonlinear Effects.....	93
c. Electro-optic Applications.....	96
d. Nonlinear Effects Applications.....	98
V. Applications of Quantum Semiconductor Structures	141
21. Electronic Devices Based on Parallel Transport.....	141
a. Simplest Model of FET.....	143
b. More Refined Models.....	146
c. Performance Analysis.....	149
d. Variants of Heterojunction FETs.....	152
22. Electronic Devices Based on Perpendicular Transport.....	155
a. Two-Terminal Devices.....	155
b. Three-Terminal Devices.....	158
23. Quantum Well Lasers.....	165
a. Basic Description of Laser Action.....	165
b. Single Quantum Well (SQW) Laser Operation.....	171
c. Multiple Quantum Well Lasers.....	176
d. The Temperature Dependence of the Threshold Current.....	178
e. Additional Features of Quantum Well Lasers.....	179
f. The GaInAsP/InP Laser Case.....	184
g. Other Materials Systems.....	187
VI. Towards 1D and 0D Physics and Devices	189
24. One- and Zero-Dimensional Systems.....	189
25. 1D and 0D Semiconductor Fabrication Techniques.....	191
26. Electrical Applications of 1D and 0D Structures.....	197
27. Devices Based on 1D and 0D Effects.....	205
28. 1D and 0D Optical Phenomena.....	209
29. 1D and 0D Optical Devices.....	215

Science and Future

Next topics: please read...

Rockett: MSS

4. ASPECTS OF MATERIALS SCIENCE 141

4.1 Structures of materials.....	141
4.1.1 Crystal lattices.....	142
4.1.2 The reciprocal lattice.....	148
4.2 Basic thermodynamics of materials.....	151
4.3 Phase diagrams.....	155
4.4 Kinetics.....	163
4.4.1 Reaction kinetics.....	164
4.4.2 Nucleation.....	166
4.4.3 Atomic transport.....	170
4.5 Organic molecules.....	172
4.6 Applications.....	178
4.6.1 A basis for phase transformations.....	178
4.6.2 Silicon crystal fabrication.....	180
4.6.3 Rapid thermal processing.....	187
4.7 Summary points.....	189
4.8 Homework.....	191
4.9 Suggested Readings and References.....	194

6. SEMICONDUCTOR ALLOYS 237

6.1 Alloy selection.....	238
6.1.1 Overview.....	238
6.1.2 Choosing alloy constituents.....	241
6.2 Semiconductor alloy thermodynamics.....	245
6.2.1 Regular solution theory revisited.....	245
6.2.2 Ternary and quaternary solutions.....	249
6.2.3 More mechanisms for alloy ordering.....	252
6.3 Band gap bowing.....	255
6.3.1 Binary and pseudobinary alloys.....	255
6.3.2 Bowing in quaternary alloys.....	260
6.4 Silicon-germanium alloys.....	261
6.4.1 Structure and solubility.....	262
6.4.2 Band gap engineering.....	264
6.4.3 Alloying and carrier mobility.....	267
6.5 Metastable semiconductor alloys.....	268
6.6 Applications.....	272
6.6.1 Heterojunction bipolar transistors.....	272
6.6.2 Solar cells.....	276
6.7 Summary points.....	280
6.8 Homework.....	282
6.9 Suggested readings & references.....	285

Compound Semiconductor Crystal Structures

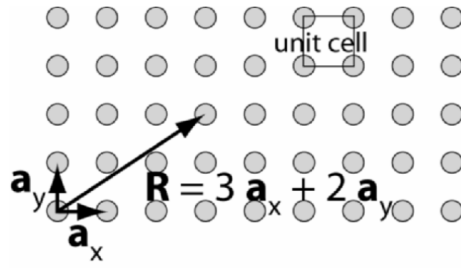
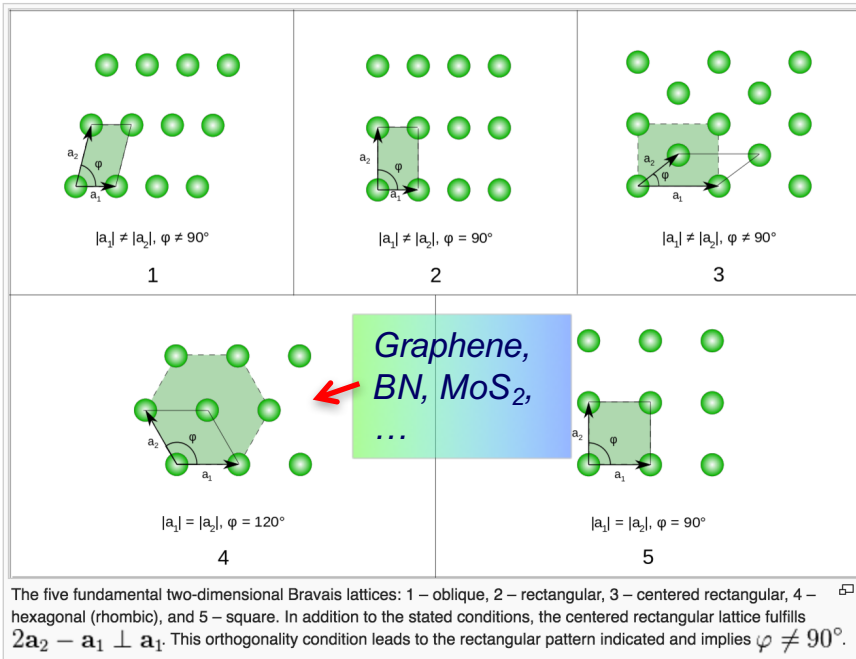


Figure 4.1: A schematic diagram of the periodic arrangement of atoms in a lattice. The basis vectors of the lattice are a_x and a_y . Any lattice point can be written as a linear combination of the two basis vectors.



Five Bravais lattices in 2-dimensions

The 7 lattice systems	The 14 Bravais lattices			
Triclinic	P			
	$\alpha, \beta, \gamma \neq 90^\circ$			
Monoclinic	P	C		
	$\beta \neq 90^\circ, \alpha, \gamma = 90^\circ$	$\beta \neq 90^\circ, \alpha, \gamma = 90^\circ$		
Orthorhombic	P	C	I	F
	$a \neq b \neq c$	$a \neq b \neq c$	$a \neq b \neq c$	$a \neq b \neq c$
	a	b	c	c
Tetragonal	P	I		
	$a \neq c$	$a \neq c$		
Rhombohedral	R or P			
	$\alpha = \beta = \gamma \neq 90^\circ$			
Hexagonal	P			
Cubic	P (fcc)	I (bcc)	F (fcc)	
	a	a	a	

14 Bravais lattices in 3-dimensions

Ga_2O_3, \dots

$CuInSe_2, \dots$

Lattice system	Volume
Triclinic	$abc\sqrt{1 - \cos^2 \alpha - \cos^2 \beta - \cos^2 \gamma + 2 \cos \alpha \cos \beta \cos \gamma}$
Monoclinic	$abc \sin \beta$
Orthorhombic	abc
Tetragonal	$a^2 c$
Rhombohedral	$a^3 \sqrt{1 - 3 \cos^2 \alpha + 2 \cos^3 \alpha}$
Hexagonal	$\frac{\sqrt{3}}{2} a^2 c$
Cubic	a^3

$GaN, AlN, ZnO, CdS, \dots$

$C, Si, Ge, GaAs, \dots$

(wikipedia)

Compound Semiconductor Crystal Structures

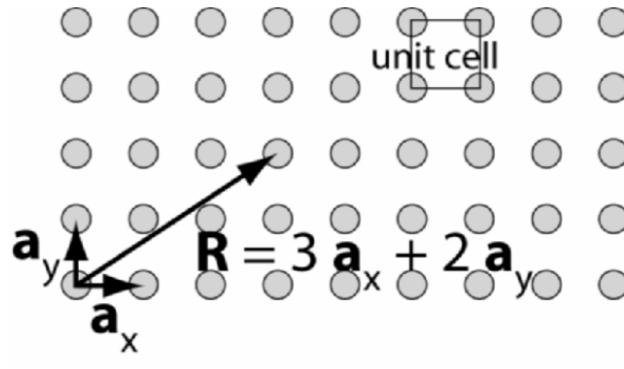


Figure 4.1: A schematic diagram of the periodic arrangement of atoms in a lattice. The basis vectors of the lattice are a_x and a_y . Any lattice point can be written as a linear combination of the two basis vectors.

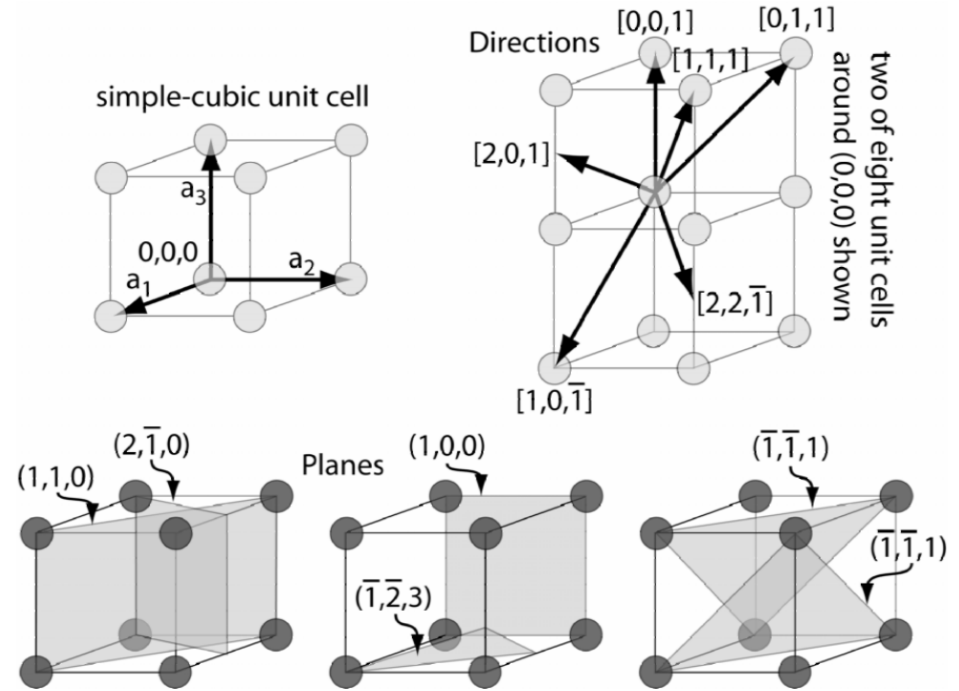


Figure 4.2: Shows the Miller indexing scheme for crystal planes and directions in a simple cubic crystal. Similar indexing methods are used in other Bravais lattices, although the basis vectors are not necessarily parallel to Cartesian coordinate axes. In hexagonal lattices an alternate labeling scheme employing four indices in which only three of the four are independent is often used. Notice that the two $(\bar{1}\bar{1}1)$ planes marked are adjacent and parallel to one another.

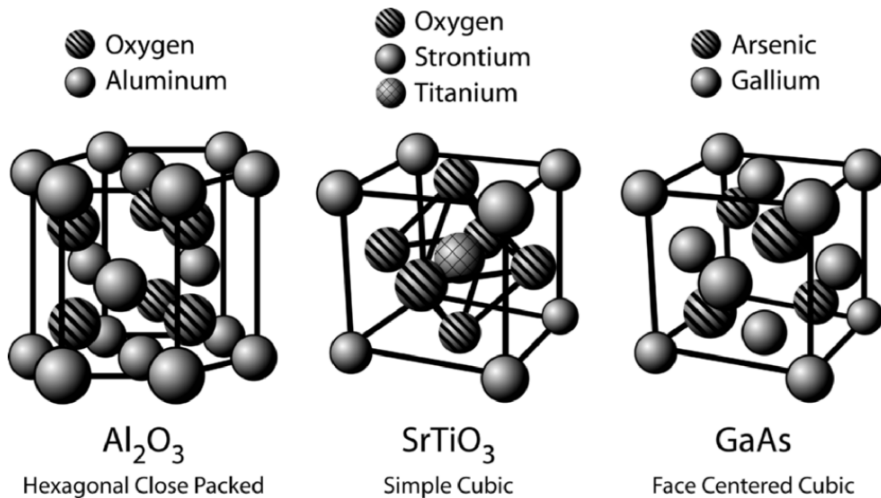


Figure 4.3: Shows the crystal structures of three compounds used in microelectronics. Each has a different Bravais lattice. To see the Bravais lattices of each compound, look only at the aluminum, strontium, and gallium atoms, respectively.

(Rockett)

Compound Semiconductor Crystal Structures

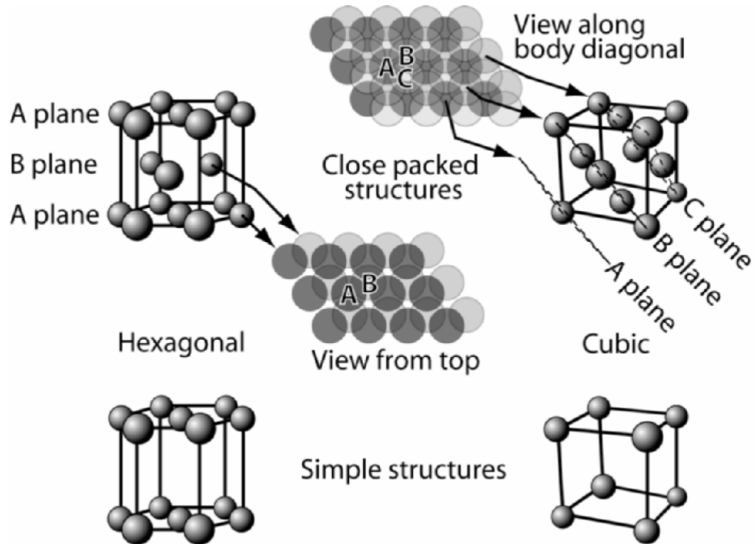


Figure 4.4: A comparison of fcc and hcp structures and their corresponding simple structures. Atoms in the "A" plane correspond to the darkest gray circles in the top view while atoms in the "B" and "C" planes are progressively lighter shades of gray.

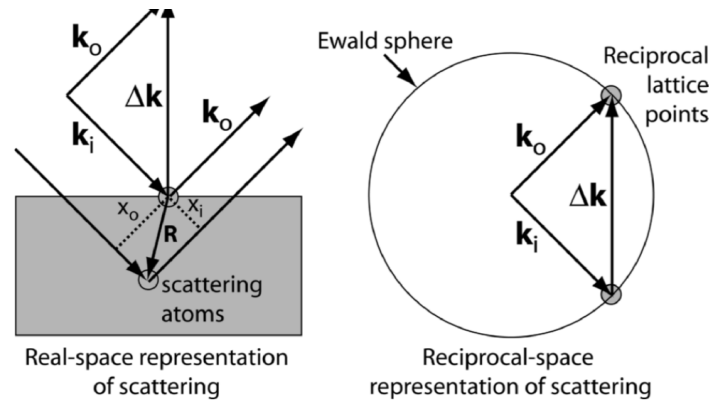


Figure 4.6: Shows the relationships among the incident, k_i , and scattered, k_o , wave vectors, the change in wave vector, Δk , the extra path lengths, x_i and x_o , of one part of the scattered wave front along the incident and outgoing waves, and the distance between two scattering centers (atoms) in real space, R . Also shown is the equivalent reciprocal space construction based on the Ewald sphere concept showing that diffraction occurs when Δk begins and ends on a reciprocal lattice point.

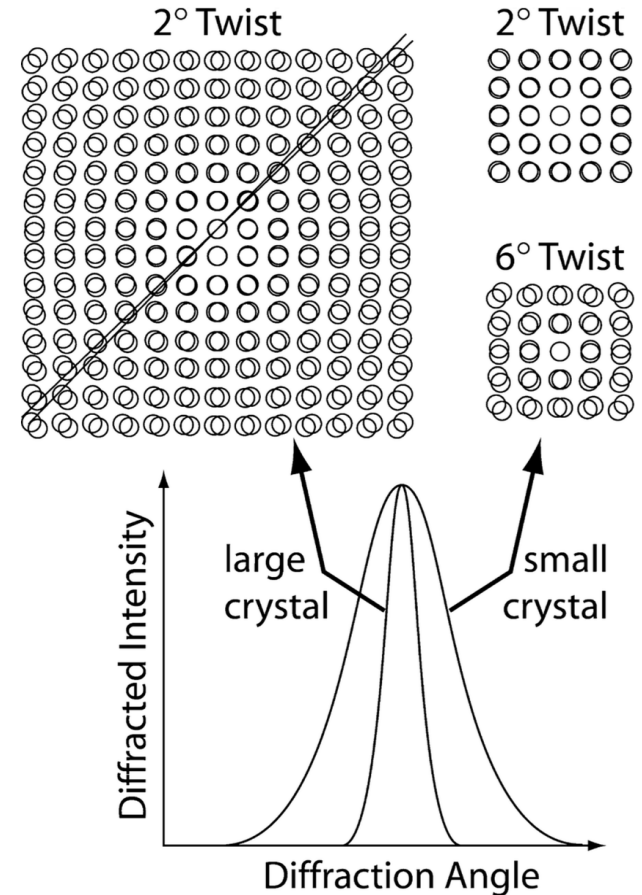


Figure 4.5: Shows the effect of crystal size on sensitivity to angular distortions. A "large" crystal shows an obvious effect of a 2° twist of one layer with respect to another. By contrast, a "small" crystal shows an almost undetectable effect. To achieve a similarly visible distortion in the small crystal a 6° twist is required. The sensitivity to variations in angle produces similar effects on diffraction patterns. Large crystals produce diffraction (constructive interference) only over a very small angular range. Small crystals allow diffracted intensity over a much larger range.

(Rockett)

Compound Semiconductor Crystal Structures

$$\mathbf{b}_1 = (\mathbf{a}_2 \times \mathbf{a}_3) / (\mathbf{a}_1 \bullet \mathbf{a}_2 \times \mathbf{a}_3)$$

$$\mathbf{b}_2 = (\mathbf{a}_3 \times \mathbf{a}_1) / (\mathbf{a}_1 \bullet \mathbf{a}_2 \times \mathbf{a}_3),$$

$$\mathbf{b}_3 = (\mathbf{a}_1 \times \mathbf{a}_2) / (\mathbf{a}_1 \bullet \mathbf{a}_2 \times \mathbf{a}_3)$$

The reciprocal lattice is defined by the set of points $h\mathbf{b}_1$, $k\mathbf{b}_2$, and $l\mathbf{b}_3$ with the basis vectors defined by Equation 4.2.

$$\frac{1}{d^2} = \frac{h^2 + k^2 + l^2}{a^2}$$

Compound Semiconductor Crystal Growth

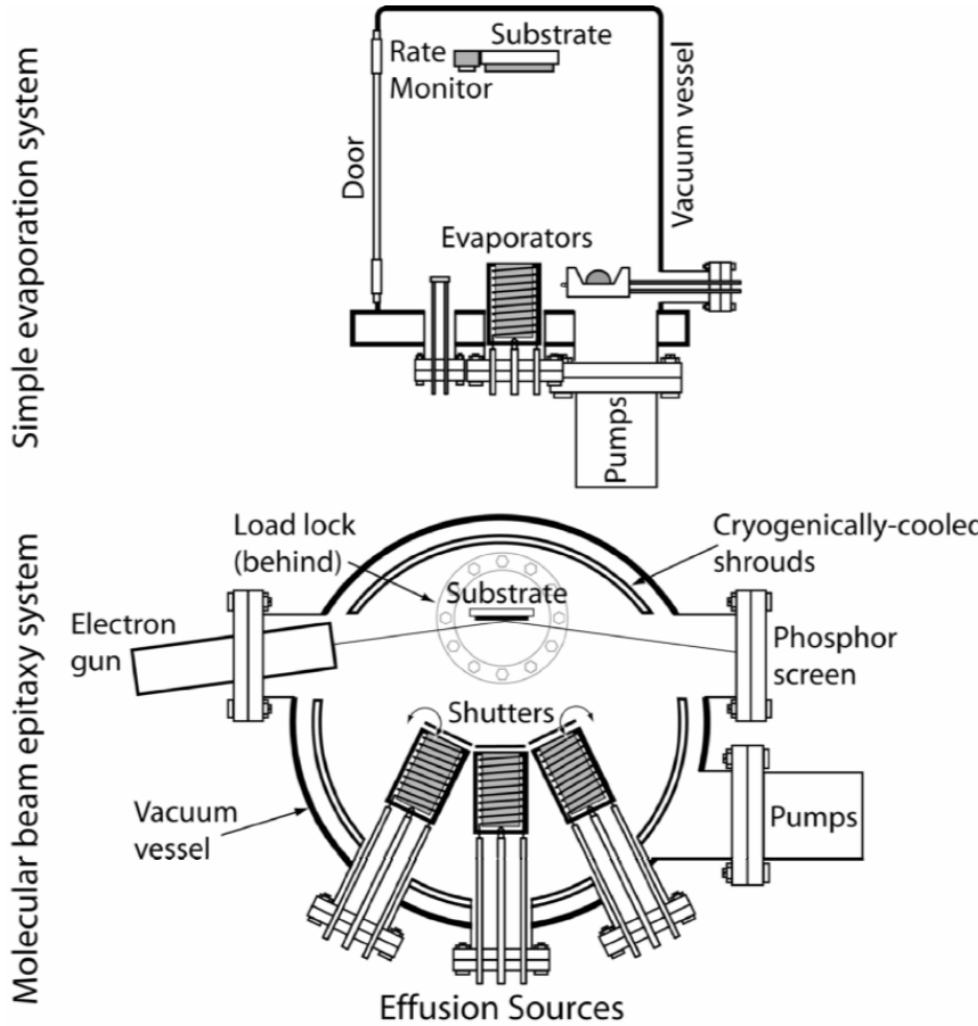


Figure 11.1: Typical evaporation system geometries. Both schematics are simplified and leave out typical components. However, the major parts are indicated. The major difference for the molecular beam epitaxy system is the increased emphasis on ultimate vacuum performance, often four to five orders of magnitude better.

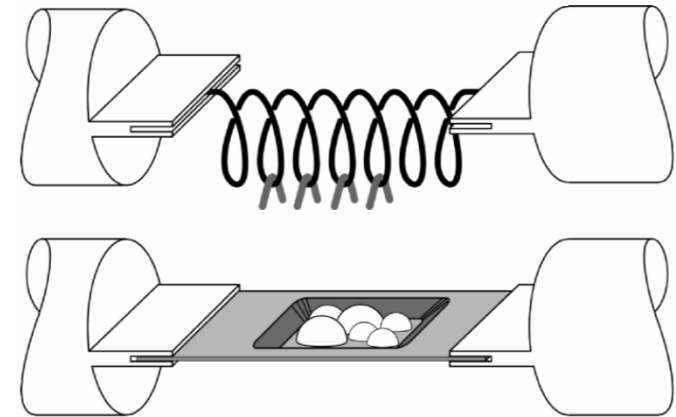


Figure 11.2: Open source evaporation boats (lower) and wire coils (upper figure). Wire coils are generally made of W although other low vapor pressure systems also work. Open boats are made in a wide variety of shapes and of a wide variety of materials including Ta, W, graphite, and other materials.

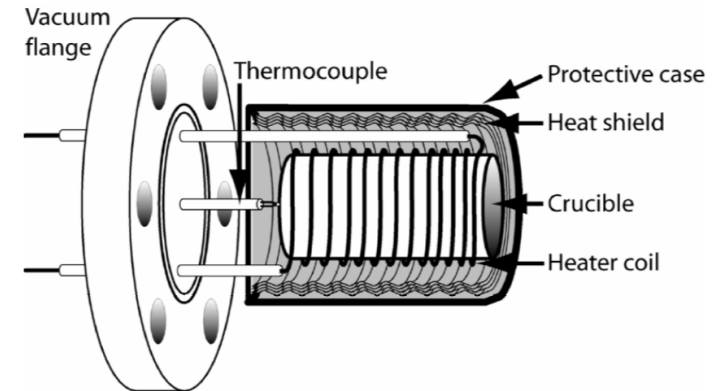


Figure 11.3: A simplified schematic sketch of a typical effusion cell. Omitted are the top cap that protects the heater windings from the evaporant as well as improving the black body environment of the crucible, the support clamps and details of the power feedthroughs, etc. The thermocouple junction is pressed gently against the base of the crucible but the black body environment assures an accurate temperature measurement. Note that the heater coils are more closely spaced near the front of the crucible to compensate for greater heat loss in that portion of the cell.

Molecular Beam Sources

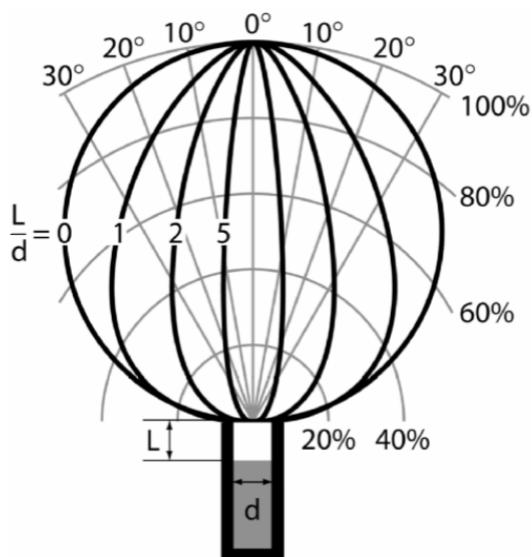


Figure 11.4: The flux distribution of atoms emitted by an effusion cell as a function of the depth in the cell of the evaporant surface relative to the diameter of the surface. [1]. Reprinted from Prog. Crystal Growth and Characterization, Vol 2, Luscher, P.E. and Collins, D.M.; “Design considerations for molecular beam epitaxy systems”, pp 15-32, Copyright 1979, with permission from Elsevier.

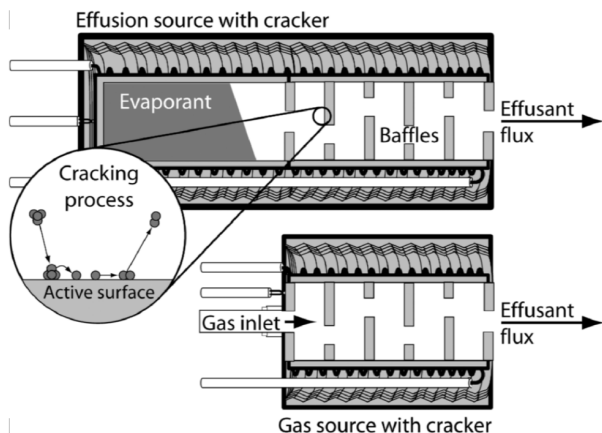


Figure 11.6: Cracking effusion sources for either a solid/liquid source (top) and for a gas source (bottom). The only difference is how the vapor to be cracked is supplied to the baffle section. Normal crackers typically have three baffles.

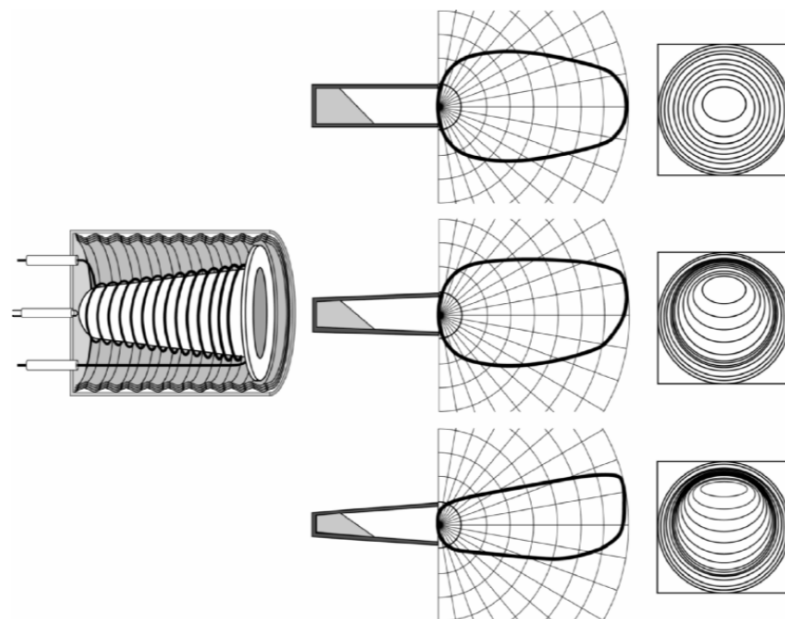


Figure 11.5: The flux patterns resulting from tapered effusion cells in both polar plots (center) and in flux contour plots (right). An isometric schematic shows the design of the tapered effusion cell with a flanged top to reduce creep of effusant out of the cell. Figure redrawn with permission from portions of Figure 3 in Tatyua Yamashita, Takashi Tomita, and Takeshi Sakurai, Japanese Journal of Applied Physics vol. 26 (1987), pages 1192-3. Copyright 1987, Institute of Pure and Applied Physics.

(Rockett, Chp 11)

Materials Sources and Detectors

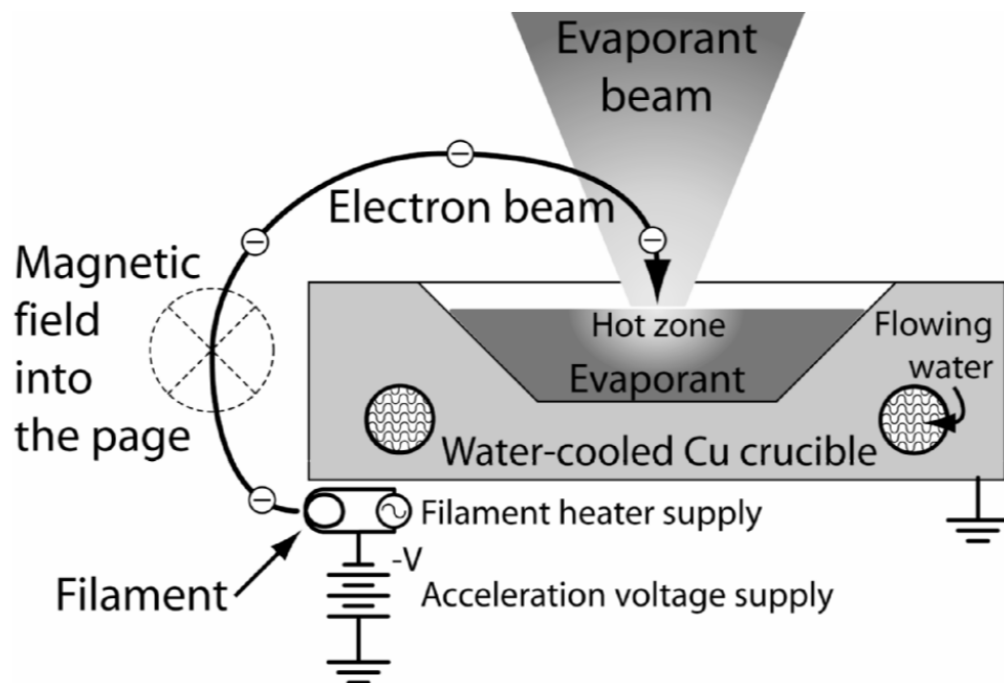


Figure 11.7: A schematic cross section of a typical electron beam evaporator. The magnetic field poles and consequently the magnetic field is out of the plane of the drawing. The high negative potential of the filament assists in electron emission and establishes the electron energy and point of impact on the crucible. Generally electrostatic deflection plates are added to sweep the electron beam into and out of the plane of the drawing.

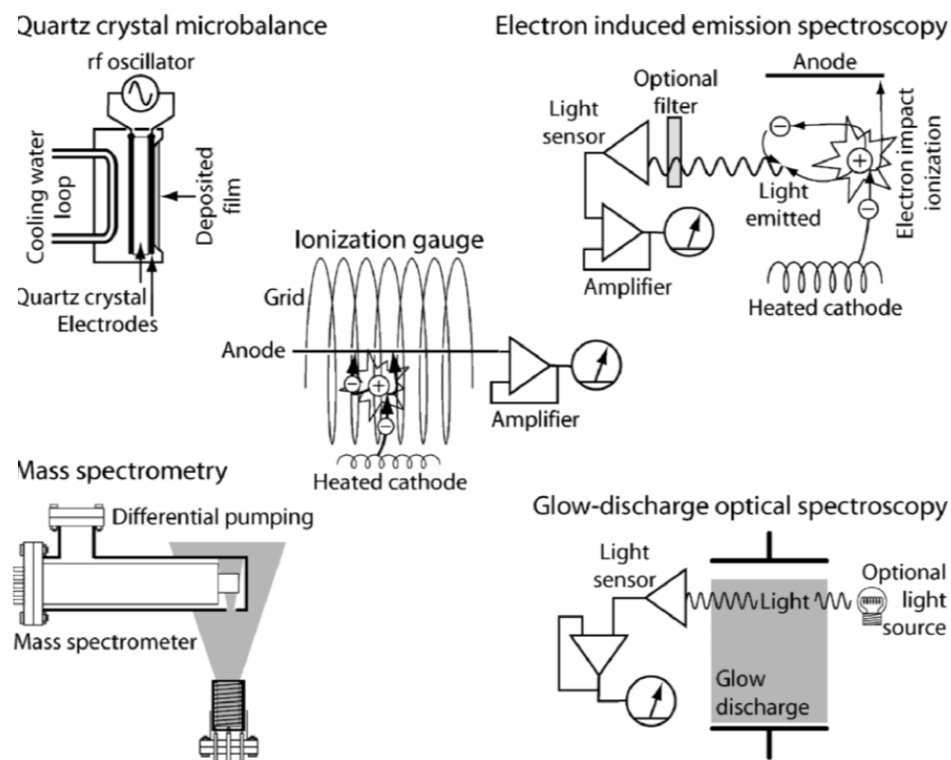


Figure 11.8: Five methods for monitoring concentrations of gas species. Many others exist.

(Rockett, Chp 11)

Tracking crystal growth in-situ using RHEED

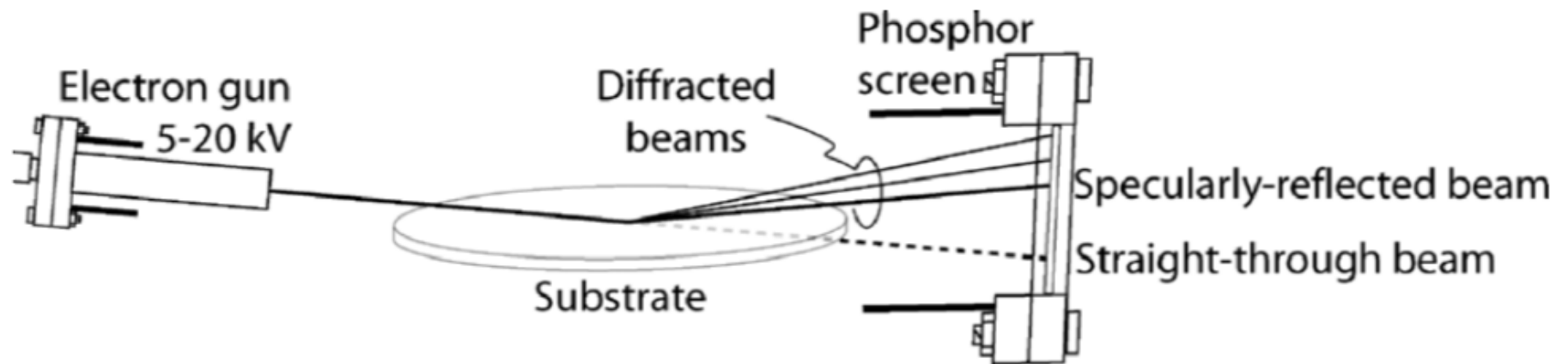


Figure 11.9: A schematic of the basic apparatus for conducting a RHEED experiment. Not shown is the remainder of the deposition system. This apparatus relies on at least high vacuum to protect the electron gun.

(Rockett, Chp 11)

Tracking crystal growth in-situ using RHEED

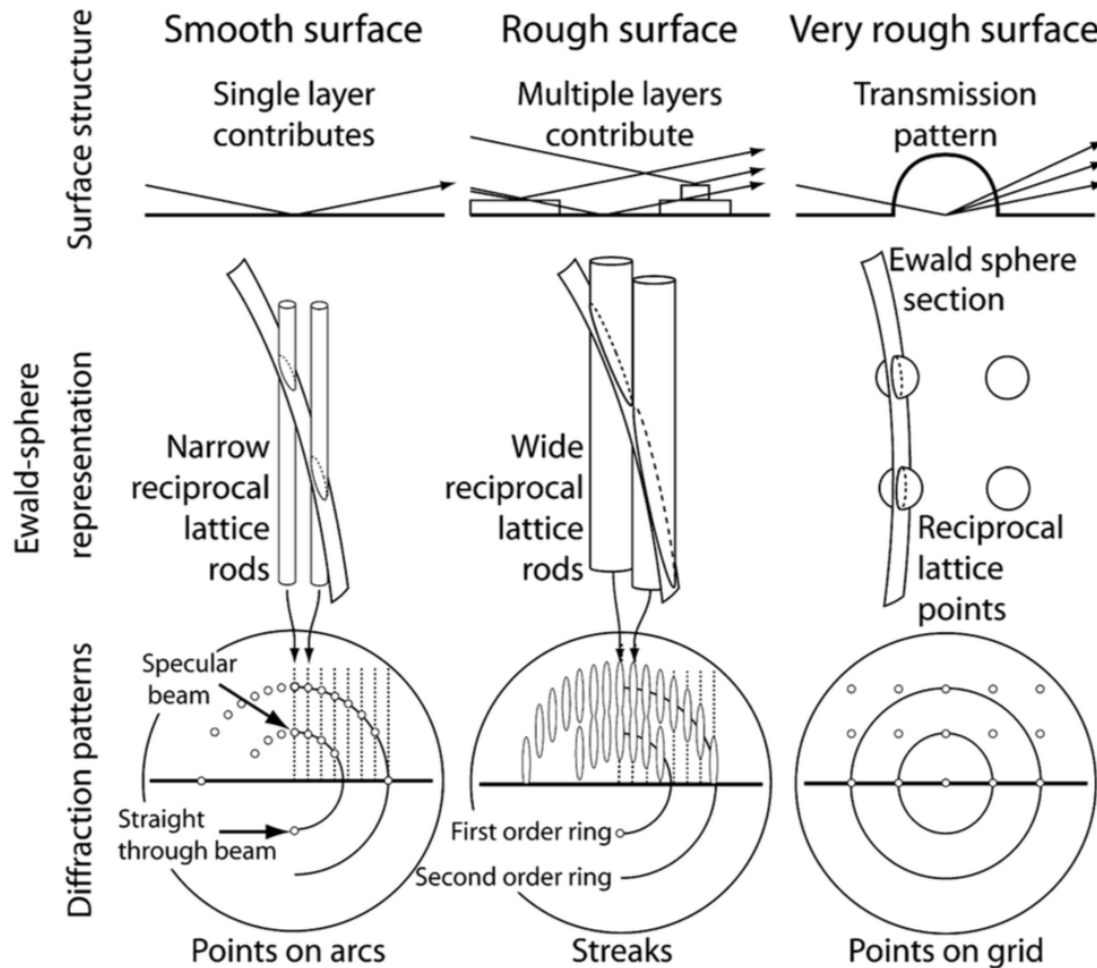


Figure 11.10: A schematic of the diffraction patterns in a RHEED experiment resulting from different surface structures. To simplify the drawing the broad rods of the rough surface are drawn as constant in width. Properly, for a two-level surface they have two non-zero Fourier coefficients and should oscillate as sine waves perpendicular to the surface. Therefore the rods should be wider and narrower along their length. See Figure 11.11 for a more accurate representation.

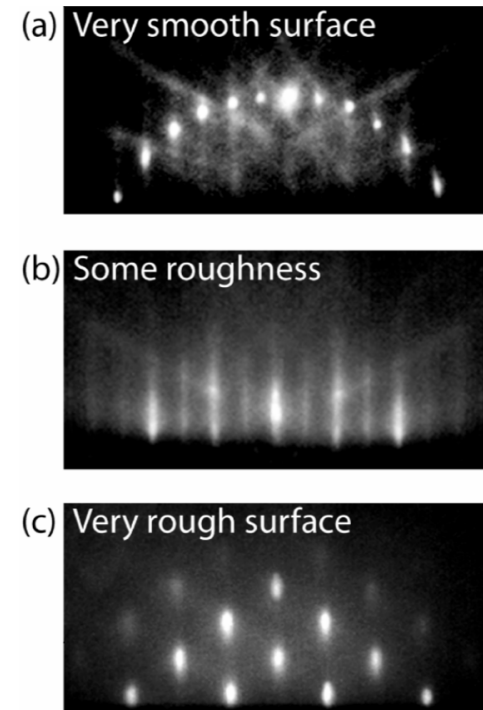


Figure 11.11: Examples of RHEED patterns obtained during non-equilibrium MBE growth of GeSn alloys. (a) Pattern for a very smooth surface as in left side of Figure 11.10 showing points on an arc. The diagonal streaks are multiple diffraction effects known as Kikuchi bands. (b) A pattern for a somewhat rougher surface corresponding to the middle drawing in Figure 11.10. Both (a) and (b) show a half-order reflection between the bright integer-order spots that results from the surface reconstruction. (b) Shows some evidence of residual Kikuchi bands. (c) A pattern for a very rough surface corresponding to the right hand drawing in Figure 11.10 where the electron beam is passing through three dimensional islands. Adapted with permission from O. Gurdal, P. Desjardins, J. R. A. Carlsson, N. Taylor, H. H. Radamson, J.-E. Sundgren, and J. E. Greene, *Journal of Applied Physics*, 83, 162 (1998). Copyright 1998, American Institute of Physics.

(Rockett, Chp 11)

Tracking crystal growth in-situ using RHEED

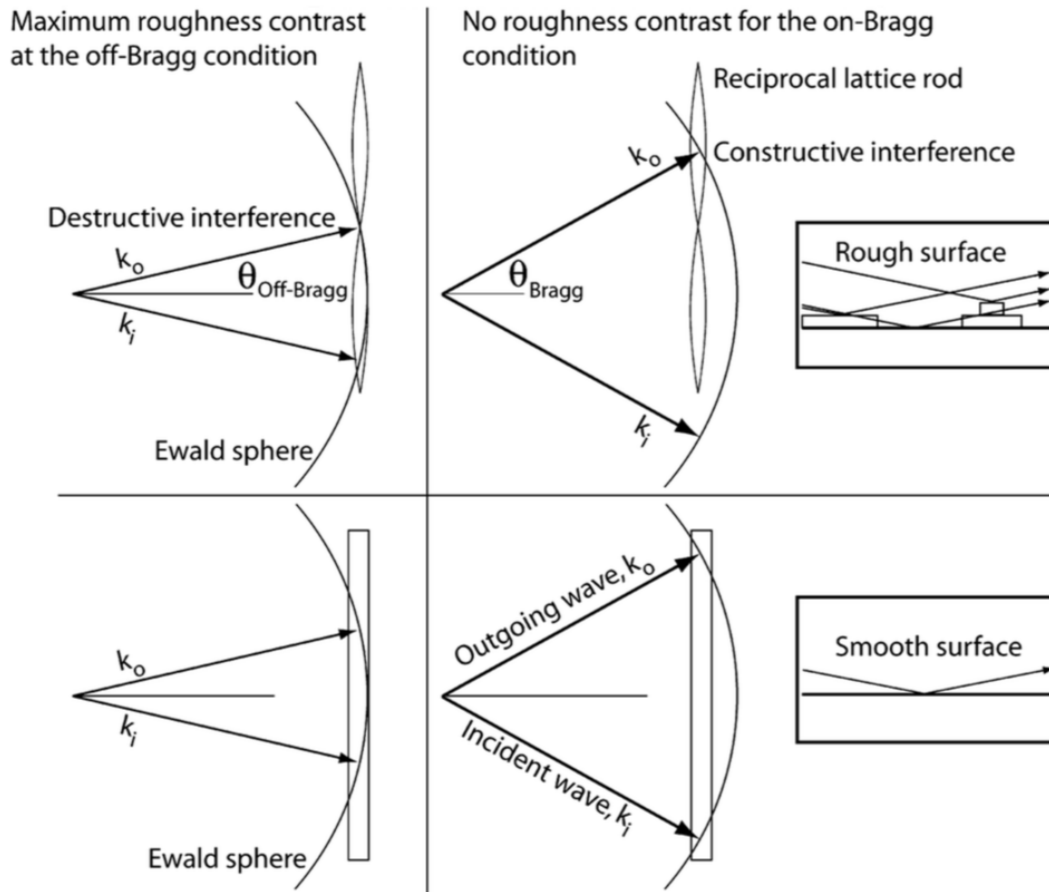


Figure 11.12: RHEED diffraction Ewald sphere constructions for the on-Bragg and off-Bragg conditions. Note that in the on-Bragg condition there is no difference in the diffracted intensity for the rough and smooth surfaces while for the off-Bragg condition alternate layers of the film interfere destructively. Therefore there is strong contrast for the intensity from rough and smooth surfaces. Refer to Figure 4.6 and related discussion for background on this construction.

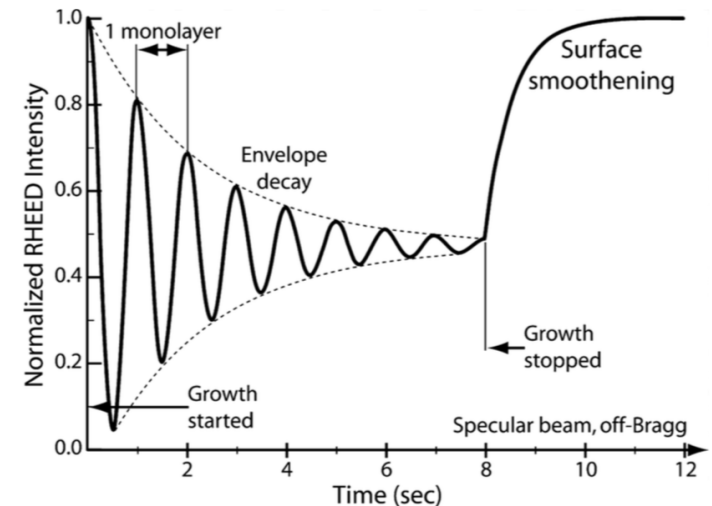


Figure 11.13: A typical example of (hypothetical) RHEED oscillation data during MBE growth at a rate of 1 monolayer/sec. Note that the surface is roughening during the 8 monolayers of deposition as shown by the decay of the oscillations but upon termination of growth the surface becomes smooth and the intensity recovers. To obtain this type of behavior the experiment is configured in the off-Bragg condition so that alternate monolayers of the film interfere destructively. This type of oscillation is observed in the intensity of all reflected and diffracted beams. The most intense is the specularly-reflected beam so that is the one normally used.

(Rockett, Chp 11)

Compound Semiconductor Growth & Energetics

A phase is a chemically and structurally homogeneous material.

$$dE = dQ + dW + dQ_B + \dots$$

$$dE = TdS - PdV + \sum_i \mu_i dN_i$$

$$E = TS - PV + \sum_i \mu_i N_i$$

$$H = TS + \sum_i \mu_i N_i$$

$$F = -PV + \sum_i \mu_i N_i$$

$$G = \sum_i \mu_i N_i$$

$$\frac{-\Delta S_{mix}}{Nk_B} = x \ln(x) - (1-x) \ln(1-x)$$

$$\frac{\Delta F}{N} = k_B T [x \ln x + (1-x) \ln(1-x)] - \frac{x(1-x)\xi}{2}$$

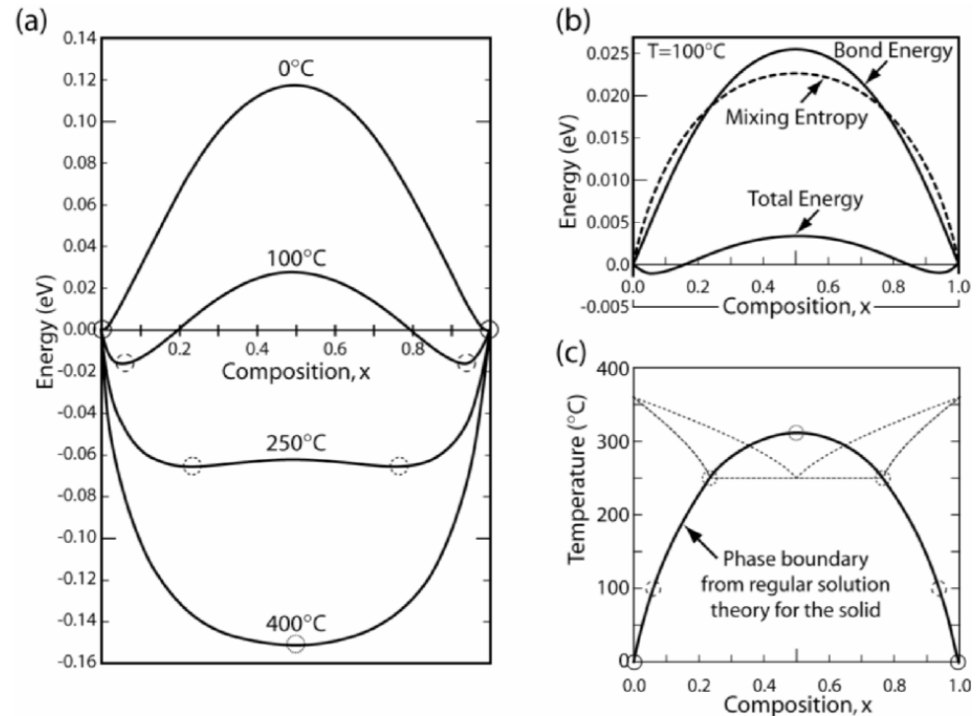
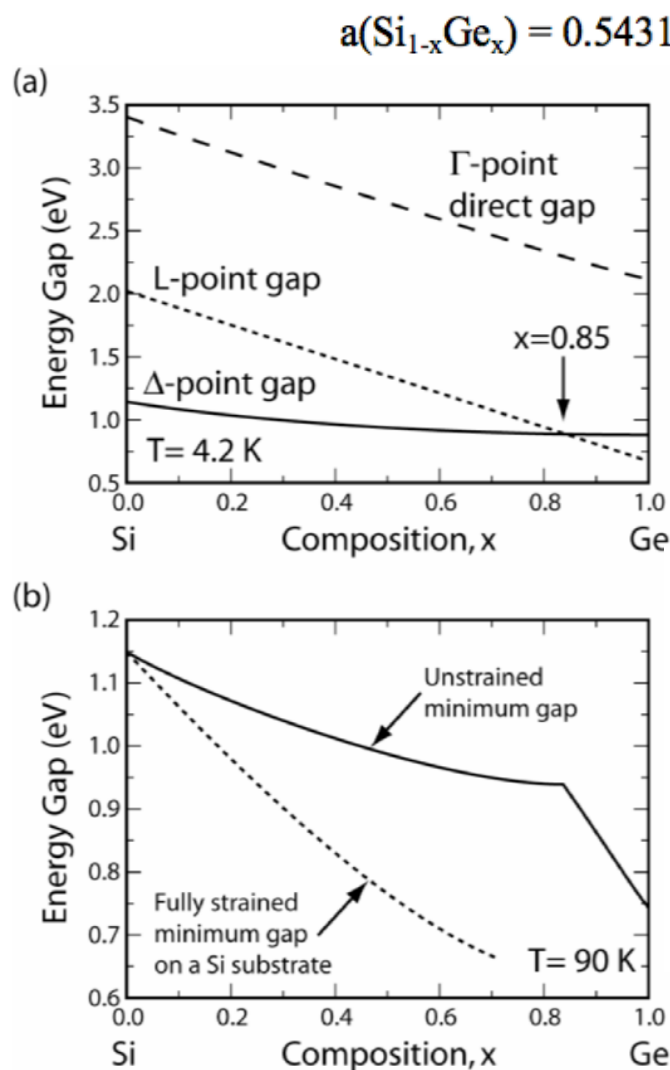
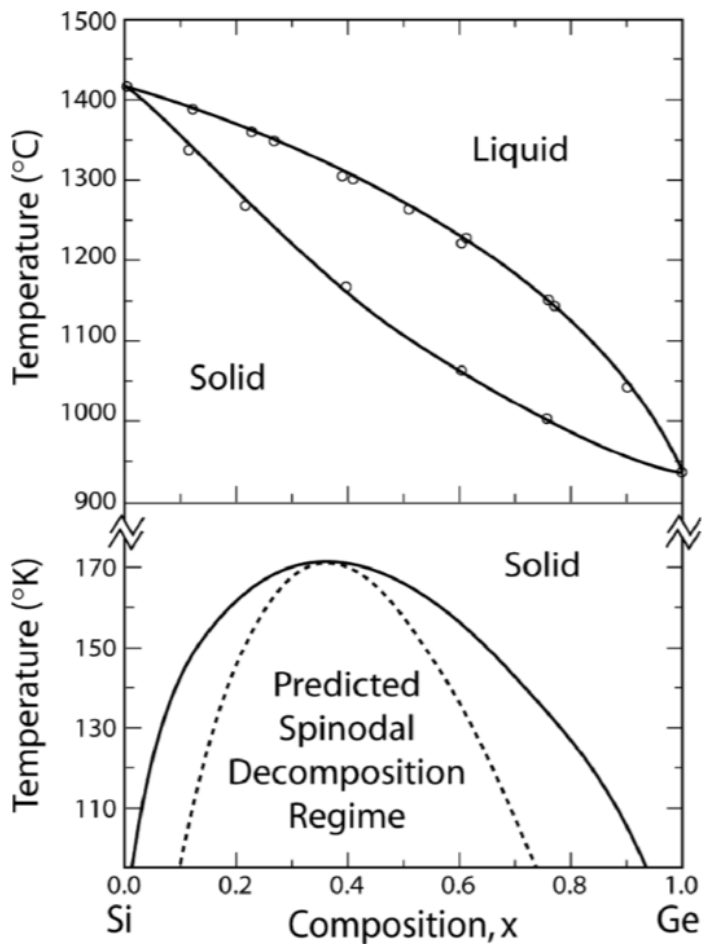


Figure 4.18: Free energy as calculated from Equations 4.25-4.29. (a) shows the free energy of mixing for several temperatures. Negative values indicate favorable mixing, while positive values indicate a preference for demixing. The more negative the energy the more favorable the mixing. (b) gives the two contributions to the energy, bond enthalpy and heat (temperature \times entropy), whose difference gives the curves in (a). Notice in particular that the entropy dependence upon x is significantly more square than the energy dependence. (c) the locus of energy minima from (a) [circles] as a function of temperature determine the boundary of the stable phase regions and the compositions which are stable in the two-phase region. This locus determines the shape of the phase boundaries in the solid phase region of a binary phase diagram. To give an idea of how the rest of the phase diagram enters, the dashed curves are added. Calculation of these requires a separate determination of the energy of the various liquid phases.

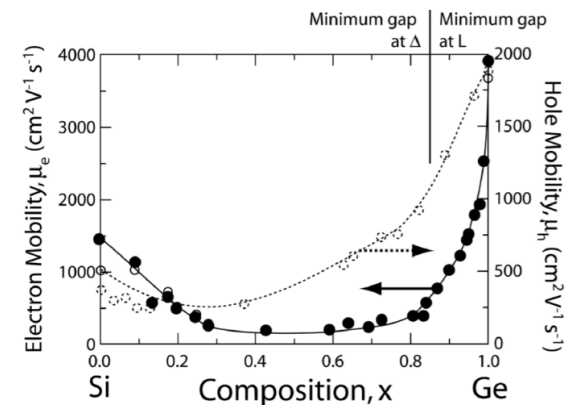
(Rockett, Chp 4)

Compound Semiconductor Growth & Energetics



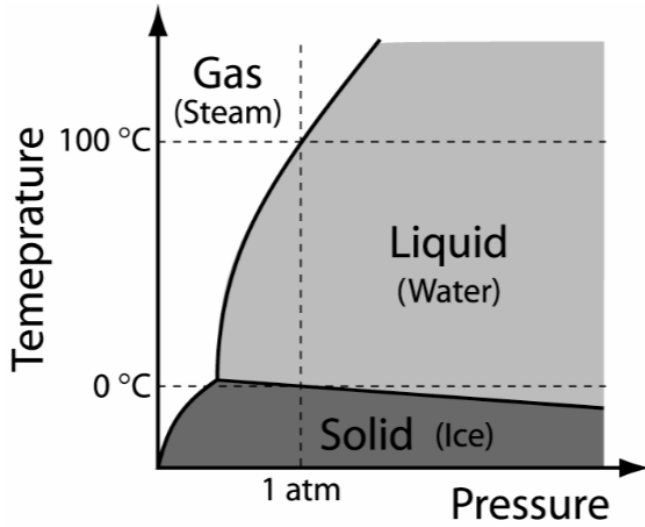
$$\Delta E_V = 0.6x - 0.07x^2$$

$$\Delta E_C = 0.44x - 0.09x^2$$



(Rockett, Chps 4 & 6)

Compound Semiconductor Growth & Energetics



$$F = C - P + 2,$$

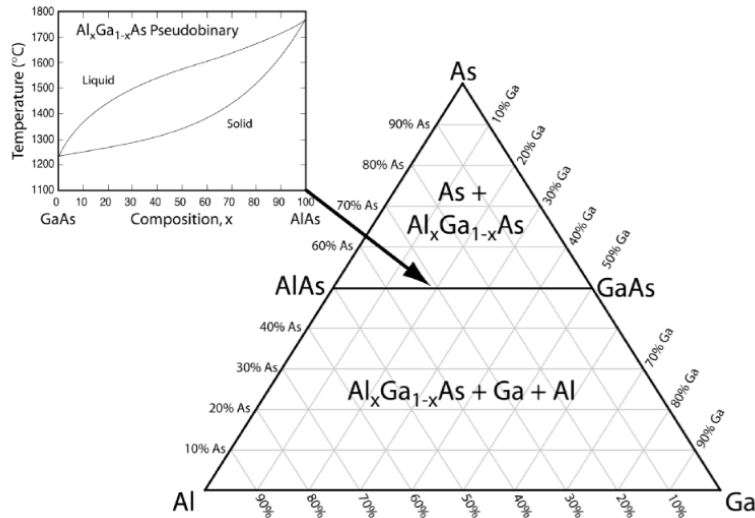
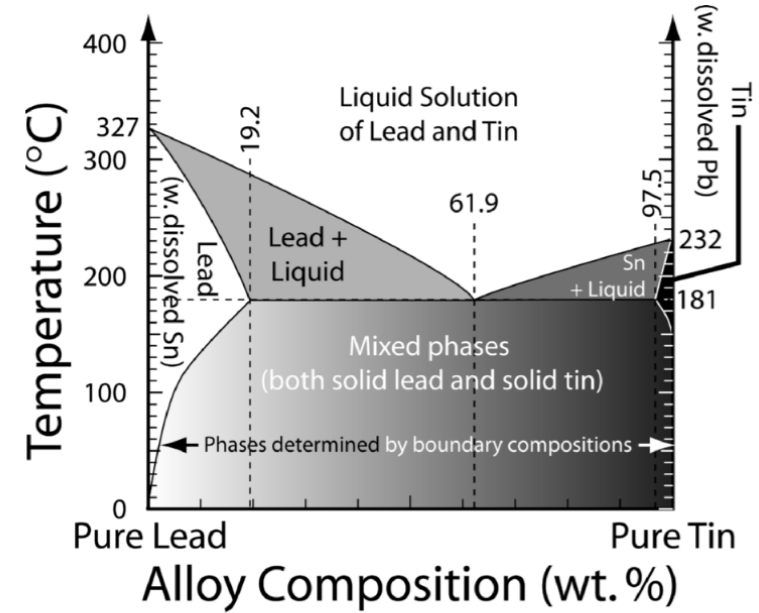


Figure 4.10: The ternary phase diagram for Al-Ga-As. Each light line represents alloys of constant composition as labeled for each line. The dark horizontal line represents the pseudobinary alloy $Al_xGa_{1-x}As$. This is a continuously-soluble alloy as shown in the inset. Figure inset based on data from Reference 1.

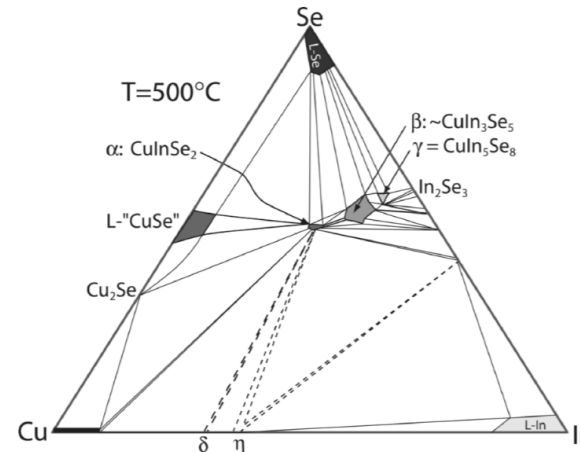


Figure 4.11: A ternary phase diagram for Cu, In, and Se at 500°C based on data in [2]. Additional data available for 750°C in [1]. Uncolored regions on the diagram are two or three phase areas. Numerous In-Se compounds occur which are not labeled to simplify the diagram. The diagram is approximate and most relevant for 500-750°C.

(Rockett, Chp 4)

Compound Semiconductor Growth & Energetics

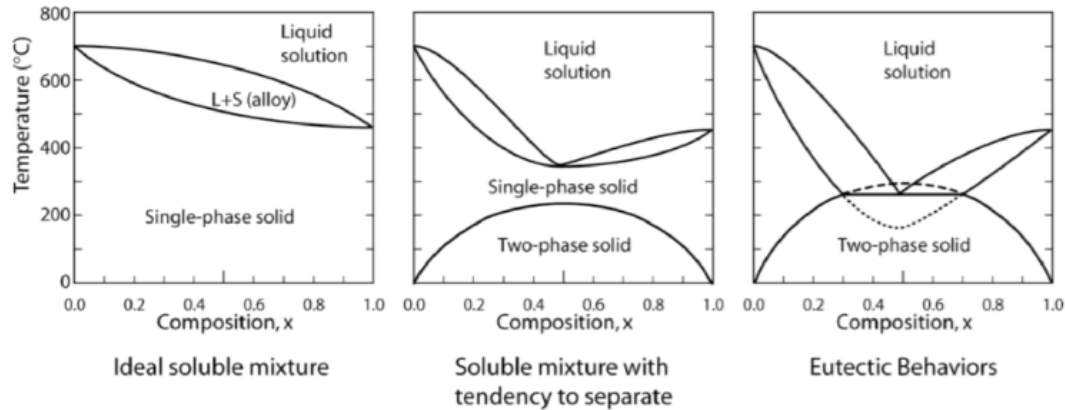


Figure 4.19: In a full calculation of a phase diagram one can include the liquid phase. An ideal solution produces a liquid-solid phase diagram as on the left side of the figure. As the bond energy difference from Equation 4.25 becomes more significant the solid tends to prefer to separate into two phases. This has consequences for both the low-temperature behavior described by Equation 4.29 and Figure 4.18 and for the liquid-solid relations. The result is the middle figure. A further increase in the tendency to phase separate leads to the behavior on the right and to a binary eutectic phase diagram as in Figure 4.8.

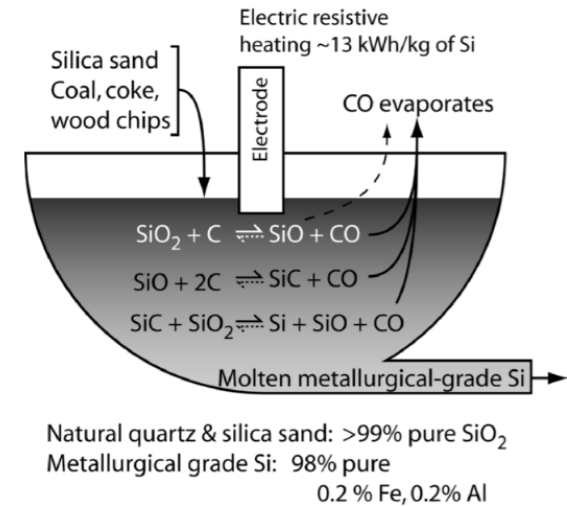


Figure 4.20: A schematic of the process for refining SiO₂ into metallurgical-grade Si using reduction by C. The product CO is removed by evaporation from the surface and is swept away in the gas. Because SiO has a moderate vapor pressure at these temperatures, some SiO also leaves the surface and condenses on cool surfaces nearby.

(Rockett, Chp 4)

Compound Semiconductor Growth & Energetics

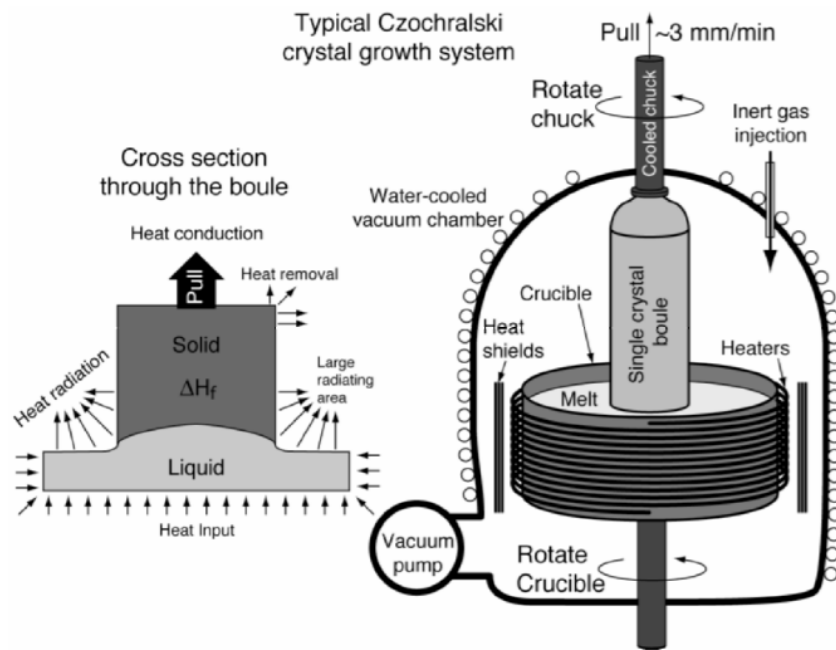


Figure 4.21: A schematic diagram of the Czochralski crystal growth process. A seed crystal mounted on a cooled chuck is lowered into a molten bath, which will solidify to start crystal growth. This seed is then withdrawn slowly and new crystal grows on the existing seed. If the seed is a single crystal then with proper care the boule will also be a single crystal with zero dislocations. The diameter of the boule is adjusted by control of the shape of the meniscus of the liquid and the shape of the solidification boundary.

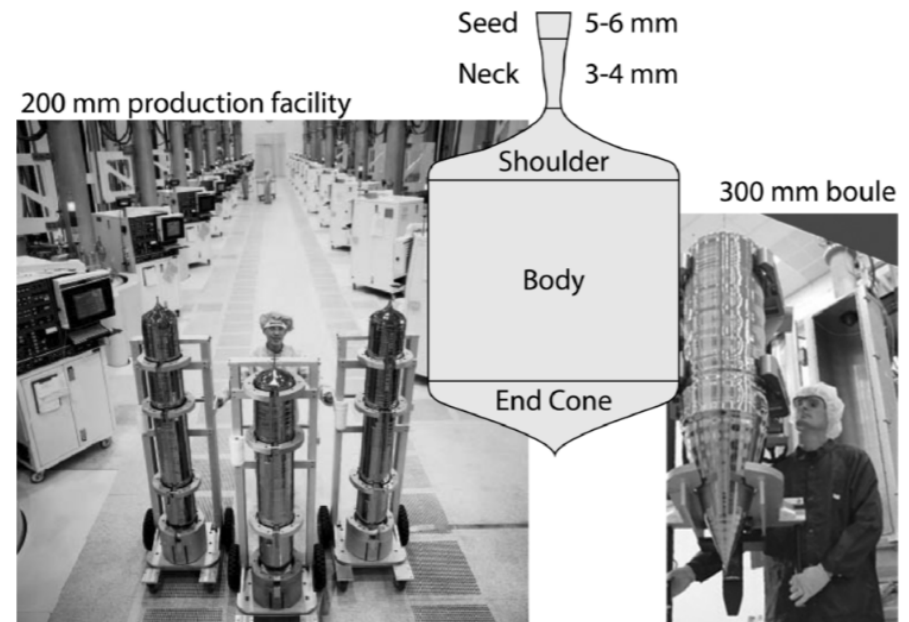


Figure 4.22: Photographs (left) of a 200-mm Si Czochralski growth facility, and a 300 mm Si boule (right) courtesy of MEMC Electronic Materials, Inc; St. Peters MO. The overlying schematic shows the regions of the boule.

(Rockett, Chp 4)

Compound Semiconductor Growth & Energetics

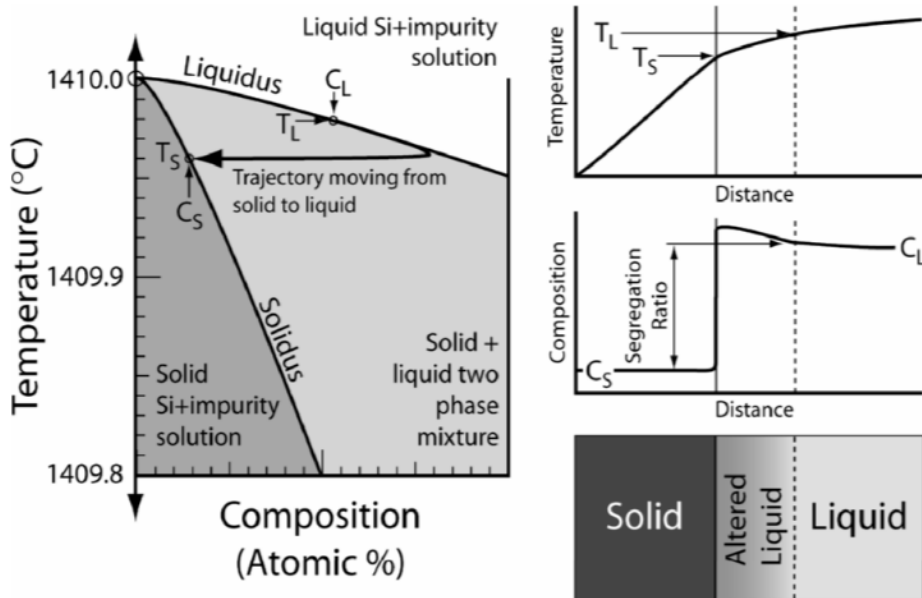


Figure 4.23: Schematic diagram of a typical binary eutectic phase diagram between Si and an impurity near the Si melting point. Insets at the right show the temperature and composition of the system across the solid/liquid interface, as well as a schematic of the interface. The binary phase diagram includes an indication of the compositions of the solid and liquid during growth and the change in both variables through the interface region. As shown, the composition of the liquid is enriched in impurity near the interface due to rejection of extra impurity from the solid during growth. This excess impurity must diffuse into the liquid and results in the composition change shown. Note that the observed segregation ratio will generally be lower during growth than the equilibrium value due to this diffusion rate limitation.

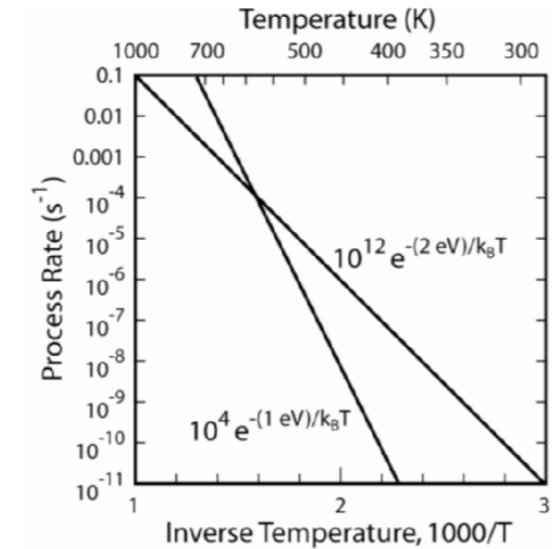


Figure 4.24: Rates for two hypothetical processes, one with an activation energy of 2 eV and a prefactor of 10^{12} sec^{-1} and a second with an activation energy of 1 eV and a prefactor of 10^4 sec^{-1} . The high activation energy process is favored by short times at high temperatures (left side of the graph) while the low activation energy process is dominant for long times at low temperatures (right).

(Rockett, Chp 4)

Compound Semiconductor Growth & Energetics

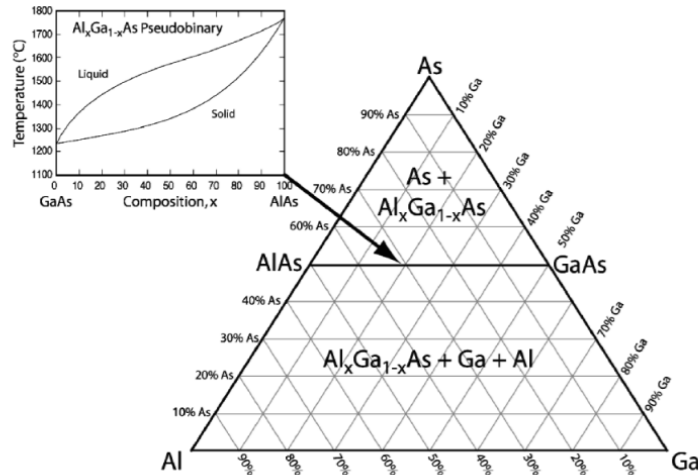


Figure 6.2: Shows the ternary phase diagram for Al-Ga-As. There is also significant solubility for Ga in Al (not indicated) and significant vapor pressure for As above a few hundred degrees C. The latter leads to As loss in open or vacuum environments. Inset based on data in Reference [1].

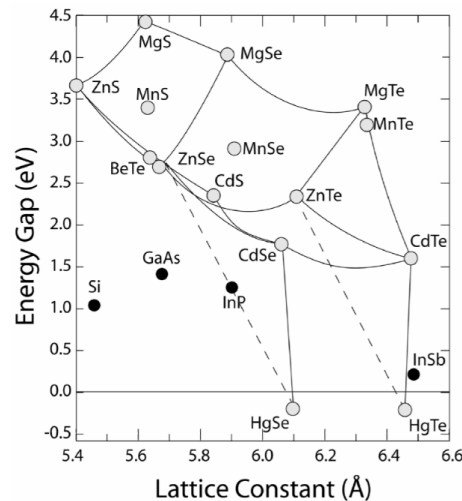


Figure 6.4: The energy gap as a function of lattice constant for II-VI compounds. All of these compounds are direct-gap. The dashed curves are linear interpolations. The real systems would exhibit lattice constant bowing. The black points indicate commonly available substrates on which the II-VI compounds can be grown. Note that HgSe and HgTe are metallic rather than semiconducting. Figure based on References [4] and [5].

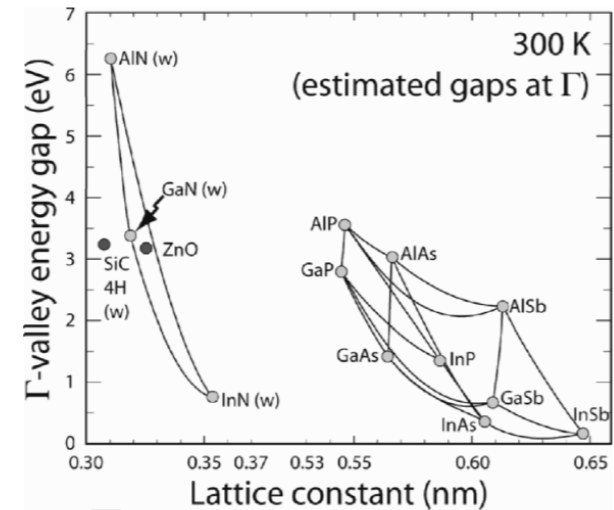
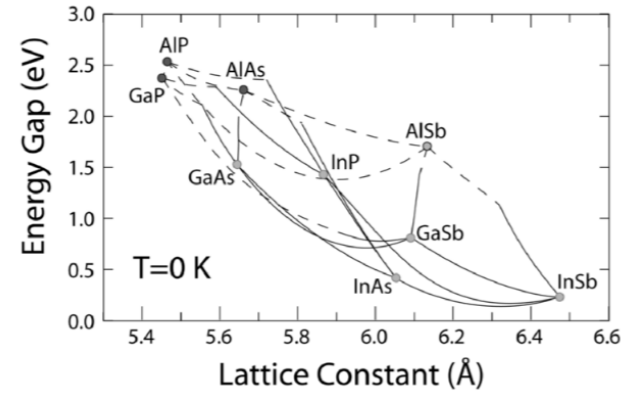


Figure 6.3: The energy gap of group III-V compounds as a function of lattice constants. The upper plot shows the minimum gaps for the alloys with dashed lines indicating indirect gaps and solid lines for direct gaps. The lower chart shows the minimum direct gaps. Based on data in References [2] and [3]. Note that the nitride values are for the hexagonal wurtzite phase (indicated with a "w"). The cubic nitride lattice constants are 0.438, 0.450, and 0.498 nm for AlN, GaN, and InN, respectively. [3] The cubic nitride energy gaps are similar to or smaller than the hexagonal phase values. Top figure redrawn with permission from I. Vurgaftman, J. R. Meyer, and L. R. Ram-Mohan, Journal of Applied Physics, 89, 5815 (2001). Copyright 2001, American Institute of Physics.

(Rockett, Chp 6)

Compound Semiconductor Growth & Energetics

$$\Delta G = \sum_i \mu_i \Delta N_i = \Delta E - T\Delta S + P\Delta V,$$

$$\Delta E = 1/2 (E_{AA} + E_{BB}) - E_{AB},$$

$$E = N \sum_j \alpha_j q_j E_j,$$

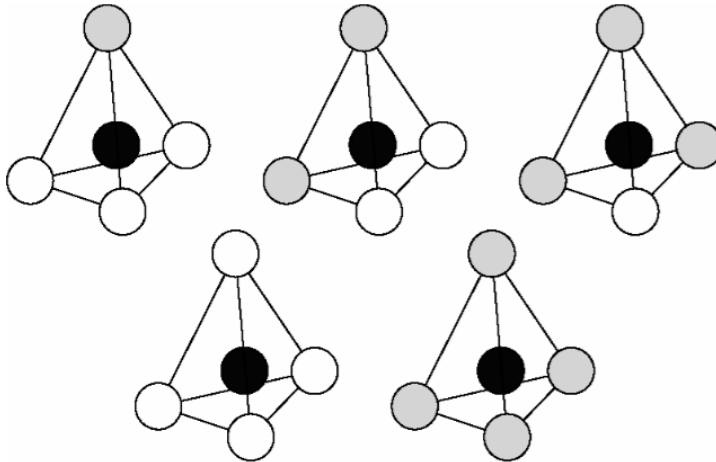


Figure 6.5: The five distinct alloy tetrahedra. White circles indicate A atoms, gray circles B atoms, and black circles C atoms in an $A_{1-x}B_xC$ type alloy. Note that each tetrahedron can be rotated to place any of the A or B atoms on a given vertex when forming the crystal. The energy of a tetrahedron is independent of its orientation. The model does not consider second-nearest neighbor interactions but can account for bond strains within each tetrahedron. A more accurate model must consider longer-range interactions.

The next step is to calculate the values of α_j . There are three rotations of the tetrahedra containing mixed A and B atoms that are, to some extent, distinct. The pure AC and pure BC tetrahedra cannot be distinguished upon rotation. Thus, for a diamond or zincblende structure, $\alpha_j=1$ for the two tetrahedra containing only A and C ($j=0$) or B and C ($j=4$) atoms, while tetrahedra including $j=1$ to 3 B atoms have $\alpha_j=C_j^4 = 4!/(j!(4-j)!)$ distinguishable rotations. Note that $\alpha_j q_j$ summed over all five values of j is unity, while the composition, x , of the alloy $A_{1-x}B_xC$ is $x = q_1 + 3q_2 + 3q_3 + q_4$. One may further show that $q_j = x^j(1-x)^{4-j}$. [6] **Note: the difference between a random and a non-random alloy is in the q_j values.** The ignored third-nearest neighbor effects in the energies are generally much smaller than the second-nearest neighbor values and so this approximation is not normally a problem. Higher order interactions can be important in establishing, for example, the difference between cubic or hexagonal structures and the precise locations of phase boundaries.

$$S = k_B N \left(3[x \ln x + (1-x) \ln(1-x)] - \sum_j \alpha_j q_j \ln q_j \right)$$

$$\sum_j \frac{\partial G}{\partial q_j} dq_j = 0 \quad \sum_j \alpha_j \delta q_j = 0$$

$$\beta = 1 - \frac{P_{AB}}{x}$$

$$\beta = 1 - \frac{q_1 + 2q_2}{x(1-x)}$$

$$\delta x = \delta q_1 + 3\delta q_2 + 3\delta q_3 + \delta q_4 = 0.$$

The energy minimization criterion can be used to develop values of the various q_j 's for given E_j values. These can, in turn, be used to calculate an order parameter. Consider for a moment the range of values β can take. For a completely phase separated alloy $P_{AB}=0$ and $\beta=1$. If a superstructure order develops in which $P_{AB}>x$ or $q_1>x(1-x)^3$, $q_2>x^2(1-x)^2$, and/or $q_3>x^3(1-x)$. This situation would yield $\beta<0$. **Hence positive β values indicate phase separation while negative β shows ordering.**

(Rockett, Chp 6)

Compound Semiconductor Growth & Energetics

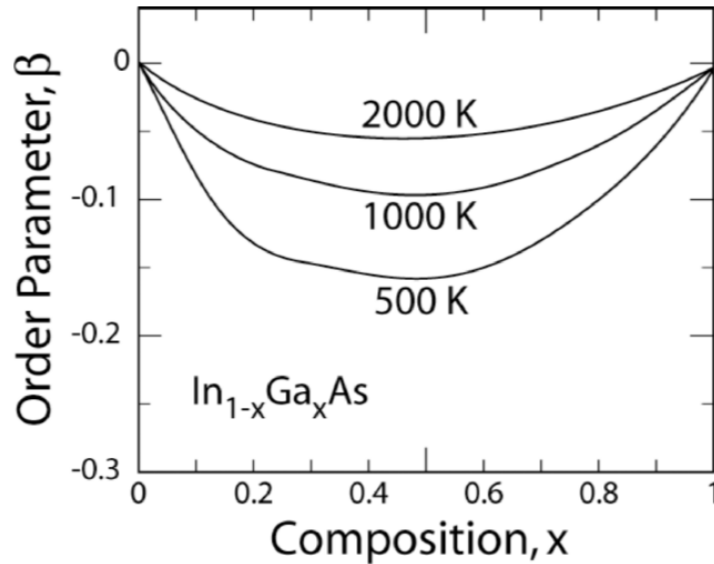


Figure 6.6: Shows the order parameter calculated for $\text{In}_{1-x}\text{Ga}_x\text{As}$ as a function of composition at several temperatures. Redrawn with permission from Masaya Ichimura and Akio Sasaki, Journal of Applied Physics, 60, 3850 (1986). Copyright 1986, American Institute of Physics.

For a quaternary $\text{A}_{1-x}\text{B}_x\text{C}_y\text{D}_{1-y}$ alloy, the stability criterion is determined by the second partial derivative of the free energy change, ΔG , for mixing:

$$\frac{\partial^2 \Delta G}{\partial x^2} \frac{\partial^2 \Delta G}{\partial y^2} - \frac{\partial^2 \Delta G}{\partial x \partial y} = 0.$$

$$\begin{aligned} \Delta E = & w_{AC}(1-x)(1-y) + w_{BC}x(1-y) + w_{AD}(1-x)y + w_{BD}xy + \\ & a_{AC-BC}(1-x)x(1-y) + a_{AD-BD}(1-x)xy + \\ & a_{AC-AD}(1-x)(1-y)y + a_{BC-BD}x(1-y)y \end{aligned}$$

$$\Delta S = Nk [(1-x) \ln(1-x) + x \ln x + (1-y) \ln(1-y) + y \ln y]$$

(Rockett, Chp 6)

Compound Semiconductor Growth & Energetics

Equilibrium Spinodal Decomposition Phase Boundaries

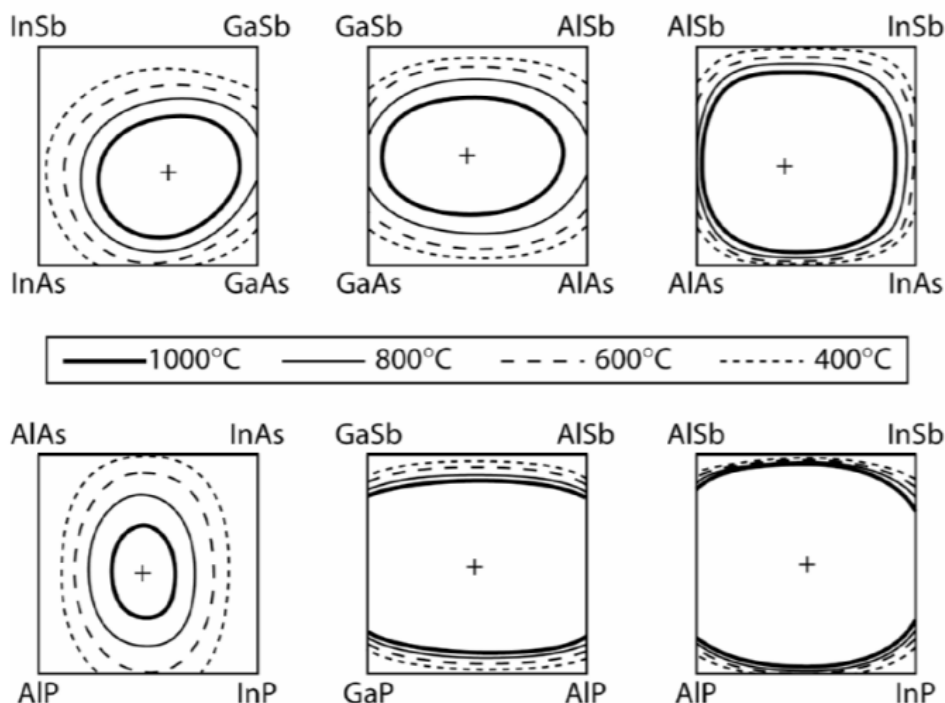


Figure 6.7: Spinodal decomposition curves for six quaternary semiconductor systems as calculated by Onabe in Reference [8]. Crosses indicate the midpoint of the spinodal decomposition regions. Ellipses are equivalent to slices through Figure 4.18c at various temperatures. Figure redrawn with permission from portions of Figure 1 in Kentaro Onabe, Japanese Journal of Applied Physics vol. 21 (1982), pages L323-5. Copyright 1982, Institute of Pure and Applied Physics.

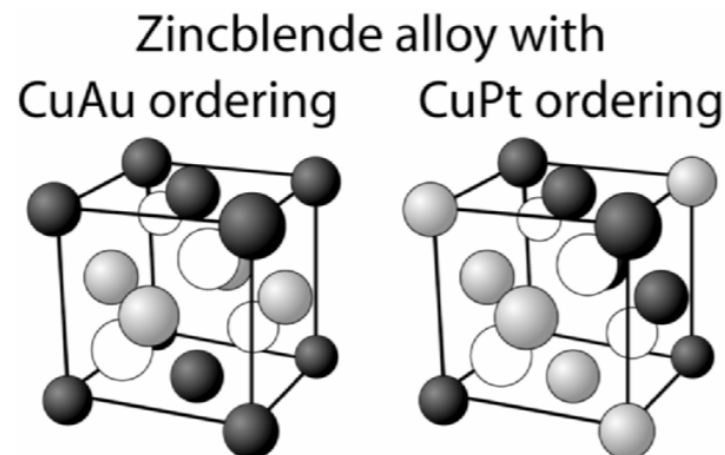


Figure 6.8: Schematics of a zincblende alloy of dark and light gray cations and white anions with CuAu and CuPt ordering on (100) and (111) planes, respectively. A common cation alloy has the same behavior.

(Rockett, Chp 6)

Compound Semiconductor Growth & Energetics

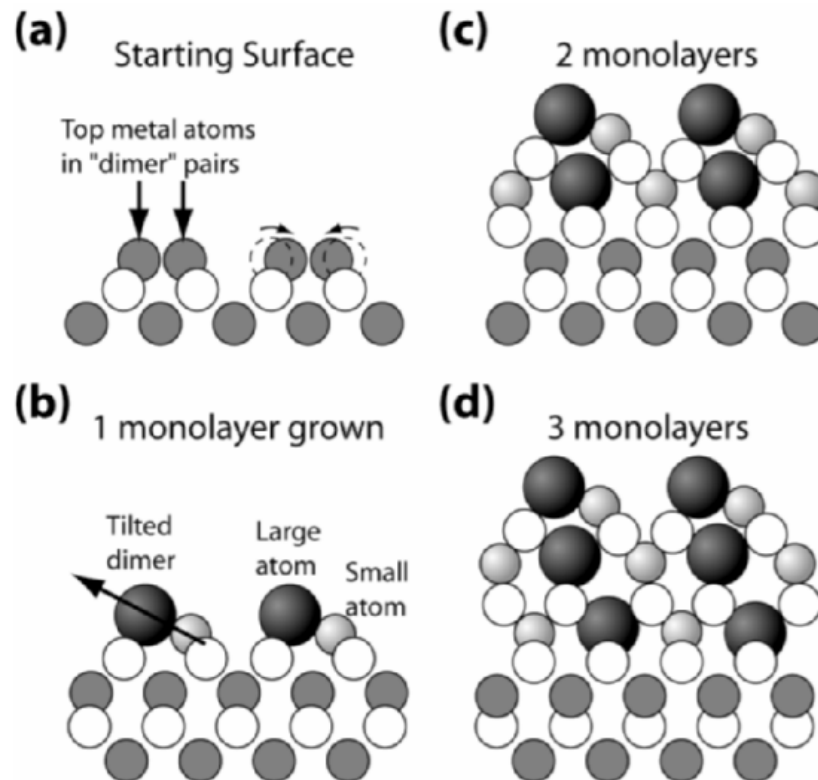


Figure 6.9: Schematic cross sections through a zincblende lattice along a (110) direction showing the dimerization of atoms on the surface of the material. The white circles represent common anions in an alloy and the large and small circles are the two cations. The medium gray circles represent the substrate cations. Strain resulting from placement of the large atoms in the second layer influences how dimers tilt on the surface. One side of these dimers favors the larger atom, which continues the underlying order.

The similar effects giving rise to both bowing and variations in the energy of the alloy tetrahedra in Figure 6.5 lead to an important conclusion. **Bowing and solubility are directly linked. Alloys with large bowings should have large regions where spinodal decomposition would favor phase separation. Thus one may expect poor miscibility in alloys with large bowing.** Examination of Equation 6.3 and the equations for the α_j and q_j terms also shows why bowing should have a maximum at $x \sim 0.5$ and why it would depend roughly on the difference in bond energies between atoms – because this is where the amplitude of core potential fluctuations should be largest relative to the unperturbed lattice.

(Rockett, Chp 6)

Compound Semiconductor Growth & Energetics

For the virtual crystal of an AB semiconductor alloy the symmetric potential term is

$$U_s = \sum_{r'} [xU_A(r') + (1-x)U_B(r')].$$

The asymmetric part is best written as

$$U_a = \sum_{r'} [U_A(r'-\tau) - U_B(r'-\tau)]c_\tau.$$

$$V_2 [A_{1-x}B_xC \text{ alloy}] = V_2^{AC} + (V_2^{BC} - V_2^{AC})x.$$

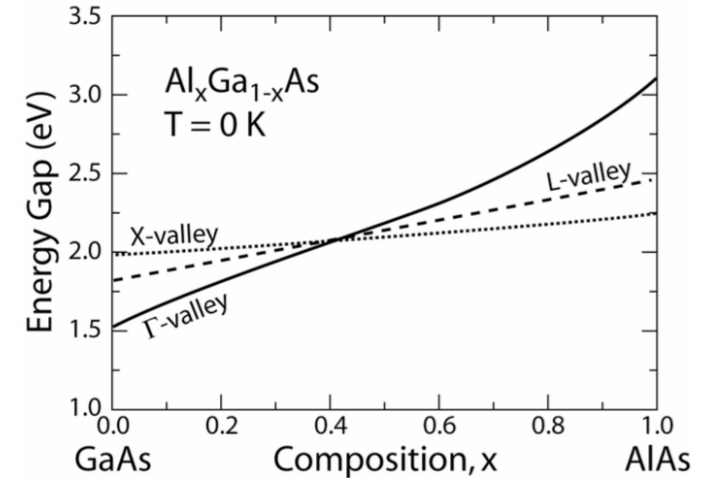


Figure 6.10: Minimum transition energy values for three primary gaps in AlGaAs alloys as a function of alloy composition. Note the direct-indirect transition at approximately 43% Al. Redrawn with permission from I. Vurgaftman, J. R. Meyer, and L. R. Ram-Mohan, Journal of Applied Physics, 89, 5815 (2001). Copyright 2001, American Institute of Physics.

Table 6.1: Semiconductor Alloy Bowing Parameters

Alloy	Bowing Parameter (eV)			Alloy	Bowing Parameter (eV)		
	Γ	X	L		Γ	X	L
AlGaAs	-0.13	0.55	0	AlAsP	0.22	0.22	0.22
AlInSb	0.43			AlAsSb	0.8	0.28	0.28
AlInP	-0.48	0.38		AlPSb	2.7	2.7	2.7
GaInAs	0.48	1.4	0.33	GaAsP	0.19	0.24	0.16
GaInSb	0.41	0.33	0.4	GaAsSb	1.43	1.2	1.2
GaAlN	1.0			InAsSb	0.67	0.6	0.6
GaInN	2.4			GaAsN	120		

All values are for the zincblende structure of the alloy. Most values and especially GaAsN, and AlGaAs and AlInP Γ -point values are composition dependent. Data are from Reference [2].

$$E_{ABCD}(x,y) = \frac{x(1-x)[(1-y)E'_{ABD}(x) + yE'_{ABC}(x)]}{x(1-x) + y(1-y)} + \frac{y(1-y)[xE'_{ACD}(y) + (1-x)E'_{BCD}(y)]}{x(1-x) + y(1-y)}$$

(Rockett, Chp 6)

Compound Semiconductor Growth & Energetics

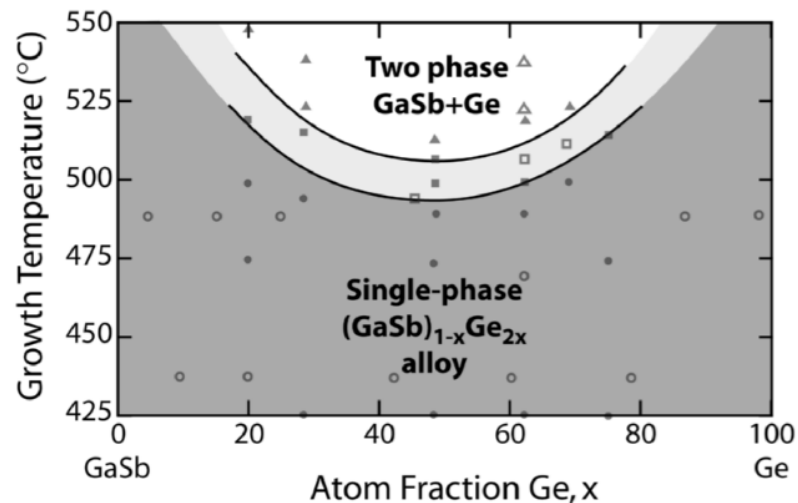


Figure 6.14: A phase diagram for the metastable $(\text{GaSb})_{1-x}\text{Ge}_{2x}$ alloy showing the phases present as a function of deposition temperature and composition based on data in Cadien et al. [20]. The darker gray area is the single-phase alloy region. The light gray region is a mixture of alloy and two-phase regions, and at sufficiently high temperature only the two equilibrium phases are found. Open data points are for films on GaAs (100) single-crystal substrates while the closed points are for films on glass.

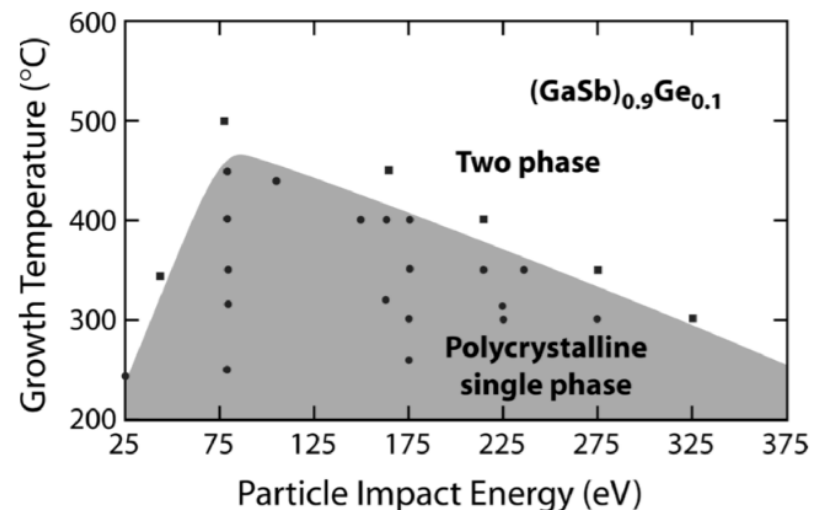


Figure 6.15: A phase diagram for the metastable $(\text{GaSb})_{0.9}\text{Ge}_{0.1}$ alloy showing the phases present as a function of deposition temperature and fast particle bombardment energy. Figure is based on data in Shah [21]. Circles indicate single-phase metastable alloys formed while square points show two-phase samples.

(Rockett, Chp 6)

Compound Semiconductor Growth & Energetics

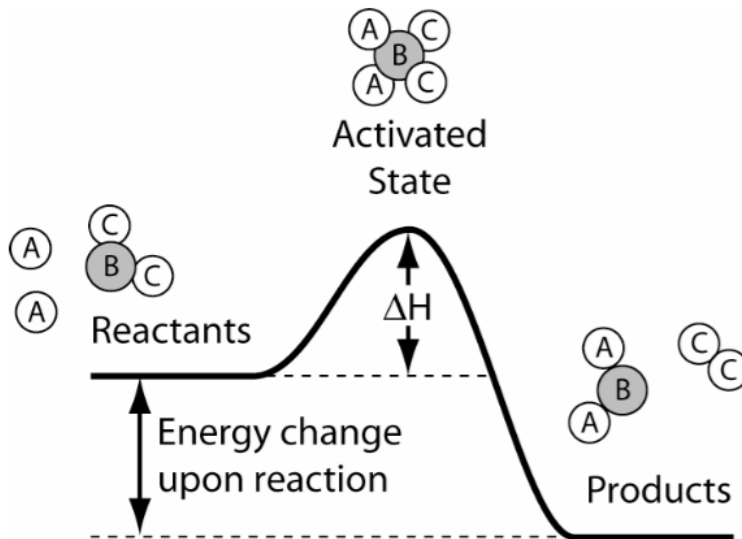
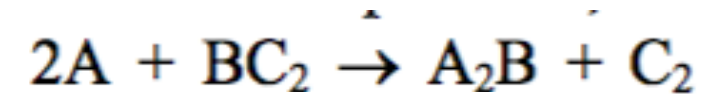
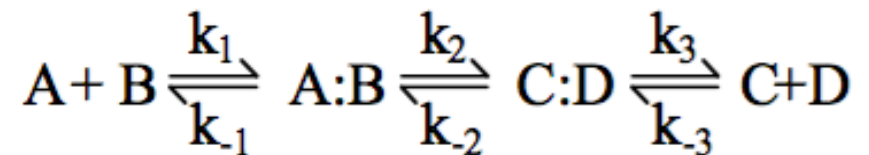


Figure 4.12: The energy of a system of atoms during the course of a reaction such as $2A + BC_2 \rightarrow A_2B + C_2$. The reactants must be configured for reaction. In the example this might mean attaching two A atoms to the BC_2 molecule prior to reaction. The reverse reaction would cross a higher energy barrier climbing the entire energy hill from the right ("Products") to the activated state energy.



$$R_f = k_f \frac{[A]^2 [BC_2]}{[A_2B][C_2]}$$

$$k_f = k_0 e^{-\Delta H / k_B T}$$



$$k_f = \frac{k_1}{1 + (k_{-1}/k_2) + (k_{-1}k_{-2}/k_2k_3)}$$

$$k_r = \frac{k_{-3}}{1 + (k_3/k_{-2}) + (k_2k_3/k_{-1}k_{-2})}$$

(Rockett, Chp 4)

Compound Semiconductor Growth & Energetics

$$E = \pi r^2 \gamma_s + (4\pi/3)r^3 \Delta H$$

$$r^* = -\frac{\gamma_s}{2\Delta H}$$

$$E^* = \frac{\pi}{12} \frac{\gamma_s^3}{\Delta H^2}$$

$$R = R_0 e^{-E^*/k_B T}$$

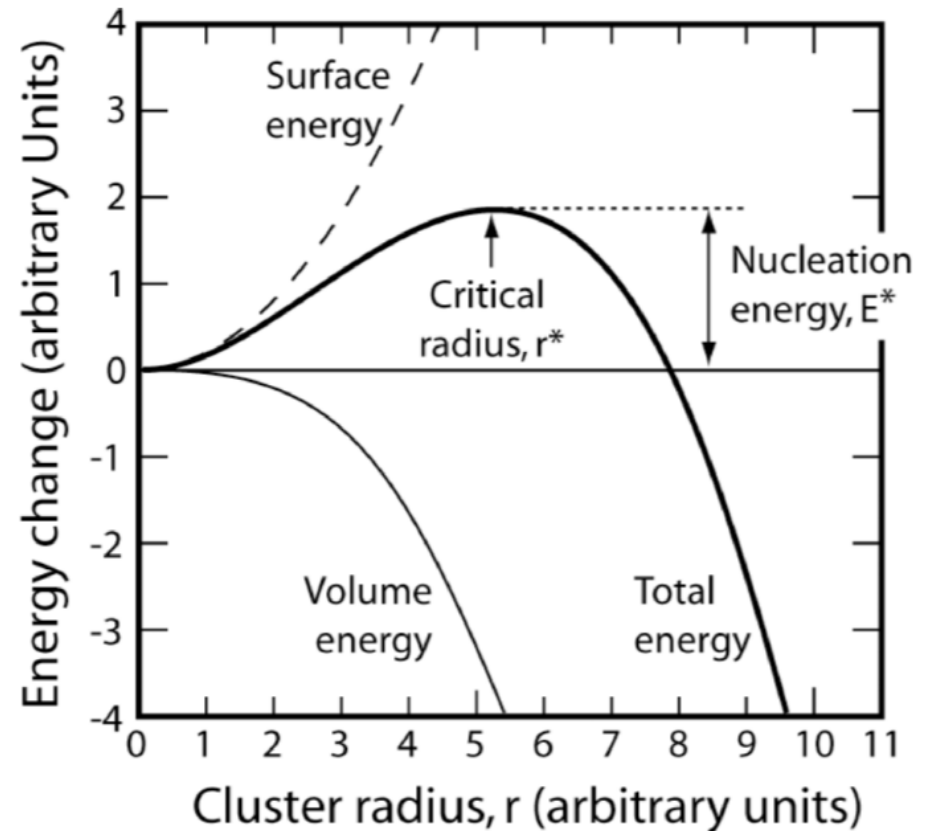
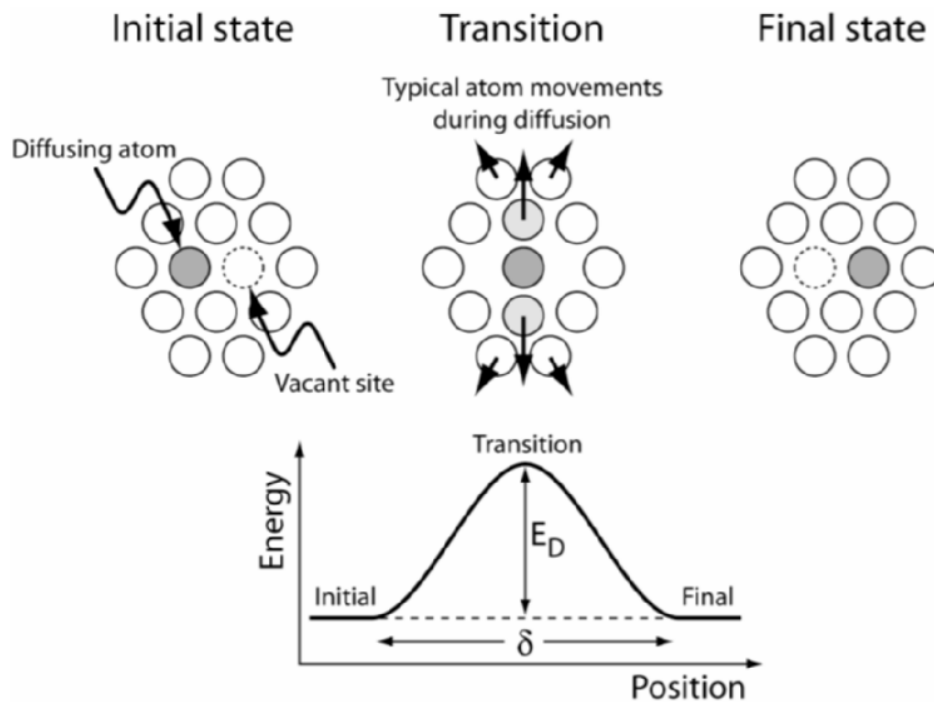


Figure 4.13: Shows the energy of a cluster of atoms during nucleation as a function of cluster size. Surface energy generally increases as r^2 , while volume energy decreases as r^3 . The energy of the cluster increases with addition of atoms up to a critical size, r^* , beyond which the energy decreases with atom addition. The maximum energy at r^* and is the activation energy barrier for nucleation.

(Rockett, Chp 4)

Compound Semiconductor Growth & Energetics



$$D = D_0 e^{-E_D / kT}$$

$$F = -D \frac{dC}{dx}$$

Figure 4.14: A schematic of the atomic movements involved in a typical substitutional diffusion process in a fcc lattice and the change in system energy throughout the process.

(Rockett, Chp 4)

Next topic: Defects in Semiconductors

Rockett: MSS

7. DEFECTS IN SEMICONDUCTORS

289

7.1 Point defects	289
7.1.1 Electronic states due to point defects	291
7.1.2 Shallow levels	295
7.1.3 Depth of intrinsic defects	299
7.1.4 Ionization of defects	300
7.1.5 Point defect densities	302
7.1.6 Vacancies and dopant diffusivity	308
7.2 Line defects	311
7.3 Strain relief in heterostructures	320
7.3.1 Energetics of strain relief	322
7.3.2 Misfit dislocations	328
7.3.3 Dislocation dynamics	329
7.3.4 Reducing problems due to strain relief	336
7.4 Planar and volume defects	337
7.4.1 Twins and stacking faults	337
7.4.2 Surfaces, interfaces, grain boundaries	340
7.4.3 Volume defects	343
7.5 SiC: a case study in stacking faults	344
7.6 Summary points	349
7.7 Homework	352
7.8 Suggested readings & references	355

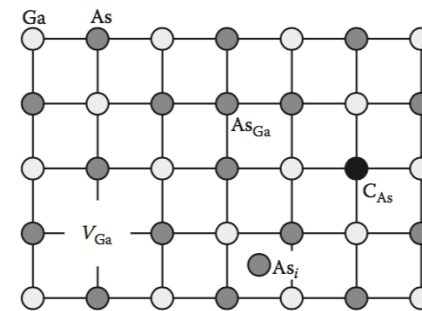


Figure 2.1 Defects in GaAs. Gallium vacancy (V_{Ga}), arsenic interstitial (As_i), arsenic antisite (As_{Ga}), and substitutional carbon (C_{As}).

(Rockett, Chp 7, Haller/McLuskey)

Materials Science of Compound Semiconductors

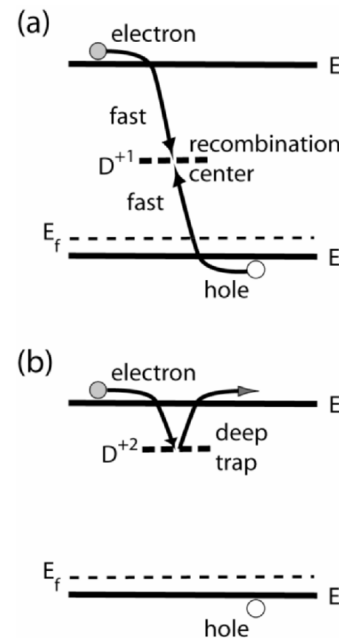
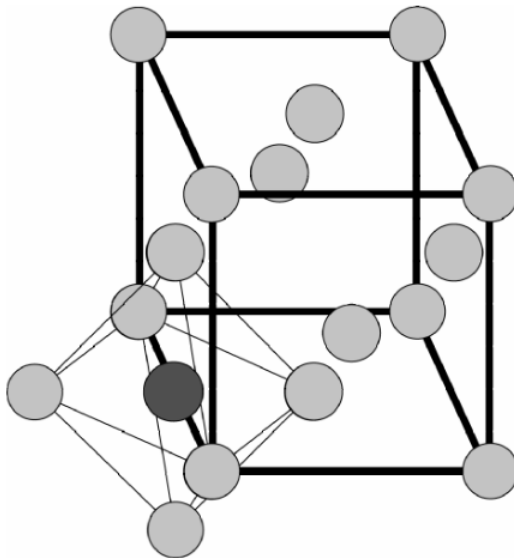
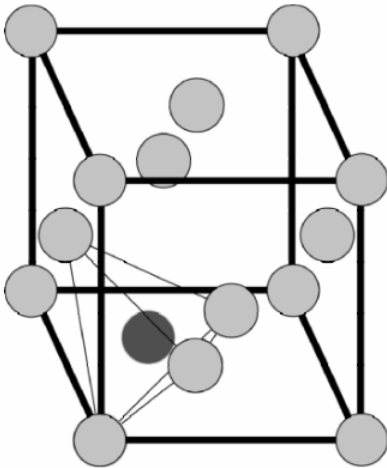
Debdeep Jena (djena@cornell.edu), Cornell University

191/xx

Interstitial sites in FCC lattices, Electronic nature

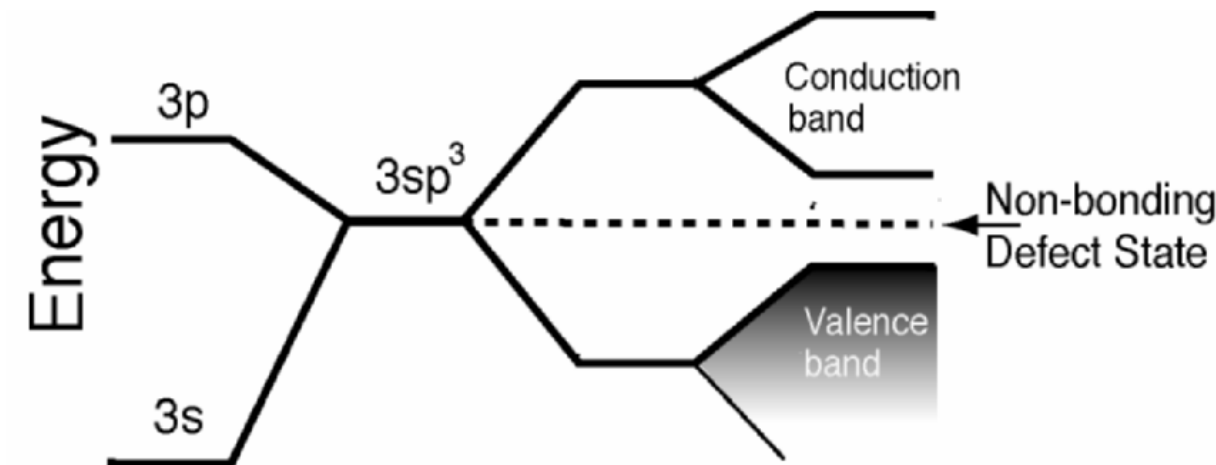
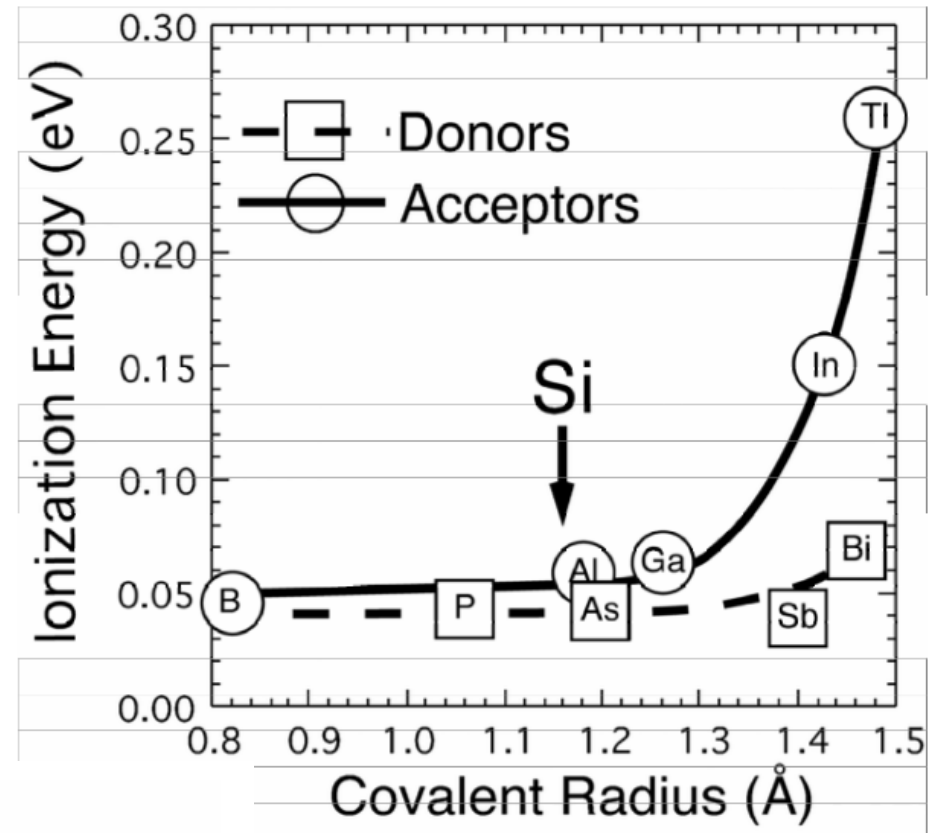
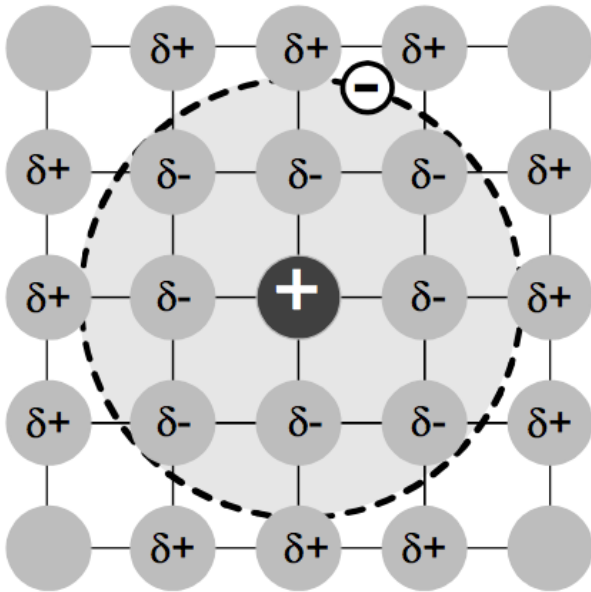
Table 7.1: Ideal Properties for Traps and Recombination Centers

Defect Property	Traps	Recombination Centers
Charge state before capture of a minority carrier:	Doubly charged, opposite to minority carriers	Singly charged, opposite to minority carriers
Cross section for minority carriers before capture:	10^{-9} to 10^{-12} cm ² (strongly attractive)	10^{-12} to 10^{-15} cm ² (moderately attractive)
Cross section for majority carriers after capture:	10^{-18} - 10^{-20} cm ² (moderately repulsive)	10^{-15} to 10^{-17} cm ² (neutral)
Depth (energy from minority carrier band edge):	Relatively small	Relatively large



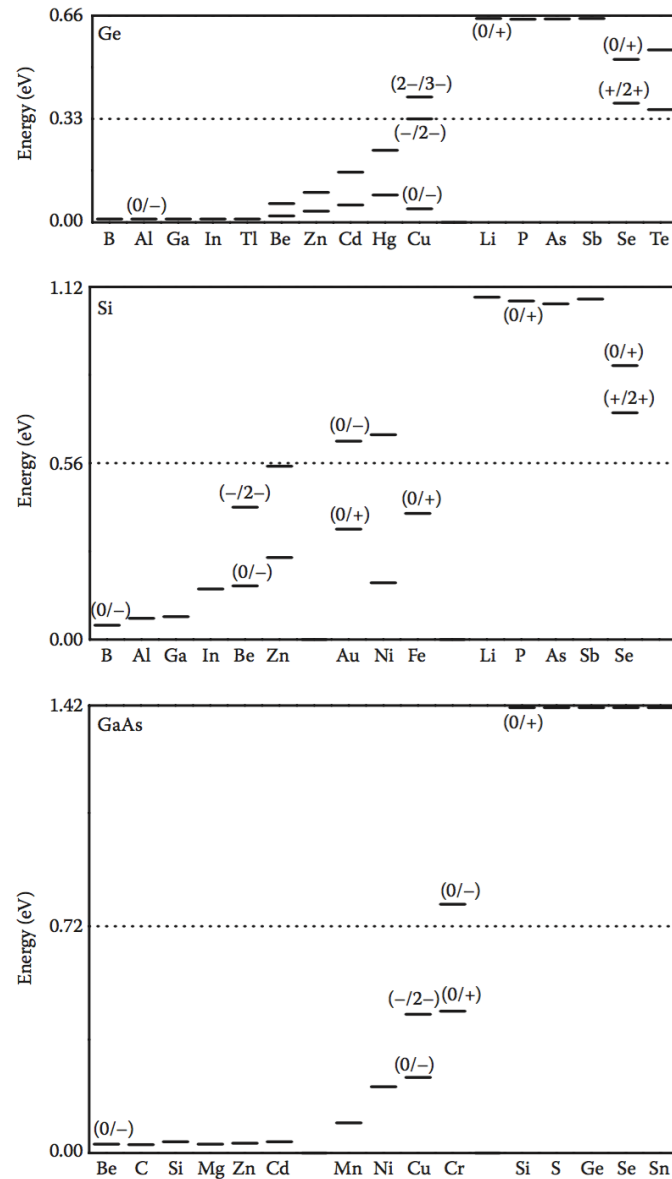
(Rockett, Chp 7, Haller/McLuskey)

Electronic Energy levels of Substitutional Dopants



(Rockett, Chp 7, Haller/McLuskey)

Electronic Energy levels of substitutional impurities



(Rockett, Chp 7, Haller/McLuskey)

Electronic Energy levels of Hydrogen Interstitial

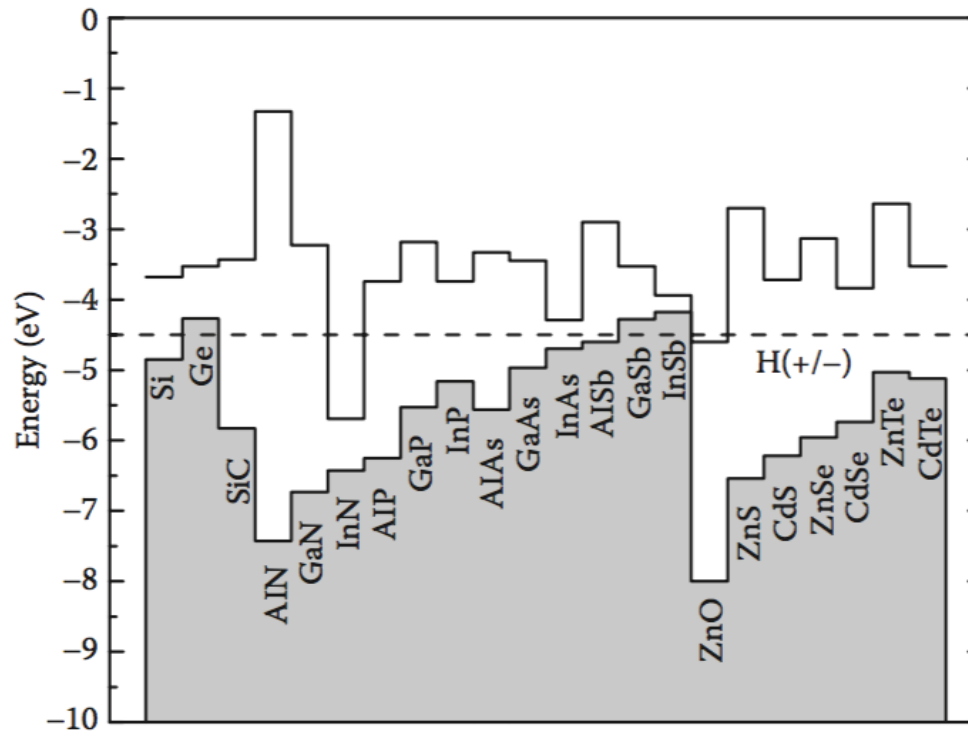
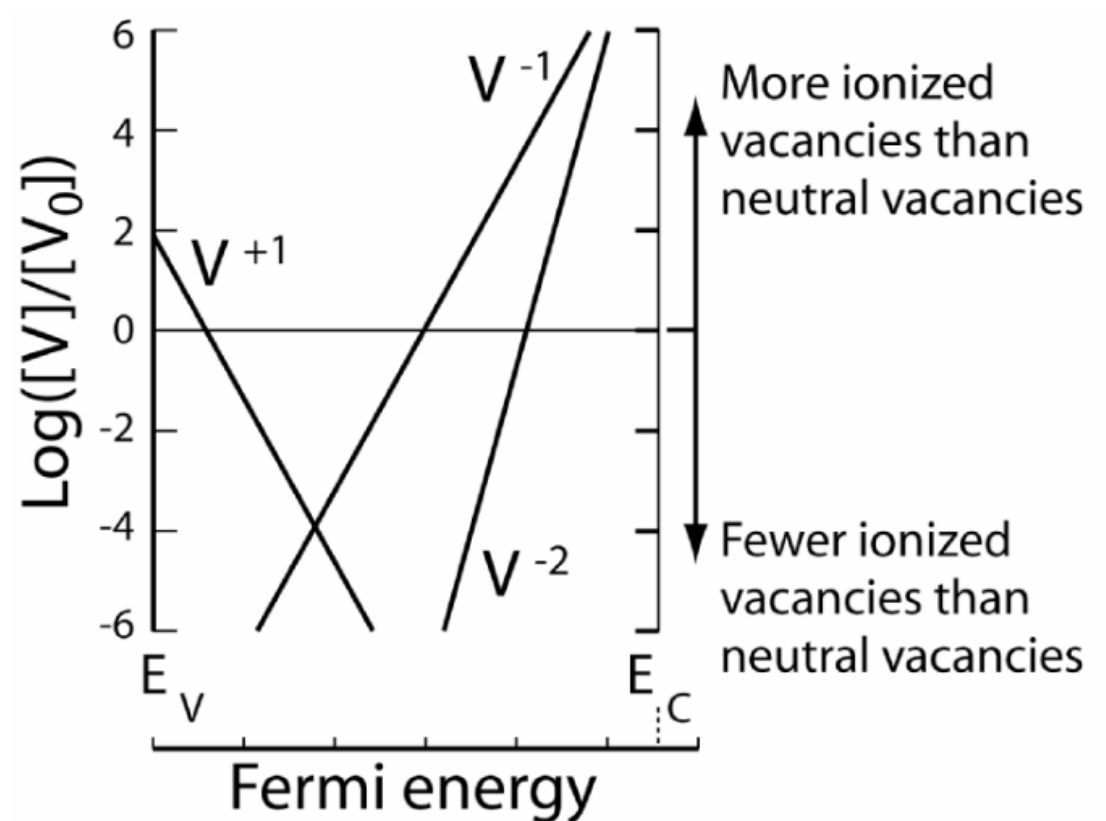


Figure 4.11 Valence band maxima and conduction band minima (solid lines), and the H(+/-) level (dashed line), as calculated by density functional theory (DFT) for various semiconductors. Here, zero energy corresponds to the vacuum level. (After Van de Walle, C.G., and Neugebauer, J., Universal Alignment of Hydrogen Levels in Semiconductors, Insulators, and Solutions, *Nature*, 423, 626–628, 2003.)

(Rockett, Chp 7, Haller/McLuskey)

Formation Energy & Statistics of Vacancies & Interstitials



To illustrate the effect of Equations 7.6 and 7.7 on the vacancy concentration, let us consider the case of undoped and doped Si. Here vacancies can occur in three charge states, +1, -1, and -2, with energies 1.0 eV below the conduction band, and 0.6 and 1.05 eV above the valence band at 300 K, respectively. The overall energy gap of Si is 1.12 eV. The energy of formation of a neutral vacancy is 2.4 eV, the vibrational entropy change per added vacancy is $1.1 k_B$, and the site density in the Si lattice is $5 \times 10^{22} \text{ cm}^{-3}$. [3]

$$\Delta E_d(q, E_f) = \Delta E_0(q) - q\Delta E_f$$

(Rockett, Chp 7, Haller/McLuskey)

Formation Energy & Statistics of Vacancies & Interstitials

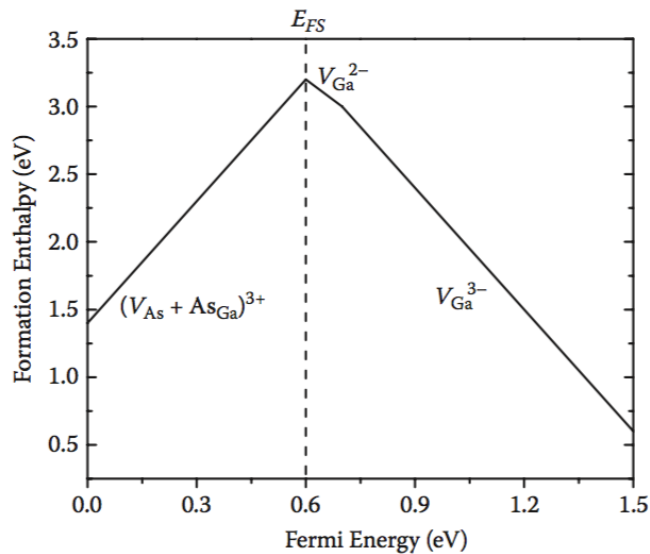


Figure 7.1 Formation enthalpies for native defects in GaAs. The Fermi stabilization energy E_{FS} is ~ 0.6 eV above the valence-band maximum. (After Walukiewicz, W., Amphoteric Native Defects in Semiconductors, *Appl. Phys. Lett.*, 54, 2094–2096, 1989.)

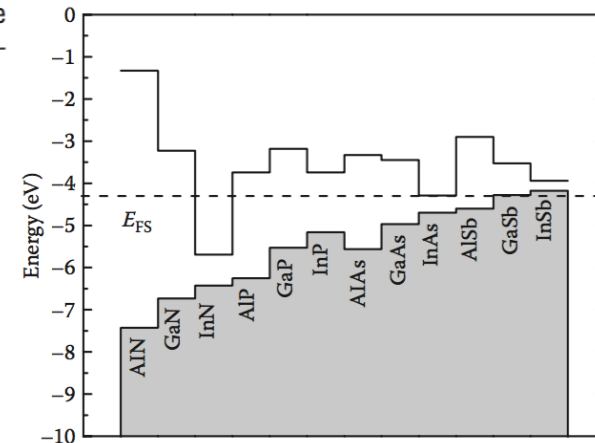


Figure 7.2 Approximate Fermi stabilization energy level E_{FS} , for various III-V semiconductors. (After Walukiewicz, W., Intrinsic Limitations to the Doping of Wide-Gap Semiconductors, *Physica B*, 302–303: 123–134, 2001. For consistency, the band alignments of Figure 4.11 were used.)

(Rockett, Chp 7, Haller/McLuskey)

Formation Energy & Statistics of Vacancies & Interstitials

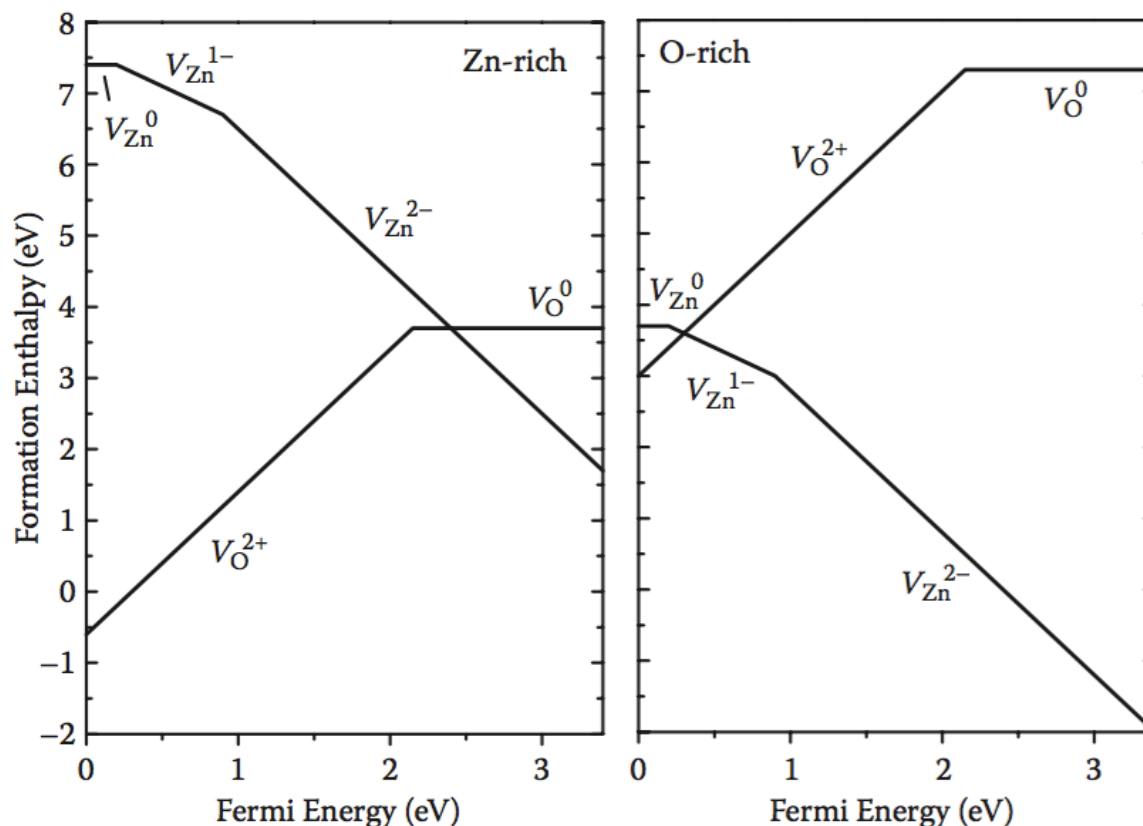


Figure 7.4 Formation enthalpies for oxygen and zinc vacancies in ZnO, for zinc-rich and oxygen-rich conditions. The Fermi energy is relative to the valence-band maximum. (After Janotti, A., and Van de Walle, C.G., Native Point Defects in ZnO, *Phys. Rev. B*, 76, 165202, 1–22, 2007.)

(Rockett, Chp 7, Haller/McLuskey)

Strain Energies: Microscopic

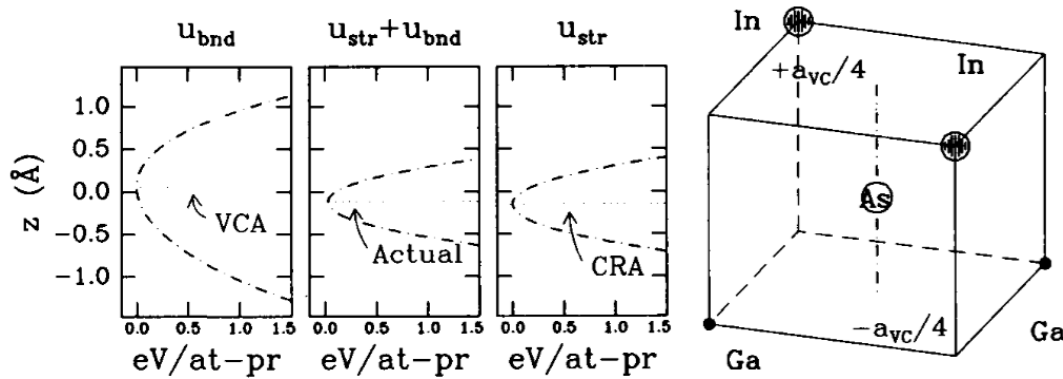


Figure 4.1: Valence force field potential energies versus As position within a 5-atom $\text{In}_{0.5}\text{Ga}_{0.5}\text{As}$ tetrahedron. Left and right panels show contributions due to bond bending and bond stretching forces; center panel shows the sum of the two contributions. The geometric center of the tetrahedron is at $z = 0$; the actual As position is shifted downward toward the Ga atoms. The predictions of the virtual crystal (VCA) and covalent radius (CRA) approximations discussed in the text are also shown.

Material	α (N/m)	β (N/m)	β/α	C_{11} (10^{10} N/m ²)	C_{12} (10^{10} N/m ²)	C_{44} (10^{10} N/m ²)
C	129.33	84.76	0.655	107.6	12.50	57.68
Si	48.50	13.81	0.285	16.57	6.39	7.96
Ge	38.67	11.35	0.294	12.89	4.83	6.71
AlSb	35.35	6.77	0.192	8.94	4.43	4.16
GaP	47.32	10.44	0.221	14.12	6.25	7.05
GaAs	41.19	8.95	0.217	11.81	5.32	5.92
GaSb	33.16	7.22	0.218	8.84	4.03	4.32
InP	43.04	6.24	0.145	10.22	5.76	4.60
InAs	35.18	5.50	0.156	8.33	4.53	3.96
InSb	29.61	4.77	0.161	6.67	3.65	3.02
ZnS	44.92	4.78	0.107	10.40	6.50	4.62
ZnSe	35.24	4.23	0.120	8.10	4.88	4.41
ZnTe	31.35	4.45	0.142	7.13	4.07	3.12
CdTe	29.02	2.43	0.084	5.35	3.68	1.99
CuCl	12.60	1.00	0.079	2.72	1.87	1.57

Table 4.1: Microscopic bond stretching (α) and bond bending (β) force constants deduced from macroscopic elastic constants (C_{11} , C_{12} , and C_{44}) of various cubic semiconducting materials.^a

$$u_{\text{str},i} = \frac{3}{8} \alpha_i \frac{(d_i^2 - d_{i,o}^2)^2}{d_{i,o}^2}$$

$$u_{\text{bnd},ij} = \frac{3}{8} \frac{\beta_i + \beta_j}{2} \frac{(\mathbf{d}_i \cdot \mathbf{d}_j - \mathbf{d}_{i,o} \cdot \mathbf{d}_{j,o})^2}{d_{i,o} d_{j,o}}$$

$$u_{\text{str}} = \sum_{i=1}^4 u_{\text{str},i}, \quad u_{\text{bnd}} = 2 \sum_{i=1}^4 \sum_{j<i} u_{\text{bnd},ij}$$

$$u_{(\triangle)} = u_{\text{str}} + u_{\text{bnd}} \approx \frac{3}{4} \left[\alpha_{\text{GaAs}} \frac{(d_{\text{GaAs}}^2 - d_{\text{GaAs},o}^2)^2}{d_{\text{GaAs},o}^2} + \alpha_{\text{InAs}} \frac{(d_{\text{InAs}}^2 - d_{\text{InAs},o}^2)^2}{d_{\text{InAs},o}^2} \right] + \frac{3}{4} \left[\beta_{\text{GaAs}} \frac{(d_{\text{GaAs}}^2 \cos^2 \theta_{\text{GaAsGa}} - d_{\text{GaAs},o}^2 \cos^2 \theta_T)^2}{d_{\text{GaAs},o}^2} + \beta_{\text{InAs}} \frac{(d_{\text{InAs}}^2 \cos^2 \theta_{\text{InAsIn}} - d_{\text{InAs},o}^2 \cos^2 \theta_T)^2}{d_{\text{InAs},o}^2} \right]. \quad ($$

(Rockett, Chp 7, Tsao, Marder)

Strain Energies: Microscopic

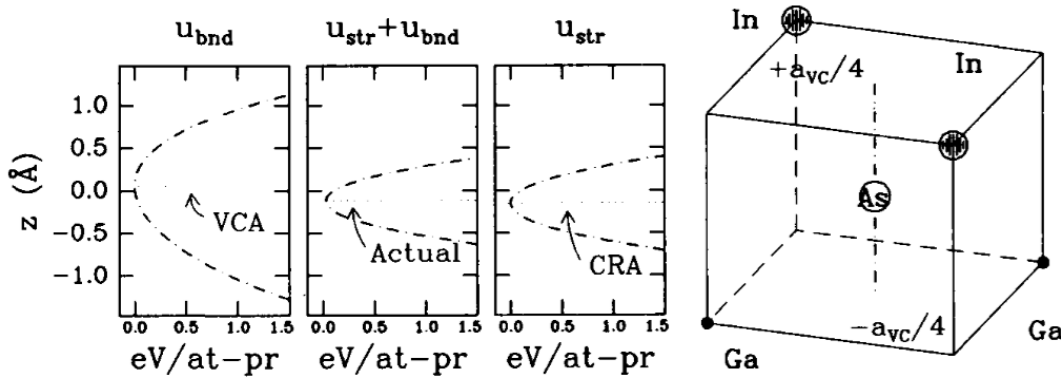


Figure 4.1: Valence force field potential energies versus As position within a 5-atom $\text{In}_{0.5}\text{Ga}_{0.5}\text{As}$ tetrahedron. Left and right panels show contributions due to bond bending and bond stretching forces; center panel shows the sum of the two contributions. The geometric center of the tetrahedron is at $z = 0$; the actual As position is shifted downward toward the Ga atoms. The predictions of the virtual crystal (VCA) and covalent radius (CRA) approximations discussed in the text are also shown.

Material	α (N/m)	β (N/m)	β/α	C_{11} (10^{10} N/m ²)	C_{12} (10^{10} N/m ²)	C_{44} (10^{10} N/m ²)
C	129.33	84.76	0.655	107.6	12.50	57.68
Si	48.50	13.81	0.285	16.57	6.39	7.96
Ge	38.67	11.35	0.294	12.89	4.83	6.71
AlSb	35.35	6.77	0.192	8.94	4.43	4.16
GaP	47.32	10.44	0.221	14.12	6.25	7.05
GaAs	41.19	8.95	0.217	11.81	5.32	5.92
GaSb	33.16	7.22	0.218	8.84	4.03	4.32
InP	43.04	6.24	0.145	10.22	5.76	4.60
InAs	35.18	5.50	0.156	8.33	4.53	3.96
InSb	29.61	4.77	0.161	6.67	3.65	3.02
ZnS	44.92	4.78	0.107	10.40	6.50	4.62
ZnSe	35.24	4.23	0.120	8.10	4.88	4.41
ZnTe	31.35	4.45	0.142	7.13	4.07	3.12
CdTe	29.02	2.43	0.084	5.35	3.68	1.99
CuCl	12.60	1.00	0.079	2.72	1.87	1.57

Table 4.1: Microscopic bond stretching (α) and bond bending (β) force constants deduced from macroscopic elastic constants (C_{11} , C_{12} , and C_{44}) of various cubic semiconducting materials.^a

$$d_{\text{GaAs}}^2 = \left(\frac{a_{\text{VC}}}{2\sqrt{2}}\right)^2 + \left(\frac{a_{\text{VC}}}{4} + z\right)^2$$

$$d_{\text{InAs}}^2 = \left(\frac{a_{\text{VC}}}{2\sqrt{2}}\right)^2 + \left(\frac{a_{\text{VC}}}{4} - z\right)^2$$

$$\cos(\theta_{\text{GaAsGa}}/2) \approx \frac{(a_{\text{VC}}/4) + z}{(\sqrt{3}a_{\text{VC}}/4) + z/\sqrt{3}}$$

$$\cos(\theta_{\text{InAsIn}}/2) \approx \frac{(a_{\text{VC}}/4) - z}{(\sqrt{3}a_{\text{VC}}/4) - z/\sqrt{3}}$$

$$u_{(\triangle)} \approx \frac{3}{2}\alpha_{\text{GaAs}} \left[\frac{\sqrt{3}}{4}a_{\text{VC}} - d_{\text{GaAs,o}} + \frac{z}{\sqrt{3}} \right]^2 + \frac{3}{2}\alpha_{\text{InAs}} \left[\frac{\sqrt{3}}{4}a_{\text{VC}} - d_{\text{InAs,o}} - \frac{z}{\sqrt{3}} \right]^2 + \frac{3}{8}\beta_{\text{GaAs}} \left[\frac{-2}{3} \left(\frac{\sqrt{3}}{4}a_{\text{VC}} - d_{\text{GaAs,o}} \right) + \frac{2}{\sqrt{3}}z \right]^2 + \frac{3}{8}\beta_{\text{InAs}} \left[\frac{-2}{3} \left(\frac{\sqrt{3}}{4}a_{\text{VC}} - d_{\text{InAs,o}} \right) - \frac{2}{\sqrt{3}}z \right]^2. \quad (4.9)$$

Then, solving for $\partial u_{(\triangle)}/\partial z = 0$, the equilibrium position can be deduced to be

$$z_{\text{equ}} = \left(\frac{-\sqrt{3}}{2}\right) \frac{\alpha_{\text{GaAs}} + \alpha_{\text{InAs}} - \beta_{\text{GaAs}}/3 + \beta_{\text{InAs}}/3}{\alpha_{\text{GaAs}} + \alpha_{\text{InAs}} - \beta_{\text{GaAs}} + \beta_{\text{InAs}}} (d_{\text{InAs,o}} - d_{\text{GaAs,o}}). \quad (4.10)$$

(Rockett, Chp 7, Tsao, Marder)

Strain Energies: Microscopic

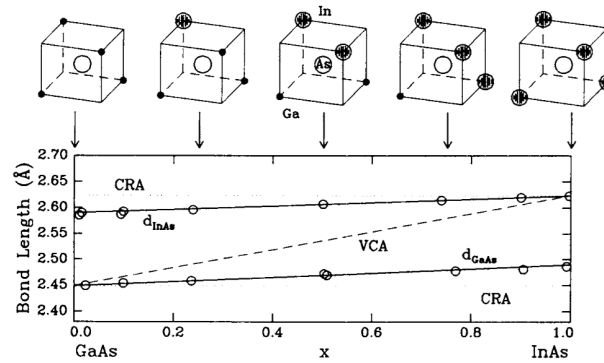


Figure 4.2: Measured and calculated Ga-As and In-As bond lengths in $\text{In}_{1-x}\text{Ga}_x\text{As}$ alloys. Experimental data are from (open circles) X-ray-absorption fine structure (EXAFS)^a measurements; calculations are based on valence-force-field potentials using either bond bending forces in the virtual crystal approximation (dashed line), bond stretching forces in the covalent radius approximation (dotted lines), or both (solid lines).^b

$$u_{(\triangle)} \approx \frac{\bar{\alpha}\bar{\beta}}{2(\bar{\alpha} + \bar{\beta})} (\Delta a_o)^2,$$

$$\Delta a_o \equiv a_{\text{InAs},o} - a_{\text{GaAs},o} = \frac{4}{\sqrt{3}} (d_{\text{InAs},o} - d_{\text{GaAs},o})$$

$$\Omega_{\text{VFF}} \approx \frac{2\bar{\alpha}\bar{\beta}}{\bar{\alpha} + \bar{\beta}} (\Delta a_o)^2$$

Material	Crystal Structure	a_o or a/c (\AA or $\text{\AA}/\text{\AA}$)	$\alpha_T = \partial \ln a_o / \partial T$ (10^{-6}K^{-1})
C	Diamond	3.56683	$0.87 + 0.0092(T - 273)$
Si	Diamond	5.43095	$3.08 + 0.0019(T - 273)$
Ge	Diamond	5.64613	$6.05 + 0.0036(T - 273)$
α -Sn	Diamond	6.48920	
SiC	Wurtzite	3.086/15.117	
BN	Zincblende	3.6150	
BP	Zincblende	4.5380	
AlP	Zincblende	5.4510	
AlAs	Zincblende	5.6605	$3.40 + 0.0064(T - 273)$
AlSb	Zincblende	6.1355	
GaN	Zincblende	3.189/5.185	
GaP	Zincblende	5.4512	5.81
GaAs	Zincblende	5.6533	$5.35 + 0.0080(T - 273)$
GaSb	Zincblende	6.0959	6.7
InP	Zincblende	5.8686	
InAs	Zincblende	6.0584	$4.33 + 0.0038(T - 273)$
InSb	Zincblende	6.4794	
ZnO	Rock Salt	4.580	
ZnS	Zincblende	5.420	$6.70 + 0.0128(T - 313)$
ZnS	Wurtzite	3.82/6.26	
CdS	Zincblende	5.8320	
CdS	Wurtzite	4.16/6.756	
CdTe	Zincblende	6.482	
CdSe	Zincblende	6.050	
PbS (Galena)	Rock Salt	5.9362	$18.81 + 0.0074(T - 273)$
PbTe (Altaite)	Rock Salt	6.4620	19.80

Table 4.2: Crystal structures, room-temperature lattice parameters and thermal expansion coefficients of various semiconductors.^a

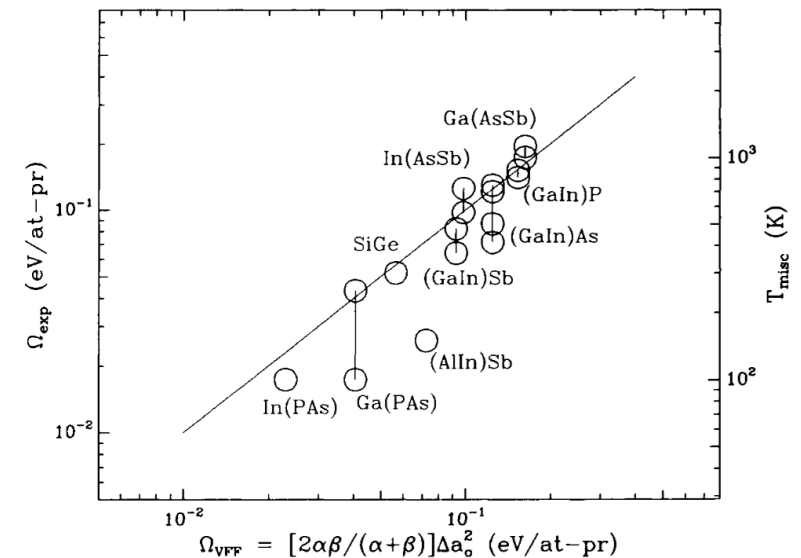


Figure 4.3: Regular solution parameters for various pseudobinary alloys. Values plotted along the bottom axis were calculated using Equation 4.13; values plotted along the left axis are experimental measurements^a; values plotted along the right axis are the critical temperatures, deduced from Equation 3.38, above which the constituent components are fully miscible.

(Rockett, Chp 7, Tsao, Marder)

Extended Defects: Dislocations

$$a_{\text{sub}} = (1 - x_{\text{sub}})a_{\text{GaAs,o}} + x_{\text{sub}}a_{\text{InAs,o}}$$

$$a_{\text{epi,||}} = a_{\text{sub}} = (1 - x_{\text{sub}})a_{\text{GaAs,o}} + x_{\text{sub}}a_{\text{InAs,o}}$$

$$\epsilon_{\text{epi,||}} \equiv 2 \frac{a_{\text{epi,||}} - a_{\text{epi,o}}}{a_{\text{epi,||}} + a_{\text{epi,o}}}$$

$$a_{\text{epi,o}} = (1 - x_{\text{epi}})a_{\text{GaAs,o}} + x_{\text{epi}}a_{\text{InAs,o}}$$

$$\begin{pmatrix} \sigma_x \\ \sigma_y \\ \sigma_z \\ \tau_{xy} \\ \tau_{yz} \\ \tau_{zx} \end{pmatrix} = \begin{pmatrix} C_{11} & C_{12} & C_{12} & 0 & 0 & 0 \\ C_{12} & C_{11} & C_{12} & 0 & 0 & 0 \\ C_{12} & C_{12} & C_{11} & 0 & 0 & 0 \\ 0 & 0 & 0 & C_{44} & 0 & 0 \\ 0 & 0 & 0 & 0 & C_{44} & 0 \\ 0 & 0 & 0 & 0 & 0 & C_{44} \end{pmatrix} \begin{pmatrix} \epsilon_x \\ \epsilon_y \\ \epsilon_z \\ \gamma_{xy} \\ \gamma_{yz} \\ \gamma_{zx} \end{pmatrix}$$

$$\sigma_{\text{epi,\perp}} = 2C_{12}\epsilon_{\text{epi,||}} + C_{11}\epsilon_{\text{epi,\perp}} = 0$$

$$\epsilon_{\text{epi,\perp}} = \frac{-2C_{12}}{C_{11}}\epsilon_{\text{epi,||}}$$

$$a_{\perp}(x_{\text{epi}}, x_{\text{sub}}) = a_{\text{epi,o}} \frac{1 + \epsilon_{\text{epi,\perp}}/2}{1 - \epsilon_{\text{epi,\perp}}/2}$$

If the epitaxial film and its substrate are oriented along one of the $\langle 100 \rangle$ cubic symmetry directions, then this equation reduces to

$$\begin{pmatrix} \sigma_{\text{epi,||}} \\ \sigma_{\text{epi,\perp}} \end{pmatrix} = \begin{pmatrix} C_{11} + C_{12} & C_{12} \\ 2C_{12} & C_{11} \end{pmatrix} \begin{pmatrix} \epsilon_{\text{epi,||}} \\ \epsilon_{\text{epi,\perp}} \end{pmatrix}. \quad (4.20)$$

(Rockett, Chp 7, Tsao, Marder)

Extended Defects: Dislocations

$$\epsilon_{i,\parallel} = 2 \frac{a_{\text{epi},\parallel} - a_{i,o}}{a_{\text{epi},\parallel} + a_{i,o}}$$

$$\epsilon_{i,\perp} = 2 \frac{a_{\text{epi},\perp} - a_{i,o}}{a_{\text{epi},\perp} + a_{i,o}}$$

$$\sigma_{\text{epi},\perp} = 2C_{12}\epsilon_{\text{epi},\parallel} + C_{11}\epsilon_{\text{epi},\perp} = 0$$

$$\epsilon_{\text{epi},\perp} = \frac{-2C_{12}}{C_{11}}\epsilon_{\text{epi},\parallel}$$

$$a_{\perp}(x_{\text{epi}}, x_{\text{sub}}) = a_{\text{epi},o} \frac{1 + \epsilon_{\text{epi},\perp}/2}{1 - \epsilon_{\text{epi},\perp}/2}$$

$$u_{i,\text{ext}} = \frac{1}{2} [2\sigma_{i,\parallel}\epsilon_{i,\parallel} + \sigma_{i,\perp}\epsilon_{i,\perp}]$$

$$= (C_{i,11} + C_{i,12})\epsilon_{i,\parallel}^2 + 2C_{i,12}\epsilon_{i,\perp}\epsilon_{i,\parallel} + \frac{1}{2}C_{i,11}\epsilon_{i,\perp}^2$$

$$\begin{pmatrix} \epsilon_x \\ \epsilon_y \\ \epsilon_z \end{pmatrix} = \frac{1}{2\mu(1+\nu)} \begin{pmatrix} 1 & -\nu & -\nu \\ -\nu & 1 & -\nu \\ -\nu & -\nu & 1 \end{pmatrix} \begin{pmatrix} \sigma_x \\ \sigma_y \\ \sigma_z \end{pmatrix} \quad \begin{pmatrix} \epsilon_{\parallel} \\ \epsilon_{\perp} \end{pmatrix} = \frac{1}{2\mu(1+\nu)} \begin{pmatrix} 1-\nu & -\nu \\ -2\nu & 1 \end{pmatrix} \begin{pmatrix} \sigma_{\parallel} \\ \sigma_{\perp} \end{pmatrix}$$

$$C_{11} = 2\mu \left(\frac{1-\nu}{1-2\nu} \right)$$

$$C_{12} = 2\mu \left(\frac{\nu}{1-2\nu} \right)$$

$$\sigma_{\parallel} = 2\mu \left(\frac{1+\nu}{1-\nu} \right) \epsilon_{\parallel}$$

(Rockett, Chp 7, Tsao, Marder)

Extended Defects: Dislocations

$$\epsilon_{\text{epi},\perp} = \frac{-2C_{12}}{C_{11}} \epsilon_{\text{epi},\parallel}$$

$$a_{\perp}(x_{\text{epi}}, x_{\text{sub}}) = a_{\text{epi},o} \frac{1 + \epsilon_{\text{epi},\perp}/2}{1 - \epsilon_{\text{epi},\perp}/2}$$

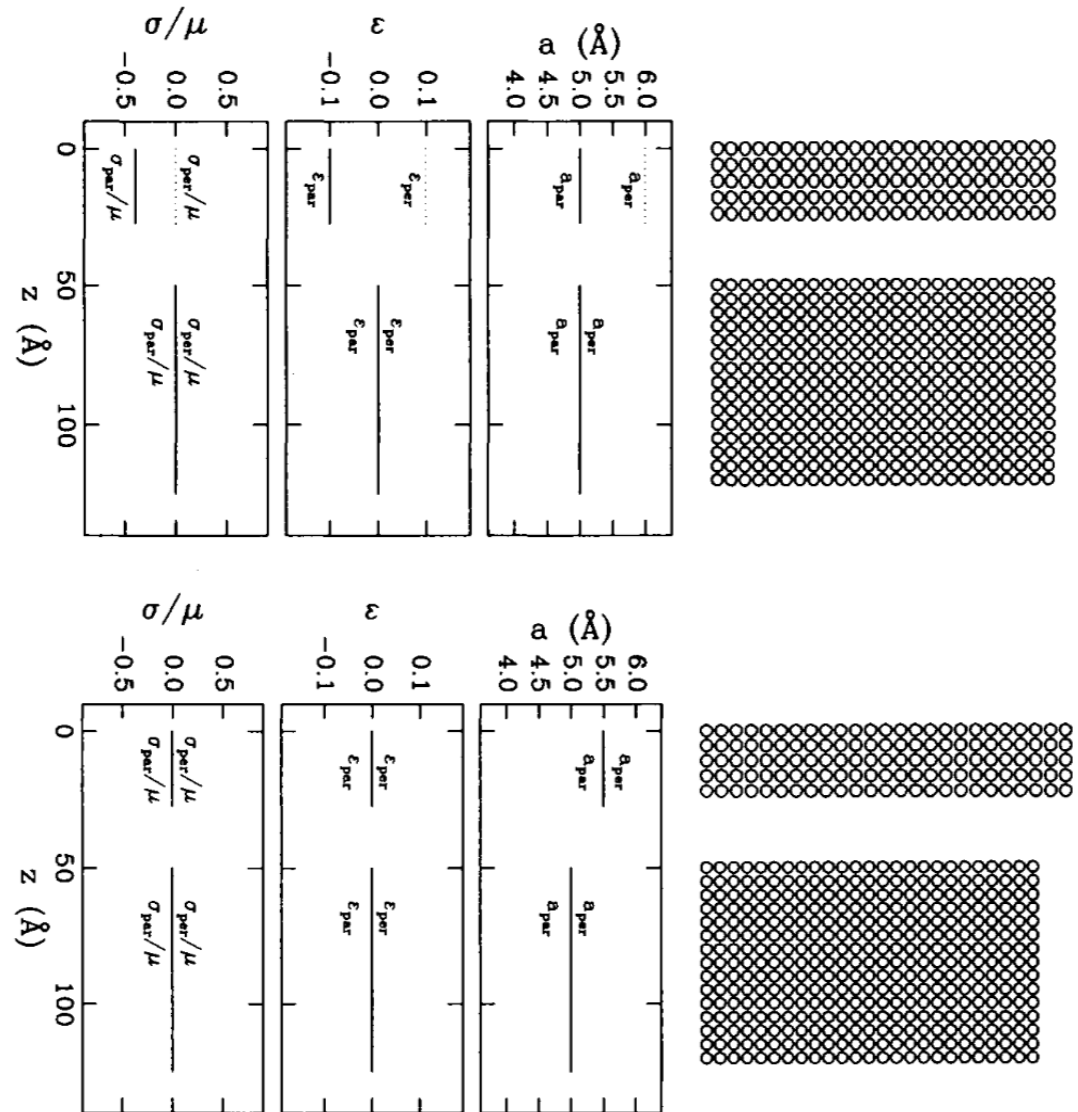
$$\begin{pmatrix} \epsilon_{\parallel} \\ \epsilon_{\perp} \end{pmatrix} = \frac{1}{2\mu(1+\nu)} \begin{pmatrix} 1-\nu & -\nu \\ -2\nu & 1 \end{pmatrix} \begin{pmatrix} \sigma_{\parallel} \\ \sigma_{\perp} \end{pmatrix}$$

$$\sigma_{\parallel} = 2\mu \left(\frac{1+\nu}{1-\nu} \right) \epsilon_{\parallel}$$

$$\epsilon_{\perp} = \frac{-2\nu}{1-\nu} \epsilon_{\parallel}$$

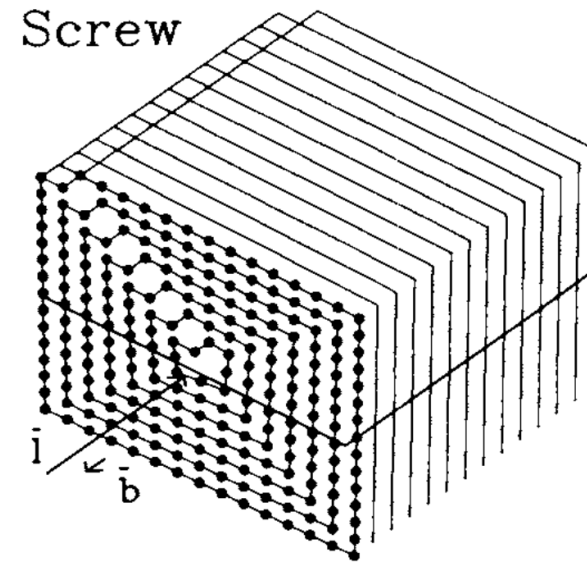
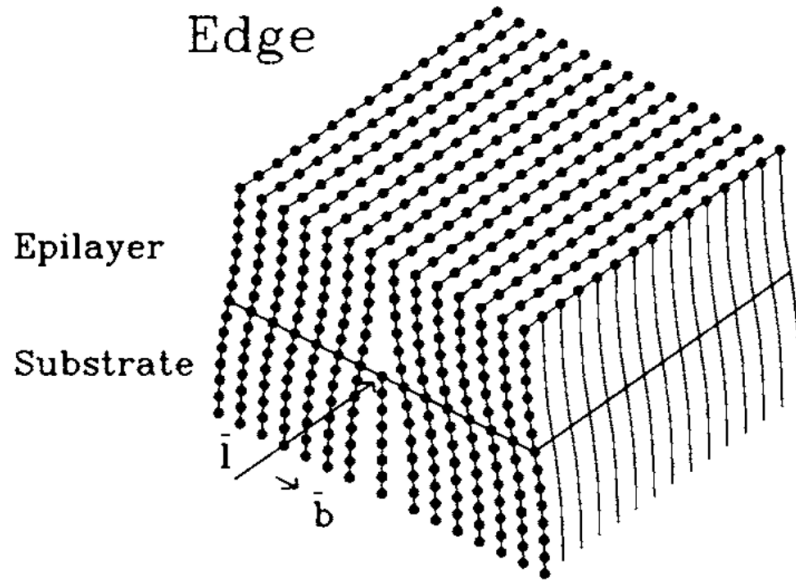
$$u_{\text{coh}} = \frac{1}{2} h (2\sigma_{\parallel} \epsilon_{\parallel} + \sigma_{\perp} \epsilon_{\perp}) = 2\mu \left(\frac{1+\nu}{1-\nu} \right) h \epsilon_{\parallel}^2$$

$$u_{\text{coh}} = 2\mu \left(\frac{1+\nu}{1-\nu} \right) \sum_i h_i \epsilon_{i,\parallel}^2$$



(Rockett, Chp 7, Tsao, Marder)

Extended Defects: Dislocations



$$b_{\text{edg},\parallel} \equiv b \cos \lambda$$

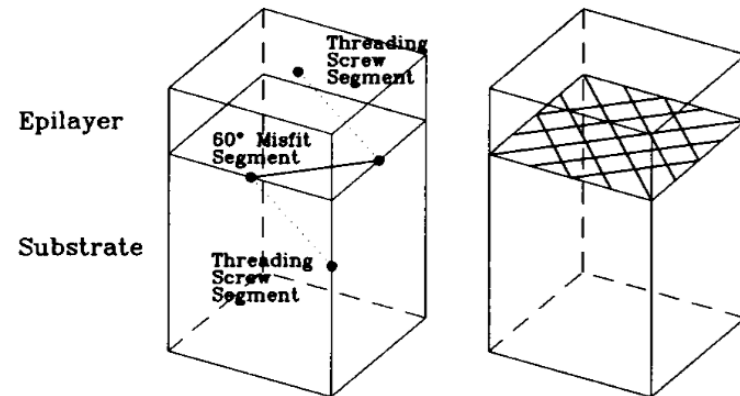
$$U_{\text{edg}} = \frac{\mu b_{\text{edg}}^2}{4\pi(1-\nu)} \ln(R/r_o)$$

$$U_{\text{scr}} = \frac{\mu b_{\text{scr}}^2}{4\pi} \ln(R/r_o),$$

$$U_{\text{dis}} = \frac{\mu b^2}{4\pi} \left(\frac{\sin^2 \beta}{1-\nu} + \cos^2 \beta \right) \ln(4R/b)$$

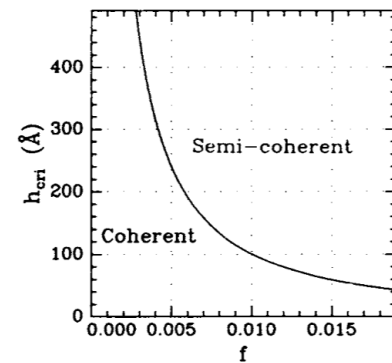
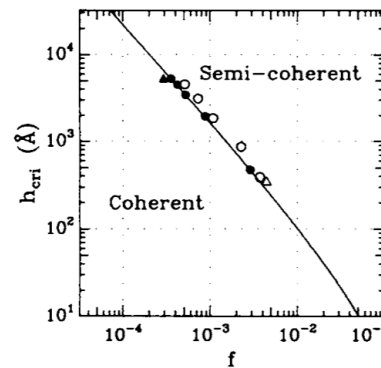
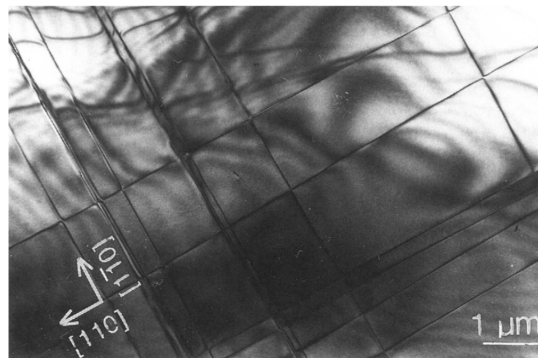
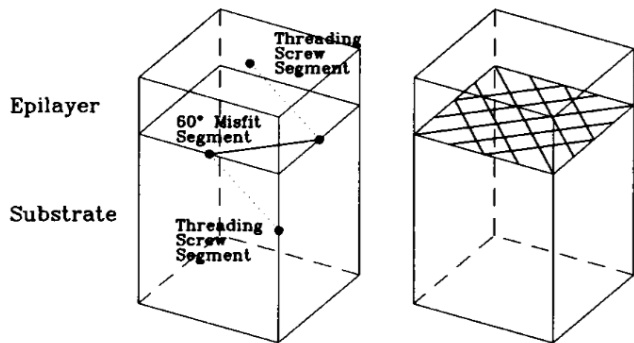
$$= \frac{\mu b^2}{4\pi} \left(\frac{1-\nu \cos^2 \beta}{1-\nu} \right) \ln(4R/b).$$

$$U_{\text{dis}} = \frac{\mu b^2}{4\pi} \left(\frac{1-\nu \cos^2 \beta}{1-\nu} \right) \ln(4h/b).$$



(Rockett, Chp 7, Tsao, Marder)

Extended Defects: Dislocations



$$U_{\text{dis}} = \frac{\mu b^2}{4\pi} \left(\frac{1 - \nu \cos^2 \beta}{1 - \nu} \right) \ln(4h/b).$$

$$f_{\text{dis}} = \rho_{\text{md}} b_{\text{edg},\parallel}$$

$$\epsilon_{\parallel} \approx f - f_{\text{dis}} = f - \rho_{\text{md}} b_{\text{edg},\parallel}$$

$$u_{\text{coh}} = 2\mu \left(\frac{1 + \nu}{1 - \nu} \right) h (f - \rho_{\text{md}} b_{\text{edg},\parallel})^2$$

$$u_{\text{dis}} \approx \rho_{\text{md}} \frac{\mu b^2}{4\pi} \left(\frac{1 - \nu \cos^2 \beta}{1 - \nu} \right) \ln \left(\frac{4h}{b} \right)$$

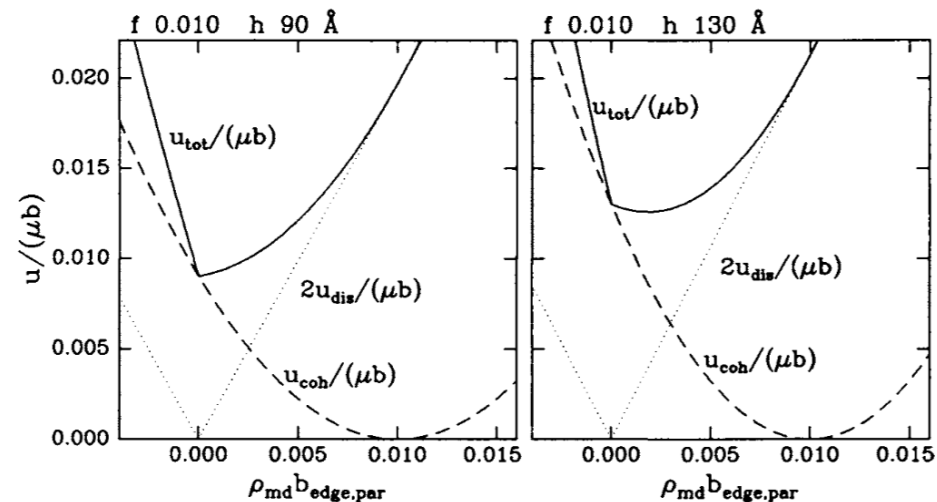
$$u_{\text{tot}} = u_{\text{coh}} + 2u_{\text{dis}}$$

$$= 2\mu \left(\frac{1 + \nu}{1 - \nu} \right) h (f - \rho_{\text{md}} b_{\text{edg},\parallel})^2$$

$$+ \rho_{\text{md}} \frac{\mu b^2}{2\pi} \left(\frac{1 - \nu \cos^2 \beta}{1 - \nu} \right) \ln \left(\frac{4h}{b} \right)$$

$$f_c = \frac{b}{8\pi h \cos \lambda} \left(\frac{1 - \nu \cos^2 \beta}{1 + \nu} \right) \ln(4h/b)$$

$$h_c = \frac{b}{8\pi f \cos \lambda} \left(\frac{1 - \nu \cos^2 \beta}{1 + \nu} \right) \ln(4h_c/b)$$



(Rockett, Chp 7, Tsao, Marder)

Extended Defects: Dislocations

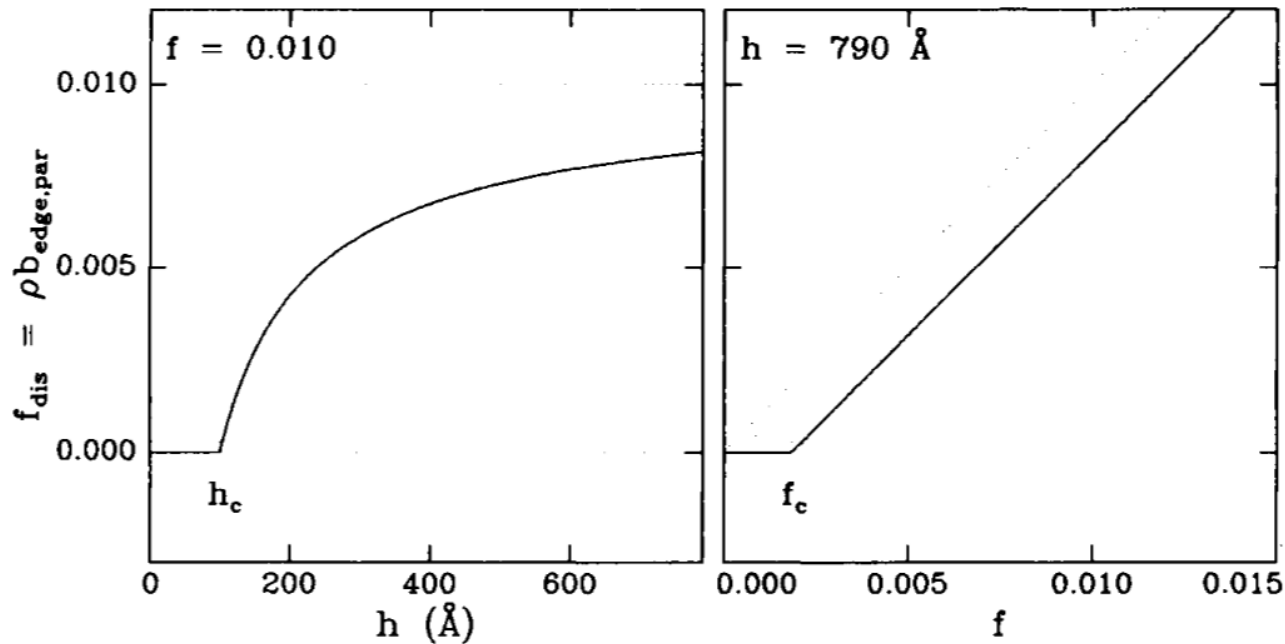


Figure 5.9: Equilibrium misfit strain (f_{dis}) taken up by dislocations as a function of thickness at constant misfit (left) or as a function of misfit at constant thickness (right). Below either the critical thickness (h_c) or critical misfit (f_c) the strain taken up by dislocations is zero; above the critical thickness or critical misfit it becomes an increasingly large fraction of the total misfit (f).

$$\rho_{\text{md,eq}} = \frac{f}{b \cos \lambda} - \frac{b}{8\pi h \cos^2 \lambda} \left(\frac{1 - \nu \cos^2 \beta}{1 + \nu} \right) \ln \left(\frac{4h}{b} \right) = \frac{f}{b \cos \lambda} \left[1 - \frac{h_c}{h} \right]$$

(Rockett, Chp 7, Tsao, Marder)

Dislocations in Buried Heterostructures & Motion

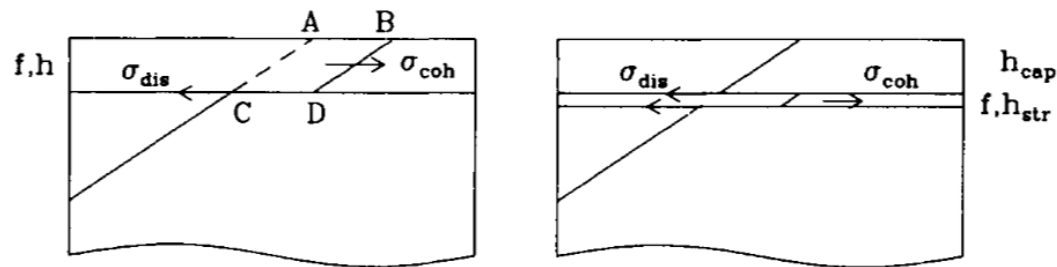


Figure 5.10: Strain relaxation by single (left) and double (right) kinking of a threading dislocation to form misfit dislocations.

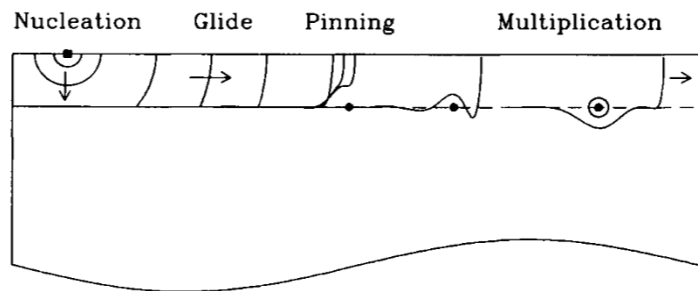


Figure 5.17: Schematic illustrations of possible microscopic deformation mechanisms operative during strain relaxation.

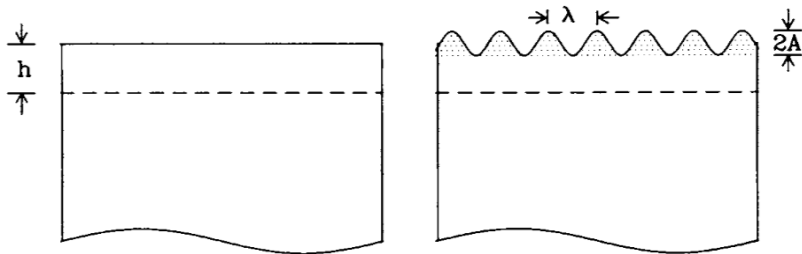


Figure 5.22: Uncorrugated (left) and corrugated (right) epitaxial strained layers.

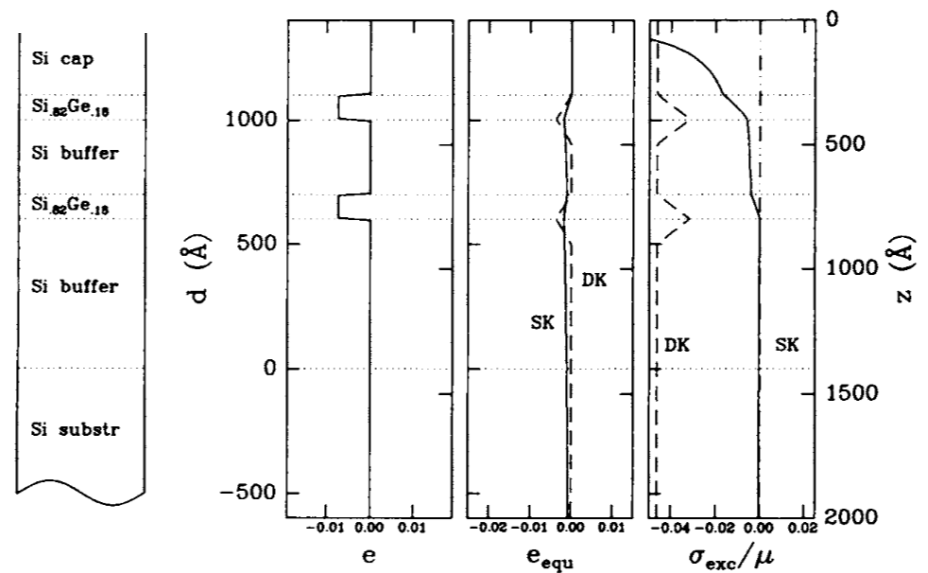


Figure 5.12: Strains, equivalent strains, and excess stresses in a double buried quantum-well heterostructure. Both the single- and double-kink excess stresses maximize at a depth of 800 Å, but only the single-kink excess stress exceeds zero, and even then just barely. Therefore, this structure is stable with respect to double-kink strain relaxation, but slightly unstable with respect to single-kink strain relaxation.

(Rockett, Chp 7, Tsao, Marder)

Extended Defects: Dislocations

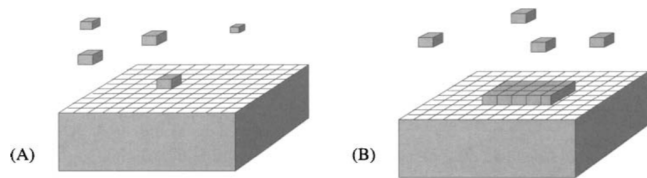
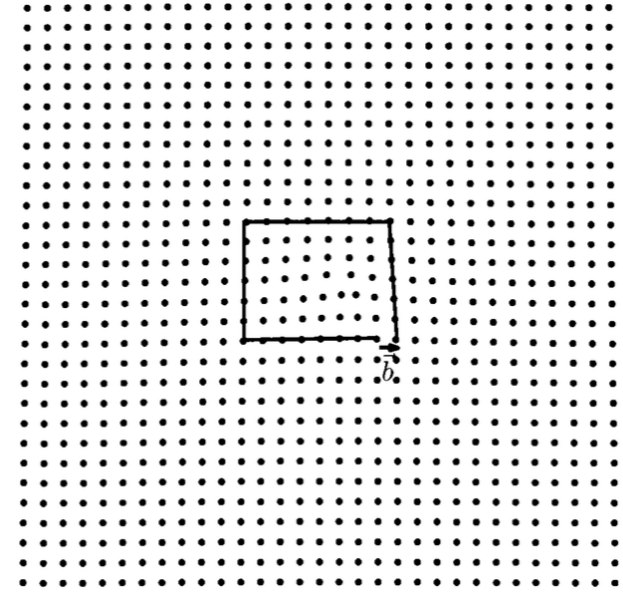
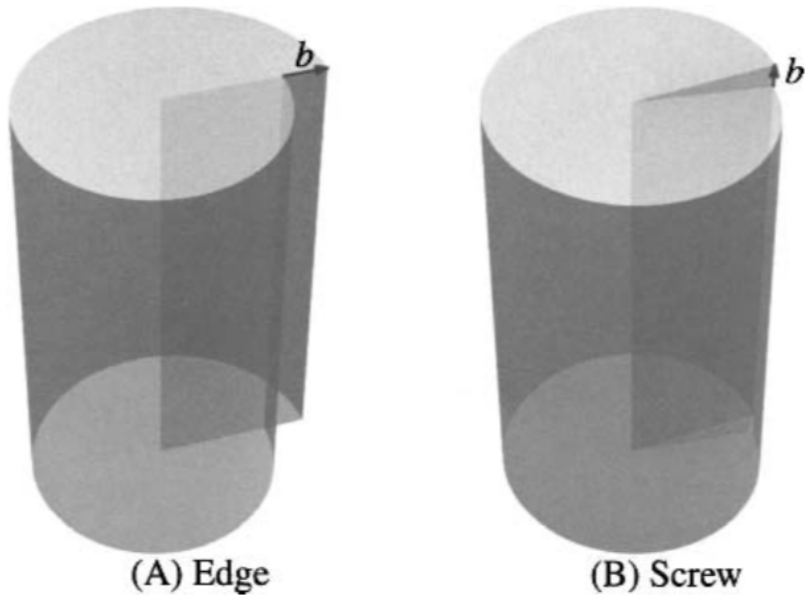


Figure 14.6. In order to add a new layer of atoms to a crystal, it is typically necessary to add a large clump of new atoms simultaneously. (A) A single atom attaching to the surface will be unstable and detach. (B) A large enough clump is stable.

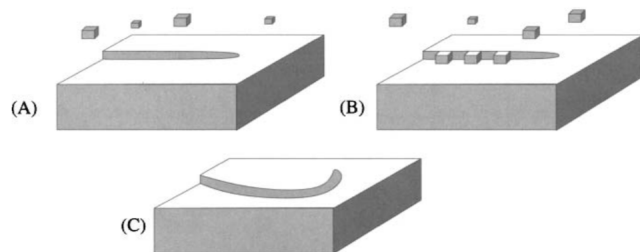


Figure 14.7. Mechanism due to Frank, showing how the presence of a screw dislocation should speed the process of crystal growth, by providing open regions to which atoms can easily attach.

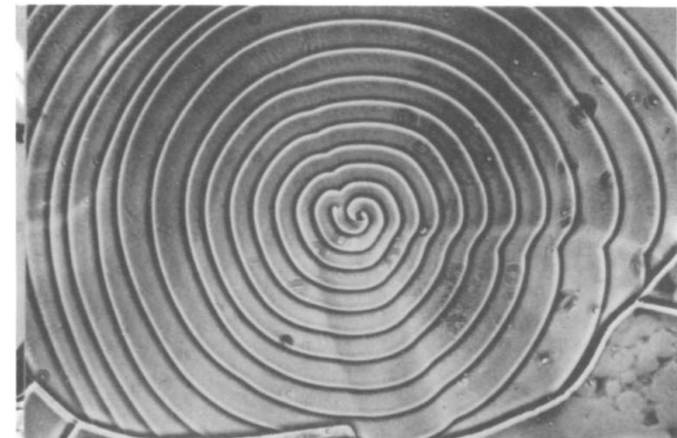


Figure 14.8. Experimental observation of growth spirals on the (0001) plane of silicon carbide. [Source: Amelinckx (1964), p. 5.]

(Rockett, Chp 7, Tsao, Marder)

Extended Defects: Dislocations

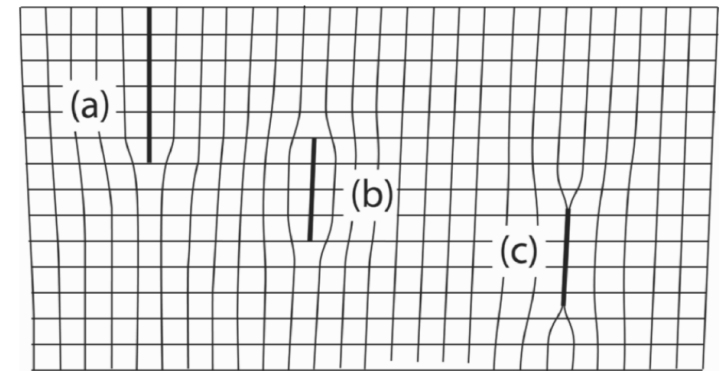
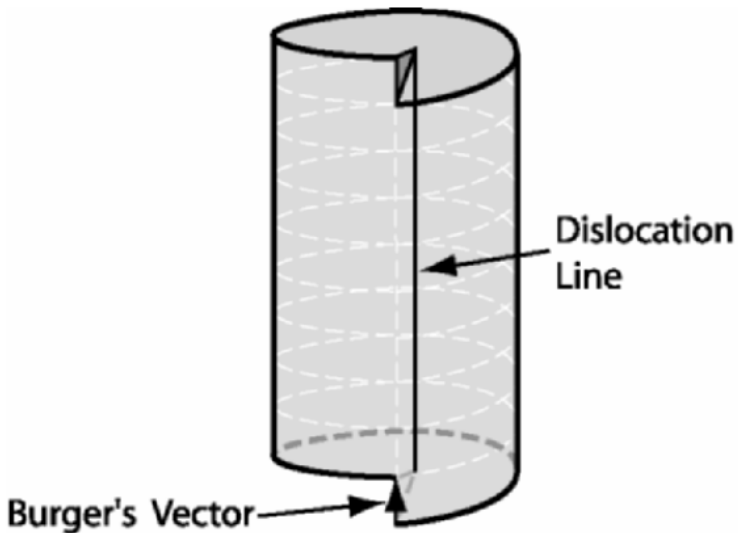
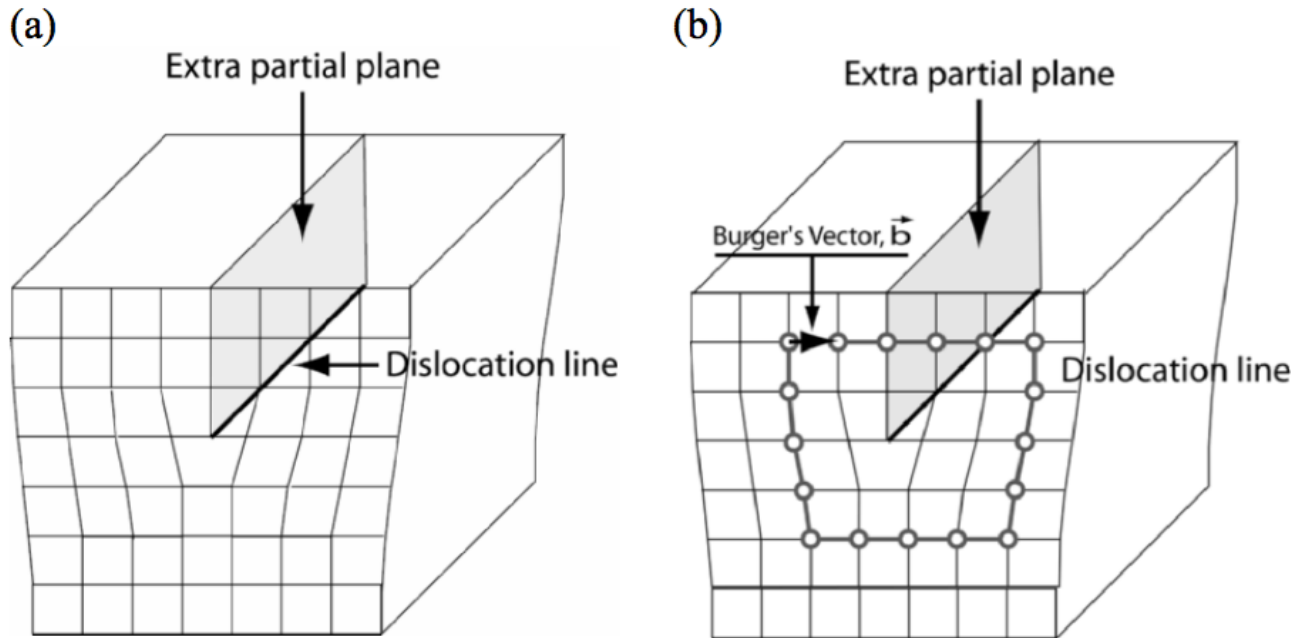


Figure 7.11: A schematic diagram of various edge dislocation configurations. (a) a classic edge dislocation with an extra half plane inserted into the material. This type of dislocation forms a loop which closes at the crystal surface. Thus, threading segments will occur. (b) and (c) are loops resulting from coalescence of interstitials and vacancies, respectively to form small planes. When these result in stacking faults, the faults are termed extrinsic and intrinsic for (b) and (c), respectively and have dislocations at their edges.

(Rockett, Chp 7, Tsao, Marder)

Dislocation Energetics and Fields

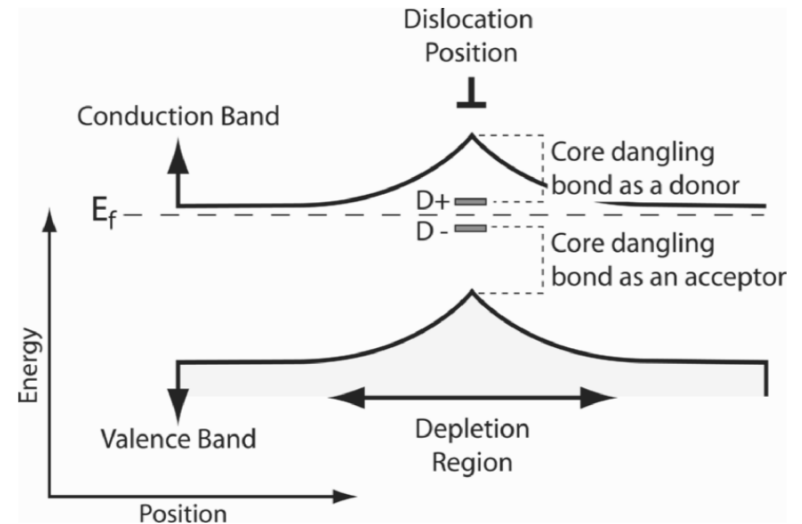
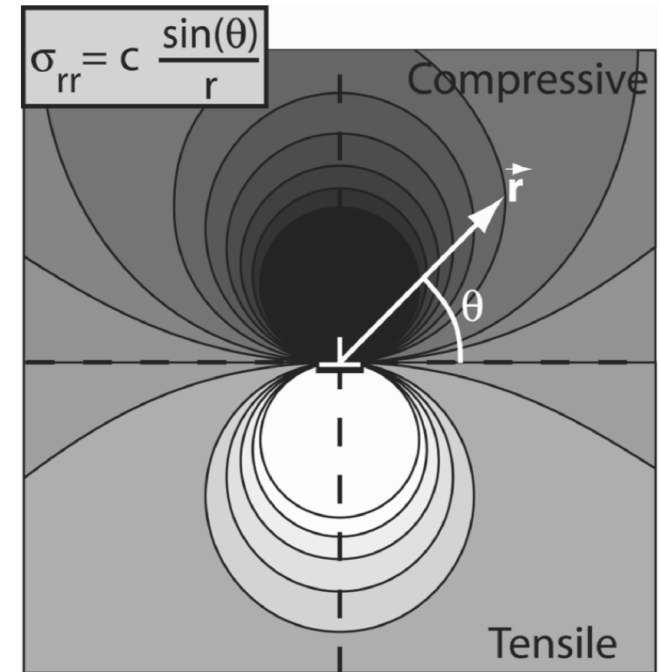
$$\Gamma_{screw} = \frac{G}{4\pi} \left[b^2 \ln\left(\frac{r}{b}\right) \right] + E_{core}$$

$$\sigma_{rr} = -\frac{Gb}{2\pi(1-\nu)r^2 l} \vec{r} \cdot \vec{\xi}$$

$$P_{edge} = -\frac{(1+\nu)Gb \sin \theta}{3\pi(1-\nu)r}$$

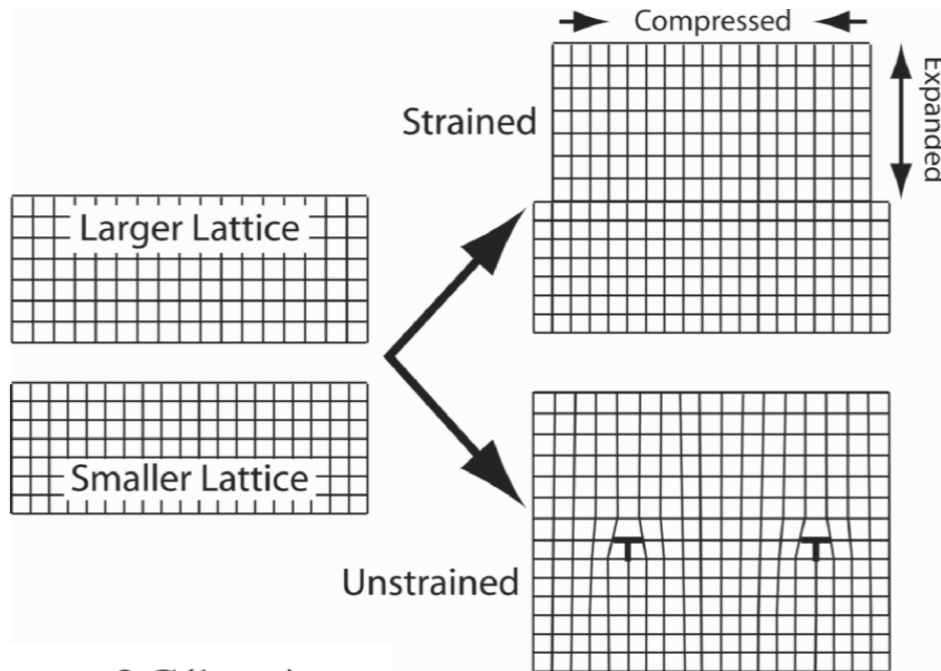
$$E = \frac{4(1+\nu)}{3(1-\nu)} \frac{R\Delta R}{r} \sin \theta$$

$$\pi R^2 N_d = \frac{f \sin \alpha}{a}$$



(Rockett, Chp 7, Tsao, Marder)

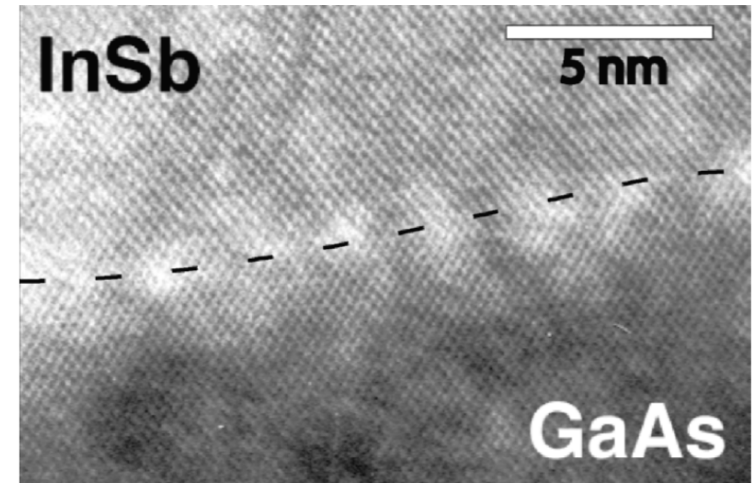
Dislocation Energetics: Critical Thickness



$$E_{el} = \frac{2G(1+\nu)}{1-\nu} f^2 h$$

$$E_{dis} = \frac{Gb^2}{4\pi} \frac{1-\nu \cos^2(\theta)}{1-\nu} \ln\left(\frac{\alpha h}{b}\right)$$

$$E_{el} = f E_{dis}$$



11% Lattice Mismatch

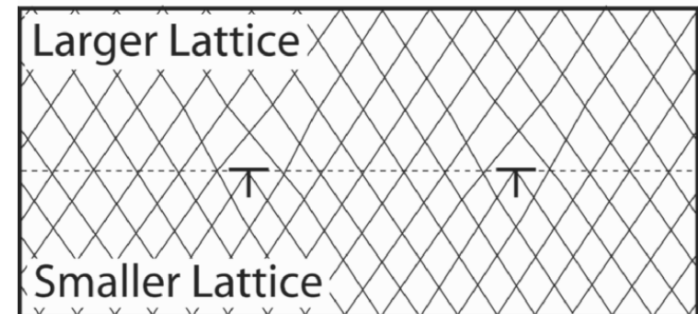
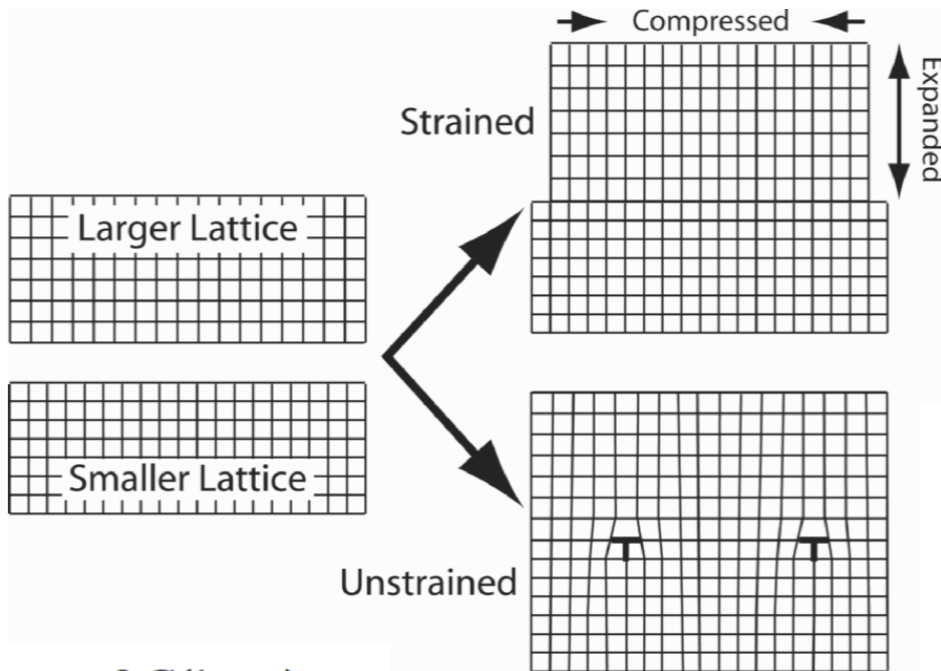


Figure 7.16: A cross-sectional transmission electron micrograph of a GaAs/InSb heterojunction. The mismatch in this system is approximately 14.6%, giving rise to a misfit dislocation roughly every seven lattice spacings. In this image, the core regions of the edge dislocations appear as brighter regions. The schematic below shows a sketch of the dislocation structure in the image above. Each marked dislocation terminates two of the (111)-type lattice fringes as shown and is located in the whiter regions along the marked interface.

(Rockett, Chp 7, Tsao, Marder)

Dislocation Energetics: Critical Thickness



$$E_{el} = \frac{2G(1+\nu)}{1-\nu} f^2 h$$

$$E_{dis} = \frac{Gb^2}{4\pi} \frac{1-\nu \cos^2(\theta)}{1-\nu} \ln\left(\frac{\alpha h}{b}\right)$$

$$E_{el} = f E_{dis}$$

$$\frac{h_c/b}{\ln(\alpha h_c/b)} = \frac{1-\nu \cos^2 \theta}{8\pi f(1+\nu) \cos \phi}$$

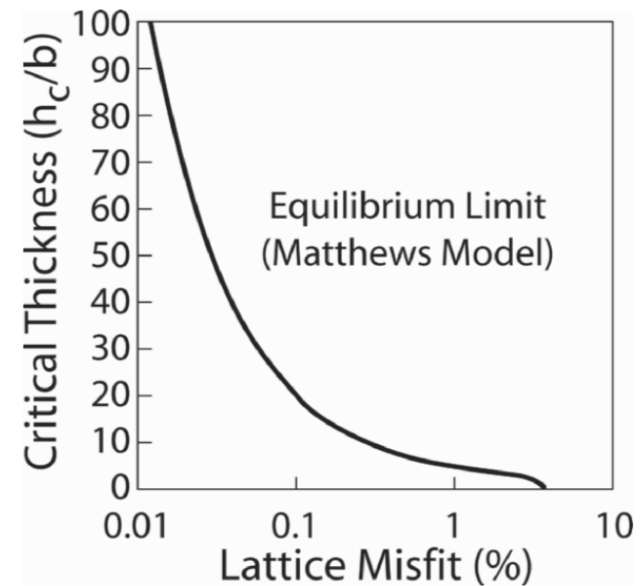
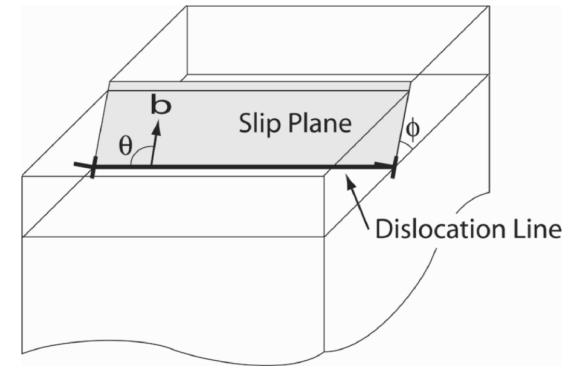


Figure 7.18: The equilibrium critical thickness for a film with a Poisson's ratio of 0.22 assuming strain relief by 60° dislocations ($\theta, \phi = 60^\circ$). The curve was calculated using Equation 7.29, with $\alpha=1$.

(Rockett, Chp 7, Tsao, Marder)

Dislocation Arrays: Critical Thickness

$$f(D) = f_{\infty} - \frac{b \cos \phi}{D}$$

$$E_{array} = \frac{Gb^2(1 - \nu \cos^2 \theta)}{8\pi(1 - \nu)D} \ln\left(\frac{\alpha h}{b}\right)$$

$$D(h) = \frac{b \cos \phi}{\frac{\Delta a}{a} - \frac{b(1 - \nu \cos^2 \theta) \ln(\alpha h/b)}{8\pi(1 - \nu) \cos \phi} h}$$

$$D(h) = \frac{b \cos \phi}{\frac{\Delta a}{a} - C \frac{\ln(\alpha h/b)}{h}}$$

$$D = \infty$$

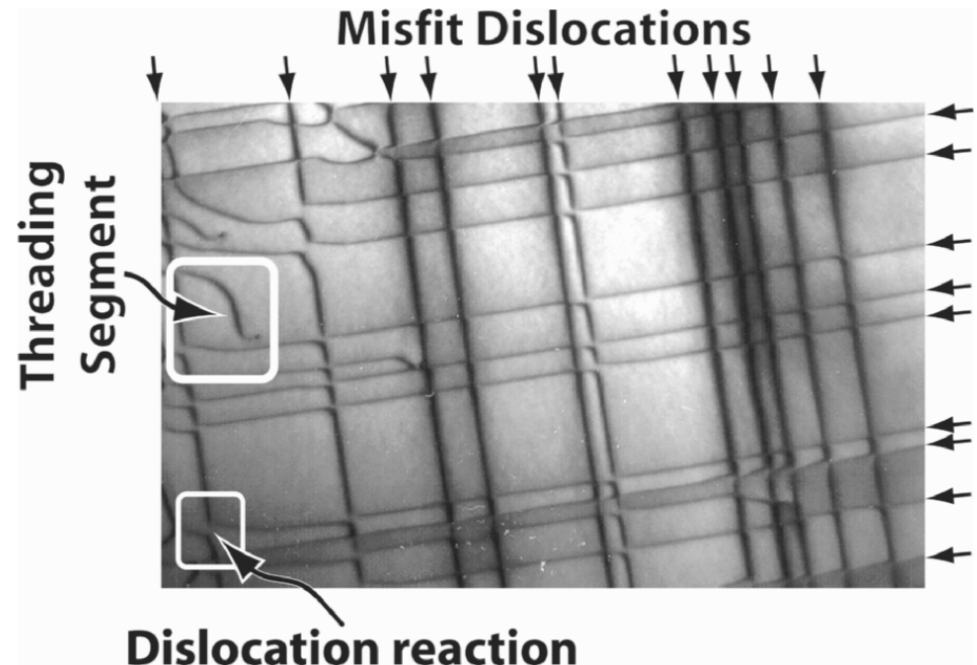


Figure 7.19: A transmission electron micrograph looking down upon the interface between a GaAs substrate and an InAs epitaxial layer. Both threading segments stretching from the heterojunction to the surface and reactions between dislocation segments are visible in the micrograph. The lines in the image are the misfit dislocations in the interface. [8]

(Rockett, Chp 7, Tsao, Marder)

Dislocation Scattering and Mobility

APPLIED PHYSICS LETTERS

VOLUME 76, NUMBER 13

27 MARCH 2000

Dislocation scattering in a two-dimensional electron gas

Debdeep Jena,^{a)} Arthur C. Gossard,^{b)} and Umesh K. Mishra
 Department of Electrical and Computer Engineering, University of California, Santa Barbara,
 California 93106

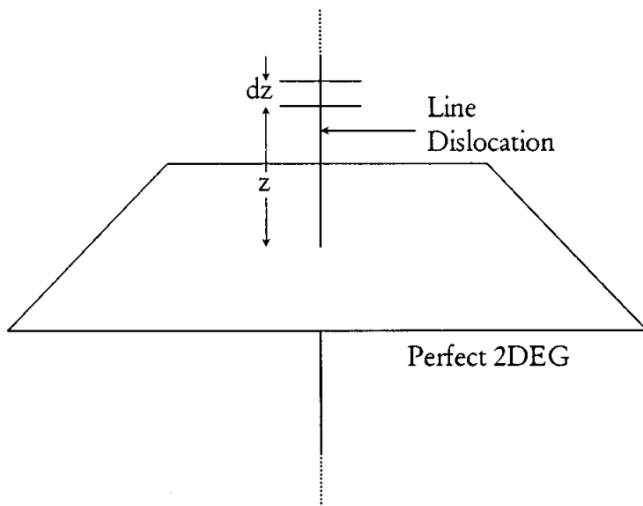


FIG. 1. Line dislocation modeled as a line of charge. The dislocation line has filled acceptor states along it. Charges on the dislocation line act as an extended remote impurity. The remote ionized impurity matrix element is integrated for all the small elemental remote impurities to account for the effect of the whole dislocation.

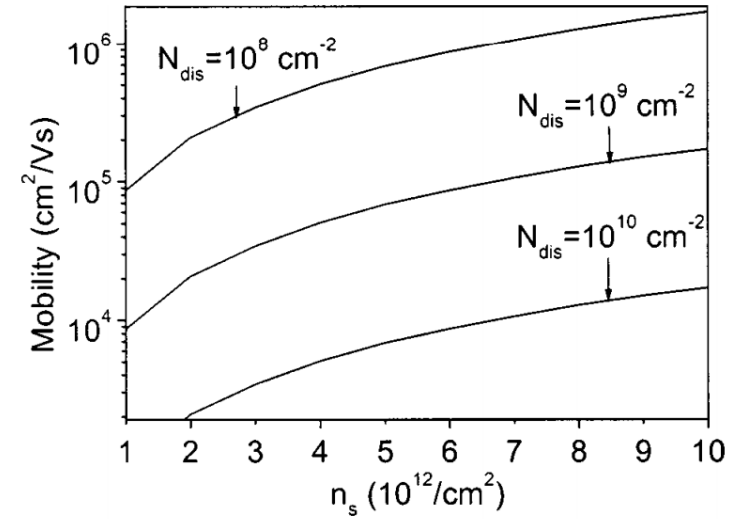


FIG. 3. Dislocation scattering inhibited 2DEG mobility. Mobilities for three different dislocation densities have been shown. Our theory predicts an approximate $n_s^{3/2}/N_{\text{dis}}$ mobility dependence, which is seen in this plot. Note the strong mobility degradation at 10^{10} cm^{-2} dislocation density.

$$\tau_{\text{dis}}^{3\text{D}} = \frac{\hbar^3 \epsilon_0^2 \epsilon_b^2 c_0^2}{N_{\text{dis}} m^* e^4 f^2} \cdot \frac{(1 + 4\lambda_D^2 k_{\perp}^2)^{3/2}}{\lambda_D^4} \propto \frac{(k_B T)^{3/2}}{\lambda_D},$$

$$\tau_{\text{dis}}^{2\text{D}} = \frac{\hbar^3 \epsilon_0^2 \epsilon_b^2 c_0^2}{N_{\text{dis}} m^* e^4 f^2} \cdot \frac{16\pi k_F^4}{I\left(\frac{q_{\text{TF}}}{2k_F}\right)}$$

$$\approx \frac{\hbar^3 \epsilon_0^2 \epsilon_b^2 c_0^2}{N_{\text{dis}} m^* e^4 f^2} \cdot \frac{16\pi k_F^4}{\left(\frac{1.84k_F}{q_{\text{TF}}} - 0.25\right)}$$

Dislocation Scattering and Mobility

APPLIED PHYSICS LETTERS

VOLUME 80, NUMBER 1

7 JANUARY 2002

Effect of scattering by strain fields surrounding edge dislocations on electron transport in two-dimensional electron gases

Debdeep Jena^{a)} and U. K. Mishra

Department of Electrical and Computer Engineering, University of California, Santa Barbara California, 93106

(Received 16 July 2001; accepted for publication 20 October 2001)

$$\Delta E_C = a_C \text{Tr}(\epsilon)$$

$$\delta V = \Delta E_C = a_C \text{Tr}(\epsilon) = -\frac{a_C b_e}{2\pi} \frac{1-2\gamma}{1-\gamma} \frac{\sin(\theta)}{r}$$

$$\mu_{\text{disl}}^{\text{strain}} = \frac{2e\hbar^3 \pi k_F^2}{N_{\text{disl}} m^{*2} b_e^2 a_C^2} \left(\frac{1-\gamma}{1-2\gamma} \right)^2 \frac{1}{I(n_s)}$$

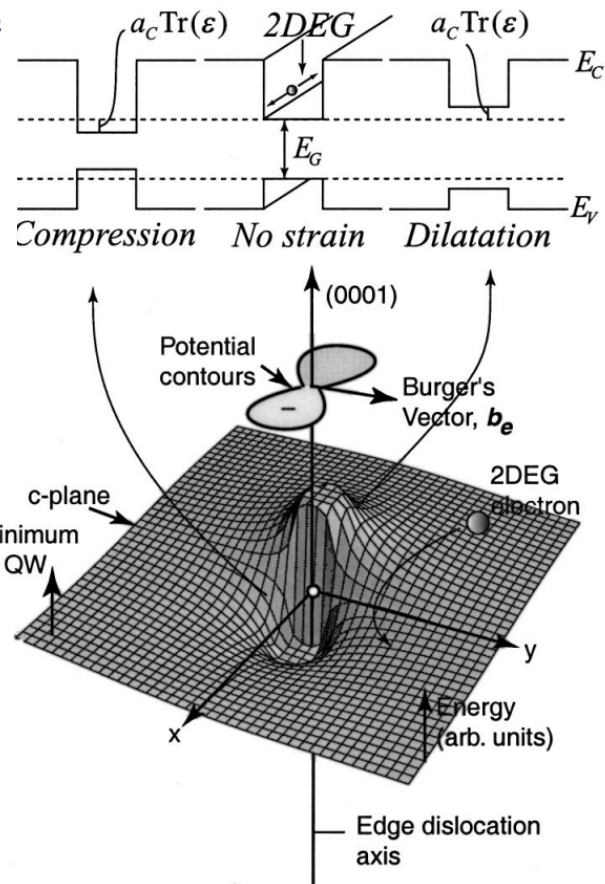
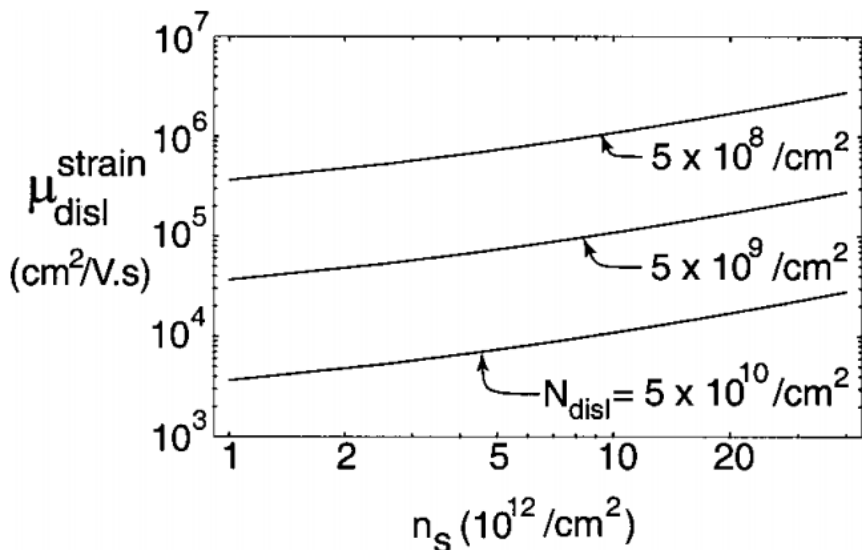


FIG. 1. The band electron experiences the depicted CB minimum fluctuation caused by strain fields around an edge dislocation. Strain is anisotropic, with maximum strain in directions perpendicular to the Burgers vector. The energy is in arbitrary units.

(Rockett, Chp 7, Tsao, Marder)

Dislocation Scattering and Mobility

phys. stat. sol. (b) **228**, No. 2, 617–619 (2001)

Electron Transport in III–V Nitride Two-Dimensional Electron Gases

D. JENA¹ (a), I. SMORCHKOVA (b), A. C. GOSSARD (a, c), and U. K. MISHRA (a)

(a) Department of Electrical and Computer Engineering, University of California,
Santa Barbara, CA 93106, USA

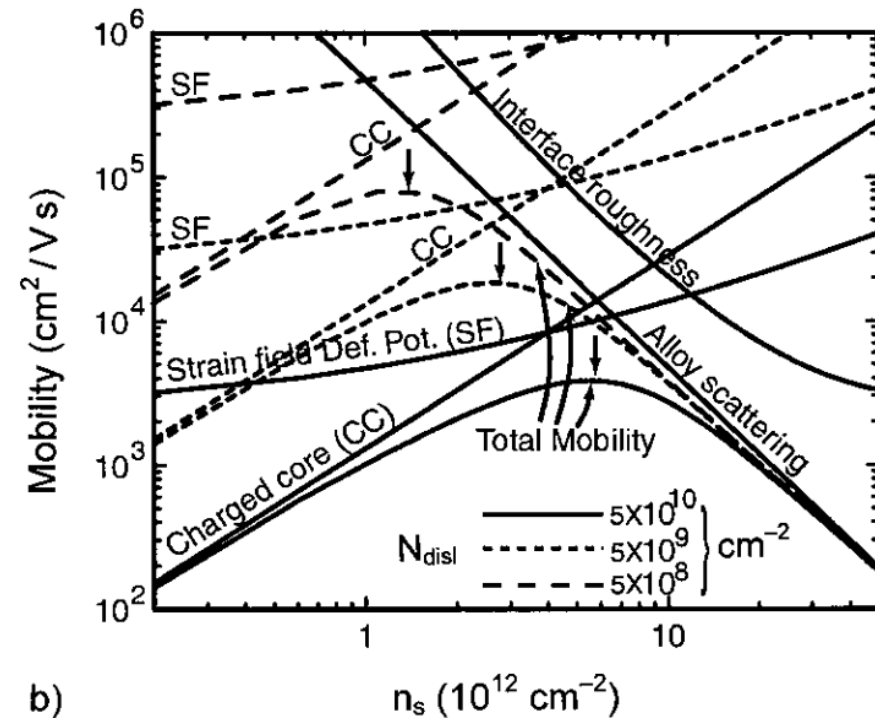
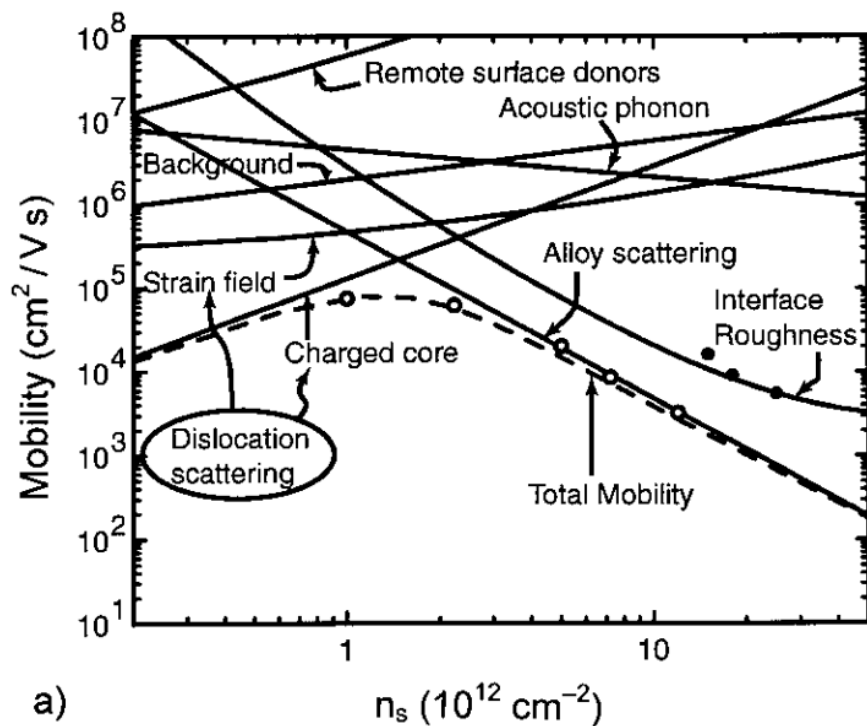


Fig. 1. a) Scattering processes limiting electron mobility in the Al(Ga)N/GaN 2DEG system evaluated for $N_{\text{disl}} = 5 \times 10^8 \text{ cm}^{-2}$; experimental data is also shown (circles). b) Effect of dislocation scattering for three different dislocation densities

Effect of Dislocations on Vertical Diodes & Transistors

Diagram and AFM image of LEO grown template

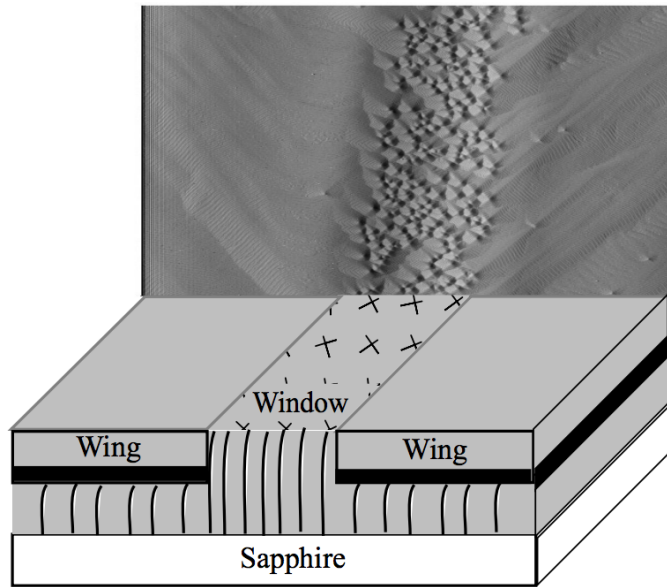


Figure 5.6: Atomic Force Microscopy image of an LEO substrate (above) showing window and ring regions. Spiral growth mode in the window region is associated with the screw component of TDs. Wing regions consist of atomically flat steps.

SEM micrograph of LEO Cross-section

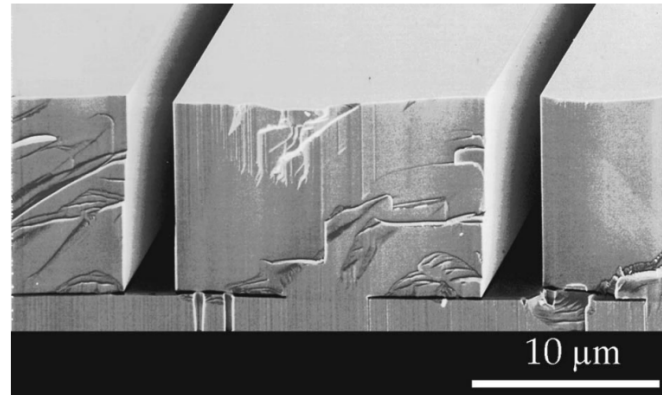


Figure 5.5: The above cross section shows an as-cleaved cross section of uncoalesced LEO stripes similar to those in the LEO template utilized for the AlGaIn/GaN HBT on LEO GaN (courtesy P. Fini [9]).

comparison of collector-emitter leakage on wing vs window

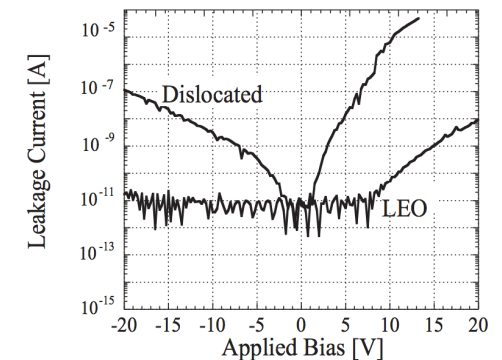


Figure 5.7: Semi log plot of leakage current of LEO window compared to wing region. Plot shows reduction of leakage by four orders of magnitude for wing region as compared to window region. The emitter mesa area for these devices was $6 \mu\text{m} \times 50 \mu\text{m}$.

Effect of Dislocations on Vertical Diodes & Transistors

APPLIED PHYSICS LETTERS 107, 232101 (2015)



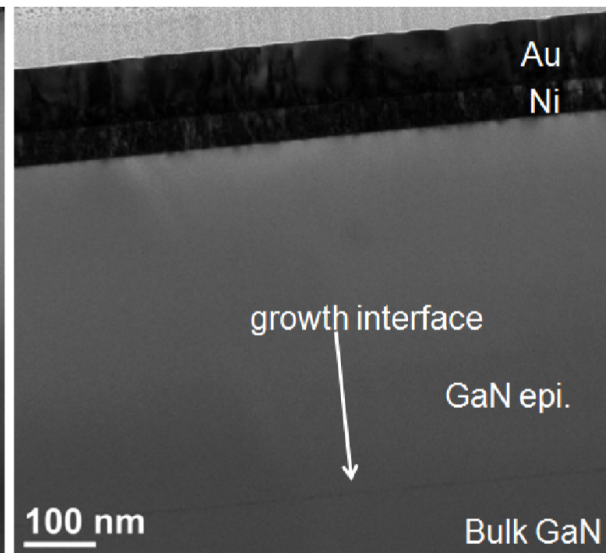
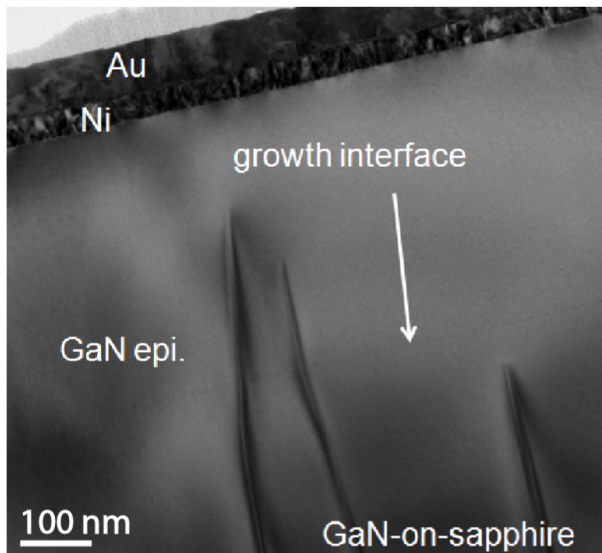
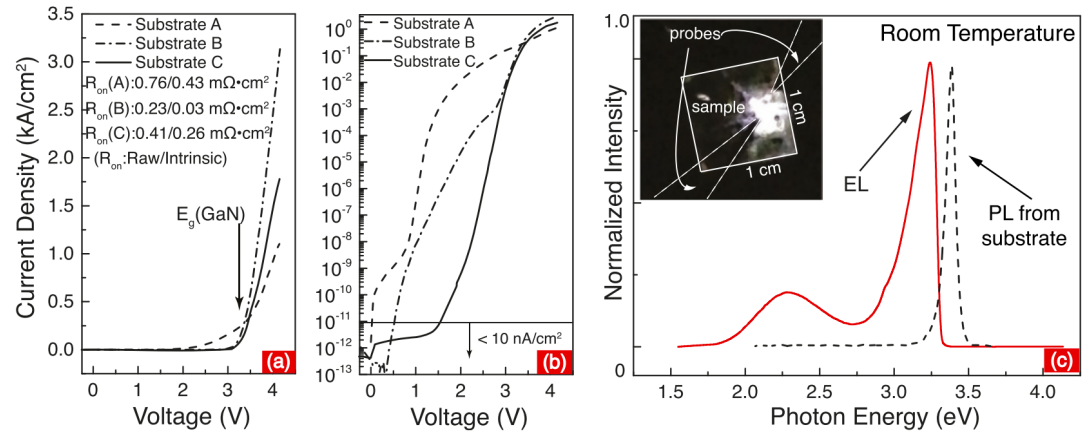
High breakdown single-crystal GaN p-n diodes by molecular beam epitaxy

Meng Qi,¹ Kazuki Nomoto,^{1,2} Mingda Zhu,^{1,2} Zongyang Hu,^{1,2} Yuning Zhao,¹ Vladimir Protasenko,^{1,2} Bo Song,^{1,2} Xiaodong Yan,¹ Guowang Li,¹ Jai Verma,¹ Samuel Bader,² Patrick Fay,¹ Huihui Grace Xing,^{1,2} and Debdeep Jena^{1,2,a)}
¹Department of Electrical Engineering, University of Notre Dame, Notre Dame, Indiana 46556, USA
²Departments of ECE and MSE, Cornell University, Ithaca, New York 14853, USA

(Received 13 October 2015; accepted 19 November 2015; published online 8 December 2015)

TABLE I. Substrates specifications for MBE grown p-n junctions. σ : carrier concentration, μ : carrier mobility, t : thickness, TD : threading dislocation density, and ρ : resistivity at 300 K.

GaN Substrate	σ (cm ⁻³)	μ (cm ² /V s)	t (μ m)	ρ (m Ω cm)	TD (cm ⁻²)
A	$\sim 4 \times 10^{18}$	107	300 ± 50	10.9 ± 1.8	$1-2 \times 10^7$
B	$\sim 3 \times 10^{18}$	211	290	7.2	$2-5 \times 10^5$
C	$\sim 10^{19}$	150	566	2.7	$< 5 \times 10^4$



Effect of Dislocations on Vertical Diodes & Transistors

Effect of doping on emitter-collector leakage

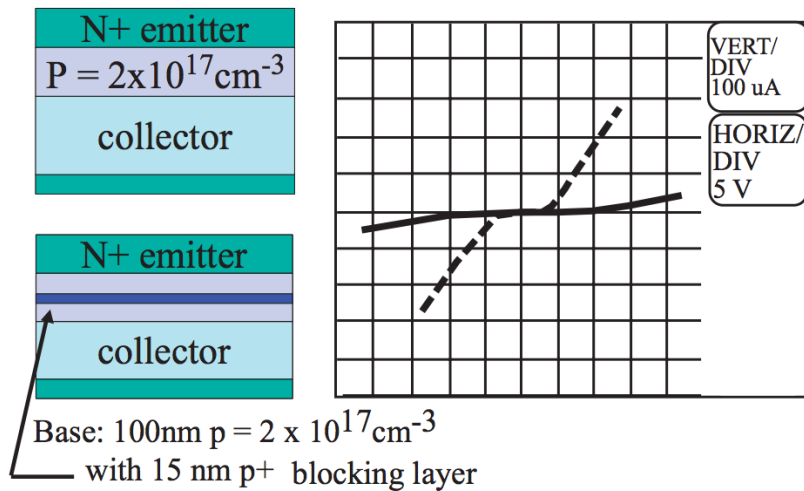


Figure 5.9: Emitter-Collector leakage is reduced by the addition of a p^+ spike in the neutral base of a transistor structure. The solid line represents the emitter-collector leakage of the device with the p^+ blocking layer, while the dashed line is corresponds to the device with a conventional base doped $p=2 \times 10^{17} \text{ cm}^{-3}$.

Lee McCarthy (PhD Thesis, 2001)

Debdeep Jena (djena@cornell.edu), Cornell University

3D Illustration of a band diagram with a dislocation

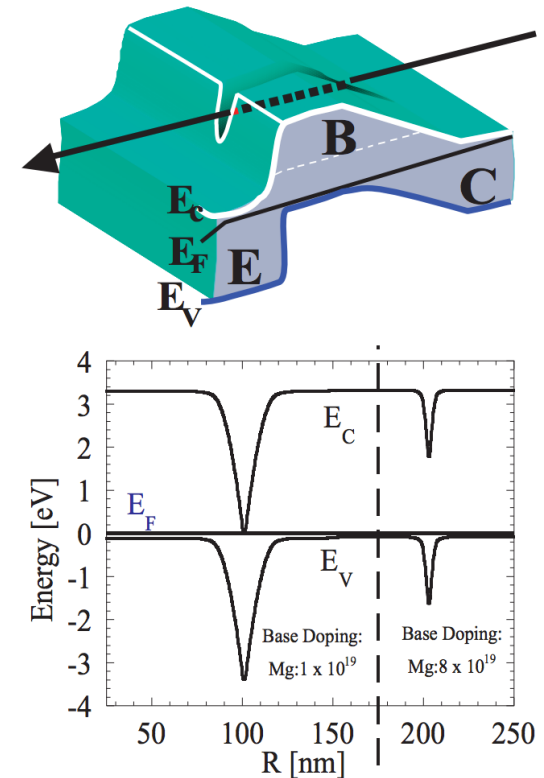


Figure 5.10:

Above: Three dimensional rendering of the proposed band diagram of an HBT with a dislocation (arrow) causing local compensation of the p-type base.

Below: Calculated cross sectional band-diagram of a locally compensated area surrounding a dislocation in p-type GaN taken at the base-emitter interface. A lightly doped base (left) is fully compensated near the dislocation, while a heavily doped base (right) is only partially compensated. The notches in the cross sectional band diagram correspond to the notch around the dislocation in the three dimensional illustration.

Effect of Dislocations on Photonic Devices

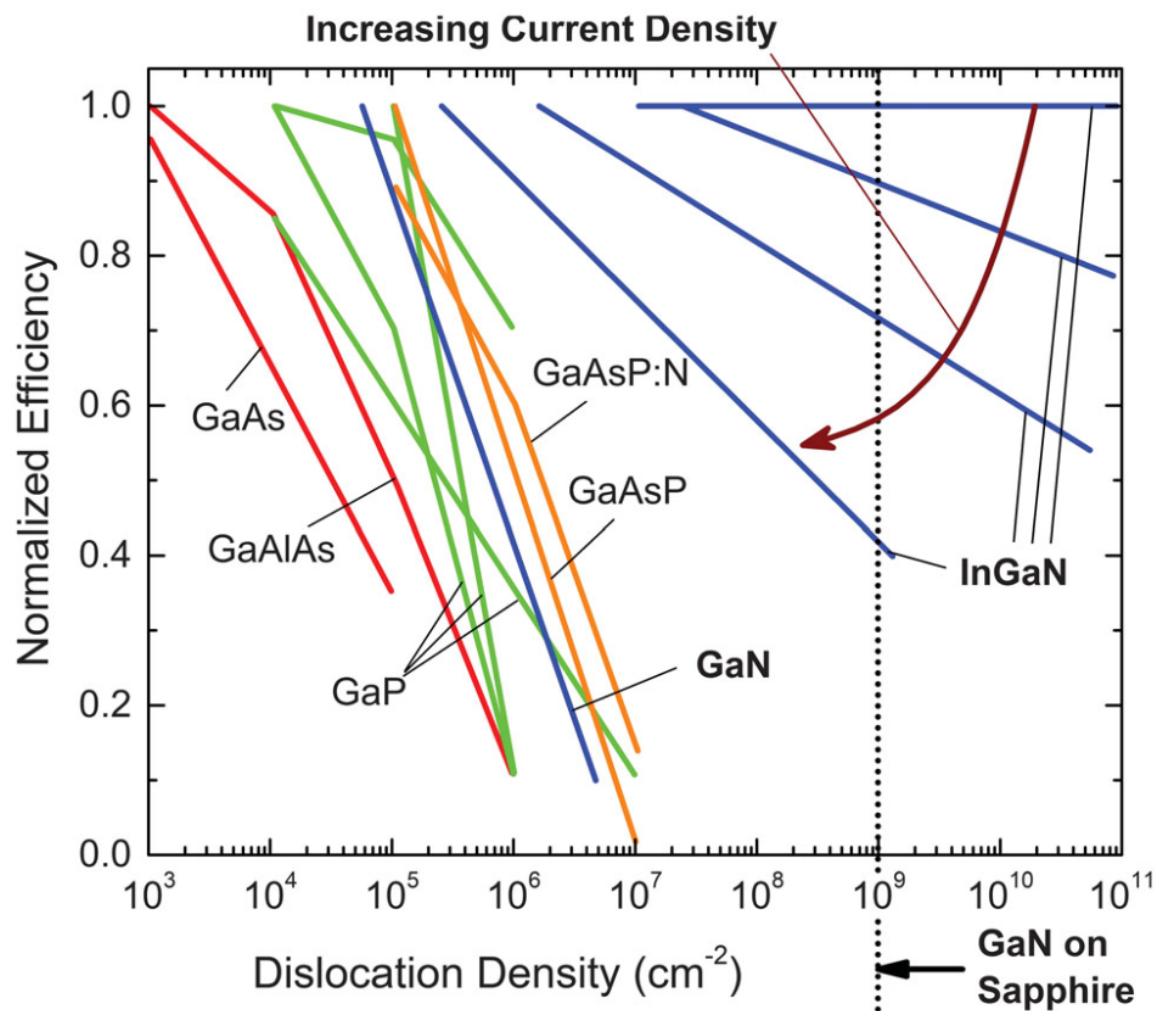


FIG. 13 (color). Dependence of LED efficiency on dislocation density for various semiconductor materials. From Lester *et al.*, 1995, Chichibu *et al.*, 1996, and Nakamura, 1998.

Advances in group III-nitride-based deep UV light-emitting diode technology

M Kneissl^{1,2}, T Kolbe¹, C Chua³, V Kueller², N Lobo¹, J Stellmach¹, A Knauer², H Rodriguez², S Einfeldt², Z Yang³, N M Johnson¹ and M Weyers²

¹ Institute of Solid State Physics, Technische Universität Berlin, Hardenbergstr. 36, D-10623 Berlin, Germany

² Ferdinand-Braun-Institut, Leibniz-Institut für Höchstfrequenztechnik, Gustav-Kirchhoff-Str. 4, D-12489 Berlin, Germany

³ Palo Alto Research Center, 3333 Coyote Hill Road, Palo Alto, CA 94304, USA

E-mail: kneissl@physik.tu-berlin.de

Received 18 June 2010, in final form 30 July 2010

Published 15 December 2010

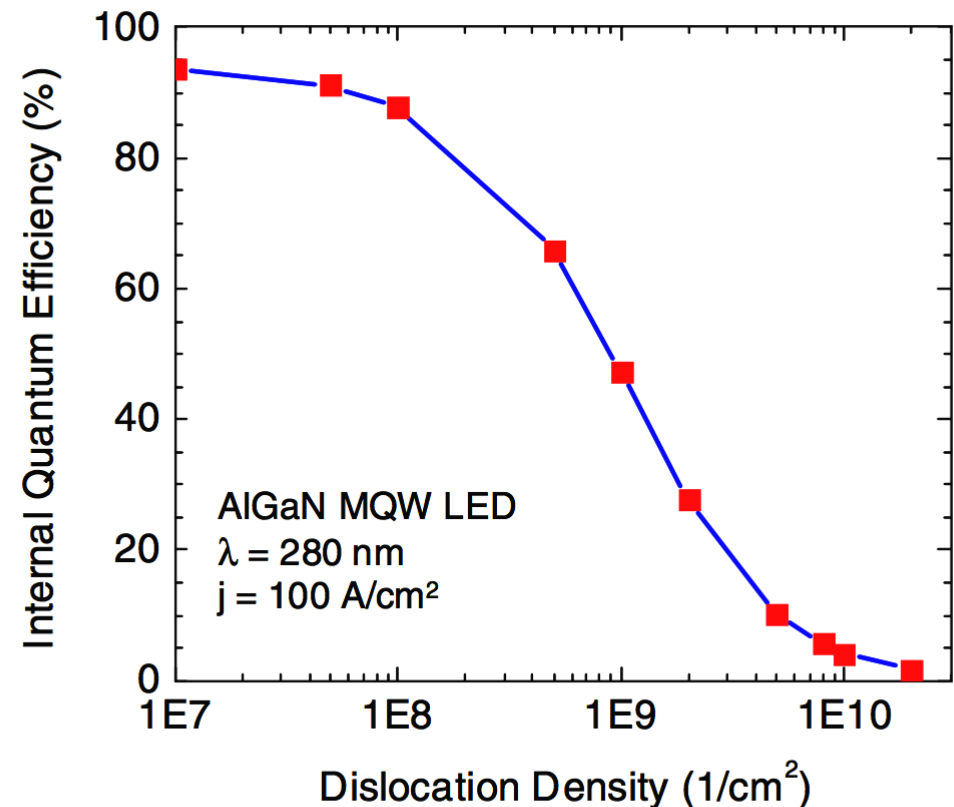
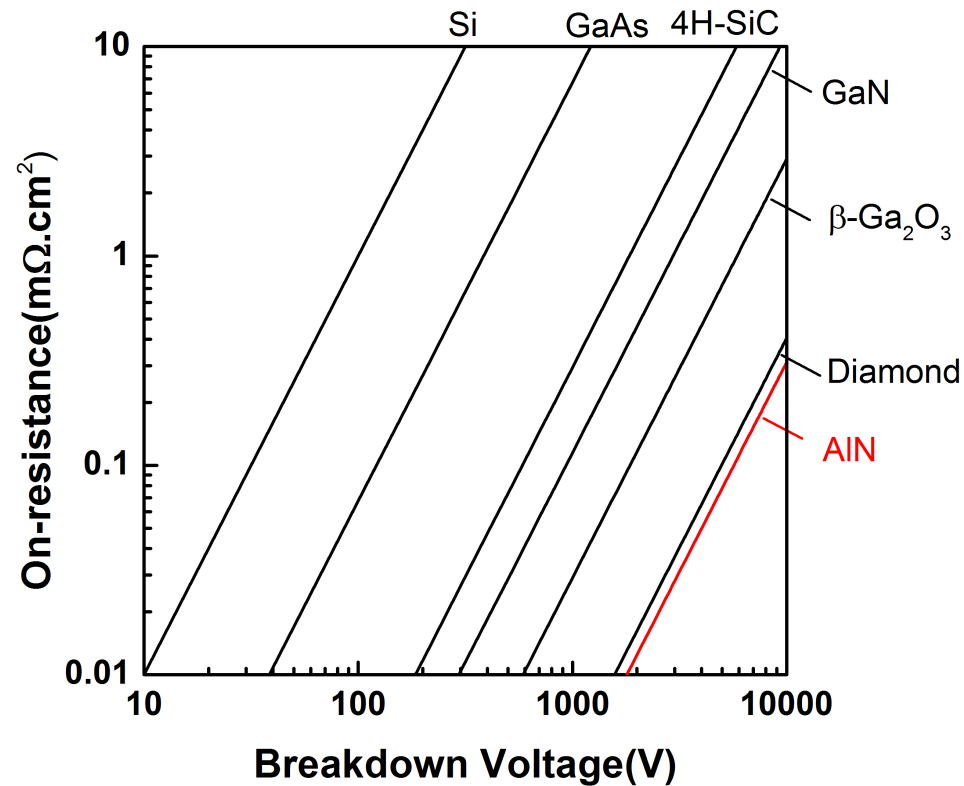


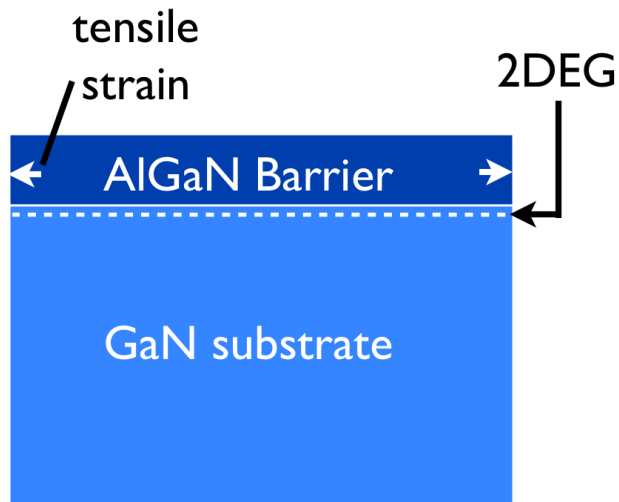
Figure 2. Simulated IQE versus the dislocation density for 280 nm UV LEDs [17].

Moving from “GaN” to AlN for electronics



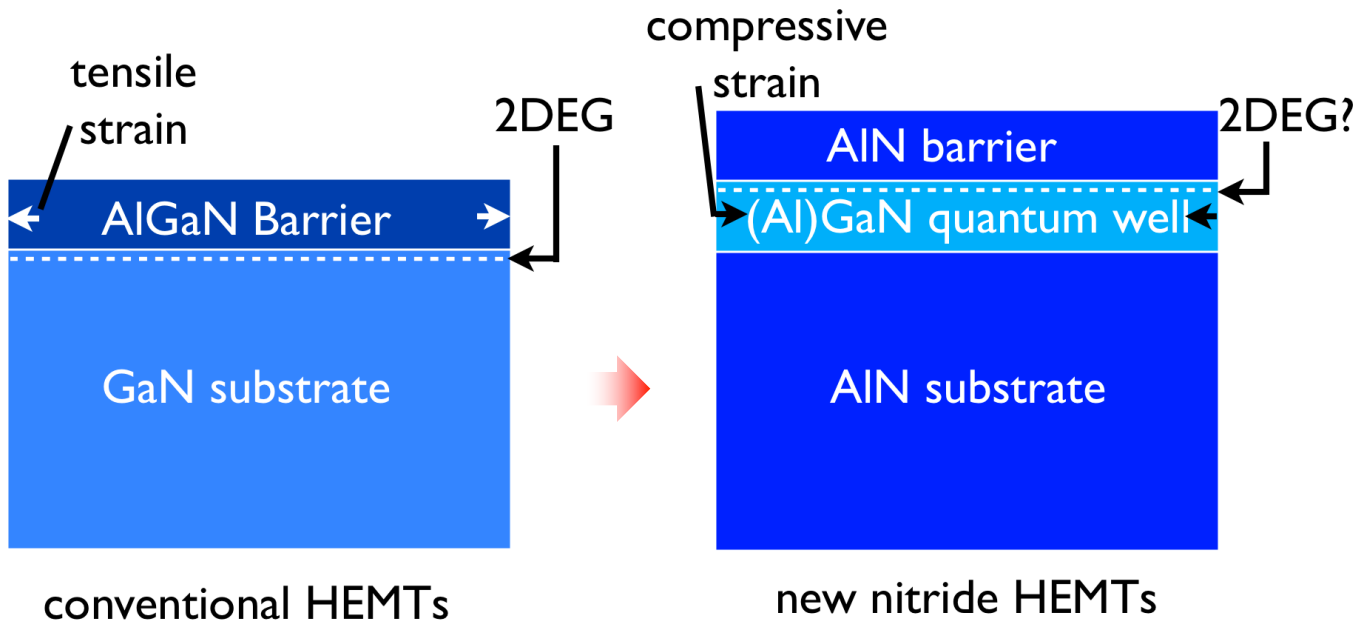
	Si	GaAs	4H-SiC	GaN	Diamond	β-Ga ₂ O ₃	AlN
Bandgap E_g (eV)	1.1	1.4	3.3	3.4	5.5	4.8-4.9	6
Electron mobility μ (cm ² /Vs)	1400	8000	1000	1200	2000	300	500
Breakdown field E_b (MV/cm)	0.3	0.4	2.5	3.3	10	8	15
Relative dielectric constant ϵ	11.8	12.9	9.7	9.0	5.5	10	8.5
Baliga's FOM $\epsilon\mu E_b^3$	1	15	340	870	24664	3444	32158

HEMTs based on the AlN platform

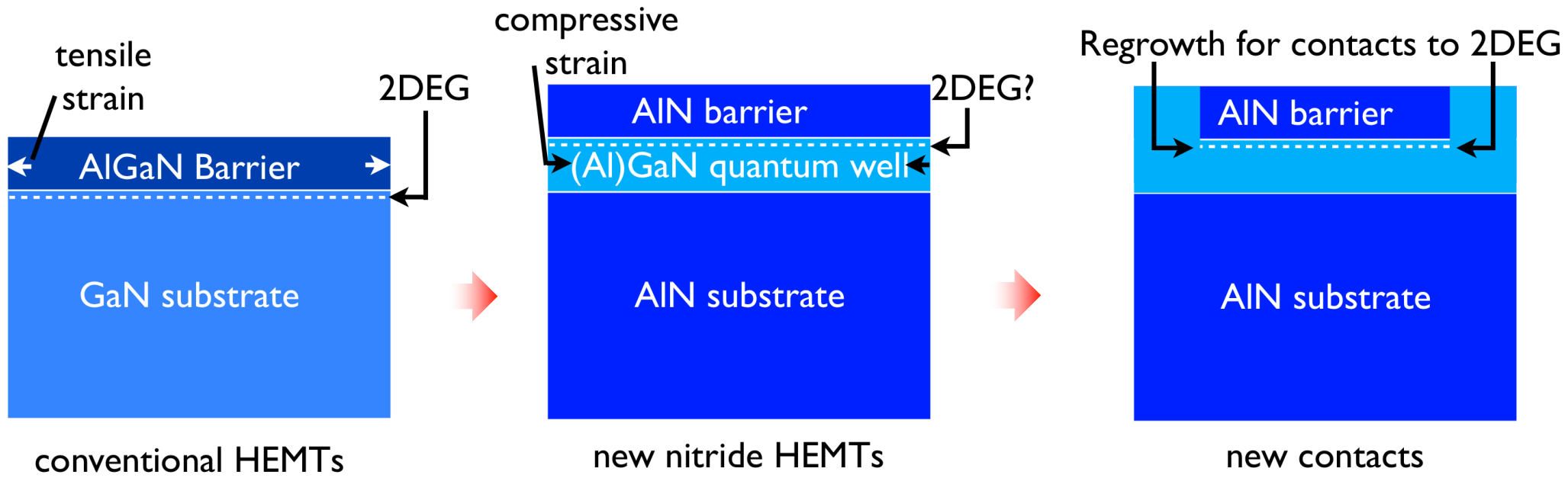


conventional HEMTs

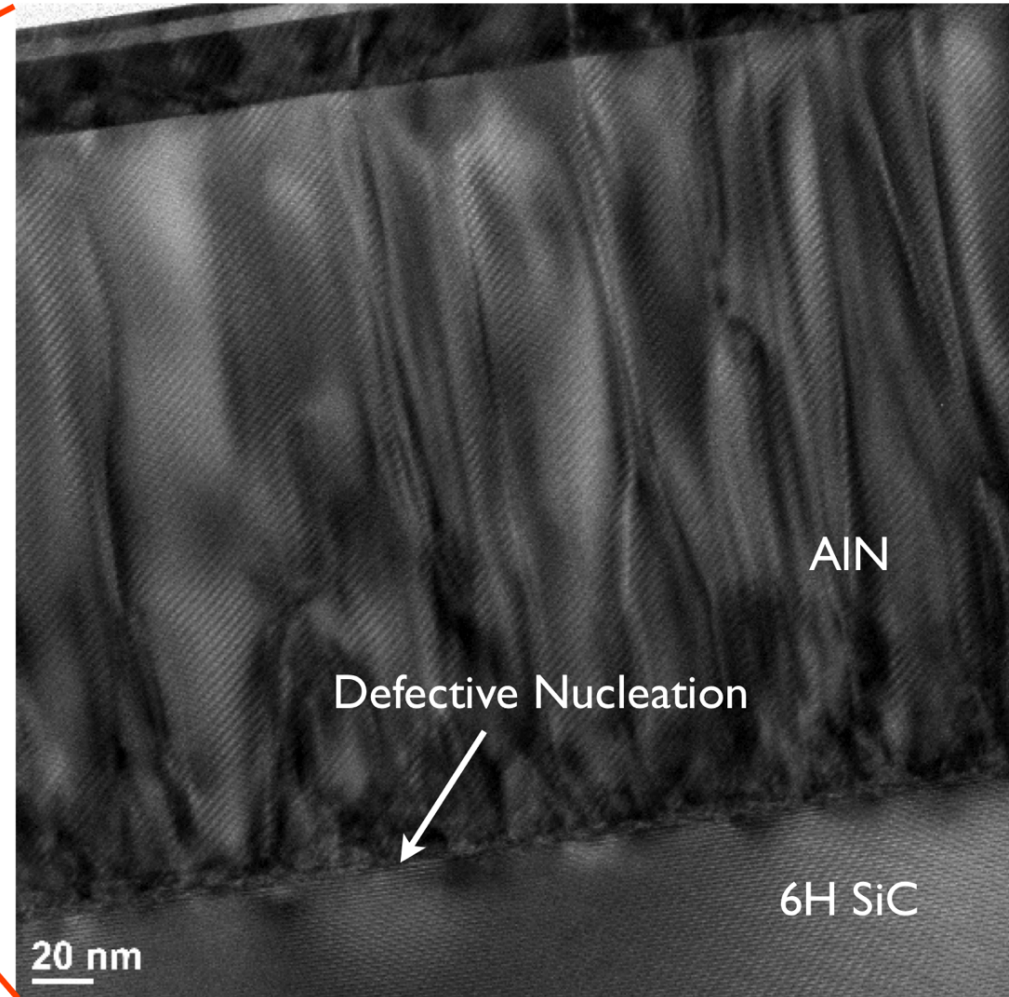
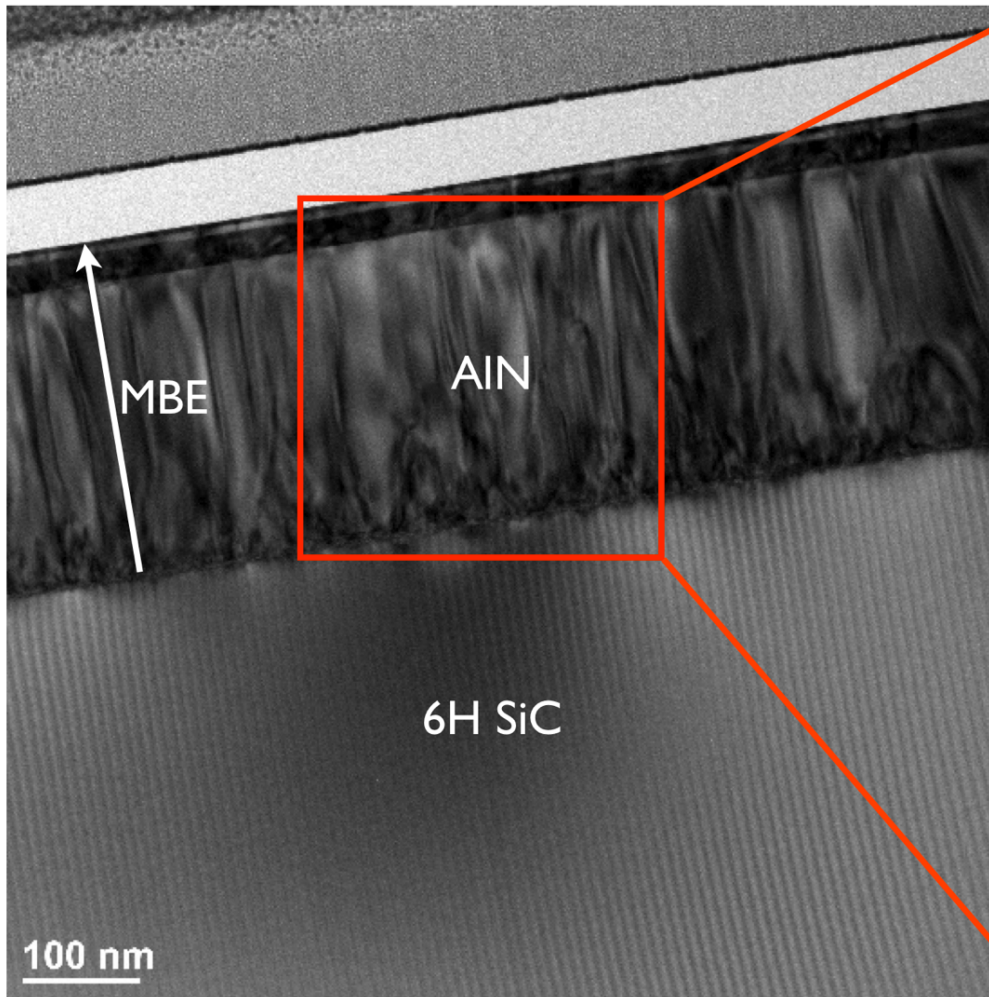
HEMTs based on the AlN platform



HEMTs based on the AlN platform

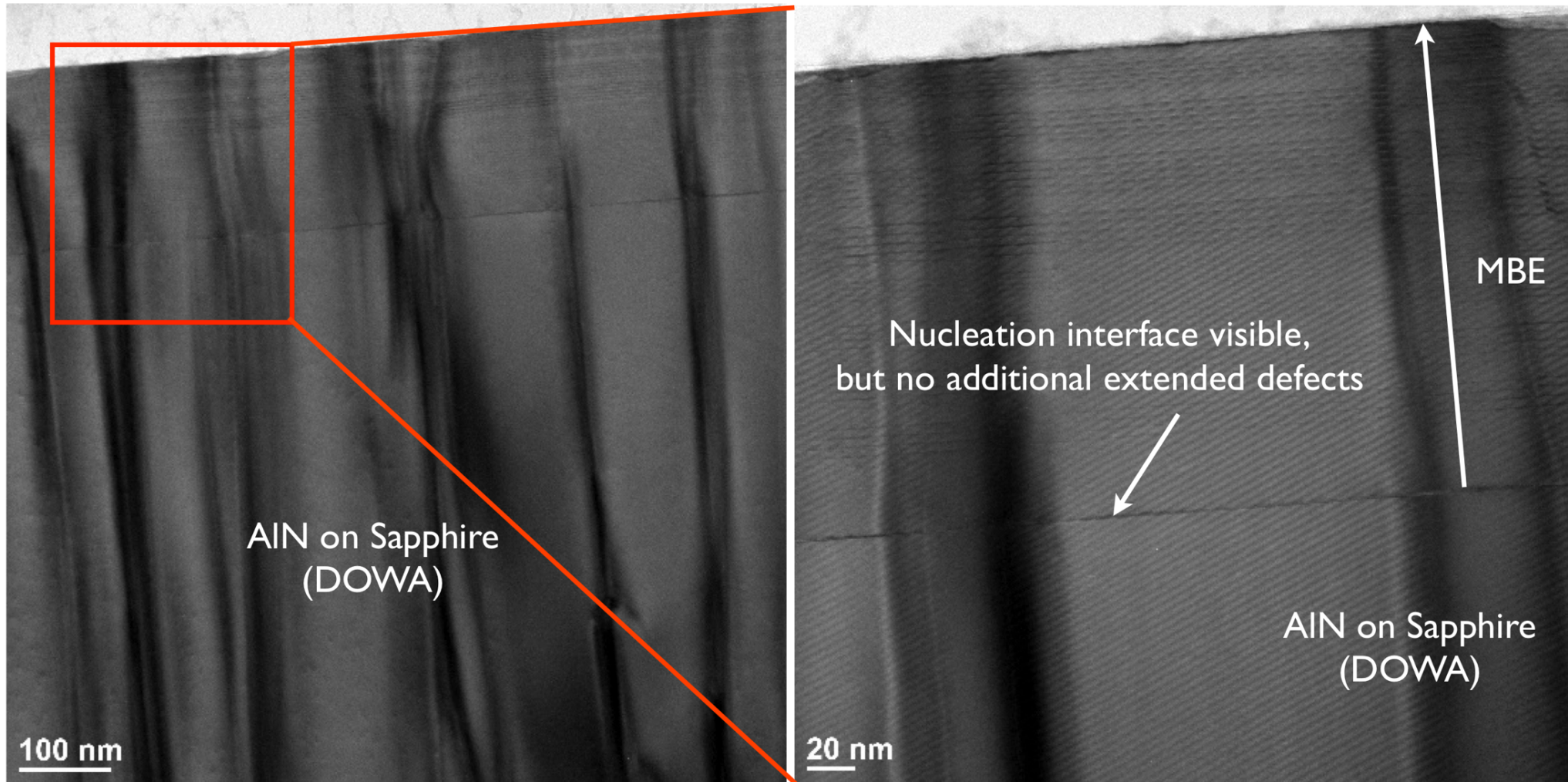


AlN nucleation on 6H SiC by MBE



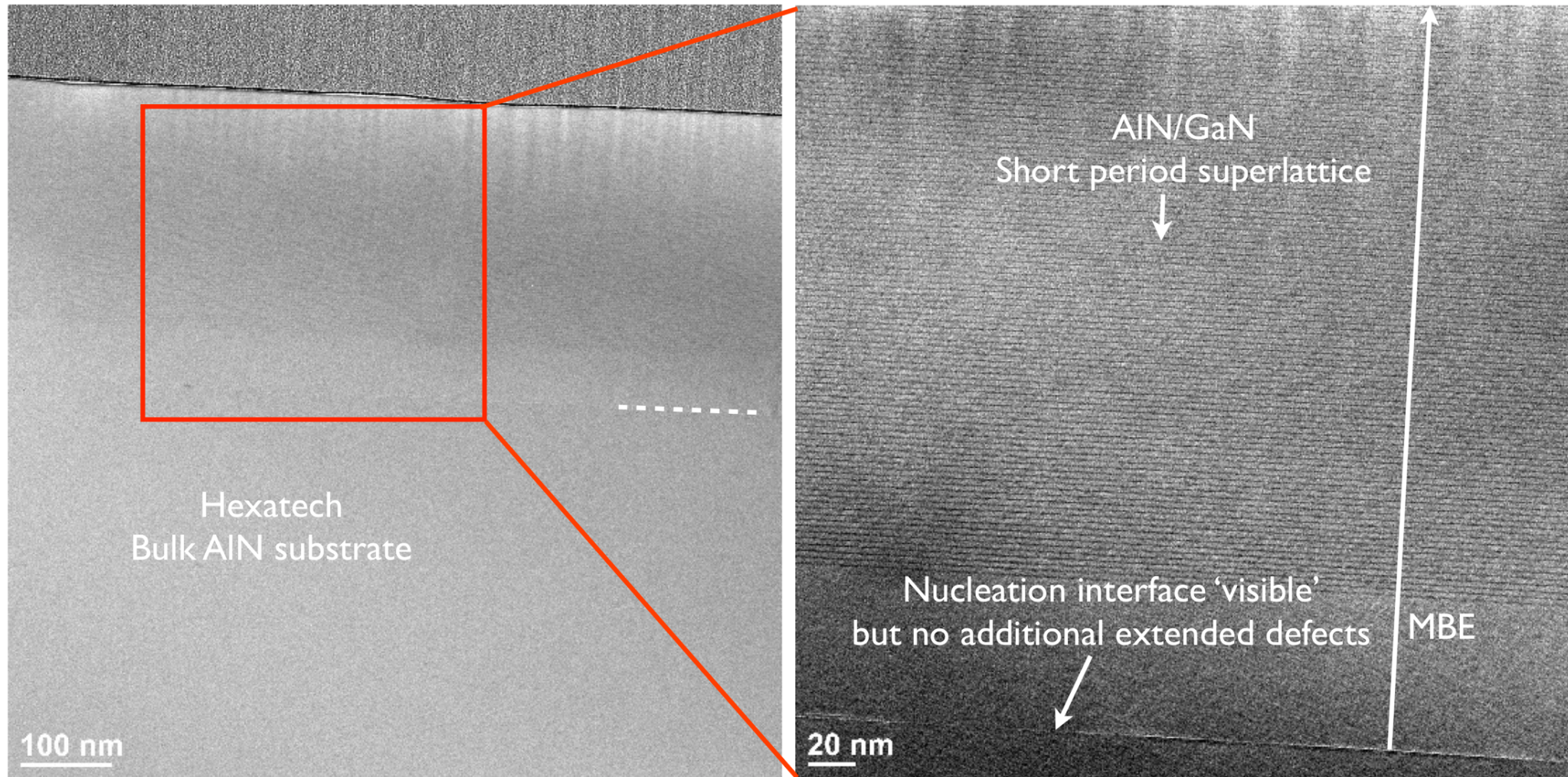
Surface treatment: Solvent clean, BHF dip, Ga-Flash in MBE
Nucleation: N-Rich AlN (or MEE) at 750 C

AlN nucleation on AlN/Sapphire by MBE



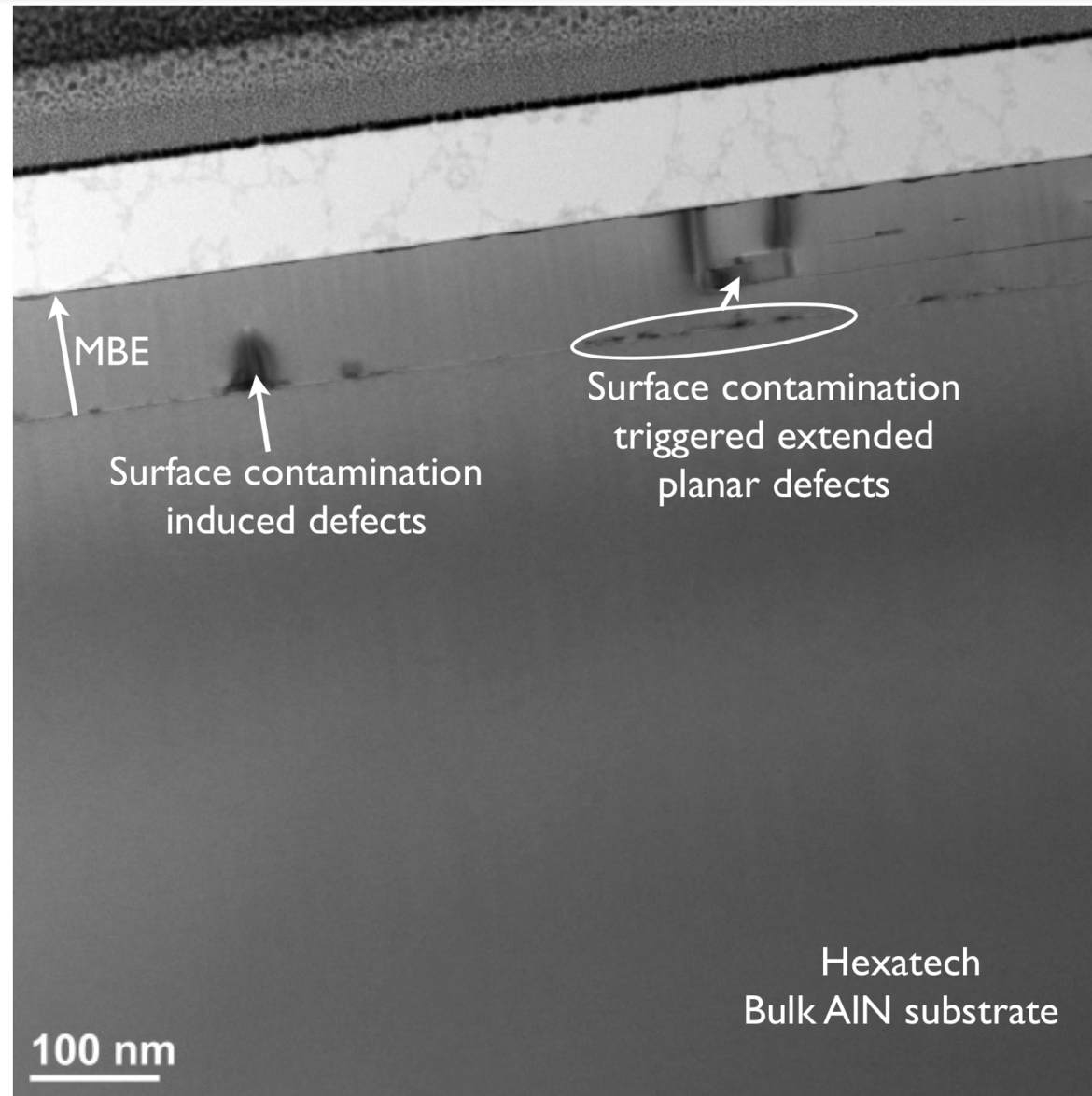
Surface treatment: Solvent clean
Nucleation: N-Rich AlN (or MEE) at 750 C

AlN nucleation on Bulk AlN substrate by MBE



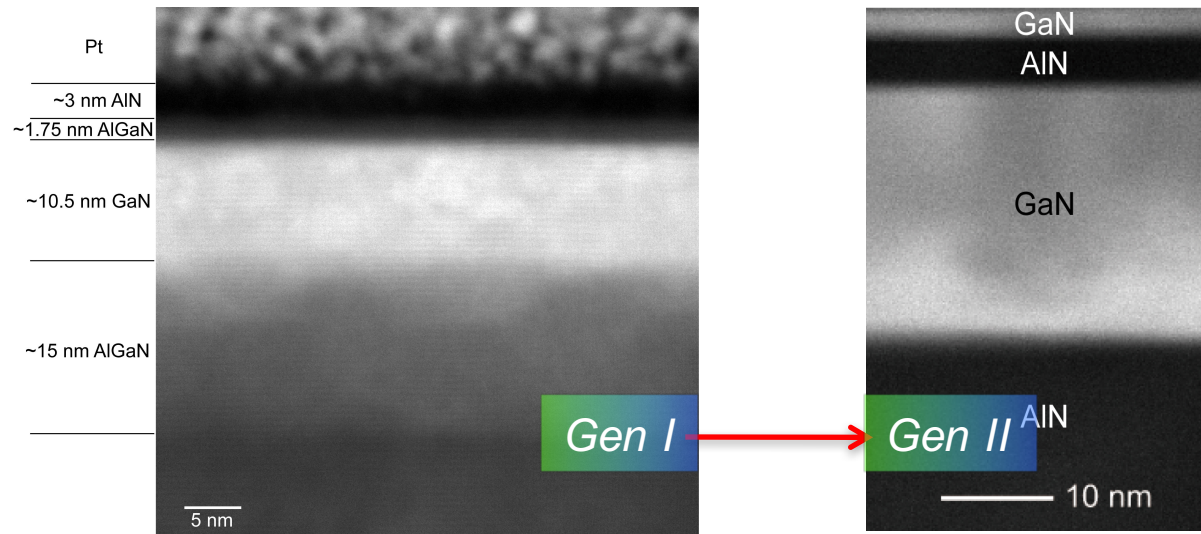
Surface treatment: Solvent clean
Nucleation: N-Rich AlN (or MEE) at 750 C

AlN nucleation on Bulk AlN substrate by MBE

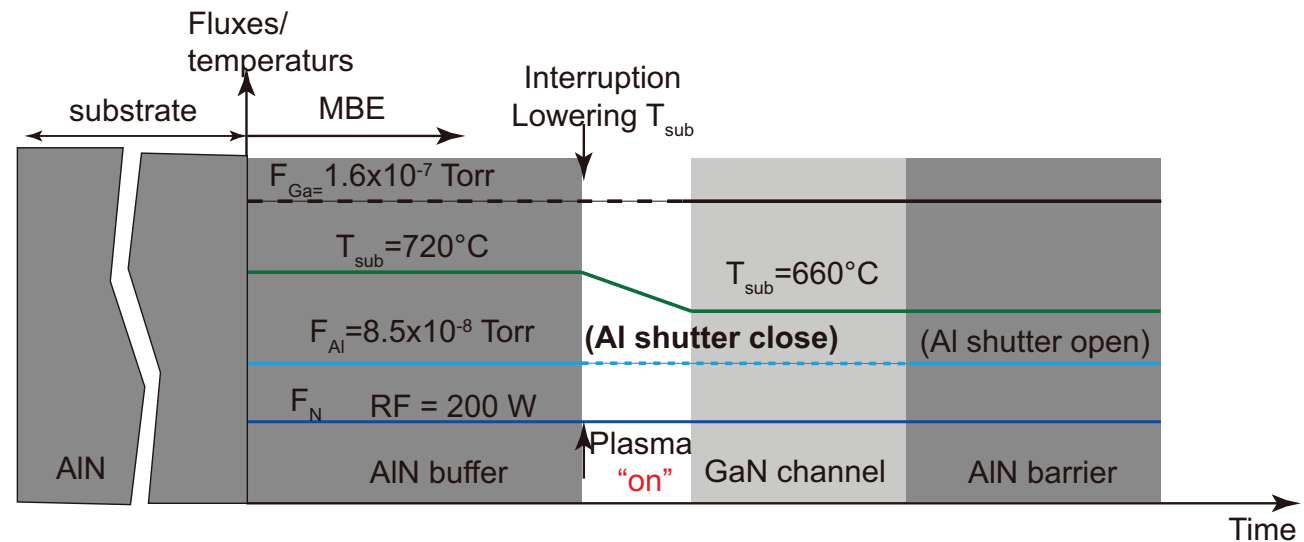


Nucleation on Bulk AlN Substrates is extremely sensitive to surface contamination. In-situ cleaning requires high temperatures.

Growth conditions for sharp heterojunctions

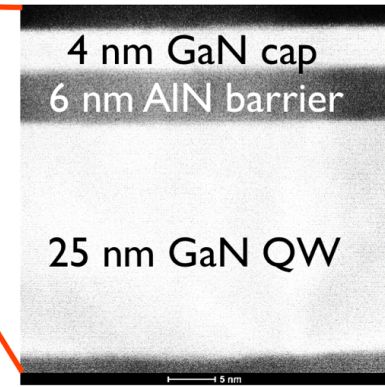
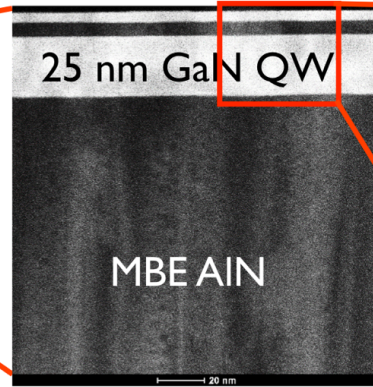
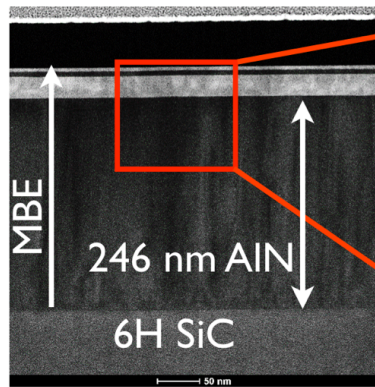


- Rough lower heterointerfaces
- Growth interrupt was found to be essential in metal-rich MBE growth to make the heterojunctions sharp

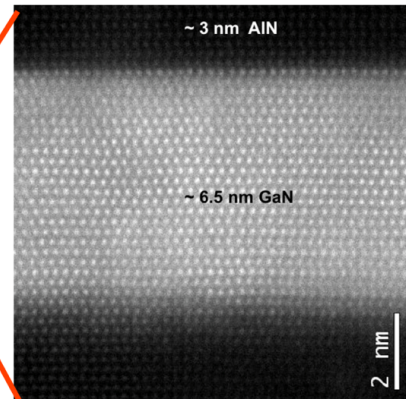
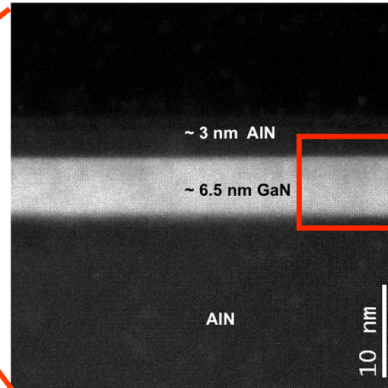
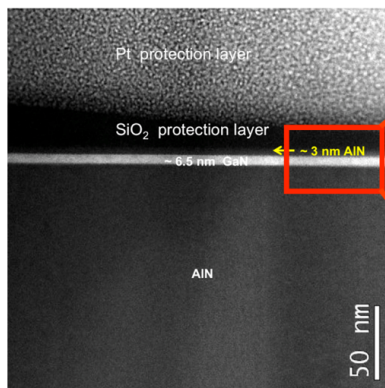


MBE growth of strained GaN Q-Well HEMTs

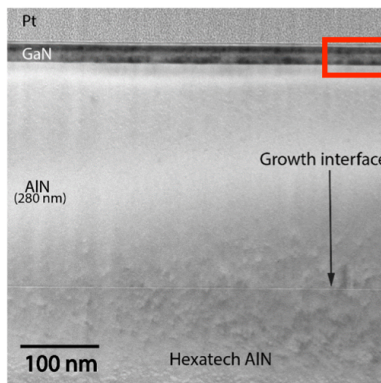
QW HEMT on SiC



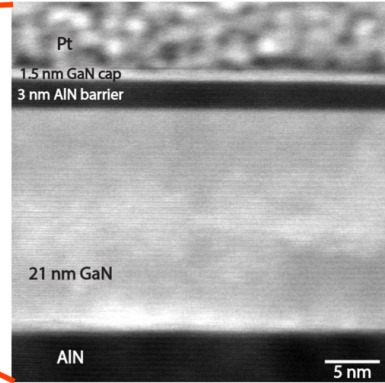
QW HEMT on
AlN/Sapphire



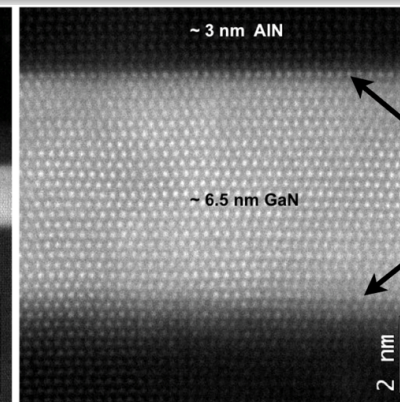
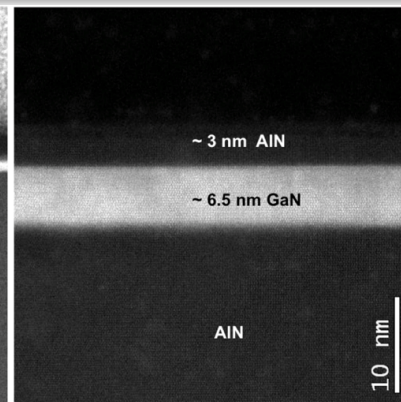
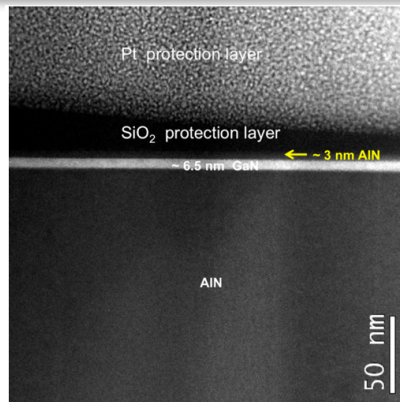
QW HEMT on
Bulk AlN



TEM courtesy:
Moon Kim (UT Dallas)

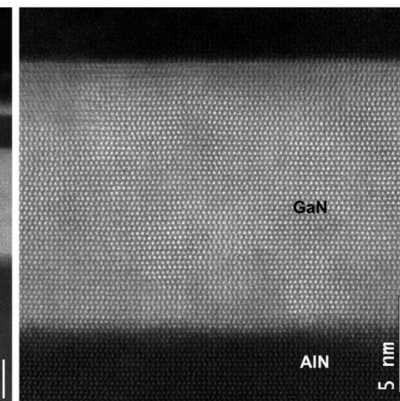
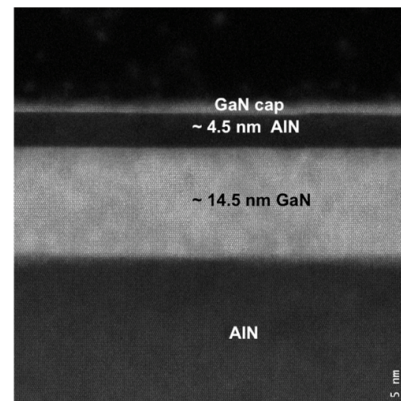


MBE growth of strained GaN Q-Well HEMTs

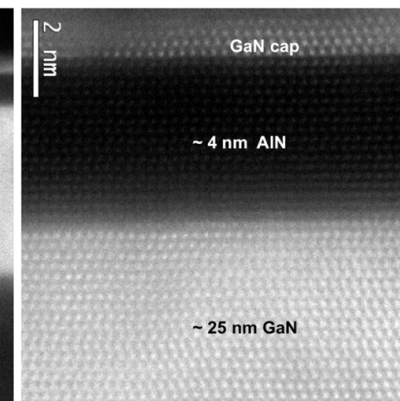
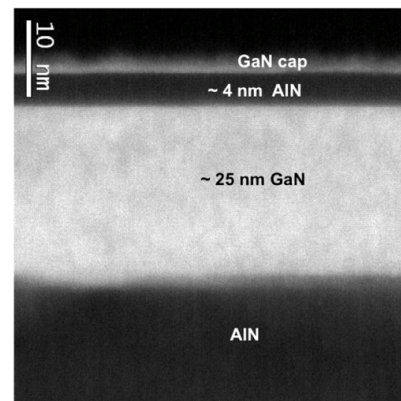


Top heterojunction is MUCH sharper than the bottom heterojunction

QW HEMT on AlN/Sapphire

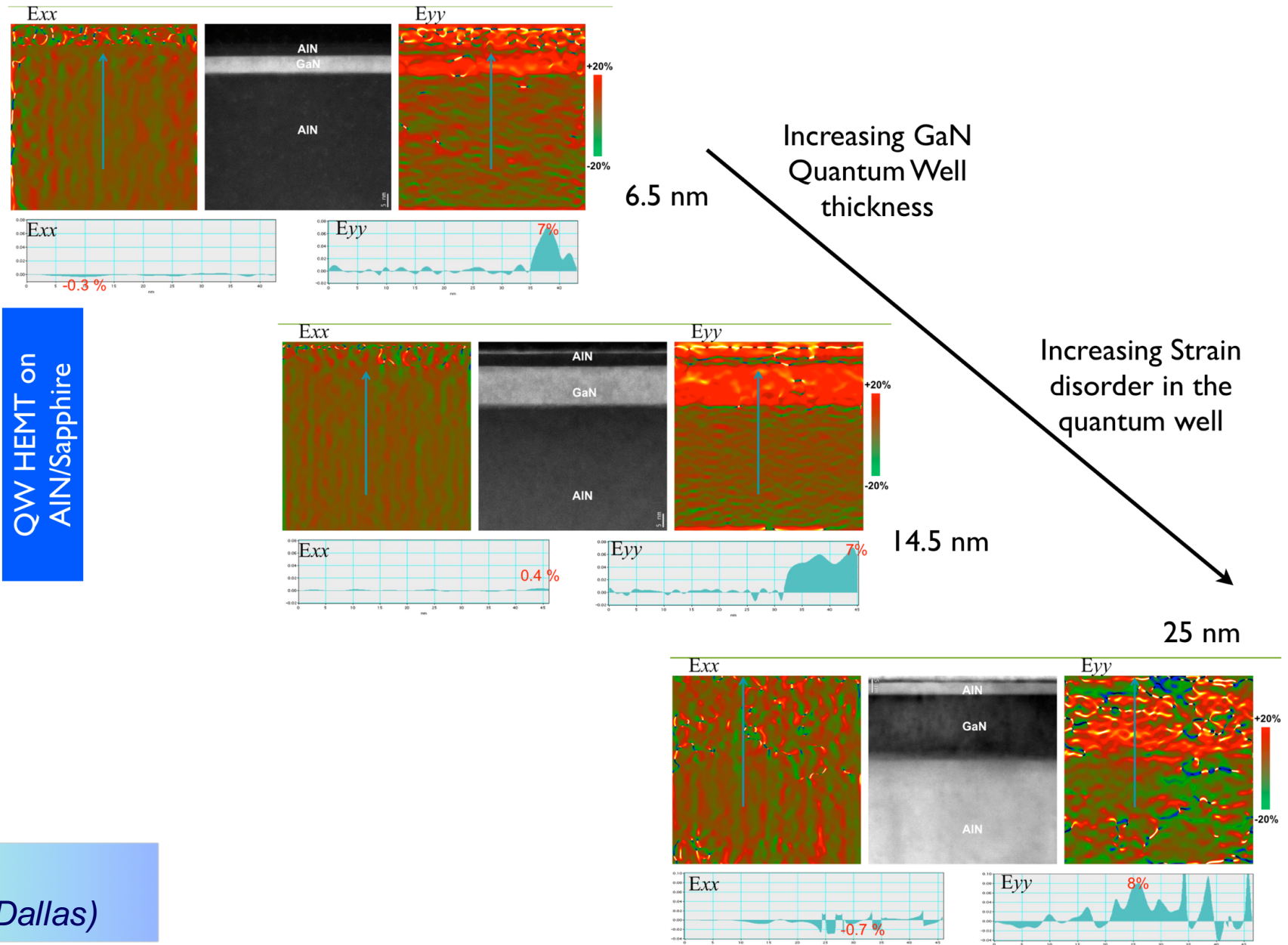


Increasing GaN Quantum Well thickness



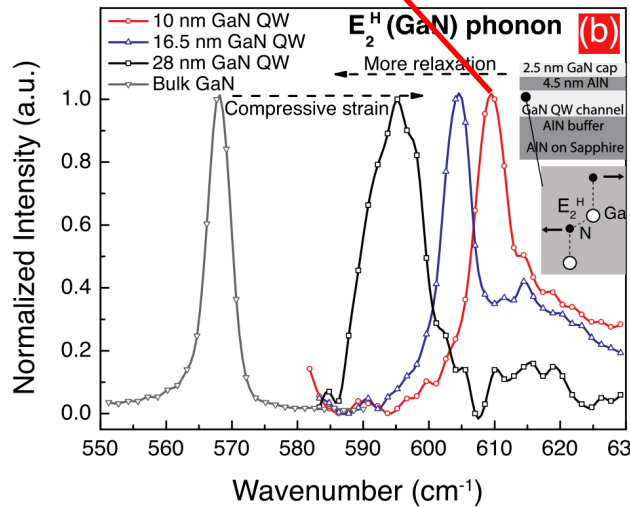
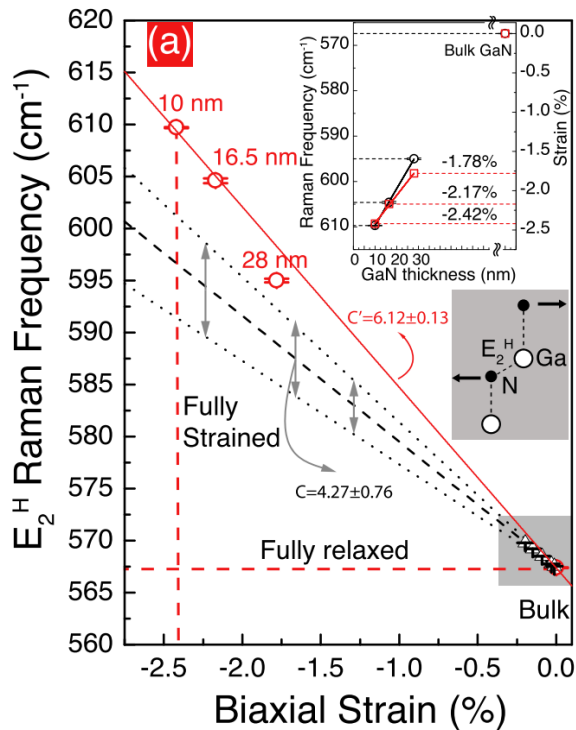
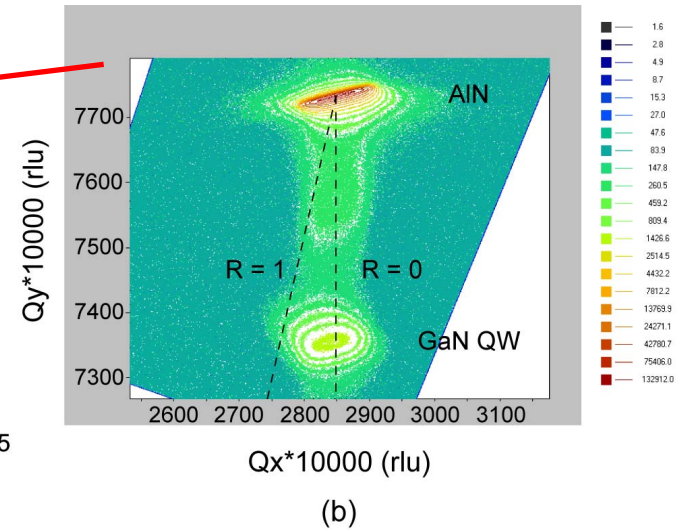
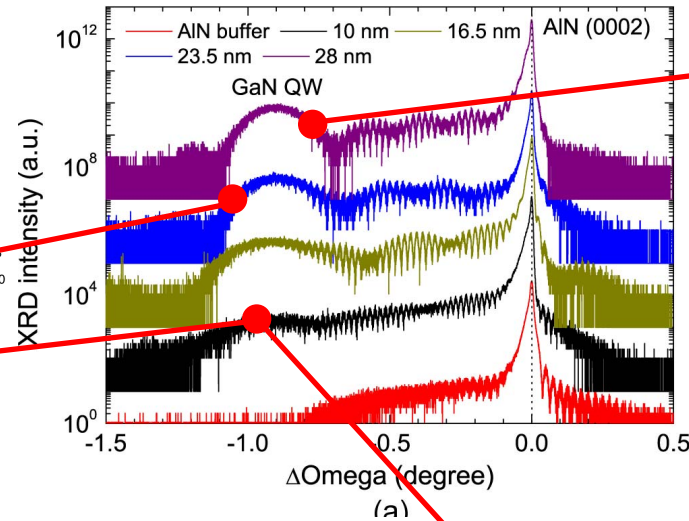
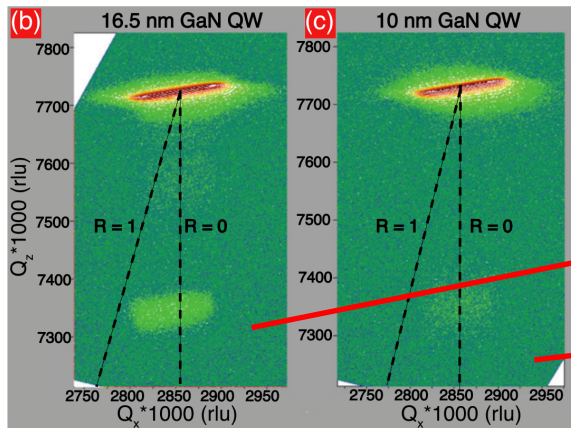
TEM courtesy: Moon Kim (UT Dallas)

Evolution of strain with GaN Q-Well thickness



TEM courtesy:
Moon Kim (UT Dallas)

Evolution of strain with GaN Q-Well thickness



APPLIED PHYSICS LETTERS 106, 041906 (2015)

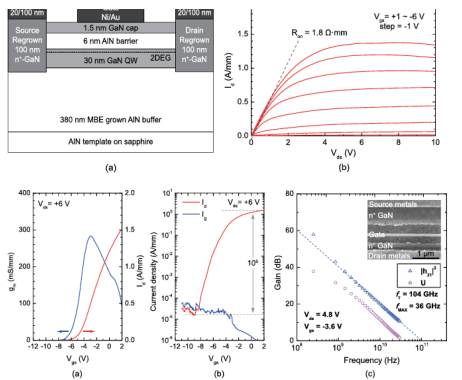


Dual optical marker Raman characterization of strained GaN-channels on AIN using AIN/GaN/AIN quantum wells and ¹⁵N isotopes

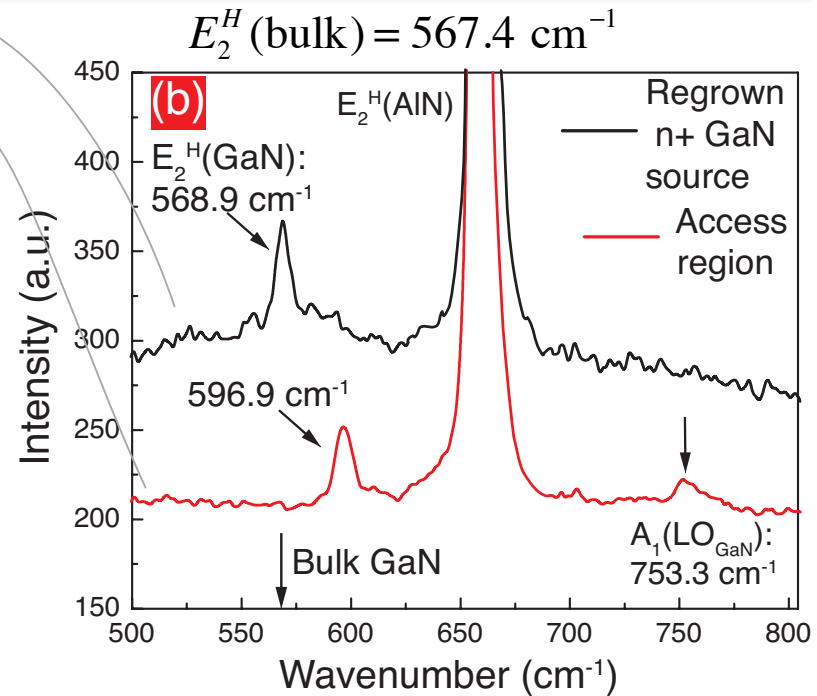
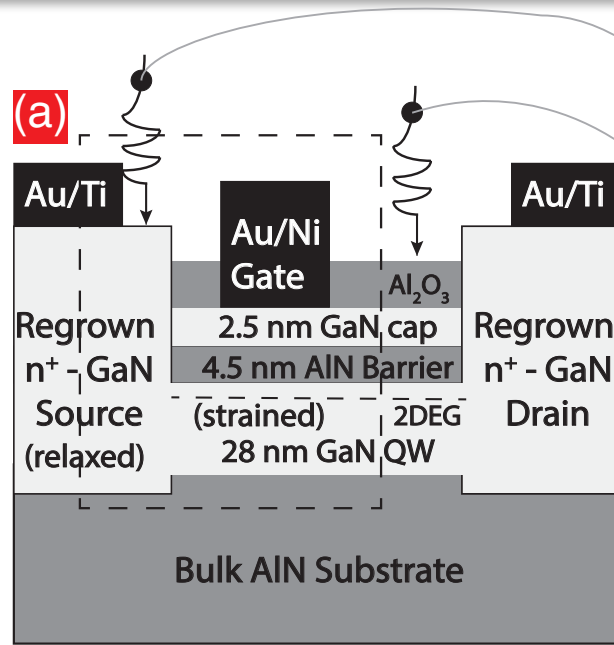
Meng Qi,¹ Guowang Li,¹ Vladimir Protasenko,¹ Pei Zhao,¹ Jai Verma,¹ Bo Song,¹ Satyaki Ganguly,¹ Mingda Zhu,¹ Zongyang Hu,¹ Xiaodong Yan,¹ Alexander Mintairov,^{1,2} Huihui Grace Xing,¹ and Debdeep Jena^{1,a)}

Strain distribution in Regrown contact HEMTs

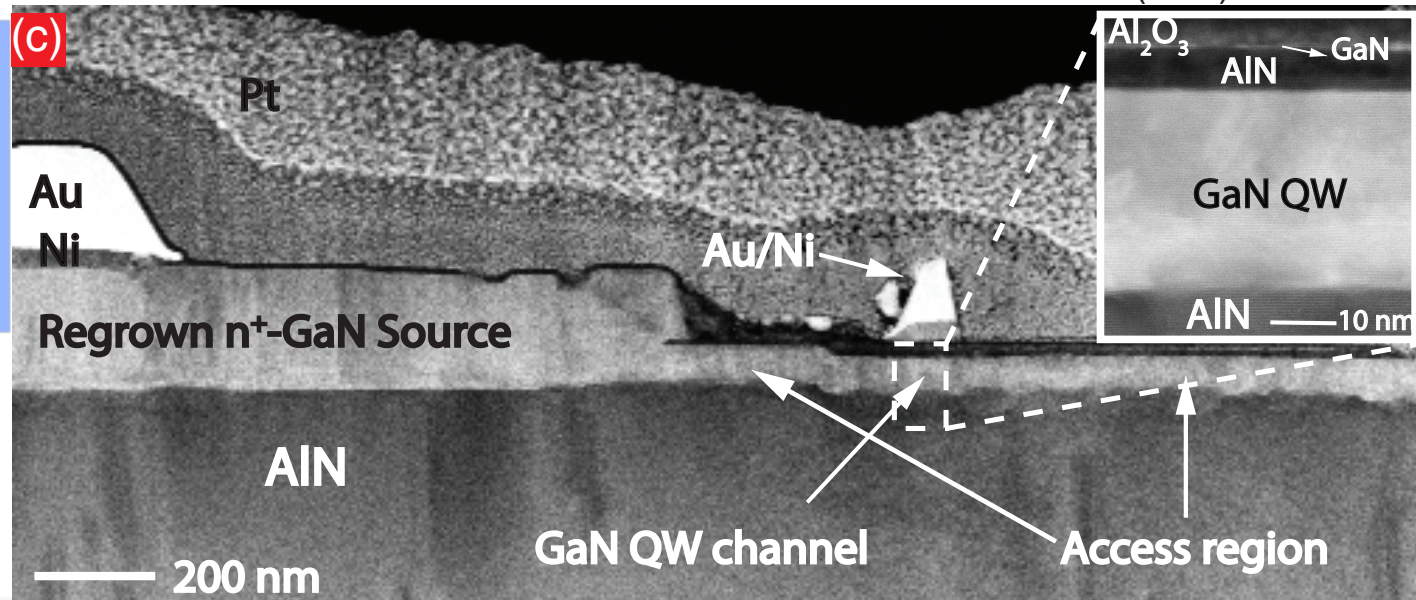
APPLIED PHYSICS LETTERS 104, 193506 (2014)



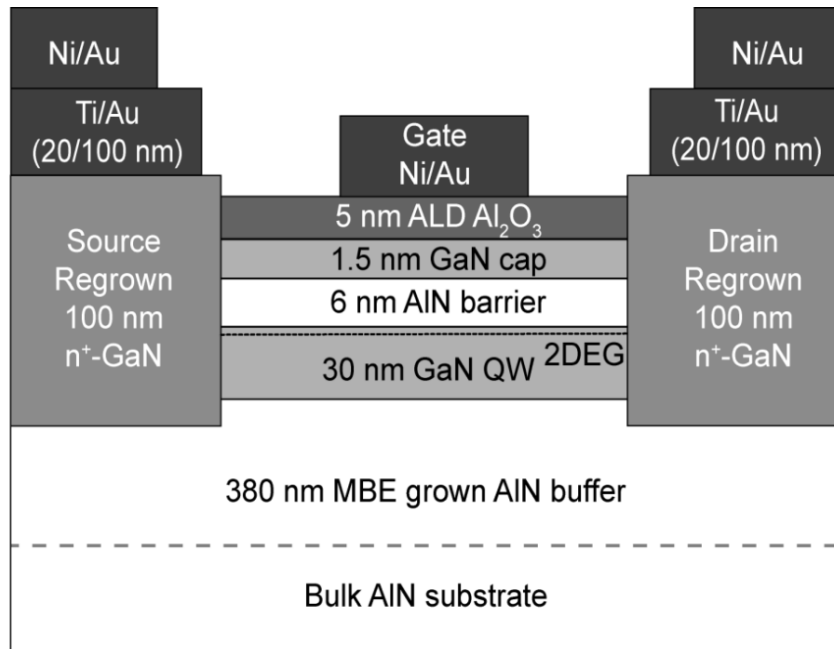
G. Li, et al



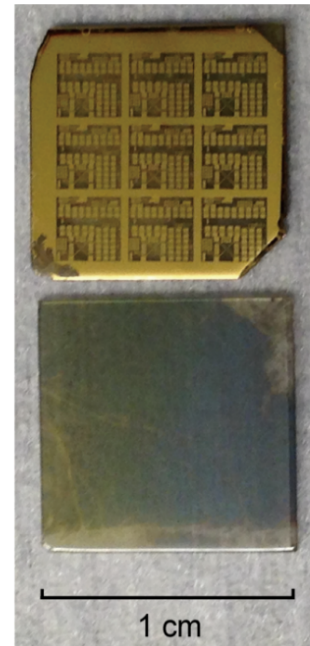
- Strain probing in lateral direction.
- Strained GaN in QW access region.
- Large relaxation in the regrown n+ GaN region.



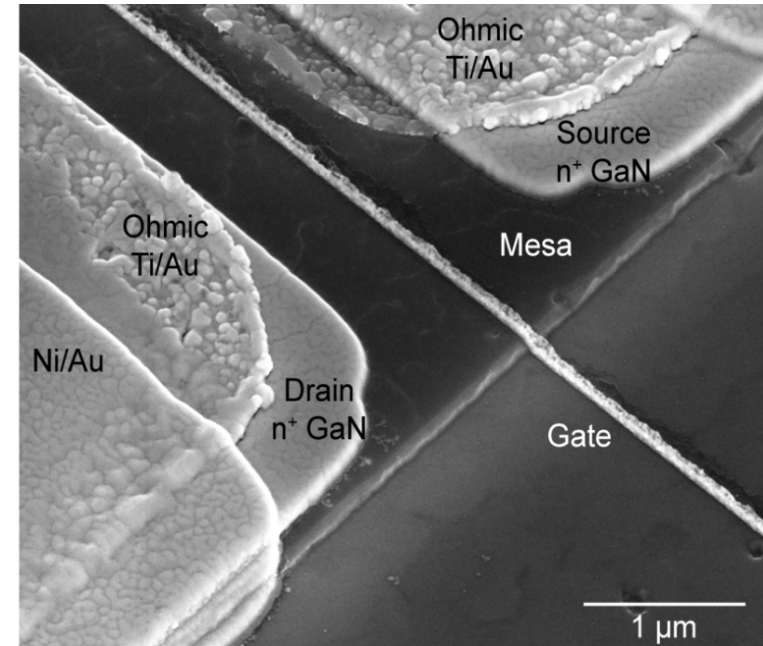
First strained GaN Quantum-Well HEMTs on bulk AlN



(a)



(b)



(c)

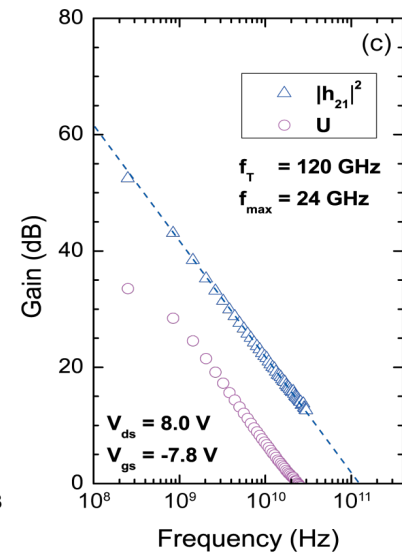
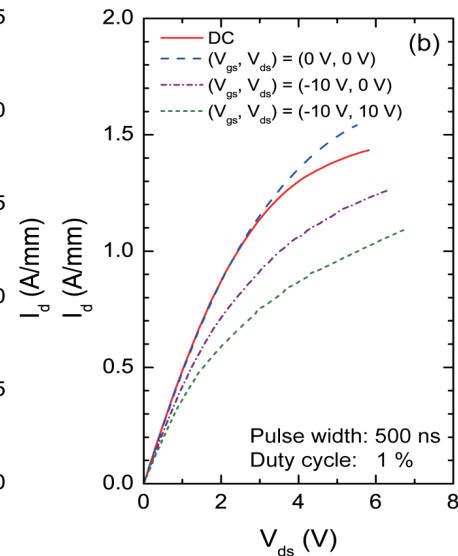
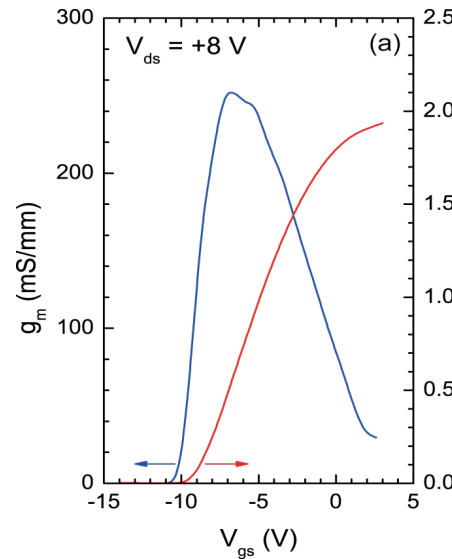
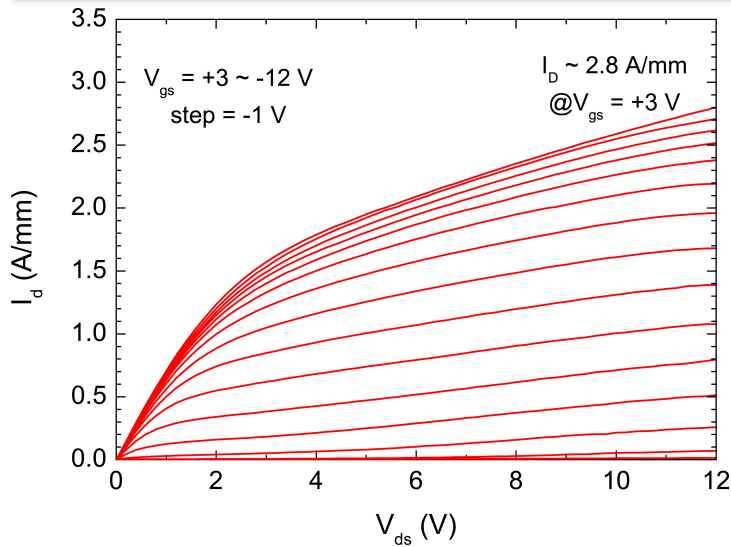
(a) Cross-sectional schematic of the AlN/GaN/GaN heterostructure FETs.

(b) Images of a grown and processed sample (top), and a bulk AlN substrate (down).

(c) SEM image of a finished device.

- We transferred everything we learnt from growth and processing on AlN-on-sapphire templates
- First demonstration of strained GaN QWs on bulk AlN substrates with MBE regrown contacts
- Latest 2DEG mobilities are up to $\sim 600 \text{ cm}^2/\text{Vs}$, but devices fabricated on $\sim 200 \text{ cm}^2/\text{Vs}$ samples

RF results of strained GaN QW HEMTs on bulk AlN

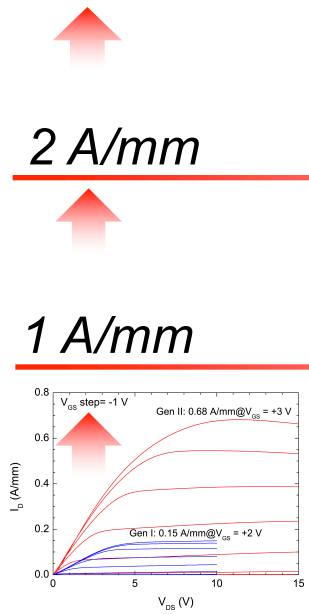


RF performance w/o passivation:

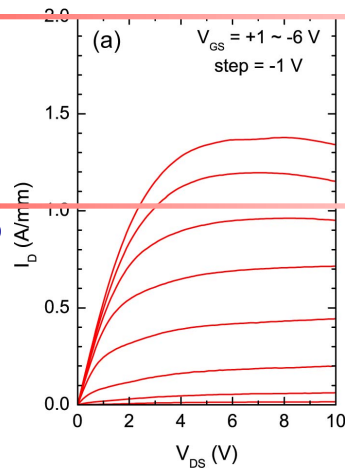
- (a) Transfer characteristics of the FETs with 65-nm-long gates in linear scale.
- (b) Pulsed I - V measurements with a 500-ns pulse width and a 0.5-ms period.
- (c) Small-signal RF characteristics of the device showing current gain and unilateral gain $f_T / f_{max} = 120/24$ GHz.

- Strained GaN QW HEMTs on bulk AlN exhibit current drives ~ 2.8 A/mm
- RF cutoff frequencies of 120 GHz on ~ 1.9 A/mm 65 nm gate devices
- Device characteristics beat those on sapphire significantly

GaN pHEMTs (Gen I \rightarrow II \rightarrow III \rightarrow IV)

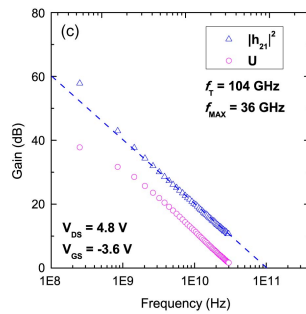
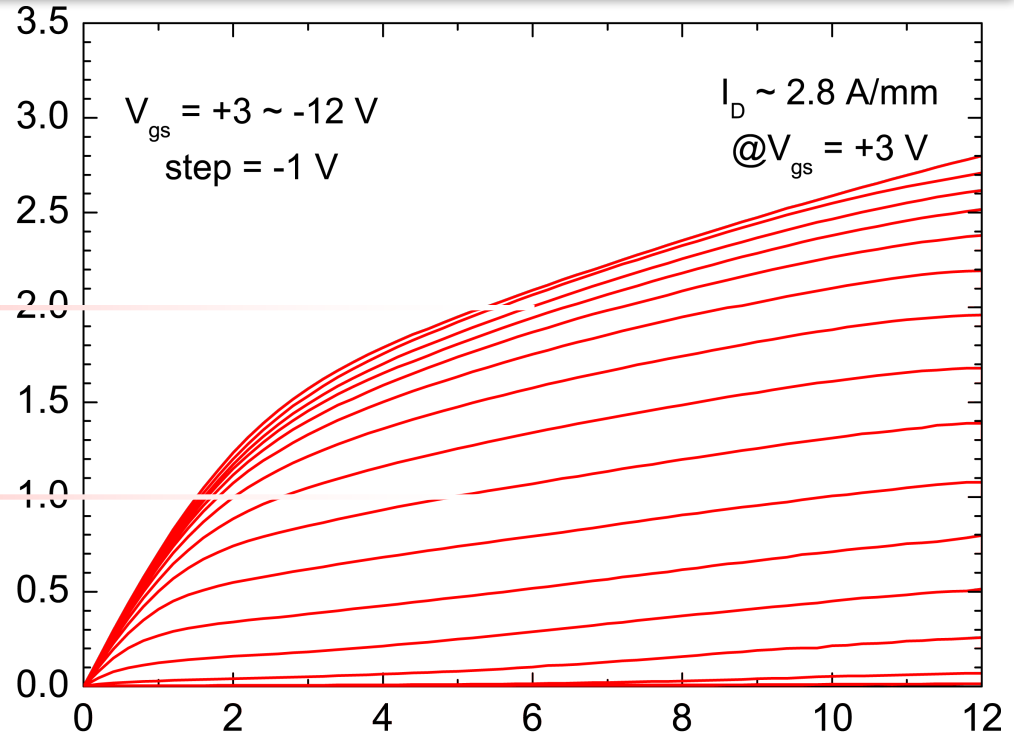


scalin
g

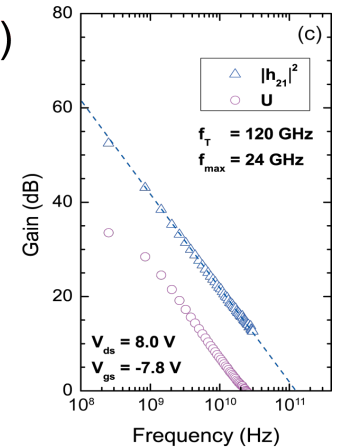


AlN substrate.s

I_d (A/mm)



V_{ds} (V)



Gen I \rightarrow Gen II

\rightarrow Gen III

\rightarrow Gen IV

Thermal Conductivity of Compound Semiconductors

$$\theta_a^2 = \frac{5\hbar^2 \int_0^{\omega_D} \omega^2 g(\omega) d\omega}{3k_B^2 \int_0^{\omega_D} g(\omega) d\omega}$$

Effective Debye Temperature

$$\kappa_L = \frac{k_B}{2\pi^2 v} \left(\frac{k_B T}{\hbar} \right)^3 \int_0^{\theta_D/T} \frac{x^4 e^x}{\tau_C^{-1} (e^x - 1)^2} dx$$

Lattice Thermal Conductivity

$$\kappa = \kappa_1 + \kappa_2$$

$$\gamma = - \frac{d \ln \omega_i}{d \ln V}$$

Grüneisen Parameter

$$\kappa_1 = \frac{1}{3} CT^3 \int_0^{\theta/T} \frac{\tau_c(x) x^4 e^x}{(e^x - 1)^2} dx \quad \kappa_2 = \frac{1}{3} CT^3 \frac{\left[\int_0^{\theta/T} \frac{\tau_c(x) x^4 e^x}{\tau_N(x) (e^x - 1)^2} dx \right]^2}{\int_0^{\theta_L/T} \frac{\tau_c(x) x^4 e^x}{\tau_N(x) \tau_R(x) (e^x - 1)^2} dx}$$

$$\kappa = A \cdot \frac{M_a \theta_a^3 \delta}{\gamma^2 T}$$

$$\kappa = A \cdot \frac{\bar{M} \theta^3 \delta}{\gamma^2 T n^{2/3}}$$

Criteria for high thermal conductivity semiconductors

- high Debye temperature,
- small Grüneisen parameter, and
- small n (simple crystal structure)

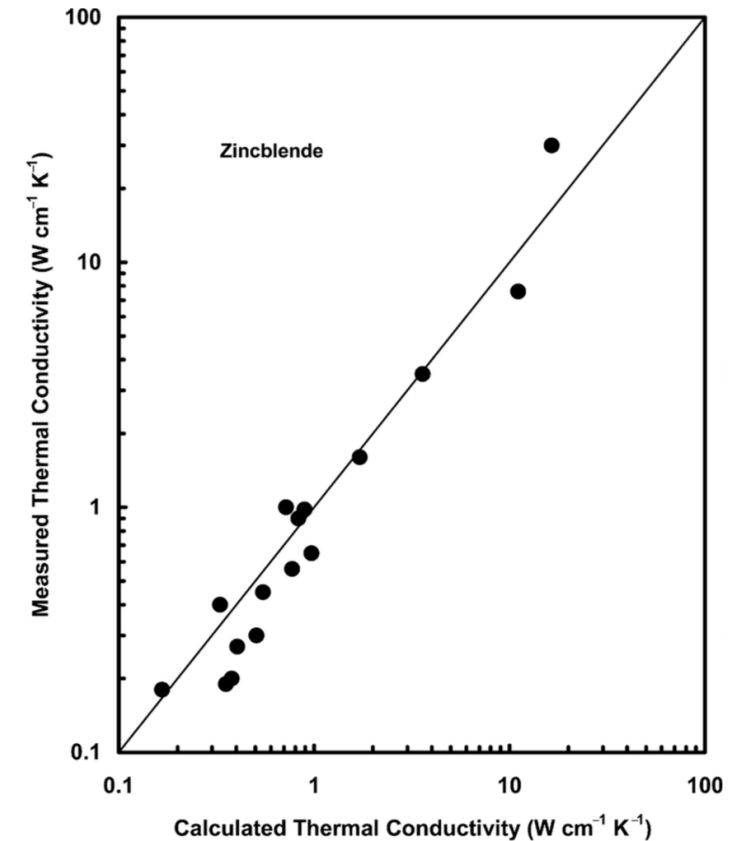
(Slack)

$$A = 3.04 \times 10^{-8}$$

Thermal Conductivity of Compound Semiconductors

Table 2.2. Calculated and experimental room-temperature thermal conductivity of several zincblende and diamond structure ($n = 2$) compounds. θ_a = high-temperature Debye temperature of the acoustic phonon branch; γ = high-temperature Grüneisen constant; δ^3 = volume per atom; M = average atomic mass; κ_{calc} = calculated thermal conductivity from Eq. (2.13); κ_{exp} = measured thermal conductivity.

Element/ Compound	θ_a (K)	γ	δ (Å)	M (amu)	κ_{calc} (Wcm ⁻¹ K ⁻¹)	κ_{exp} (Wcm ⁻¹ K ⁻¹)
C	1450	0.75	1.78	12.01	16.4	30
Si	395	1.06	2.71	28.08	1.71	1.66
Ge	235	1.06	2.82	72.59	0.97	0.65
BN	1200	0.7	1.81	12.41	11.05	7.6
BP	670	0.75	2.27	20.89	3.59	3.5
BAs	404	0.75	2.39	42.87	1.70	
AlP	381	0.75	2.73	28.98	1.10	
AlAs	270	0.66	2.83	50.95	0.89	0.98
AlSb	210	0.6	3.07	74.37	0.77	0.56
GaP	275	0.75	2.73	50.35	0.72	1.00
GaAs	220	0.75	2.83	72.32	0.55	0.45
GaSb	165	0.75	3.05	95.73	0.33	0.4
InP	220	0.6	2.94	72.90	0.83	0.93
InAs	165	0.57	3.03	94.87	0.51	0.3
InSb	135	0.56	3.24	118.29	0.38	0.2
ZnS	230	0.75	2.71	48.72	0.40	0.27
ZnSe	190	0.75	2.84	72.17	0.35	0.19
ZnTe	155	0.97	3.05	96.49	0.17	0.18
CdSe	130	0.6	3.06	95.68	0.23	
CdTe	120	0.52	3.23	120.00	0.296	0.075

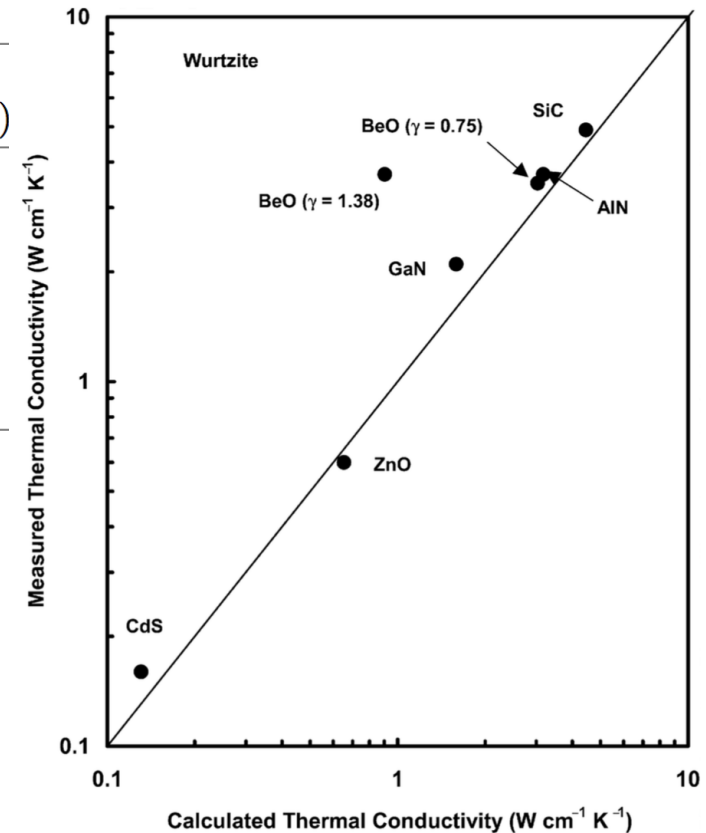


(Slack)

Thermal Conductivity of Compound Semiconductors

Table 2.3. Calculated and experimental room-temperature thermal conductivity of several wurtzite ($n = 4$) compounds. θ_a = high-temperature Debye temperature of the acoustic phonon branch; γ = high-temperature Grüneisen constant; δ^3 = volume per atom; M = average atomic mass; κ_{calc} = calculated thermal conductivity from equation (2.13); κ_{exp} = measured thermal conductivity.

Compound	θ_a (K)	γ	δ (Å)	M (amu)	κ_{calc} (Wcm ⁻¹ K ⁻¹)	κ_{exp} (Wcm ⁻¹ K ⁻¹)
SiC	740	0.75	2.18	20.0	4.45	4.9
AlN	620	0.7	2.18	20.49	3.03	3.5
GaN	390	0.7	2.25	41.87	1.59	2.1
ZnO	303	0.75	2.29	40.69	0.65	0.6
BeO	809	1.38/0.75	1.90	12.51	0.90/3.17	3.7
CdS	135	0.75	2.92	72.23	0.13	0.16



(Slack)

High Thermal Conductivity Semiconductors

boundary

Point defects

Intrinsic Umklapp

$$\kappa_L = \frac{k_B}{2\pi^2 v} \left(\frac{k_B T}{\hbar} \right)^3 \int_0^{\theta_D/T} \frac{x^4 e^x}{\tau_C^{-1} (e^x - 1)^2} dx$$

$$\tau_C^{-1} = \frac{v}{L} + A\omega^4 + B\omega^2 T \exp\left(-\frac{\theta_D}{3T}\right)$$

Phonon Scattering Rate

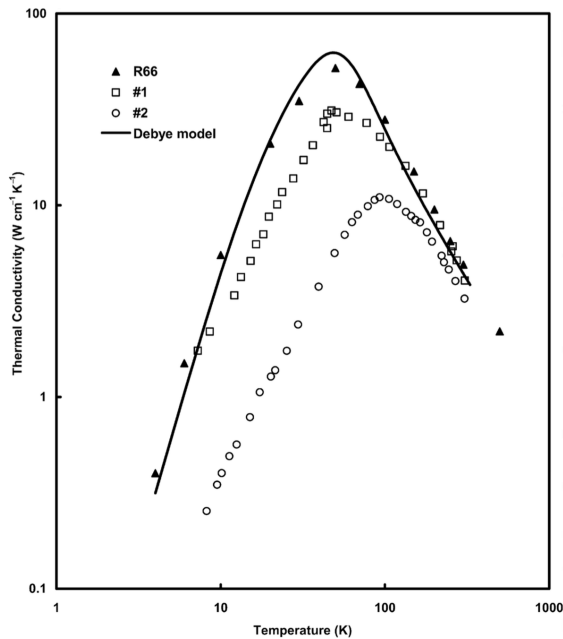


Fig. 2.7. Thermal conductivity of various single crystals of SiC. R66: pure crystal Slack [65]; #1 and #2: crystals [67] with electron concentrations of 3.5×10^{16} and $2.9 \times 10^{18} \text{ cm}^{-3}$, respectively.

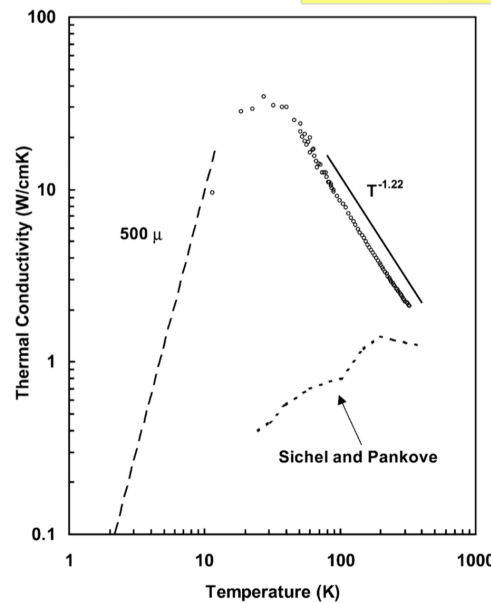


Fig. 2.8. Thermal conductivity of GaN as a function of temperature. Open points: data of Slack et al. [74]; lower dotted line: results of Sichel and Pankove [71]. Dashed line shows low-temperature boundary limit, assuming a crystal dimension of 50 microns.

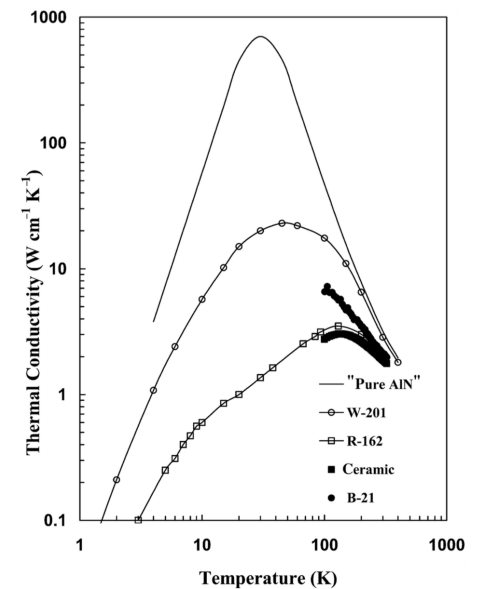


Fig. 2.9. Thermal conductivity of single-crystal AlN. "Pure AlN" is the calculated result for a crystal containing no impurities; samples W-201, R-162, and B-21 are single crystals with varying amounts of oxygen concentrations; see text. A ceramic sample is shown for comparison.

Electrically active defects have stronger effect on thermal conductivity than neutral impurities
 Example: Oxygen significantly degrades the thermal conductivity of AlN, because it creates Aluminum vacancies, that have large $dM/M!$

(Slack)

Thermal Conductivity of Layered Semiconductors

Table 2.6. Thermal conductivity of graphite and BN in the basal plane (xy) and perpendicular to the c -axis (z).

Compound	n	θ_a (K)	γ	δ (Å)	M (amu)	κ_{calc} (Wcm ⁻¹ K ⁻¹)	κ_{exp} (Wcm ⁻¹ K ⁻¹)
Graphite- xy	4	1562	0.75	2.05	12.01	27	10–20
Graphite- z	4	818	2	2.05	12.01	0.5	0.06
BN- xy	4	1442	0.75	2.05	12.40	22	2–3
BN- z	4	755	2	2.05	12.4	0.4	~0.02

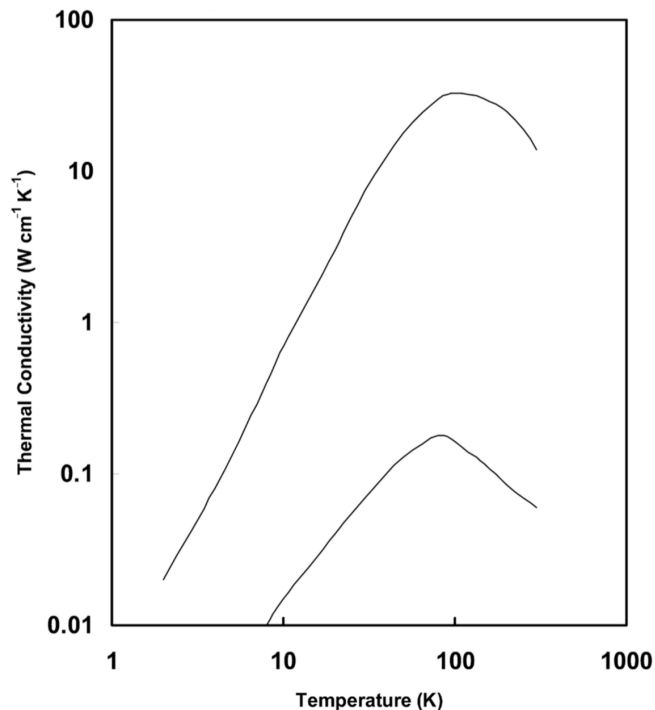


Fig. 2.6. Thermal conductivity of highly oriented graphite parallel (upper curve) and perpendicular (lower curve) to the basal plane.

(Slack)

Thermal Conductivity: Isotope Effects

Table 2.7. Percentage Increase in Room-Temperature Thermal Conductivity due to the Isotope Effect in Some Group IV and Group III–V semiconductors.

Element/ Compound	$\Delta\kappa/\kappa^*$ (%)	$\Delta\kappa/\kappa^{**}$ (%)	$\Delta\kappa/\kappa^{***}$ (%)
Ge	30	28	30
Si		12	60
C		23	35–45
SiC		36	
GaN		5	
BN		125	

* Model [59].

** Model [60].

*** Experimental results.

(Slack)

Compound Semiconductor Crystal Growth

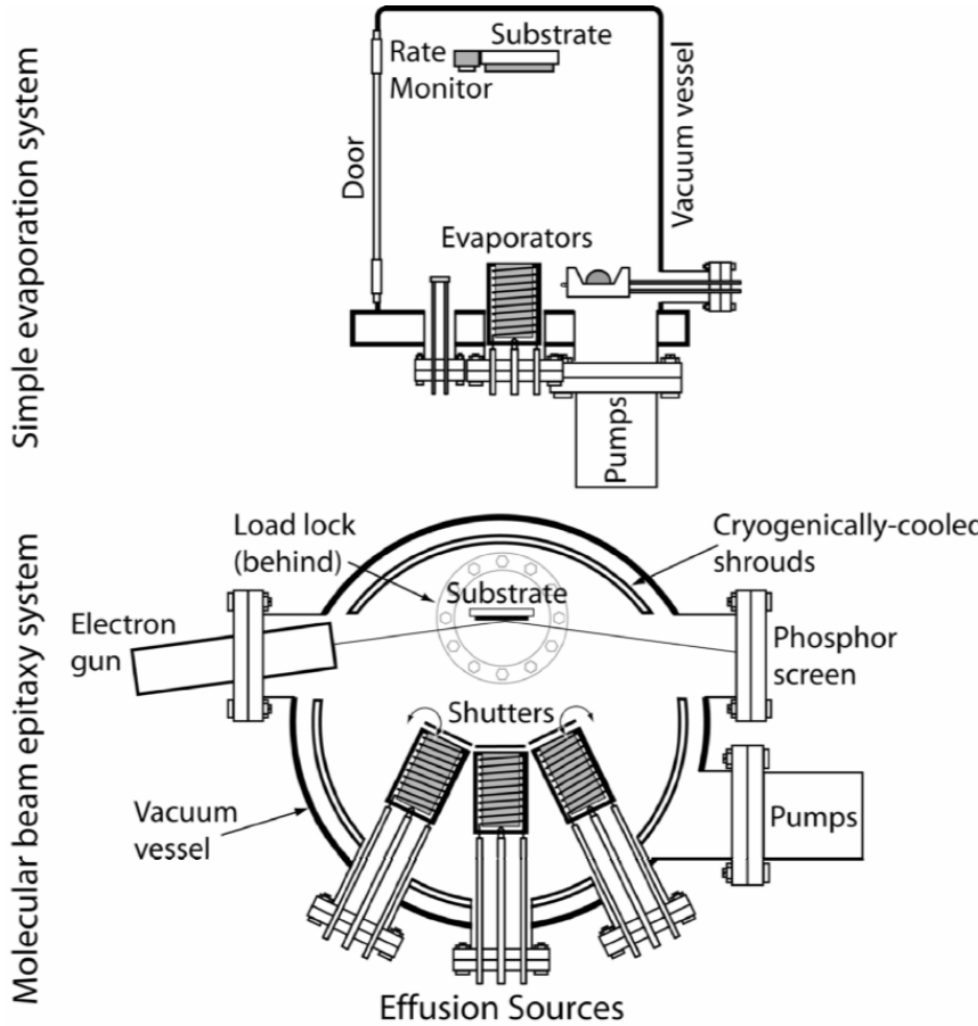


Figure 11.1: Typical evaporation system geometries. Both schematics are simplified and leave out typical components. However, the major parts are indicated. The major difference for the molecular beam epitaxy system is the increased emphasis on ultimate vacuum performance, often four to five orders of magnitude better.

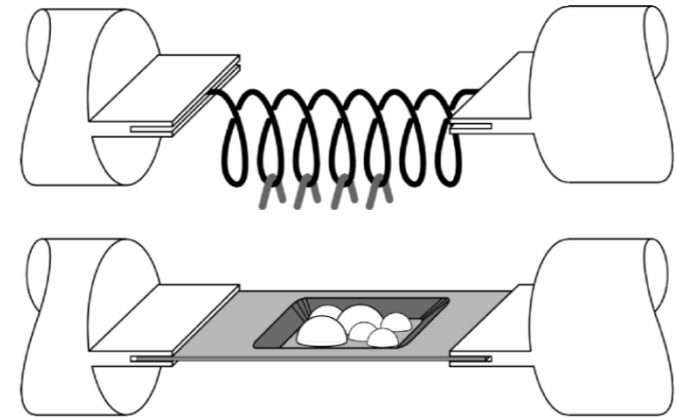


Figure 11.2: Open source evaporation boats (lower) and wire coils (upper figure). Wire coils are generally made of W although other low vapor pressure systems also work. Open boats are made in a wide variety of shapes and of a wide variety of materials including Ta, W, graphite, and other materials.

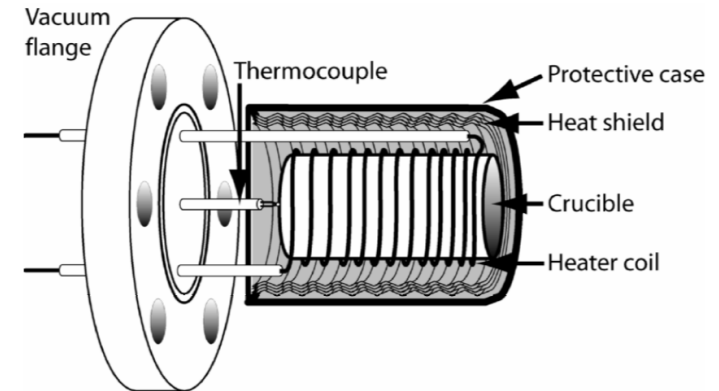


Figure 11.3: A simplified schematic sketch of a typical effusion cell. Omitted are the top cap that protects the heater windings from the evaporant as well as improving the black body environment of the crucible, the support clamps and details of the power feedthroughs, etc. The thermocouple junction is pressed gently against the base of the crucible but the black body environment assures an accurate temperature measurement. Note that the heater coils are more closely spaced near the front of the crucible to compensate for greater heat loss in that portion of the cell.

Compound Semiconductor Growth

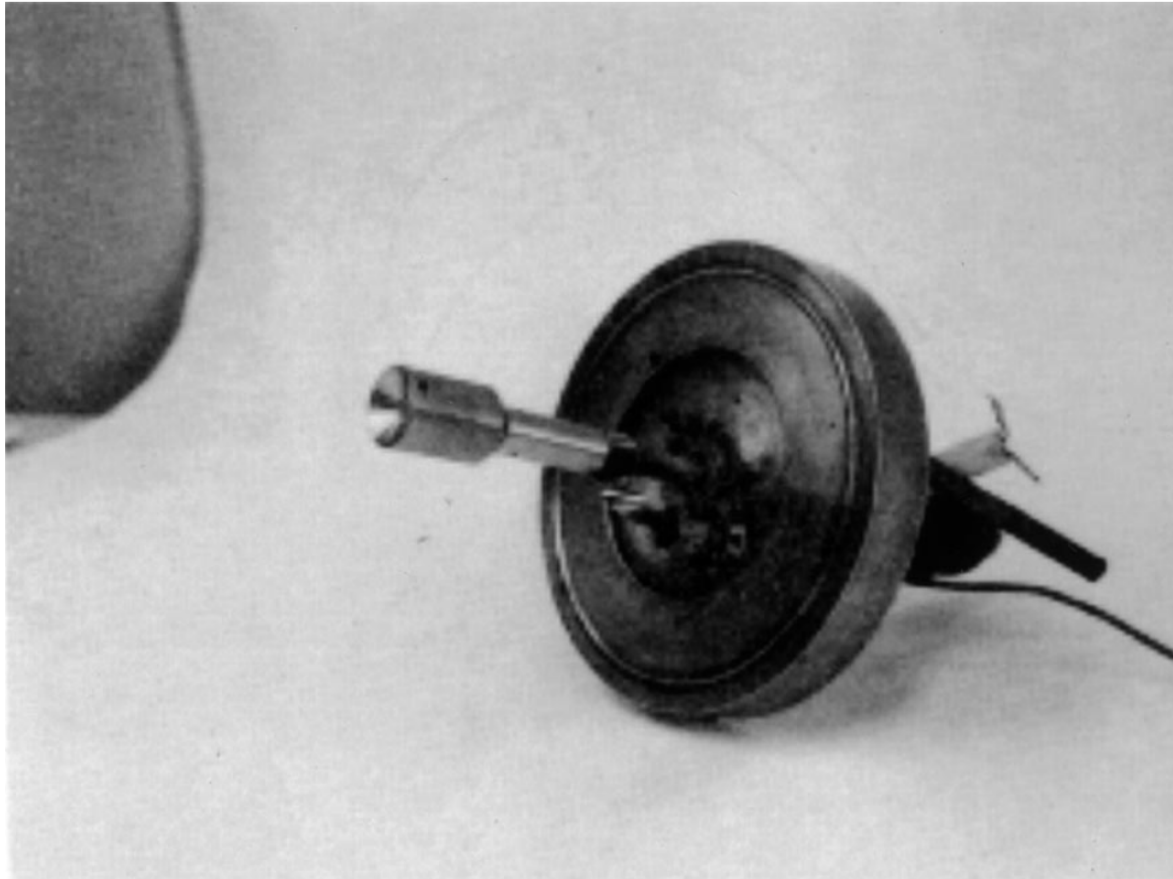


Fig. 3. Effusion cell used for Cs ion beam experiment for ion propulsion in 1964.

*Molecular Beam Epitaxy: Effusion cell design comes from space propulsion systems!
Ion beam sources were developed for altitude control, station keeping, and changing orbit.*

Compound Semiconductor Growth

Effusion Cells

PBN CRUCIBLE – (Alumina, PG & W also available). Each cell is designed to accept one specific size of crucible – see pages 8–11 for details.

STANDOFFS – Mo rods. Standoff length can be varied to suit the dimensions of a particular deposition system

POWER CONNECTORS – Screw-on (Amphenol-type) or push-on. Screw-on connectors supplied with mate.

THERMOCOUPLE CONNECTOR – Omega-type.

MOUNTING FLANGE – 2.75", 4.5", or 6.0" CF.

HEAT SHIELDING – Layered Tantalum.

THERMOCOUPLE (not shown) – Wide-area contact thermocouple. Standard: W5%Re vs W26%Re. Optional: W3%Re vs W25%Re; Chromel/Alumel; Pt/Rh.

FILAMENT (not shown) – Non-inductively wound Ta wire, with PBN insulators. Exception: The High Temperature Cell (W wire, self-supported).

Water cooling is available for cells on 4.5" or 6.0" flanges. This capability is provided via a 3mm dia. seamless stainless steel coil.

Fig. 4. Effusion cell used for molecular beam epitaxy (photograph courtesy of EPI).

Molecular Beam Sources

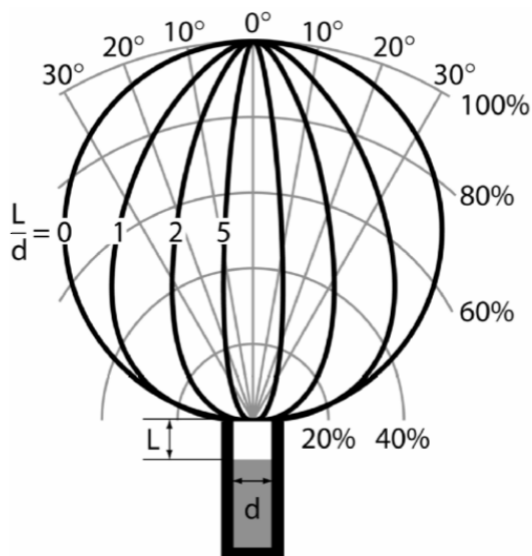


Figure 11.4: The flux distribution of atoms emitted by an effusion cell as a function of the depth in the cell of the evaporant surface relative to the diameter of the surface. [1]. Reprinted from Prog. Crystal Growth and Characterization, Vol 2, Luscher, P.E. and Collins, D.M.; “Design considerations for molecular beam epitaxy systems”, pp 15-32, Copyright 1979, with permission from Elsevier.

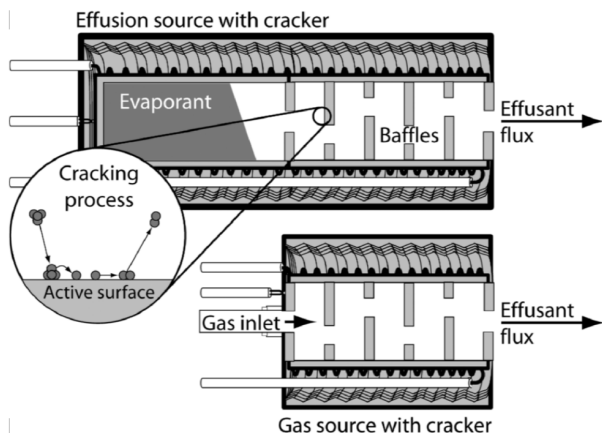


Figure 11.6: Cracking effusion sources for either a solid/liquid source (top) and for a gas source (bottom). The only difference is how the vapor to be cracked is supplied to the baffle section. Normal crackers typically have three baffles.

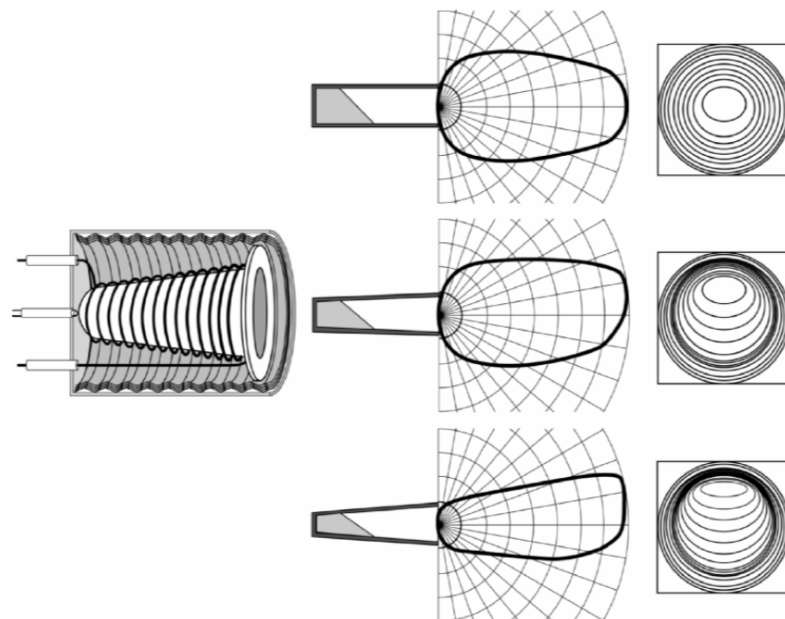


Figure 11.5: The flux patterns resulting from tapered effusion cells in both polar plots (center) and in flux contour plots (right). An isometric schematic shows the design of the tapered effusion cell with a flanged top to reduce creep of effusant out of the cell. Figure redrawn with permission from portions of Figure 3 in Tatyua Yamashita, Takashi Tomita, and Takeshi Sakurai, Japanese Journal of Applied Physics vol. 26 (1987), pages 1192-3. Copyright 1987, Institute of Pure and Applied Physics.

(Rockett, Chp 11)

Compound Semiconductor Growth

JOURNAL OF APPLIED PHYSICS

VOLUME 40, NUMBER 8

JULY 1969

Mean Adsorption Lifetimes and Activation Energies of Silver and Gold on Clean, Oxygenated, and Carburized Tungsten Surfaces

A. Y. CHO* AND C. D. HENDRICKS

Department of Electrical Engineering, University of Illinois, Urbana, Illinois 61801

(Received 29 July 1968; in final form 17 February 1969)

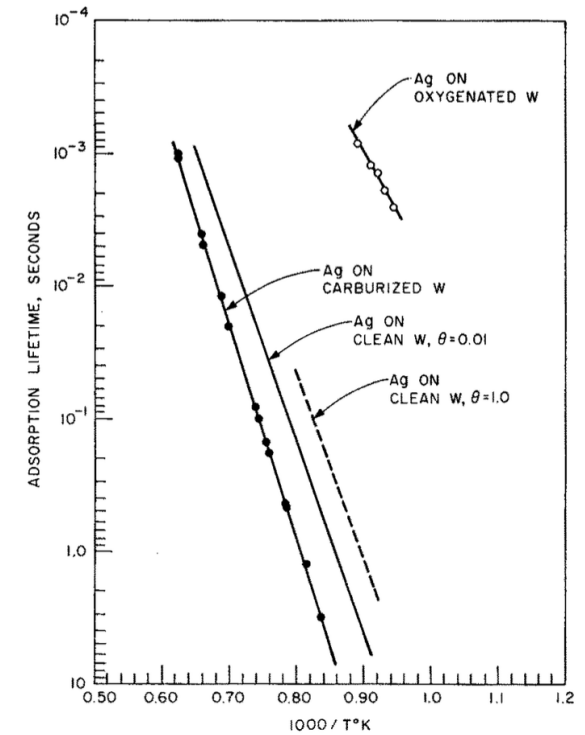
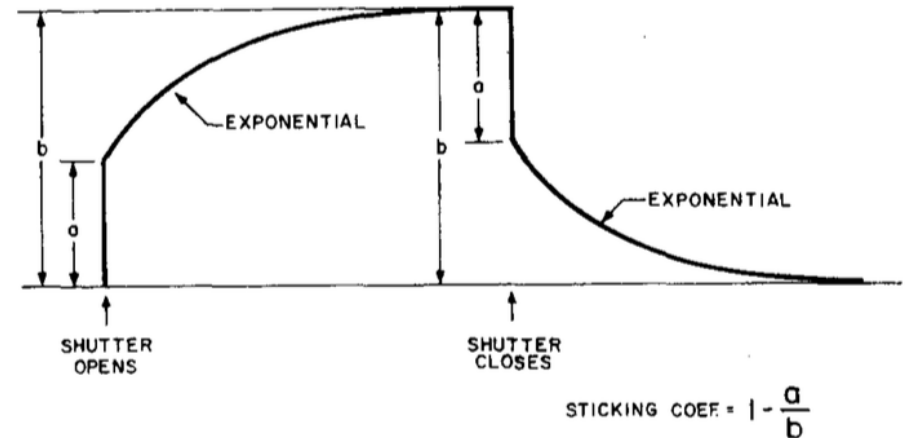
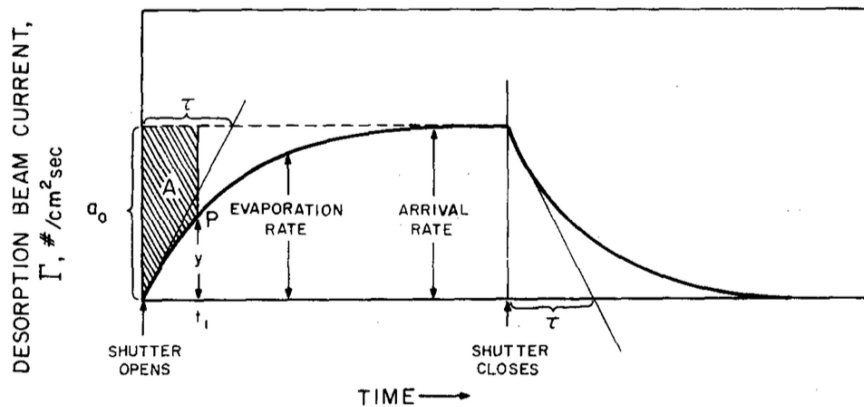
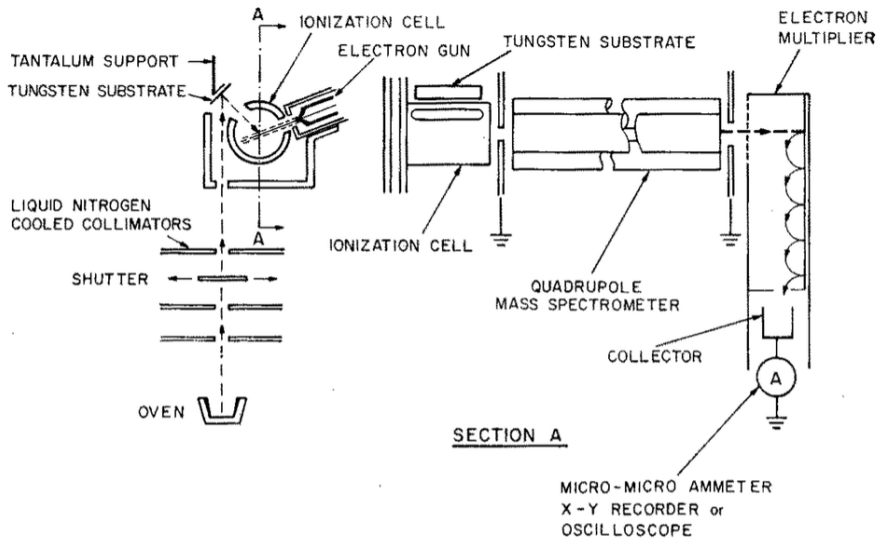


FIG. 9. The adsorption lifetime of silver on an oxygenated and a carburized tungsten surface.

Materials Sources and Detectors

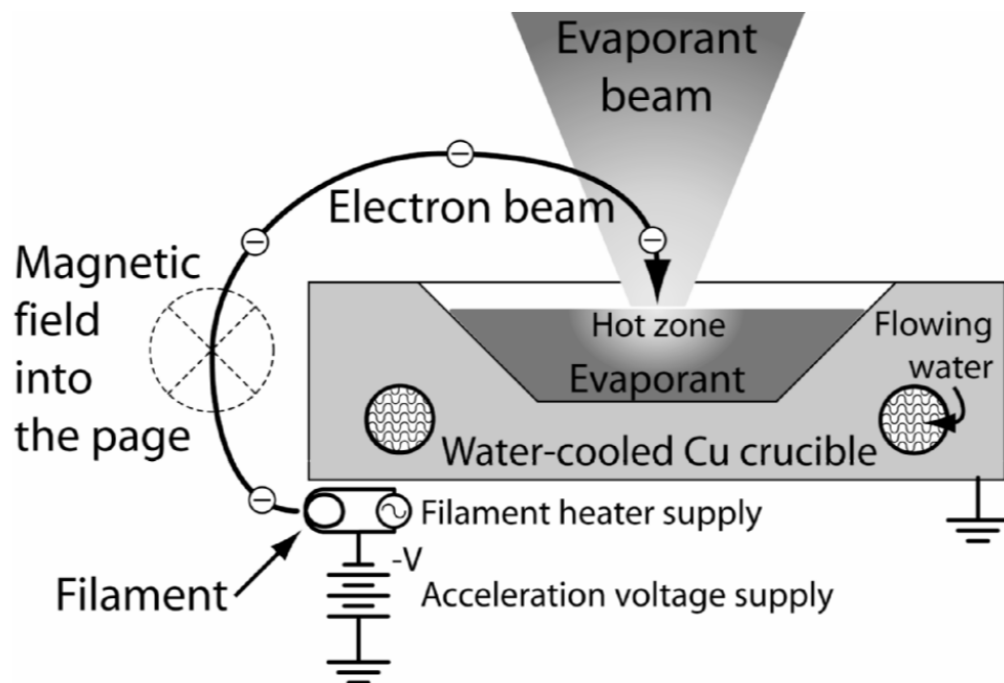


Figure 11.7: A schematic cross section of a typical electron beam evaporator. The magnetic field poles and consequently the magnetic field is out of the plane of the drawing. The high negative potential of the filament assists in electron emission and establishes the electron energy and point of impact on the crucible. Generally electrostatic deflection plates are added to sweep the electron beam into and out of the plane of the drawing.

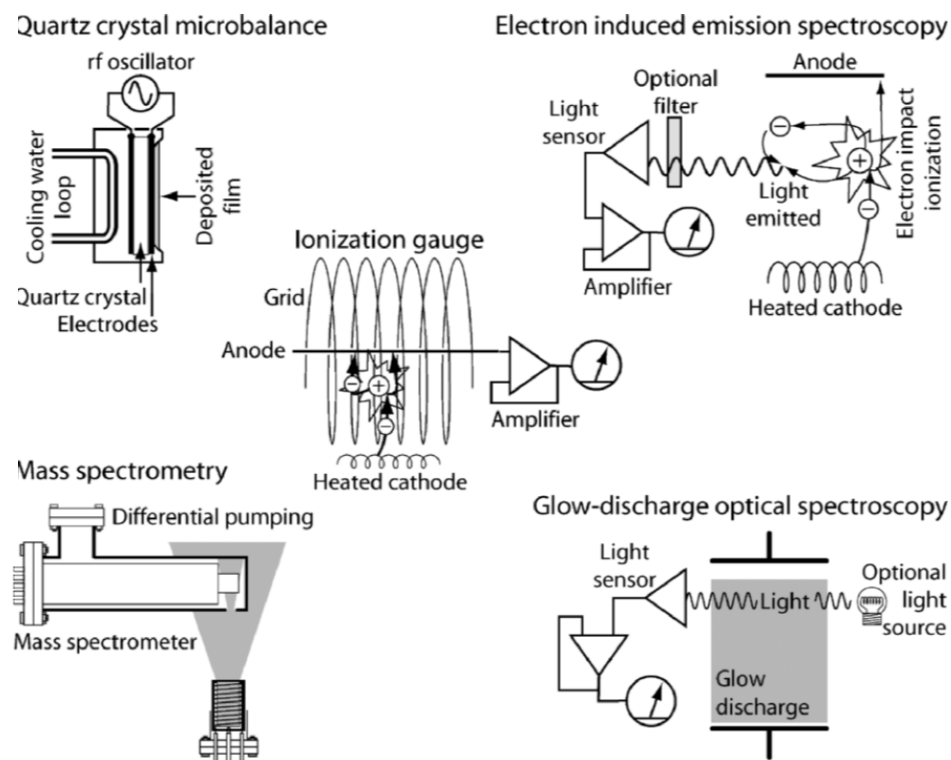


Figure 11.8: Five methods for monitoring concentrations of gas species. Many others exist.

(Rockett, Chp 11)

Tracking crystal growth in-situ using RHEED

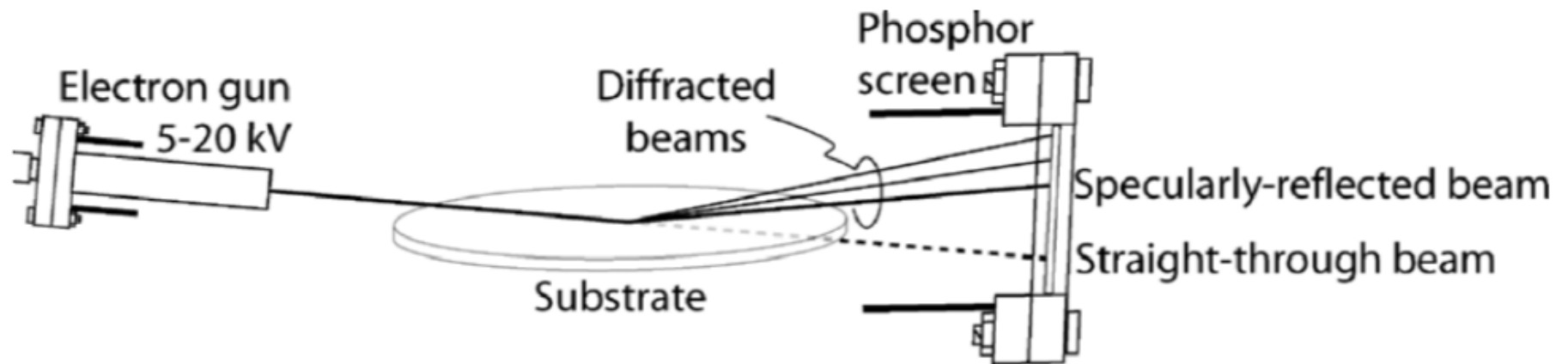


Figure 11.9: A schematic of the basic apparatus for conducting a RHEED experiment. Not shown is the remainder of the deposition system. This apparatus relies on at least high vacuum to protect the electron gun.

(Rockett, Chp 11)

Tracking crystal growth in-situ using RHEED

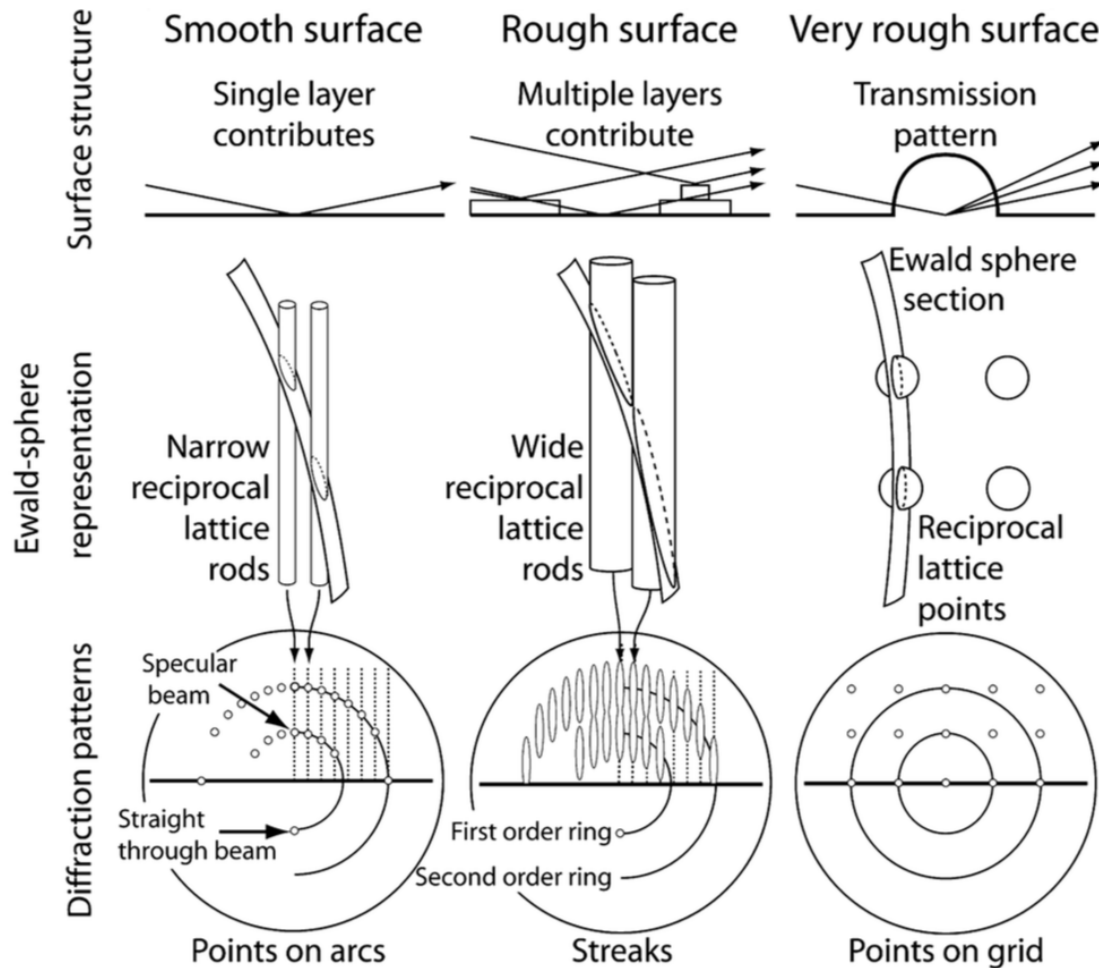


Figure 11.10: A schematic of the diffraction patterns in a RHEED experiment resulting from different surface structures. To simplify the drawing the broad rods of the rough surface are drawn as constant in width. Properly, for a two-level surface they have two non-zero Fourier coefficients and should oscillate as sine waves perpendicular to the surface. Therefore the rods should be wider and narrower along their length. See Figure 11.11 for a more accurate representation.

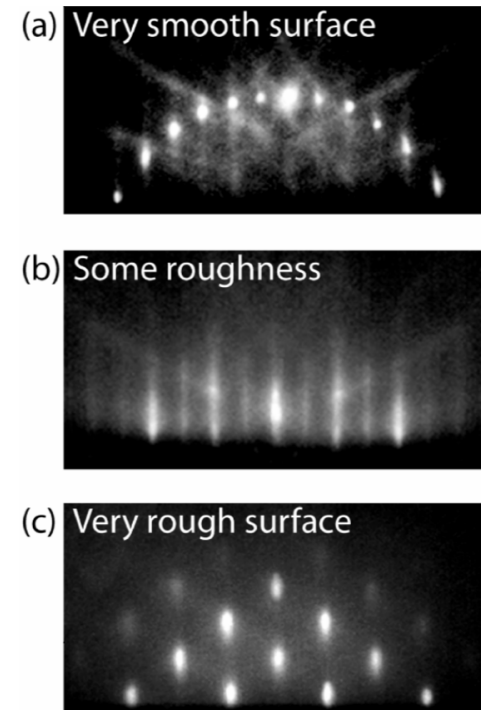


Figure 11.11: Examples of RHEED patterns obtained during non-equilibrium MBE growth of GeSn alloys. (a) Pattern for a very smooth surface as in left side of Figure 11.10 showing points on an arc. The diagonal streaks are multiple diffraction effects known as Kikuchi bands. (b) A pattern for a somewhat rougher surface corresponding to the middle drawing in Figure 11.10. Both (a) and (b) show a half-order reflection between the bright integer-order spots that results from the surface reconstruction. (b) Shows some evidence of residual Kikuchi bands. (c) A pattern for a very rough surface corresponding to the right hand drawing in Figure 11.10 where the electron beam is passing through three dimensional islands. Adapted with permission from O. Gurdal, P. Desjardins, J. R. A. Carlsson, N. Taylor, H. H. Radamson, J.-E. Sundgren, and J. E. Greene, *Journal of Applied Physics*, 83, 162 (1998). Copyright 1998, American Institute of Physics.

(Rockett, Chp 11)

Tracking crystal growth in-situ using RHEED

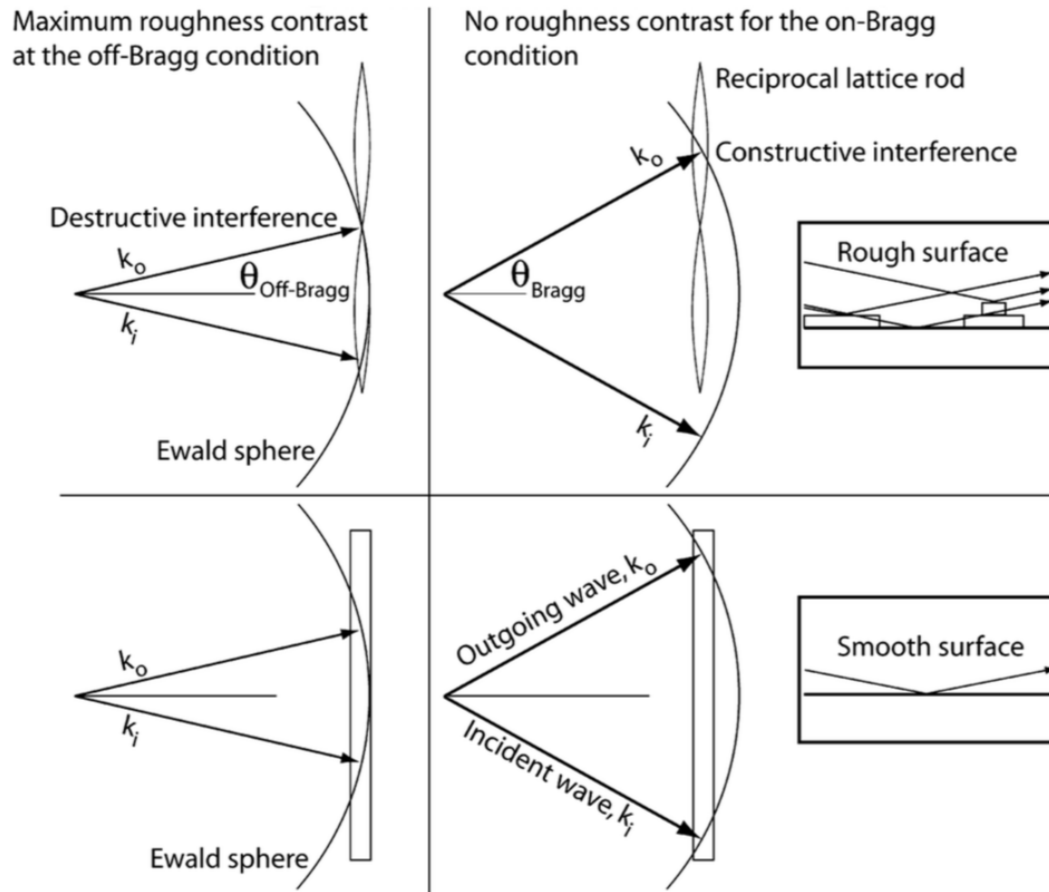


Figure 11.12: RHEED diffraction Ewald sphere constructions for the on-Bragg and off-Bragg conditions. Note that in the on-Bragg condition there is no difference in the diffracted intensity for the rough and smooth surfaces while for the off-Bragg condition alternate layers of the film interfere destructively. Therefore there is strong contrast for the intensity from rough and smooth surfaces. Refer to Figure 4.6 and related discussion for background on this construction.

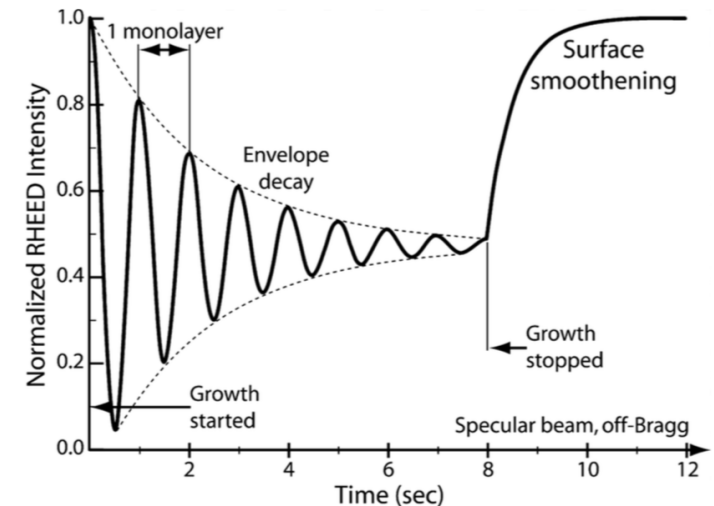


Figure 11.13: A typical example of (hypothetical) RHEED oscillation data during MBE growth at a rate of 1 monolayer/sec. Note that the surface is roughening during the 8 monolayers of deposition as shown by the decay of the oscillations but upon termination of growth the surface becomes smooth and the intensity recovers. To obtain this type of behavior the experiment is configured in the off-Bragg condition so that alternate monolayers of the film interfere destructively. This type of oscillation is observed in the intensity of all reflected and diffracted beams. The most intense is the specularly-reflected beam so that is the one normally used.

(Rockett, Chp 11)

Compound Semiconductor Growth

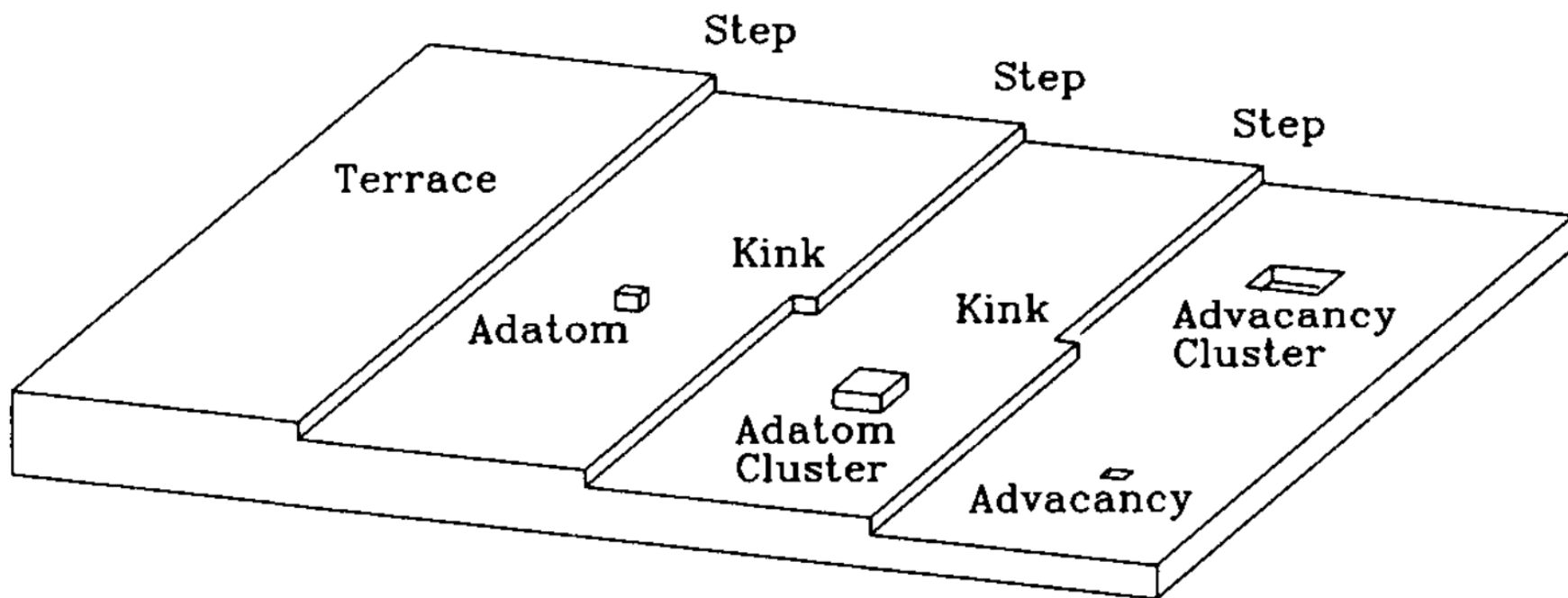


Figure 6.1: Terraces, ledges, kinks, adatoms, adatom clusters, advacancies, and advacancy clusters on a Kossel crystal.

(Rockett chp 10,11, Tsao)

Compound Semiconductor Growth

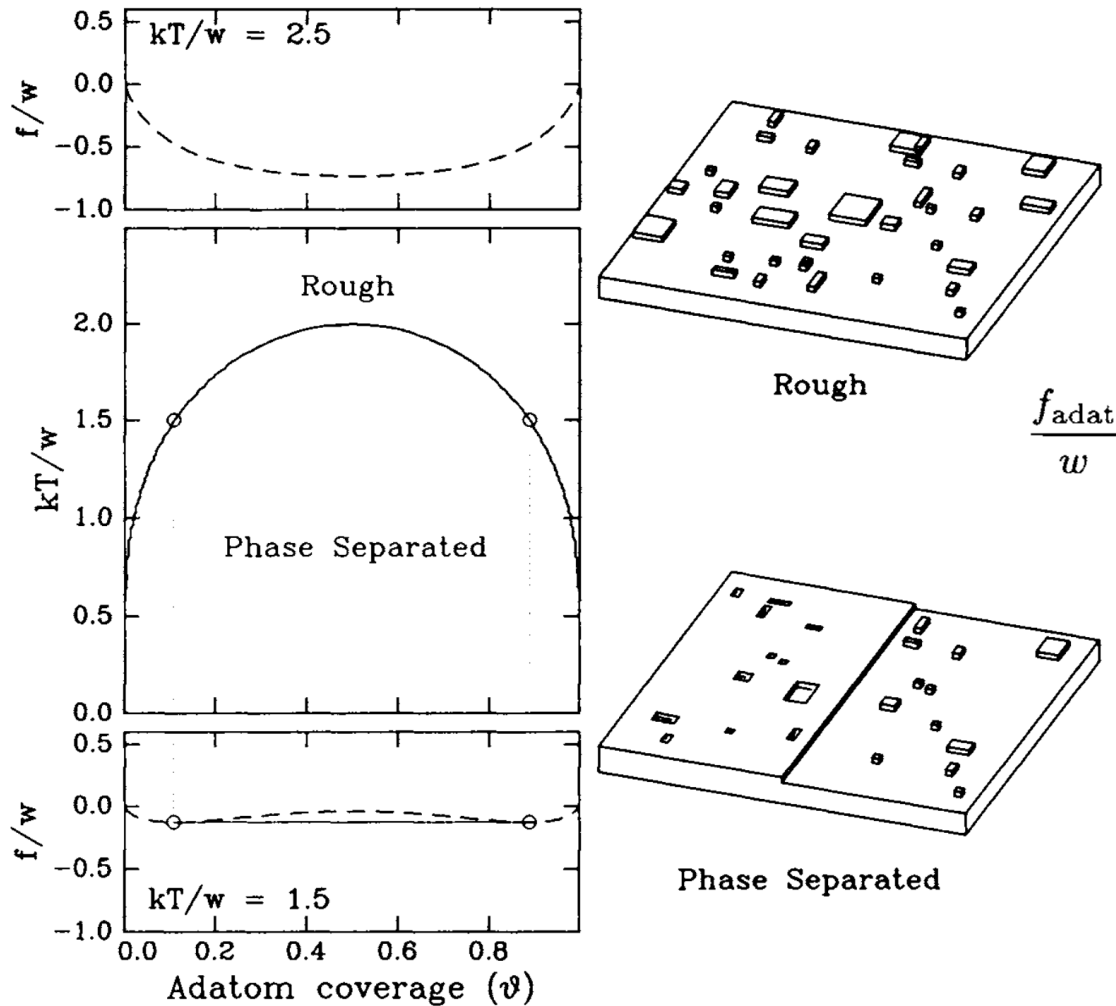


Figure 6.2: x - T phase diagrams for surface roughening. Above and below each phase diagram are also shown the normalized molar free energies of the adlayer phases at $kT/w = 2.5$ and $kT/w = 1.5$, their common tangents, and the critical compositions (open circles) determined by those common tangents.

$$u_{\text{adat}} = 4w\theta(1 - \theta)$$

$$-\frac{s_{\text{adat}}}{k} = \theta \ln \theta + (1 - \theta) \ln(1 - \theta)$$

$$\begin{aligned} \frac{f_{\text{adat}}}{w} &= \frac{u_{\text{adat}} - Ts_{\text{adat}}}{w} \\ &= 4\theta(1 - \theta) + \frac{kT}{w} [\theta \ln \theta + (1 - \theta) \ln(1 - \theta)] \end{aligned}$$

$$[\partial^2 f / \partial \theta^2]_{\theta=0.5} = 0$$

$$T_{r,\text{adat}} = 2w/k$$

$$\Delta h_{\text{sub}} = 3w$$

$$T_{r,\text{adat}} \approx \frac{2}{3} \Delta h_{\text{sub}}$$

(Rockett chp 10,11, Tsao)

Compound Semiconductor Growth

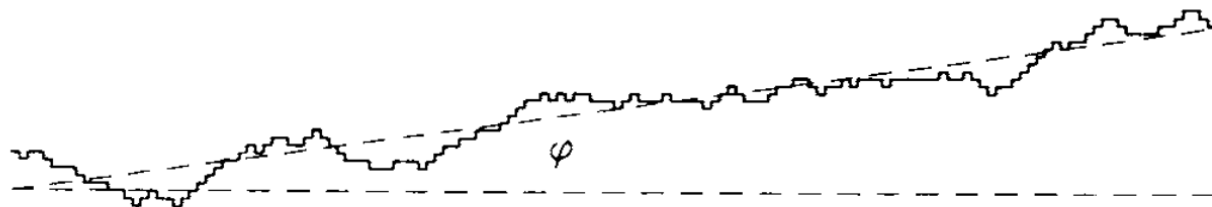


Figure 6.3: A step wandering on the surface of a Kossel crystal due to randomly distributed kinks.

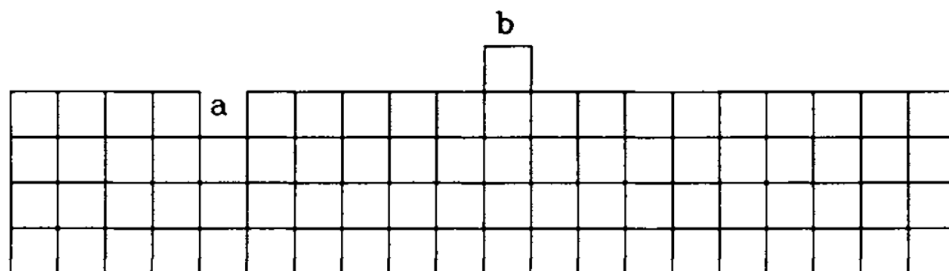


Figure 6.4: In moving an atom from position a to position b, two net bonds are broken, but four kinks are formed. If the bond energy is w , then the energy per kink is $\epsilon_{\text{kink}} = 2w/4 = w/2$.

$$\begin{aligned}
 f_{\text{step}} = & \epsilon_{\text{step}} + \epsilon_{\text{kink}}(p_+ + p_-) \\
 & + kT[(p_{\text{ext}} + p_{\text{int}}/2) \ln(p_{\text{ext}} + p_{\text{int}}/2) + (p_{\text{int}}/2) \ln(p_{\text{int}}/2) \\
 & + (1 - p_{\text{ext}} - p_{\text{int}}) \ln(1 - p_{\text{ext}} - p_{\text{int}})]. \quad (6.9)
 \end{aligned}$$

(Rockett chp 10,11, Tsao)

Compound Semiconductor Growth

$$f_{\text{step}} = \epsilon_{\text{step}} + \epsilon_{\text{kink}}(p_+ + p_-) + kT[(p_{\text{ext}} + p_{\text{int}}/2) \ln(p_{\text{ext}} + p_{\text{int}}/2) + (p_{\text{int}}/2) \ln(p_{\text{int}}/2) + (1 - p_{\text{ext}} - p_{\text{int}}) \ln(1 - p_{\text{ext}} - p_{\text{int}})].$$

$$\frac{\partial f_{\text{step}}}{\partial p_{\text{int}}} = \epsilon_{\text{kink}} + kT[(1/2) \ln(p_{\text{ext}} + p_{\text{int}}/2) + (1/2) \ln(p_{\text{int}}/2) - (1/2) \ln(1 - p_{\text{ext}} - p_{\text{int}})] = 0.$$

$$p_+ p_- = p_o^2 e^{-2\epsilon_{\text{kink}}/kT}$$

$$p_o^{\text{equ}} = \frac{1 - \sqrt{1 - (1 - 4e^{-2\epsilon_{\text{kink}}/kT})(1 - \tan^2 \phi)}}{1 - 4e^{-\epsilon_{\text{kink}}/kT}}$$

$$p_+^{\text{equ}} = \frac{\tan \phi}{2} + \sqrt{p_o^2 e^{-2\epsilon_{\text{kink}}/kT} + \frac{1}{4} \tan^2 \phi}$$

$$p_-^{\text{equ}} = -\frac{\tan \phi}{2} + \sqrt{p_o^2 e^{-2\epsilon_{\text{kink}}/kT} + \frac{1}{4} \tan^2 \phi}.$$

$$\begin{aligned} u_{\text{step}} &= \epsilon_{\text{step}} + 2\epsilon_{\text{kink}}p_- \\ -\frac{s_{\text{step}}}{k} &= 2p_- \ln p_- + (1 - 2p_-) \ln(1 - 2p_-) \\ f_{\text{step}} &= u_{\text{step}} - Ts_{\text{step}}. \end{aligned}$$

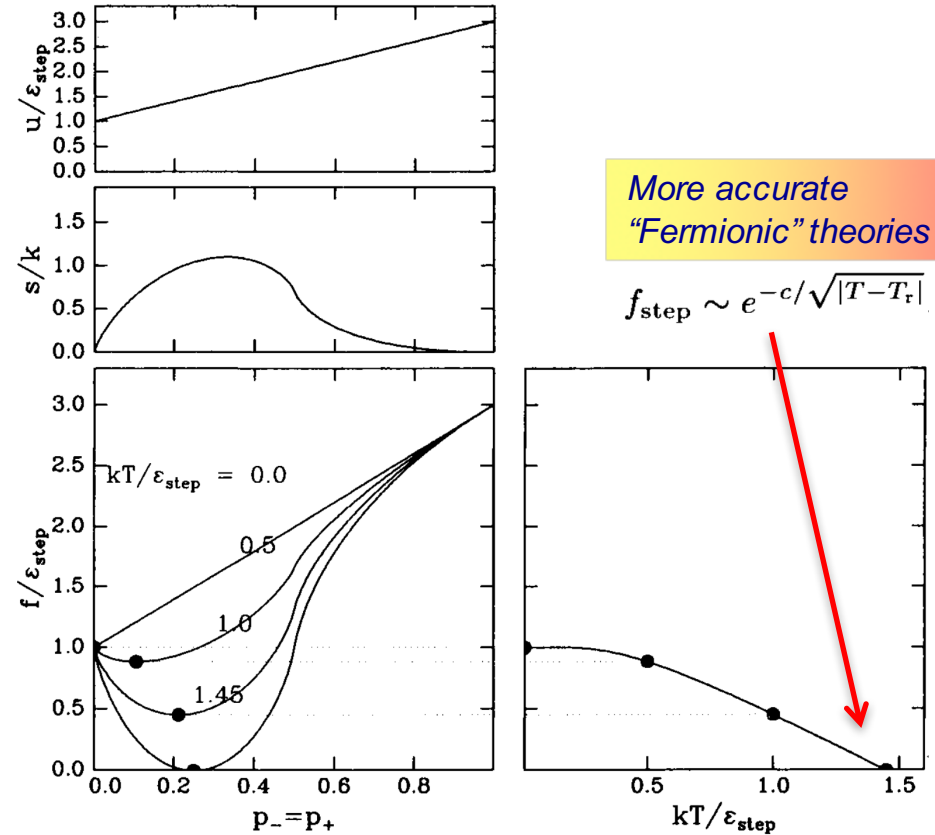


Figure 6.6: Dependences of the energy, entropy, and free energy of a step on the probability of intrinsic kinks. The step is assumed to have no extrinsic kinks, and a kink is assumed to add an additional energy equal to half the energy of a straight step. The energies and free energies are normalized to the energy of a straight step. As the temperature increases, the intrinsic kink probability that minimizes the free energy of the step increases, and the minimum free energy decreases.

(Rockett chp 10,11, Tsao)

Growth Physics: Connection to Ising Models

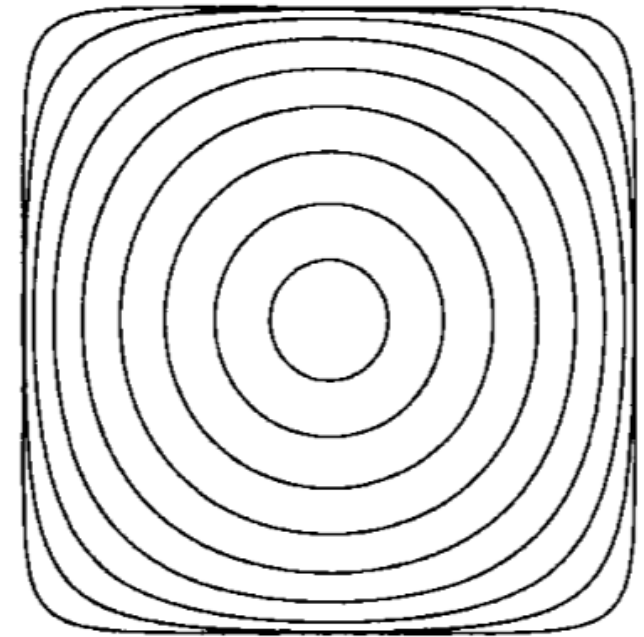
Exercise: In a lattice gas model for crystal growth, a density variable n_i at a lattice site i takes a value 1 when the site is occupied by an atom, or it is 0 when the site is empty. If a broken chemical bond from a crystal atom costs an energy J , the interaction energy is expressed as

$$\mathcal{H} = J \sum_{\langle ij \rangle} [n_i(1 - n_j) + (1 - n_i)n_j] - \Delta\mu \sum_i n_i, \quad (8.1)$$

where $\langle ij \rangle$ means the summation over the nearest neighbor sites pairs, and $\Delta\mu$ is the chemical potential gain by crystallization. Show that the Hamiltonian (8.1) can be transformed to the two-dimensional Ising Hamiltonian

$$\mathcal{H}_I = -\frac{J}{2} \sum_{\langle ij \rangle} S_i S_j - H \sum_i S_i. \quad (8.2)$$

Here an Ising spin variable $S_i = 2n_i - 1$ takes values $+1$ or -1 , and the field is $H = \Delta\mu/2$ [128].



$$\frac{\beta(\theta)}{k_B T} = |\cos \theta| \sinh^{-1}(\alpha |\cos \theta|) + |\sin \theta| \sinh^{-1}(\alpha |\sin \theta|)$$

$$\alpha = \frac{2}{b} \left(\frac{1 - b^2}{1 + \sqrt{\sin^2 2\theta + b^2 \cos^2 2\theta}} \right)^{1/2}$$

$$b = \frac{2 \sinh(J/k_B T)}{\cosh^2(J/k_B T)}$$

$$\mathcal{H} = -\frac{J}{2} \sum_{\langle ij \rangle} S_i S_j + \frac{NzJ}{4}$$

$$\frac{k_B T_c}{J} = \frac{1}{\ln(\sqrt{2} + 1)} = 1.1346 \dots$$

(Saito, *Stat. Phys. of Crystal Growth*)

Compound Semiconductor Growth

$$f_{\text{surf}} = f_{\text{terr}} + f_{\text{step}} \tan \theta,$$

$$b^2 \equiv p_+ a^2 + p_- a^2$$

$$\frac{\Delta s_{\text{step}}}{k} = \frac{\pi^2 b^2 / 2}{6 l^2} = \frac{\pi^2 b^2}{12 a^2} \tan^2 \phi$$

$$f_{\text{surf}} = f_{\text{terr}} + f_{\text{step}} \tan \phi + kT \frac{\pi^2 b^2}{12 a^2} \tan^3 \phi$$

$$\Delta u_{\text{step}} = A \left[\frac{1}{(l+x)^2} + \frac{1}{(l-x)^2} \right] \approx \frac{2A}{l^2} (1 + x^2/l^2)$$

$$\frac{d(\Delta u_{\text{step}} - T \Delta s_{\text{step}})}{dx} = \frac{d}{dx} \left[\frac{2A}{l^2} \left(1 + \frac{x^2}{l^2} \right) + kT \frac{\pi^2 b^2}{12 x^2} \right] = 0$$

$$d = \left(\frac{\pi^2 kT b^2}{24 A} \right)^{1/4} l.$$

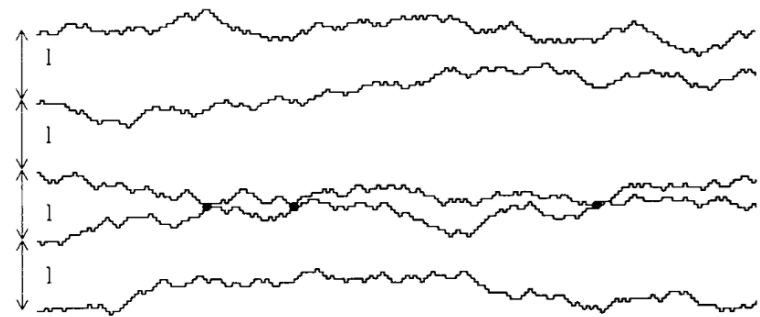


Figure 6.7: Five wandering steps of average spacing l . Two of the steps intersect, by chance, three times.

(Rockett chp 10,11, Tsao)

Compound Semiconductor Growth

$$f_{\text{surf}} = f_{\text{terr}} + f_{\text{step}} \tan \theta,$$

$$b^2 \equiv p_+ a^2 + p_- a^2$$

$$\frac{\Delta s_{\text{step}}}{k} = \frac{\pi^2 b^2 / 2}{6 l^2} = \frac{\pi^2 b^2}{12 a^2} \tan^2 \phi$$

$$f_{\text{surf}} = f_{\text{terr}} + f_{\text{step}} \tan \phi + kT \frac{\pi^2 b^2}{12 a^2} \tan^3 \phi$$

$$\Delta u_{\text{step}} = A \left[\frac{1}{(l+x)^2} + \frac{1}{(l-x)^2} \right] \approx \frac{2A}{l^2} (1 + x^2/l^2)$$

$$\frac{d(\Delta u_{\text{step}} - T \Delta s_{\text{step}})}{dx} = \frac{d}{dx} \left[\frac{2A}{l^2} \left(1 + \frac{x^2}{l^2} \right) + kT \frac{\pi^2 b^2}{12 x^2} \right] = 0$$

$$d = \left(\frac{\pi^2 kT b^2}{24 A} \right)^{1/4} l,$$

$$\Delta f_{\text{step}} = \frac{2A}{l^2} \left(1 + \sqrt{\frac{\pi^2 kT b^2}{6A}} \right)$$

$$f_{\text{surf}} = f_{\text{terr}} + (f_{\text{step}} + \Delta f_{\text{step}}) \tan \theta$$

$$= f_{\text{terr}} + f_{\text{step}} \tan \theta + \frac{2A}{a^2} \left(1 + \sqrt{\frac{\pi^2 kT b^2}{6A}} \right) \tan^3 \theta.$$

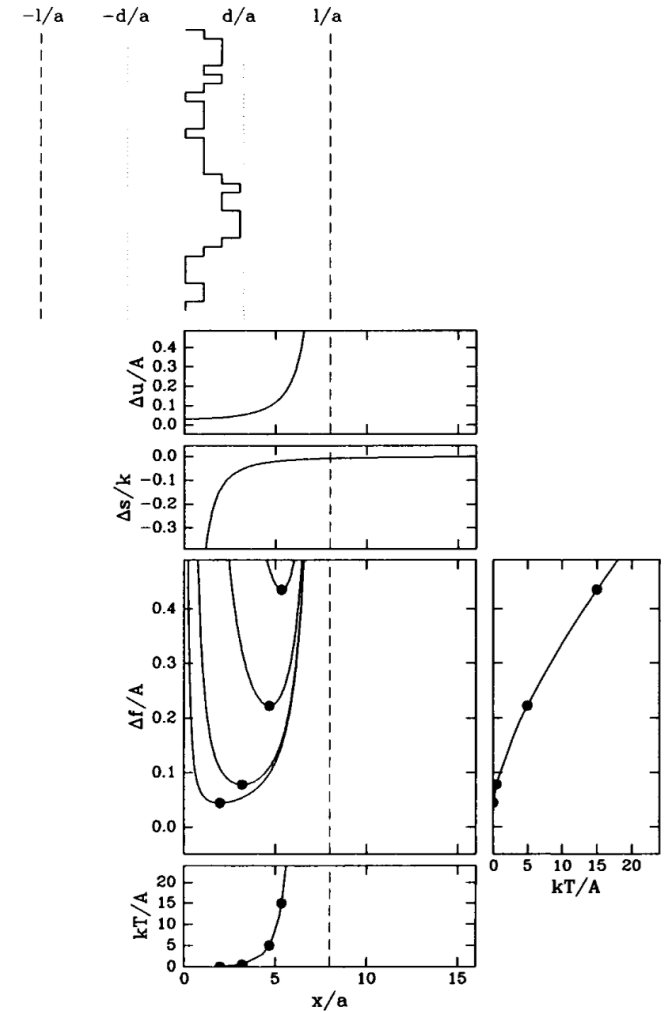


Figure 6.8: Changes in energy, entropy, and free energy as the width of the alley (x/a , in units of lattice constants) within which a step is allowed to wander increases. Both the energy and entropy increase as the width of the alley increases and approaches the mean step spacing (l/a , in units of lattice constants). The equilibrium alley width (d/a , in units of lattice constants) is that which minimizes the free energy. As the ratio between the temperature and the strength of the interaction between steps (kT/A) increases, both the equilibrium alley width and the free energy at that equilibrium alley width increase.

Compound Semiconductor Growth

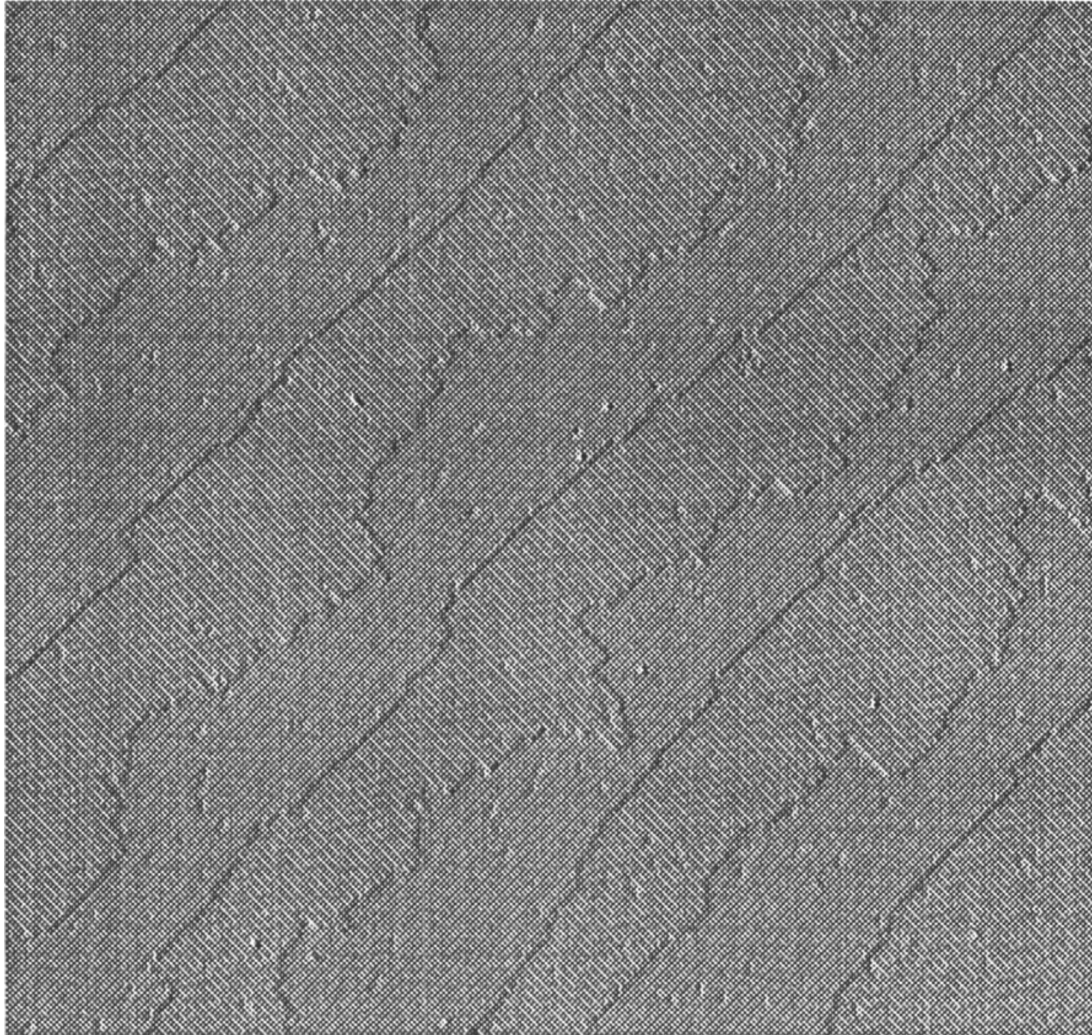
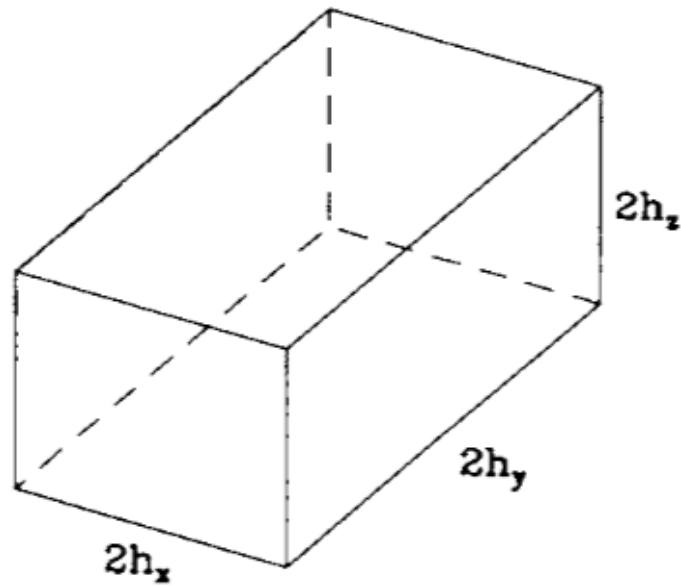


Figure 6.5: Scanning tunneling micrograph of a Si surface misoriented 0.5° from (001) toward [110]. The surface height decreases from upper left to lower right.^a On this surface, alternate single-height steps are referred to as type *SA* and *SB*, and are smooth and rough, respectively, reflecting the relative energies of kink formation.

(Rockett chp 10,11, Tsao)

Compound Semiconductor Growth



$$E = 2\gamma_x h_y h_z + 2\gamma_y h_x h_z + 2\gamma_z h_x h_y$$

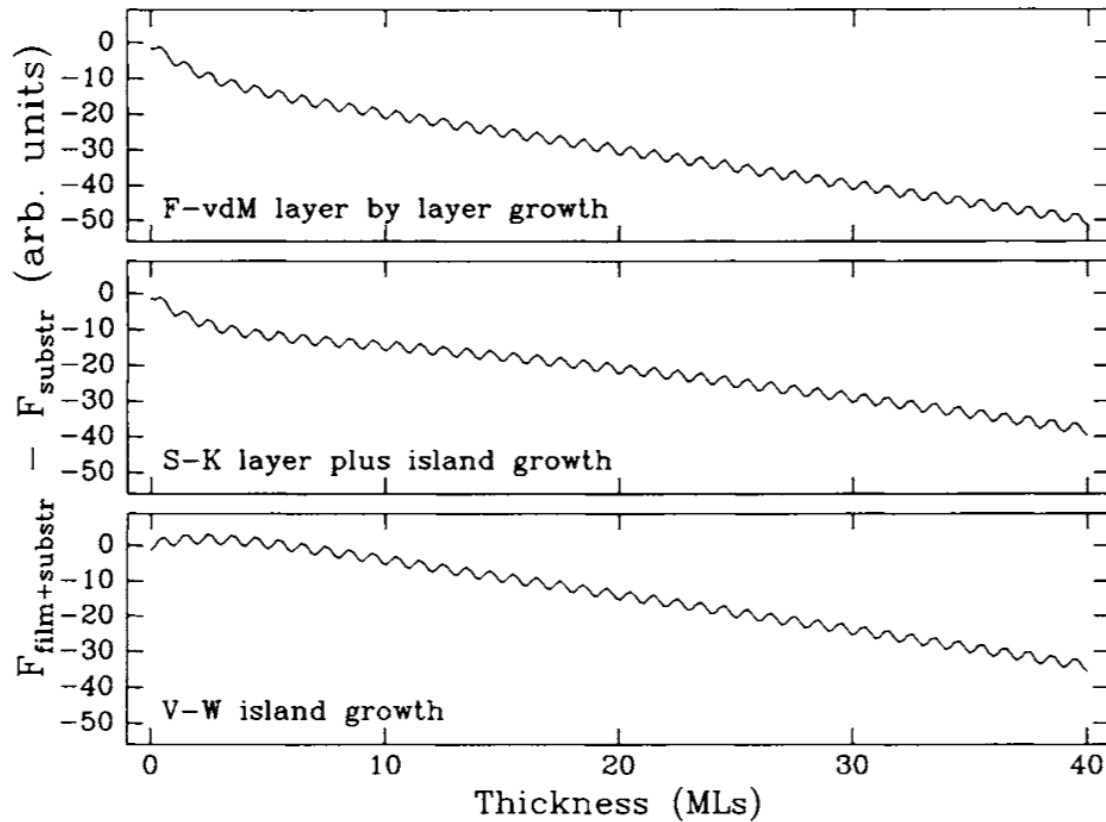
$$E = \frac{\gamma_x V}{4h_x} + \frac{\gamma_y V}{4h_y} + 2\gamma_z h_x h_y.$$

$$\gamma_x h_y h_z = \gamma_y h_x h_z = \gamma_z h_x h_y = (\gamma_x \gamma_y \gamma_z)^{1/3} V^{2/3} = \text{constant}$$

$$\frac{\gamma_x}{h_x} = \frac{\gamma_y}{h_y} = \frac{\gamma_z}{h_z} = \left(\frac{\gamma_x \gamma_y \gamma_z}{V} \right)^{1/3}$$

(Rockett chp 10,11, Tsao)

Compound Semiconductor Growth

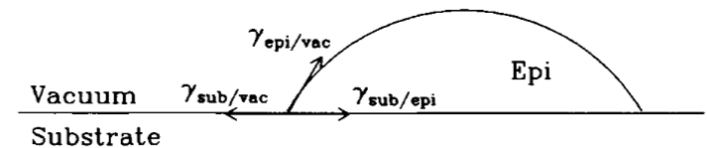
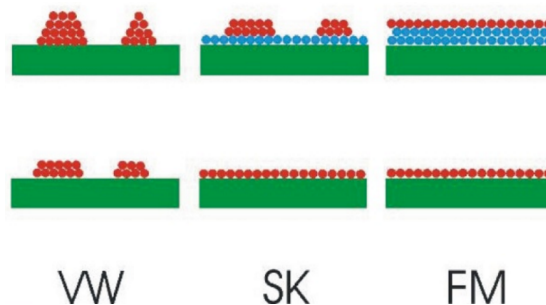


$$\gamma_{e/v} + \gamma_{s/e} < \gamma_{s/v}$$

$$\gamma_{e/v} + \gamma_{s/e} > \gamma_{s/v}$$

$$\gamma_{e/v} + \gamma_{s/e} > \gamma_{s/v}$$

Figure 6.20: Thickness dependences of total free energies for the three classical heteroepitaxial growth modes.



(Rockett chp 10,11, Tsao)